The Role of Composition on the Ammonia Synthesis Activity of Nitrides, Carbonitrides, Carbides and Osmium Based Compounds

Angela Daisley

Submitted in fulfilment of the requirements for the Degree of Doctor of Philosophy

School of Chemistry
College of Science and Engineering
University of Glasgow

July 2020

Abstract

The industrial route for producing ammonia is via the Haber-Bosch Process and requires high temperatures and pressures. When considered in its entirety, including the production of the necessary feedstreams, the process is stated to account for 2% of the world's energy demand and 1.6% of global anthropogenic CO_2 emissions. If a more active ammonia synthesis catalyst was developed, it may prove possible to operate under more moderate conditions, facilitating localised and sustainable production. One potential approach to the development of catalysts with enhanced activity by-passing the limiting scaling relationship invoked for metal catalysts is ammonia production via the Mars-van Krevelen mechanism, as possibly exhibited by some metal nitrides, such as Co_3Mo_3N.

The role composition and crystal structure type have on the ammonia synthesis activity of mixed metal nitrides, carbonitrides and carbides was investigated within this thesis. Fe_3Mo_3C, Ni_6Mo_6C, Ni_3Mo_3C and $Ni_2Mo_3C_xN_y$ have been tested for their ammonia synthesis capabilities, to discover if the presence of lattice nitrogen was required. Fe_3Mo_3C was found to be inactive for ammonia synthesis at 400°C. However, when the temperature was increased to 500°C, the material became active, which may be related to the substitution of lattice carbon with nitrogen. Ni_6Mo_6C and Ni_3Mo_3C were inactive for ammonia synthesis at 400°C and 500°C, respectively. When Ni_6Mo_6C and Ni_3Mo_3C were investigated at 700°C, an induction period occurred before the two materials developed activity for ammonia synthesis; during this period, nitridation of the lattice occurred eventually leading to the formation of Ni_2Mo_3N. Ni_2Mo_3C could not be synthesised via a topotactic route from Ni_2Mo_3N and the carbonitride phase which was formed was active for ammonia synthesis at 400°C.

The lattice nitrogen in the filled β-Mn structured Ni_2Mo_3N and η-carbide structured Ni_2GaMo_3N was observed to exhibit different behaviour to that in the filled β-Mn structured Co_2Mo_3N and η-carbide structured Co_3Mo_3N and Fe_3Mo_3N. For Ni_2Mo_3N and Ni_2GaMo_3N, the bulk lattice nitrogen appeared to be relatively unreactive at 900°C, whereas Co_2Mo_3N, Co_3Mo_3N and Fe_3Mo_3N decomposed under these conditions. This suggests that both composition and crystal structure type may have an impact on the lattice nitrogen reactivity.

The potential structure sensitivity of osmium for ammonia synthesis was examined and it was found that the metal was more active when it was more highly dispersed. Supported mixed metal carbonyl clusters were also tested and were observed to have different activities to the supported monometallic equivalents.

Table of Contents

List of Figures

List of Tables

List of Equations

Acknowledgements

First and foremostly, I would like to thank my supervisor Prof. Justin Hargreaves for giving me this opportunity and for his assistance throughout. Without his support and help, I do not think I would have reached this stage.

I would also like to thank the technical staff at University of Glasgow, with special mention to Jim Gallagher for his help with the SEM and EDX, Andy Monaghan for his help with Raman and TGA measurements, along with his interesting stories, and Gangi Reddy Ubbara for running the elemental analysis.

Furthermore, I would like to thank Prof. Jean-Francois Lamonier for the opportunity to perform ToF-SIMS measurements at UCCS, Alessandro Faccinetto and especially Nicolas Nuns for their assistance with the acquisition and analysis of the ToF-SIMS data.

Thanks also to the students I have collaborated with over the last four years for making the experience fun, with special mention to Nicholas Stephen, Shane McKenna and Lucy Costley-Wood for the enjoyable lab experiences.

A special mention must also go to Yalinu Poya for her friendship, support and help over the last four years. The PhD experience would not have been as enjoyable without you and I really appreciate the time we spent together. I would also like to thank the members of the Hargreaves, Jackson, Gibson and Lennon groups. Kathleen you are amazing and an inspiration, Kate for her assistance and positivity at the start of the project, Caitlin for making the lab a fun place, Mustapha for the friendship, Nicola and Adam for the enjoyable time and Said for his help with my many questions. Yoshi it was great getting to know you, thank you for your support and I will always remember our time in Aachen.

In addition, I would like to thank my friends for their support, especially David for his encouragement, interesting conversations and for inspiring me.

Finally, many thanks go to my family for their support over the years, helping me out when needed and Sparkle for her company.

Author's Declaration

I declare that this thesis is the result of my own work, except where reference is made to the contribution of others. This work has not been submitted for any other degree at the University of Glasgow or any other institution.

Publications

- Kirste, K.; McAulay, K.; Bell, T. E.; Stoian, D.; Laassiri, S.; Daisley, A.; Hargreaves, J. S. J.; Mathisen, K.; Torrente-Murciano, L., CO_x-Free Hydrogen Production from Ammonia – Mimicking the Activity of Ru Catalysts with Unsupported Co-Re Alloys, *Applied Catalysis B: Environmental*, **2021**, 280, 119405.
- Goto, Y.; Daisley, A.; Hargreaves, J. S. J., Towards Anti-Perovskite Nitrides as Potential Nitrogen Materials for Chemical Looping Ammonia Production: Reduction of Co_3ZnN, Ni_3ZnN, Co_3InN, Ni_3InN under Hydrogen, *Catalysis Today*, **2020**, In Press, (doi: 10.1016/j.cattod.2020.03.022).
- Daisley, A.; Hargreaves, J. S. J.; Hermann, R.; Poya, Y.; Wang, Y., A Comparison of the Activities of Various Supported Catalysts for Ammonia Synthesis, *Catalysis Today*, **2020**, In Press, (doi: 10.1016/j.cattod.2019.06.009).
- Daisley, A.; Hargreaves, J. S. J., The Role of Interstitial Species upon the Ammonia Synthesis Activity of Ternary Fe-Mo-C(N) and Ni-Mo-C(N) Phases, *Journal of Energy Chemistry*, **2019**, 39, 170 – 175.
- AlShibane, I.; Daisley, A.; Hargreaves, J. S. J.; Hector, A. L.; Laassiri, S.; Rico, J. L.; Smith, R. I., The Role of Composition for Cobalt Molybdenum Carbide in Ammonia Synthesis, *ACS Sustainable Chem. Eng.*, **2017**, 5, 9214 – 9222.

Definitions/Abbreviations

Abbreviation	Definition
SEM	Scanning Electron Microscopy
EDX	Energy Dispersive X-ray Spectroscopy
BET Surface Area	Brunauer-Emmett-Teller Surface Area
PXRD	Powder X-ray Diffraction
CHN	Carbon, Hydrogen, Nitrogen
TGA	Thermogravimetric Analysis
TPO	Temperature Programmed Oxidation
IR	Infrared Spectroscopy
ToF SIMS	Time of Flight Secondary Ion Mass Spectroscopy
TPR	Temperature Programmed Reduction
JCPDS	Joint Committee on Powder Diffraction Standards
a.u.	Arbitrary units
TOF	Turnover Frequency

1. Introduction

1.1 Fixation of N_2 in Nature

Nitrogen is essential to sustain the life of animals and plants. Many biomolecules, including nucleotides and amino acids, contain nitrogen and are necessary for producing the proteins in muscle and the skin [1]. Nitrogen is widely available, with almost 80% being present in air [1]. However, due to the strong nitrogen triple bond making N_2 relatively inert, plants and many life forms cannot uptake nitrogen in this form. Instead, plants obtain nitrogen when N_2 is converted into ammonia or nitrate [2]. In nature, nitrogen fixation can occur by two methods. The first is the transformation of N_2, oxygen and water to nitrate by lightening [3]. The second is by the enzyme, nitrogenase, found in a small number of prokaryotes [2]. Nitrogenase forms ammonia at ambient temperature and pressure according to the following equation:

$$N_2 + 8e^- + 8H^+ + 16\ ATP \rightarrow 2NH_3 + H_2 + 16\ ADP + 16P_i$$

Equation 1: Formation of ammonia by nitrogenase [2]

Nitrogenase contains two main proteins, the iron protein and the molybdenum-iron protein [2] [4]. There also exist nitrogenases with vanadium or iron in place of molybdenum [5]. The structure of the Mo containing nitrogenase is presented in Figure 1. Three clusters exist within this structure, the F, P and M clusters. The F cluster consists of the iron protein and is responsible for hydrolysis of adenosine triphosphate (ATP) to adenosine diphosphate (ADP) [4]. The electrons formed by this process are transferred to the FeMo cofactor (M cluster) through the P cluster [2]. The M cluster is the active site for binding of the nitrogen and reduces H^+ and N_2 to H_2 and NH_3 [2].

It was originally thought that the M cluster contained an interstitial nitrogen atom that could be exchanged during dinitrogen reduction [6]. However, later studies revealed that the atom was not exchangeable [7] and was instead carbon [2] [8]. The active site for this process is Fe_7MoS_9C [2]. It has been proposed that the formation of ammonia by nitrogenase occurs through an associative mechanism in which protonation of N_2 occurs prior to its dissociation [2] [9]. Through nitrogenase catalysed nitrogen fixation, 110 Tg of nitrogen is fixed per year on land and 140 Tg of nitrogen per year in the ocean [10].

However, not enough nitrogen is fixed by the enzyme to sustain the current human population. The biological process contributes 50% of the fixed nitrogen required for current agricultural production [2] [10]. When nitrogen levels are low in the soil, plant growth becomes limited and food production is low. This problem can be solved by adding

fixed nitrogen to the soil in the form of fertiliser. Therefore, it was necessary that an industrial process was developed to produce the synthetic fertiliser and support the growing population.

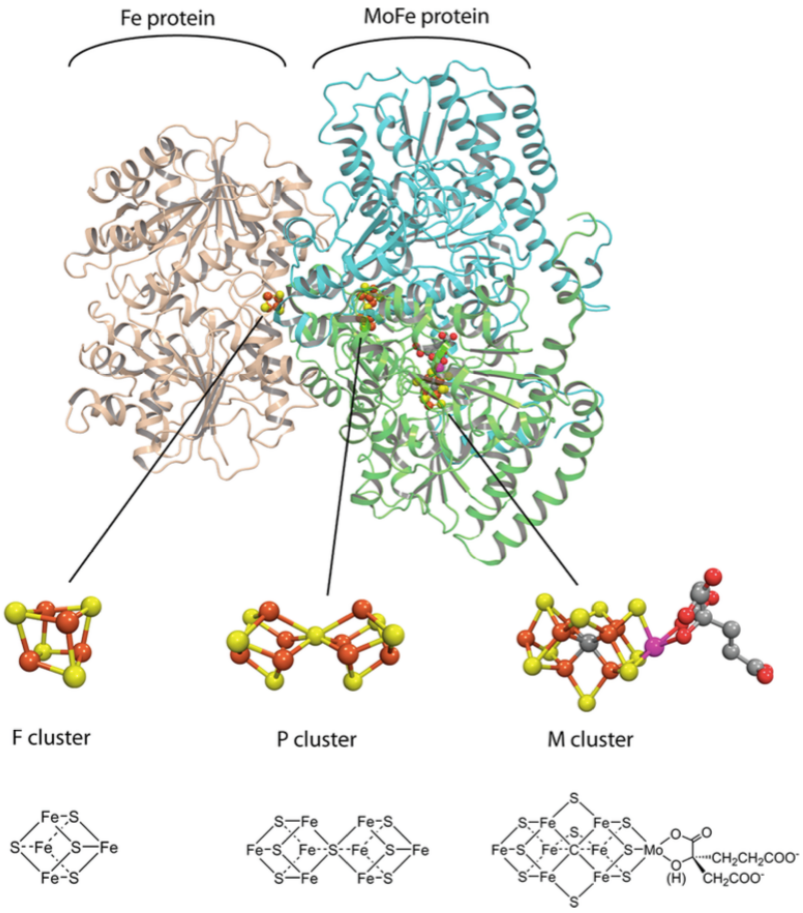

Figure 1: Structure of Mo nitrogenase. [2]

1.2 Industrial Processes for Producing Ammonia

1.2.1 Haber-Bosch Process

The development of the Haber-Bosch Process was one of the most important achievements of the twentieth century. It allowed the production of ammonia from the direct combination of nitrogen with hydrogen. This reaction is possible by the use of an iron catalyst doubly promoted with Al_2O_3 and K_2O. The reaction takes place at a moderate temperature of between 400-500^oC and high pressures of approximately 200 atmospheres [11] [12]. The reaction is as follows:

$$N_2 + 3H_2 \leftrightarrow 2NH_3 \ (\Delta H^0 = -92 \text{ kJ/mol})$$

Equation 2: Reaction of nitrogen and hydrogen to produce ammonia

As the reaction is exothermic and equilibrium limited, thermodynamically it is favoured at low reaction temperatures. However, higher temperatures are used industrially to achieve satisfactory reaction kinetics. As suggested in a patent by Haber and Rossignol, the

ammonia in the gas leaving the reactor is removed by cooling it to a liquid state [13]. The unreacted nitrogen and hydrogen are then recycled to increase the percentage conversion to ammonia from 15% to an overall conversion of 97% on subsequent passes [14].

Mittasch and co-workers studied a wide range of metals for the process, including iron, molybdenum, osmium, uranium and nickel [15]. Iron metal was found to initially have a good activity for ammonia synthesis but was observed to deactivate quickly [16]. Therefore, iron was originally removed from contention as the catalyst for the process. However, Mittasch discovered that mixing the iron oxide (Fe_3O_4) precursor with metal oxides, such as Al_2O_3 and K_2O enhanced the activity and stability of the resultant iron based catalyst [16]. The alumina acts as a structural promoter and prevents the sintering of α-iron, which is formed after reduction of the iron oxide [17]. Potassium increases the activity of the catalyst by donating electron charge to the iron, resulting in a weakening of the N_2 bond upon adsorption [18]. The reduced iron catalyst has a network of pores with diameters of 25 – 50 nm [19].

The process facilitated the formation of ammonia on an industrial scale. Ammonia has many uses but the most significant, is as a synthetic fertiliser and ammonia is also gaining interest as a potential fuel. The fertiliser formed from ammonia is necessary for sustaining crops and for providing food for a large fraction of the world's population. Almost 130 million tonnes of ammonia was produced in the year 1999 [20], with more than 80% of this being converted to fertilizers. However, there are some disadvantages to this process. The production of ammonia from the Haber-Bosch Process requires 1 – 2% of the world's manmade energy demand when the process is considered in its entirety including feed gas generation [11] [21]. Furthermore, the hydrogen feedstream obtained from natural gas, results in 2.2 tonnes of CO_2 being generated per tonne of ammonia being produced [22]. When coal is used as the source of hydrogen, 16.7 tonnes of CO_2 per tonne of ammonia is formed [22]. This results in ammonia production accounting for 1.6% of global manmade CO_2 emissions [21].

If a more active catalyst than the one used in the Haber-Bosch Process was developed, it may prove possible to operate under more moderate conditions, facilitating localised and sustainable production where the H_2 feedstream is derived from renewable hydrogen generated via electrolysis from electricity sources derived from wind, solar or tidal power. The reduction in temperature would allow the possible increase in percentage per-pass yield due to more favourable equilibrium conditions. This would require the discovery of a

new catalyst. However, it is important to consider that iron, as is currently used on the large scale, is inexpensive and abundant, although it is highly susceptible to poisoning. Any new catalyst must be highly active and, ideally, be less susceptible to poisoning.

1.2.2 Kellogg Advanced Ammonia Process (KAAP)

One alternative process that has been developed is the Kellogg Advanced Ammonia Process, which uses a promoted ruthenium on graphite catalyst [23]. The catalyst is stated to be 10 – 20 times more active than the iron-based one used in the Haber-Bosch Process. This high activity of the ruthenium catalyst has been explained in relation to its nitrogen binding energy [24]. Ruthenium was shown to have close to optimal adsorption energy for nitrogen chemisorption, resulting in high ammonia turnover frequencies.

Aika and Ozaki focused on studying ruthenium based catalysts for ammonia synthesis [25] [26] [27]. They showed that promoting the ruthenium with both Cs^+ and Ba^{2+} resulted in a highly active catalyst [28]. It is proposed that the promoters transfer charge to the ruthenium, acting similarly to the potassium component in the Haber Bosch catalyst in enhancing N_2 activation. The choice of support was also shown to affect the rate, with carbon and alumina supported ruthenium having the highest activity [27]. The authors suggested that the support acts as a medium for the electron transfer. Due to the interest generated by Aika and Ozaki in ruthenium catalysts, BP developed a doubly promoted ruthenium catalyst supported on methanation resistant high surface area graphitised carbon (Ru/Cs/Ba/HSAG) for ammonia synthesis [29].

The Ru/Cs/Ba/HSAG catalyst contains an 8 wt.% loading of ruthenium and high loadings of the two promoters [29]. The HSAG is formed by a three stage heat treatment up to approximately 2000^{o}C. The resultant material has a mesoporous structure that stabilises the ruthenium particles and is resistant to methanation at high pressures of hydrogen [29].

As the Ru/Cs/Ba/HSAG catalyst is more active than the Haber Bosch catalyst, the KAAP can be operated at lower pressures, which results in a lower operational cost [30]. The process can also retain a high activity at lower temperatures and higher ammonia concentrations than the Haber Bosch Process. The catalyst can operate with a range of hydrogen to nitrogen feedstream ratios. The Haber-Bosch Process operates with 3:1 H_2/N_2, whereas for the ruthenium based catalyst, the optimum ratio is lower than stoichiometric [30]. This is due to ruthenium being strongly inhibited by hydrogen and thus, the catalyst has a higher activity when higher nitrogen pressures are used [31]. The first KAAP plant was in operation by 1992 as part of the Ocelet project [29] and by 2004, there were 7

plants in operation [32]. However, there is further interest in producing a highly active catalyst operative under even less severe conditions which are more applicable to localised sustainable ammonia synthesis.

1.3 Metal Nitrides

Another alternative being considered is the use of binary and ternary nitrides as catalysts for ammonia synthesis. Mittasch discovered that molybdenum nitride and uranium nitride were particularly active for ammonia synthesis [15] [16]. Uranium nitride was one of the early contenders for the Haber Bosch Process before the iron catalyst was discovered [33]. The uranium could be promoted with certain metals to provide an ammonia yield of between 1% and 2.5% at 550^{o}C and 100 atmospheres pressure [15]. However, the uranium catalyst was expensive and, therefore, it was necessary to find an alternative that was as effective and more commercially acceptable [15].

During the search for a catalyst for the Haber Bosch Process, Mittasch observed that molybdenum formed a nitride under the ammonia synthesis conditions [15] [16]. The molybdenum had an advantage over pure iron as it was less easily poisoned. Mittasch also stated that molybdenum was the most efficient of the easily obtainable materials [15]. As the molybdenum was transformed into the nitride, the activity increased and therefore, it was proposed that the nitride was the active form of the catalyst [16]. Molybdenum nitride was observed to have an ammonia synthesis yield of 1.5% at 550^{o}C and 100 atmospheres pressure [15]. The activity of the material could be increased by combining molybdenum with cobalt, nickel or iron and promoting molybdenum with alkali metals. However, oxides of the alkali metals were observed to have a negative impact. The promoted molybdenum material had an ammonia yield of up to 4% at 550^{o}C and 100 atmospheres pressure [15].

Kojima and Aika also studied molybdenum nitride (γ-Mo_2N) for ammonia synthesis and obtained a rate of 48 μmol h^{-1} g^{-1} at 400^{o}C and atmospheric pressure [34]. Generally, ternary molybdenum nitrides, such as Co_3Mo_3N, Ni_2Mo_3N and Fe_3Mo_3N, are reported to be more active [35] [36]. This supports the observations made by Mittasch that alloying the molybdenum with one of these metals increases the activity. It has been shown that the Co_3Mo_3N has high activity for ammonia synthesis and even exceeds the activity of the iron based industrial catalyst, particularly when doped with Cs^+ [37].

Materials that have recently been developed which show promise with respect to the commercially applied promoted iron and ruthenium based systems are $CoRe_4$ and Cs^+ on

Co_3Mo_3N. $CoRe_4$ has an extremely high activity of 943 ± 44 μmol h^{-1} g^{-1} at 400°C and ambient pressure [38]. However, the high cost of rhenium is a disadvantage to using this material. A disadvantage to the Cs^+ on Co_3Mo_3N is that phase instability can occur [39]. Therefore, any material that is prepared has to be highly active, stable and reasonably cost effective, as well as being suitable for application under transient operation and in addition less harsh reaction conditions than the Haber Bosch Process.

1.4 Sustainability for Ammonia Synthesis

Finding ways to produce ammonia in a sustainable way has grown in importance over the years [11] [22] [40]. One possible solution is to use renewable sources, such as solar, tidal or wind energy, instead of fossil fuels to form the H_2 feedstream via electrolysis of water. Localised production, where the fertiliser is formed near the crop growing fields where it would be applied, would also be desirable. However, for this to occur, a more active catalyst would need to be developed, in order that more moderate conditions suitable for ammonia production on a farm could be utilised.

One proposed method related to catalysis is chemical looping [40] [41]. This process requires multiple steps in order to produce ammonia via the intermediacy of a metal nitride as seen in Figure 2. Either H_2O or H_2 can be used in the looping process. For the H_2O cyclic looping, the first reaction step involves oxidising a metal nitride with water to form ammonia and a metal oxide. Then, the metal oxide is reacted with a reducing agent, such as carbon, and then N_2 to generate the recycled metal nitride [41] [42]. In order to remove the oxygen from the metal oxide to produce the metal nitride, energy has to be supplied. This energy could be supplied from solar power using parabolic mirror devices to attain the high temperatures necessary to make this process sustainable. Another advantage of this process is that it can be applied at ambient pressure [40]. However, the need for reducing agents containing carbon and the formation of carbon monoxide are drawbacks to this process. The regeneration of the metal nitride from the metal oxide can occur by thermal treatment but requires high temperatures (above 1200°C) [41] [43].

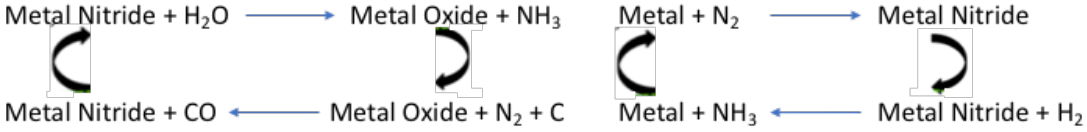

Figure 2: Chemical looping processes to produce ammonia

One potential cycle for this process involves AlN/Al_2O_3, where AlN is produced from Al_2O_3 by carbothermal reduction under N_2 and is subsequently, hydrolysed to form

ammonia and Al_2O_3 [44]. The procedure was performed at ambient pressure and the energy required for the reduction step was provided by thermal radiation [45]. Michalsky and Pfromm studied a range of metals for this process and observed that Mg_3N_2 had a rate of $1.1 \pm 0.2 \times 10^{-3}$ mol_{NH3} mol_{metal}^{-1} s^{-1} at 500°C, with 69.9 mol. % of lattice nitrogen converted to ammonia [12]. However, Mg_3N_2 generates a large amount of heat during the hydrolysis stage. The authors suggested that Mo_2N was a more suitable material. Manganese nitrides have also shown promise for this process [42] [43].

For the hydrogen-based cyclic looping to produce ammonia, the first stage is the same as the H_2O cyclic looping, where a metal is nitrided with N_2 to form a metal nitride. However, H_2 is used to reduce the metal nitride to form ammonia and the starting metal [41]. The use of a carbothermal reduction agent would therefore, not be required. The hydrogen applied in this process could be generated from, for example, solar powered electrolysis of water. Michalsky et al examined a range of binary nitrides for this process [46]. The ammonia production rates for Sr_3N_2 and Ca_3N_2 under H_2 at 1 atmosphere and 550°C were stated to be 2.1 ± 0.2 and 1.3 ± 0.4 μmol NH_3 (mol metal x s)$^{-1}$, respectively. The nitrides were observed to transform into SrH_2 and Ca_2NH. The authors concluded that the insertion of hydrogen increased the formation of ammonia from the lattice nitrogen [46]. Other studies have shown that manganese based materials are active for this process, with Li-Mn-N having a high activity at 400°C under 1:3 N_2/H_2 [47].

However, the materials produced so far are somewhat unstable and have unsatisfactory reactivities. Finding a material for this sustainable process is of importance and is the next challenge for the ammonia synthesis process.

As the aim is to reduce the pressure and temperature that the ammonia synthesis process occurs, this would make the materials more environmentally friendly than those currently used in industry.

1.5 Aims

The influence of composition and structure type on the ammonia synthesis activity of ternary and quaternary molybdenum materials and Group 8 metals will be investigated within this thesis. Nitrides (Ni_2Mo_3N, Ni_2GaMo_3N, Co_2Mo_3N and Fe_3Mo_3N) with different metal compositions and either a η-carbide structure or a filled β-manganese structure will be tested for ammonia synthesis activity and lattice nitrogen reactivity. This will be performed in order to study the effect metal composition and crystal structure type may have on the activity. The performance of ternary carbides (Ni_6Mo_6C, Ni_3Mo_3C and

Fe_3Mo_3C) and a carbonitride ($Ni_2Mo_3C_xN_y$) will also be examined and compared with their corresponding nitrides, in order to gain an insight into the effect the interstitial carbon/nitrogen may have on the activity. In Chapter 6, the possible structure sensitivity of osmium for ammonia synthesis will be investigated and compared with the other Group 8 metals and possible structure-activity relationships will be explored. Supported mixed metal clusters will also be prepared and tested for ammonia synthesis activity, in order to try and optimise the activity of the Group 8 cluster materials.

2. Experimental

2.1 Materials Preparation

2.1.1 Preparation of $Ni_2Mo_3C_xN_y$

Nickel molybdenum oxide precursor ($Ni_2Mo_3O_x$) was prepared as described elsewhere by Bion et al. [36], who applied a modified form of the Pechini method. The necessary amounts of ammonium molybdate tetrahydrate ($(NH_4)_6Mo_7O_{24}\cdot 4H_2O$, Fluka Analytical, puriss. p.a., ACS reagent, ≥ 99.0%), nickel nitrate hexahydrate ($Ni(NO_3)_2\cdot 6H_2O$, Janssen Chimica) and citric acid monohydrate ($C_6H_8O_7.H_2O$, Sigma Aldrich, ACS reagent, ≥ 99.0%), were dissolved in a 10% aqueous solution of nitric acid. The mixture was stirred at room temperature, until a clear solution was obtained. Then, the solvent was evaporated off at 70 °C, until a green coloured gel had formed. The gel was calcined in air at 500°C (60°C/min) for 2 hours to form the oxide.

Nickel molybdenum nitride (Ni_2Mo_3N) was prepared by nitridation of the oxide precursor by using a 3:1 ratio of 60 mL/min H_2/N_2 gas mixture (BOC, H_2 99.998%, N_2 99.995%) at 700°C for three hours. A ramp rate of 10°C/min was used to reach 700°C. The material was then cooled after the three hours under H_2/N_2.

The carburised material ($Ni_2Mo_3C_xN_y$) was prepared by carburisation of Ni_2Mo_3N with a 20% CH_4/H_2 gas mixture (BOC, 99.98%) at a flow rate of 12 mL/min. The ramp rate used was 6°C/min until the reactor had reached 350°C and was then changed to 1°C/min up to 560°C. The reactor was kept at 560°C for 2 hours and then the sample was cooled down at a ramp rate of 10°C/min under CH_4/H_2.

2.1.2 Preparation of Ni_6Mo_6C

Nickel molybdenum oxide precursor ($Ni_3Mo_3O_x$) was prepared by using a similar method to the one described in section 2.1.1. Stoichiometric amounts of nickel nitrate hexahydrate ($Ni(NO_3)_2\cdot 6H_2O$, Janssen Chimica) and ammonium molybdate tetrahydrate ($(NH_4)_6Mo_7O_{24}\cdot 4H_2O$, Fluka Analytical, puriss. pa., ACS reagent, ≥99.0%) were dissolved in 200mL of 10% nitric acid. Then, 26.547g of citric acid monohydrate ($C_6H_8O_7.H_2O$, Sigma Aldrich, ACS reagent, ≥ 99.0%) was added to the mixture and this was stirred until the solution was clear. The mixture was heated at 70°C, until a gel had formed. The gel was then dried in an oven for 12 hours at 120°C. The material was not calcined.

Nickel molybdenum carbide (Ni_6Mo_6C) was prepared by reducing the uncalcined oxide precursor under a 3:1 ratio of H_2/Ar gas mixture (BOC, 99.98%) at a flow rate of

60 mL/min. The citric acid was used as the source of carbon. The material was reduced at either 700°C or 750°C for 6 hours. The ramp rate used was 10°C/min until the reactor had reached 350°C and then it was changed to 5°C/min until the required temperature was attained. The sample was cooled down under H_2/Ar to room temperature.

2.1.3 Preparation of Ni_3Mo_3C

Two methods were used in attempting to prepare nickel molybdenum carbide (Ni_3Mo_3C):

1) The first method used a similar process as described by Regmi and Leonard [48]. Uncalcined oxide precursor ($Ni_3Mo_3O_x$) and excess activated charcoal (0.0156g, British Drug Houses Ltd., powder, washed with acid) were ground together for 20 minutes using a pestle and mortar to obtain a homogeneous mixture. Subsequently, the material was prepared under a 60 mL/min flow rate of Ar gas (BOC, 99.998%) at 1000°C. The ramp rate used for heating was 1°C/min. Once the furnace reached 1000°C, the furnace was cooled down to room temperature under Ar.

2) The second method prepared the material by using the carburisation reactor described in section 2.1.11. Ni_6Mo_6C was carburised in 20% CH_4/H_2 (BOC, 99.98%) at a flow rate of 12 mL/min. The material was loaded into a quartz reactor tube and placed into the microreactor. The material was heated to either 560°C or 800°C at a ramp rate of 50°C/min. After 5 hours at the required temperature, the sample was cooled down to room temperature under 20% CH_4/H_2.

2.1.4 Preparation of Ni_2GaMo_3N

Nickel gallium molybdenum oxide precursor ($Ni_2GaMo_3O_x$) was prepared using a modified Pechini method as described in section 2.1.1. Stoichiometric amounts of nickel nitrate hexahydrate ($Ni(NO_3)_2 \cdot 6H_2O$, Janssen Chimica), gallium (III) nitrate hydrate ($Ga(NO_3)_3.xH_2O$, Sigma Aldrich, 99.9% metals basis) and ammonium molybdate tetrahydrate ($(NH_4)_6Mo_7O_{24} \cdot 4H_2O$, Fluka Analytical, puriss. pa., ACS reagent, ≥99.0%) were dissolved in 100mL of 10% nitric acid. Then, 13.226g of citric acid monohydrate ($C_6H_8O_7.H_2O$, Sigma Aldrich, ACS reagent, ≥ 99.0%) was added to the mixture and this was stirred until the solution was clear. Following this, the mixture was evaporated off at 70 °C, until a gel had formed. The gel was dried in an oven overnight at 150°C and then, was calcined in air at either 500°C, 600°C or 650°C (60°C/min) for 2 hours to form the oxide.

Nickel gallium molybdenum nitride (Ni_2GaMo_3N) was prepared using the ammonolysis reactor (as described in section 2.1.9). $Ni_2GaMo_3O_x$ was nitrided with 95 mL/min of NH_3 (BOC, 99.98 %) at 785°C for 5 hours. The temperature was increased from room temperature to 357°C at a ramp rate of 5.6°C/min, then, to 447°C at a ramp rate of 0.2°C/min. Finally, the ramp rate was increased at 2.1°C/min until the final temperature had been reached. After 5 hours at 785°C, the material was cooled down to room temperature under 95 mL/min of NH_3. The reactor was then flushed with nitrogen for 30 minutes to remove any residual NH_3. Subsequently, the material was passivated for 1 hour by using a mixture of 25 mL/min 2% O_2/Ar diluted with nitrogen.

2.1.5 Preparation of Fe_3Mo_3C

Iron molybdenum oxide ($FeMoO_4$) was prepared by following the procedure outlined by Bem et al. [49]. A green 0.25 M aqueous solution of 37.1 mL of iron (II) chloride tetrahydrate ($FeCl_2.4H_2O$, Sigma Aldrich, ReagentPlus, 98%) was added dropwise to a 0.66 M aqueous solution of 14 mL of sodium molybdate dihydrate ($Na_2MoO_4.2H_2O$, Hopkin and Williams, Analar, 99.0 - 102.0%). $FeCl_2.4H_2O$ was weighed out in a glovebox. A solid formed immediately when the solutions were mixed together. Once all the aqueous solution of iron (II) chloride tetrahydrate was added, the mixture was left to stir for 1 hour. A brown precipitate was acquired after vacuum filtration and this was washed twice with distilled water and once with ethanol. The solid was dried overnight in an oven at 150°C. Then, it was calcined under 60 mL/min of nitrogen at 500°C (10°C/min) for 6 hours. The solid was cooled down to room temperature under nitrogen.

Iron molybdenum nitride (Fe_3Mo_3N) was formed by ammonolysis of approximately 0.6 g of $FeMoO_4$ with 95 mL/min of NH_3 (BOC, 99.98 %) at 785°C for 5 hours. The ammonolysis reactor was used as described in section 2.1.9. The temperature was increased from room temperature to 357°C at a ramp rate of 5.6°C/min. Then, to 447°C at a ramp rate of 0.2°C/min and finally, the ramp rate was increased at 2.1°C/min until the final temperature had been reached. After 5 hours at 785°C, the material was cooled down under 95 mL/min of NH_3. At room temperature, the reactor was flushed with nitrogen for 30 minutes to remove any NH_3. Then, the material was passivated for 1 hour by using a mixture of 25 mL/min 2% O_2/Ar diluted with nitrogen.

Iron molybdenum carbide (Fe_3Mo_3C) was prepared from Fe_3Mo_3N, which was carburised by using a 12 mL/min flow of 20% CH_4/H_2 gas mixture (BOC, 99.98%) at 560°C for 2 hours. The ramp rate used was 6°C/min until the reactor had reached 350°C and was then

changed to 1°C/min up to the final temperature. After 2 hours, the sample was cooled down to room temperature at a ramp rate of 10°C/min under CH_4/H_2.

2.1.6 Preparation of Co_2Mo_3N

Cobalt molybdenum oxide was synthesised by using three different methods:

1) The first method used a modified form of the Pechini method as described by Bion et al. [36]. To give a 2:3 ratio of Co:Mo, the necessary amounts of cobalt (II) nitrate hexahydrate ($Co(NO_3)_2 \cdot 6H_2O$, Alfa Aesar, ACS, 98.0 – 102.0%, crystalline) and ammonium molybdate tetrahydrate ($(NH_4)_6Mo_7O_{24} \cdot 4H_2O$, Fluka Analytical, puriss. p.a., ACS reagent, ≥ 99.0%) were dissolved in a 10% aqueous solution of nitric acid. Then, citric acid monohydrate ($C_6H_8O_7.H_2O$, Sigma Aldrich, ACS reagent, ≥ 99.0%) was added. The mixture was stirred at room temperature, until a clear solution was obtained. Then, the mixture was treated at 70°C, until a red coloured gel had formed. The gel was dried in an oven overnight at 120°C. Subsequently, the gel was calcined in air at 500°C (60°C/min) for 2 hours to form the oxide.
2) 2.22 g of ammonium molybdate tetrahydrate $(NH_4)_6Mo_7O_{24}.4H_2O$, Fluka Analytical, puriss. p.a., ACS reagent, ≥ 99.0%) and 3.64 g of cobalt (II) nitrate hexahydrate ($Co(NO_3)_2 \cdot 6H_2O$, Alfa Aesar, ACS, 98.0 – 102.0%, crystalline) were dissolved separately in 100 mL of deionised water. The solution containing cobalt was added dropwise to the solution of molybdenum under stirring. Then, the solution was heated to 85°C and left at this temperature until approximately 75 mL of solution remained. A purple precipitate was obtained after vacuum filtration and this was washed twice with deionised water and once with ethanol. The solid was dried overnight in an oven at 150°C and was then calcined in air at 500°C (10°C/min) for 3 hours.
3) A similar method was used as outlined by Hunter et al. [50]. 4.00 g of ammonium molybdate tetrahydrate $(NH_4)_6Mo_7O_{24}.4H_2O$, Fluka Analytical, puriss. p.a., ACS reagent, ≥ 99.0%) and 4.40 g of cobalt (II) nitrate hexahydrate ($Co(NO_3)_2 \cdot 6H_2O$, Alfa Aesar, ACS, 98.0 – 102.0%, crystalline) were dissolved in 200 mL of deionized water. The solution was then heated to 85°C and left at this temperature until approximately 75 mL of deionised water remained. The resulting purple precipitate of $CoMoO_4 \cdot nH_2O$ was vacuum filtered and then, washed twice with deionised water and once with ethanol. The sample was dried overnight in an oven at 150°C. The material was not calcined.

Cobalt molybdenum nitride (Co_2Mo_3N) was prepared by nitridation of the oxide precursor by using a 3:1 ratio of 60 mL/min H_2/N_2 gas mixture (BOC, H_2 99.998%, N_2 99.995%). The material was prepared at different temperatures of either 600°C, 650°C or 700°C for one, two or three hours. A ramp rate of 10°C/min was used to reach the required temperature. The material was then cooled after the reaction time under H_2/N_2.

2.1.7 Preparation of Osmium

The osmium metal sample was purchased from Acros Organics (99.9%, trace metal basis) and was used as provided.

2.1.8 Preparation of Supported Metal Carbonyl Compounds

2.1.8.1 Preparation of 5% $Os_3(CO)_{12}$ on Support

Triosmium dodecacarbonyl ($Os_3(CO)_{12}$, Sigma Aldrich, 98%) was supported onto silica (Silica-amorphous, precipitated, Sigma Aldrich) or alumina (γ-alumina, Condea chemie, alumina extrudates) by the method outlined by Collier et al. [51]. The support was impregnated with a solution of $Os_3(CO)_{12}$ in dichloromethane (DCM, VRW chemicals, ≥99%, stab. with 0.2% ethanol). The volume of dichloromethane required was determined by point of wetness for each support. The material was then dried at 40°C to remove the dichloromethane to produce a yellow powder of supported $Os_3(CO)_{12}$. The material was prepared to target a percentage loading of 5% by weight of osmium. The silica was either used as supplied (the hydroxylated support) or was dried at 500°C (10°C/min) for 16 hours under a 60 mL/min flow of nitrogen prior to being impregnated (the dehydroxylated support).

2.1.8.2 Preparation of 5% $Os_3(CO)_{12}$ on Silica in Inert Conditions

Triosmium dodecacarbonyl ($Os_3(CO)_{12}$, Sigma Aldrich, 98%) and silica (Silica-amorphous, precipitated, Sigma Aldrich) were weighed out in a nitrogen filled glove box. These were then placed in a sealed Schlenk flask and connected to a Schlenk line. Dry dichloromethane was added to the Schlenk line and was added dropwise, by a syringe, to the silica support and $Os_3(CO)_{12}$. The material was prepared under nitrogen. The volume of dry dichloromethane needed was determined from the point of wetness for silica. A vacuum was applied to the material to evaporate off any excess dry DCM. The material was prepared to give a percentage loading of 5% by weight of osmium.

2.1.8.3 Preparation of 5% $Os_3(CO)_{12}$ on Silica and 1% KOH

5% $Os_3(CO)_{12}$/silica was prepared as described in section 2.1.8.1. Potassium hydroxide (KOH, Sigma Aldrich, puriss. p.a., Reag. Ph. Eur., ≥ 85%, pellets) was added to the 5%

$Os_3(CO)_{12}$/silica by wetness impregnation. A solution of KOH in deionised water was added to give a 1% loading of potassium. The material was dried at 100°C for 3 hours.

2.1.8.4 Preparation of 1% $Fe_3(CO)_{12}$ on Support

Triiron dodecacarbonyl ($Fe_3(CO)_{12}$, Alfa Aesar, 96% (dry wt.), stab. with 5-10% methanol) supported on either silica (Silica-amorphous, precipitated, Sigma Aldrich) or alumina (γ-alumina, Condea chemie, alumina extrudates) was prepared by the method described by Collier et al. [44]. A solution of $Fe_3(CO)_{12}$ in dichloromethane was impregnated onto the support. The amount of dichloromethane required to fill the pore volume of the support was determined from the point of wetness. After impregnation, the material was dried at 40°C to remove the dichloromethane. The material was prepared to give a percentage loading of 1% by weight of iron.

2.1.8.5 Preparation of 1% $Fe_2(CO)_9$ on Alumina

Diiron nonacarbonyl ($Fe_2(CO)_9$, Sigma Aldrich, 98%) was supported on alumina (γ-alumina, Condea chemie, alumina extrudates) to give a percentage loading of 1% by weight of iron. A solution of $Fe_2(CO)_9$ in dichloromethane was impregnated onto the support. The amount of dichloromethane needed was decided from the point of wetness for the support. Weighing of the $Fe_2(CO)_9$ was performed in a glove box due to the material being air sensitive.

2.1.8.6 Preparation of 2% $Ru_3(CO)_{12}$ on Support

Triruthenium dodecacarbonyl ($Ru_3(CO)_{12}$, Sigma Aldrich, 99%) was supported on silica (Silica-amorphous, precipitated, Sigma Aldrich) or alumina (γ-alumina, Condea chemie, alumina extrudates). The support was impregnated with a solution of $Ru_3(CO)_{12}$ in dichloromethane. The material was then dried at 40°C to remove the dichloromethane to produce a powder of supported $Ru_3(CO)_{12}$. The material was prepared to give a percentage loading of 2% by weight of ruthenium.

2.1.8.7 Preparation of 5% Ru on Alumina and 1% KOH

The 5% Ru/Al_2O_3 was a commercial material purchased from Sigma Aldrich (powder, reduced, dry) and was used as provided. Potassium hydroxide (KOH, Sigma Aldrich, puriss. p.a., Reag. Ph. Eur., ≥ 85%, pellets) was added by wetness impregnation. The material was treated with a solution of KOH in deionised water to produce a loading of 1% by weight of potassium. Then, the material was dried overnight at 110°C in an oven.

2.1.8.8 Preparation of 5% $Os_3(CO)_{12}$ and 2% $Ru_3(CO)_{12}$ on Silica

The formation of a supported bimetallic cluster was attempted by using an approach suggested by Kulkarni and Gates [52]. First, triosmium dodecacarbonyl ($Os_3(CO)_{12}$, Sigma Aldrich, 98%) was supported onto silica (Silica-amorphous, precipitated, Sigma Aldrich) as described in section 2.1.8.1. The resulting material was a yellow powder. Then, triruthenium dodecacarbonyl ($Ru_3(CO)_{12}$, Sigma Aldrich, 99%) was supported on the silica as detailed in section 2.1.8.6. The material was prepared to target a percentage loading of 5% by weight of osmium and 2% by weight of ruthenium. The material produced was an orange powder of $Os_3(CO)_{12}$ and $Ru_3(CO)_{12}$ on silica.

2.1.8.9 Preparation of 5% $Os_3(CO)_{12}$ and 1% $Fe_3(CO)_{12}$ on Silica

Initially, triosmium dodecacarbonyl ($Os_3(CO)_{12}$, Sigma Aldrich, 98%) was supported onto silica (Silica-amorphous, precipitated, Sigma Aldrich) as outlined in section 2.1.8.1. Then, triiron dodecacarbonyl ($Fe_3(CO)_{12}$, Alfa Aesar, 96% (dry wt.), stab. with 5-10% methanol) was supported onto the material as described in section 2.1.8.4. The material was prepared to target a percentage loading of 5% by weight of osmium and 1% by weight of iron. The material produced was a green powder of $Os_3(CO)_{12}$ and $Fe_3(CO)_{12}$ on silica.

2.1.8.10 Preparation of 2% $Ru_3(CO)_{12}$ and 1% $Fe_3(CO)_{12}$ on Silica

The first step involved supporting triruthenium dodecacarbonyl ($Ru_3(CO)_{12}$, Sigma Aldrich, 99%) onto silica, following the method described in section 2.1.8.6. Then, triiron dodecacarbonyl ($Fe_3(CO)_{12}$, Alfa Aesar, 96% (dry wt.), stab. with 5-10% methanol) was supported onto the material as explained in section 2.1.8.4. The material was prepared to target a percentage loading of 2% by weight of ruthenium and 1% by weight of iron. The resulting material was a green powder of $Ru_3(CO)_{12}$ and $Fe_3(CO)_{12}$ on silica.

2.1.9 Ammonolysis Reactor

The sample oxide was placed in a quartz reactor tube (10.5 mm internal diameter), which had a quartz sintered disk fitted halfway along the tube. A small amount of quartz wool was placed on top of the sample. The reactor tube was placed vertically inside the Carbolite furnace, which was set to go through various heating programmes by using a temperature controller. Ammonia (NH_3, BOC, grade N3.8) was introduced into the reactor through ¼ inch stainless steel tubing (Swagelok). A Brooks 5850 TR mass flow controller regulated the flow rate of ammonia. The vented gas was passed through an empty conical flask, to act as a dead volume, and then, a dilute sulfuric acid solution to neutralise any unreacted ammonia. After the reaction, the reactor was cooled down to room temperature and then was flushed with nitrogen for 30 minutes to remove any residual NH_3. Resultant

nitrides were passivated at room temperature by using a gas mixture containing 2% O_2/Ar diluted with N_2. Figure 3 shows the experimental set up used for nitriding materials by ammonolysis.

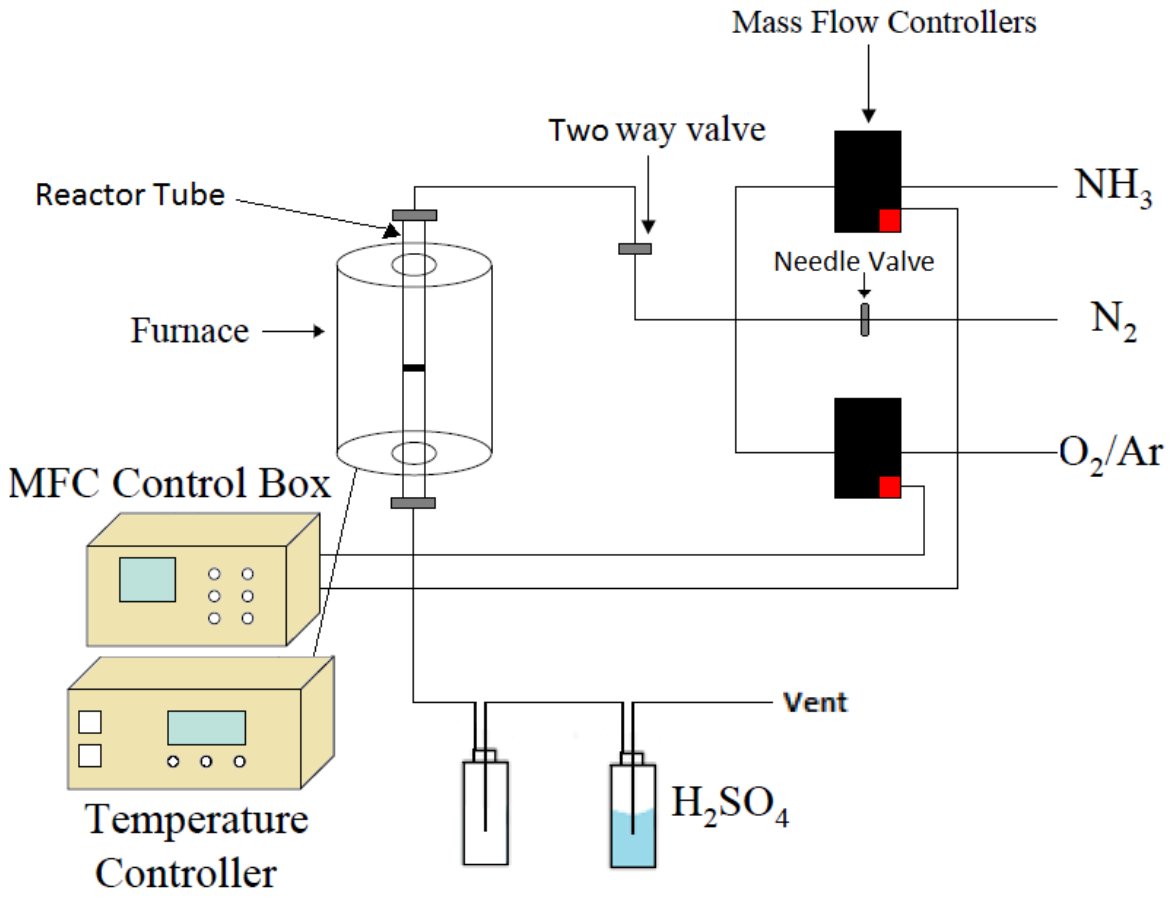

Figure 3: Rector Set Up for Ammonolysis

2.1.10 Reactor for Nitridation with N_2/H_2

A schematic of the microreactor system applied for nitridation with the N_2/H_2 reaction gas mixture is displayed in Figure 4. The sample oxide was loaded into a quartz reactor tube (8 mm internal diameter) and was packed at each end with quartz wool. This was then positioned in the centre of the Carbolite furnace, which was used to control the temperature. A Brooks 5850 TR MFC controlled the flow rate of 3:1 H_2/N_2 and the gas was flowed through ¼ inch stainless steel tubing. The resulting nitride was cooled to room temperature under the flowing gas mixture.

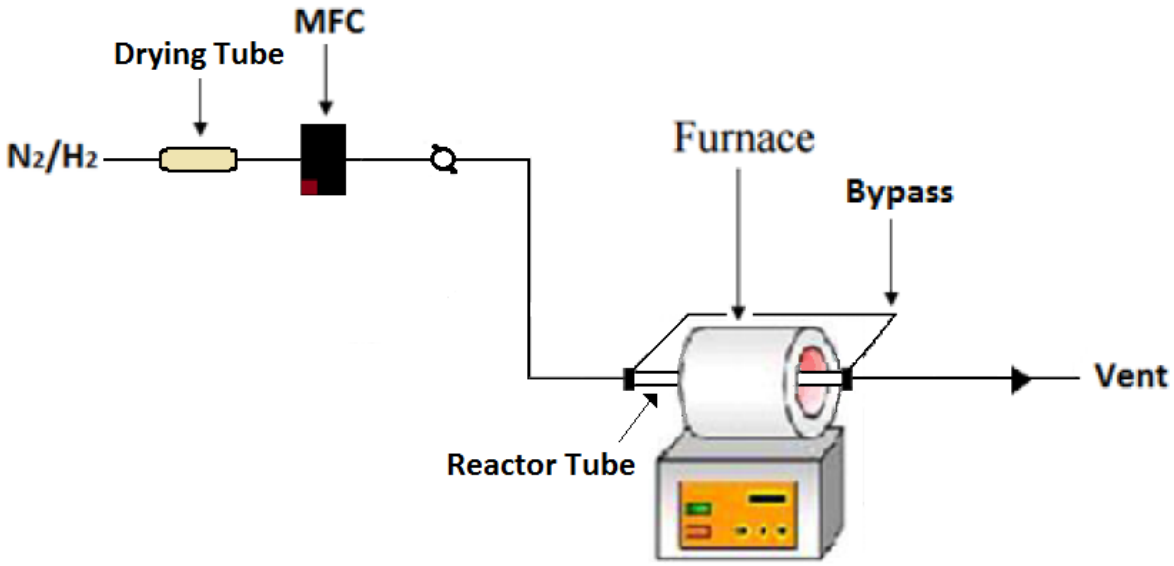

Figure 4: Reactor Set Up for Nitridation by N_2/H_2

2.1.11 Carburisation and Reduction Reactor

The apparatus set up for the carburisation and reduction processes is shown in Figure 5. The sample was loaded into a quartz reactor tube (8 mm internal diameter) and was packed between quartz wool plugs. The reactor tube was placed in the Carbolite furnace, which was used to control the temperature. Brooks 5850 TR MFCs controlled the flow rates for both the 3:1 H_2/Ar (BOC, 99.98 %) and 20% CH_4/H_2 (BOC, 99.98 %) gas mixtures when applied. The gases were flowed through ¼ inch stainless steel tubing. The resulting material was cooled to room temperature under the flowing gas mixture.

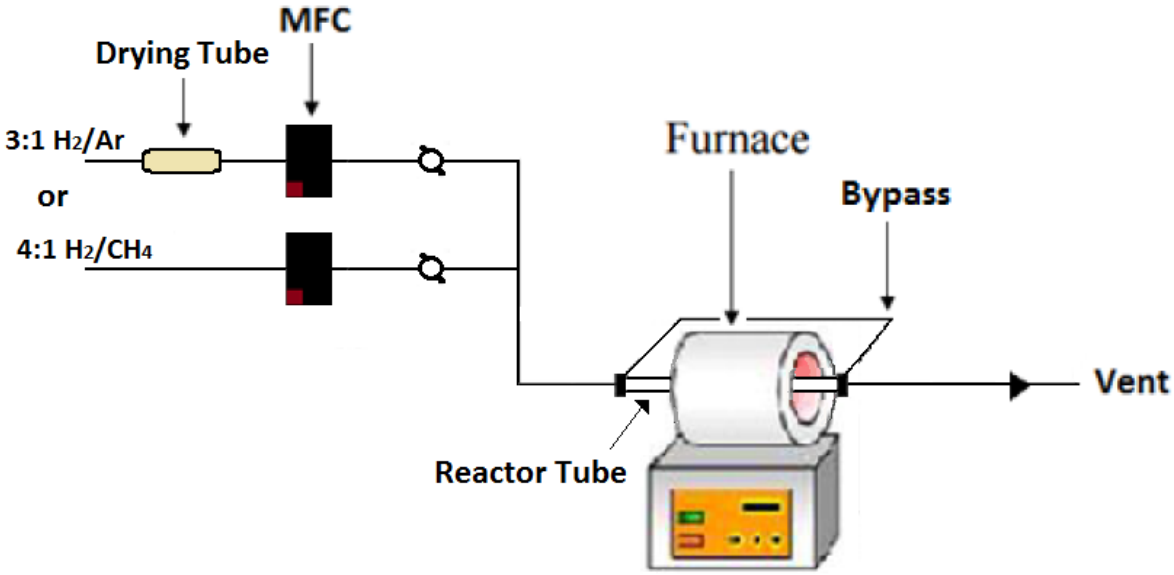

Figure 5: Reactor Set Up for Carburisation or Reduction

2.2 Materials Testing

2.2.1 Reactor for Ammonia Synthesis

The success of a material at producing ammonia was measured by the change in conductivity of a sulfuric acid solution (200 mL, 0.00108 mol/L) over time. The exit gas from the reactor was passed through the sulfuric acid solution and the conductivity decrease was measured. This decrease in conductivity corresponds to the formation of ammonium ions upon reaction of the ammonia with protons. The experimental method applied was related to the one developed by McKay [53]. A schematic of the ammonia synthesis reactor is displayed in Figure 6. The material was located in a quartz reactor tube (8 mm internal diameter) and was held in place between quartz wool plugs. This was then positioned in the centre of the Carbolite furnace, which was used to control the temperature. Reactions were performed at atmospheric pressure under either a 3:1 ratio of H_2/N_2 (BOC, H_2 99.998%, N_2 99.995%) or a 3:1 ratio of H_2/Ar (BOC, 99.98 %) with a gas flow rate of 60 mL/min. Flow rates were controlled by Brooks 5850 TR MFCs and the gases were flowed through ¼ inch stainless steel tubing. The conductivity was measured using a HACH HQ14d portable conductivity meter. The calibration value used to calculate ammonia synthesis rates is provided in Appendix I.

2.2.2 Experimental Method

Some of the samples were pre-treated before the reaction. Pre-treatment of these materials was performed at 700°C (except when specified otherwise) for two hours with either 1:3 N_2/H_2 or 1:3 Ar/H_2 gas mixtures. The flow rate of each gas applied was 60 mL/min. A ramp rate of 10°C/min was used to heat the furnace to the required temperature. After the two hours, the reactor was then cooled down to 400°C or 500°C and the ammonia synthesis reaction was started. All the ammonia synthesis reactions were performed at atmospheric pressure. The exit gas was passed through the sulfuric acid solution and the conductivity values were recorded periodically, every five minutes.

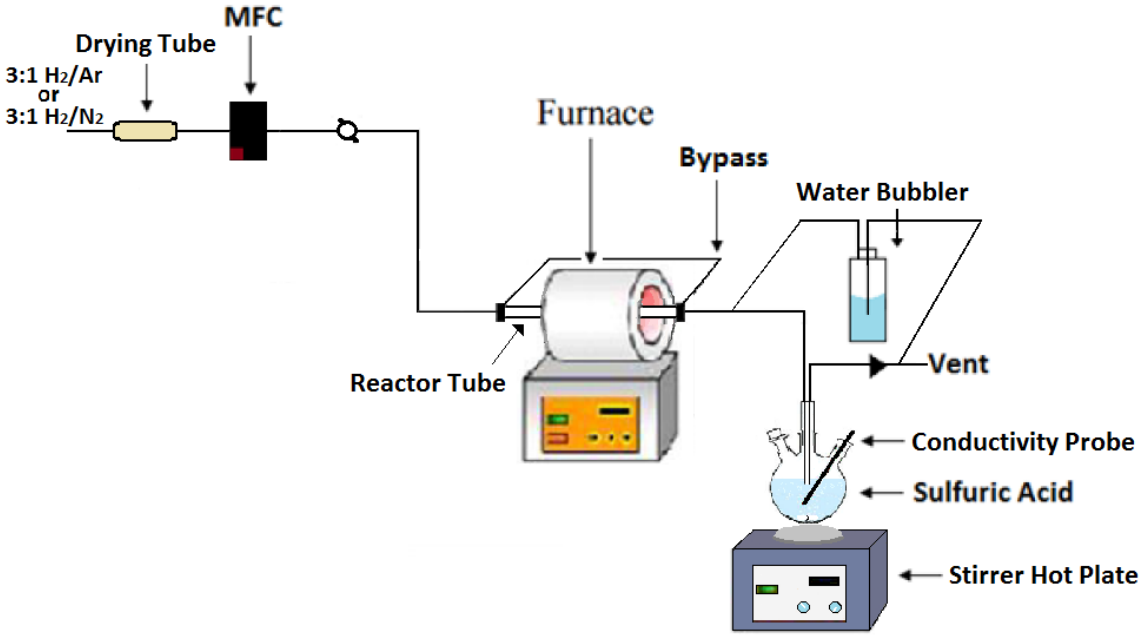

Figure 6: Reactor Set Up for Ammonia Synthesis Testing

2.3 Material Characterisation

2.3.1 Powder X-ray Diffraction (PXRD)

XRD patterns were obtained for the materials pre- and post-reaction by using a PANalytical X-Pert Pro Diffractometer (40kV, 40mA) with a monochromatised CuK alpha radiation source (1.5418 Å). A scanning range of 5-85° 2θ with a total scan time of 51 minutes and a step size of 0.0167° was used. Identification of phases was performed by comparing the patterns with JCPDS database files.

2.3.2 CHN Analysis

Carbon, hydrogen and nitrogen (CHN) analysis for pre- and post-reaction samples was very kindly performed by Mr Gangi Reddy Ubbara at the University of Glasgow. Elemental analysis was performed by combustion by using a CE-440 elemental analyzer made by Exeter Analytical, Inc.

2.3.3 Scanning Electron Microscopy (SEM) and Energy Dispersive X-ray Spectroscopy (EDX)

A Philips XL30E-Scanning electron microscope fitted with a tungsten filament and secondary electron detector was used to take SEM images. A beam of 20 kV and a spot size setting of 5 was applied. The spot size is an instrumental size and relates to the diameter of the beam on the sample. The microscope was also used to obtain Energy-Dispersive X-ray spectroscopy (EDX), which is applied to give the composition of the materials. EDX was measured by Oxford Instruments AZtec Software with X-act 10 mm^2 SDD detector.

The samples were placed onto carbon tabs and covered with a film of gold/palladium to reduce electron charging. This was done with a Polarn SC7640 Auto high-resolution sputter coater.

2.3.4 Raman Spectroscopy

The Raman spectra of the pre- and post-reaction samples were collected by using a Horiba Jobin Yvon LabRAM High Resolution spectrometer. A Ventus 532 nm green laser at 100 mW was used as the excitation source. The samples were focused by using a 50x objective lens. The laser was focused for 10 seconds, with a repetition of 3 and a grating of 600 cm^{-1}. The spectral region measured was from 50 - 3000 cm^{-1}. The Raman spectra were collected at room temperature on a glass slide.

2.3.5 Thermogravimetric Analysis with Mass Spectrometry (TGA-MS)

A TA Instruments SDT Q600 coupled to an ESS evolution mass spectrometer was used to perform thermogravimetric analyses on the materials. Mass spectrometry was performed in multiple ion detection mode (MID mode). The sample was heated from room temperature to 1000°C at a ramp rate of 10°C/min under a gas flow comprising either 3:1 H_2/Ar or 5% H_2/N_2. TGA-MS was very kindly performed by Mr Andrew Monaghan at the University of Glasgow.

2.3.6 Temperature Programmed Oxidation (TPO)

Thermogravimetric analysis of the uncalcined and calcined nickel gallium molybdenum oxide was performed on a TA Instruments TGA Q500. The samples were heated from room temperature to 900°C at a ramp rate of 10°C/min under 90 mL/min of air. TPO was very kindly performed by Mr Andrew Monaghan at the University of Glasgow.

2.3.7 Infrared Measurement

Infrared spectroscopy was performed on the materials derived from organometallic clusters. Infrared analysis for the samples was performed with a 10 mm KBr cell inserted into a Shimadzu IR Affinity-1S instrument. A background was taken before each sample and was subtracted to give the IR spectra for the corresponding metal carbonyl complex. The spectra were collected in the carbonyl region of 1500 – 2800 cm^{-1}, the resolution was 4 cm^{-1} and the number of scans undertaken was 50.

2.3.8 BET Surface Area

Surface areas of the pre- and post-reaction materials were measured from a Quadrasorb evo Gas Sorption Surface Area and Pore Size Analyzer manufactured by Quantachrome.

Before each measurement, approximately 0.1 g of sample was degassed overnight under vacuum at 110°C with a Flovac degasser. The programme used to analyse the data was Quadrawin software.

2.3.9 Time of Flight Secondary Ion Mass Spectroscopy (ToF SIMS)

A ToF-SIMS ION-TOF was used to characterise iron molybdenum and nickel molybdenum carbides and carbonitrides. The equipment has a bismuth ion gun and a time of flight mass analyser. Secondary ion mass spectra and depth profiles were recorded using Bi^{3+} as primary ions. The bismuth pulse duration was 1 ns with an AC current. For depth profiling, Cs was used for sputtering in the negative mode. The sputtering area was 300 µm x 300 µm and the area of analysis was 100 µm x 100 µm. The sputter current was 42.79 nA and the Cs primary ion beam energy was 0.5 keV. The analysis was performed at the Unite de Catalyse et Chimie du Solide (UCCS) in Lille with the very kind help of M. Nicolas Nuns. The placement of the samples in the sample holder is shown in Figure 7 and images of the ToF-SIMS V ION-TON instrument are provided in Figure 8.

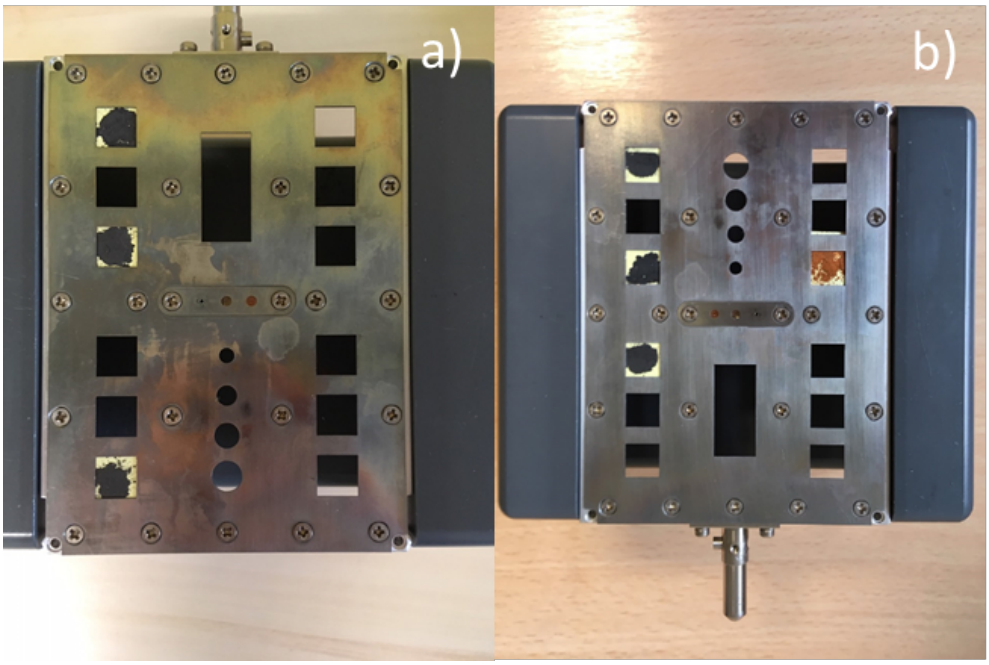

Figure 7: Images showing the samples placed in the sample holder, a) nickel molybdenum samples and b) iron molybdenum samples.

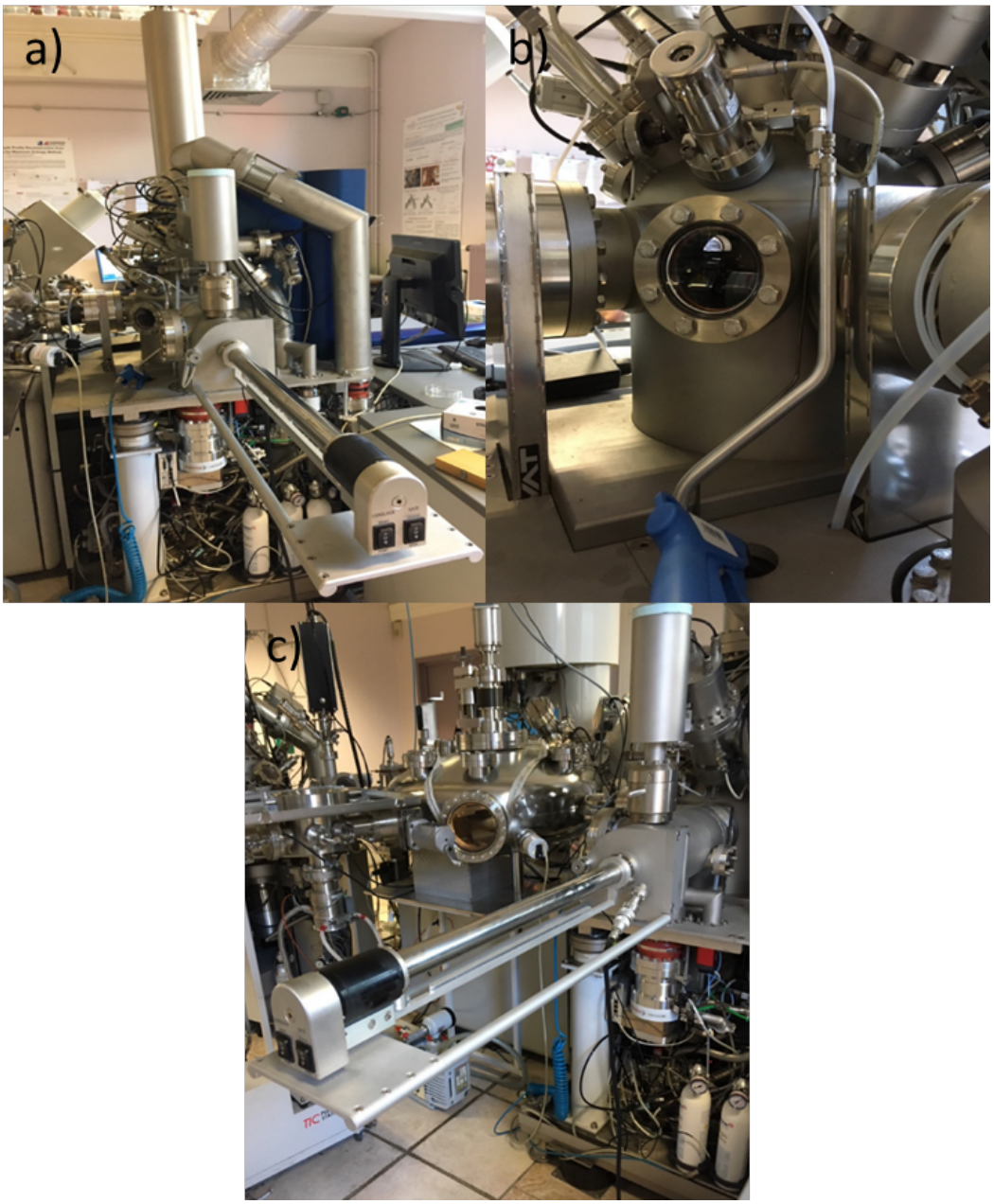

Figure 8: Images showing the ToF-SIMS V ION-TOF instrument, a) the overall ToF-SIMS V ION-TOF instrument, b) chamber where the samples are located during measurements and c) arm used to place the samples in the chamber.

3. Nickel Molybdenum Materials

3.1 Introduction

Nickel molybdenum nitride is a known ammonia synthesis material with relatively high activity of 395 ± 6 μmol h^{-1} g^{-1} at 400°C and atmospheric pressure [36] [39]. Co_3Mo_3N has been shown to have the highest activity of the nitrides at atmospheric pressure, with a rate of 652 μmol h^{-1} g^{-1} at 400°C [39] and 489 ± 17 μmol h^{-1} g^{-1} at 500°C [54]. The ternary nitrides tend to have higher rates than the binary nitrides as seen for γ-Mo_2N having a rate of 195 ± 7 μmol h^{-1} g^{-1} at 500°C [55].

Molybdenum carbide promoted with nickel has also been investigated as a catalyst for the hydrodesulfurization of dibenzothiophene (DBT) [56]. It was reported that Ni-Mo_2C had 96.25% conversion, with this being 1.57 times higher than for unpromoted Mo_2C. Ni-Mo_2C could be carburised at 50°C lower than Mo_2C and, therefore, had a higher BET surface area.

Ni_3Mo_3C has been examined for use as an anode electrocatalyst for high performance microbial fuel cells and was found to be 19% more active than Mo_2C and 62% as active as a Pt anode [57]. Ni_3Mo_3C and Ni_6Mo_6C mixed with Ketjen carbon were also found to have a good activity for anodic hydrogen oxidation, with the Ni_6Mo_6C containing catalyst having 15% of the activity of Pt catalyst and the Ni_3Mo_3C containing catalyst having a current density of 21 mA/cm^2 at 0.6 V [58]. These results suggest the potential of nickel molybdenum materials for electrochemistry.

The ammonia synthesis activity of ternary nitrides has tended to focus on Co_3Mo_3N, with Ni_2Mo_3N receiving less attention. This work focuses on the influence of phase composition and crystal structure on the ammonia synthesis activity.

3.1.1 Synthesis of Nickel Molybdenum Nitride

When trying to form the nickel molybdenum nitride (Ni_2Mo_3N) from its oxide ($NiMoO_4$), issues arise due to the difference in metal ratios between the precursor and the nitride. This causes impurities to form along with the required product [59] [36]. The presence of nickel metal in this material results in a lower catalytic activity for ammonia synthesis. The Ni_2Mo_3N and Ni material has been incorrectly reported as the Ni_3Mo_3N phase in the literature in a number of instances [49] [60]. The presence of impurities caused by this difference in ratio suggests that a different method is essential in order to obtain a single

phase nitride. The Ni_3Mo_3N phase has not been synthesised to date and instead there is a preference for the formation of the β-manganese structured Ni_2Mo_3N.

One way to overcome this problem of impure phase formation is to use freeze-dried polymetallic precursors [61]. Aqueous solutions containing the suitable metal salts were prepared so as to give the ratio of 2:3 for Ni:Mo. Heating the mixed oxide precursor with ammonia gas at 950°C resulted in single phase Ni_2Mo_3N. However, impurities were formed depending on the rate of the cooling process. The single phase nitride can also be prepared via a sol-gel precursor by using a modified Pechini method [36]. An oxide precursor with a 2/3 Ni/Mo ratio is formed and this yields the desired nitride when nitrided under a $N_2/3H_2$ mixture. The ammonia synthesis activity of this nitride prepared via the sol-gel route was compared to the one prepared from $NiMoO_4$ precursor [36]. It was found that the activity was significantly enhanced when the modified Pechini method was used. Therefore, the preparation route has an important impact on the catalytic activity of the nitride.

3.1.2 Synthesis of Nickel Molybdenum Carbides

When the TPR method was used to prepare nickel molybdenum carbides with CH_4/H_2, some issues arose as reported in the literature. When trying to prepare the carbide from the oxide precursor, β-Mo_2C and nickel metal are formed instead [62] [63]. Nagai et al. investigated the carburisation of nickel molybdenum oxides with different Ni:Mo ratios [62]. The $Ni_{0.25}Mo_{0.75}$ catalyst was carburised at 600°C and was shown to contain β-Mo_2C and $NiMoC_{3.6}O_{1.4}$. This could be transformed to the Ni_6Mo_6C phase when heated to 900°C under helium. The Ni_6Mo_6C structure has been studied by Newsam et al [64], who prepared the material by carburising the precursor with CO/CO_2 gas at 1000°C. It was observed that all the carbon atoms are located at the (0,0,0) sites in Ni_6Mo_6C, leaving the 1/8 sites empty.

A similar study by Hirose et al. focused on varying the carburisation temperature to prepare nickel molybdenum carbide from the oxide [65]. X-ray diffraction (XRD) data and temperature programmed carburisation (TPC) showed the transformation of the starting oxides as the carburisation temperature increased. MoO_3 was transformed to MoO_2 and $NiMoO_4$ to $NiMoO_xC_y$, which was further converted to β-Mo_2C and Ni metal. Therefore, reduction of Ni^{2+} to Ni results in the decomposition of the oxide. These results suggest that the Ni_2Mo_3C cannot be produced from the oxide precursor.

Puello-Polo and Brito have compared the carburisation of different starting precursors and their resulting products [66]. An activated carbon support was co-impregnated with ammonium heptamolybdate and a nickel salt. The XRD patterns showed that the carburisation of Ni-Mo sulfate precursor caused the formation of a $Ni_6Mo_6C_2$ phase along with nickel metal. However, when the Ni-Mo nitrate precursor was used, β-Mo_2C and nickel metal was produced, comparable to when the oxide precursor was used. Thus, different precursors may go through different intermediates and so can affect the final product that is formed.

Instead of using an oxide precursor, Alconchel et al. looked at using Ni_2Mo_3N as the starting precursor in the carburisation process [67]. The idea was that the structure would remain unaltered and the nitrogen atoms would be exchanged for carbon in a topotactic manner. From this method, a new carbonitride was produced, $Ni_2Mo_3C_xN_y$, which had the filled β-Mn structure.

Other sources of carbon have also been used to synthesise carbides. Smirnov et al. claim to have made Ni_2Mo_3C and $Ni_6Mo_6C_{1.06}$ from a Pechini based method by using citric acid as a complexing agent and by adding ethylsilicate-32 [68]. They prepared Ni_yMoC-SiO_2 materials with different Ni to Mo ratios. Their XRD patterns show that a mixture of phases were formed with impurities of β-Mo_2C and an alloy Ni_xMo_{1-x}. For all the prepared samples, XRD indicated that only a small amount of Ni_2Mo_3C was produced, with β-Mo_2C being the majority phase for the $Ni_{0.5}MoC$-SiO_2 material. Zhao et al. have also prepared a mixed phase Ni_6Mo_6C by using citric acid and ethylene glycol as the sources of carbon [69]. These results suggest that this method is not ideal for producing a single phase nickel molybdenum carbide.

Ni_6Mo_6C and Ni_3Mo_3C have been prepared by using decolourising carbon as the carburisation source [48]. The lower carbon content Ni_6Mo_6C was prepared at a lower temperature of 975°C and the Ni_3Mo_3C was formed at 1030°C. Therefore, the different phases can be formed depending on the carbothermic reduction temperature. The authors were able to show through XRD patterns that the transformation from Ni_6Mo_6C to Ni_3Mo_3C resulted in the material decomposing, before recombining to form the high carbon content phase. Therefore, this transition did not occur by the insertion of carbon into Ni_6Mo_6C.

3.1.3 Structures of Nickel Molybdenum Nitrides and Carbides

Bimetallic nitrides and carbides often form crystal structures where the non-metal atom is located in the interstitial sites between the metal atoms. In face-centered cubic (fcc) and hexagonal closed packed (hcp) structures this position is often in the octahedral sites as these are the largest available interstitial sites. It has been stated that the crystal structure is determined by two important factors [70]. The first is Hägg's rule, which states that if the number generated by dividing the atomic radii of the metal by the non-metal lies between 0.41 and 0.59, then an interstitial compound will be formed [71]. The second factor relates to Engel-Brewer theory for metals and alloys, which connects the structure to the number of valence electrons in certain orbitals [72]. Thus, the number of valence electrons in carbon and nitrogen can affect the structure. For example, molybdenum carbide forms an hcp based structure whereas the nitride forms an fcc based structure. However, despite the explanations offered by these theories, it is still unclear why certain compositions are formed and not others. For example, Ni_3Mo_3C, Co_3Mo_3N and Fe_3Mo_3N are known phases whereas Ni_3Mo_3N has not been successfully synthesised to date.

The two crystal structures of interest in this thesis are the η-carbide and filled β-manganese structures.

3.1.4 Filled β-Manganese Structure

The filled β-manganese structure has a cubic unit cell corresponding to the $P4_132$ space group. Ni_2Mo_3N is one example of a nitride that has the filled β-Mn structure [59]. There are two types of metal atom sites in this structure, the Wyckoff 8c site and 12d site. For Ni_2Mo_3N, the nickel atoms occupy the 8c sites and are arranged in a (10,3)-a network. Molybdenum atoms occupy the 12d sites and form corner sharing Mo_6 octahedra, with the non-metal atom occupying the interstitial site by binding to the six molybdenum atoms. Therefore, the filled β-manganese structure can be considered as two separate subunits. The Mo_6N octahedra and the nickel framework in Ni_2Mo_3N are shown in Figure 9.

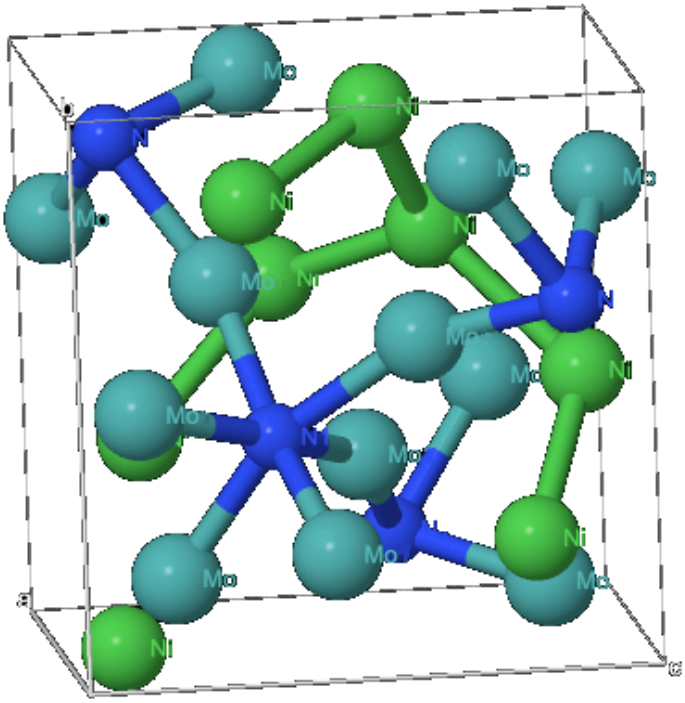

Figure 9: The crystal structure of Ni_2Mo_3N, showing the Mo_6N octahedra and the Ni-Ni bonding framework. Data plotted from Ni_2Mo_3N structure reported by Prior and Battle [73]. Elements: Nickel (green), molybdenum (light blue) and nitrogen (dark blue).

3.1.5 η-Carbide Structure

The η-carbide structure has a primitive cubic unit cell corresponding to the space group Fd3m. A range of carbides and nitrides with the formula $M_3M'_3X$ (M, M' = metals and X = non-metal) are known to have this structure, including Co_3Mo_3C and Fe_3Mo_3N [64] [74]. The structure consists of a distorted face centred cubic (fcc) arrangement of the M metal atoms. As in the filled β-manganese structure, the non-metal atom is situated in the interstitial site and is surrounded by six M' atoms to form an M'_6X octahedron. These octahedra are corner sharing and have mainly ionic bonding. The M' atoms are located on the 48f Wyckoff sites and the non-metals on the 16c Wyckoff sites. The M atoms occupy the 16d and 32e Wyckoff sites. The atoms on the 32e sites form a tetrahedron and are capped at each end by M on the 16d sites. Thus, forming pseudo-icosahedron, which share corners to produce a network of metal atoms [60]. These pseudo-icosahedra have metallic character. The Mo_6N and nickel network in Ni_3Mo_3C is displayed in Figure 10.

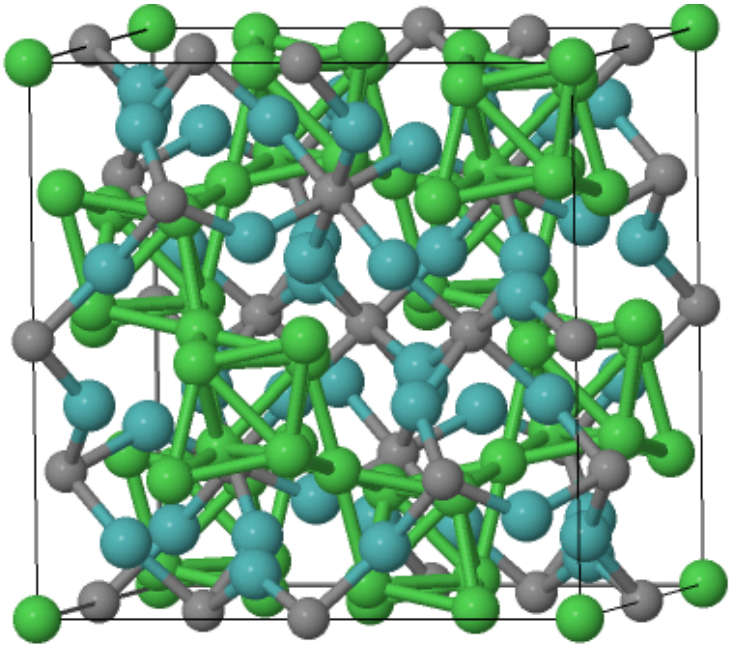

Figure 10: The crystal structure of Ni_3Mo_3C, showing the Mo_6N octahedra and the Ni-Ni bonding framework. Data plotted from Ni_3Mo_3C structure reported by Ettmayer and Suchentrunk [75]. Elements: Nickel (green), molybdenum (blue) and carbon (grey).

The η-carbide structure also has a low non-metal content variant phase, with stoichiometry of $M_6M'_6X$ and is denoted as η-12 structure. In this case, the non-metal is located in the 8a octahedral Wyckoff site and the rest of the structure remains the same. Examples of materials that adopt this structure are Co_6Mo_6C and Ni_6Mo_6C [64]. The crystal structure of Ni_6Mo_6C is presented in Figure 11. It has been observed that topotactic cycling can occur between the low and high nitrogen content cobalt molybdenum nitrides analogous phases [50].

Contrasting with the η-carbide structure, the filled β-Mn structure does not possess a low non-metal content analogue with partly occupied interstitial sites. However, Ni_2Mo_3N can exchange some nitrogen under certain pre-treatment conditions [36]. The local nitrogen environment between the η-carbide and the filled β-Mn structured nitrides is very similar. This is of interest as Co_3Mo_3N possibly operates via a Mars-van Krevelen mechanism for ammonia synthesis [54], where lattice N mobility is important and therefore, other nitrides may also operate via this mechanism.

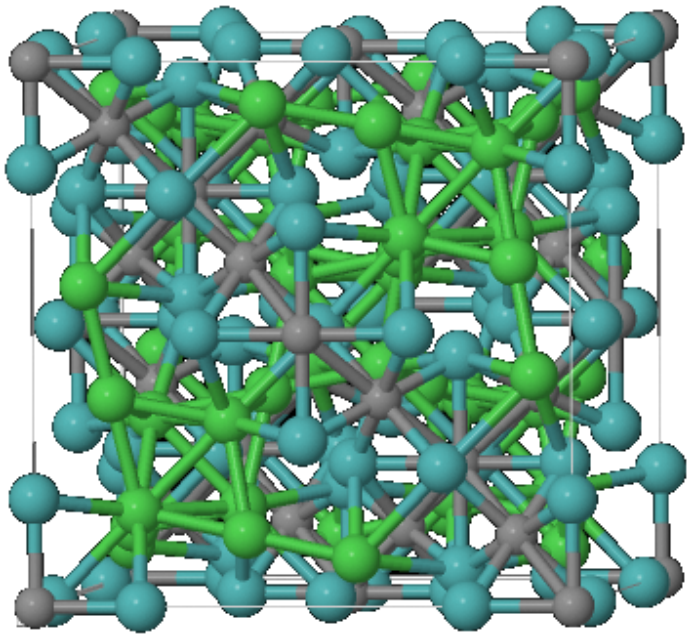

Figure 11: The crystal structure of Ni_6Mo_6C, showing the Mo_6N octahedra and the Ni-Ni bonding framework. Data plotted from Ni_6Mo_6C structure reported by Newsam et al. [64]. Elements: Nickel (green), molybdenum (blue) and carbon (grey).

Both the η-carbide and the filled β-Mn structures exhibit interesting behaviour, with influences from covalent, ionic and metallic bonding. They are known to have high hardness and incompressibility [76], suggesting that they are covalently bonded. However, they also have conductivities that are associated with metallic properties. This is due to the bond distances between the metals and metal and non-metal. The bonds for Mo-Ni are shown to have distances similar to covalent bonding, although they possess a degree of ionic character. The Ni-Ni bond distances are shorter and are more similar to metallic bonding [59].

3.1.6 Co_3Mo_3C/Co_3Mo_3N System for Ammonia Synthesis

Co_3Mo_3N has the comparatively high rate of 652 μmol h^{-1} g^{-1} for ammonia synthesis at 400°C and ambient pressure. This is higher than the commercial Haber Bosch catalyst under the same conditions (330 μmol h^{-1} g^{-1}) [39]. Through nitrogen isotopic exchange studies, it was seen that lattice N exchanged with $^{15}N_2$, suggesting that the nitride may operate under a Mars-van Krevelen mechanism as stated earlier [77]. Furthermore, half of the lattice nitrogen can be removed from Co_3Mo_3N to form Co_6Mo_6N, the high and low N variants of the η-carbide structure, when reacted under 1:3 Ar/H_2 [50], showing the high lattice nitrogen reactivity and mobility of this material.

Supported Co-Mo nanoparticles reportedly have 20 times the ammonia synthesis activity of bulk Co_3Mo_3N [78]. The nanoparticles are observed to transform to Co_3Mo_3N during the reaction. The formation of nitrogen vacancies on the nanoparticles is easier compared

to the bulk material and this has been stated to indicate that the creation of these vacancy sites is important for nitrogen activation [79].

One possible explanation for the high activity of Co_3Mo_3N is advanced by Norskov's volcano plot as shown in Figure 12. As can be seen, the combination of cobalt and molybdenum has almost optimal binding energy for nitrogen to give a high turnover frequency (TOF) for ammonia synthesis. Therefore, in relation to this explanation, it is proposed that CoMo is the active phase and the lattice nitrogen has no active role. Instead, the nitrogen is stated to be only required in order to give the correct structural ordering such that the (111) face comprising both Co and Mo is expressed. An alternative suggestion for the high activity of Co_3Mo_3N is that, as mentioned above, it operates via a Mars-van Krevelen mechanism and therefore, the lattice nitrogen is the active component. In this explanation, the lattice nitrogen is hydrogenated to yield ammonia, creating a transient lattice vacancy, which is then replenished by nitrogen from the reactant gas.

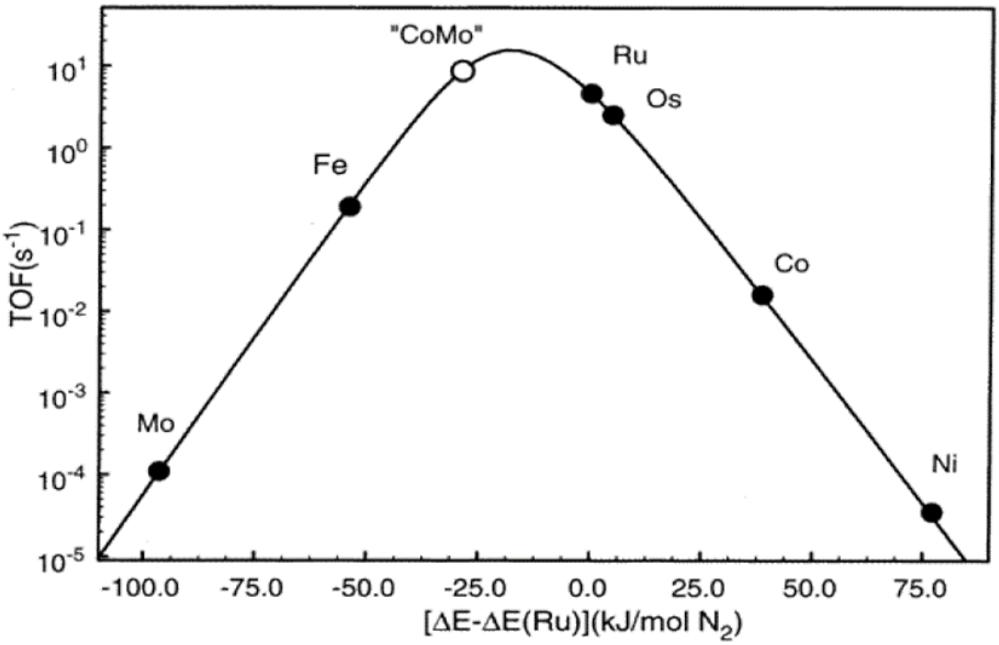

Figure 12: Calculated turnover frequencies (TOF) for ammonia synthesis against the adsorption energy for nitrogen for different elements [24].

In order to examine the effect of composition on activity, the corresponding carbide phase has been synthesised [54]. The carbide was prepared by carburisation of the Co_3Mo_3N with 20% CH_4/H_2 at 700°C for 2 hours. The formation of Co_3Mo_3C from Co_3Mo_3N is stated to be topotactic and pseudomorphic [80] and therefore, any difference in activity between these materials would not be due to a difference in morphology. The ammonia synthesis activities of Co_3Mo_3N and Co_3Mo_3C are shown in Figure 13. A reaction temperature of 500°C was required for activity to be exhibited by Co_3Mo_3C. However, the corresponding

nitride was active at 400°C. An induction period was required for the carbide at 500°C before it became active.

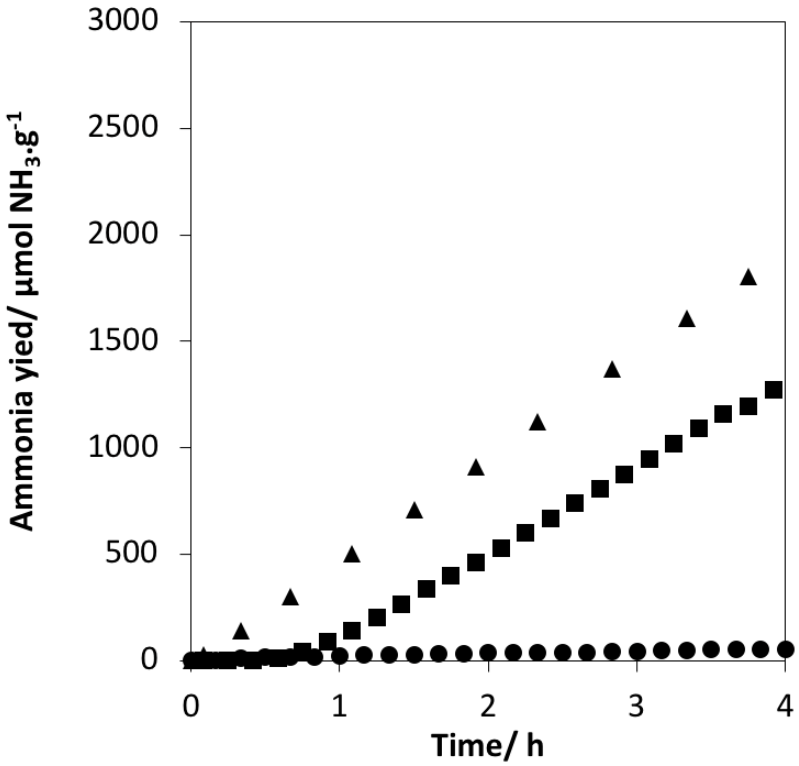

Figure 13: Ammonia yield under 60 ml/min of H_2/N_2 at 500°C (▲) Co_3Mo_3N, (■) Co_3Mo_3C and (●) Co_6Mo_6C [54].

During this period, nitridation of the Co_3Mo_3C lattice occurred, which eventually lead to the formation of Co_3Mo_3N upon prolonged reaction time. This substitution of carbon with nitrogen, going through an intermediate carbonitride phase, is displayed in Figure 14. Through computational modelling studies, it has also been proposed that nitrogen vacancies in Co_3Mo_3N occur and that the vacancy concentrations are significant at the temperatures necessary for ammonia synthesis [81]. These results suggest that ammonia synthesis activity in the cobalt molybdenum systems could be associated with its lattice nitrogen via a Mars-van Krevelen mechanism.

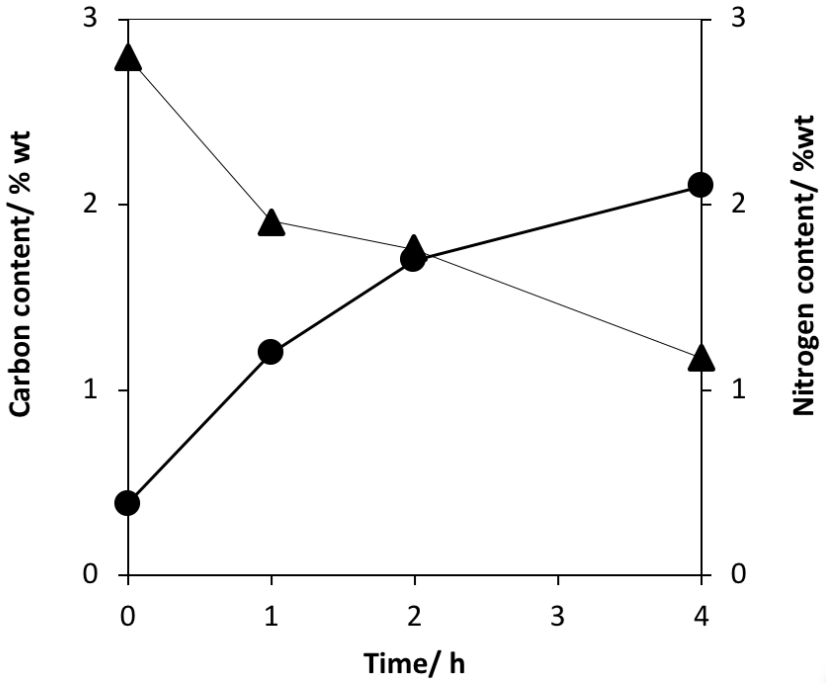

Figure 14: Co_3Mo_3C composition against reaction time during ammonia synthesis reaction at 500°C (▲) fractional carbon content and (●) fractional nitrogen content [54].

In comparison, the production of ammonia from Ni_2Mo_3N under an Ar/H_2 treatment is minimal, suggesting that bulk lattice nitrogen appears to be relatively unreactive. As both Ni_2Mo_3N and Co_3Mo_3N have different lattice nitrogen reactivities, it suggests that this is not a direct indicator of ammonia synthesis activity. It is interesting to note that the lattice nitrogen in these two nitrides have similar environments by being coordinated to six molybdenum species. However, nitrogen isotopic exchange studies of Ni_2Mo_3N indicate a degree of lattice nitrogen is exchangeable depending on the pre-treatment conditions [11] and the observation of lattice nitrogen exchange for Ni_2Mo_3N suggests the possibility of a surface limited Mars-van Krevelen mechanism for ammonia synthesis for this material. Thus, it would be of interest to prepare and test the activity of the corresponding carbide as has been performed for the cobalt molybdenum system. This would therefore give a greater understanding on the part the lattice nitrogen plays in the activity for this nitride.

3.2 Results and Discussion

Part I: Filled β-Mn Structured Materials

3.2.1 Nickel Molybdenum Carbonitride ($Ni_2Mo_3C_xN_y$)

3.2.1.1 Nickel Molybdenum Oxide ($Ni_2Mo_3O_x$)

At atmospheric pressure, there are four phases of $NiMoO_4$: the low temperature α-phase (α-$NiMoO_4$) [82], the α'-phase (a distorted form of the α-phase) [67], the high temperature β-phase (β-$NiMoO_4$) [83] and the hydrate ($NiMoO_4 \cdot nH_2O$) [84]. The phase can be identified from the XRD pattern by matching the peak positions between 20–36° 2θ with

the corresponding JCPDS files. For the material prepared in this work, it appears that the α-$NiMoO_4$ phase had been formed as seen in Figure 15 (JCPDS file number 00-033-0948). Al Sobhi et al. [85], who used the same preparation method, also obtained the α-$NiMoO_4$ phase. However, the presence of the peak at 26.7° 2θ, which is characteristic for β-$NiMoO_4$ [86], suggests that the material was a mixture of α-$NiMoO_4$ and β-$NiMoO_4$. A previous study has shown that β-$NiMoO_4$ can be synthesised at low temperature by using a sol-gel route [87]. Furthermore, there have been reports of mixed phase α, β-$NiMoO_4$ in the literature [88] [86].

From Figure 15, it can be seen that the oxide precursor also contained a MoO_3 phase fraction. This observation is consistent with the previously published work that used the sol-gel method to prepare Ni_2Mo_3N [85] [36]. This mixture of oxides is preferential as the difference in metal ratios of the Ni and Mo between the $NiMoO_4$ (1:1) and the nitride (2:3) can lead to impurities of nickel metal when the nitride is synthesised [36]. Therefore, this mixture of oxide phases was targeted to form stoichiometric Ni_2Mo_3N.

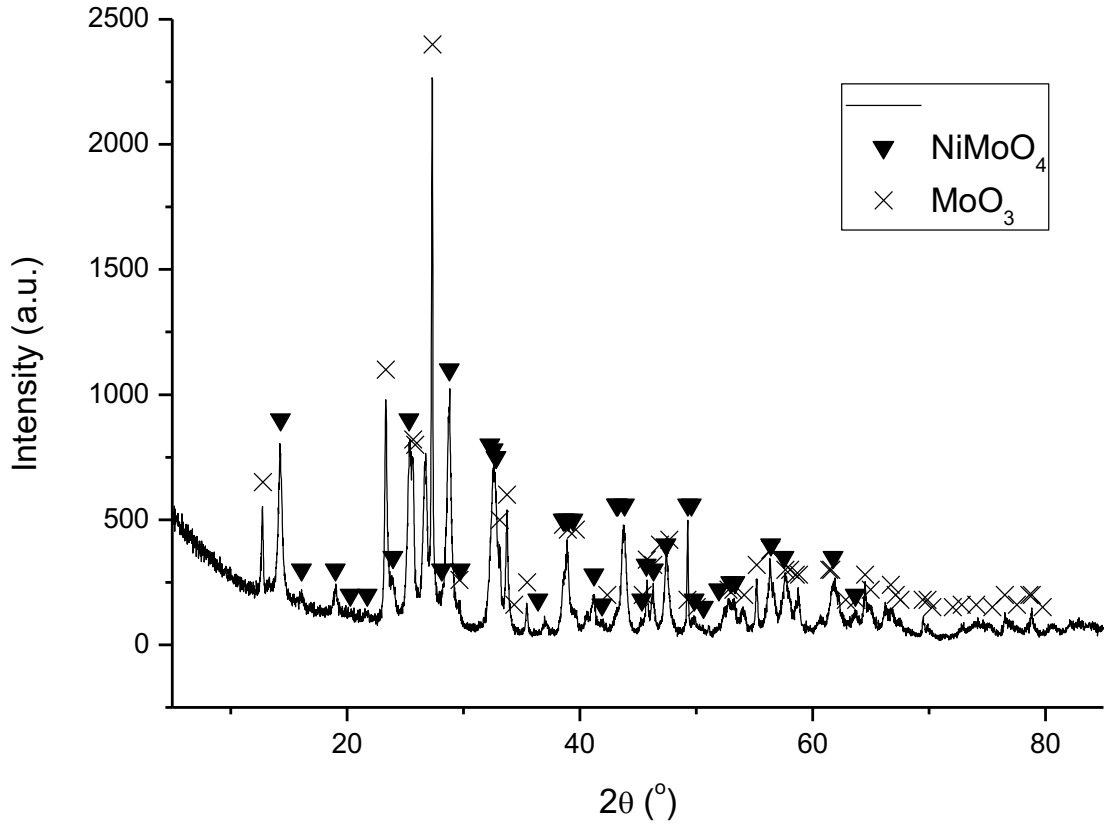

Figure 15: XRD pattern of nickel molybdenum oxide ($Ni_2Mo_3O_x$). Reflections marked: ▼ $NiMoO_4$ (JCPDS file number 00-033-0948) and X MoO_3 (JCPDS file number 00-035-0609).

The elemental analysis shows that there were only trace amounts of carbon and nitrogen present in the material after calcination (C: 0.70 wt. %, H: 0.00 wt. % and N: 0.01 wt. %).

This suggests that the citric acid and any other nitrogen from the starting precursors had largely been removed from the oxide during calcination.

Raman spectroscopy is a very good technique for characterising oxide materials and distinguishing between different oxide phases. The Raman spectrum of this material was analysed by comparing Figure 16 with the spectra of $NiMoO_4$ published in the literature. The Raman bands at positions of approximately 961, 913 and 706 cm^{-1} were attributed to α-$NiMoO_4$ [89]. These Raman shifts are in very good agreement with $NiMoO_4$ spectra reported in the literature [67]. The bands at 961 and 913 cm^{-1} have been assigned in the literature as the symmetric and asymmetric stretching modes of the terminal Mo=O bond [90]. The band at 706 cm^{-1} was assigned to the Ni-O-Mo symmetric stretch [67] [89]. However, another report in the literature suggests that the band at 818 cm^{-1} is due to either the symmetric or asymmetric stretching mode of Mo-O and the band at 706 cm^{-1} is due to the asymmetric mode of Ni-O-Mo bonds [91]. The weak bands at approximately 420, 390, 370 cm^{-1} are attributed to α-$NiMoO_4$ in the literature [89] and have been assigned to the bending mode of Mo−O. The weak band at 265 cm^{-1} has also been assigned to α-$NiMoO_4$ and is associated with the deformation mode of Mo−O−Mo [89].

The bands at 995, 818 and 665 cm^{-1} are related to MoO_3 [90] and are attributed to the Mo=O stretching mode, Mo-O-Mo asymmetric stretching mode and the Mo-O-Mo symmetric stretching mode respectively [67]. The Raman bands at 336 and 283 cm^{-1} have also been assigned to MoO_3 and are most likely due to the Mo-O bending and Mo-O-Mo deformation mode [90].

The presence of bands for both $NiMoO_4$ and MoO_3 agrees with the XRD results, which showed that both these oxides were present. Alconchel et al. [67] also observed the occurrence of bands for both these oxides in their starting precursor.

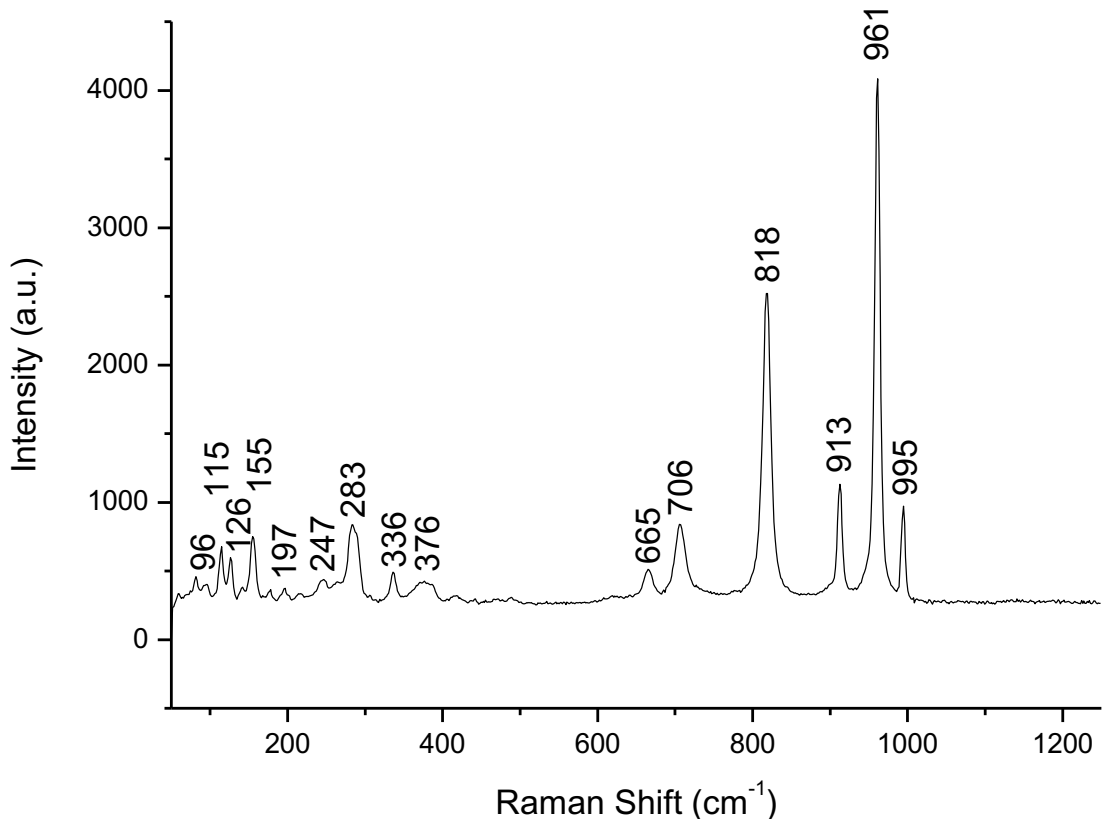

Figure 16: Raman spectrum of nickel molybdenum oxide ($Ni_2Mo_3O_x$)

Representative SEM images for the oxide precursor are displayed in Figure 17. The material appears to be porous with pores ranging in diameter from approximately 1 – 10 µm. The material had a surface area of 46 m^2/g, a pore volume of 0.26 cc/g and an average pore radius of 26.44 Å. To the author's knowledge, previous studies by groups that used the same sol-gel method, did not publish SEM images for the oxide and therefore, a comparison cannot be made [85] [36] [92]. Umapathy et al. published SEM images for $NiMoO_4$, which was prepared by a sol-gel method that used ethyl cellulose [93]. Their images showed that the material contained agglomerated particle-like nanostructures.

The elemental map in Figure 18 shows that the nickel, molybdenum and oxygen were evenly dispersed across the sample, as expected. The EDX analysis showed that nickel, molybdenum and oxygen were the only elements present in the sample.

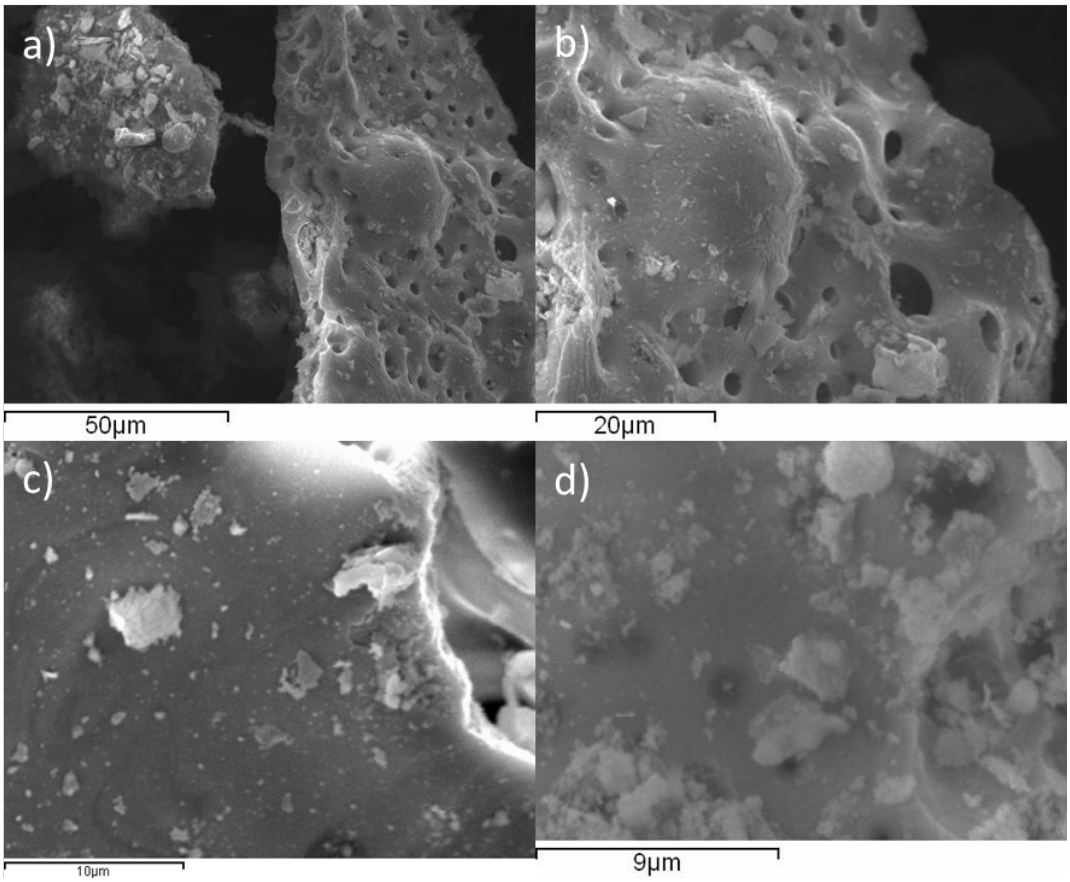

Figure 17: SEM images of nickel molybdenum oxide ($Ni_2Mo_3O_x$). a) 1000x magnification, b) 2000x magnification, c) 4000x magnification and d) 6000x magnification.

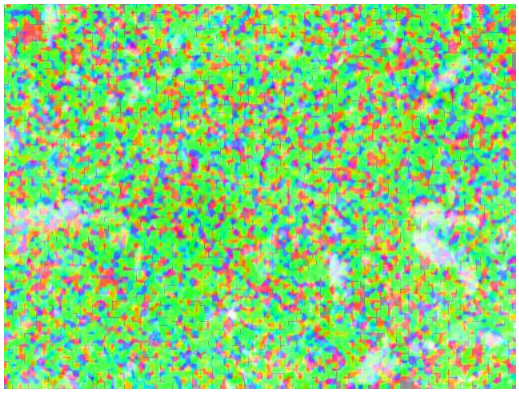

Figure 18: Element Map for $Ni_2Mo_3O_x$. Elements: Ni (red), Mo (green) and O (blue).

The EDX data in Table 1 details the weight percentages for each element. The stoichiometric percentage of nickel, molybdenum and oxygen in $NiMoO_4$ is 26.85 wt. %, 43.88 wt. % and 29.27 wt. % respectively. From the table, it can be seen that the oxygen weight percentage was higher than predicted and the nickel percentage was lower. From the XRD pattern, it was shown that the material consisted of both $NiMoO_4$ and MoO_3. Therefore, the stoichiometric percentage of nickel, molybdenum and oxygen in the theoretical $NiMo_2O_7$ ($Ni_2Mo_3O_{11}$) would be 16.19% (20.20%), 52.92% (49.52%) and 30.89% (30.28%) respectively. The theoretical composition $NiMo_2O_7$ assumes that there

was a 1:1 ratio of $NiMoO_4$ and MoO_3. $Ni_2Mo_3O_{11}$ was stated as the product when the oxide is formed by the modified Pechini method [36].

Area	Ni weight (%)	Mo weight (%)	O weight (%)
1	16	44	40
2	21	42	38
3	22	42	36
4	17	44	40
5	21	40	40
6	14	40	46
Average	18	42	40

Table 1: EDX values for nickel molybdenum oxide ($Ni_2Mo_3O_x$)

3.2.1.2 Nickel Molybdenum Nitride (Ni_2Mo_3N)

The filled β-Mn structured Ni_2Mo_3N is a known ammonia synthesis catalyst [39] [94]. Ni_2Mo_3N was prepared via temperature programmed nitridation of the bimetallic oxide, which was obtained via a sol-gel route. The preparation of this material was inspired by prior literature that reported the formation of Ni_2Mo_3N without nickel impurity [36]. An advantage of the Ni_2Mo_3N phase is that it can be prepared directly by nitridation of the oxide with N_2/H_2 at 700°C. Therefore, ammonolysis is not required in its preparation and this overcomes problems with using ammonia at a large scale [95].

As can be seen in Figure 19, the desired ternary nitride phase had been formed without any nickel impurities. However, a minor impurity phase of β-Mo_2N can be observed at 37.6° 2θ. The XRD pattern confirms that the material was free from reflections relating to molybdenum metal or any metal oxide phases. This result is consistent with previously published literature [36] [85].

The elemental analysis shows that there was no carbon or hydrogen present in the material after nitridation with N_2/H_2 (C: 0.00 wt. %, H: 0.00 wt. % and N: 4.58 wt. %). The percentage of nitrogen present in the material was higher than the expected stoichiometric value of 3.34 wt. %. Any residual NH_x species formed on the surface of the nitride would contribute towards this value. The β-Mo_2N phase content which could contribute to excess N content looks to be minimal as inferred from the XRD pattern and therefore, the contribution from this phase would be small. Therefore, it is unclear where the extra nitrogen originated from.

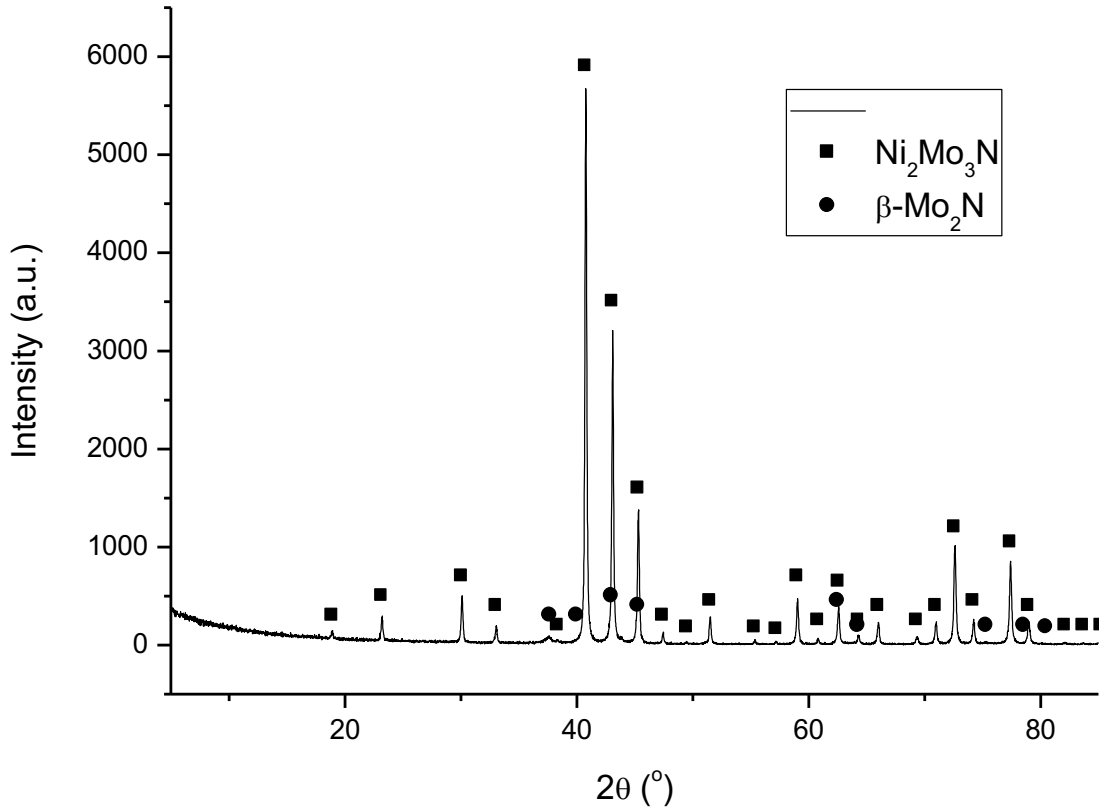

Figure 19: XRD pattern of nickel molybdenum nitride (Ni_2Mo_3N). Reflections marked: ■ Ni_2Mo_3N (JCPDS file number 01-089-4564) and ● β-Mo_2N (JCPDS file number 01-075-1150).

Raman spectroscopy is a valuable technique to characterise surface oxide species. These oxide species may affect the ammonia synthesis activity and therefore, it is important to observe if they are present on the surface of the material. The Raman spectra of Ni_2Mo_3N was taken at two different areas with 10% and 25% filters. The spectra are presented in Figure 20. The Raman spectra are very different between the two different areas. However, both show the formation of a surface oxide layer on the nitride, consisting of either α-$NiMoO_4$ or β-$NiMoO_4$. The formation of an oxide surface layer was observed in previous work investigating cobalt molybdenum nitrides [55].

For the area taken with a 10% filter, the Raman bands at positions of approximately 962, 914 and 709 cm^{-1} were attributed to α-$NiMoO_4$. These Raman shifts are in very good agreement with α-$NiMoO_4$ spectra reported in the literature [67] and match with the spectrum in Figure 16 for the oxide precursor. The weak bands at approximately 420, 390, 370, and 265 cm^{-1} are also attributed to α-$NiMoO_4$ in the literature [89]. The bands at 962 and 914 cm^{-1} have been assigned in the literature as the symmetric and asymmetric stretching modes of the terminal Mo=O bond. The band at 709 cm^{-1} was assigned to the Ni-O-Mo symmetric stretch [67]. The weak bands at 420, 390, and 370 cm^{-1} have been

assigned to the bending mode of Mo−O. The other weak band at 265 cm^{-1} is associated with the deformation mode of Mo−O−Mo [89].

At the second area with a 25% filter, Raman bands were detected at 344, 370, 820, 894 and 941 cm^{-1}. These bands match well with the literature values for β-$NiMoO_4$, which has bands at 370, 818, 890 and 936 cm^{-1} [96]. The bands at 894 and 941 cm^{-1} are due to the asymmetric and symmetric Mo-O vibration of Mo in a tetrahedral environment [96] [97]. The band at 820 cm^{-1} has been reported to be due to either the asymmetric stretching mode of the Ni-O-Mo bond [96] or the Mo-O vibration of Mo in tetrahedral coordination [97]. Furthermore, the band at 370 cm^{-1} has been assigned to the bending mode of Mo-O [96]. The presence of β-$NiMoO_4$ in the Raman spectra of Ni_2Mo_3N has been reported previously in the literature [67].

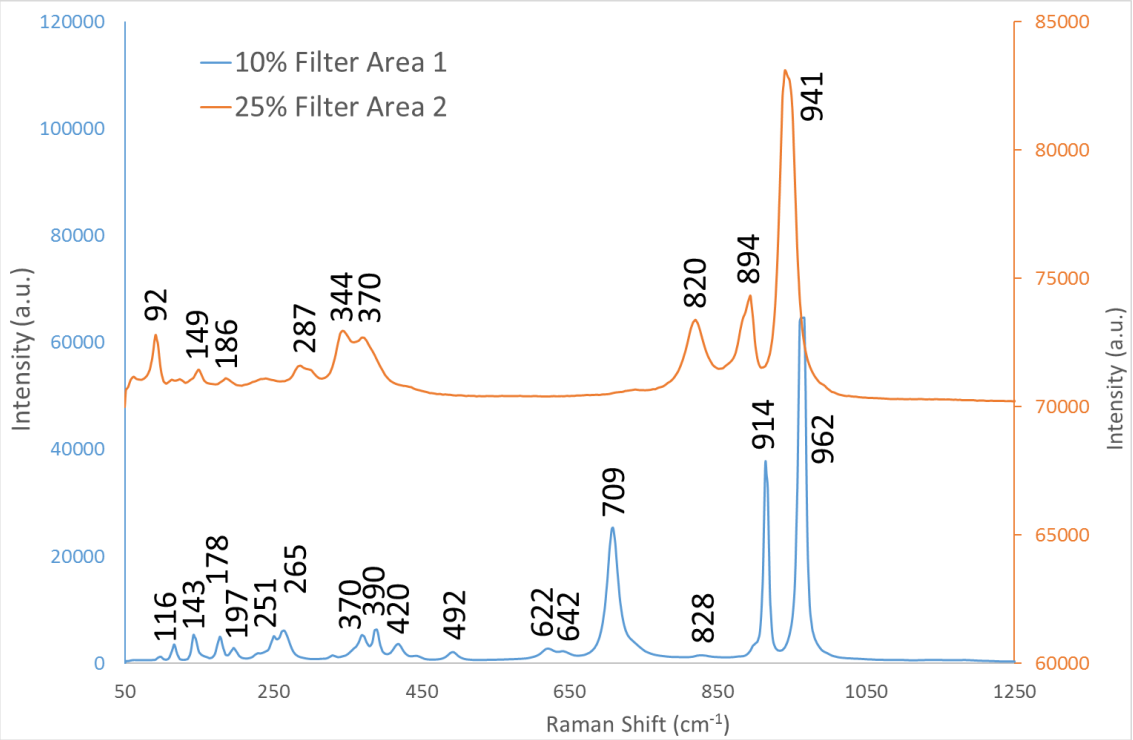

Figure 20: Raman spectra of nickel molybdenum nitride (Ni_2Mo_3N). The two spectra were taken at different points of the material and either at 10% or 25% filter.

It is important to investigate the morphology of a material as this can affect the ammonia synthesis activity. Figure 21 displays representative SEM images for Ni_2Mo_3N. The SEM images show a similar morphology to that of the oxide precursor. The sample consisted of rounded porous particles with an uneven surface. The nitride had a BET surface area of 5 m^2/g, a pore volume of 0.04 cc/g and an average pore radius of 15.92 Å. These values are lower than those for the oxide precursor. However, as observed from the Raman spectra for Ni_2Mo_3N, when the sample was in contact with air for a short time, a surface oxide

phase formed. Therefore, the BET surface area value for the nitride might not be a representative measurement in terms of the material under reaction conditions.

To the author's knowledge, only SEM images for Ni_2Mo_3N prepared by ammonolysis are published in the literature [85] [36] [59]. The morphology of the ammonolysis prepared samples are very different, comprising of well-formed rounded particles.

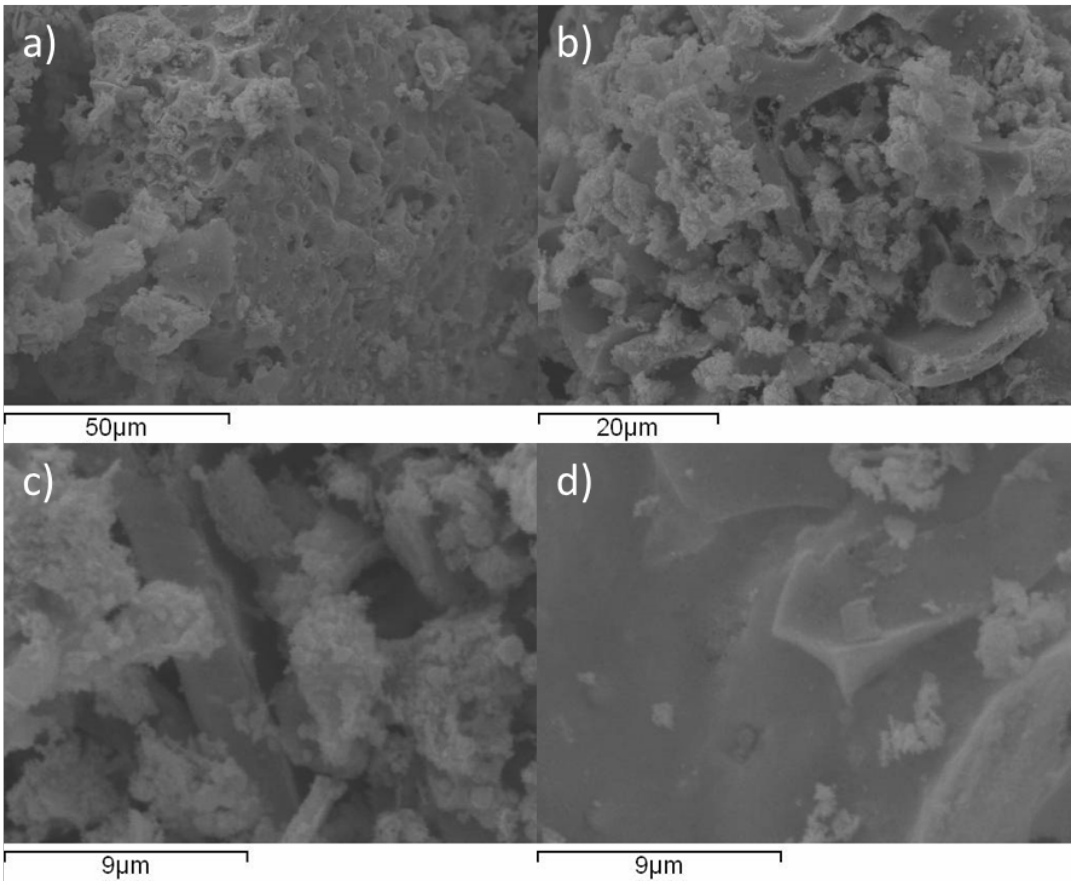

Figure 21: SEM images of nickel molybdenum nitride (Ni_2Mo_3N). a) 1000x magnification, b) 2000x magnification, c) 6000x magnification and d) 6000x magnification.

The element maps in Figure 22 show that there was an even distribution of nickel, molybdenum and nitrogen over the sample and that there was more molybdenum present than nickel.

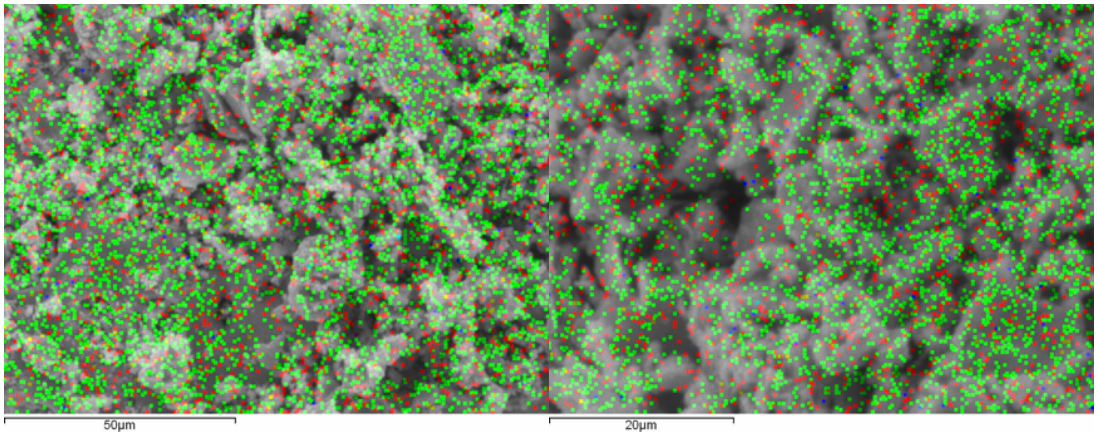

Figure 22: Element Maps for Ni_2Mo_3N. Elements: Ni (red), Mo (green) and N (blue).

The EDX analysis for the sample is shown in Table 2. The stoichiometric percentage of nickel, molybdenum and nitrogen for Ni_2Mo_3N is 28.00 wt. %, 68.66 wt. % and 3.34 wt. % respectively. The nitrogen weight percentage from EDX was greater than the stoichiometric nitrogen predicted for Ni_2Mo_3N. This could possibly be due to the limitations of EDX for light element analysis. The percentage of molybdenum and nickel was approximately as expected, suggesting that the weight ratio of Ni to Mo was close to that expected for Ni_2Mo_3N.

Area	Ni weight (%)	Mo weight (%)	N weight (%)
1	34	62	4
2	25	68	8
3	29	64	7
4	28	65	7
5	27	65	7
Average	28	65	7

Table 2: EDX values for nickel molybdenum nitride (Ni_2Mo_3N)

3.2.1.2.1 Lattice Nitrogen Reactivity of Ni_2Mo_3N

Ni_2Mo_3N has been explored for its ammonia synthesis activity [36] [39] and lattice nitrogen reactivity [36] [92] [98]. Most of the ammonia synthesis reactions were performed at 400°C and atmospheric pressure. The highest ammonia synthesis rates for Ni_2Mo_3N reported under these conditions are 383 ± 22 µmol h^{-1} g^{-1} [36] and 275 µmol h^{-1} g^{-1} [39]. For the nitride prepared with N_2/H_2, the rate was stated to be 395 ± 6 µmol h^{-1} g^{-1} at 400°C [36] and 466 µmol h^{-1} g^{-1} at 500°C [85] when there was no nickel impurity. The presence of nickel metal in the material drastically reduces the ammonia synthesis rate [36] [98]. Therefore, it is of importance to form the pure phase bimetallic nitride.

In order to determine the reactivity of lattice nitrogen in Ni_2Mo_3N, the material has been reacted under 1:3 Ar/H_2 from 400°C to 700°C [98] and isotopic exchange studies with $^{15}N_2$ have been performed [36] [92]. If the lattice nitrogen was active for ammonia synthesis via

a Mars-van Krevelen mechanism, there would be a reduction in the nitrogen content of Ni_2Mo_3N when reduced under Ar/H_2. Furthermore, there may be a transformation of the structure. The studies showed that the lattice N was only slightly reactive under Ar/H_2 up to 700°C and that there was no phase transition for the nitride. However, it was seen through nitrogen isotopic exchange studies that some lattice nitrogen exchanges with $^{15}N_2$ depending on the pre-treatment conditions [36].

In order to understand the role of lattice nitrogen reactivity in Ni_2Mo_3N, the material was reduced at 900°C under 1:3 ratio of Ar/H_2 at atmospheric pressure for 7 hours. The vent gas was passed through a dilute solution of H_2SO_4 and the conductivity was recorded over the reaction. A linear decrease in conductivity over time would represent a steady state reaction. As observed from the conductivity data in Figure 23, the rate was non-steady state. The R^2 value of the straight-line fit was 0.9751 and the data deviates from this at the start and the end. The conductivity decreased by only 49 µS/cm over the 7 hours. This result suggests that the lattice nitrogen in Ni_2Mo_3N is fairly unreactive with respect to ammonia production even at elevated temperatures. It must be noted that ammonia formation at this temperature is greatly unfavoured [99] and that the lattice nitrogen may be lost as N_2 instead, which would not result in a change in conductivity of the H_2SO_4 solution through which the reactor effluent gas is flowed.

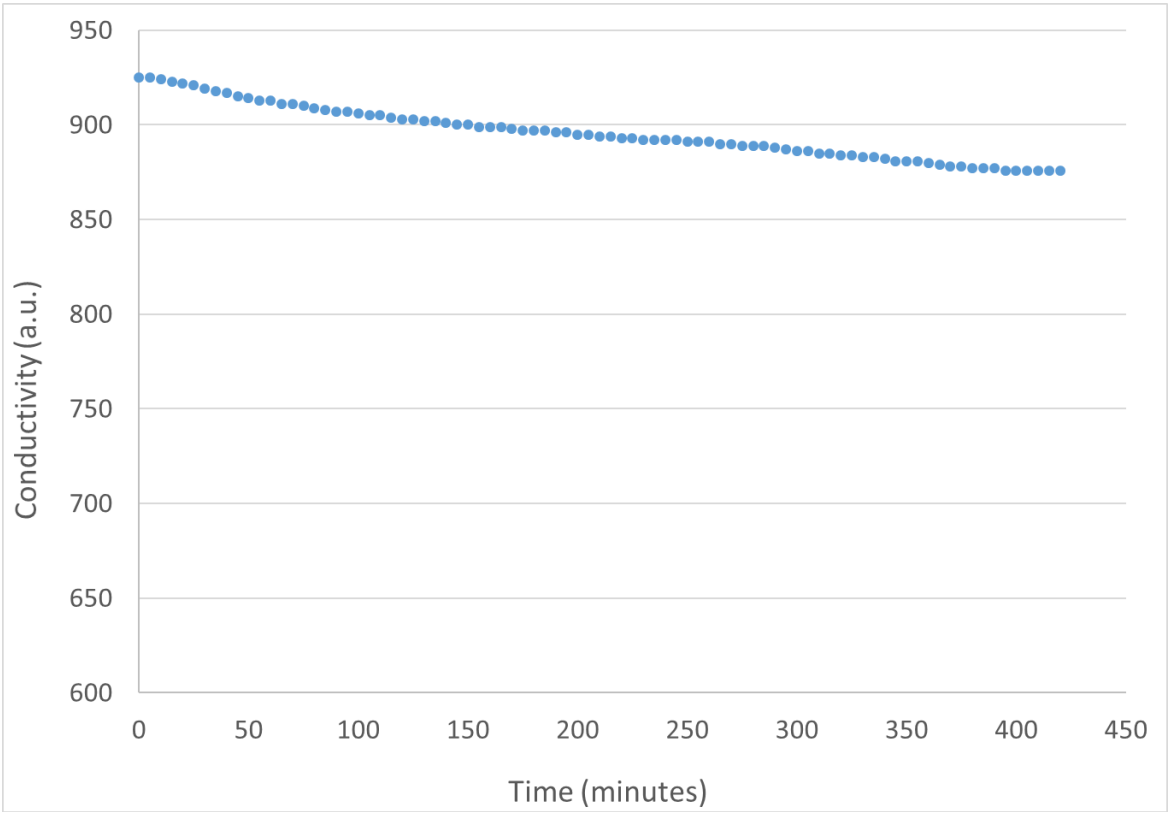

Figure 23: Conductivity profile for $Ni_2Mo_3C_xN_y$ reacted with 3:1 H_2/Ar at 900°C for 7 hours.

The XRD pattern in Figure 24 shows that the filled β-Mn structure was maintained after the reaction. There does not appear to be any major change in phase compared to pre-reaction suggesting that the material was not reduced under these conditions. The very minor Mo_2N phase present in the material was reduced to Mo metal during the reaction as evidenced by the XRD pattern post-reaction. The XRD pattern confirms that the bulk lattice nitrogen in Ni_2Mo_3N was fairly unreactive under these conditions.

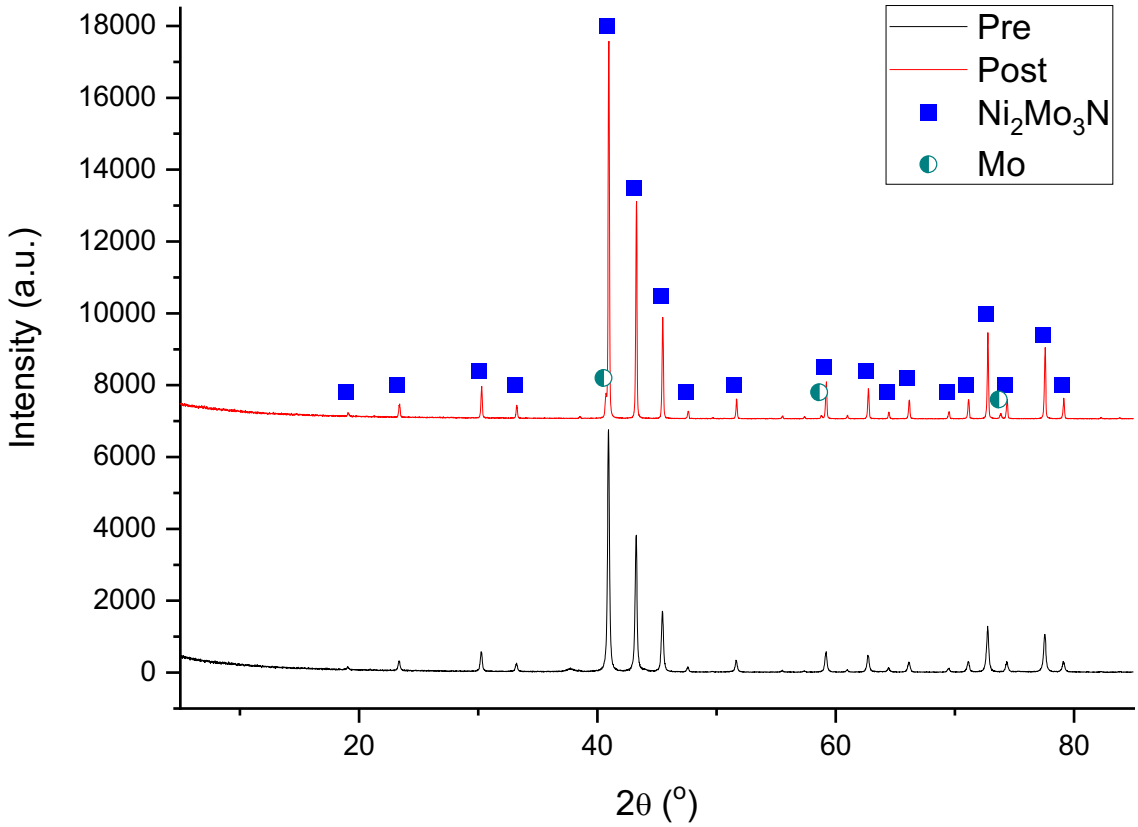

Figure 24: Comparison of XRD patterns for Ni_2Mo_3N pre- and post-reaction with 3:1 H_2/Ar at 900°C for 7 hours. Reflections marked: ■ Ni_2Mo_3N (JCPDS file number 01-089-4564) and ◐ Mo (JCPDS file number 01-089-5023).

Figure 25 illustrates that there was no lattice shift between the pre- and post-reaction samples. This is consistent with the results published in the literature for Ni_2Mo_3N tested under Ar/H_2 up to 700°C [36] [92].

The elemental analysis shows that the percentage of nitrogen present in the material after reduction with 1:3 Ar/H_2 had slightly decreased (C: 0.00 wt. %, H: 0.00 wt. % and N: 3.94 wt. %) compared to pre-reaction (4.58 wt. %). The percentage of nitrogen present in the material was still higher than the expected stoichiometric value of 3.34 wt. %. The decrease in nitrogen could be due to the reduction of the β-Mo_2N to molybdenum or the loss of some surface nitrogen from nickel molybdenum nitride. Assuming the loss of

nitrogen was solely due to the Ni_2Mo_3N, the percentage of lattice nitrogen lost that was converted to ammonia was 34.22%.

Ni_2Mo_3N and Co_3Mo_3N display very different behaviour with respect to one another under Ar/H_2 treatment. This may be explained by the difference in structure type or composition between these two nitrides and the origin of this difference will be explored further in this thesis.

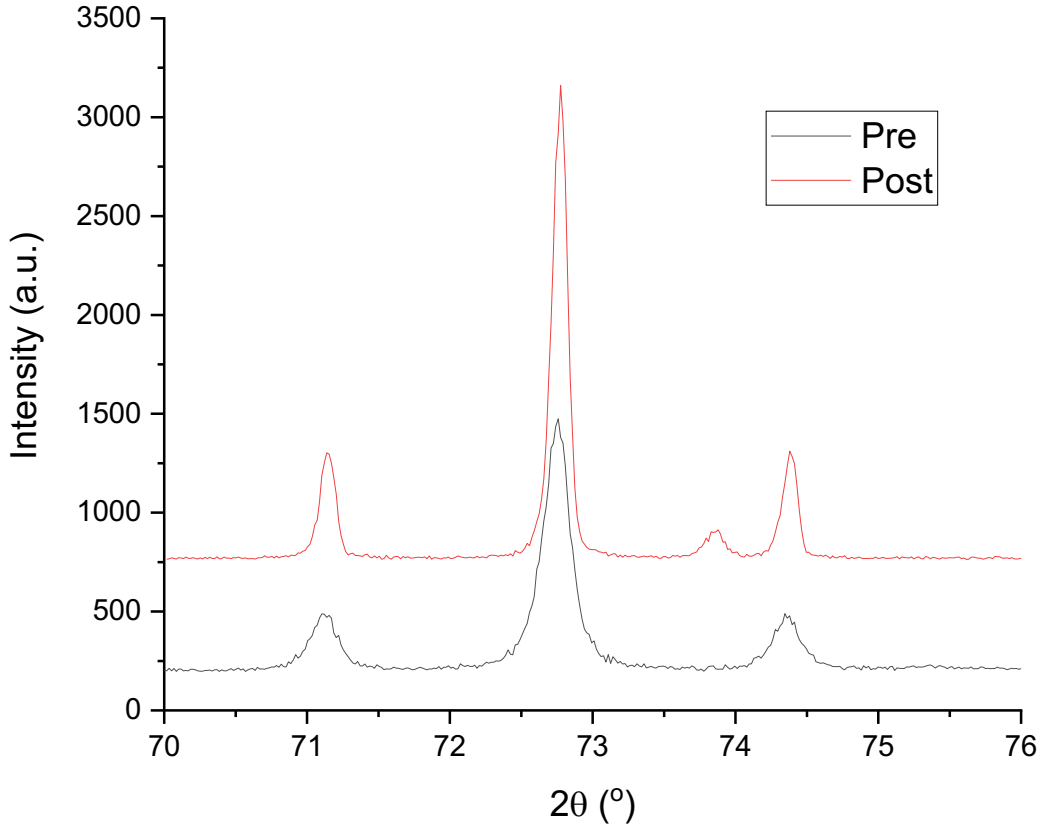

Figure 25: Comparison of XRD patterns between Ni_2Mo_3N pre- (black) and post-reaction (red) with 3:1 H_2/Ar at 900°C for 7 hours.

SEM analysis was conducted in order to investigate if there was any change in morphology of Ni_2Mo_3N during the reaction. Figure 26 displays characteristic SEM images at different magnifications of the post-reaction Ni_2Mo_3N. The sample consisted of porous particles with pores ranging in diameter from 0.5 μm to 10 μm. The crystallite shape and size had been retained compared to pre-reaction. However, there appeared to be smaller pores in the particles.

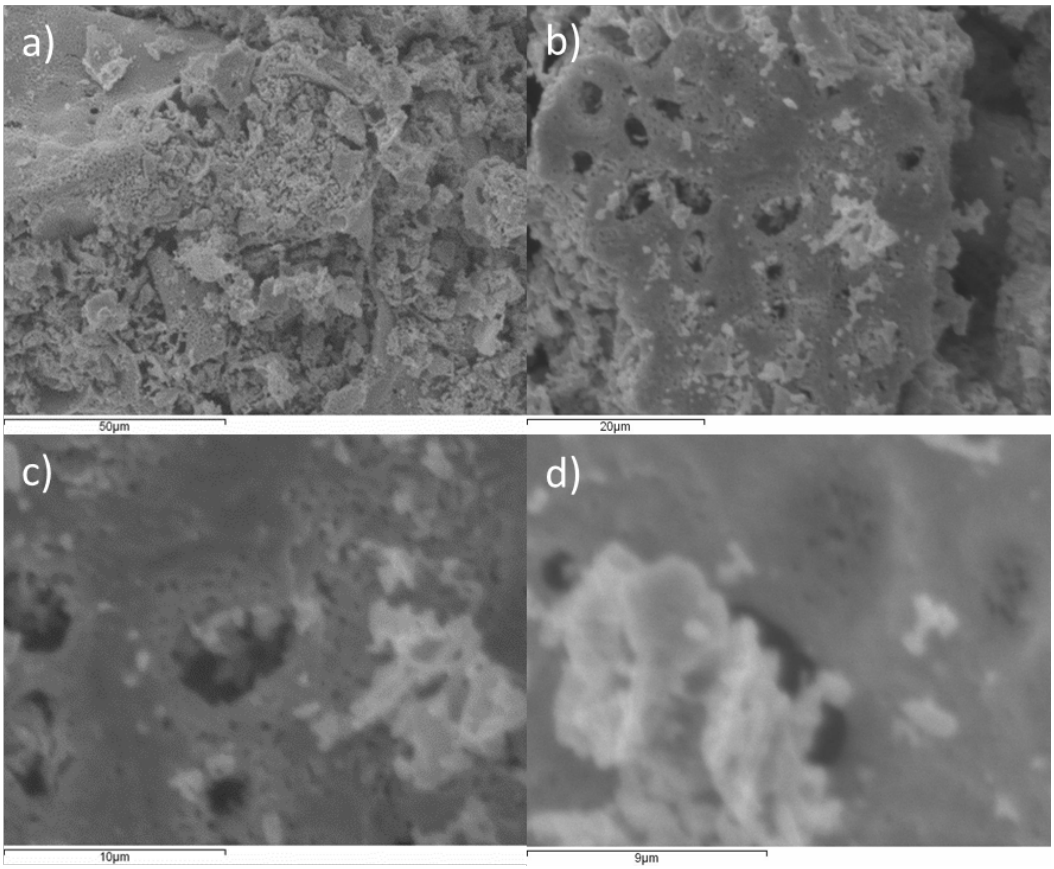

Figure 26: SEM images of nickel molybdenum nitride (Ni_2Mo_3N) post-reaction with 3:1 H_2/Ar at 900°C. a) 1000x magnification, b) 2000x magnification, c) 5000x magnification and d) 6000x magnification.

The nickel, molybdenum and nitrogen appear to have been evenly distributed across the material as evidenced by the element maps in Figure 27. This confirms that there had been no phase separation under the reducing conditions.

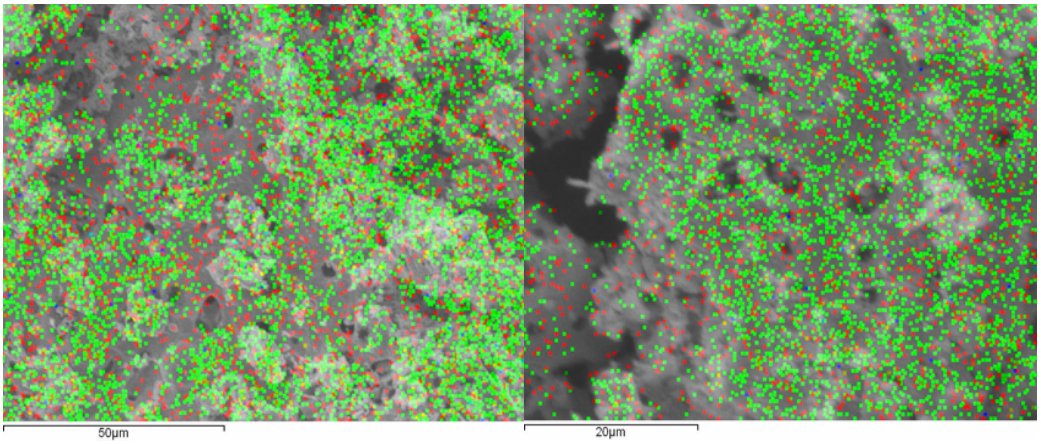

Figure 27: Element Maps for Ni_2Mo_3N post-reaction with 3:1 H_2/Ar at 900°C. Elements: Ni (red), Mo (green) and N (blue).

The EDX analysis for the post-reaction sample is presented in Table 3. The stoichiometric percentage of nickel, molybdenum and nitrogen for Ni_2Mo_3N is 28.00 wt. %, 68.66 wt. % and 3.34 wt. % respectively, as stated previously. The nitrogen weight percentage from

EDX was much lower than the predicted stoichiometric value and the result obtained from CHN analysis. However, there are limitations to EDX for measuring light elements. The percentage of nickel was higher than expected and therefore the mass ratio of Ni to Mo was higher than predicted for Ni_2Mo_3N. This is in contrast to the XRD pattern, which showed that the Ni_2Mo_3N phase had been retained post-reaction.

Area	Ni weight (%)	Mo weight (%)	N weight (%)	O weight (%)
1	33	58	9	0
2	31	69	0	0
3	31	69	0	0
4	42	58	0	0
5	36	64	0	0
6	32	68	0	0
7	63	37	0	0
8	41	59	0	0
9	30	70	0	0
10	29	71	0	0
11	25	70	5	0
12	33	61	6	0
13	36	64	0	0
14	35	65	0	0
15	38	62	0	0
16	40	60	0	0
17	30	70	0	0
18	28	72	0	0
19	30	70	0	0
Average	35	64	1	0

Table 3: EDX values for nickel molybdenum nitride (Ni_2Mo_3N) post-reaction with 3:1 H_2/Ar at 900°C.

3.2.1.3 Nickel Molybdenum Carbide (Ni_2Mo_3C)

3.2.1.3.1 Preparation with 20% CH_4/H_2

In order to have a greater understanding on the role lattice nitrogen plays in the ammonia synthesis activity of Ni_2Mo_3N, determination of the reactivity of the corresponding isostructural carbide would be of interest. From this it may prove possible to determine the influence phase composition has upon ammonia synthesis performance. Similar studies have been undertaken for the Co_3Mo_3N/Co_3Mo_3C system [54]. Although, the reactivity of lattice nitrogen in Ni_2Mo_3N has been shown to be very low, it has been observed and the topotactic replacement of the nitrogen with carbon to form a nickel molybdenum carbonitride has been reported in the literature [67].

The activity of Ni_2Mo_3N could be explained by Norskov's volcano plot [24], which states that the combination of Mo, which binds N_2 strongly and Ni, which binds N_2 weakly,

results in a suitable binding energy for N_2 to give high ammonia synthesis activity. The lattice nitrogen is assumed to be non-reactive in this explanation and therefore, Ni_2Mo_3C would be expected to display similar performance to its nitride counterpart.

Preparation of Ni_2Mo_3C was attempted initially via carburisation of Ni_2Mo_3N with 20% CH_4/H_2. The pure phase carbide was not produced under these conditions, with instead the material decomposing at high temperatures. The optimum preparation temperature was found to be 560 °C, which produced a carbonitride phase containing 1.42 wt. % carbon and 1.93 wt. % nitrogen as shown in Table 4. When the temperature was increased above 560°C, with the intention of substituting more of the lattice nitrogen with carbon, the material began to decompose. At temperatures above 600°C, the material fully decomposed to give mixed phases of Ni and α-Mo_2C as demonstrated in Figure 28. The decomposition of the material observed agrees with what has been reported in the literature [62] [65]. The formation of a nickel molybdenum carbonitride phase has been reported by Alconchel et al. [67], who formed the phase by carburisation of Ni_2Mo_3N with CH_4/H_2/Ar gas mixture at 650°C.

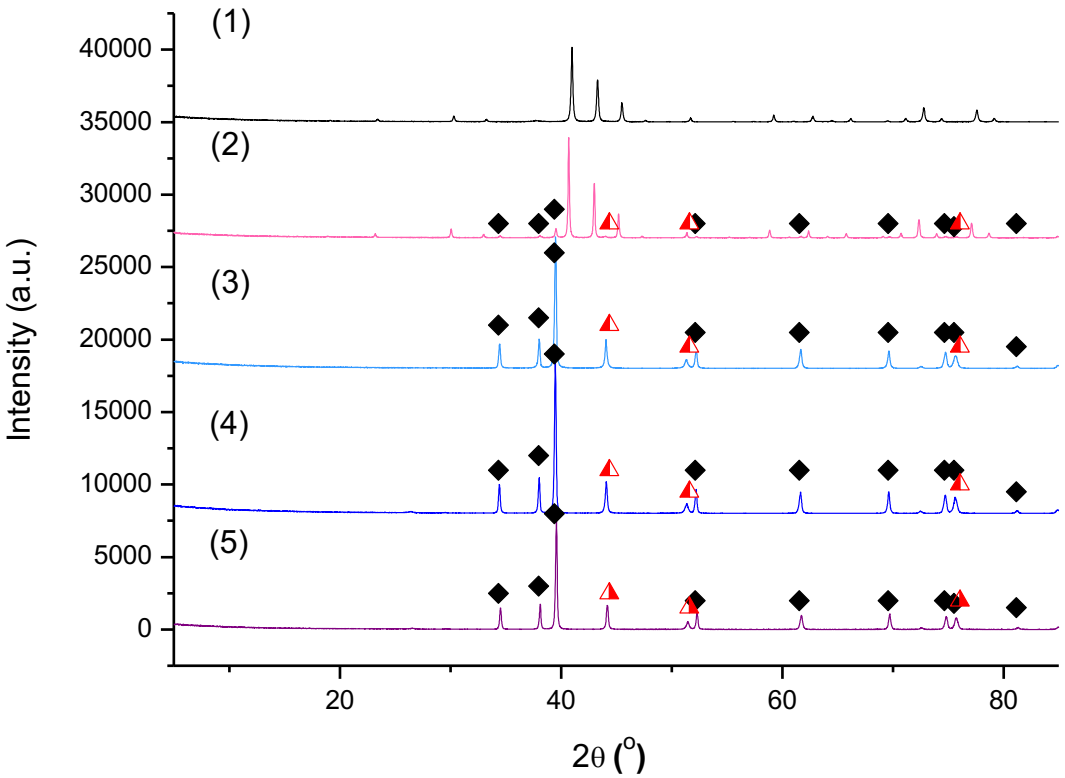

Figure 28: XRD patterns of nickel molybdenum materials prepared at different carburisation temperatures with 20% CH_4/H_2: (1) 560°C, (2) 600°C, (3) 650°C, (4) 700°C and (5) 725°C. Reflections marked: ◆ α-Mo_2C (JCPDS file number 00-035-0787) and ◭ Ni (JCPDS file number 00-001-1258).

Material	Carbon Content from Elemental Analysis (wt. %)	Hydrogen Content from Elemental Analysis (wt. %)	Nitrogen Content from Elemental Analysis (wt. %)
560°C	1.42	0.00	1.93
600°C	1.98	0.00	1.00
650°C	3.93	0.00	0.05
700°C	11.80	0.01	0.00
725°C	11.39	0.01	0.01

Table 4: Elemental Analysis for the nickel molybdenum materials prepared at different carburisation temperatures with 20% CH_4/H_2.

SEM was conducted to investigate the effect carburisation had on the morphology. The SEM results of the nickel molybdenum materials prepared at different carburisation temperatures are shown in Figure 29. As can be seen, the morphology of the materials was similar, even though the higher temperature materials decomposed. The BET surface area was observed to decrease as the carburisation temperature increased as shown in Table 5.

Material	Surface Area (m^2/g)	Pore Volume (cc/g)	Average Pore Radius (Å)
560°C	9	0.10	22.94
650°C	7	0.05	15.90
700°C	7	0.05	17.86
725°C	5	0.08	20.20

Table 5: BET surface area, pore volume and average pore radius for the nickel molybdenum materials prepared at different carburisation temperatures with 20% CH_4/H_2.

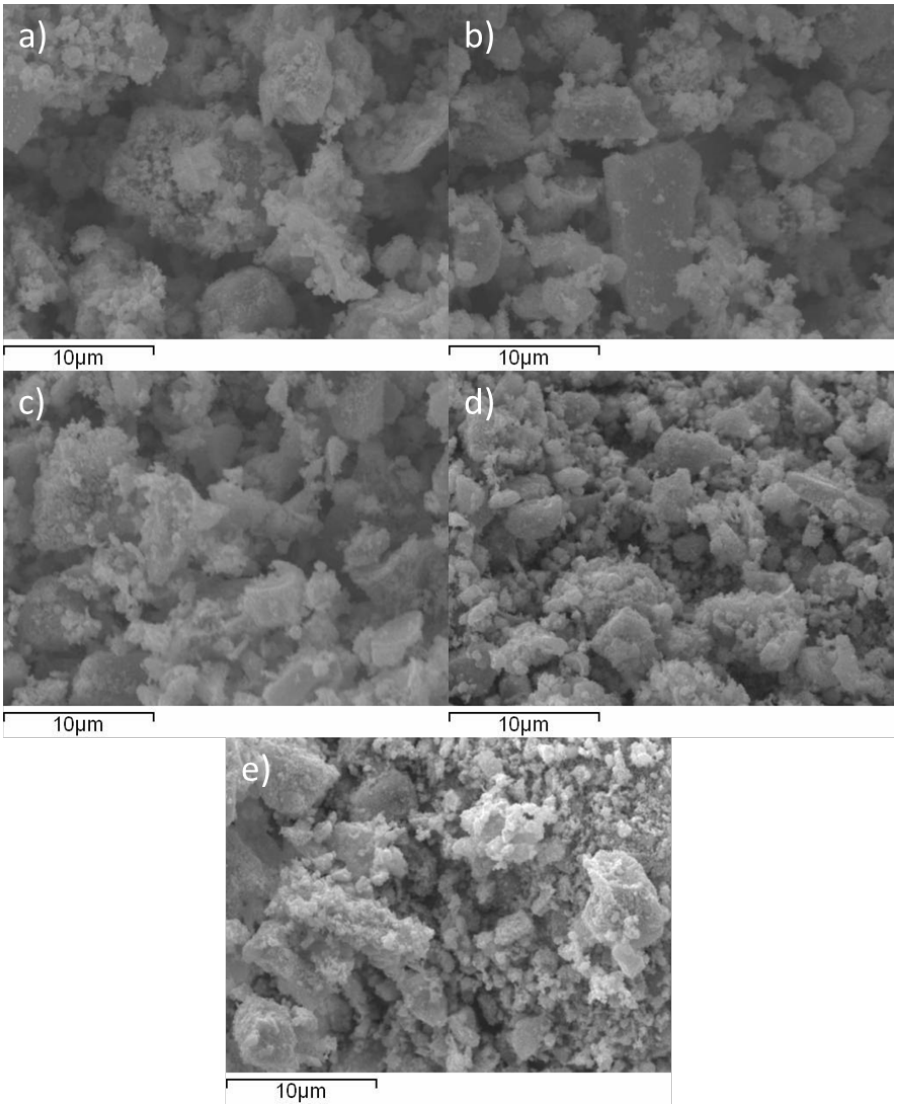

Figure 29: SEM images of nickel molybdenum materials prepared at different carburisation temperatures with 20% CH_4/H_2: a) 560°C, b) 600°C, c) 650°C, d) 700°C and e) 725°C. All of the images were taken at 4000x magnification.

The element maps in Figure 30 show the phase separation as the carburisation temperature increases. In Figure 30 (a), the nickel and molybdenum appear to be fairly evenly distributed over the material. As the carburisation temperature was increased to 600°C, phase separation was apparent (Figure 30 (b)) with areas of molybdenum and nickel. This is the same at the higher carburisation temperatures. In Figure 30 (d), it can be seen that carbon is only located in areas where there was molybdenum present. This is consistent with the XRD patterns that show only the molybdenum has formed a carbide phase whereas Ni was present as Ni metal.

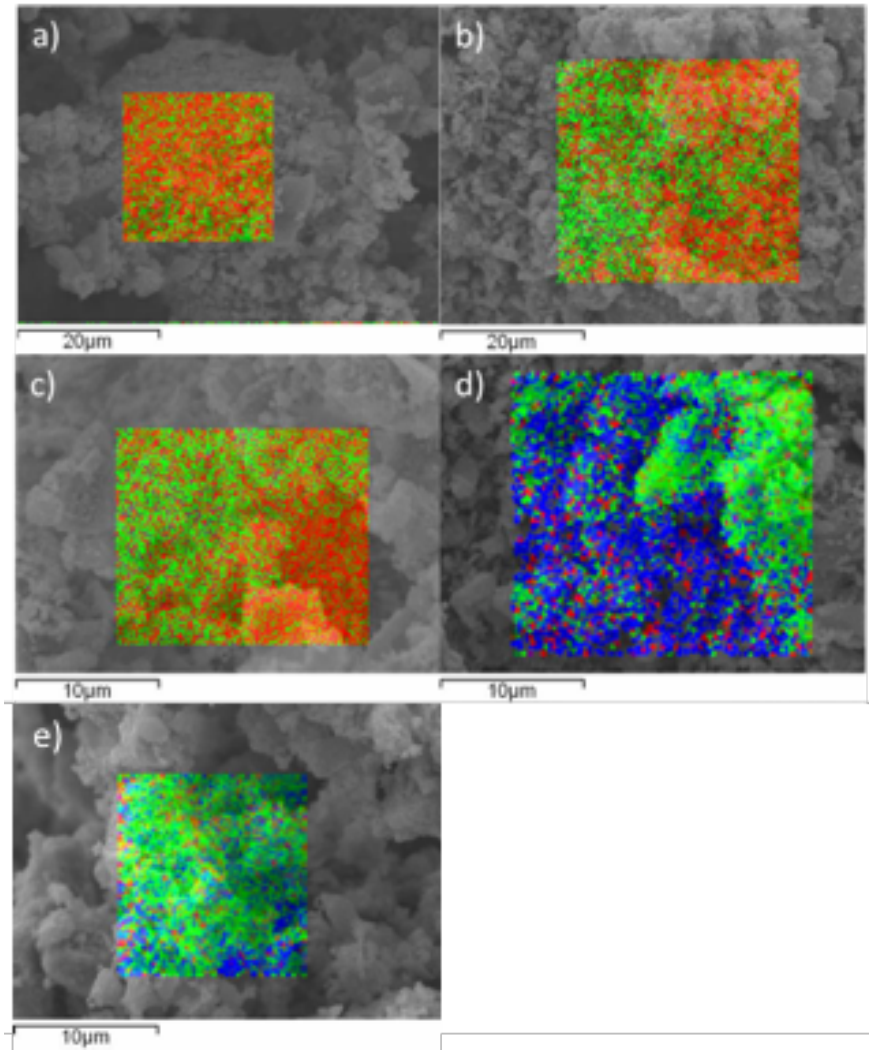

Figure 30: Element Maps for nickel molybdenum materials prepared at different carburisation temperatures with 20% CH_4/H_2. Elements: Ni (green), Mo (red) and C (blue). a) 560°C, b) 600°C, c) 650°C, d) 700°C and e) 725°C.

The EDX results show that the molybdenum weight percentage decreased as the carbon content increased as observed in Table 6. However, care needs to be taken as the samples were not homogeneous and EDX is semi-quantitative. The stoichiometric percentage of nickel, molybdenum and nitrogen for Ni + Mo_2C (assuming a Ni:Mo ratio of 2:3) is 27.74 wt. %, 68.01 wt. % and 4.26 wt. %, respectively. There is no nitrogen present in the material after carburisation temperature at 650°C, which agrees with the CHN analysis. Areas with more nickel content have a lower percentage of carbon (EDX tables provided in Appendix II). This is consistent with the XRD and element maps that show the nickel has not formed a carbide phase. The percentages of carbon were higher than expected and there did not appear to be any evidence for carbon in the XRD patterns. However, the EDX measurements are semi-quantitative and restrictive for light elements.

Area	Ni weight (%)	Mo weight (%)	C weight (%)	N weight (%)
560°C Average	24	54	17	5
600°C Average	28	51	19	1
650°C Average	24	54	22	0
700°C Average	24	43	33	0
725°C Average	19	43	38	0

Table 6: EDX values for nickel molybdenum materials prepared at different carburisation temperatures with 20% CH_4/H_2

3.2.1.3.2 Preparation with 30% CH_4/H_2

In order to prepare a pure phase bimetallic carbide, the methane content of the gas feed was increased to 30% CH_4/H_2. From section 3.2.1.3.1, it can be seen that higher temperatures may be required in order to replace all of the lattice nitrogen of Ni_2Mo_3N with carbon. The reaction was carried out the same way as for the materials prepared with the 20% CH_4/H_2. The carbide was prepared by carburisation of the nitride in 30% CH_4/H_2 at a flow rate of 12 mL/min. The material was heated to 350°C at a ramp rate of 6°C/min and then, the ramp rate was changed to 1°C/min to reach a final temperature of 650°C. The sample was kept at this temperature for two hours, then cooled down to room temperature under the CH_4/H_2.

The elemental analysis shows that carbon and nitrogen were present in the material after carburisation (C: 3.50 wt. %, H: 0.00 wt. % and N: 0.32 wt. %). The XRD pattern for the material post-carburisation is provided in Figure 31. It can be seen that there are still peaks relating to a nickel molybdenum phase in this material, suggesting that the material has not completely decomposed under these conditions. When the nitride was carburised with 20% CH_4/H_2 at the same temperature, the material had completely decomposed as observed in its XRD pattern (Figure 28). Therefore, the material did not decompose as much when there was a higher methane percentage in the gas feed. However, the ternary carbide phase was not formed under 30% CH_4/H_2 and the material had started to decompose at 650°C carburisation temperature. The carburisation temperature could be lowered in order to try and form the carbide and prevent the observed decomposition. However, as nitrogen was still present in the material at 650°C, this would suggest that at lower carburisation temperature, the carbonitride would be formed. Thus, the pure carbide phase cannot be formed under 30% CH_4/H_2 in the procedure adopted.

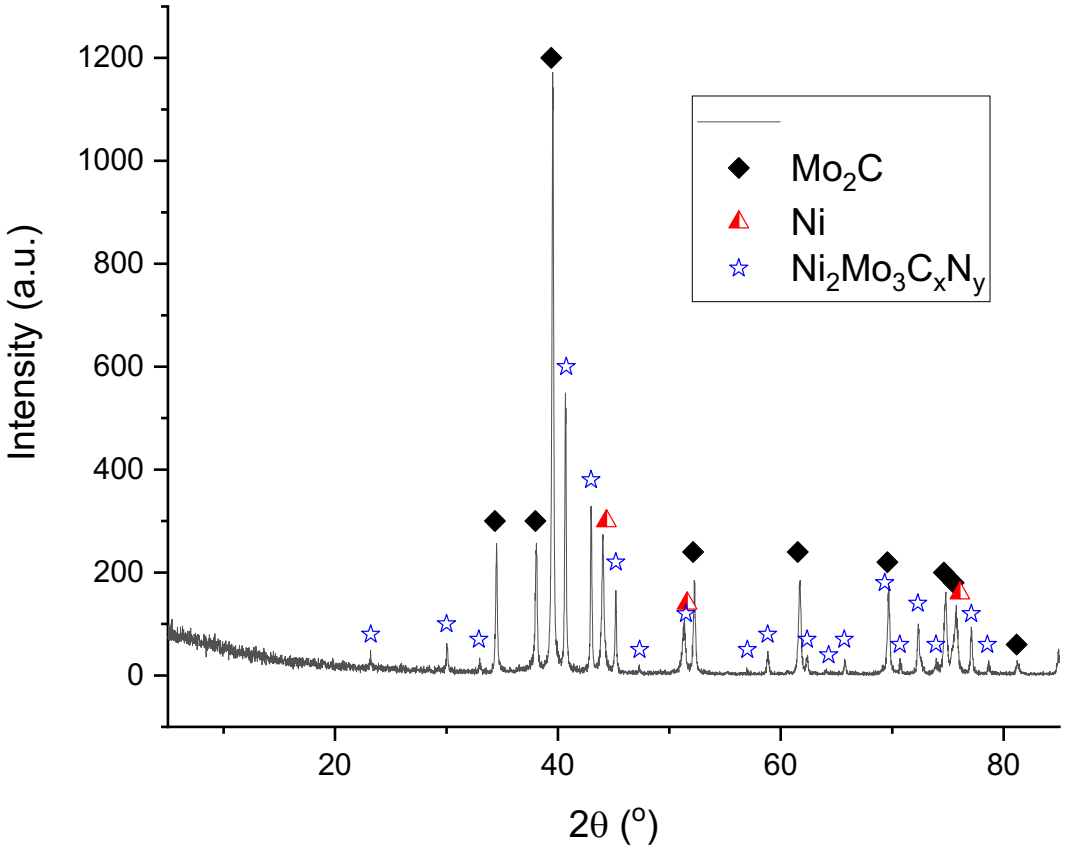

Figure 31: XRD pattern of the nickel molybdenum material prepared at 650°C carburisation temperature with 30% CH_4/H_2. Reflections marked: ◆ α-Mo_2C (JCPDS file number 00-035-0787) and ◭ Ni (JCPDS file number 00-001-1258).

SEM images of the material post-carburisation are displayed in Figure 32. The morphology of the sample was similar to the morphology of the materials prepared under 20% CH_4/H_2 (Figure 29).

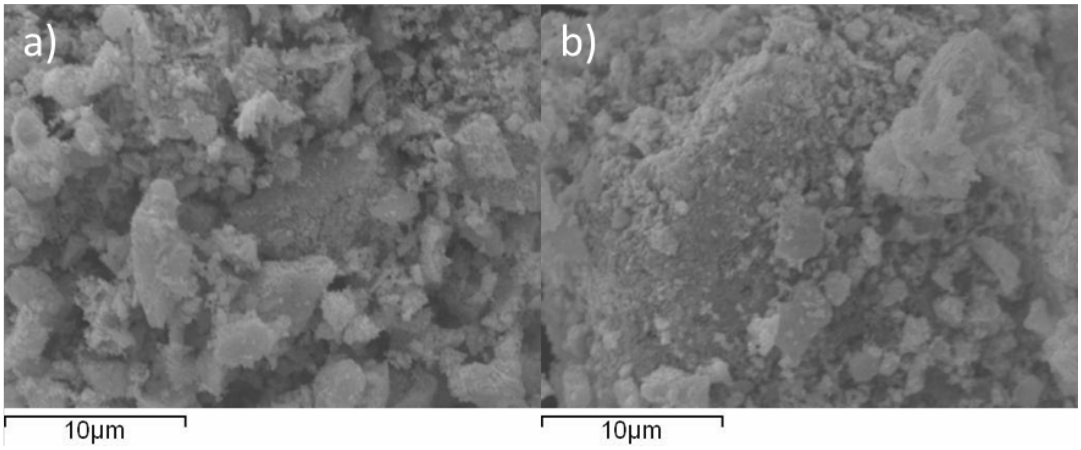

Figure 32: SEM images of nickel molybdenum material prepared at 650°C carburisation temperature with 30% CH_4/H_2. Both images were taken at 4000x magnification.

The element map also shows the phase segregation between the nickel and molybdenum as displayed in Figure 33. The average EDX values for this material were 25 wt. %, 50 wt. % and 25 wt. % for nickel, molybdenum and carbon respectively. There was no nitrogen

detected in the areas that were examined. This is in disagreement with the CHN analysis, which showed that 0.32 wt. % of nitrogen was present. However, it needs to be borne in mind that detecting light elements by EDX can be problematic.

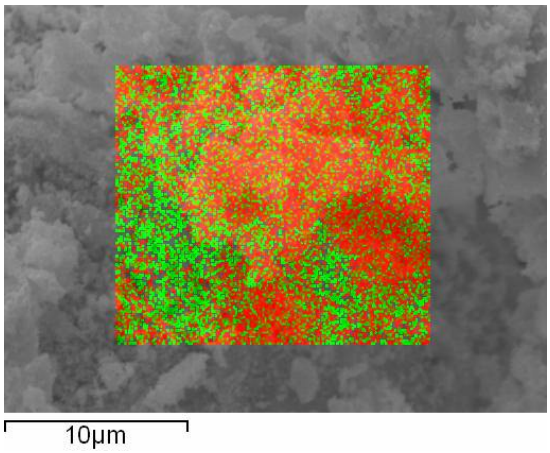

Figure 33: Element Map for nickel molybdenum material prepared at 650°C carburisation temperature with 30% CH_4/H_2. Elements: Ni (red) and Mo (green).

3.2.1.3.3 Preparation with Pure C_2H_6

Methane was substituted with ethane to investigate the effect a more reactive source of carbon had on obtaining pure phase Ni_2Mo_3C from Ni_2Mo_3N. The material was prepared by carburisation of the nitride in C_2H_6 at 500°C, 550°C and 575°C. The XRD patterns for these materials are displayed in Figure 34. However, this proved unsuccessful with a carbonitride phase being formed instead as seen from the elemental analysis presented in Table 7. Only 30% of the lattice nitrogen was removed from the materials at all three temperatures tested and the stoichiometries of the carbonitrides formed are shown in Table 8.

Material	Carbon Content from Elemental Analysis (wt. %)	Hydrogen Content from Elemental Analysis (wt. %)	Nitrogen Content from Elemental Analysis (wt. %)
500°C	1.02	0.00	2.41
550°C	1.17	0.00	2.33
575°C	1.32	0.00	2.32

Table 7: Elemental Analysis for the nickel molybdenum materials prepared at different carburisation temperatures with C_2H_6.

Material	Proposed Stoichiometry
500°C	$Ni_2Mo_3C_{0.35}N_{0.72}$
550°C	$Ni_2Mo_3C_{0.41}N_{0.70}$
575°C	$Ni_2Mo_3C_{0.46}N_{0.69}$

Table 8: Stoichiometry proposed for the bulk sample for nickel molybdenum materials prepared at different carburisation temperatures with C_2H_6.

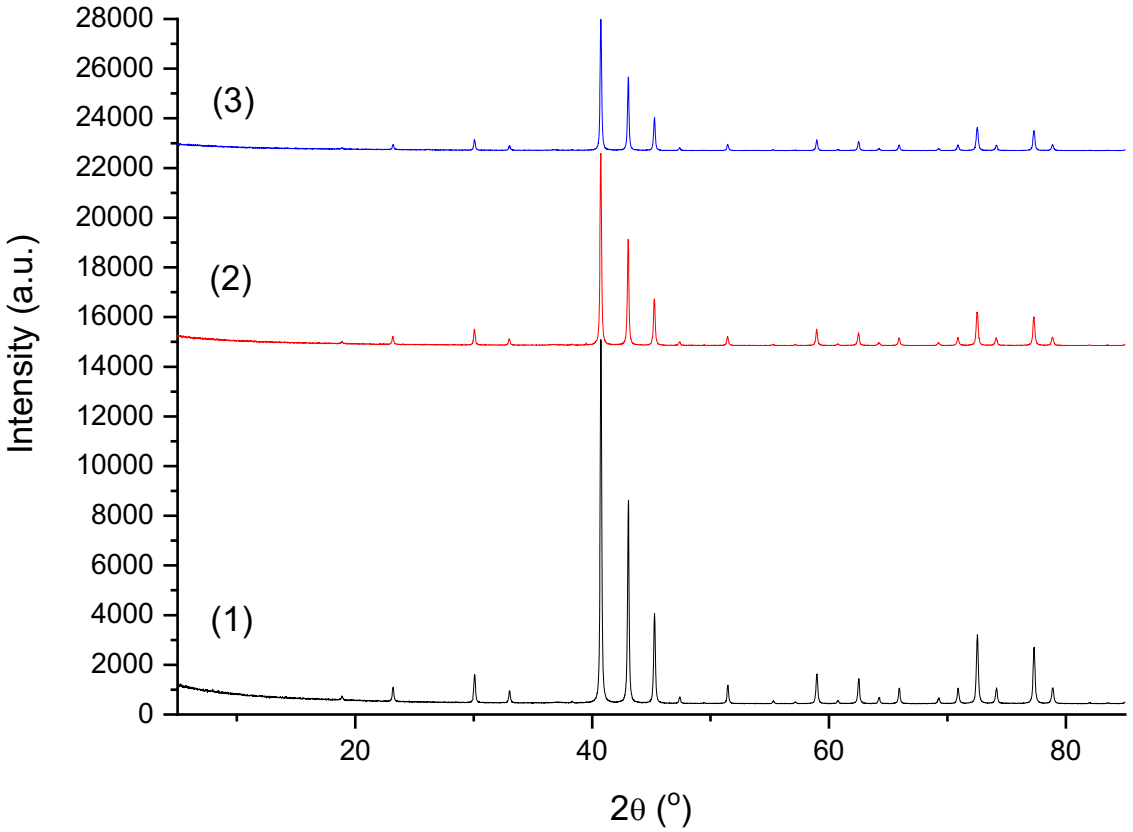

Figure 34: XRD patterns of nickel molybdenum materials prepared at different carburisation temperatures with C_2H_6: (1) 500°C, (2) 550°C and (3) 575°C.

As can be seen in Figure 35, there was almost no shift in peak positions between the three samples. This suggests that lattice nitrogen was not being substituted by more carbon at the higher temperature.

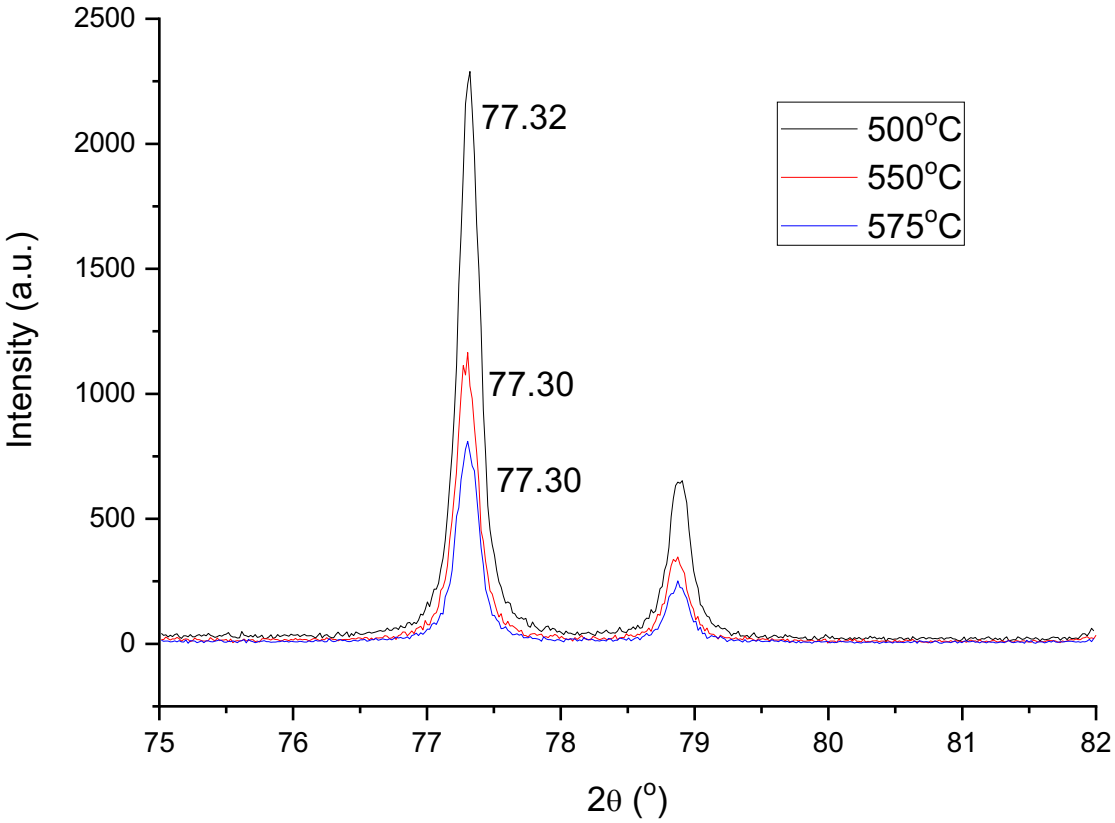

Figure 35: Comparison of XRD patterns for nickel molybdenum materials prepared at different carburisation temperatures with C_2H_6: 500°C (black), 550°C (red) and 575°C (blue).

3.2.1.3.4 Preparation with 10% C_2H_6/H_2

Due to the inability to form the nickel molybdenum carbide under pure ethane, hydrogen was added to the feed stream to assist with the carbide formation. The material was prepared by carburisation of Ni_2Mo_3N in 10% C_2H_6/H_2 at a flow rate of 12 mL/min at 520°C, 560°C and 610°C. From the XRD patterns in Figure 36, it can be seen that the resulting material at 560°C was similar to the material carburised under 20% CH_4/H_2 at the same temperature. However, at the carburisation temperature of 610°C, it can be seen that the material possessed a higher relative intensity of molybdenum carbide and nickel reflections compared to the material carburised at 600°C under 20% CH_4/H_2. This suggests that more of the material had decomposed under the ethane atmosphere. This is consistent with what would be expected. According to literature, ethane lowers the temperature at which the carbide is formed [100] [101] [102]. The formation of a pure phase Ni_2Mo_3C was unsuccessful when an ethane and hydrogen gas mixture was applied to the nitride. Instead, the nickel molybdenum carbonitride was formed as was the case when methane was used as the carbon source.

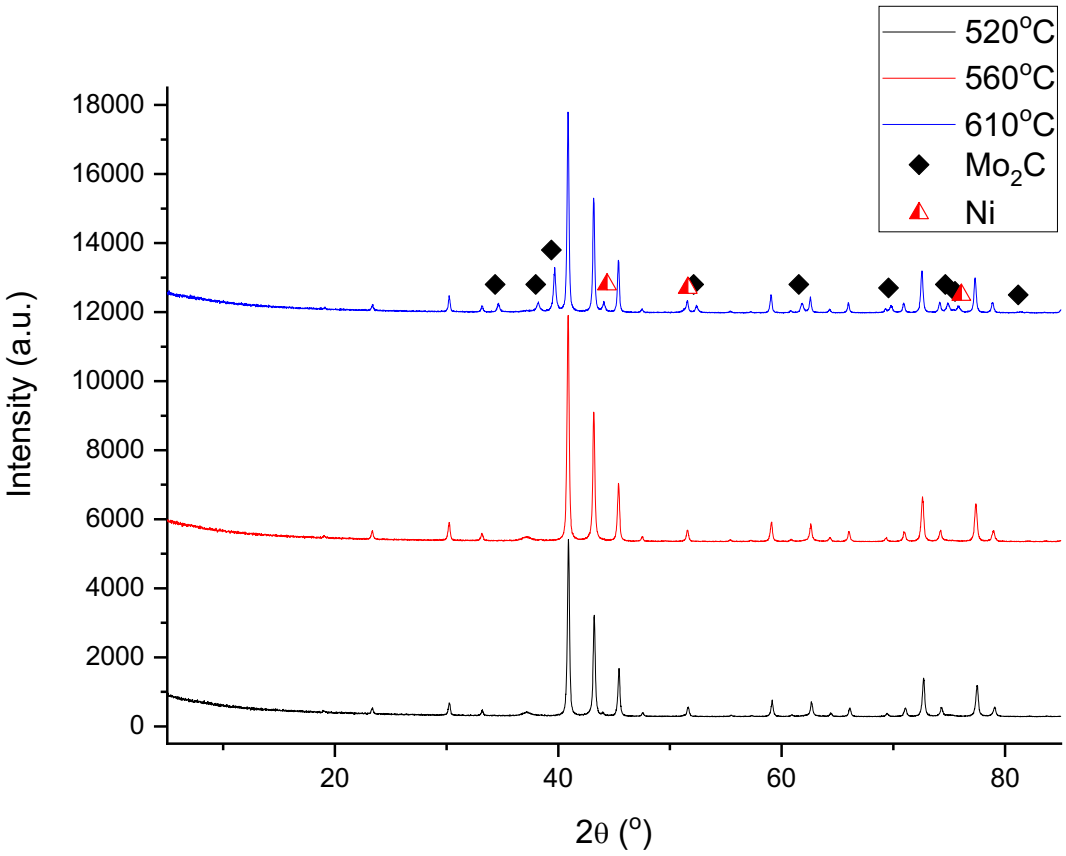

Figure 36: XRD patterns of nickel molybdenum materials prepared at different carburisation temperatures with 10% C_2H_6/H_2: 520°C (black), 560°C (red) and 610°C (blue). Reflections marked: ◆ α-Mo_2C (JCPDS file number 00-035-0787) and ◭ Ni (JCPDS file number 00-001-1258).

The stoichiometries proposed for the bulk samples prepared at 520°C and 560°C were $Ni_2Mo_3C_{0.20}N_{0.66}$ and $Ni_2Mo_3C_{0.43}N_{0.66}$ respectively, as predicated from the elemental analysis shown in Table 9. The sample carburised at 610°C contains Mo_2C and therefore, this contributes to the carbon content and a stoichiometry relating to a ternary phase cannot be proposed. The material prepared at 560°C under 20% CH_4/H_2 had a stoichiometry of $Ni_2Mo_3C_{0.49}N_{0.58}$. The sample prepared with 10% C_2H_6/H_2 would be expected to contain more carbon due to the ethane lowering the temperature for carburisation. From elemental analysis and the proposed stoichiometry, it is seen that this is not the case. However, when comparing the 600°C carburised materials it can be observed that more carbon is present for the material carburised with 10% C_2H_6/H_2.

Material	Carbon Content from Elemental Analysis (wt. %)	Hydrogen Content from Elemental Analysis (wt. %)	Nitrogen Content from Elemental Analysis (wt. %)
520°C	0.59	0.07	2.19
560°C	1.23	0.13	2.20
610°C	2.26	0.05	0.92

Table 9: Elemental Analysis for the nickel molybdenum materials prepared at different carburisation temperatures with 10% C_2H_6/H_2.

A comparison of the XRD patterns of the materials carburised at 560°C with 20% CH_4/H_2, pure C_2H_6 and 10% C_2H_6/H_2 are presented in Figures 37 and 38. It must be noted that the nitride carburised with pure ethane was reacted at a lower temperature of 550°C. When comparing the shift in peak positions, it can be seen that the material carburised with 10% C_2H_6/H_2 had the smallest shift to lower 2θ values. When consideration is given to the relative atomic radii of N and C with C being larger, this is in contrast with the elemental analysis that showed the material carburised with pure ethane had the lowest amount of carbon present and therefore, would be expected to have the smallest shift in peak positions. However, the carbon values from elemental analysis for the materials prepared under C_2H_6 and 10% C_2H_6/H_2 are within experimental error, as observed in Table 10. This lower shift in peak position for the material carburised with 10% C_2H_6/H_2 suggests that not all the carbon may be incorporated into the lattice. Instead, some of the carbon may be laid down on the surface of the material. Although, there is no peak associated with graphitic carbon in the XRD pattern for this material, the carbon may be in a different form or in trace amounts that the XRD can't detect.

Material	Carbon Content from Elemental Analysis (wt. %)	Hydrogen Content from Elemental Analysis (wt. %)	Nitrogen Content from Elemental Analysis (wt. %)
20% CH_4/H_2	1.42	0.00	1.93
C_2H_6	1.17	0.00	2.33
10% C_2H_6/H_2	1.23	0.13	2.20

Table 10: Elemental Analysis for the nickel molybdenum materials prepared with 20% CH_4/H_2, C_2H_6 and 10% C_2H_6/H_2.

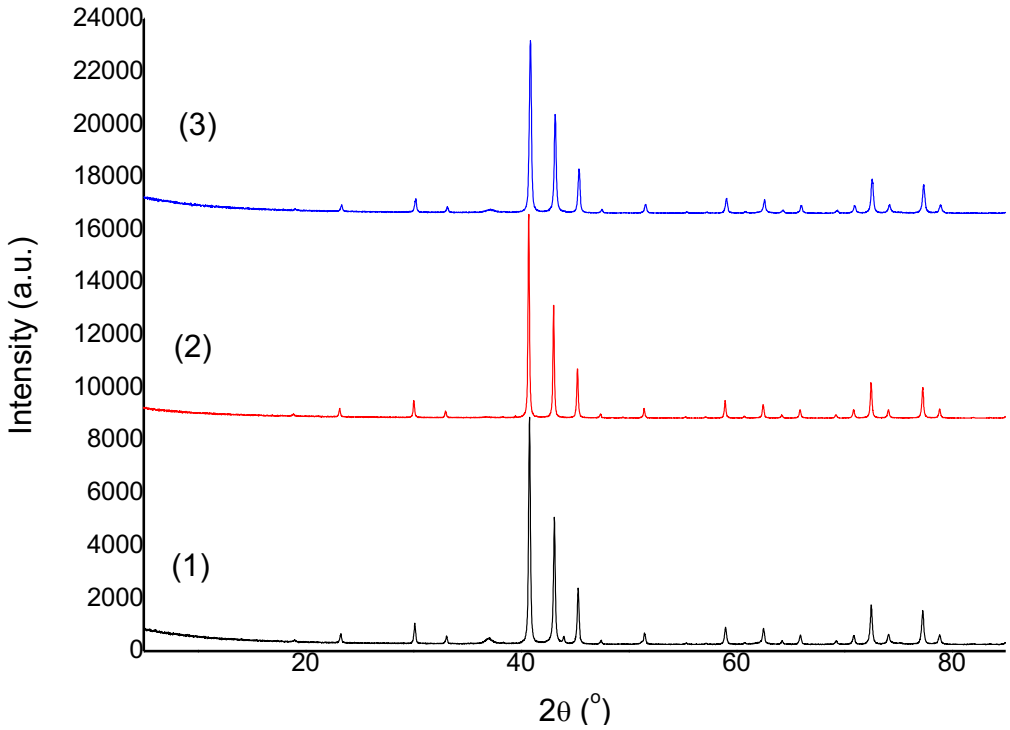

Figure 37: XRD patterns of nickel molybdenum materials prepared at 560°C with different carburisation sources: (1) 20% CH_4/H_2, (2) C_2H_6 (550°C) and (3) 10% C_2H_6/H_2.

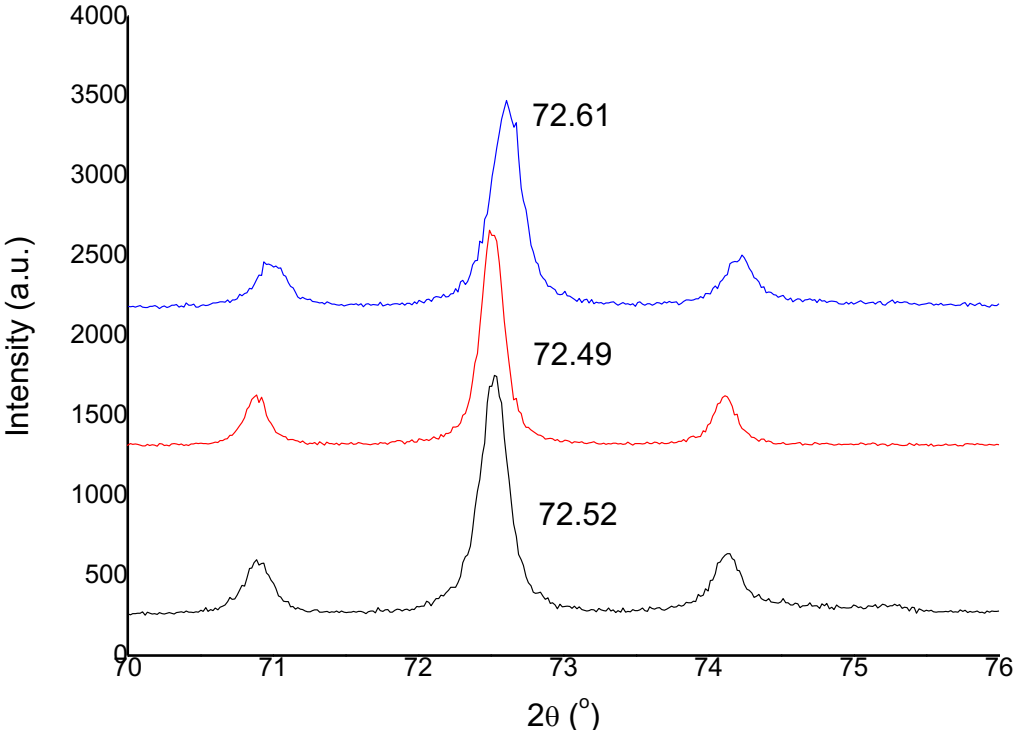

Figure 38: Comparison of XRD patterns for nickel molybdenum materials prepared at 560°C with different carburisation sources: 20% CH_4/H_2 (black), C_2H_6 (550°C, red) and 10% C_2H_6/H_2 (blue).

3.2.1.4 Nickel Molybdenum Carbonitride ($Ni_2Mo_3C_xN_y$)

As discussed in the introduction, the production of ammonia from Ni_2Mo_3N could be due to either a Mars van Krevelen mechanism, where lattice nitrogen is an active component, or the combination of nickel and molybdenum having a good binding energy for N_2.

Therefore, it is of interest to examine the behaviour of the carbonitride for ammonia synthesis and relate it to its nitride counterpart.

The carbonitride that was prepared with 20% CH_4/H_2 at 560°C was analysed further as it was the material that gave the highest apparent substitution of lattice nitrogen with carbon. It has been previously reported that the ratio of 20% CH_4/H_2 is the most efficient way of forming β-Mo_2C from MoO_3 [103]. From Figure 39, it can be seen that the material corresponds to the filled β-Mn structure. The identity of the impurity phase marked with a star in Figure 39 is currently unknown. Pattern matches with the JCPDS database were performed for β-Mo_2N, Mo_3N_2, Mo_5N_6, α-Mo_2C, β-Mo_2C and β-$Mo_{1.93}C_{0.96}$. However, none of these materials aligned with the peak at 37° 2θ. One possible suggestion for this impurity is that it was a molybdenum carbonitride phase due to the shift of the peak to lower 2θ values by 0.6016° 2θ from the position for β-Mo_2N.

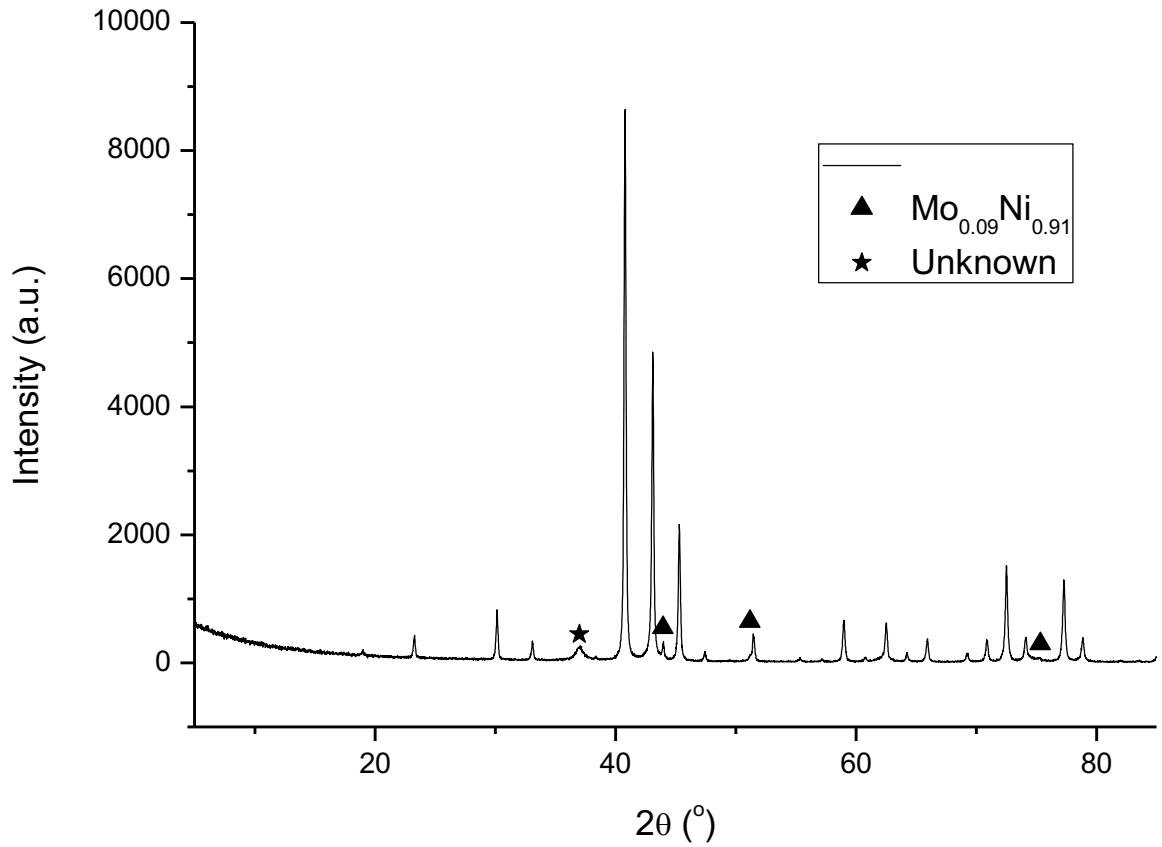

Figure 39: XRD pattern of nickel molybdenum carbonitride ($Ni_2Mo_3C_xN_y$). Reflections marked: ▲ $Mo_{0.09}Ni_{0.91}$ (JCPDS file number 01-071-9766), the peak marked with ★ is an unknown phase and the unmarked reflections are due to $Ni_2Mo_3C_xN_y$.

The elemental analysis shows that carbon and nitrogen were present in the material after carburisation (C: 1.42 wt. %, H: 0.00 wt. % and N: 1.93 wt. %). The expected stoichiometric value for carbon in Ni_2Mo_3C is 2.88 wt. %. The carbon content of the material was approximately half of the calculated stoichiometric value. The shift in peak

position compared to the nitride (Figure 40) and elemental analysis suggests that a carbonitride phase may have been formed. The stoichiometry proposed for the bulk sample is $Ni_2Mo_3C_{0.49}N_{0.58}$. From the stoichiometry, it is observed that the nitrogen content was higher than expected. This could be due to the possible molybdenum nitride phase contributing to the nitrogen percentage.

The absence of a peak at 25° 2θ suggests that the carbon was not present as graphitic carbon and had instead been incorporated into the bimetallic lattice.

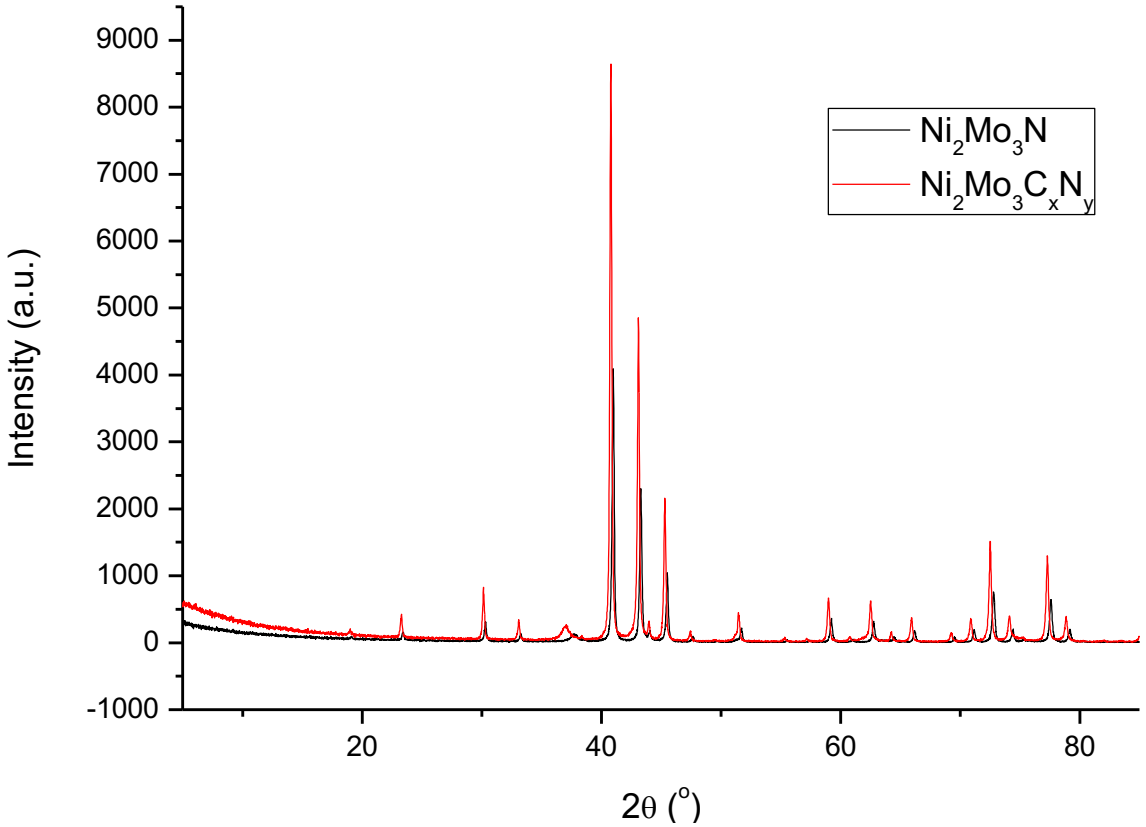

Figure 40: Comparison of XRD patterns for Ni_2Mo_3N and $Ni_2Mo_3C_xN_y$ showing the shift in reflections.

Raman spectroscopy was performed to investigate if there were any surface oxide species on the material. The Raman spectra were collected to 3000 cm^{-1} and there were no bands observed above 1000 cm^{-1}. The absence of D and G bands suggests that the carbon present in the material was not due to carbon laydown on the nitride but that it was instead incorporated into the lattice, which, as mentioned above, is consistent with the XRD results. The spectra are presented in Figure 41. As seen with Ni_2Mo_3N, the Raman spectra were different between the two different areas measured. Both areas show either the presence of α-$NiMoO_4$ or β-$NiMoO_4$, which is consistent with the formation of a surface oxide layer on the carbonitride. The bands at 368, 815, 888 and 936 cm^{-1} match well with the literature values for β-$NiMoO_4$ [96]. Raman bands at positions of approximately 953,

905 and 700 cm^{-1} were attributed to α'-$NiMoO_4$ [104]. Alconchel et al. [67] did not detect any bands in the Raman spectrum for their nickel molybdenum carbonitride. However, this group used a lower laser power (80 mW) compared to this study and also they did not state the filter percentage they used for taking Raman spectra.

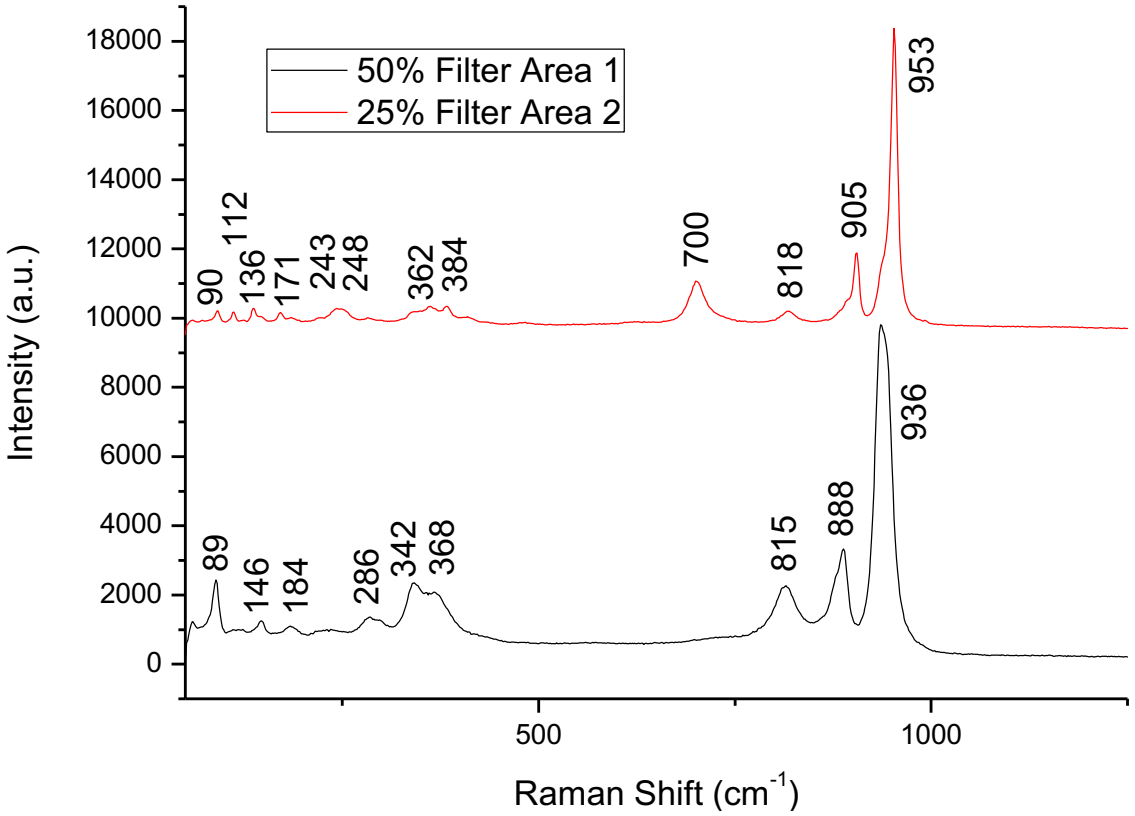

Figure 41: Raman spectra of nickel molybdenum carbonitride ($Ni_2Mo_3C_xN_y$). The two spectra were taken at different points of the material and either at 25% or 50% filter.

The ammonia synthesis activity of a material can be affected by its morphology and therefore, SEM analysis was performed for $Ni_2Mo_3C_xN_y$. Typical SEM images of $Ni_2Mo_3C_xN_y$ at different magnifications are presented in Figure 42. It can be seen that the carbonitride consisted of a porous structure and that the morphology had been retained from the nitride precursor. It has been previously reported that the conversion of Ni_2Mo_3N to the carbonitride is topotactic and pseudomorphic [67]. The topotactic production of carbides from their corresponding nitride has been reported for Co_3Mo_3C [54] [105], Fe_3Mo_3C [105], $Mo_2Ta_2C_x$, $Mo_3Nb_2C_x$ and $W_9Nb_8C_x$ [102]. Therefore, any difference in activity between Ni_2Mo_3N and the carbonitride is not due to a difference in morphology between the two materials.

The nickel molybdenum carbonitride had a surface area of 9 m^2/g, a pore volume of 0.10 cc/g and an average pore radius of 22.94 Å. The BET surface area had increased compared to the nitride, which had a value of 5 m^2/g. However, it must be noted that the measure of

very low surface areas using nitrogen as the adsorbate can give large inaccuracies. Therefore, it would be better to use krypton rather than nitrogen for BET surfaces areas that are small. Furthermore, as with the nitride, the formation of the oxide layer on the surface of the material may mean that the BET surface area value is inaccurate in the sense that it does not strictly conform to the material under operation.

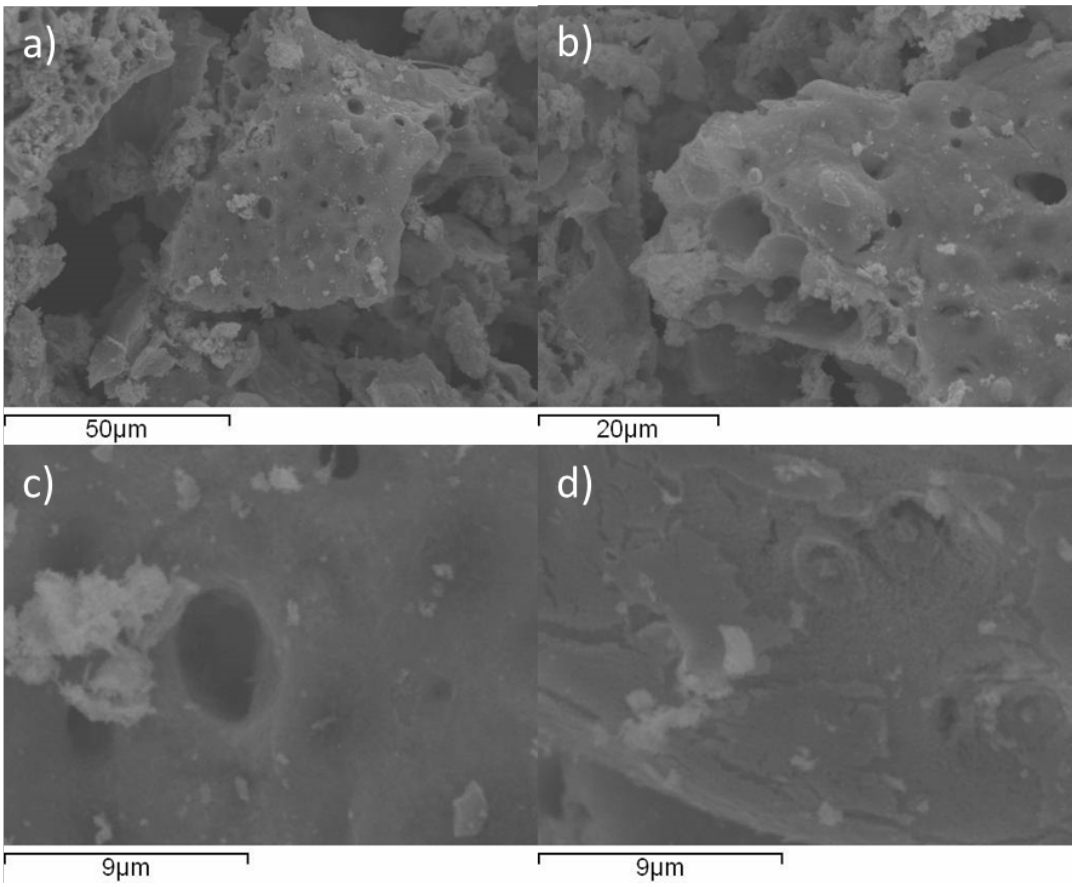

Figure 42: SEM images of nickel molybdenum carbonitride ($Ni_2Mo_3C_xN_y$). a) 1000x magnification, b) 2000x magnification, c) 6000x magnification and d) 6000x magnification.

The element map in Figure 43 illustrates that there was an even distribution of nickel and molybdenum over the sample and that there was more molybdenum present.

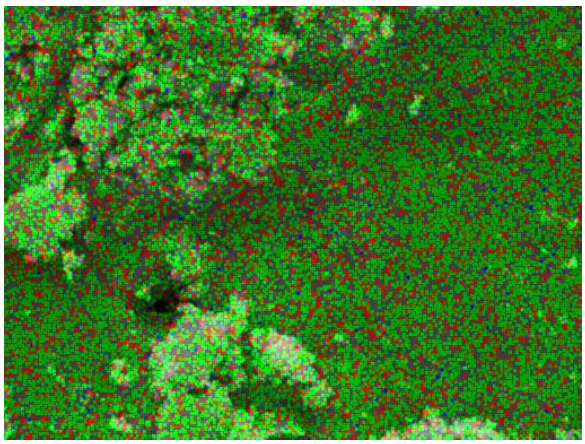

Figure 43: Element Map for $Ni_2Mo_3C_xN_y$. Elements: Ni (red) and Mo (green).

The weight percentages obtained from EDX for $Ni_2Mo_3C_xN_y$ are provided in Table 11. From CHN analysis, the stoichiometry calculated for the bulk sample is $Ni_2Mo_3C_{0.49}N_{0.58}$. Therefore, the stoichiometric percentage of nickel, molybdenum, carbon and nitrogen in the sample is 28.00 wt. %, 68.66 wt. %, 1.40 wt. % and 1.94 wt. % respectively. The carbon and nitrogen weight percentages were greater than the stoichiometric values expected for $Ni_2Mo_3C_{0.49}N_{0.58}$. However, EDX can be problematic in analysing light elements and also carbon stubs are used to mount the samples. The molybdenum percentage was lower than the expected stoichiometric value. However, EDX is semi-quantitative and therefore, these values may not be representative.

Area	Ni weight (%)	Mo weight (%)	C weight (%)	N weight (%)
1	25	50	23	2
2	22	53	16	9
3	25	57	15	3
4	30	48	20	3
5	22	40	34	4
6	27	49	20	4
Average	25	49	21	4

Table 11: EDX values for nickel molybdenum carbonitride ($Ni_2Mo_3C_xN_y$)

3.2.1.4.1 Ammonia Synthesis at 400°C for $Ni_2Mo_3C_xN_y$

The $Ni_2Mo_3C_xN_y$ was tested for ammonia synthesis activity at 400°C and atmospheric pressure under 3:1 H_2/N_2 atmosphere for 36 hours. This was performed to establish the influence the phase composition had upon ammonia synthesis activity. Performing the reaction at atmospheric pressure is not thermodynamically desirable. However, it is easier to follow the influence the transformation of phase has on the development of activity since it will be expected to occur on a longer timescale than when running under higher pressure, since compositional changes are expected to be more gradual.

The activity of this carbonitride was very different compared to Co_3Mo_3C at 400°C [54]. The carbonitride material had steady state activity and there was no induction period, as shown in Figure 44. Therefore, the surface oxide layer did not impede the ammonia synthesis activity. Two different rates have been calculated and are shown in Table 12 as the system was accidentally interrupted during the reaction run. The Ni_2Mo_3N nitride material prepared by the modified Pechini method has been tested previously and gave an activity of 395 ± 6 μmol h^{-1} g^{-1} [36].

To determine the reproducibility of the $Ni_2Mo_3C_xN_y$ activity for ammonia synthesis, the material was tested for a second time by reacting it with 3:1 H_2/N_2 at 400°C for ten hours. The rate exhibited by the material was 211 μmol h^{-1} g^{-1}. The stoichiometry proposed for

this bulk sample is $Ni_2Mo_3C_{0.50}N_{0.49}$, meaning that the initial amount of carbon in each sample is comparable. However, there was approximately 16% more nitrogen present pre-reaction in the sample that was tested for 36 hours.

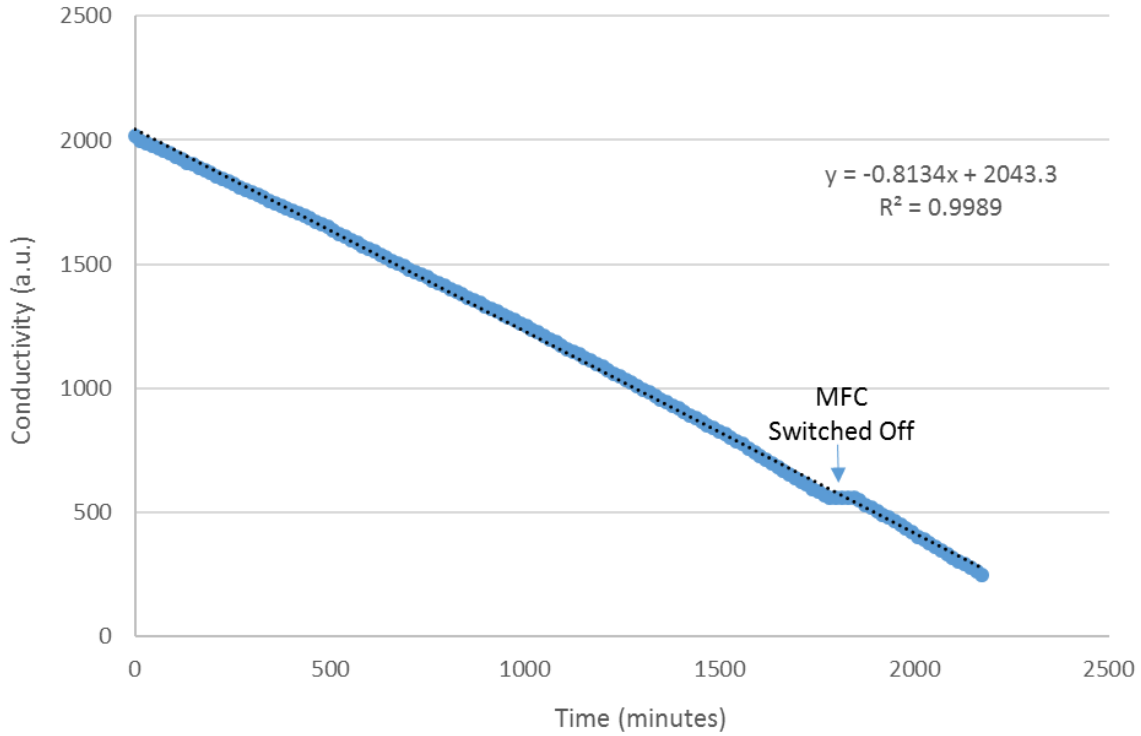

Figure 44: Conductivity profile for $Ni_2Mo_3C_xN_y$ reacted with 3:1 H_2/N_2 at 400°C for 36 hours.

Catalyst	Rate (μmol h^{-1} g^{-1}) at 400°C
$Ni_2Mo_3C_xN_y$ Before MFC was switched off	174
$Ni_2Mo_3C_xN_y$ After the MFC was switched back on	206

Table 12: Ammonia synthesis rates for $Ni_2Mo_3C_xN_y$ at 400°C and reacted with 3:1 H_2/N_2 for 36 hours.

The XRD pattern of the material post-reaction is displayed in Figure 45. If the material underwent nitridation during the reaction as observed for Co_3Mo_3C [54], the XRD pattern would be expected to show a change in lattice parameter. As nitrogen is smaller than carbon, it would be expected that the unit cell would decrease in size and the XRD peaks would shift to larger angles with progressive incorporation of N. After reaction, as seen in Figure 46, the shifts in peak positions were not consistent with the expected change in lattice parameter due to replacement of carbon with nitrogen. This observation requires further investigation as the reason for it is currently unknown. If oxygen was incorporated into the lattice the peaks would be expected to shift to higher 2θ values.

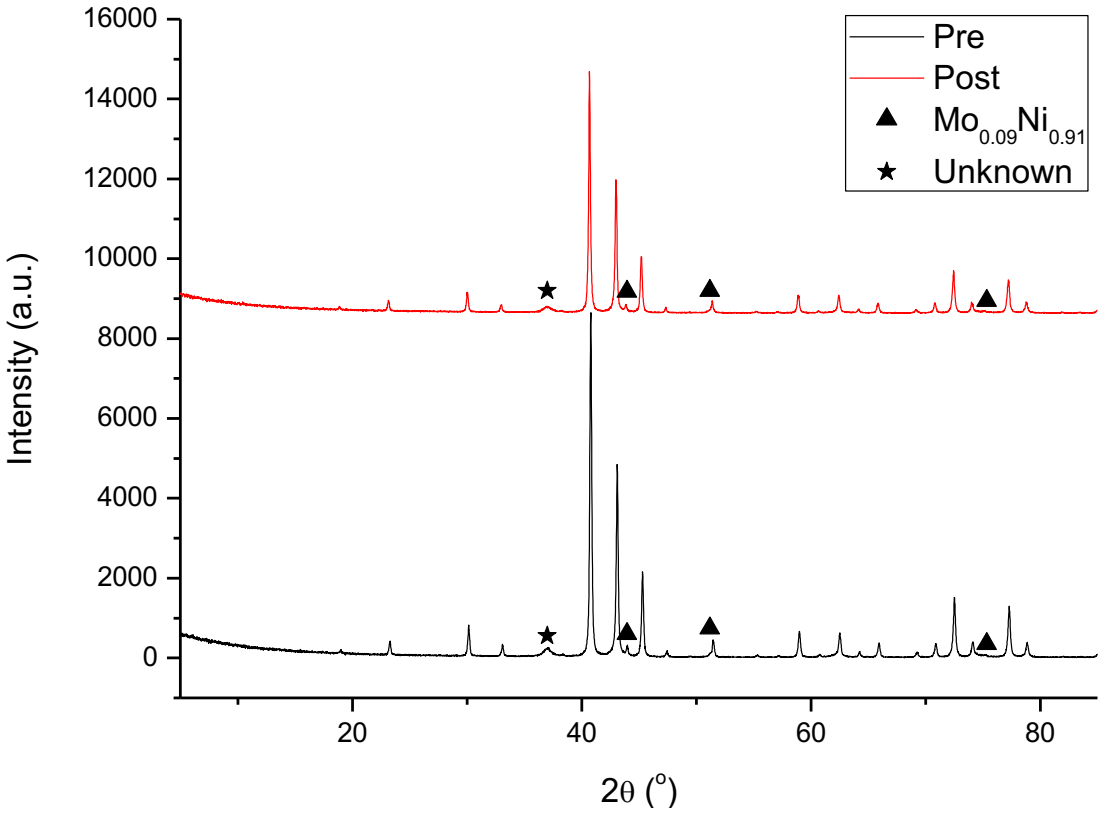

Figure 45: Comparison of XRD patterns for $Ni_2Mo_3C_xN_y$ pre and post reaction with 3:1 H_2/N_2 at 400°C for 36 hours. Reflections marled: ▲ $Mo_{0.09}Ni_{0.91}$ (JCPDS file number 01-071-9766) and the peak marked with ★ is an unknown phase.

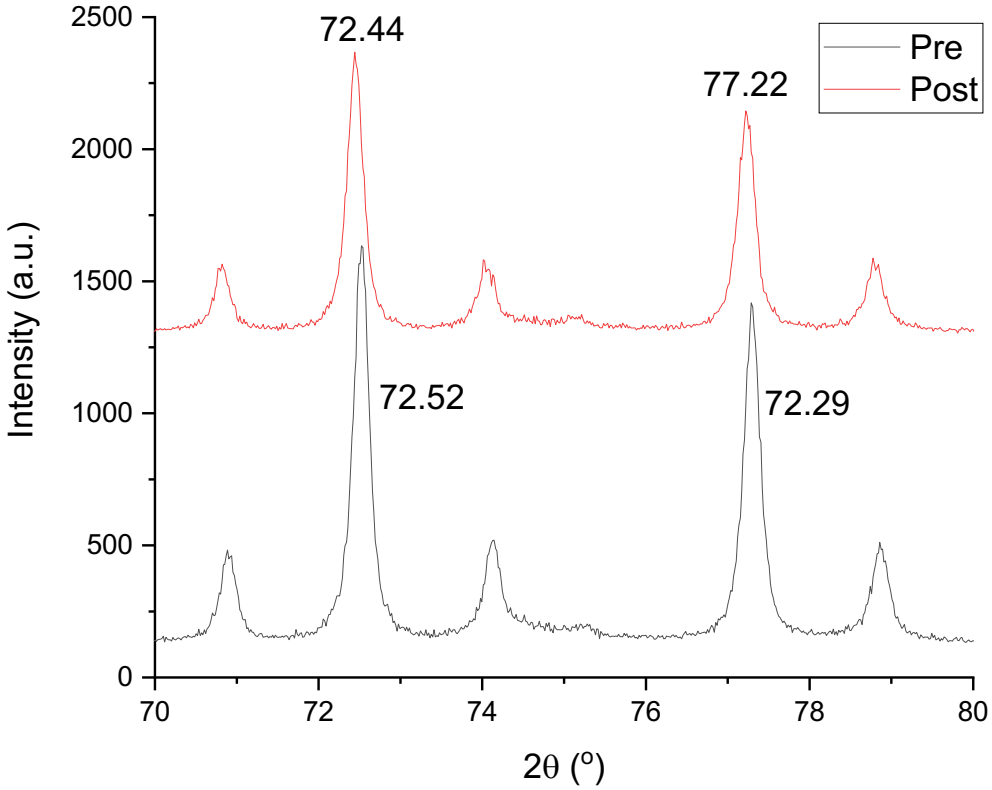

Figure 46: Comparison of XRD patterns for $Ni_2Mo_3C_xN_y$ pre- (black) and post-reaction (red) with 3:1 H_2/N_2 at 400°C for 36 hours.

The elemental analysis for the post reaction material is provided in Table 13. Post-reaction, it is observed that the nitrogen content of the nickel molybdenum carbonitride had slightly increased and the carbon content of the material had decreased. The stoichiometry proposed for the bulk sample is now $Ni_2Mo_3C_{0.43}N_{0.61}$. However, this increase in nitrogen content has not resulted in a discernible shift of the peak positions in the XRD to higher 2θ values, possibly due to the increase being small.

Material	Calculated Stoichiometric Nitrogen Content (wt. %)	Calculated Stoichiometric Carbon Content (wt. %)	Nitrogen Content from Elemental Analysis (wt. %)	Carbon Content from Elemental Analysis (wt. %)
$Ni_2Mo_3C_xN_y$ Pre-Reaction	-	2.88	1.93	1.42
$Ni_2Mo_3C_xN_y$ Post-Reaction	-	2.88	2.04	1.24

Table 13: Elemental Analysis for $Ni_2Mo_3C_xN_y$ comparing pre- and post-reaction with 3:1 H_2/N_2 at 400°C for 36 hours.

SEM analysis was performed in order to examine any changes in the morphology and structure of $Ni_2Mo_3C_xN_y$ during the ammonia synthesis reaction. Representative SEM images of the post-reaction material are presented in Figure 47. The material had a porous structure and the morphology was similar to the pre-reaction material. Therefore, the lower ammonia synthesis activity of the carbonitride compared to the nitride was not due to a change in morphology upon carburisation.

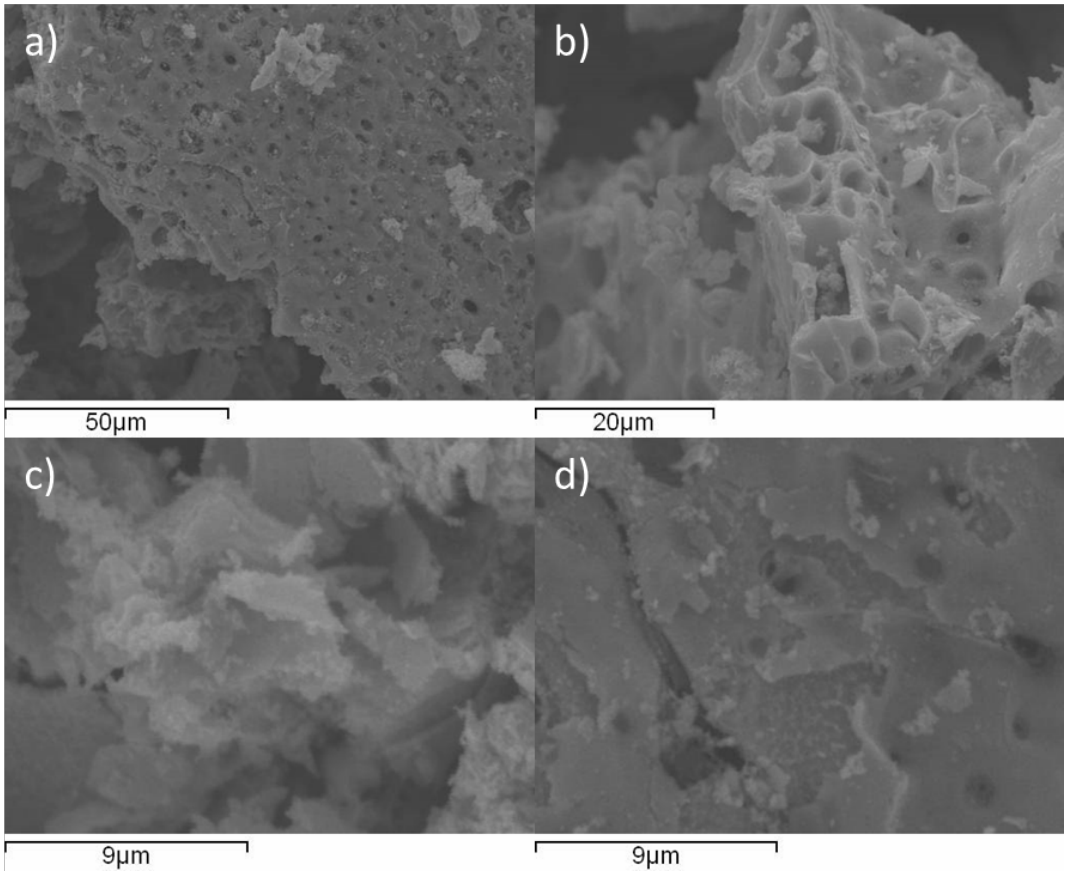

Figure 47: SEM images of nickel molybdenum carbonitride ($Ni_2Mo_3C_xN_y$) post-reaction with 3:1 H_2/N_2 at 400°C for 36 hours. a) 1000x magnification, b) 2000x magnification, c) 6000x magnification and d) 6000x magnification.

The element map in Figure 48 shows that the even nickel and molybdenum distribution had been retained.

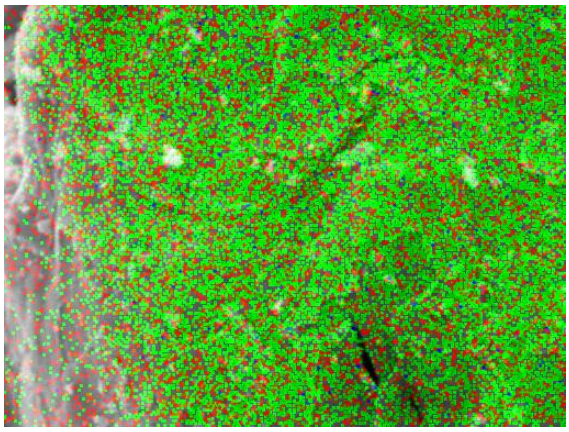

Figure 48: Element Map for $Ni_2Mo_3C_xN_y$ post-reaction with 3:1 H_2/N_2 at 400°C. Elements: Ni (red) and Mo (green).

Table 14 gives the weight percentage for each element from the EDX for the post-reaction $Ni_2Mo_3C_xN_y$. The CHN analysis shows that the stoichiometry for the bulk sample post 36 hour reaction at 400°C was $Ni_2Mo_3C_{0.43}N_{0.61}$. Thus, the stoichiometric content of nickel, molybdenum, carbon and nitrogen in the sample should be 28.02 wt. %, 68.71 wt. %, 1.23 wt. % and 2.04 wt. % respectively. As with the pre-reaction sample, the carbon and

nitrogen percentages were higher than expected. However, the amount of carbon decreased by 5.59 wt. % and the weight percentage of nitrogen increased by 1.05 wt. % compared to pre-reaction. These values compare very well with the stoichiometric differences between the pre- ($Ni_2Mo_3C_{0.49}N_{0.58}$) and post-reaction sample. The molybdenum percentage increased by 5.10 wt. % compared to the pre-reaction $Ni_2Mo_3C_xN_y$.

Area	Ni weight (%)	Mo weight (%)	C weight (%)	N weight (%)
1	27	55	15	4
2	26	56	14	5
3	24	48	23	6
4	22	59	15	4
5	23	55	13	8
6	27	53	16	5
Average	25	54	16	5

Table 14: EDX values for nickel molybdenum carbonitride ($Ni_2Mo_3C_xN_y$) post reaction with 3:1 H_2/N_2 at 400°C for 36 hours.

The formation of the oxide layer on the surface of the carbonitride and its potential effect on the ammonia synthesis activity of the material where examined by ToF-SIMS. It is important to understand if the development of activity requires removal of the oxide layer and/or restructuring of the near surface region of the material. ToF-SIMS is a surface sensitive technique and therefore, can give information on the elements present at the surface of a material. This technique can also be used for depth profiling and in this work, could be used to determine the depth of the oxide surface layer.

The ToF-SIMs instrument used a pulsed Cs^+ ion beam to remove species from the top layer of the carbonitride surface. Bi^{3+} was used as the primary ion for depth profiling. The removed molecules from the surface are the secondary ions and their mass are determined by the time they take to reach the detector.

The mass spectrum for molybdenum can be complex due to the element having seven naturally occurring isotopes of 92, 94, 95, 96, 97, 98 and 100. In $Ni_2Mo_3C_xN_y$, the nitrogen and carbon are bonded to six molybdenum species as explained in the introduction. Therefore, the mass fragments for this material would contain MoC and MoN. The mass spectrum of MoC, MoN and MoO fragments overlap. Therefore, there was no peak that was attributable solely to a MoN fragment. The peak at 106 m/z can result from both ^{94}MoC and ^{92}MoN. In this study, to show the depth profiling of a MoN fragment, the contribution of ^{94}MoC was subtracted from the total intensity for 106 m/z to give the intensity for ^{92}MoN. The ^{94}MoC contribution was calculated by comparing the expected ratio of the isotopes with ^{92}MoC at 104 m/z (^{92}Mo is 14.8% and ^{94}Mo is 9.2%).

The pre- and post- 36 hour reaction materials were examined by ToF-SIMS and the data is provided in Appendix III. For both the pre- and post-reaction samples, nitrogen and carbon were present at a depth of 10 nm, suggesting that although there was an oxide layer, these elements were present near the surface. Oxygen was also present in the materials and the intensity appeared to decrease as the depth increased, which is consistent with this being a surface layer. From this analysis, it can be determined that although there was an oxygen passivation layer, due to the presence of nitrogen and carbon near the surface, this would not need to be removed significantly in order for the material to be active.

As the pre- and post-reaction mass spectra appeared to be very similar, this suggests that the material has not undergone restructuring (i.e. segregation) during the reaction. However, the intensity of the ^{92}MoN peak had increased post-reaction compared to pre-reaction and the intensities of the ^{92}MoC and MoO_3^- peaks had decreased. This suggests that more nitrogen was present near the surface of the material after the reaction, as expected.

The mass peak due to oxygen (m/z = 16) was observed to reach saturation during the depth profiling of the material. It was suggested that the vacuum may have been insufficient to remove the oxygen from the chamber and therefore, there may have been a problem with the sample reabsorbing the oxygen.

3.2.1.4.2 Ammonia Synthesis at 500°C for $Ni_2Mo_3C_xN_y$

$Ni_2Mo_3C_xN_y$ was tested for ammonia synthesis activity at 500°C and atmospheric pressure under 3:1 H_2/N_2 to investigate if the increase in temperature would have a more notable effect on the phase composition. At this temperature, there is an induction period of approximately 50 minutes before the material develops steady state ammonia synthesis activity, as seen in Figure 49. The steady state activity of the material after the induction period is shown in Figure 50. This is in contrast to the material tested at 400°C, which had no induction period and therefore, an instantaneous decrease in conductivity. The reason as to why this was observed was unclear. However, the induction period may be due to removal of an oxide surface layer and/or restructuring of the material. The ammonia synthesis rate of the material at 500°C was determined to be 619 ± 14 μmol h^{-1} g^{-1}. In comparison, the rate at 400°C was calculated to be approximately 197 ± 23 μmol h^{-1} g^{-1}. Hence, beyond the induction period, the material is much more active at the higher temperature as might be expected. Co_3Mo_3C was stated to have a rate of 461 ± 17 μmol h^{-1} g^{-1} at 500°C under the same conditions [54], suggesting that $Ni_2Mo_3C_xN_y$ is yet more

reactive, although the comparative surface areas of the materials would need to be considered in drawing further inferences. The cobalt molybdenum material also had an induction period that lasted for 40 minutes before it became active during which the material underwent nitridation to form a carbonitride. $Co_3Mo_3C_xN_y$ was active for ammonia synthesis at 500°C and had similar activity to the corresponding nitride [54].

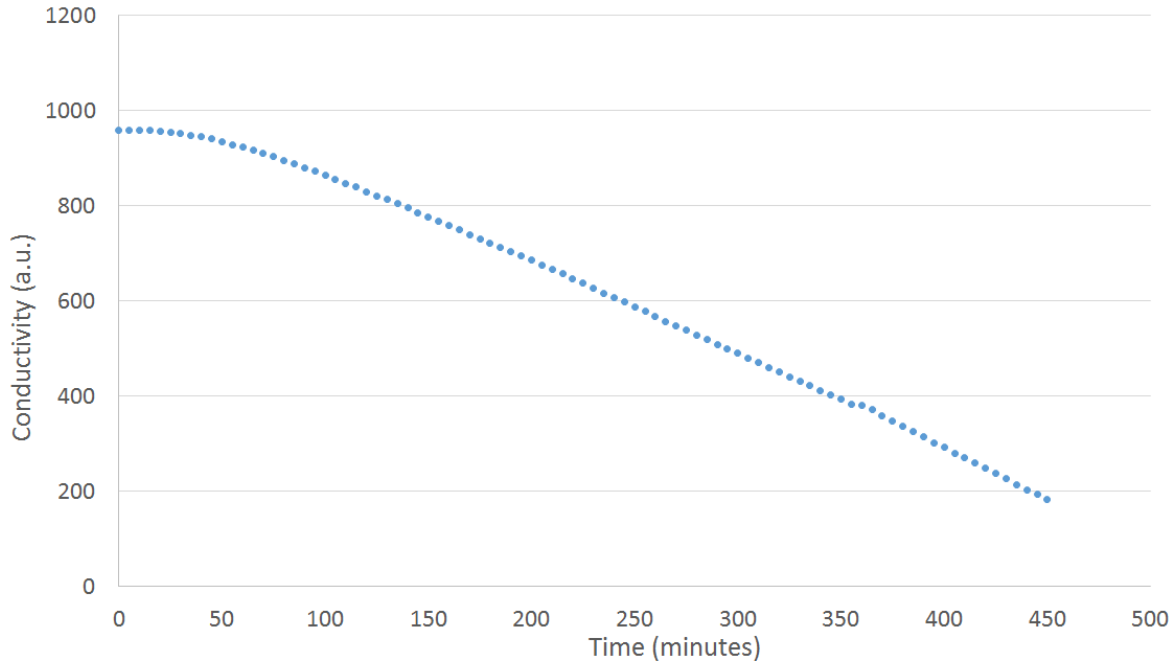

Figure 49: Conductivity profile for $Ni_2Mo_3C_xN_y$ reacted with 3:1 H_2/N_2 at 500°C for 7.5 hours.

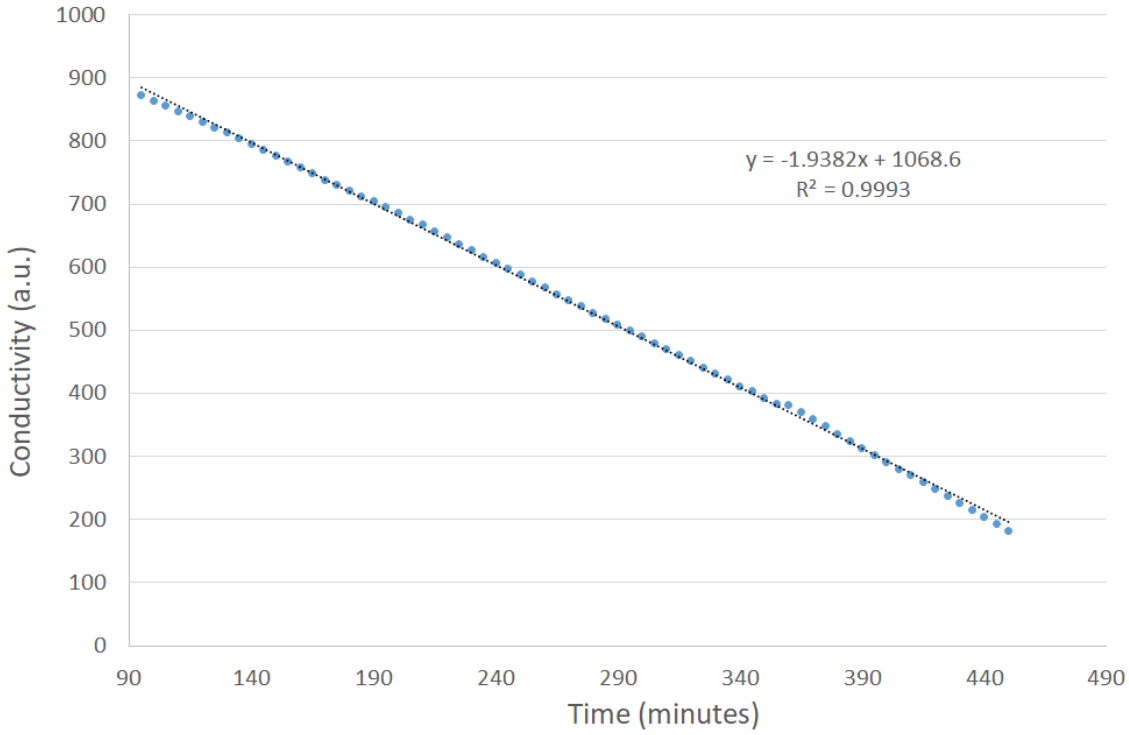

Figure 50: Conductivity profile for $Ni_2Mo_3C_xN_y$ reacted with 3:1 H_2/N_2 at 500°C for 7.5 hours, highlighting the linear part of the graph used for calculating the rate.

The XRD patterns in Figures 51 and 52 show a small shift in the position of the peaks to higher 2θ values between pre- and post-reaction. All the XRD reflections of $Ni_2Mo_3C_xN_y$ are shifted to higher 2θ angles after the reaction. This implies that the lattice carbon is being replaced with nitrogen to give a material with a composition containing more nitrogen. The XRD patterns illustrate a more notable effect on the phase transformation at the higher reaction temperature.

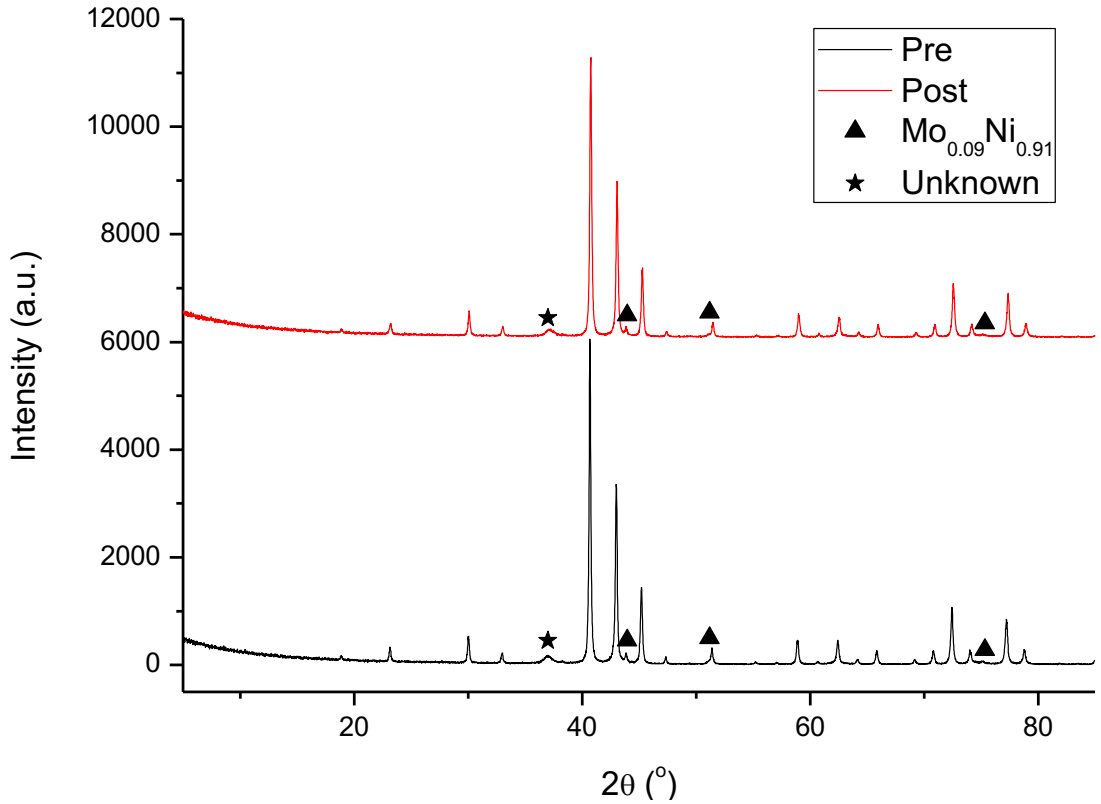

Figure 51: Comparison of XRD patterns for $Ni_2Mo_3C_xN_y$ pre- and post-reaction with 3:1 H_2/N_2 at 500°C for 7.5 hours. Reflections marked: ▲ $Mo_{0.09}Ni_{0.91}$ (JCPDS file number 01-071-9766) and the peak marked with ★ is an unknown phase.

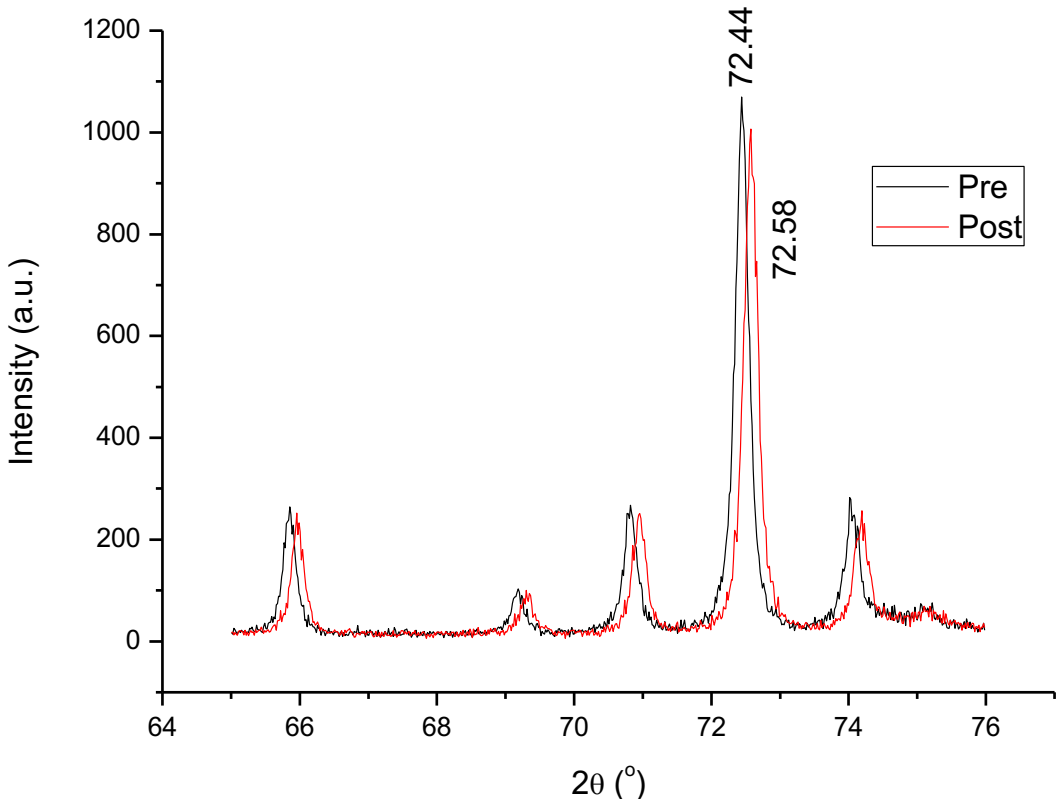

Figure 52: Comparison of XRD patterns for $Ni_2Mo_3C_xN_y$ pre- (black) and post-reaction (red) with 3:1 H_2/N_2 at 500°C for 7.5 hours.

From the elemental analysis, it appears that some of the carbon had been removed from the sample and had been replaced with nitrogen, as observed in Table 15. The stoichiometry proposed for the bulk sample is now $Ni_2Mo_3C_{0.15}N_{0.83}$. This is a significant change in composition compared to pre-reaction ($Ni_2Mo_3C_{0.43}N_{0.61}$). The post-reaction elemental analysis confirms that the carbon was not completely removed from the carbonitride to form the corresponding nitride. However, at 500°C reaction temperature, the replacement of lattice carbon with nitrogen is much more noticeable. A similar transformation was seen for Co_3Mo_3C, which formed $Co_3Mo_3C_xN_y$ when reacted with 3:1 H_2/N_2 at 500°C [54].

Material	Calculated Stoichiometric Nitrogen Content (wt. %)	Calculated Stoichiometric Carbon Content (wt. %)	Nitrogen Content from Elemental Analysis (wt. %)	Carbon Content from Elemental Analysis (wt. %)
$Ni_2Mo_3C_xN_y$ Pre-Reaction	-	2.88	2.04	1.24
$Ni_2Mo_3C_xN_y$ Post 500°C Reaction	-	2.88	2.78	0.42

Table 15: Elemental Analysis for $Ni_2Mo_3C_xN_y$ comparing pre- and post-reaction with 3:1 H_2/N_2 at 500°C for 7.5 hours.

A representative Raman spectrum of the post 500ºC reaction carbonitride is displayed in Figure 53. Alconchel et al. [67] observed no Raman bands for $Ni_2Mo_3C_xN_y$ and they suggested that the carbonitride was less oxygen sensitive compared to the corresponding nitride. In the pre-reaction material, Raman bands were observed corresponding to a passivation layer (Figure 41). These bands were not observed in the Raman spectra post-reaction. This would suggest that the induction phase observed for this material could be due to the removal of the oxide layer, although surface segregation effects also need to be considered. However, the induction phase could also be due to restructuring of the material.

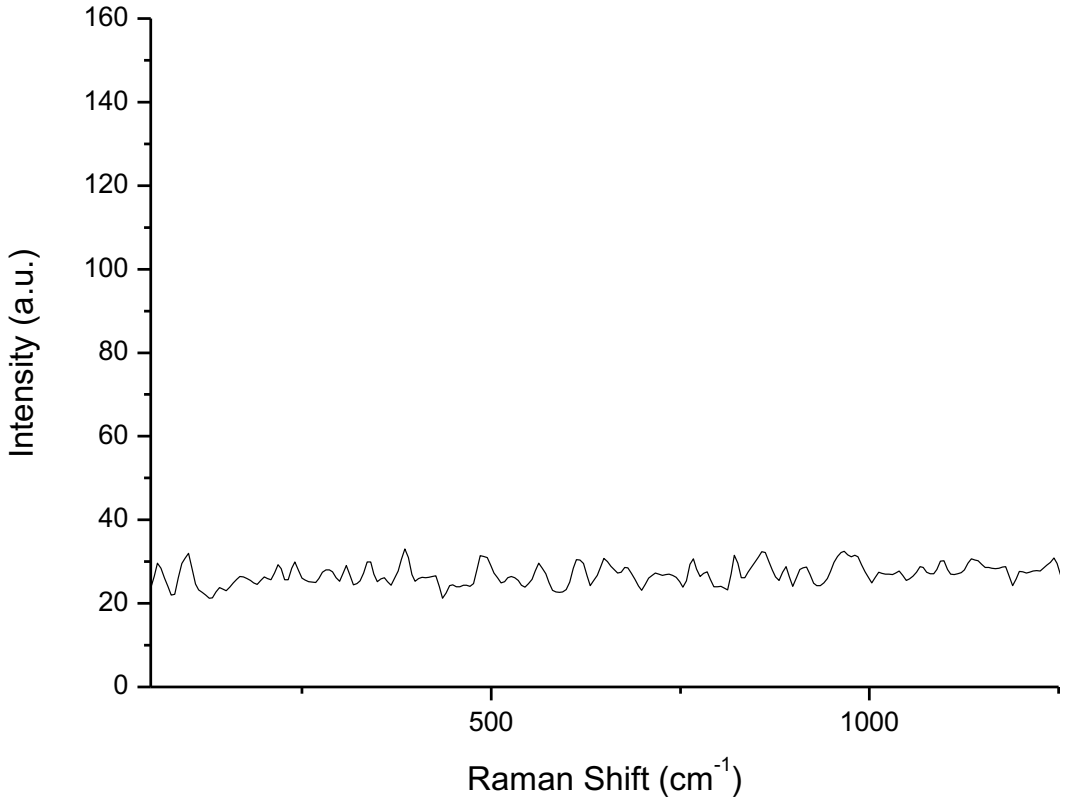

Figure 53: Raman spectrum of nickel molybdenum carbonitride ($Ni_2Mo_3C_xN_y$) post-reaction with 3:1 H_2/N_2 at 500°C for 7.5 hours.

ToF-SIMS was utilised to determine the reason for the induction period for $Ni_2Mo_3C_xN_y$ before it obtained steady state activity. The mass spectrum for the post-reaction material is displayed in Appendix III. Oxygen was observed at the surface and therefore, the material had an oxide surface layer. This is in contrast to the Raman spectrum that showed no bands for an oxide. However, ToF-SIMS is a very sensitive technique with amounts in the ppm/ppb range being detected. Carbon and nitrogen were also detected at the surface of the material. This suggests that the removal of an oxide layer might not straightforwardly be the reason for the induction period.

Part II: η-Carbide Structured Materials

3.2.2 Nickel Molybdenum Carbide (Ni_6Mo_6C)

Although there have been reports of Ni_3Mo_3N formation in the literature, this phase is not currently established [60] [35]. Instead, nitridation of the $NiMoO_4$ precursor results in a mixture of Ni and Ni_2Mo_3N. In contrast, the carbide, Ni_3Mo_3C, is an established phase and therefore, its preparation and possible topotactic nitridation during ammonia synthesis might be a route to preparing Ni_3Mo_3N. The nitridation of carbides and carbonitrides has been reported for $Ni_2Mo_3C_xN_y$ in this thesis and for Co_3Mo_3C [54]. Comparison of the catalytic performance of Ni_3Mo_3C and Ni_2Mo_3C would also give information on the effect structure (η-carbide versus filled β-Mn) has on the ammonia synthesis activity.

Attempts have been made to prepare nickel molybdenum carbide directly from the bimetallic oxide by using methane as the carburising source. However, this has proved to be difficult, with reports in the literature showing the formation of β-Mo_2C and Ni instead [62]. Therefore, in this work, a different approach was undertaken in order to prepare Ni_3Mo_3C. The citric acid used in the preparation of the oxide precursor via the modified Pechini method, was used as the carburising source. Other studies have shown that a precursor can be used as the carbon source to form carbides, for example hexamethylenetetramine (HMTA) [106] and glucose [107]. Ni_6Mo_6C has been previously synthesised by reduction of citric acid under Ar or H_2 [69] [108] [68]. However, the materials were not pure phase, with impurities of β-Mo_2C, a nickel molybdenum alloy and Ni_3C being formed. A pure phase Ni_6Mo_6C had been formed by Newsam et al. [64] under CO/CO_2 at 1000°C.

3.2.2.1 Nickel Molybdenum Oxide ($Ni_3Mo_3O_x$)

To prepare the nickel molybdenum carbide, first the oxide precursor was synthesised via the modified Pechini method. The oxide was not calcined in order for the citric acid to be used as the source of carbon. The XRD pattern of the material is shown in Figure 54 and a broad peak was observed at approximately 24° 2θ. This peak may be due to carbon or graphite, which shows a peak at 26° 2θ. The 2° 2θ difference in d-spacing may be due to the poorly defined nature of the peak due to the disordered nature of the material. Elemental analysis of the oxide material showed that there was a large percentage of carbon present (C: 23.31%, H: 2.95% and N: 1.32%). Nitrogen was also detected in this material and possibly originated from the $Ni(NO_3)_2 \cdot 6H_2O$ and $((NH_4)_6Mo_7O_{24} \cdot 4H_2O$ starting materials.

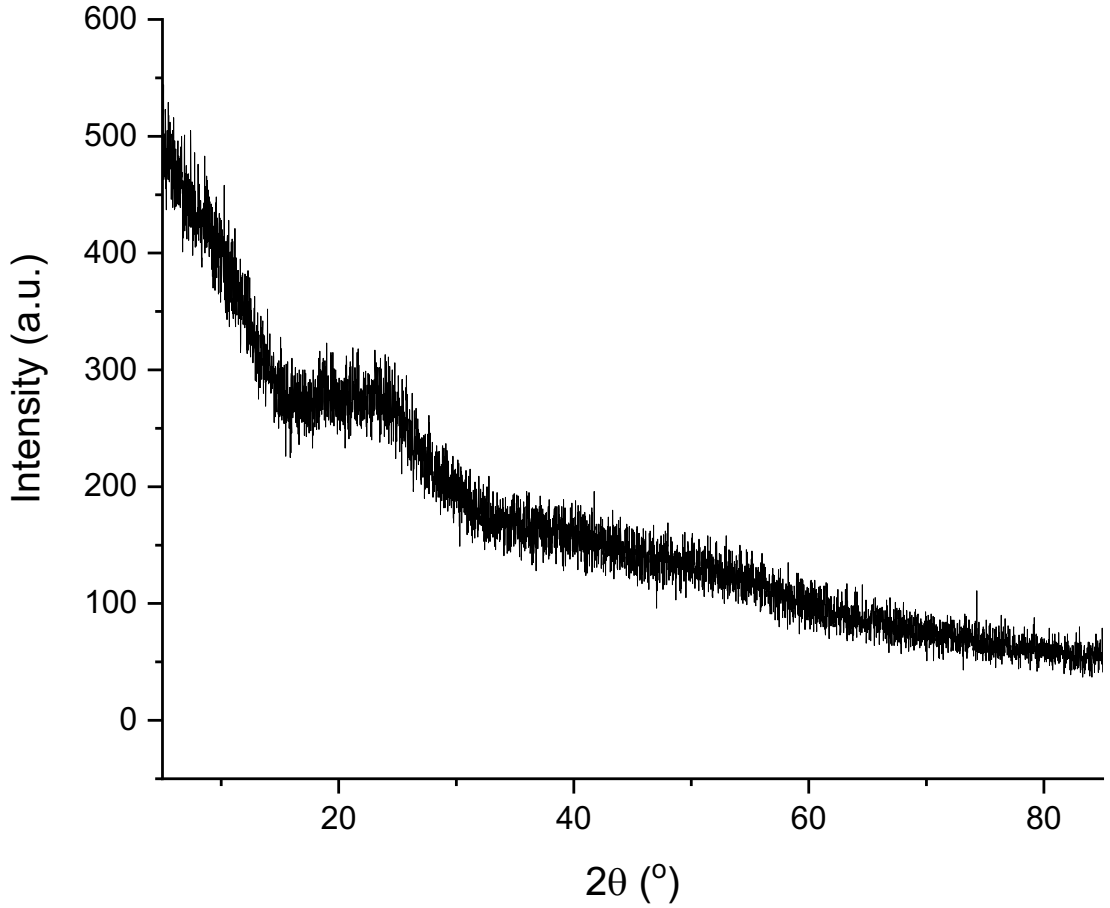

Figure 54: XRD pattern of uncalcined nickel molybdenum oxide ($Ni_3Mo_3O_x$).

As the XRD pattern showed that the material was amorphous, Raman analysis was conducted for this material to examine the oxide species present. In addition, information on the type of carbon can be obtained from Raman analysis. The Raman spectrum of uncalcined $Ni_3Mo_3O_x$ has a strong band at 943 cm^{-1} along with bands at 895, 822 and 376 cm^{-1}, as shown in Figure 55. These bands match well with those reported in the literature for β-$NiMoO_4$ [109] [110]. The bands at 943, 895 and 822 cm^{-1} are attributed in the literature to symmetric and asymmetric stretching modes of the Mo-O bond [88] [91]. The band at 376 cm^{-1} has been assigned to the bending mode of Mo-O [96]. The weak band at 290 cm^{-1} has been assigned to the deformation mode of Mo–O–Mo [91].

There are also two broad bands at 1368 and 1572 cm^{-1}, which are associated with the D and G bands of graphitic carbon. Carbon is present in the material from the starting citric acid precursor and is used as the source of carbon when the material is reduced. The D band at 1368 cm^{-1} is attributed to defects characteristic of disorder in the graphite, whereas the G band is due to the vibration of sp^2 bonded carbon atoms and relates to the E_{2g} mode of graphite [111]. In the literature, heating from the laser has been shown to shift the position of the G band down as far as 1567 cm^{-1} [112]. For the spectrum taken with a 50% filter, the G band shifts down to 1572 cm^{-1}, which suggests that laser-induced heating has

shifted this band. However, other research states that the shift in band position is due to the number of layers of graphene present [113] [114]. As the number of layers increases, the G band shifts to lower wavenumber. It has been suggested that this is due to a slight weakening of the bonds as each additional layer is added [114].

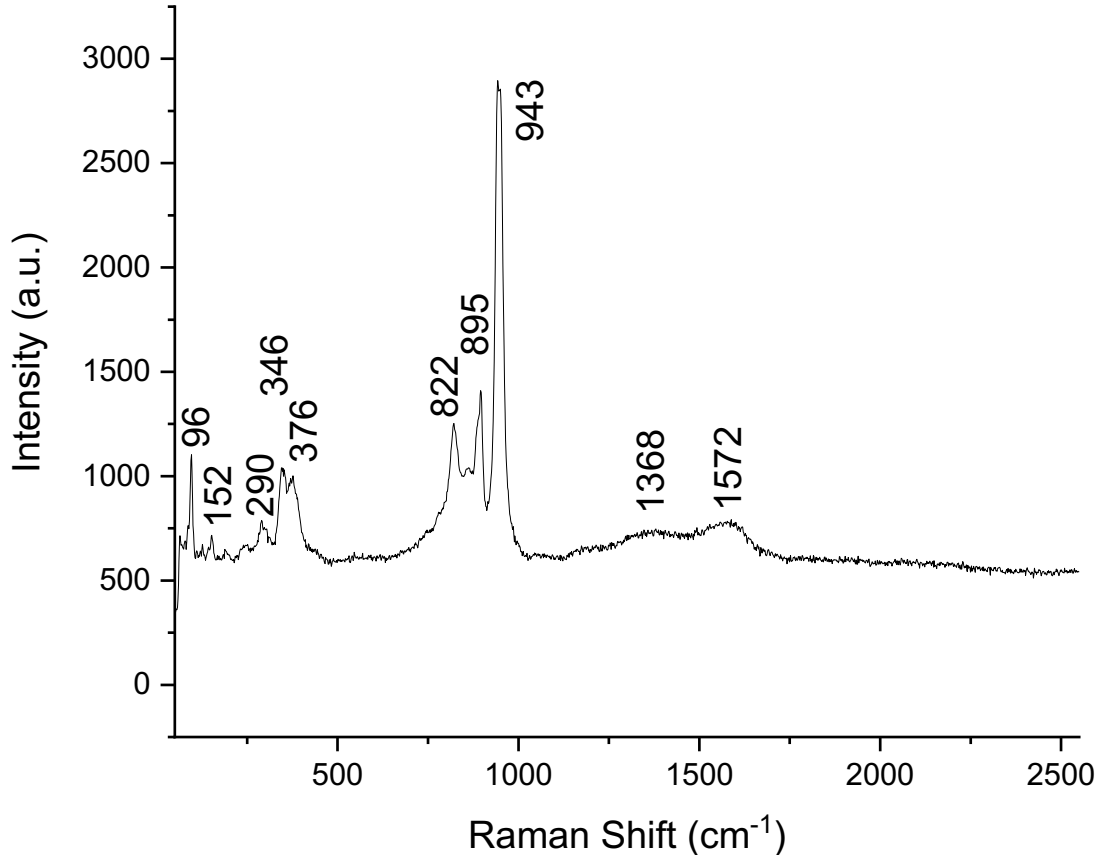

Figure 55: Raman spectrum of uncalcined nickel molybdenum oxide ($Ni_3Mo_3O_x$).

3.2.2.2 Nickel Molybdenum Carbide (Ni_6Mo_6C)

Nickel molybdenum carbide was prepared by reducing the uncalcined oxide precursor under a 3:1 ratio of H_2/Ar gas mixture at 700°C. The XRD pattern in Figure 56 shows that the low carbon content Ni_6Mo_6C was formed. There were also impurities of Mo_2C and Ni_2Mo_3N present in the material. Nitrogen was observed in the oxide precursor and possibly resulted from the $Ni(NO_3)_2 \cdot 6H_2O$ and $(NH_4)_6Mo_7O_{24} \cdot 4H_2O$ used in the Pechini method. The Ni_2Mo_3N and Ni_6Mo_6C have many XRD reflections that overlap. However, unique reflections for Ni_6Mo_6C are observed at 35.9°, 50.2° and 60.7° 2θ and for Ni_2Mo_3N at 30.1° and 45.3° 2θ. This result demonstrates that the nickel molybdenum carbide can be prepared by using citric acid as the carbon source. Both Ni_6Mo_6C and Ni_3Mo_3C have a similar η-carbide structure. The material was also prepared at a temperature of 750°C. However, the intensity of the Ni_2Mo_3N peaks increased suggesting that the nitride formation is favoured at higher temperatures. It is currently unclear why this is the case.

The stoichiometric weight percentage of carbon expected in Ni_6Mo_6C is 1.28%. Elemental analysis of the 'Ni_6Mo_6C' material prepared at 700°C showed that the amount of carbon present was almost the same as the stoichiometric percentage (C: 1.18 wt. %, H: 0.15 wt. % and N: 0.65 wt. %). However, the Mo_2C impurity will contribute towards this value. The nitrogen present is likely due to the apparent occurrence of the Ni_2Mo_3N phase. The material that was prepared at 750°C had a higher nitrogen percentage according to CHN analysis.

The formation of Ni_6Mo_6C suggests that there may be a preference for the carbon to reside in the 8a Wyckoff site compared to the 16c site that would be required to form Ni_3Mo_3C. The 8a Wyckoff site is a more perfect octahedral site, which could explain this apparent preference.

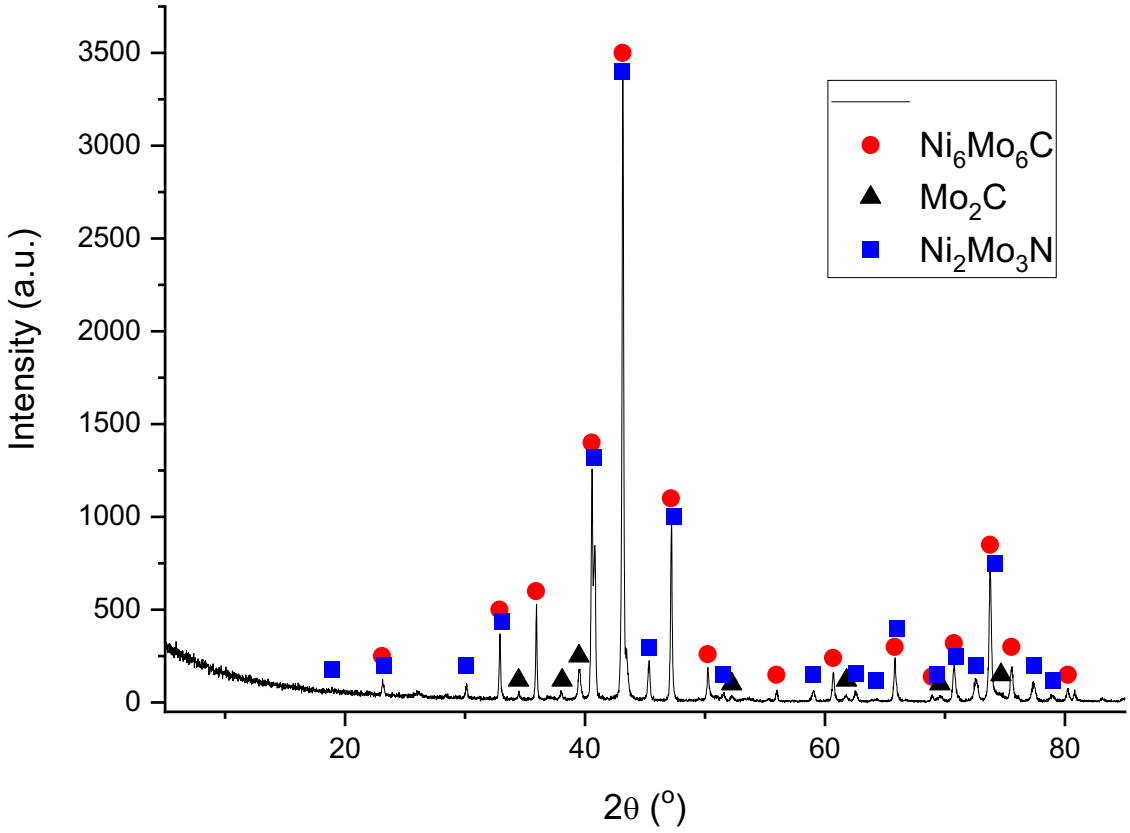

Figure 56: XRD pattern of nickel molybdenum carbide (Ni_6Mo_6C). Reflections marked: ● Ni_6Mo_6C (JCPDS file number 03-065-4436), ■ Ni_2Mo_3N (JCPDS file number 01-072-6569) and ▲ Mo_2C (JCPDS file number 00-001-1188).

Raman analysis was performed to investigate if there was oxide species on the surface of the material. The Raman spectrum of 'Ni_6Mo_6C' has bands at 937, 885, 813 and 704 cm^{-1}, as seen in Figure 57, that match well with those reported in the literature for β-$NiMoO_4$ [109] [110]. This result suggests that an oxide layer was present on the surface of the

carbide. The bands at 937, 885 and 813 cm^{-1} are attributed in the literature to symmetric and asymmetric stretching modes of the Mo-O bond [88] [91]. The band at 704 cm^{-1} was assigned to the symmetric stretch of Ni–O–Mo [67]. The bands at 477 cm^{-1} and 126 cm^{-1} could be due to α-MoO_3 [115], which would result from the passivation layer on Mo_2C. To the author's knowledge, there are no Raman spectra for Ni_6Mo_6C reported in the literature. There were no bands associated with graphitic and other forms of extra-lattice carbon seen in the Raman spectrum, suggesting that the carbon is incorporated into the lattice of the carbide.

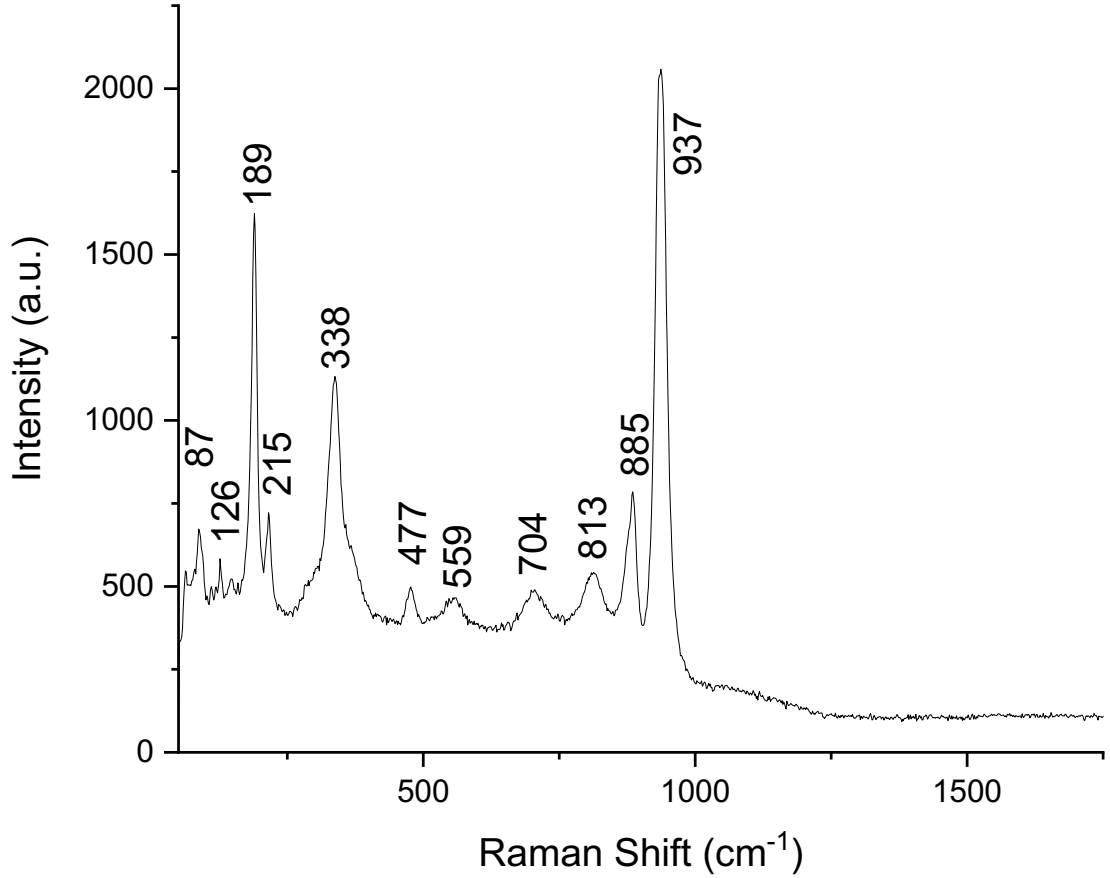

Figure 57: Raman spectrum of nickel molybdenum carbide (Ni_6Mo_6C).

SEM images of the mixed phase 'Ni_6Mo_6C' are presented in Figure 58 illustrate that the material was porous with pores ranging in diameter from approximately 1 – 10 µm. The EDX data in Table 16 gives the element weight percentages for 'Ni_6Mo_6C'. The stoichiometric percentage of nickel, molybdenum and carbon in Ni_6Mo_6C is 37.47 wt. %, 61.25 wt. % and 1.28 wt. %, respectively. From the table, it can be seen that the carbon weight percentage was much higher than predicted. Correspondingly, the nickel and molybdenum percentages were lower. This could suggest that there is a large amount of carbon laydown on the material. However, the Raman spectrum showed no evidence of carbon laydown and the XRD pattern did not contain any peaks associated with carbon. It must be noted that the samples are placed on carbon stubs for SEM and EDX analysis and

therefore, this may have contributed to the carbon percentage. From the XRD pattern, it was shown that the material consisted of Ni_6Mo_6C, Mo_2C and Ni_2Mo_3N. However, nitrogen was not detected for the material by EDX suggesting that the amount was low. The EDX data appears to support the assignment of the composition as Ni_6Mo_6C.

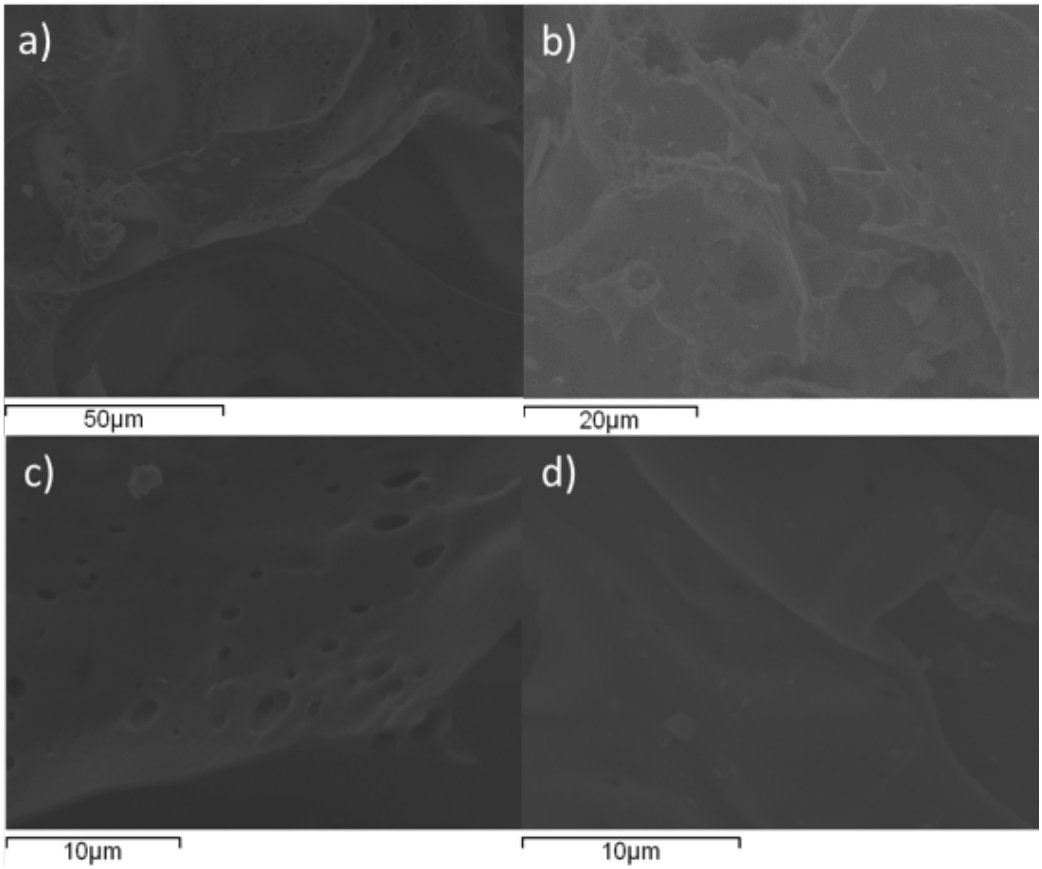

Figure 58: SEM images of nickel molybdenum carbide (Ni_6Mo_6C). a) 1000x magnification, b) 2000x magnification, c) 4000x magnification and d) 5000x magnification.

Area	Ni weight (%)	Mo weight (%)	C weight (%)
1	15	13	72
2	13	23	63
3	18	6	76
4	13	22	65
5	11	23	66
6	13	20	67
7	14	16	69
8	11	12	77
9	14	19	67
10	11	17	71
11	13	16	71
Average	13	17	69

Table 16: EDX values for nickel molybdenum carbide (Ni_6Mo_6C) prepared under 3:1 H_2/Ar at 700°C.

3.2.2.2.1 Ammonia Synthesis at 400°C for Ni_6Mo_6C

'Ni_6Mo_6C' was tested for ammonia synthesis activity at 400°C and atmospheric pressure under 3:1 H_2/N_2 atmosphere for 8.5 hours. This was performed to establish the influence the phase composition had upon ammonia synthesis activity. The conductivity only decreased by a small amount over the time the material was tested as observed in Figure 59. For the first 150 minutes, there is a small decrease in conductivity. However, after this time, the conductivity began to level off and therefore, ammonia was no longer being produced. Whilst there seems to be Ni_2Mo_3N contained within this material, which would be expected to be active, the XRD pattern suggests it to be at only a very low level.

The behaviour of 'Ni_6Mo_6C' was similar to the performance of Co_6Mo_6C tested at 500°C for ammonia synthesis [54]. Co_6Mo_6C was found to be inactive at 500°C, even upon extended reaction times of 48 hours. It is interesting to note that Ni_2Mo_3N and $Ni_2Mo_3C_xN_y$ are active for ammonia synthesis at 400°C, which implies that the relatively small phase fraction of Ni_2Mo_3N present in the current material does not significantly contribute activity under these conditions. This suggests that the carbide is relatively stable in comparison to the carbonitride and nitride. There may be a relationship between the ammonia synthesis activity and structure of these materials. Both Ni_2Mo_3N and $Ni_2Mo_3C_xN_y$ have the filled β-Mn structure whereas Ni_6Mo_6C has the η-carbide structure, although the difference in interstitial element may also affect the ammonia synthesis activity.

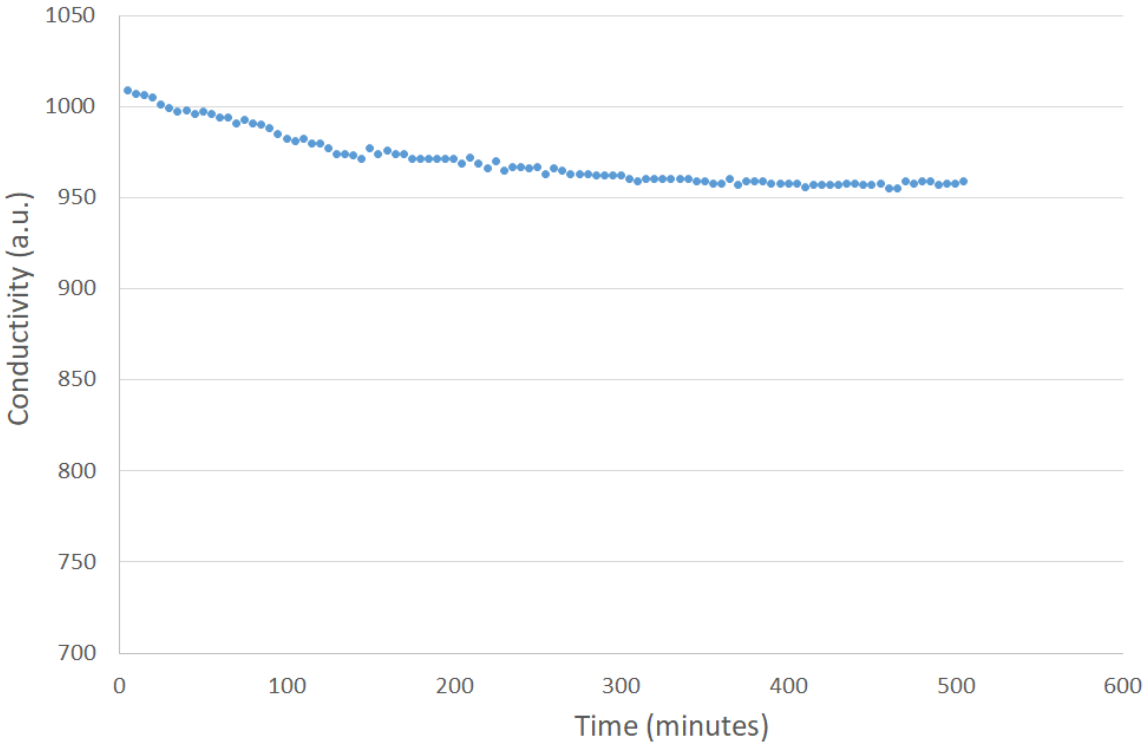

Figure 59: Conductivity profile for 'Ni_6Mo_6C' reacted with 3:1 H_2/N_2 at 400°C for 8.5 hours.

The XRD patterns presented in Figure 60 show that the η-carbide structure of Ni_6Mo_6C was maintained after the reaction. There does not appear to be any change in phase compared to pre-reaction suggesting that the material does not undergo nitridation during the reaction.

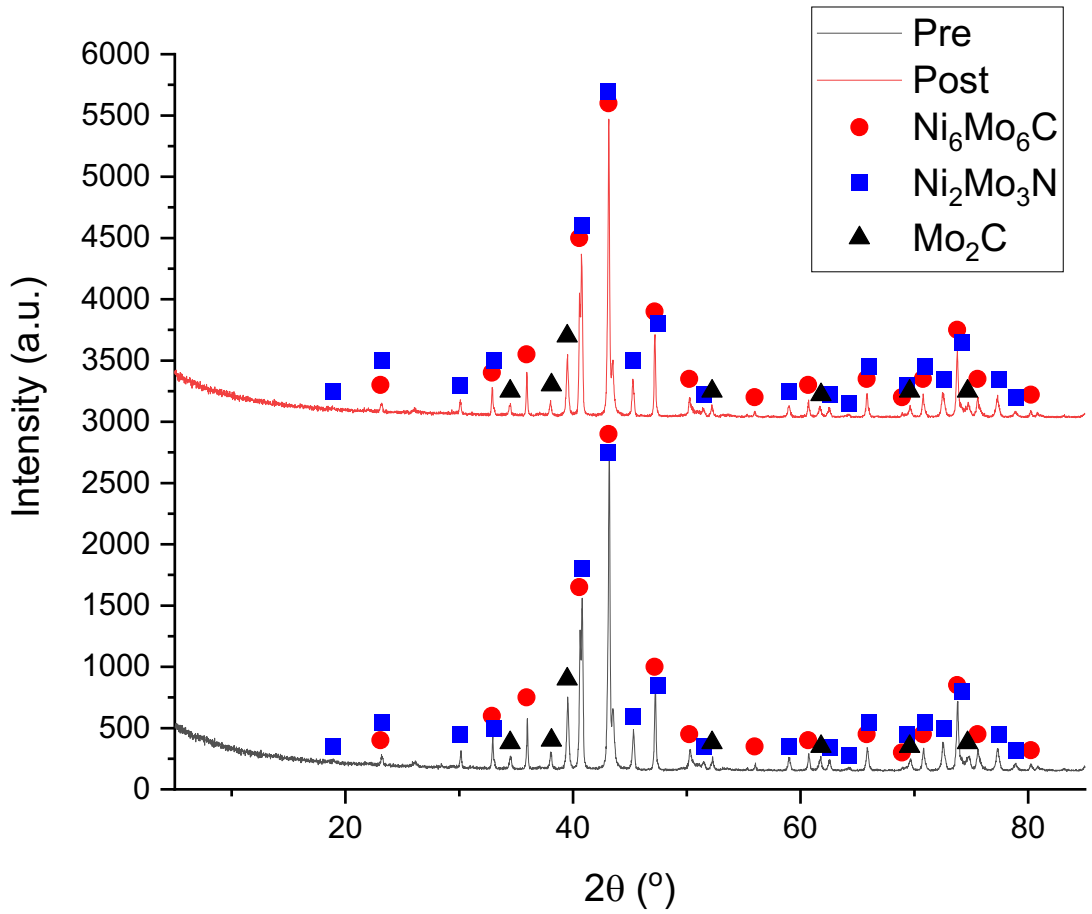

Figure 60: Comparison of XRD patterns for 'Ni6Mo6C' pre- and post-reaction with 3:1 H_2/N_2 at 400°C for 8.5 hours. Reflections marked: ● Ni_6Mo_6C (JCPDS file number 03-065-4436), ■ Ni_2Mo_3N (JCPDS file number 01-072-6569) and ▲ Mo_2C (JCPDS file number 00-001-1188).

Figure 61 confirms that the peaks due to Ni_6Mo_6C do not shift in position compared to the pre-reaction material. These results may suggest that the inactivity of 'Ni6Mo6C' is due to the material not undergoing nitridation. It has been suggested that Co_3Mo_3C does not become active for ammonia synthesis until nitrogen is incorporated into the lattice [54]. It was observed that Co_3Mo_3C was inactive at 400°C and became active when the temperature was increased to 500°C. The higher reaction temperature may be required in order to incorporate nitrogen into the material.

The elemental analysis demonstrates that the percentage of carbon present in the material post-reaction has slightly increased (C: 1.23 wt. %, H: 0.00 wt. % and N: 0.48 wt. %) compared to pre-reaction (1.18 wt. %). This increase may be due to the nitrogen

percentage slightly decreasing or the error within the CHN analysis, which is ± 5%. The expected stoichiometric percentage of carbon in Ni_6Mo_6C is 1.28 wt. % and therefore, the elemental analysis for carbon agrees very well with this value. However, the Mo_2C impurity will contribute towards this value.

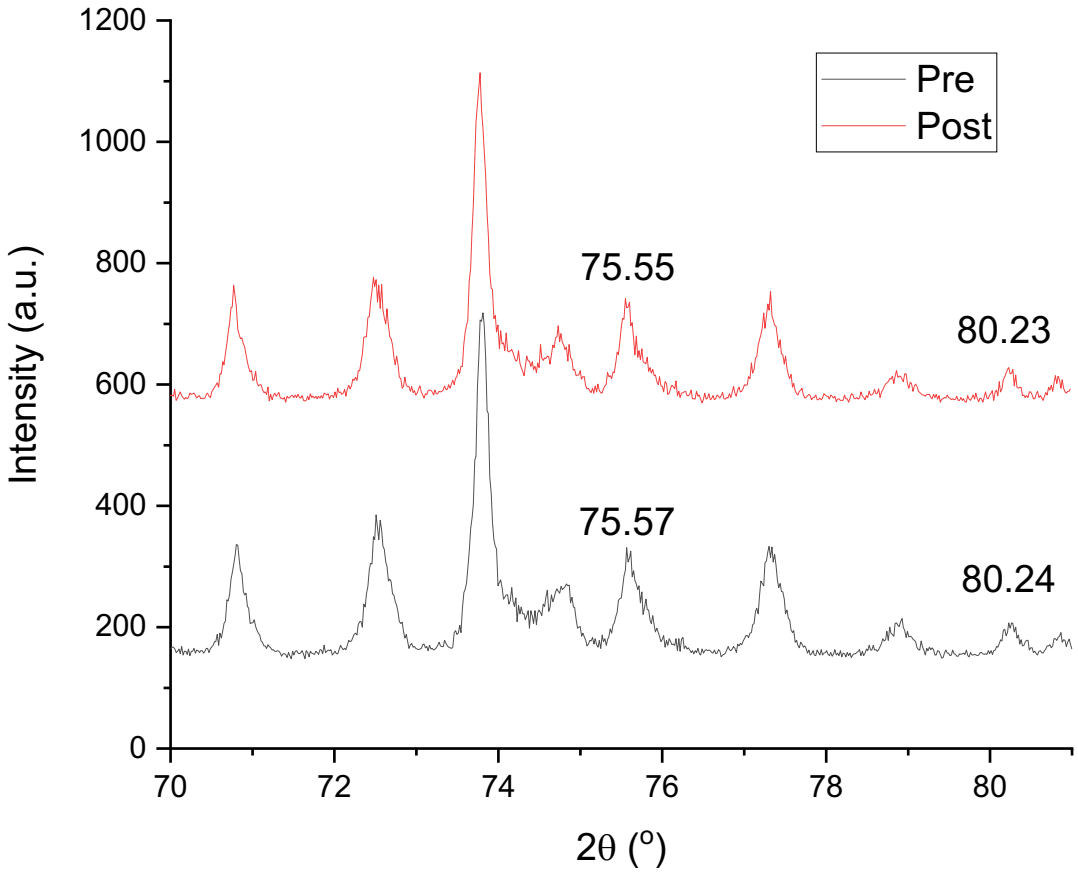

Figure 61: Comparison of XRD patterns for 'Ni_6Mo_6C' pre- (black) and post-reaction (red) with 3:1 H_2/N_2 at 400°C for 8.5 hours, highlighting the 2θ values for peaks due only to Ni_6Mo_6C.

For the post-reaction material, there was one very weak band at 2332 cm^{-1} relating to the 2D band for carbon, as shown in Figure 62. The 2D band is the second order of the D band and involves a two phonon process [111]. The 2D band can be used to determine the graphene thickness from its intensity and shape. When successive layers of graphene are added, the 2D band separates into overlapping modes due to the decrease in symmetry. The unique shape differences of this band can give information on the number of layers of graphene. Therefore, the low intensity of this band suggests that there were few layers of carbon present in this material.

There is also a broad band between 550 and 1050 cm^{-1} that could be assigned to $NiMoO_4$. However, there were no well-defined peaks, which suggests that there was only a very

small passivation layer on the material post reaction. This result suggests that the oxide layer is removed during the reaction.

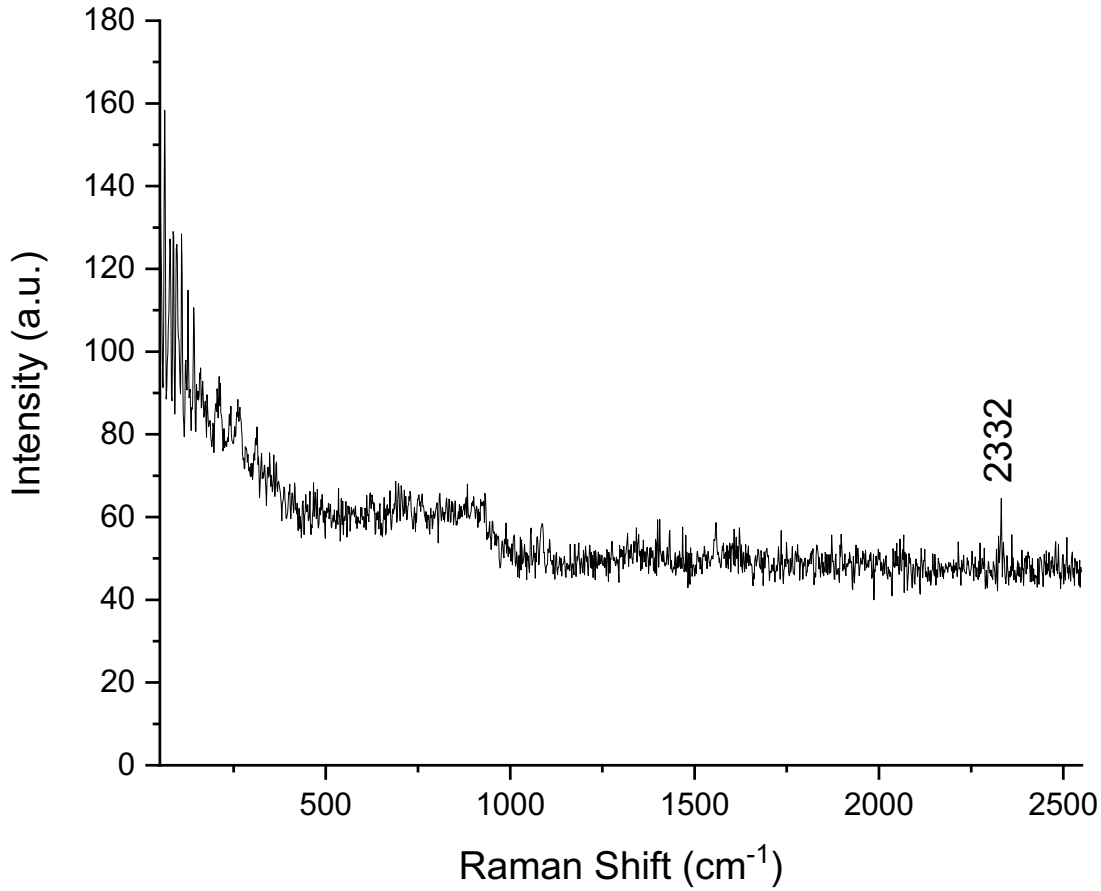

Figure 62: Raman spectrum of 'Ni_6Mo_6C' post-reaction with 3:1 H_2/N_2 at 400°C for 8.5 hours.

SEM analysis was performed to see if there was any change in the morphology of the material during the ammonia synthesis reaction. Representative SEM images of post 400°C reaction 'Ni_6Mo_6C' are displayed in Figure 63. The material is porous and retains the morphology of the pre-reaction material. The stoichiometric percentage of nickel, molybdenum and carbon in Ni_6Mo_6C is 37.47 wt. %, 61.25 wt. % and 1.28 wt. %, respectively. The EDX data displayed in Table 17 shows that the carbon and nickel weight percentages were higher compared to pre-reaction and that the molybdenum percentage was lower. However, it must be noted that EDX is a semi-quantitative technique and therefore, care needs to be taken when considering statistical relevance etc. The Raman spectrum showed a small amount of carbon laydown. However, the amount of carbon detected by EDX was much greater and therefore, the carbon stub on which the material was placed must have contributed to this value. Nitrogen was not detected by EDX suggesting that the contribution of nitrogen from Ni_2Mo_3N must be small.

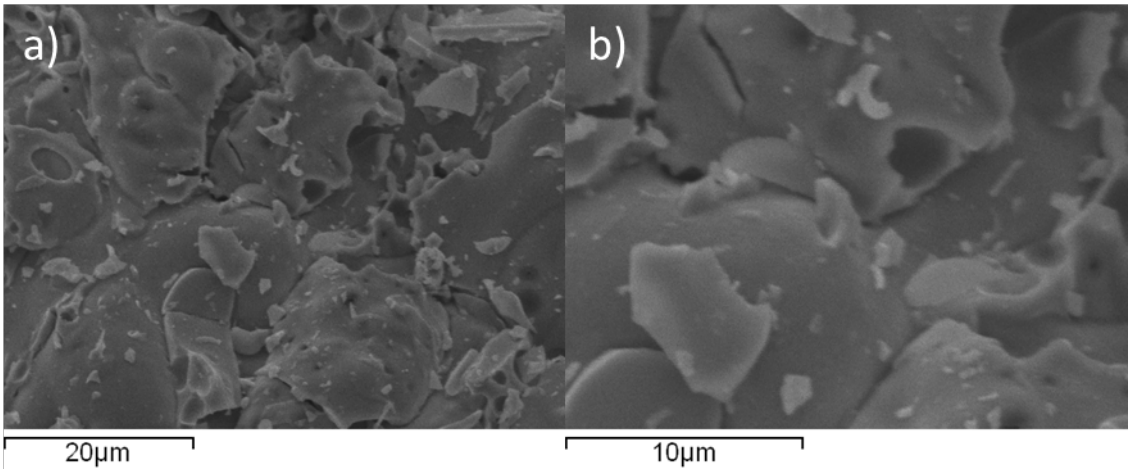

Figure 63: SEM images of 'Ni_6Mo_6C' post-reaction with 3:1 H_2/N_2 at 400°C for 8.5 hours. a) 2000x magnification and b) 5000x magnification.

Area	Ni weight (%)	Mo weight (%)	C weight (%)
1	13	13	74
2	14	12	74
3	16	12	72
4	16	5	80
Average	15	10	75

Table 17: EDX values for 'Ni_6Mo_6C' post-reaction with 3:1 H_2/N_2 at 400°C for 8.5 hours.

3.2.2.2.2 Ammonia Synthesis at 700°C for Ni_6Mo_6C

As the material was inactive for ammonia synthesis at 400°C, the temperature was increased to 700°C, despite ammonia synthesis being thermodynamically unfavourable at this temperature. The conductivity profile for the material at 700°C is provided in Figure 64.

The ammonia synthesis rate for the material at 700°C was calculated to be 152 ± 89 µmol h^{-1} g^{-1}. For the first 20 minutes, there was a lag period before the material became active. The lag period could possibly be explained by the incorporation of nitrogen into the lattice and therefore, the transition of the material from the carbide to the nitride or due to surface segregation/restructuring.

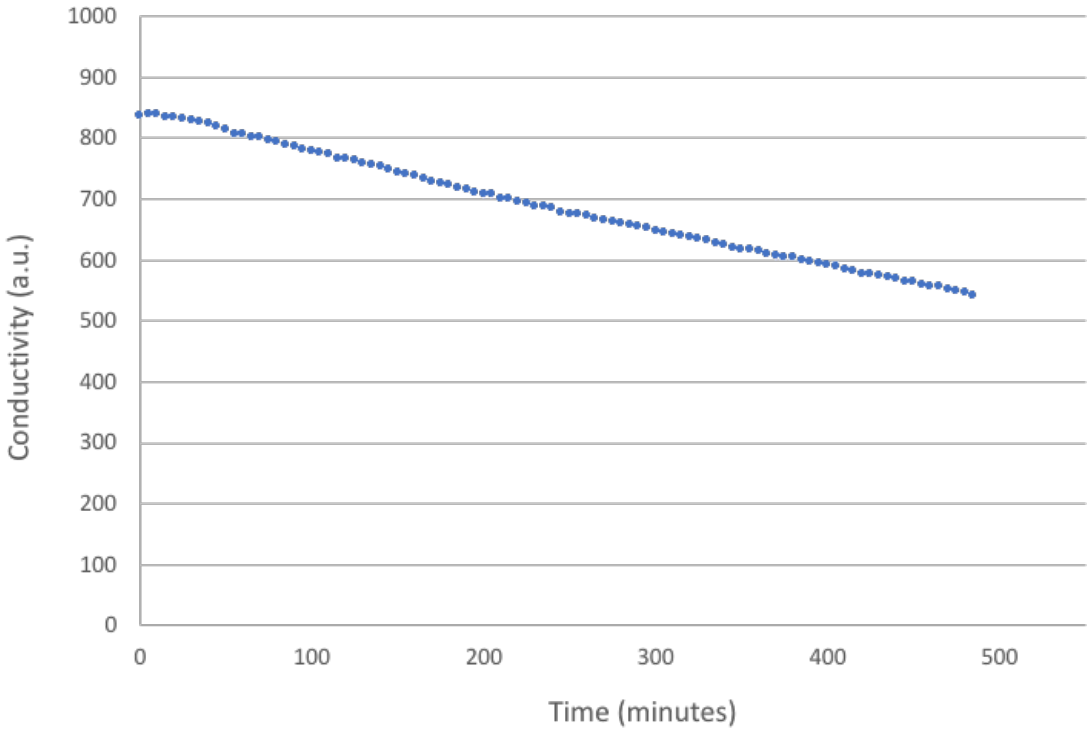

Figure 64: Conductivity profile for 'Ni_6Mo_6C' reacted with 3:1 H_2/N_2 at 700°C for 8 hours.

The XRD pattern of the material post 700°C reaction shows that Ni_2Mo_3N and $Mo_{0.09}Ni_{0.91}$ are the only phases present, as observed in Figure 65. This suggests that Ni_6Mo_6C has undergone nitridation during the reaction and could explain the reason for the material becoming active. The formation of either nickel or a nickel molybdenum alloy, alongside Ni_2Mo_3N, have been reported in the literature [36] [98]. Rietveld refinement by Conway and Prior [60] confirms that the structure is Ni_2Mo_3N and not Ni_3Mo_3N. The nitride has previously been reported to be active for ammonia synthesis [39] [94] [36]. Therefore, it is of interest to know whether the material was active due to the incorporation of nitrogen into the lattice to form the nitride or if nitrogen was present because the carbide was active thereby producing NH_3, which further nitrided the sample.

Co_6Mo_6C has been shown to form Co_3Mo_3N when reacted under 3:1 H_2/N_2 at 600°C [55]. Co_6Mo_6N was not formed as an intermediate phase but instead only $Co_6Mo_6C_x$ and $Co_3Mo_3N_x$ phases were observed during the transformation.

Almost all of the carbon had been removed from the material during the reaction as seen from the elemental analysis (C: 0.08 wt. %, H: 0.02 wt. % and N: 2.16 wt. %). The nitrogen content has also significantly increased. This further confirms that a nitride phase has been formed during the reaction. The expected stoichiometric percentage of nitrogen in Ni_2Mo_3N, taking into account the presence of additional nickel, is 2.93 wt. %. The obtained value of 2.16 wt. % for the material agrees quite well with this expected value.

This replacement of carbon with nitrogen contrasts with the observation for Co_6Mo_6C, which showed no incorporation of nitrogen [54]. However, the material was not tested at a temperature of 700°C and therefore, the higher temperature may be required for the replacement to occur in that case.

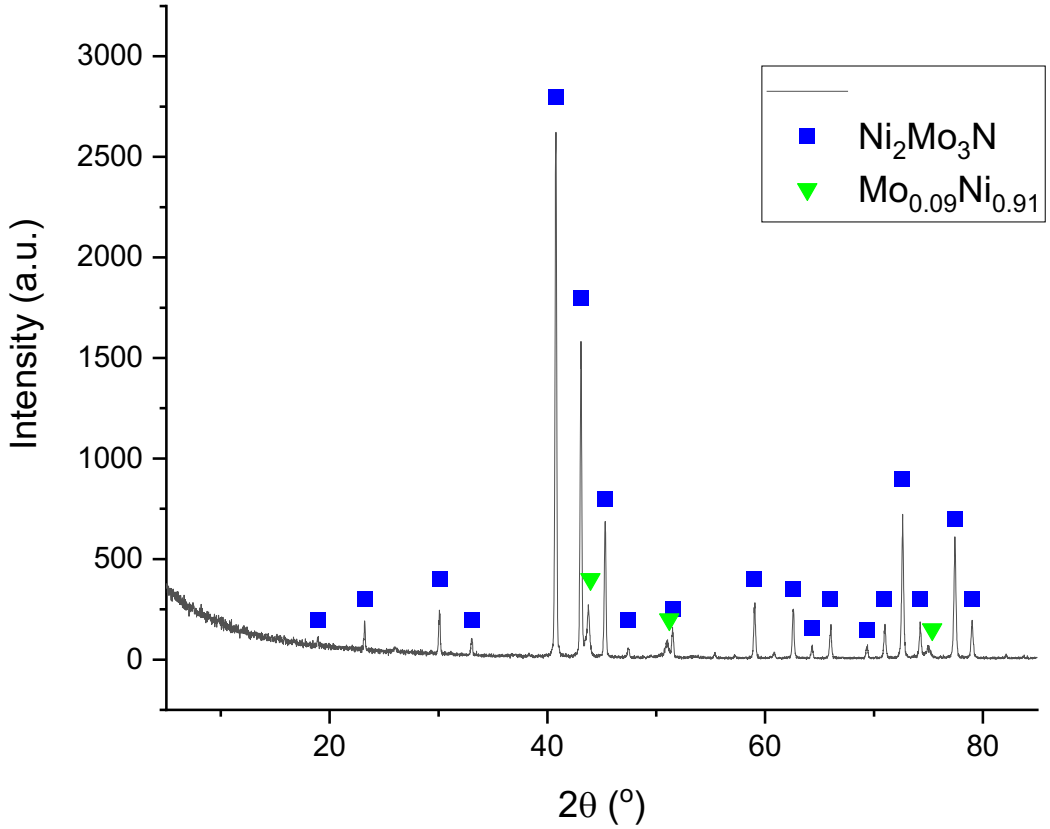

Figure 65: XRD pattern of 'Ni_6Mo_6C' post-reaction with 3:1 H_2/N_2 at 700°C for 8 hours. Reflections marked: ■ Ni_2Mo_3N (JCPDS file number 01-072-6569) and ▼ $Mo_{0.09}Ni_{0.91}$ (JCPDS file number 01-071-9766).

The Raman spectrum of the post-reaction material appears to be similar to the one for the pre-reaction sample, as shown in Figure 66. This suggests that there is a passivating oxide layer on the surface of the material. The Raman bands at 936, 887, 816 and 704 cm^{-1} can be attributed to β-$NiMoO_4$. Bands due to α-MoO_3 are also observed at 478 and 126 cm^{-1}. Another area of the sample was examined and there appeared to be no well-defined bands as was seen for the sample post 400°C reaction.

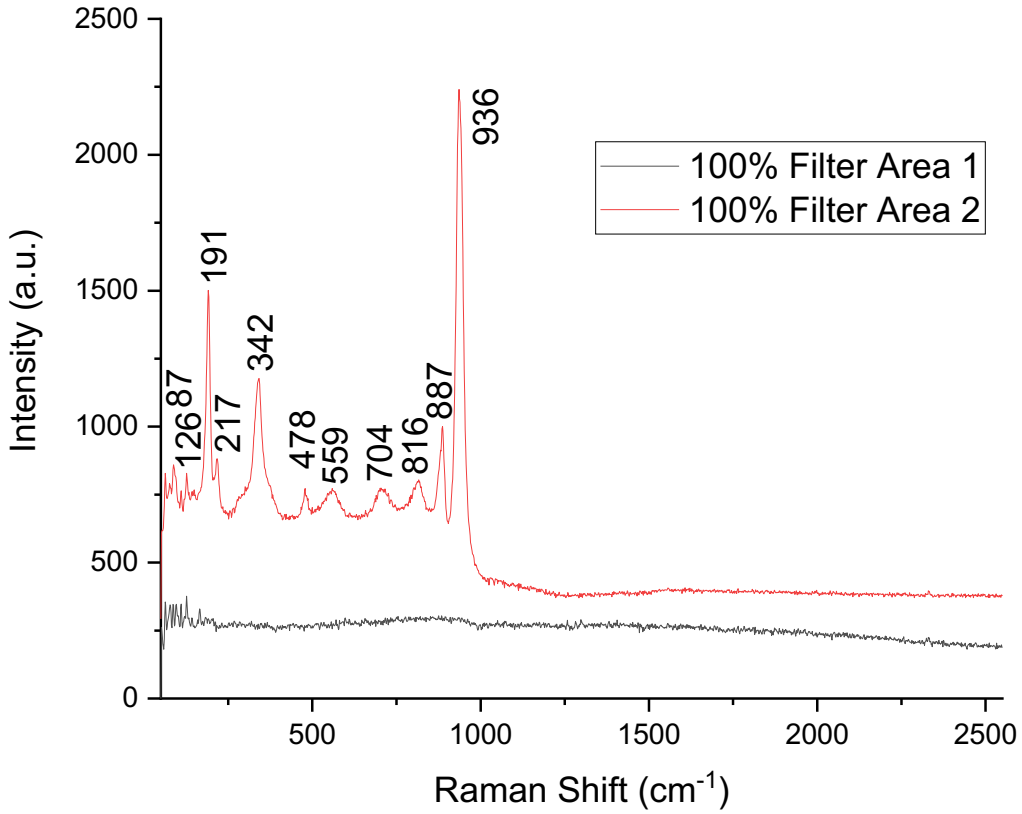

Figure 66: Raman spectra of 'Ni_6Mo_6C' post-reaction with 3:1 H_2/N_2 at 700°C for 8 hours. The spectra were taken at two different areas with a 100% filter.

As there was a change in phase, as evidenced by the XRD pattern, SEM analysis was performed on the material to see if there was also a change in the morphology. The SEM images of 'Ni_6Mo_6C' post 700°C reaction in Figure 67 show that the morphology has been retained compared to the pre-reaction material. This suggests that the nitridation process is pseudomorphic. The stoichiometric percentage of nickel, molybdenum and nitrogen in Ni_2Mo_3N is 28.00 wt. %, 68.66 wt. % and 3.34 wt. %, respectively. The EDX data presented in Table 18 shows that nitrogen was detected, which was not observed in the pre-reaction material. This further indicates that the carbide had transformed to Ni_2Mo_3N during the reaction. A large percentage of carbon was detected for this material but this may be due to the carbon stub the sample was placed on for EDX analysis.

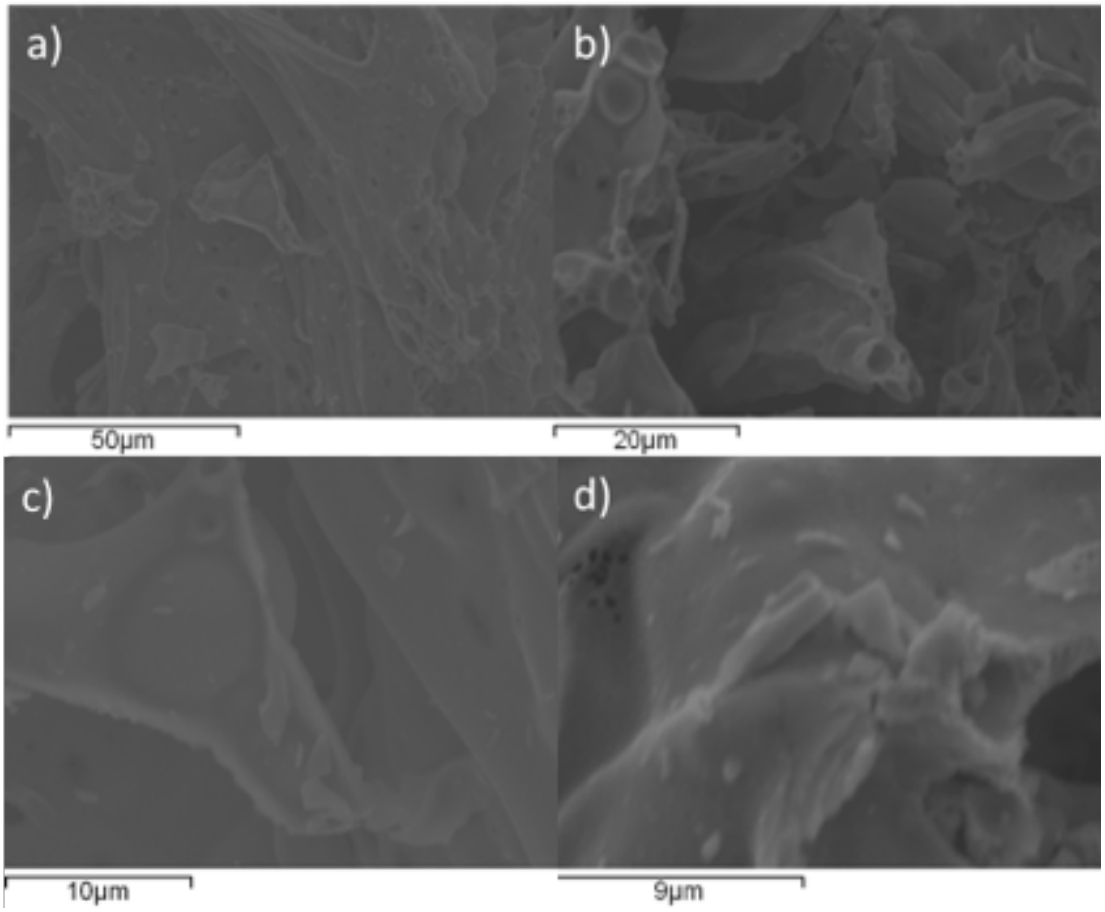

Figure 67: SEM images of 'Ni_6Mo_6C' post-reaction with 3:1 H_2/N_2 at 700°C for 8 hours. a) 1000x magnification, b) 2000x magnification, c) 4000x magnification and d) 6000x magnification.

Area	Ni weight (%)	Mo weight (%)	C weight (%)	N weight (%)
1	31	50	13	6
2	27	47	15	7
3	28	48	17	7
4	18	20	63	0
5	24	15	61	0
6	19	12	69	0
7	16	23	61	0
8	14	18	69	0
9	18	23	60	0
10	18	23	60	0
11	14	7	79	0
12	16	23	61	0
13	25	48	19	8
14	19	41	29	11
15	34	48	15	4
Average	21	30	46	3

Table 18: EDX values for 'Ni_6Mo_6C' post-reaction with 3:1 H_2/N_2 at 700°C for 8 hours.

The formation of the nitride from Ni_6Mo_6C was investigated by thermogravimetric analysis of the pre-reaction material under 5% H_2/N_2. Mass spectrometry was employed to determine the product formed when Ni_6Mo_6C was nitrided to Ni_2Mo_3N and $Mo_{0.09}Ni_{0.91}$. The TGA curve and first derivative weight change of 'Ni_6Mo_6C' is presented in Figure 68. The material was heated from room temperature to 1000°C at a ramp rate of 10°C/min under 5% H_2/N_2. The first feature of the TGA curve is a weight loss of approximately 0.4% at 358°C. Whilst methane may be the expected product, the mass spectral ion curves of 2 and 44 m/z show peaks at this temperature, as seen in Figure 69 and Figure 70, suggesting the loss of H_2 and either CO_2 or C_3H_8. The oxygen present in any CO_2 produced could arise from the oxygen surface layer on the material and therefore, this weight loss would correspond to the removal of the passivation layer. The weight loss could also be due to the reaction of lattice carbon to form propane. The loss of carbon from Ni_6Mo_6C would result in a weight loss of 1.28%. However, only a weight loss of 0.4% was observed, suggesting that only a small amount of carbon was being removed from the material. Therefore, this needs to be investigated further.

The second feature of the TGA curve is a weight gain of approximately 0.6% at 777°C. It is observed that after TGA, the final material has gained a small amount of weight. It is not certain what the weight gain is due to but the ion curve of H_2 (m/z = 2) shows a peak at this temperature. The mass spectra of 14, 15, 16, 17, 18, 28, 30, 32 and 46 m/z were investigated but they did not show any features. Assuming the following equation to be true, the formation of Ni_2Mo_3N and Ni from Ni_6Mo_6C would result in a weight gain of 1.70%. This does not take into account the presence of Ni_2Mo_3N and Mo_2C in the starting material. The total weight gain at 906°C was observed to be only 0.1%.

$$Ni_6Mo_6C + N_2 \rightarrow 2\ Ni_2Mo_3N + 2\ Ni + C$$

Equation 3: Equation for the formation of Ni_2Mo_3N from Ni_6Mo_6C

The mass began to decrease again after 906°C and resulted in a 0.2% weight loss. This reduction in mass could be due to the loss of nitrogen from the material and therefore, the reduction of the material to nickel and molybdenum metal. The total loss of nitrogen from the material would equate to a weight loss of 2.93%. This would suggest that only a small percentage of nitrogen had been removed from the material.

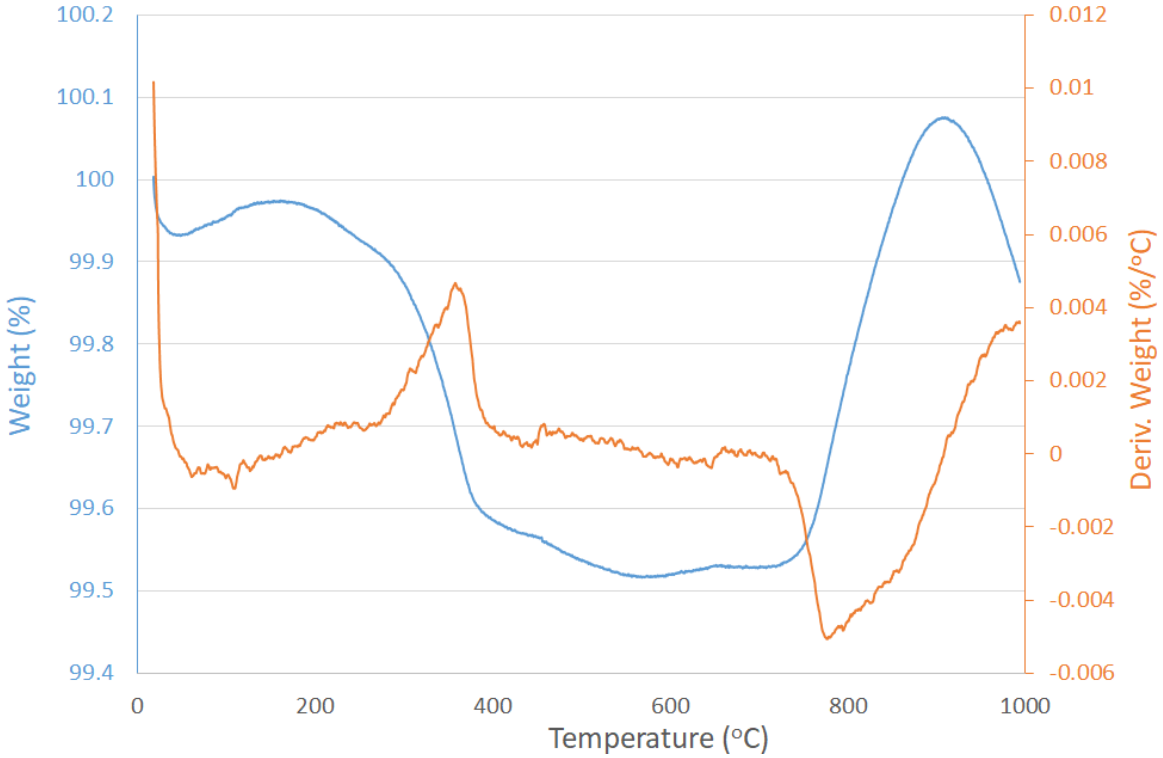

Figure 68: TGA and derivative weight profile of 'Ni_6Mo_6C' under 5%H_2/N_2 in the range from room temperature to 1000°C.

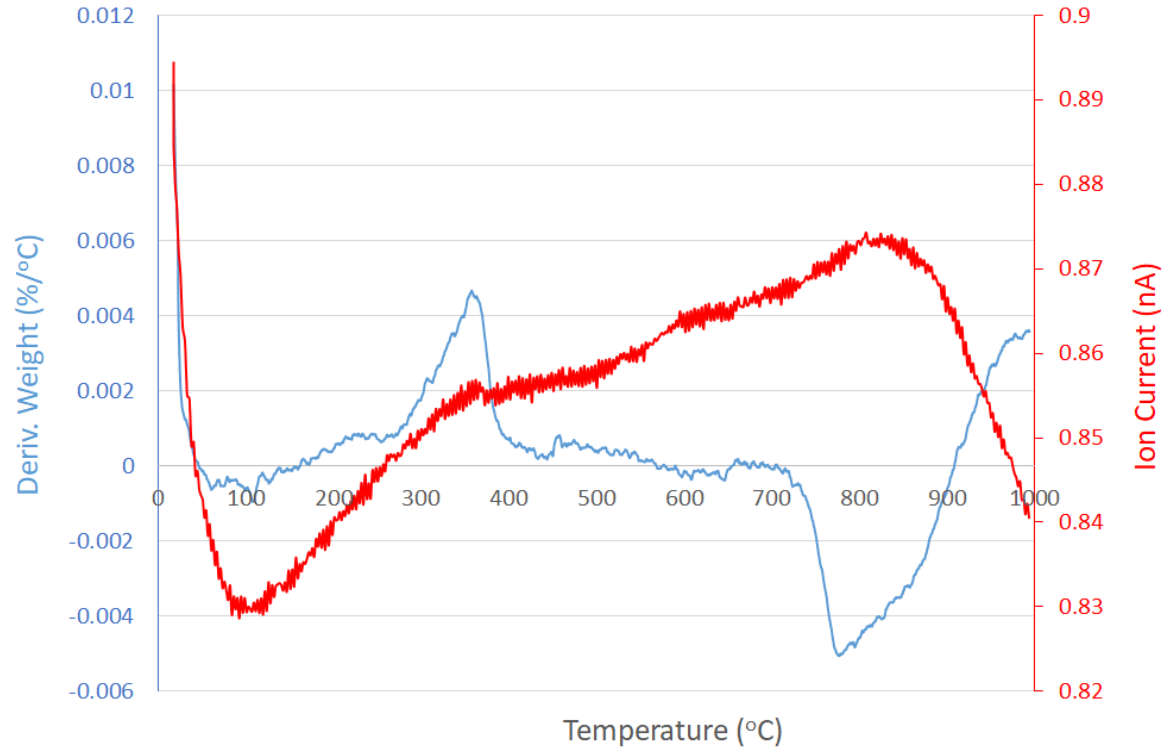

Figure 69: The mass spectrum ion curve for 2 m/z and the derivative weight profile.

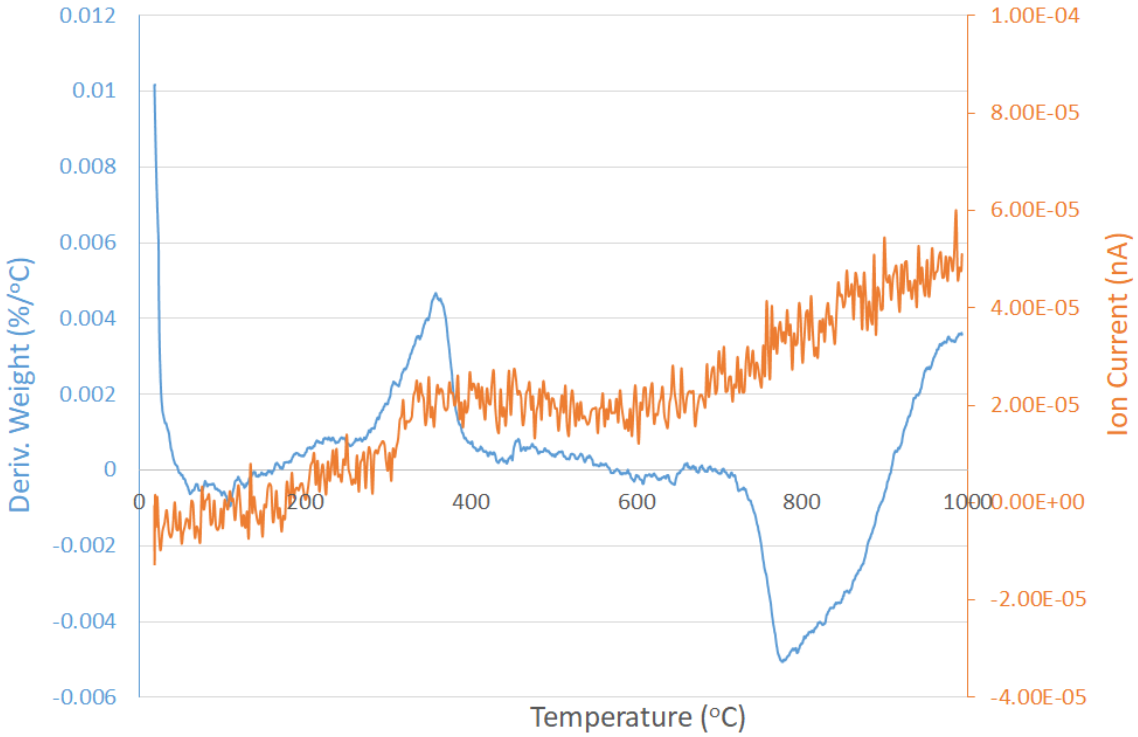

Figure 70: The mass spectrum ion curve for 44 m/z and the derivative weight profile.

Attempting to prepare the Ni_3Mo_3C phase has proved to be difficult. The oxide is seen to decompose to Mo_2C and nickel metal at temperatures above 600°C when carburised with 20% CH_4/H_2 as seen in section 3.2.1.3. However, Ni_6Mo_6C has been easier to synthesise by using citric acid as the source of carbon. 'Ni_6Mo_6C' was active for ammonia synthesis at 700°C and was seen to undergo nitridation to form Ni_2Mo_3N and $Mo_{0.09}Ni_{0.91}$ during the reaction. It is therefore proposed that this transformation of the carbide is required for the material to be active. However, further work needs to be performed to understand if the carbide or the nitrided material is the active phase for the ammonia synthesis activity. Testing the Ni_3Mo_3C phase for ammonia synthesis may provide an explanation and also the preference of the carbide to form Ni_2Mo_3N instead of Ni_3Mo_3N when it is nitrided.

3.2.3 Nickel Molybdenum Carbide (Ni_3Mo_3C)

3.2.3.1 Preparation with Activated Charcoal

Regmi and Leonard have prepared Ni_3Mo_3C by mixing nickel molybdenum oxide with decolourising carbon and reacting the material at high temperature [48]. Therefore, this method was replicated in order to form Ni_3Mo_3C. Part of the work outlined in this section was undertaken in collaboration with Shane Mckenna, who was a final year project student that helped with the preparation of the material. To try and reduce the amount of carbon lost as methane during the preparation, hydrogen was removed from the gas mixture. Excess activated charcoal was mixed with the oxide precursor ($Ni_3Mo_3O_x$) and then, this was heated to 1000°C under argon. Contrary to the literature, Ni_3Mo_3C has not formed

under these conditions in the present study as shown by the XRD pattern in Figure 71. The material has instead decomposed to Mo_2C and $Mo_{0.09}Ni_{0.91}$, with small amounts of Ni_6Mo_6C present. Regmi and Leonard suggest that the Ni_3Mo_3C is formed at a temperature of 1030°C using this method [48]. From XRD patterns, the authors were able to show that Ni_6Mo_6C forms at a lower temperature of 975°C. During the transformation of the carbide from Ni_6Mo_6C to Ni_3Mo_3C, the material apparently decomposed into a mixture of $MoNi_4$ and a Mo-Ni phase with the W type structure at 990°C. The alloys then react with carbon to form Ni_3Mo_3C at 1030 °C. However, these phases are different to the ones reported here and therefore, it is concluded that this material has not followed this transformation pathway.

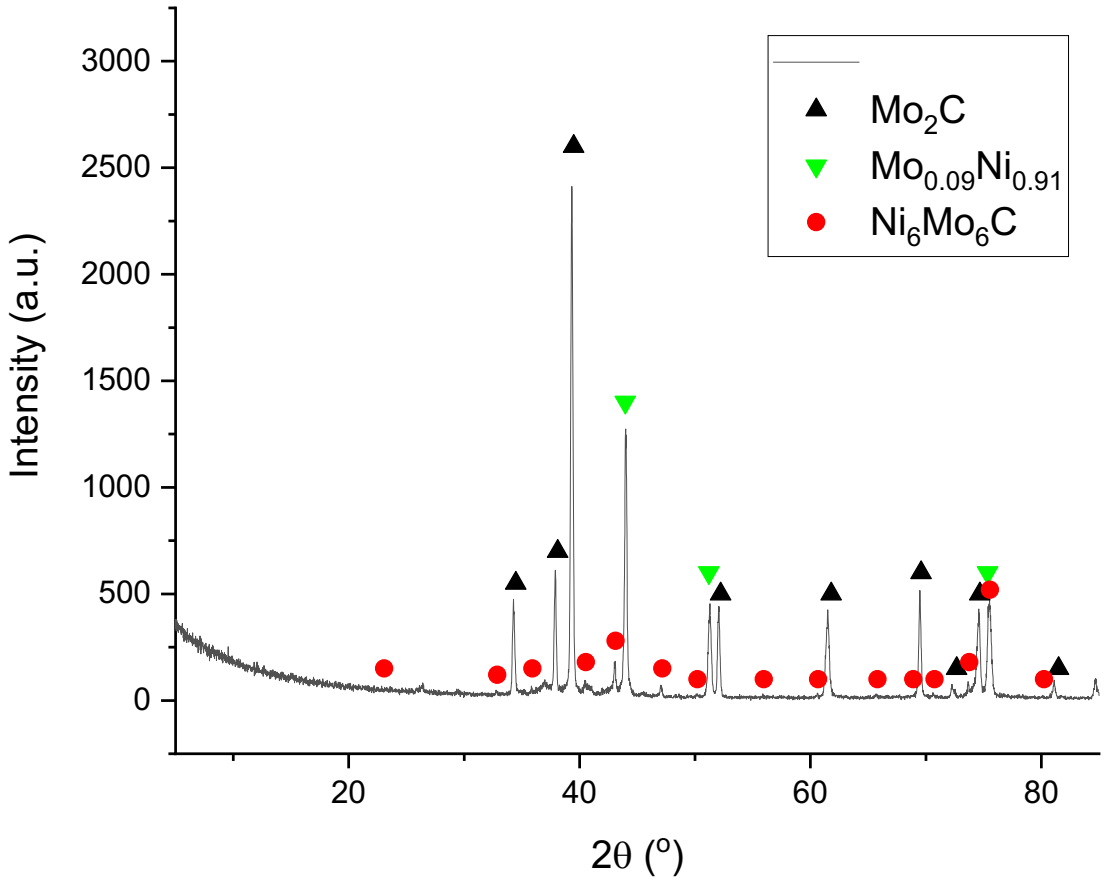

Figure 71: XRD pattern of $Ni_3Mo_3O_x$ + C post-preparation at 1000°C under argon. Reflections marked: ● Ni_6Mo_6C (JCPDS file number 03-065-4436), ▲ Mo_2C (JCPDS file number 00-001-1188) and ▼ $Mo_{0.09}Ni_{0.91}$ (JCPDS file number 01-071-9766).

The elemental analysis showed that the starting oxide precursor had 23.74 wt. % carbon in the material after activated carbon had been added (C: 23.74 wt. %, H: 3.06 wt. %, N: 5.11 wt. %). A high percentage of nitrogen was also present, which could result from the starting nickel and molybdenum materials used in the Pechini method. The amount of carbon in the material was higher than the expected amount from using a stoichiometric

ratio of oxide precursor to carbon. However, this excess carbon can be accounted for, as it originates from the citric acid used in the preparation method. Both the carbon and nitrogen percentage decreased after treatment at 1000°C under Ar (C: 14.57 wt. %, H: 0.07 wt. %, N: 1.71 wt. %). The carbon percentage was greater than the expected stoichiometric percentage for Mo_2C (5.89 wt. %) and Ni_6Mo_6C (1.28 wt. %), which are phases present in the material according to the XRD pattern. Therefore, this suggests that there may be carbon laydown on the material. A peak is observed at approximately 26° 2θ, which is expected to relate to carbon and thus confirms the presence of deposited carbon.

As the Ni_3Mo_3C phase was not formed by this method, even with a large percentage of carbon remaining after the preparation, it suggests that hydrogen was required in the gas feed to form the targeted phase.

Raman analysis was conducted for this material to investigate if there was carbon laydown due to the activated carbon and if there was any surface oxide species. The Raman spectra taken at two different areas of the material exhibit different spectra, as observed in Figure 72. In the first area, the Raman spectrum shows the presence of carbon with the D band at 1338 cm^{-1}, the G band at 1570 cm^{-1} and the 2D band observed at 2681 cm^{-1}. There are also bands present at approximately 2450 cm^{-1} and 2950 cm^{-1} attributed to D+D'' and D+G respectively [116]. The intensity of the G band is related to the number of layers of graphene present. As the number of layers of graphene increases, the intensity of the band increases, and therefore this can be used to determine the thickness of graphene. The 2D band can also be used to determine the graphene thickness from its intensity and shape. The unique shape differences of this band can give information on the number of layers of graphene. Furthermore, the intensity ratio of the 2D and G bands, I_{2D}/I_G, for graphene without defects is two. As the intensity of the 2D band in this sample is less than half of the G band this suggests that graphene is not present in the material and instead consists of graphite. Although, the symmetrical shape of the 2D band suggests that the material is composed of graphene, it must be noted that turbostratic graphite has a similar shaped band [117]. Turbostratic carbon has multiple graphene layers that are rotated and thus reduced orbital hybridisation.

Additional Raman bands associated with an oxide phase were detected at 934 and 887 cm^{-1} and could be due to $NiMoO_4$. When the filter size was increased, the bands due to carbon significantly decreased and the bands due to the oxide became more prominent. This suggests that the laser had removed the graphite from the material.

In the second area examined, the bands due to carbon were not detected. Instead, bands due to β-$NiMoO_4$ were observed at 940, 884, 811 cm^{-1}. Bands due to α-MoO_3 are also observed at 481, 287, 218, 192 and 148 cm^{-1} [118].

The XRD pattern demonstrated that the material had decomposed to Mo_2C and $Mo_{0.09}Ni_{0.91}$ and only a small intensity was observed for Ni_6Mo_6C. However, the Raman spectra showed that there were bands due to β-$NiMoO_4$. These bands could be related to the nickel molybdenum alloy or the Ni_6Mo_6C phase. The large amount of carbon laydown observed from the Raman bands suggests that the carbon from the citric acid is relatively unreactive under the argon atmosphere. Therefore, hydrogen is required in the feed stream in order to carburise the material.

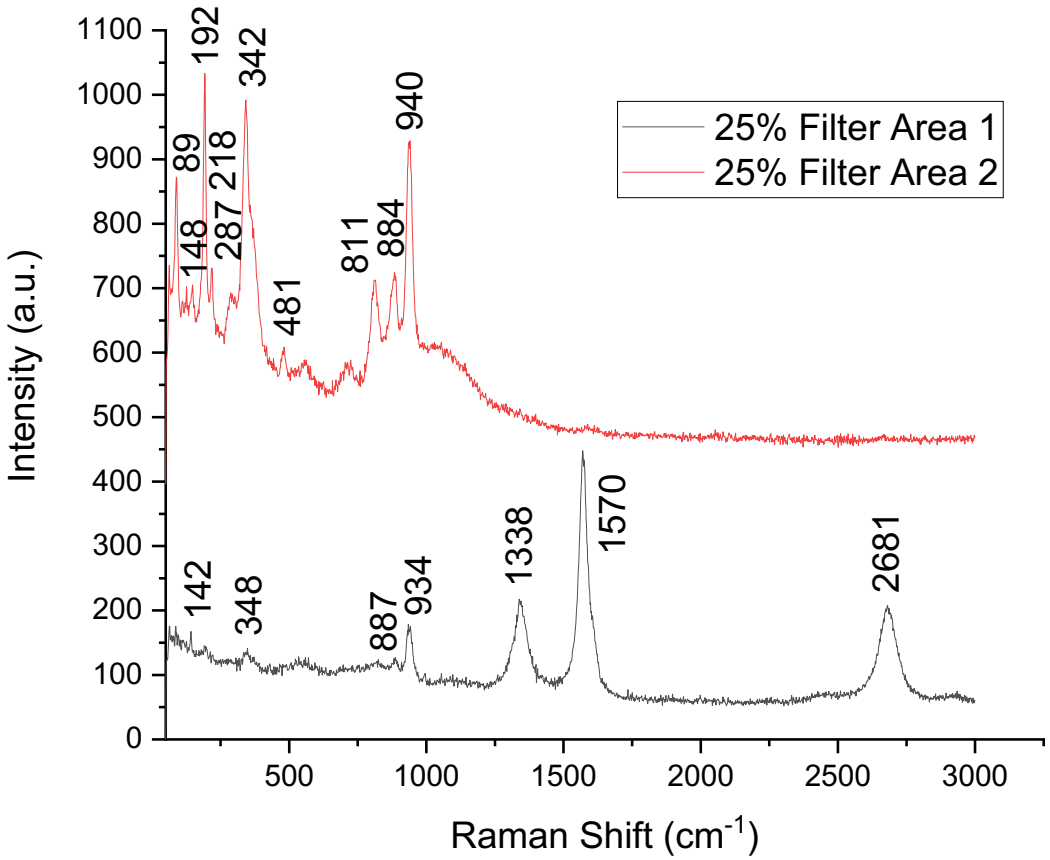

Figure 72: Raman spectra of Mo_2C + $Mo_{0.09}Ni_{0.91}$ prepared at 1000°C under Ar. The spectra were taken at two different areas with a 25% filter.

The SEM images displayed in Figure 73 show that the morphology of this material is similar to the morphology observed for the Mo_2C + Ni materials described in section 3.2.1.3.1 (Figure 29). The EDX results in Table 19 show that there was a large percentage of carbon present in this material, which agrees with the carbon laydown observed in the Raman spectrum. The stoichiometric percentage of nickel, molybdenum and nitrogen for Ni + Mo_2C (assuming a Ni:Mo ratio of 1:1) is 36.54 wt. %, 59.72 wt. % and 3.74 wt. %,

respectively. However, the stoichiometric ratio of Ni to Mo from the EDX analysis does not appear to be as expected. Instead, there appears to be more molybdenum present in the material.

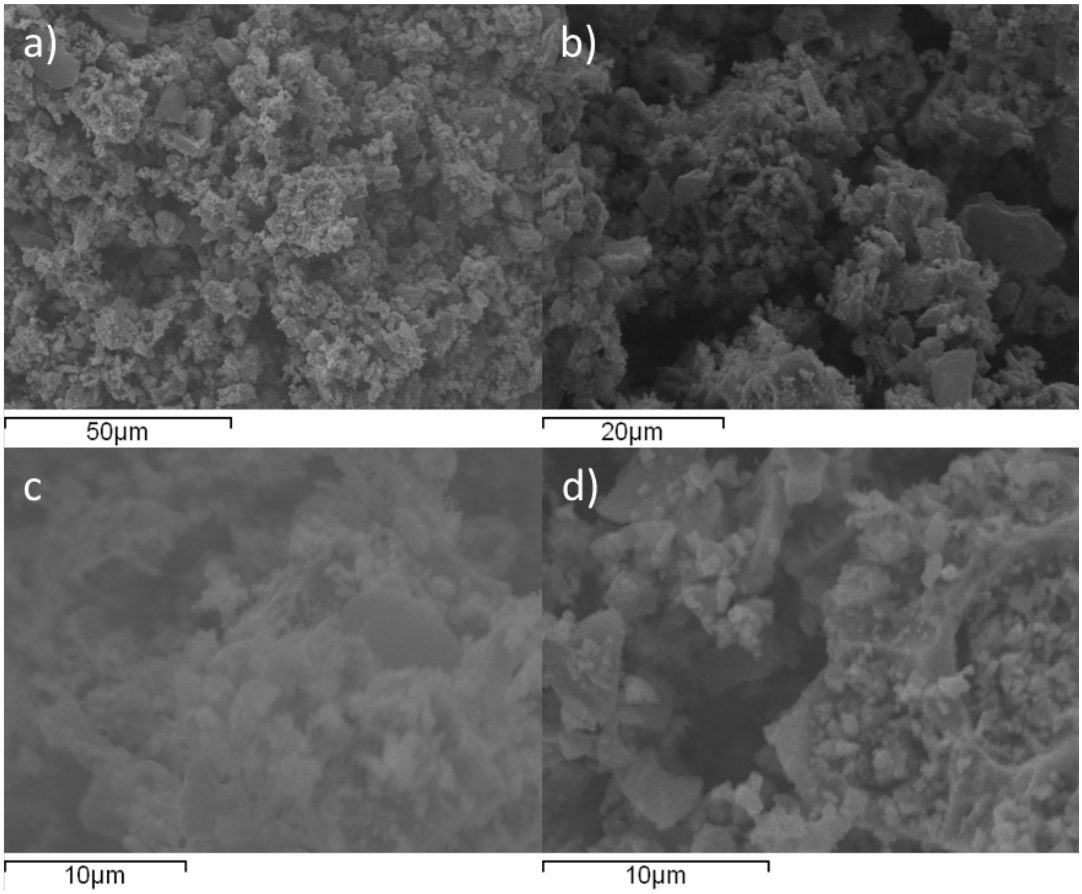

Figure 73: SEM images of $Ni_3Mo_3O_x$ + C post-preparation at 1000°C under argon. a) 1000x magnification, b) 2000x magnification, c) 4000x magnification and d) 5000x magnification.

Area	Ni weight (%)	Mo weight (%)	C weight (%)
1	8	11	81
2	8	15	77
3	8	14	78
4	10	12	78
5	3	21	76
6	3	17	80
7	9	15	76
8	8	10	82
9	8	14	78
Average	7	14	78

Table 19: EDX values for $Ni_3Mo_3O_x$ + C post-preparation at 1000°C under argon.

3.2.3.1.1 Ammonia Synthesis at 700°C for Mo_2C and $Mo_{0.09}Ni_{0.91}$

The conductivity profile of the material at 700°C is presented in Figure 74. The ammonia synthesis rate for the material at 700°C was 252 μmol h^{-1} g^{-1}. This value is very similar to Ni_6Mo_6C. There was a lag period of 10 minutes at the start before the material became active. This may be due to the transition of the material to form the nitride as was observed for Ni_6Mo_6C. The activity of this material can be explained by the XRD pattern and elemental analysis.

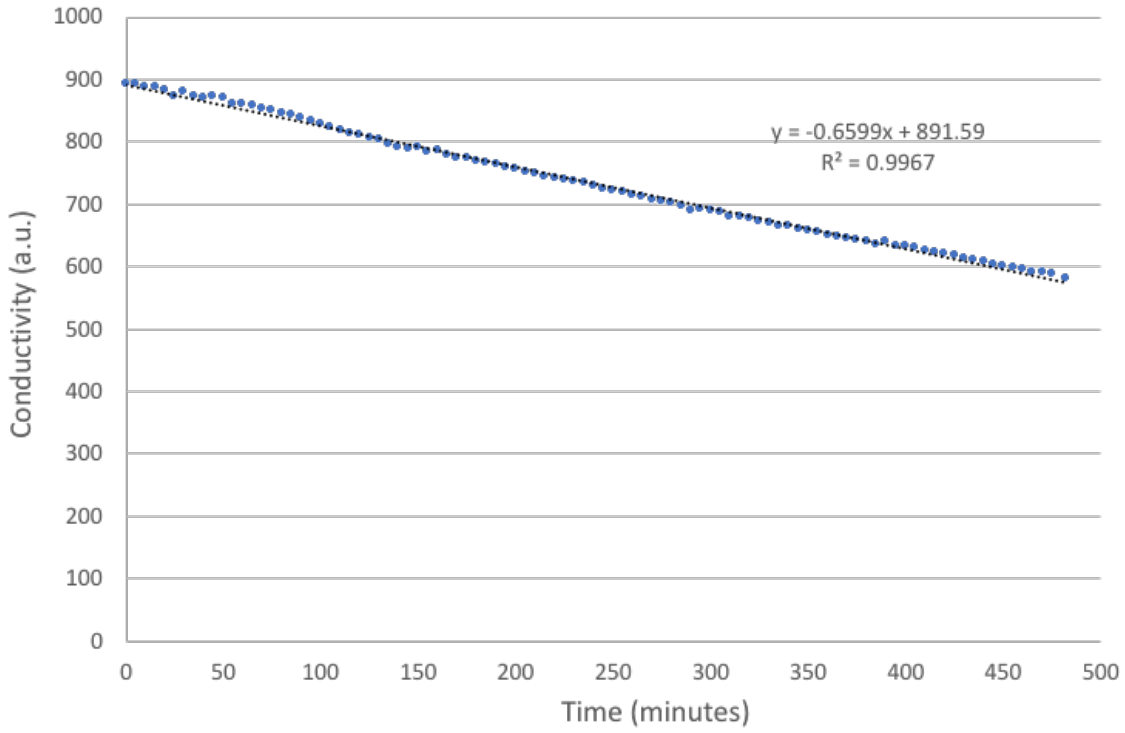

Figure 74: Conductivity profile for Mo_2C + $Mo_{0.09}Ni_{0.91}$ reacted with 3:1 H_2/N_2 at 700°C for 8 hours.

The XRD pattern of the material in Figure 75 shows that Ni_2Mo_3N had indeed been formed during the reaction. This suggests that the Mo_2C and nickel phases combined at this temperature to form the nitride. Nickel metal and Mo_2C were also still present in the sample, however, the intensity of the reflections associated with them had decreased compared to pre-reaction.

A large percentage of the carbon has been removed from the material during the reaction as can be seen from the elemental analysis (C: 0.95 wt. %, H: 0.00 wt. %, N: 1.97 wt. %). This result confirms that the material underwent nitridation as observed by the XRD pattern. The remaining carbon was most likely due to the Mo_2C phase present in the material. The nitrogen content had increased a small amount compared to pre-reaction (1.71 wt. %). The expected stoichiometric percentage of nitrogen in Ni_2Mo_3N, taking into

account the presence of Ni and Mo_2C, is 2.05 wt. %. The obtained value of 1.97 wt. % for the material agrees quite well with this expected value.

The conversion of the material to form the nitride may explain the similar activities of the Ni_6Mo_6C and the mixed Mo_2C and $Mo_{0.09}Ni_{0.91}$. Therefore, the nitride may be responsible for the activity of these materials and not the carbide. As mentioned previously, the induction period may be due to the materials undergoing nitridation and once a sufficient amount of nitrogen is incorporated into the lattice, the material becomes active.

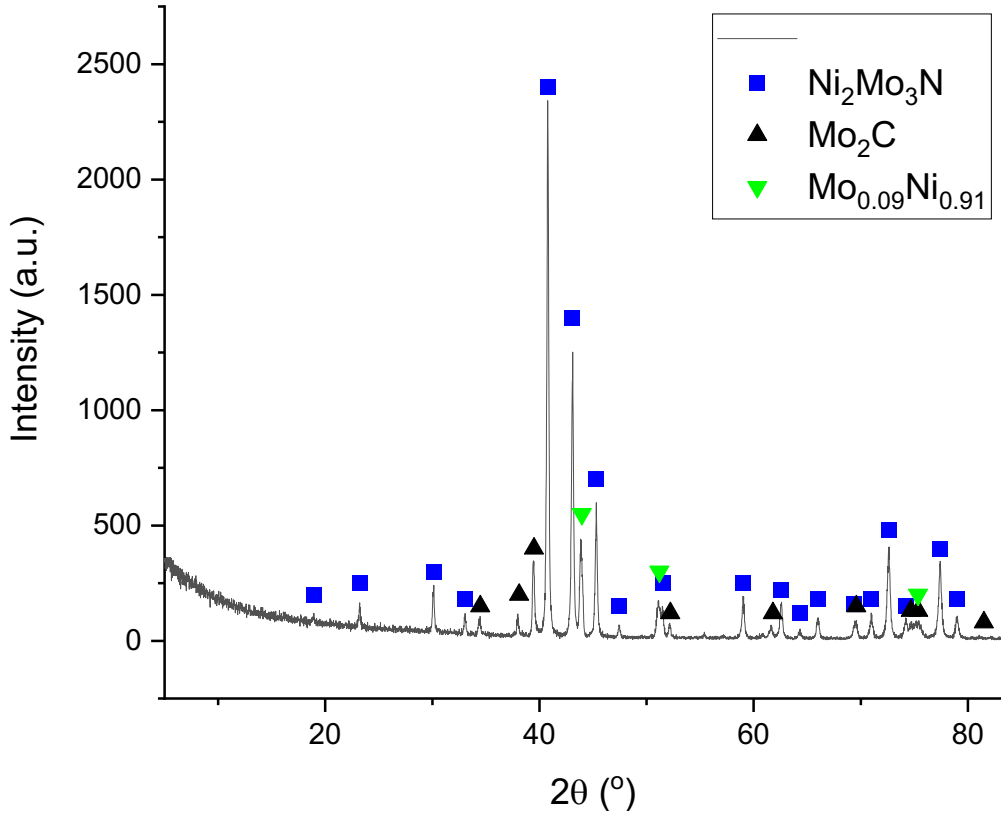

Figure 75: XRD pattern of Mo_2C + $Mo_{0.09}Ni_{0.91}$ post-reaction with 3:1 H_2/N_2 at 700°C for 8 hours. Reflections marked: ■ Ni_2Mo_3N (JCPDS file number 01-072-6569), ▼ $Mo_{0.09}Ni_{0.91}$ (JCPDS file number 01-071-9766) and ▲ Mo_2C (JCPDS file number 00-001-1188).

The Raman spectrum is very similar to that for β-$NiMoO_4$, as seen in Figure 76, which most likely relates to a passivation layer on the surface of the sample. The Raman bands at 937, 888, 811, 345 and 284 cm^{-1} can be accredited to β-$NiMoO_4$ [96] [97]. There were no bands observed for carbon in the areas that were investigated. This agrees with the elemental analysis that showed almost all the of the carbon had been removed from the material.

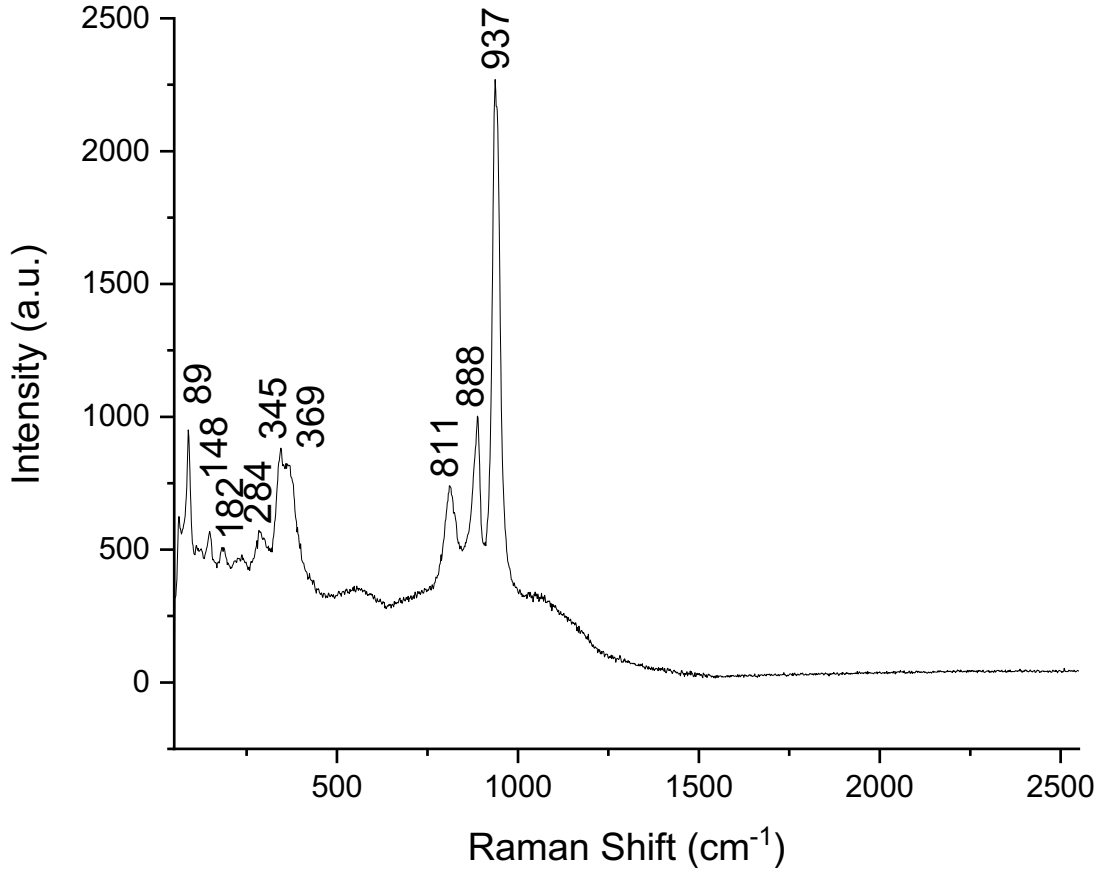

Figure 76: Raman spectrum of Mo_2C + $Mo_{0.09}Ni_{0.91}$ post-reaction with 3:1 H_2/N_2 at 700°C for 8 hours.

As the material changed phase during the reaction, SEM analysis was performed to see if this resulted in a change in the morphology. Representative SEM images for the material post-reaction are displayed in Figure 77. The morphology of this material was different to the Ni_2Mo_3N discussed in section 3.2.1.2 and the pre-reaction material. The material consists of fine needles and possesses porous surfaces. The difference in morphology from the pre-reaction material may be due to the formation of Ni_2Mo_3N. The stoichiometric percentage of nickel, molybdenum and nitrogen for Ni_2Mo_3N is 28.00 wt. %, 68.66 wt. % and 3.34 wt. % respectively. However, the EDX results in Table 20 show that the stoichiometric ratio of Ni to Mo from the EDX analysis is not the expected mass ratio as the amount of molybdenum is lower than expected. However, it must be noted that the EDX measurement is semi-quantitative and therefore, care must be taken when comparing results. Furthermore, a large percentage of carbon was detected in this material, which was difficult to determine due to the samples being placed on carbon stubs.

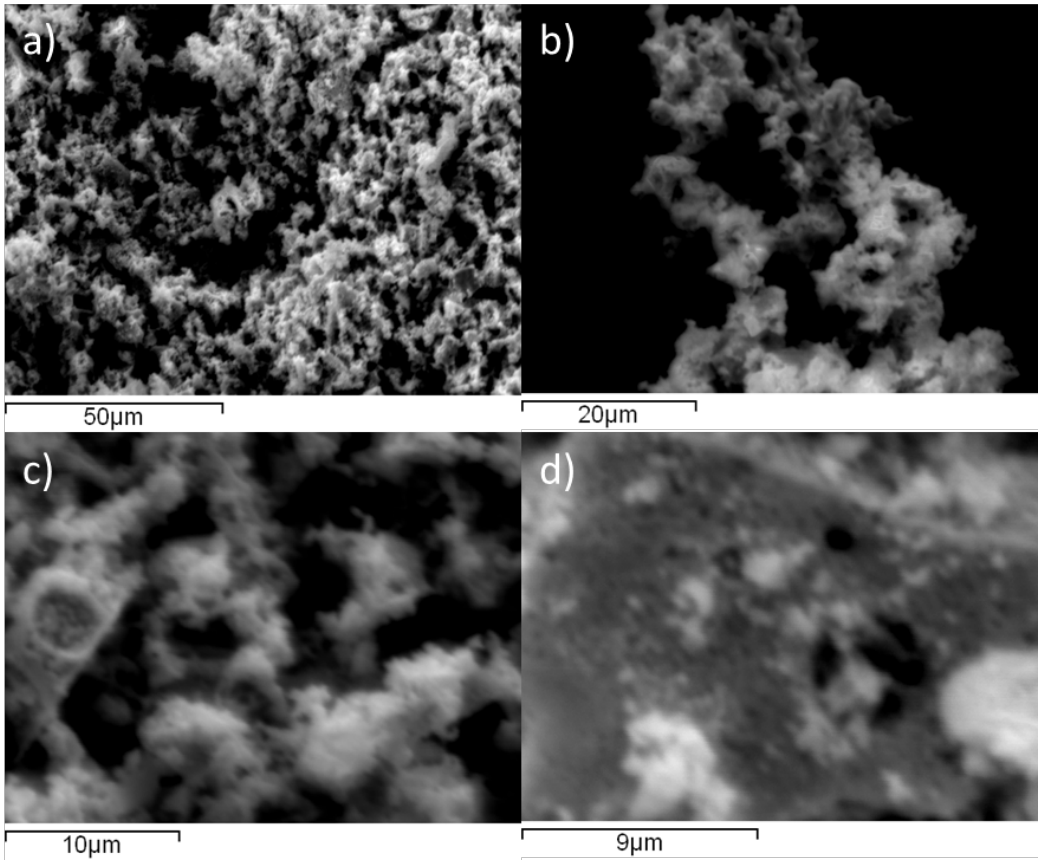

Figure 77: SEM images of Mo_2C + $Mo_{0.09}Ni_{0.91}$ post-reaction with 3:1 H_2/N_2 at 700°C for 8 hours. a) 1000x magnification, b) 2000x magnification, c) 4000x magnification and d) 6000x magnification.

Area	Ni weight (%)	Mo weight (%)	C weight (%)	N weight (%)
1	30	45	21	4
2	36	50	9	4
3	34	38	28	0
4	22	32	46	0
5	27	42	27	3
6	28	46	23	3
7	30	53	11	6
8	22	35	43	0
9	21	32	47	0
10	29	53	13	5
Average	28	42	27	3

Table 20: EDX values for Mo_2C + $Mo_{0.09}Ni_{0.91}$ post-reaction with 3:1 H_2/N_2 at 700°C for 8 hours.

3.2.3.2 Preparation of Ni_6Mo_6C by Carburisation

The apparent difficulty in forming Ni_3Mo_3C is interesting considering the relative ease in forming Co_3Mo_3C. Co_3Mo_3C can be prepared from its nitride analogue at 700°C under 20% CH_4/H_2 [54]. Interestingly, Co_6Mo_6C can be prepared via reduction of the Co_3Mo_3C under Ar/H_2 at a higher temperature of 900°C for 5 hours. It has also proved possible to form Co_3Mo_3C from Co_6Mo_6C by reacting it with 75% CH_4/N_2 at 800°C for 8 hours [119].

However, the material contained impurities of β-Mo_2C and graphite. The authors noted that the carbon located in the 0 0 0 (8a) site moved to the 1/8 1/8 1/8 (16c) sites and thus formed the Co_3Mo_3C phase. It has also been shown that transitioning from low to high nitrogen content Co_6Mo_6N and Co_3Mo_3N was possible by using a N_2/H_2 gas mixture at 400°C and N_2 alone at 700°C [50] [120]. From this work, it appears that the Ni_6Mo_6C can be formed under Ar or Ar/H_2. The material is more phase pure when prepared with Ar/H_2, however, it must be noted that the temperature was lower under these conditions. The higher temperature of 1000°C used when applying Ar may have resulted in the decomposition of Ni_6Mo_6C to Mo_2C and $Mo_{0.09}Ni_{0.91}$. However, from the characterisation results, it appears that the carbon was not incorporated into the lattice but instead resulted in carbon laydown. Following on from these reports in the literature, attempts were made to prepare Ni_3Mo_3C from Ni_6Mo_6C. The Ni_6Mo_6C prepared with Ar/H_2 at 700°C was used as the precursor. 'Ni_6Mo_6C' was carburised in 20% CH_4/H_2 at 800°C for 6 hours to replicate the conditions used to form Co_3Mo_3C from Co_6Mo_6C.

The XRD pattern in Figure 78 shows that the Ni_6Mo_6C decomposed to give a mixture of molybdenum carbides and nickel metal. There was also graphitic carbon present in the material. Therefore, it appears that the carburisation temperature needs to be lowered to form the Ni_3Mo_3C phase. Elemental analysis of the material post carburisation shows that there was a large percentage of carbon present, which was most likely due to the graphitic carbon (C: 23.90 wt. %, H: 0.00 wt. %, N: 0.15 wt. %).

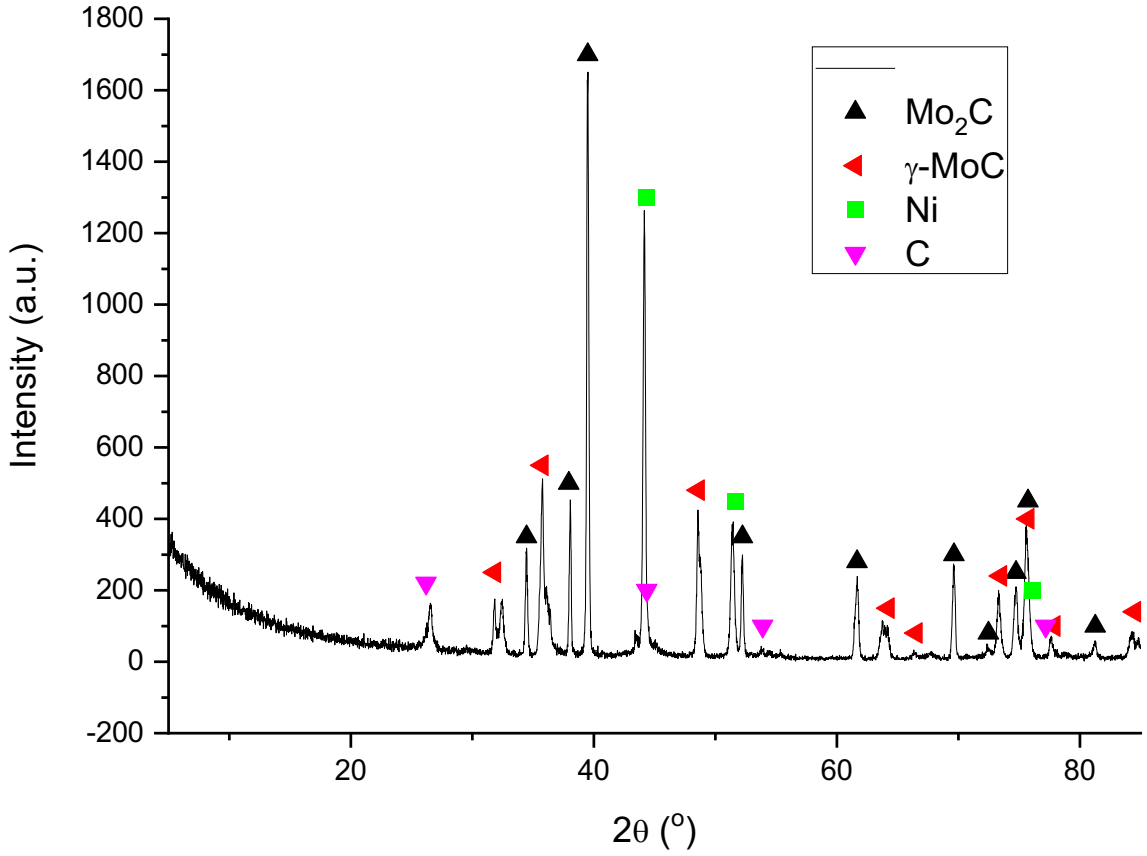

Figure 78: XRD pattern of 'Ni_6Mo_6C' post-preparation at 800°C under 20% CH_4/H_2. Reflections marked: ▲ Mo_2C (JCPDS file number 00-001-1188), ◀ γ-MoC (JCPDS file number 03-065-6664), ■ Ni (JCPDS file number 01-089-7128) and ▼ C (JCPDS file number 01-071-4630).

As the material decomposed at the high temperature, the carburisation temperature was lowered to 560°C. 'Ni_6Mo_6C' was carburised in 20% CH_4/H_2 for 6 hours. The XRD pattern of the material shows that Ni_3Mo_3C has been formed at this temperature along with impurities of Mo_2C and Ni_2Mo_3N. Ni_2Mo_3N was observed in the starting Ni_6Mo_6C precursor and the nitrogen most likely resulted from the $Ni(NO_3)_2{\cdot}6H_2O$ and $(NH_4)_6Mo_7O_{24}{\cdot}4H_2O$ used to prepare the oxide. However, the peaks associated with Ni_2Mo_3N appear to have shifted to lower 2θ values as seen in Figure 79, which suggests that the nitride has undergone carburisation to form $Ni_2Mo_3C_xN_y$.

The expected stoichiometric percentage of carbon in Ni_3Mo_3C is 2.52% and in Ni_6Mo_6C is 1.28%. The elemental analysis of the material post carburisation was as follows, C: 1.84 wt. %, H: 0.00 wt. % and N: 0.42 wt. %. The carbon percentage had increased compared to pre-reaction (1.18 wt. %). This could be due to both Ni_6Mo_6C undergoing carburisation to Ni_3Mo_3C and the nitride forming the carbonitride. The nitrogen percentage had decreased post-reaction, which suggests that some nitrogen had been lost in the formation of the carbonitride.

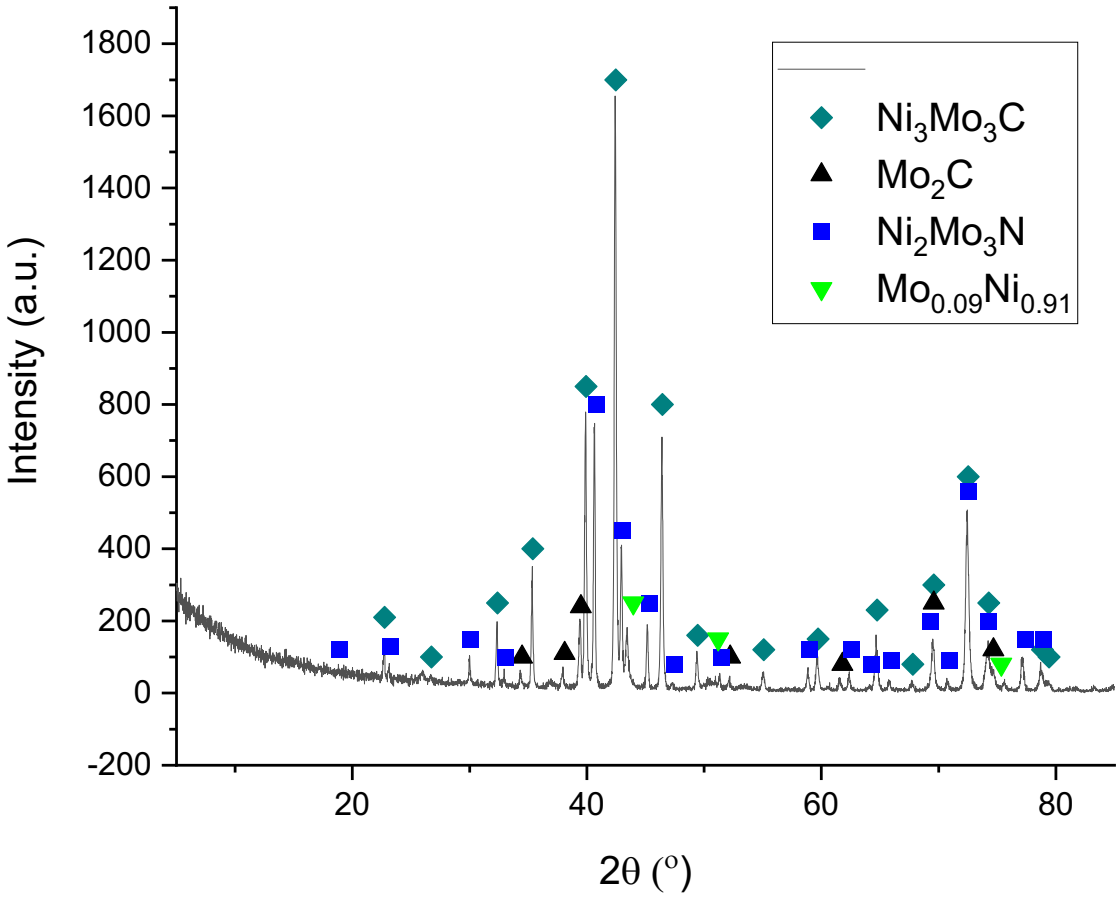

Figure 79: XRD pattern of 'Ni$_3$Mo$_3$C' prepared at 560°C under 20% CH$_4$/H$_2$. Reflections marked: ◆ Ni$_3$Mo$_3$C (JCPDS file number 01-089-4883), ▲ Mo$_2$C (JCPDS file number 00-001-1188), ▼ Mo$_{0.09}$Ni$_{0.91}$ (JCPDS file number 01-071-9766) and ■ Ni$_2$Mo$_3$N (JCPDS file number 01-072-6569).

The Raman spectra were taken at two areas of the material and display different spectra, as observed in Figure 80. In the first area, the Raman spectrum shows the presence of carbon with weak bands at 1557 cm^{-1} and 2332 cm^{-1} corresponding to the G band and the 2D band, respectively. As the intensities of the G band and 2D band were low, this suggests that there was not much carbon laydown on this material.

In the second area inspected, the bands due to carbon were more prominent with bands at 1350, 1577 and 2332 cm^{-1} relating to the D band, G band and 2D band, respectively. Bands due to β-NiMoO$_4$ were also observed at 941, 891, 820 cm^{-1}. Bands due to α-MoO$_3$ were also detected at 486, 291, 222, 197 and 143 cm^{-1} [118]. This result is consistent with the formation of a passivation layer on the material.

The XRD pattern showed that the material consisted of Ni$_3$Mo$_3$C, Ni$_2$Mo$_3$N, Mo$_2$C and Mo$_{0.09}$Ni$_{0.91}$. The Raman bands due to β-NiMoO$_4$ might result from the passivation layer on the Ni$_3$Mo$_3$C and Ni$_2$Mo$_3$N and the bands due to α-MoO$_3$ might result from the surface

oxygen layer on Mo_2C. The carbon laydown observed from the Raman spectra contrasts somewhat with the elemental analysis that showed only 1.84 wt. % of carbon was present in the material.

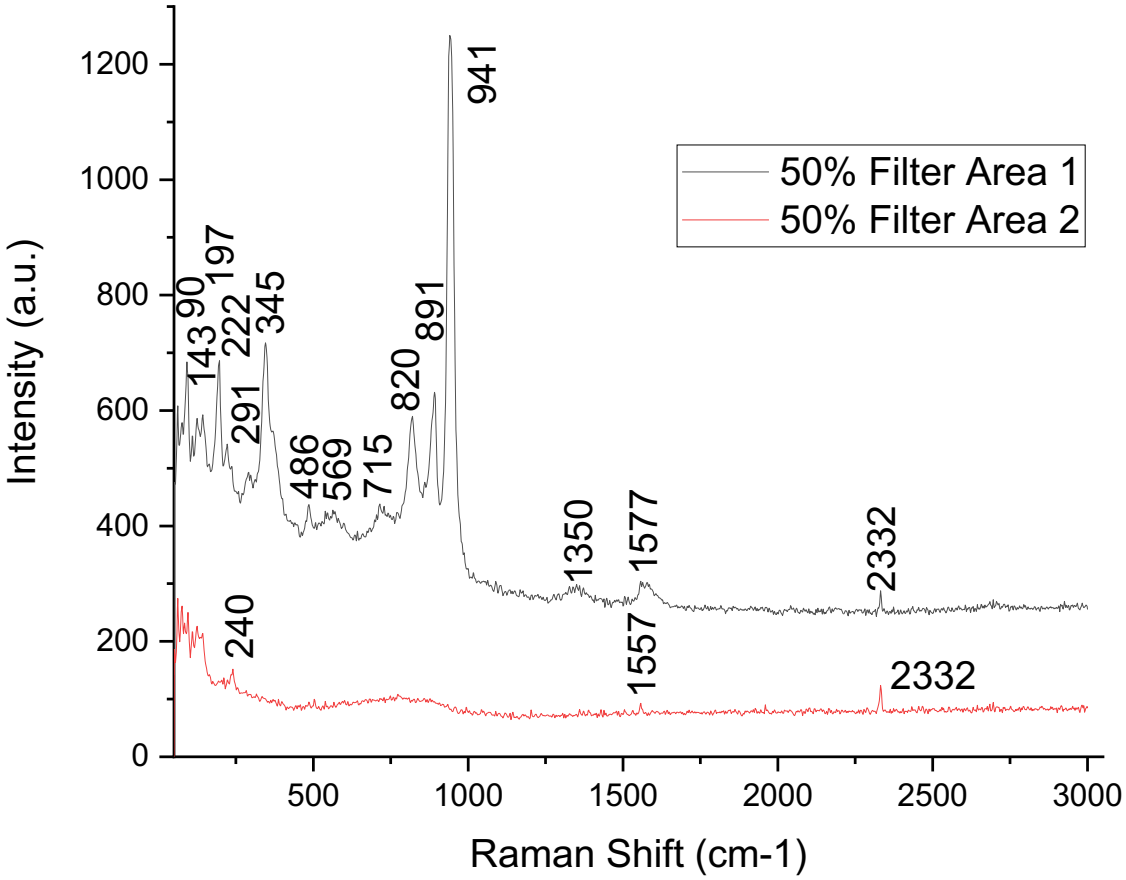

Figure 80: Raman spectra of 'Ni_3Mo_3C' prepared at 560°C with 20% CH_4/H_2. The spectra were taken at two areas with a 50% filter.

SEM was used to investigate the effect the carburisation process had on the morphology of the material. Figure 81 exhibits representative SEM images for 'Ni_3Mo_3C'. The material has a similar morphology to the 'Ni_6Mo_6C' precursor and suggests that the carburisation process was pseudomorphic. The sample was porous with pores ranging in diameter from approximately 1 – 10 μm.

The EDX analysis in Table 21 gives the element weight percentages for 'Ni_3Mo_3C'. The stoichiometric percentage of nickel, molybdenum and carbon in Ni_3Mo_3C is 37.00 wt. %, 60.48 wt. % and 2.52 wt. %, respectively. From the table, it can be seen that the carbon weight percentage was higher than predicted and nitrogen was present in the material. Furthermore, the molybdenum percentage was lower. This result suggests that there was a large amount of carbon laydown on the material, although obtaining accurate carbon percentages was difficult due to the use of carbon stubs. In addition, EDX measurements

are limiting for light elements such as carbon and nitrogen. The Raman spectra showed only weak bands associated with carbon laydown. From the XRD pattern, it was shown that the material consisted of Ni_2Mo_3N and this therefore, accounts for the presence of nitrogen observed by EDX. The EDX data shows that the mass ratio of Ni to Mo was not as predicted as the percentage of molybdenum was lower than expected. However, some areas contained a lot less molybdenum than others as observed in Table 21.

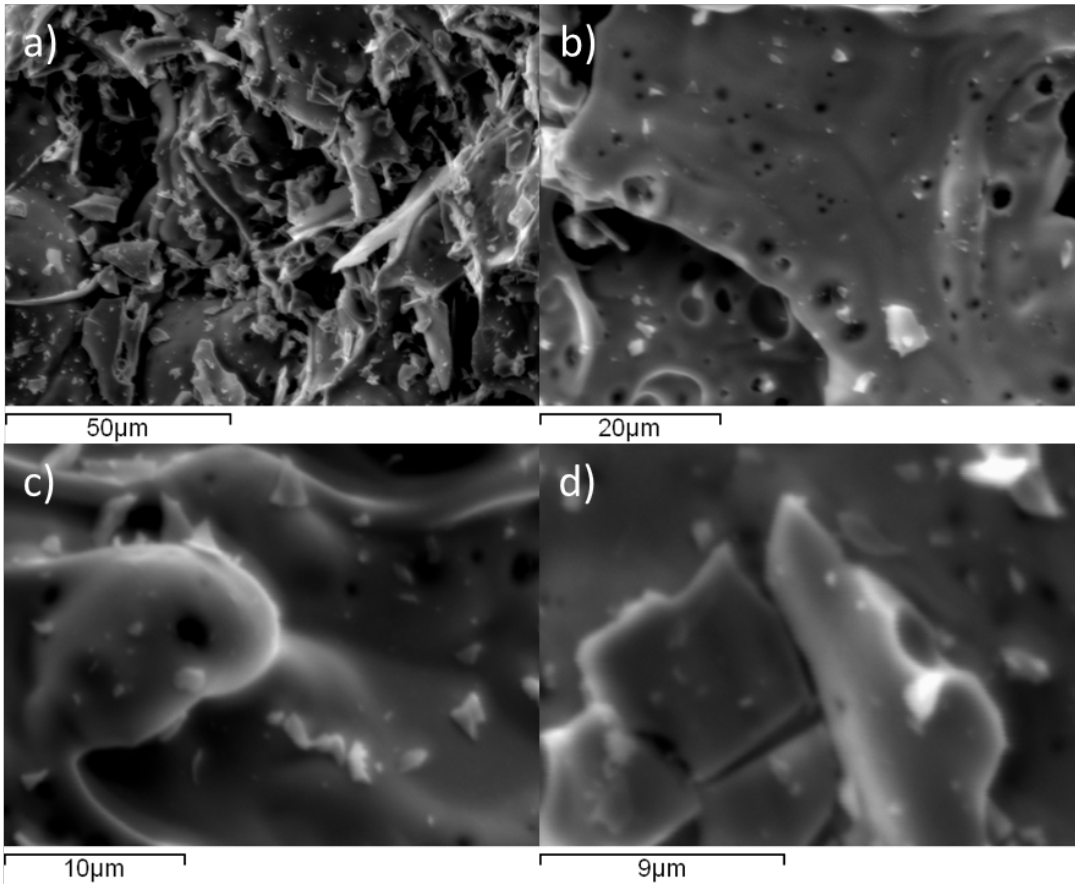

Figure 81: SEM images of 'Ni_3Mo_3C' prepared at 560°C with 20% CH_4/H_2. a) 1000x magnification, b) 2000x magnification, c) 4000x magnification and d) 6000x magnification.

The element map in Figure 82 shows that molybdenum was evenly distributed across the sample. However, there were areas that contained more nickel and carbon, suggesting that there was phase separation over the sample.

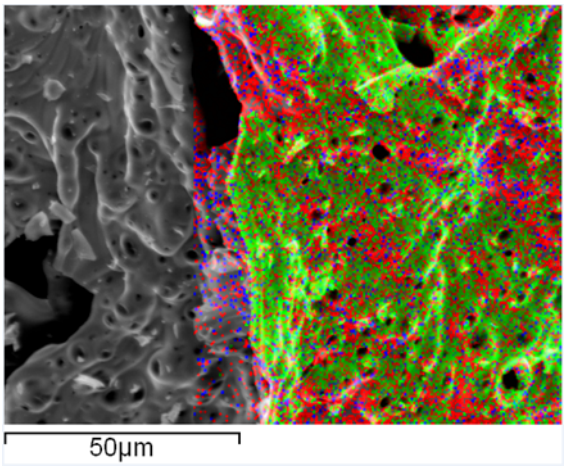

Figure 82: Element Map for 'Ni_3Mo_3C'. Elements: Ni (red), Mo (green) and C (blue).

Area	Ni weight (%)	Mo weight (%)	C weight (%)	N weight (%)
1	49	27	24	0
2	48	11	41	0
3	72	23	5	0
4	41	46	13	0
5	33	43	24	0
6	29	51	19	2
7	28	49	23	0
8	28	49	19	5
9	45	3	52	0
10	45	3	52	0
11	28	49	20	3
12	29	49	19	3
13	27	50	19	4
Average	39	35	25	1

Table 21: EDX values for 'Ni_3Mo_3C' prepared at 560°C with 20% CH_4/H_2.

3.2.3.2.1 Ammonia Synthesis at 500°C for Ni_3Mo_3C

'Ni_3Mo_3C' was tested for ammonia synthesis at 500°C under a 3:1 H_2/N_2 atmosphere. The activity testing of 'Ni_3Mo_3C' may give an understanding on the role structure and composition play in ammonia synthesis activity. Furthermore, if Ni_3Mo_3C undergoes nitridation during the reaction, as observed in the case of Co_3Mo_3C, it might prove possible to form Ni_3Mo_3N. The steady state ammonia synthesis rate of 'Ni_3Mo_3C' at 500°C was calculated to be 41 µmol h^{-1} g^{-1}. The ammonia synthesis rate of $Ni_2Mo_3C_xN_y$ at 500°C was 619 ± 14 µmol h^{-1} g^{-1} and for Co_3Mo_3C was 461 ± 17 μmol_{NH3} h^{-1} g^{-1} [54]. Therefore, 'Ni_3Mo_3C' had a much lower activity. The conductivity of the sulfuric acid solution through which the reactor effluent was flowed appeared to decrease at a greater rate for the first 60 minutes before it reached steady state, as observed in Figure 83. This is the opposite of the behaviour observed for $Ni_2Mo_3C_xN_y$ and Co_3Mo_3C, which initially had an induction period before the materials became active.

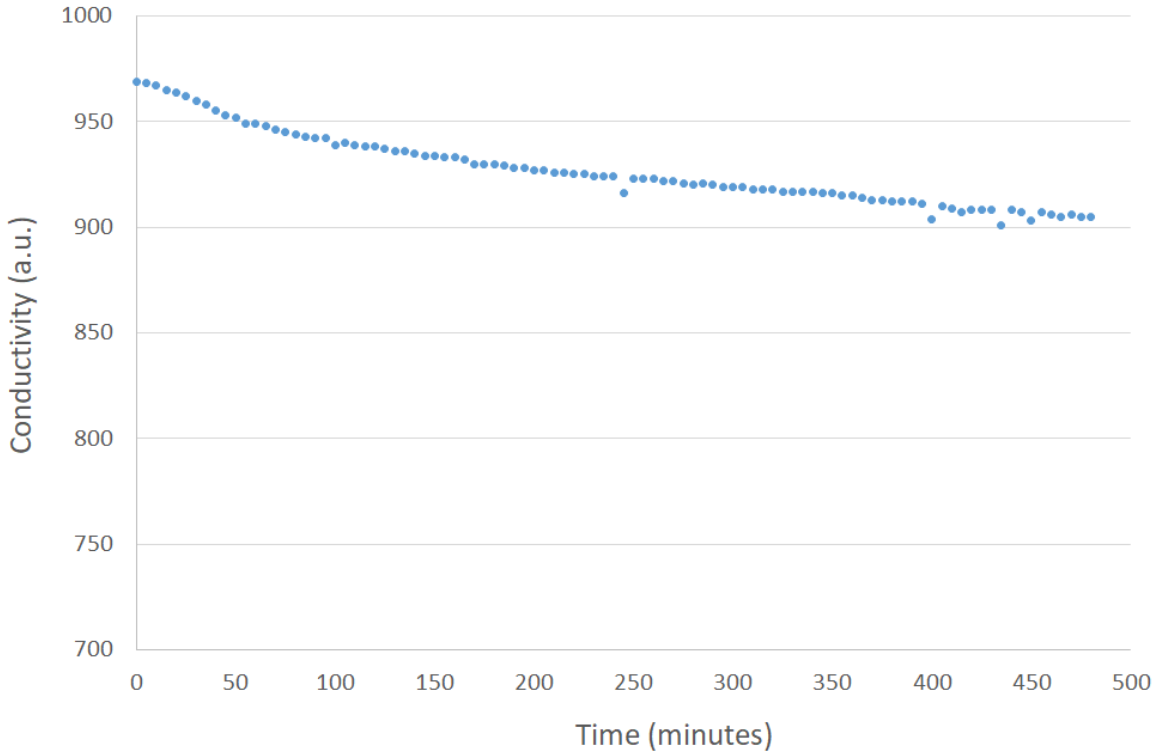

Figure 83: Conductivity profile for Ni_3Mo_3C + $Ni_2Mo_3C_xN_y$ reacted with 3:1 H_2/N_2 at 500°C for 8 hours.

The steady state activity of the material after the initial 60 minutes is shown in Figure 84.

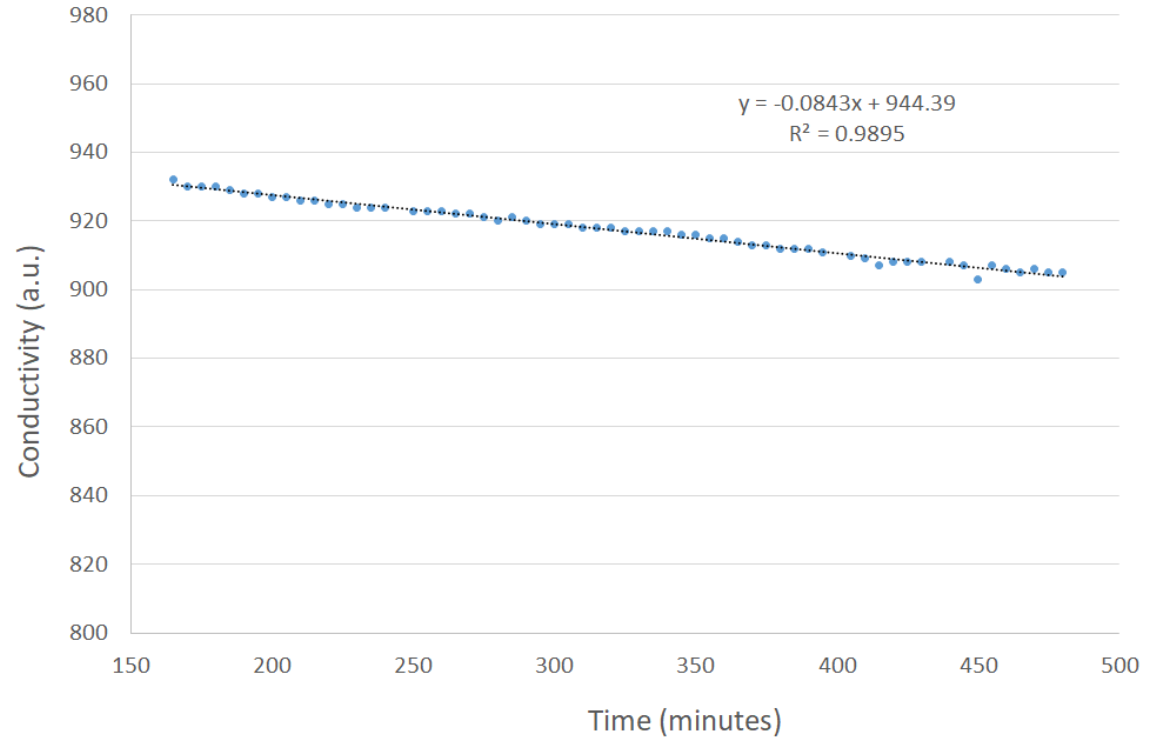

Figure 84: Conductivity profile for Ni_3Mo_3C + $Ni_2Mo_3C_xN_y$ reacted with 3:1 H_2/N_2 at 500°C for 8 hours, highlighting the linear part of the graph used for calculating the rate.

The XRD pattern of the material post-reaction shows that the Ni_3Mo_3C phase had apparently been maintained during the reaction, as shown in Figure 85.

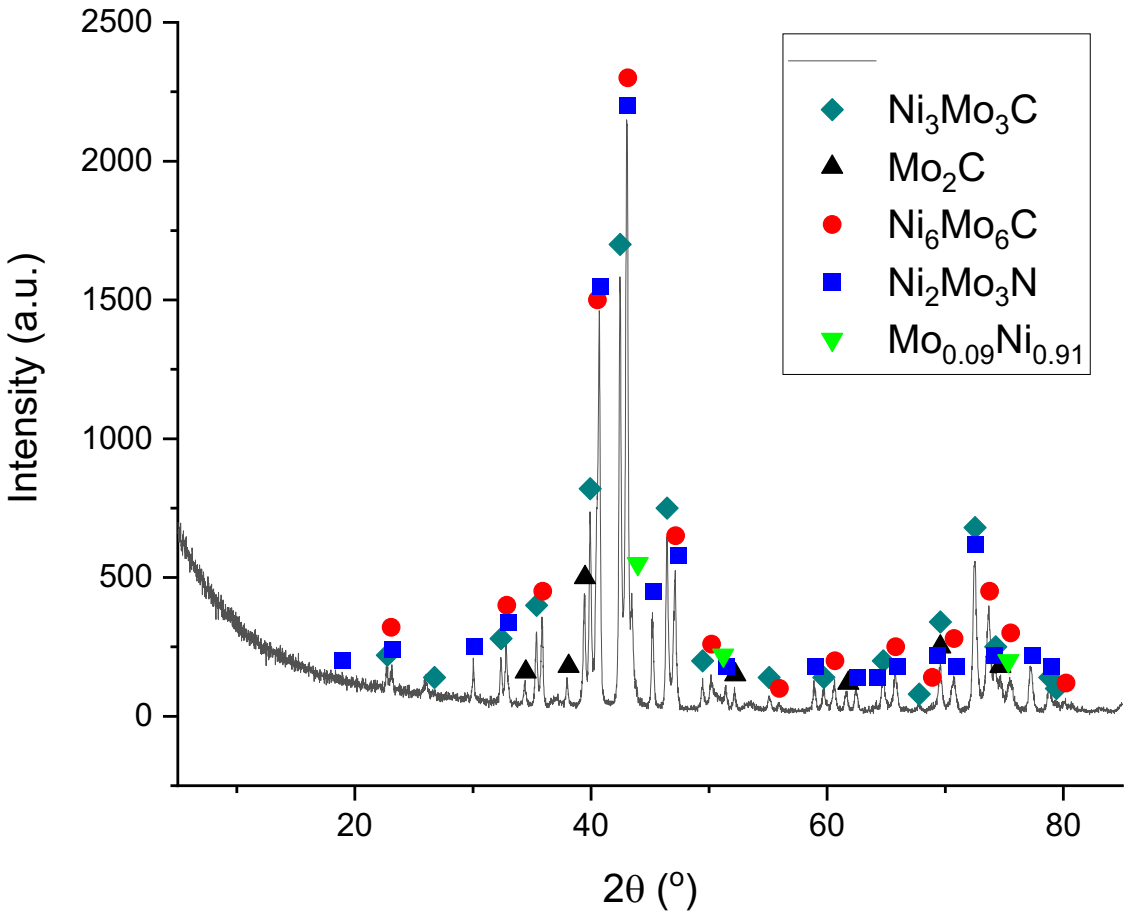

Figure 85: XRD pattern of Ni_3Mo_3C + $Ni_2Mo_3C_xN_y$ post-reaction with 3:1 H_2/N_2 at 500°C for 8 hours. Reflections marked: ◆ Ni_3Mo_3C (JCPDS file number 01-089-4883), ▲ Mo_2C (JCPDS file number 00-001-1188), ● Ni_6Mo_6C (JCPDS file number 03-065-4436), ■ Ni_2Mo_3N (JCPDS file number 01-072-6569) and ▼ $Mo_{0.09}Ni_{0.91}$ (JCPDS file number 01-071-9766).

However, as can be seen in Figure 86, the positions of the peaks due to $Ni_2Mo_3C_xN_y$ have shifted to higher 2θ values compared to pre-reaction and therefore, the material had undergone a degree of nitridation during the reaction. The peak positions for Ni_3Mo_3C have not shifted position suggesting that this phase had not been nitrided. However, peaks due to Ni_6Mo_6C are observed in the XRD pattern, which were not present in the pre-reaction material. This suggests that Ni_3Mo_3C lost carbon to form the Ni_6Mo_6C phase. Co_3Mo_3C was shown to undergo nitridation during the ammonia synthesis reaction and the peak positions were shifted to higher 2θ values [54]. This suggests that Ni_3Mo_3C is more stable than the cobalt molybdenum material and is less susceptible to nitridation. As can be seen in Figure 86, the intensity of the peaks due to $Ni_2Mo_3C_xN_y$ have increased compared

to pre-reaction. However, Ni_6Mo_6C has similar peak positions and therefore, this phase is contributing to the intensity.

It is unclear whether Ni_3Mo_3C or the Ni_2Mo_3N impurity is the active component for ammonia synthesis. Therefore, it would be beneficial to produce a pure phase Ni_3Mo_3C and test this material.

The elemental analysis of the material post-reaction at 500°C was C: 1.43 wt. %, H: 0.00 wt. % and N: 0.50 wt. %. The pre-reaction material contained 1.84 wt. % carbon and therefore this suggests that some carbon had been lost during the reaction as would be expected for the transformation of Ni_3Mo_3C to Ni_6Mo_6C. The nitrogen percentage had increased slightly compared to pre-reaction (0.42 wt. %). These results could be due to Ni_3Mo_3C or the $Ni_2Mo_3C_xN_y$ phase undergoing nitridation during the reaction.

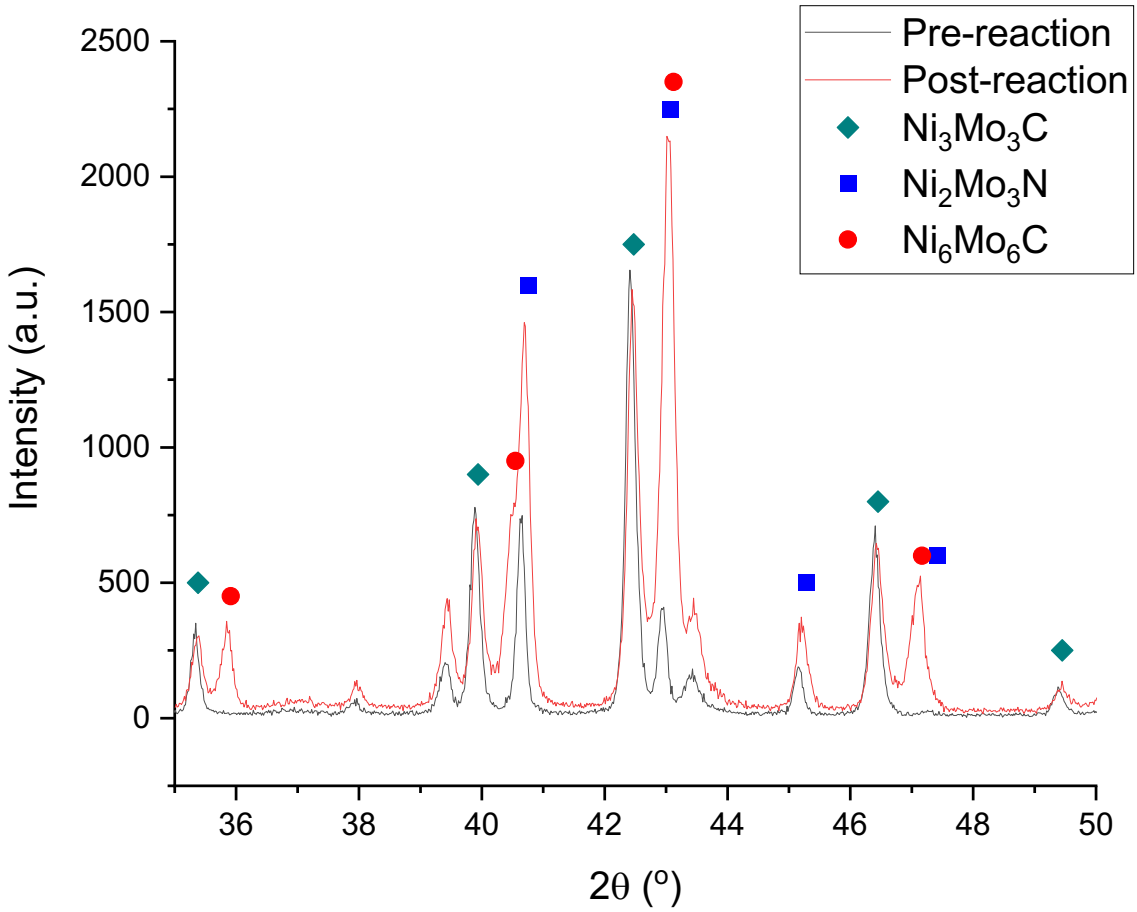

Figure 86: Comparison of XRD patterns for Ni_3Mo_3C + $Ni_2Mo_3C_xN_y$ pre- (black) and post-reaction (red) with 3:1 H_2/N_2 at 500°C for 8 hours, highlighting the peaks due to Ni_3Mo_3C, Ni_6Mo_6C or Ni_2Mo_3N.

The Raman spectrum showed that there was carbon laydown on the material with bands for carbon observed at 1559 and 2332 cm^{-1}, corresponding to the G band and the 2D band, respectively, as shown in Figure 87. The intensities of these bands were low and therefore,

there was not much carbon on the surface of the material. A wide band was observed between 500 – 1000 cm^{-1}.

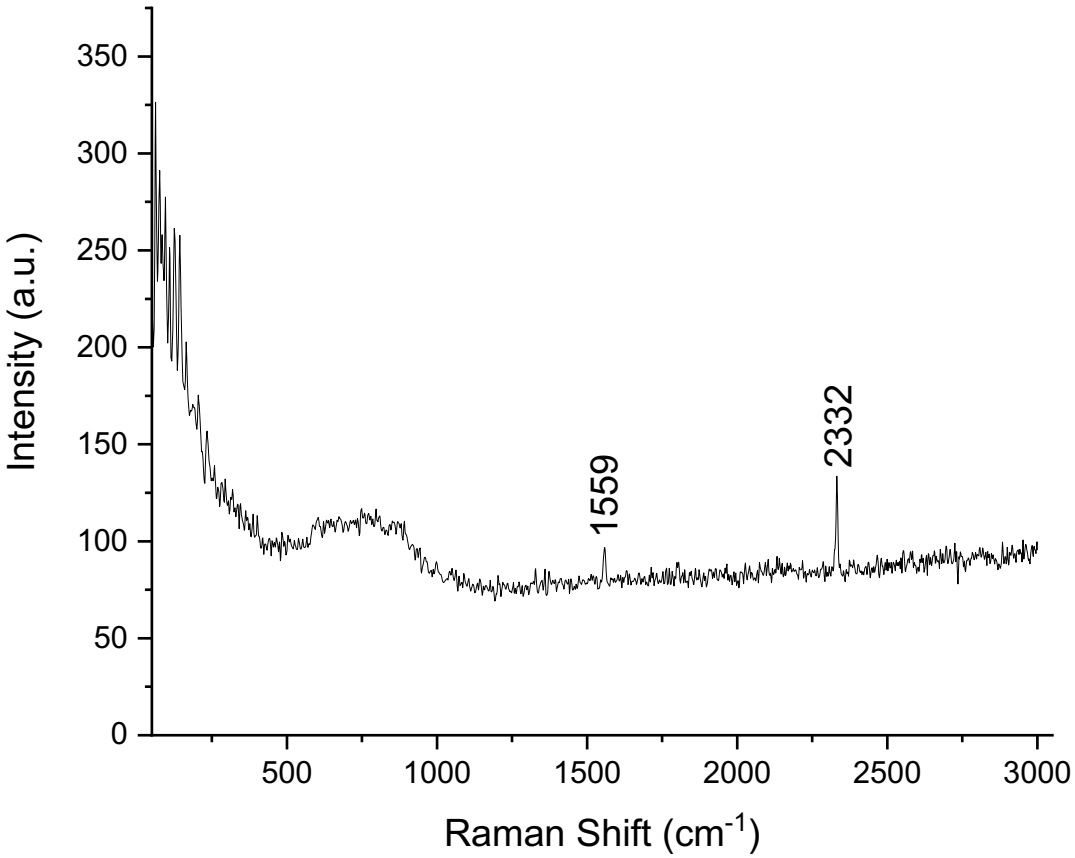

Figure 87: Raman spectrum of Ni_3Mo_3C + $Ni_2Mo_3C_xN_y$ post-reaction with 3:1 H_2/N_2 at 500°C for 8 hours.

Typical SEM images of mixed phase 'Ni_3Mo_3C' post 500°C reaction are displayed in Figure 88. It can be seen that the material consists of a porous structure and that the morphology had been retained from the pre-reaction material. The weight percentages obtained from EDX for 'Ni_3Mo_3C' are provided in Table 22. The stoichiometric percentage of nickel, molybdenum and carbon for Ni_3Mo_3C is 37.00 wt. %, 60.48 wt. % and 2.52 wt. %, respectively. The carbon weight percentage was greater than the stoichiometric value expected but the measurement of light elements by EDX can be restrictive. The molybdenum and nickel percentages were lower than the expected stoichiometric values and from these values the mass ratio of nickel and molybdenum can be observed to not be as predicted. However, EDX is semi-quantitative and therefore, these values may not be representative. The nickel and carbon percentages had decreased compared to the pre-reaction material and the molybdenum and nitrogen values had increased. This may suggest that the material was transforming from Ni_3Mo_3C to Ni_2Mo_3N and Ni.

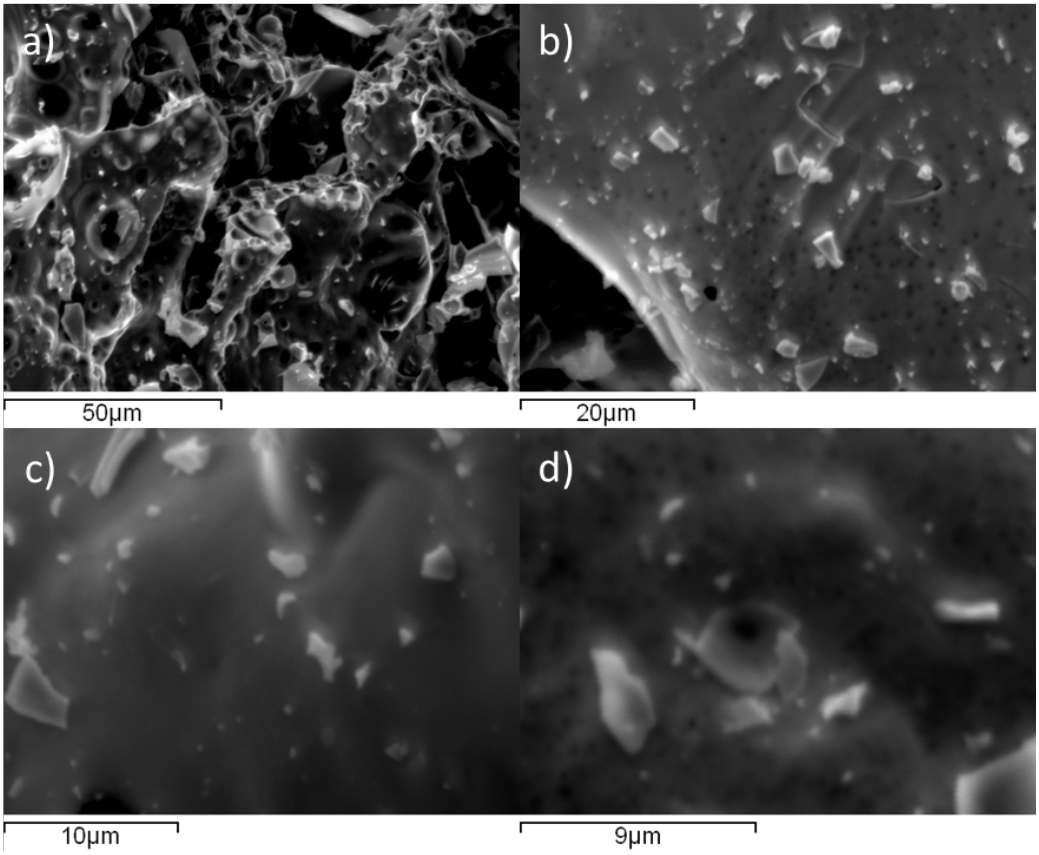

Figure 88: SEM images of Ni_3Mo_3C + $Ni_2Mo_3C_xN_y$ post-reaction with 3:1 H_2/N_2 at 500°C for 8 hours. a) 1000x magnification, b) 2000x magnification, c) 4000x magnification and d) 6000x magnification.

The element maps in Figure 89 demonstrate that the nickel was more evenly distributed compared to the pre-reaction sample.

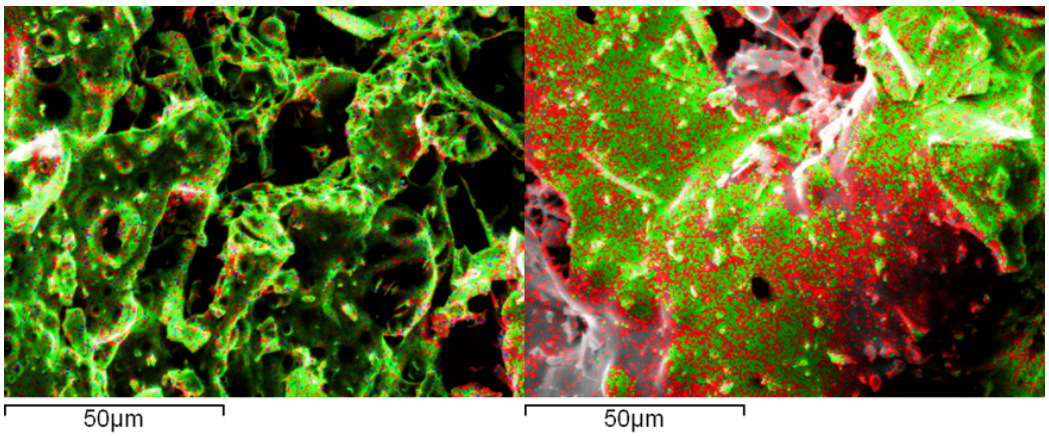

Figure 89: Element Maps for Ni_3Mo_3C + $Ni_2Mo_3C_xN_y$ post-reaction with 3:1 H_2/N_2 at 500°C for 8 hours. Elements: Ni (red) and Mo (green).

Area	Ni weight (%)	Mo weight (%)	C weight (%)	N weight (%)
1	44	41	15	0
2	29	47	25	0
3	33	51	13	3
4	30	52	13	4
5	36	40	24	0
6	38	37	24	0
7	28	53	16	4
8	28	51	18	4
9	36	52	10	2
10	34	52	12	2
11	33	53	12	2
Average	33	48	17	2

Table 22: EDX values for Ni_3Mo_3C + $Ni_2Mo_3C_xN_y$ post-reaction with 3:1 H_2/N_2 at 500°C for 8 hours.

3.2.3.2.2 Ammonia Synthesis at 700°C for Ni_3Mo_3C

As the Ni_3Mo_3C did not undergo nitridation to form a carbonitride phase at 500°C, the reaction temperature was increased to 700°C. The ammonia synthesis rate for the material at 700°C was calculated to be 80 μmol h^{-1} g^{-1} when at steady state. This is possibly lower than the rate obtained for Ni_6Mo_6C at 700°C (152 ± 89 μmol h^{-1} g^{-1}). There is a small induction period of 10 minutes at the start of the reaction before the material became active. This may be due to the transformation of the material from the carbide to the nitride as observed for the Ni_6Mo_6C phase. The conductivity decreased at a faster rate for the first 180 minutes before it became steady state, as observed in Figure 90. This behaviour was similar when the material was tested at 500°C. The steady state activity of the material after the initial 180 minutes is shown in Figure 91.

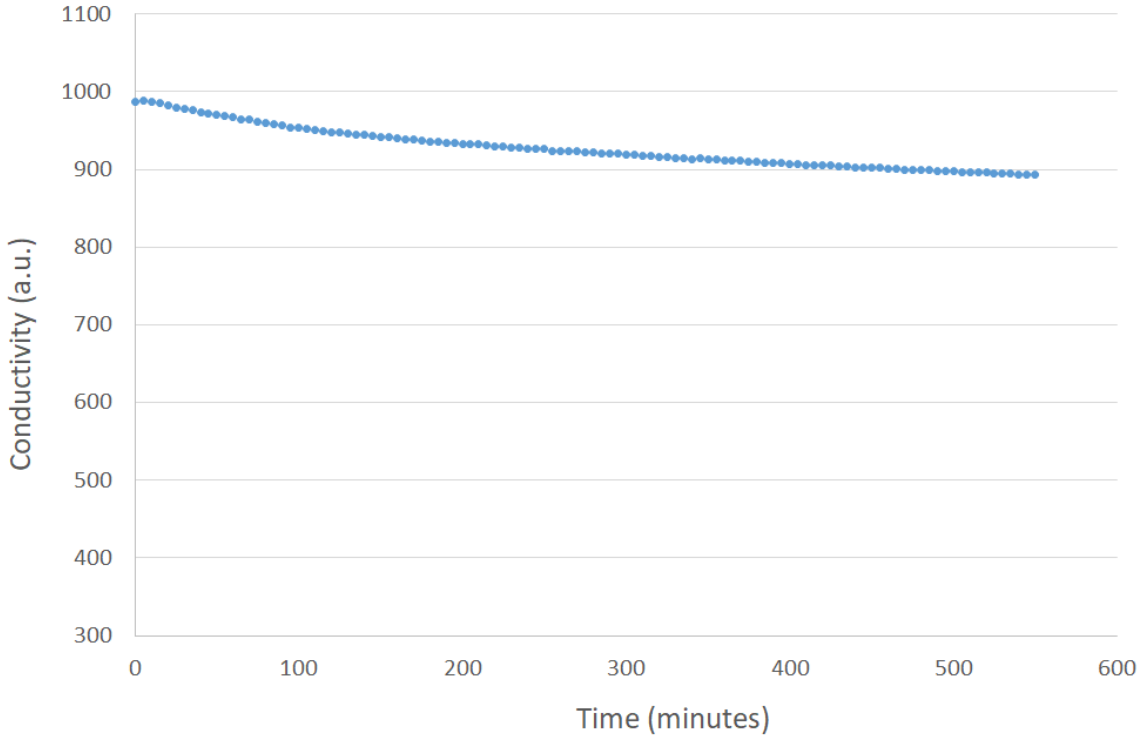

Figure 90: Conductivity profile for Ni_3Mo_3C + $Ni_2Mo_3C_xN_y$ reacted with 3:1 H_2/N_2 at 700°C for 9 hours.

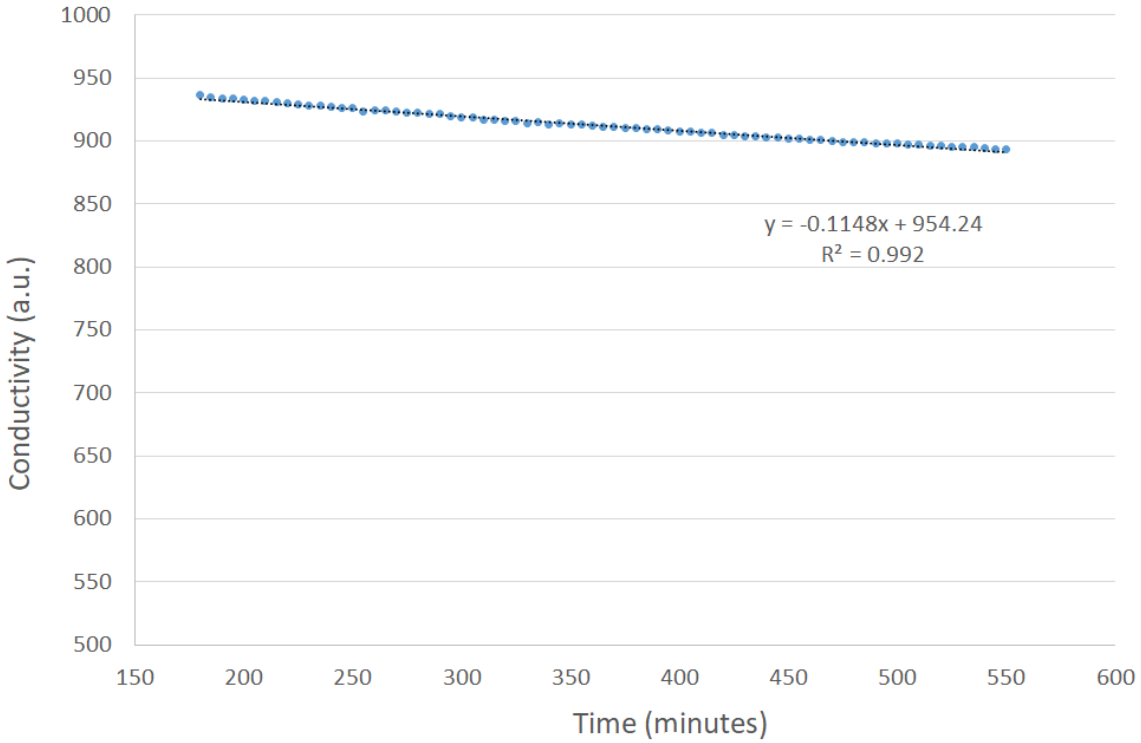

Figure 91: Conductivity profile for Ni_3Mo_3C + $Ni_2Mo_3C_xN_y$ reacted with 3:1 H_2/N_2 at 700°C for 9 hours. Highlighting the linear part of the graph used for calculating the rate.

The XRD of the material post-reaction shows that Ni_3Mo_3C has undergone nitridation to form Ni_2Mo_3N and nickel metal, as shown in Figure 92. Ni_6Mo_6C was also present in the material, which suggests that Ni_3Mo_3C is reduced and loses carbon to form Ni_6Mo_6C. This suggests that the Ni_3Mo_3C does not form a carbonitride of composition $Ni_3Mo_3C_xN_y$ and

therefore, Ni_3Mo_3N cannot be easily formed from the corresponding carbide. The XRD pattern appears to show that the Ni_3Mo_3C phase may first lose half of the lattice carbon to form Ni_6Mo_6C and then this is nitrided to form Ni_2Mo_3N.

Elemental analysis shows that the sample had been nitrided during the reaction with a large percentage of the carbon having been removed (C: 0.28 wt. %, H: 0.03 wt. %, N: 2.00 wt. %). The percentage of nitrogen was lower than the expected stoichiometric value (3.34 wt. %). However, the contribution due to Ni_6Mo_6C must be taken into consideration.

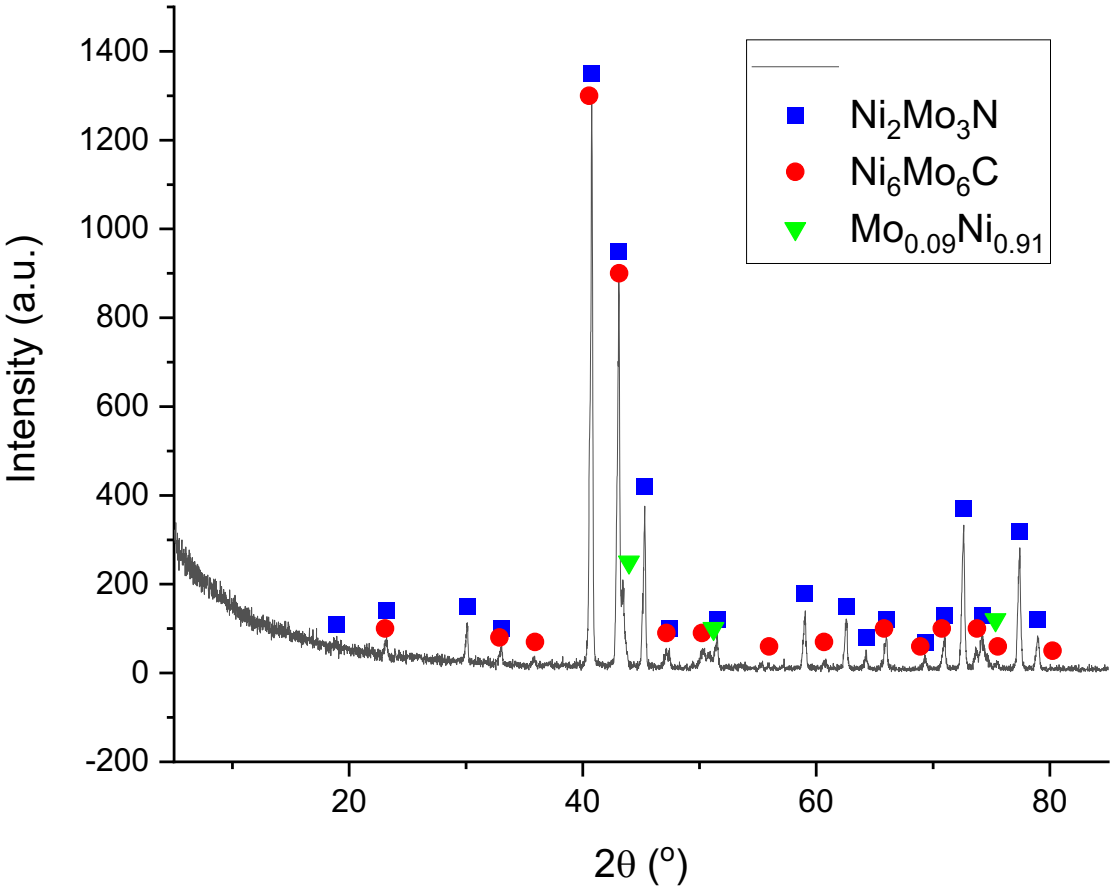

Figure 92: XRD pattern of Ni_3Mo_3C + $Ni_2Mo_3C_xN_y$ post-reaction with 3:1 H_2/N_2 at 700°C for 9 hours. Reflections marked: ● Ni_6Mo_6C (JCPDS file number 03-065-4436), ■ Ni_2Mo_3N (JCPDS file number 01-072-6569) and ▼ $Mo_{0.09}Ni_{0.91}$ (JCPDS file number 01-071-9766).

The Raman spectra in Figure 93 were taken from two areas of the material and show different spectral bands. Both areas show G and 2D bands relating to carbon suggesting that the material has carbon laydown even after reaction at 700°C. In one of the areas, bands due to an oxide surface layer were observed. The Raman bands at 944, 897 and 820 cm^{-1} are due to β-$NiMoO_4$ and are assigned to asymmetric and symmetric Mo-O vibration of Mo in a tetrahedral environment [96] [97] or for the band at 820 cm^{-1} to the asymmetric stretching mode of the Ni-O-Mo bond [96]. The band at 820 cm^{-1} is also observed in the Raman spectra for MoO_3 [90]. A weak band due to α-MoO_3 was also detected at 995 cm^{-1}

[90] [118]. Bands due to α-MoO_3 were observed in the pre-reaction material and were likely due to a surface oxide layer. The elemental analysis showed that only 0.28 wt. % of carbon was present in the material and therefore, this contrasts with the carbon laydown observed from the Raman bands.

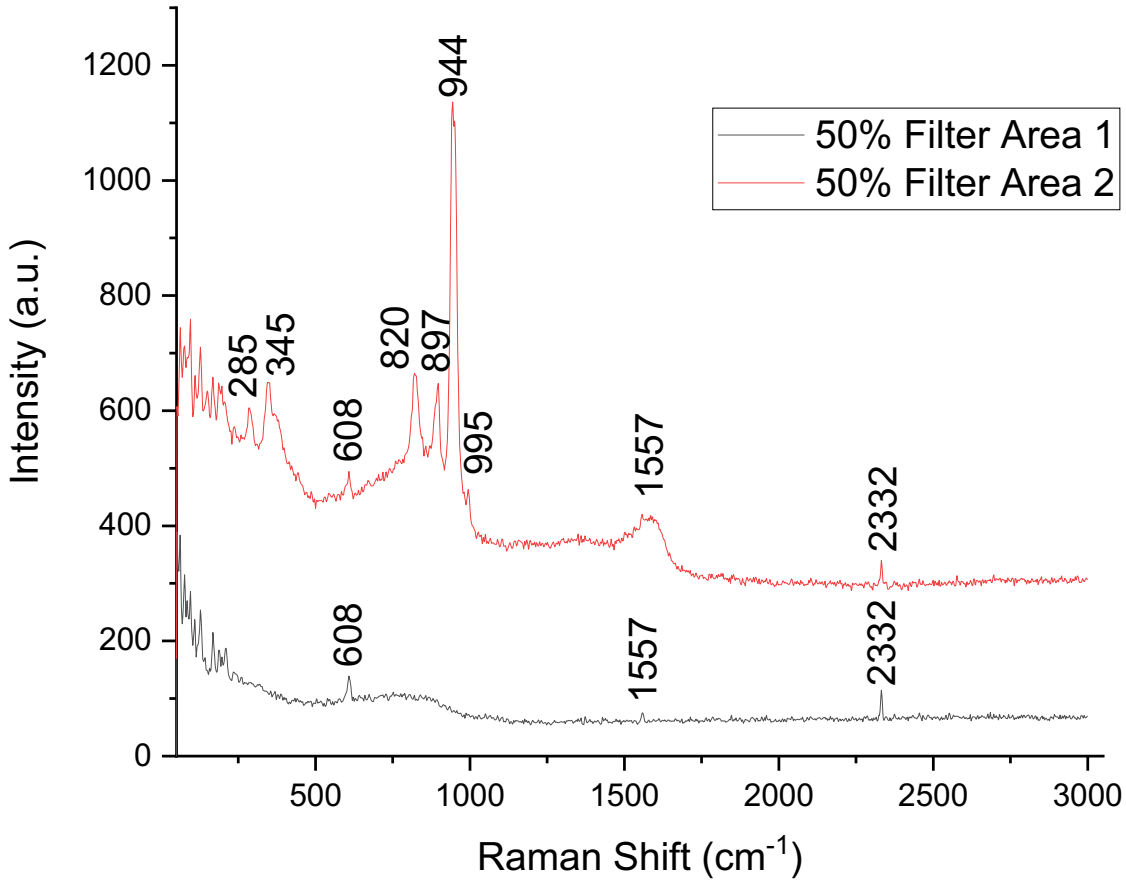

Figure 93: Raman spectra of Ni_3Mo_3C + $Ni_2Mo_3C_xN_y$ post-reaction with 3:1 H_2/N_2 at 700°C for 9 hours. The spectra were taken at two areas with a 50% filter.

SEM analysis was performed in order to examine any changes in the morphology and structure of 'Ni_3Mo_3C' during the ammonia synthesis reaction. Representative SEM images of the post-reaction material are displayed in Figure 94. The material had a porous structure and the morphology was similar to the pre-reaction material. Therefore, although the sample underwent nitridation, the morphology did not change. The EDX analysis for the material post 700°C reaction is shown in Table 23. The stoichiometric percentage of nickel, molybdenum and nitrogen for Ni_2Mo_3N is 28.00 wt. %, 68.66 wt. % and 3.34 wt. % respectively. The EDX weight percentage for nitrogen was greater than the stoichiometric nitrogen predicted for Ni_2Mo_3N. The amount of nitrogen was higher than the pre-reaction material and was detected in every area inspected. This suggests that the material had transformed to the nitride. The percentage of molybdenum was higher compared to the

pre-reaction material and nickel value was lower suggesting that the material was transforming from Ni_3Mo_3C to Ni_2Mo_3N and nickel metal.

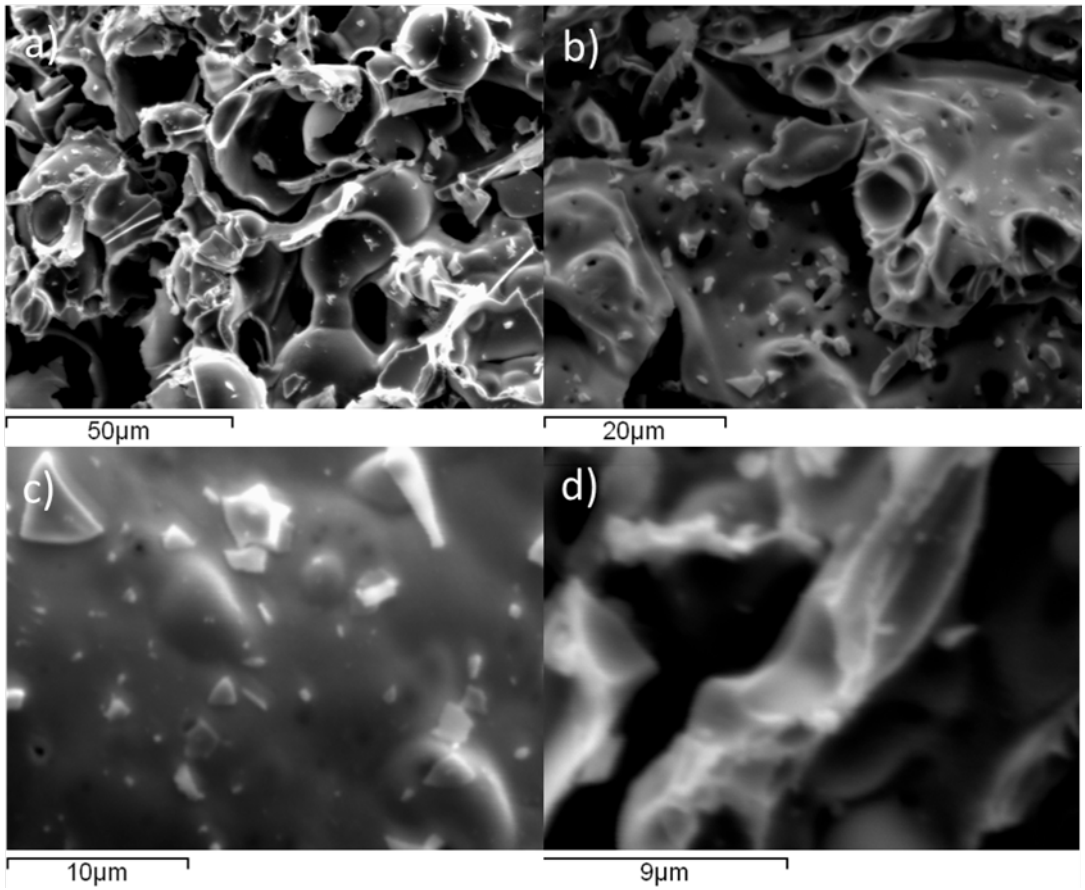

Figure 94: SEM images of Ni_3Mo_3C + $Ni_2Mo_3C_xN_y$ post-reaction with 3:1 H_2/N_2 at 700°C for 9 hours. a) 1000x magnification, b) 2000x magnification, c) 4000x magnification and d) 6000x magnification.

The nickel and molybdenum were evenly distributed across the sample as evidenced from the element maps in Figure 95.

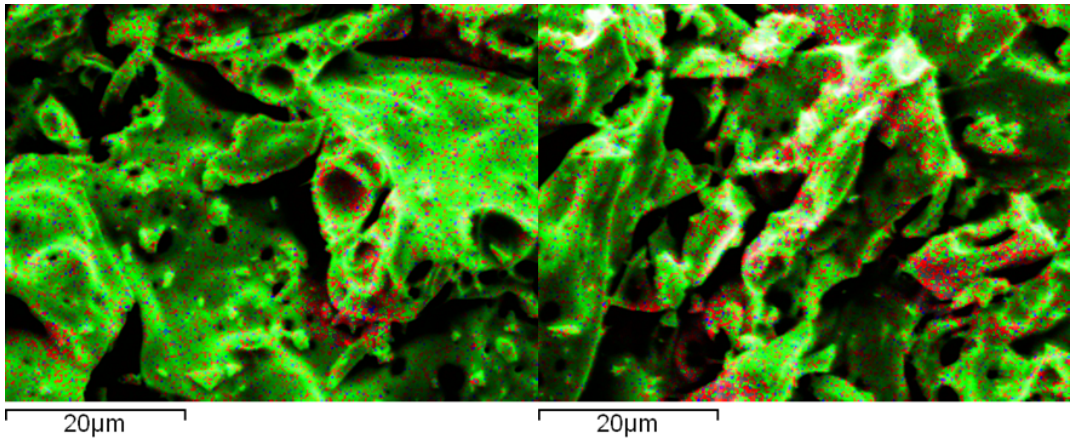

Figure 95: Element Maps for Ni_3Mo_3C + $Ni_2Mo_3C_xN_y$ post-reaction with 3:1 H_2/N_2 at 700°C for 9 hours. Elements: Ni (red), Mo (green) and N (blue).

Area	Ni weight (%)	Mo weight (%)	C weight (%)	N weight (%)
1	28	51	14	7
2	35	47	14	4
3	37	50	10	4
4	28	52	13	7
5	32	50	12	6
Average	32	50	12	6

Table 23: EDX values for Ni_3Mo_3C + $Ni_2Mo_3C_xN_y$ post-reaction with 3:1 H_2/N_2 at 700°C for 9 hours.

The formation of the nitride and reduction of the material to Ni_6Mo_6C was investigated by thermogravimetric analysis of 'Ni_3Mo_3C' under 5% H_2/N_2. The TGA curve and first derivative weight change of 'Ni_3Mo_3C' is provided in Figure 96. The material was heated from room temperature to 1000°C at a ramp rate of 10°C/min. The material only lost 0.43% of its weight from room temperature to 600°C. This can possibly explain why Ni_3Mo_3C did not show nitridation when tested at 500°C, although the TGA procedure was not performed under the same ratio of N_2:H_2.

A major weight loss is observed from 600°C and corresponds to a loss of 5.65%. There appears to be two weight losses from 600°C to 1000°C, a main peak at 860°C and a shoulder peak at 790°C. The formation of Ni_6Mo_6C from Ni_3Mo_3C would result in a weight loss of 1.26%. Therefore, this does not account for the 5.65% decrease observed. However, between 600°C and 700°C, there is a weight loss of 0.74%. From the XRD pattern of the material post 700°C reaction, it was observed that Ni_3Mo_3C had been reduced to Ni_6Mo_6C and Ni_2Mo_3N had been formed.

$$3Ni_3Mo_3C + ½\ N_2 \rightarrow Ni_6Mo_6C + Ni_2Mo_3N + Ni + 2C$$

Equation 4: Equation for the formation of Ni_6Mo_6C and Ni_2Mo_3N from Ni_3Mo_3C

The formation of Ni_2Mo_3N and Ni from Ni_3Mo_3C would result in a weight gain of 0.42%. Taking this into consideration, the transformation of Ni_3Mo_3C into Ni_6Mo_6C, Ni_2Mo_3N and Ni would result in a 0.84% total loss in mass. Ni_2Mo_3N was shown in section 3.2.1.2.1 to maintain its structure when reduced with 25% Ar/H_2 at 900°C. Therefore, this would suggest that the weight loss observed above 700°C is not due to Ni_2Mo_3N decomposing. If Ni_2Mo_3N decomposed to molybdenum and nickel metal, the weight loss for the material would be 3.34%. The mass spectrum for 28 m/z showed an increased ion current during this temperature range as seen in Figure 97. Therefore, this suggests that the material is losing nitrogen and may be decomposing. The mass spectra of 2, 15, 16, 17, 18, 30, 32, 44 and 46 m/z were followed but they did not show any features.

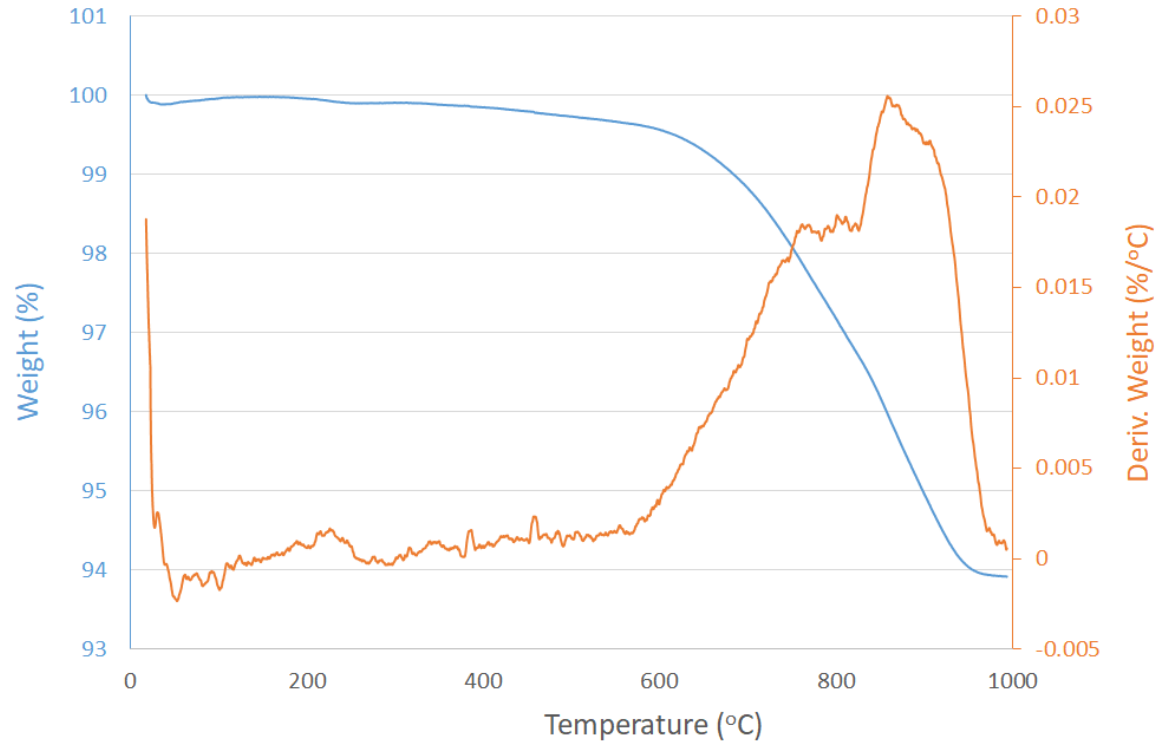

Figure 96: TGA and derivative weight profile of 'Ni_3Mo_3C' under 5%H_2/N_2 in the range from room temperature to 1000°C.

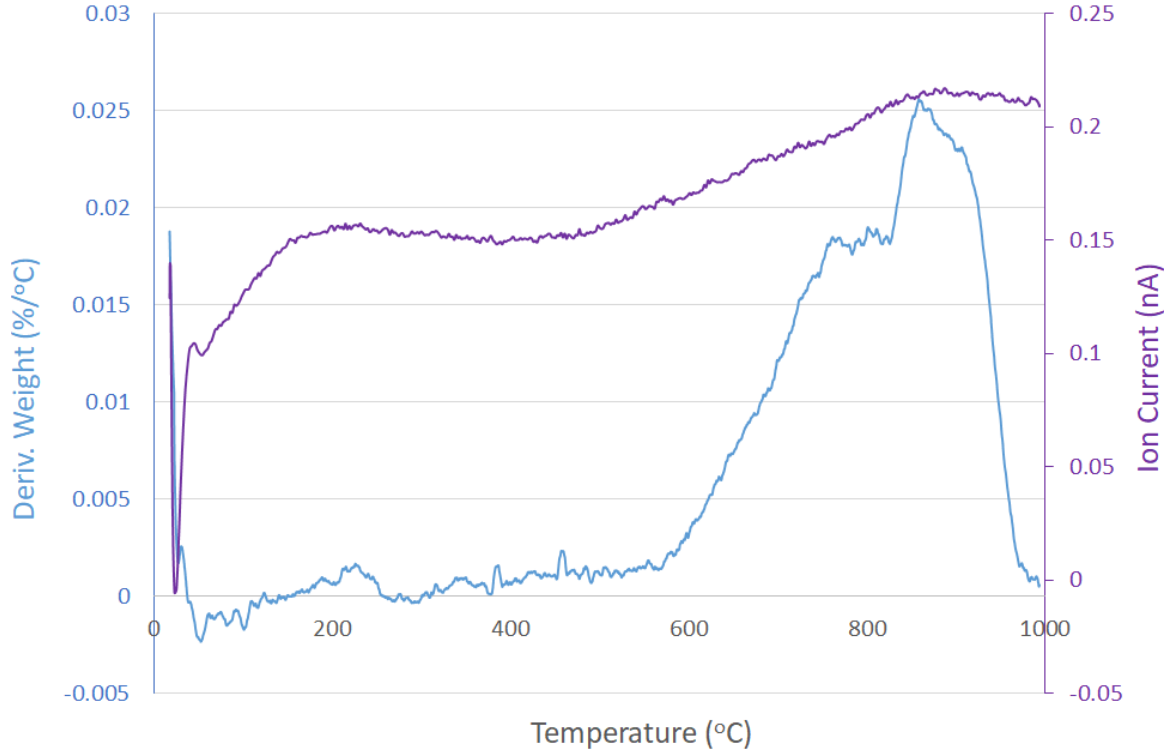

Figure 97: The mass spectrum ion curve for 28 m/z and the derivative weight profile.

The results in this thesis suggest that there may be a possible limitation to the idea that combining metals based on their N_2 binding energy will give a highly active ammonia synthesis catalyst. 'Ni_6Mo_6C' was not active at 400°C and 'Ni_3Mo_3C' was not active at 500°C. The materials became active when the temperature was increased to 700°C and this

activity may be associated with the substitution of lattice carbon with nitrogen. This behaviour is similar to Co_3Mo_3C and suggests that lattice nitrogen is required for these materials to be active. Although, conversely, lattice nitrogen may be present in these materials as a direct result of them being active. It has proved difficult to form phase-pure Ni_2Mo_3C with a carbonitride phase being formed instead. $Ni_2Mo_3C_xN_y$ was active at 400ºC for ammonia synthesis and may suggest that lattice nitrogen is required for the materials to be active at lower temperatures. $NiCoMo_3N$ has been tested for ammonia synthesis activity and lattice nitrogen reactivity and was found to behave similar to Ni_2Mo_3N [92]. Cobalt was introduced into Ni_2Mo_3N to give it a closer electronic structure to Co_3Mo_3N and this result would therefore suggest that the structure may be more important than electronic considerations.

3.2.4 Nickel Gallium Molybdenum Nitride (Ni_2GaMo_3N)

A nickel and molybdenum containing nitride that has an η-carbide structure has been prepared to give a further understanding on the relationship between structure and ammonia synthesis activity. Prior and Battle [121] have previously published work on Ni_2GaMo_3N and have shown that the nickel and gallium are completely ordered with nickel residing in the 32e sites and gallium in the 16d sites. The authors suggest that this ordering may be due to the sizes of these metal atoms, electronic factors or a result that is outwith the first coordination shell as the mean bond lengths of the 32e and 16d sites were similar. Ordering of such mixed metal atoms in η-carbide structured compounds is uncommon, with one other example being Al_2NiTi_3N [122]. The structure of Ni_2GaMo_3N is presented in Figure 98.

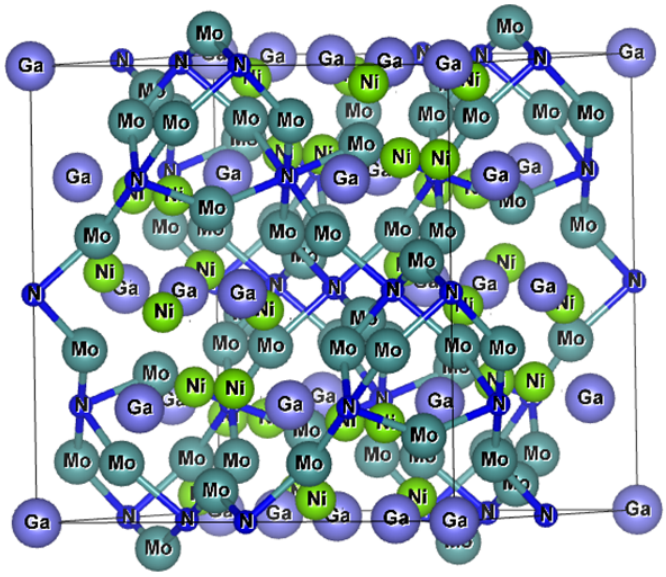

Figure 98: The crystal structure of Ni_2GaMo_3N, showing the Mo_6N octahedra. Data plotted on VESTA from Ni_2GaMo_3N structure from Springer Materials [123].

It is of interest that both η-carbide Ni_2GaMo_3N and Ni_2GeMo_3N [124] can be synthesised but Ni_3Mo_3N has proved much harder to form. As with Ni_2GaMo_3N, the nickel atoms in Ni_2GeMo_3N, reside in the 32e sites and the germanium or gallium atoms are located in the 16d sites, suggesting that the nickel atoms, which are larger than gallium and germanium atoms, are not favoured in the smaller 16d sites. Therefore, it could be proposed that Ni_3Mo_3N cannot be synthesised, as the nickel atoms are too large to fit in these sites. The empirical atomic radii of nickel, gallium and germanium are 135 pm, 130 pm and 125 pm respectively [125]. However, there is a deviation from these values depending on the method used to measure the radius. The empirical method calculates the radii by assuming that the atomic distance of two atoms forming a bond in a crystal is the sum of their radii. It must be noted, however, that Co has been stated to have the same empirical atomic radius (135 pm) as nickel [125] and can form Co_3Mo_3N.

3.2.4.1 Nickel Gallium Molybdenum Oxide ($Ni_2GaMo_3O_x$)

Ni_2GaMo_3N was prepared by ammonolysis of a nickel gallium molybdenum oxide. The oxide was synthesised by using a similar modified Pechini method as was used to prepare Ni_2Mo_3N [36]. From TPO analysis of the uncalcined starting material, it was found that a higher calcination temperature was needed than for Ni_2Mo_3N. As can be seen from Figure 99, carbon was removed from the material at 610°C, resulting in a weight loss of 10.40%. This value agrees with the 6 – 8% of carbon observed from the elemental analysis for the oxide that was calcined at 500°C. When the material was calcined at 500°C, there were two major weight losses at 560°C and 725°C as seen in Figure 100. The weight loss at 560°C was proposed to be due to carbon. All the carbon and water observed below 500°C had been removed from the calcined sample. The weight loss at 560°C was 5.96%, which corresponds to the expected percentage of carbon from elemental analysis. A weight loss of 17.88% was observed at 725°C. The results from the TPO suggest that the material should be calcined at a temperature of 650°C.

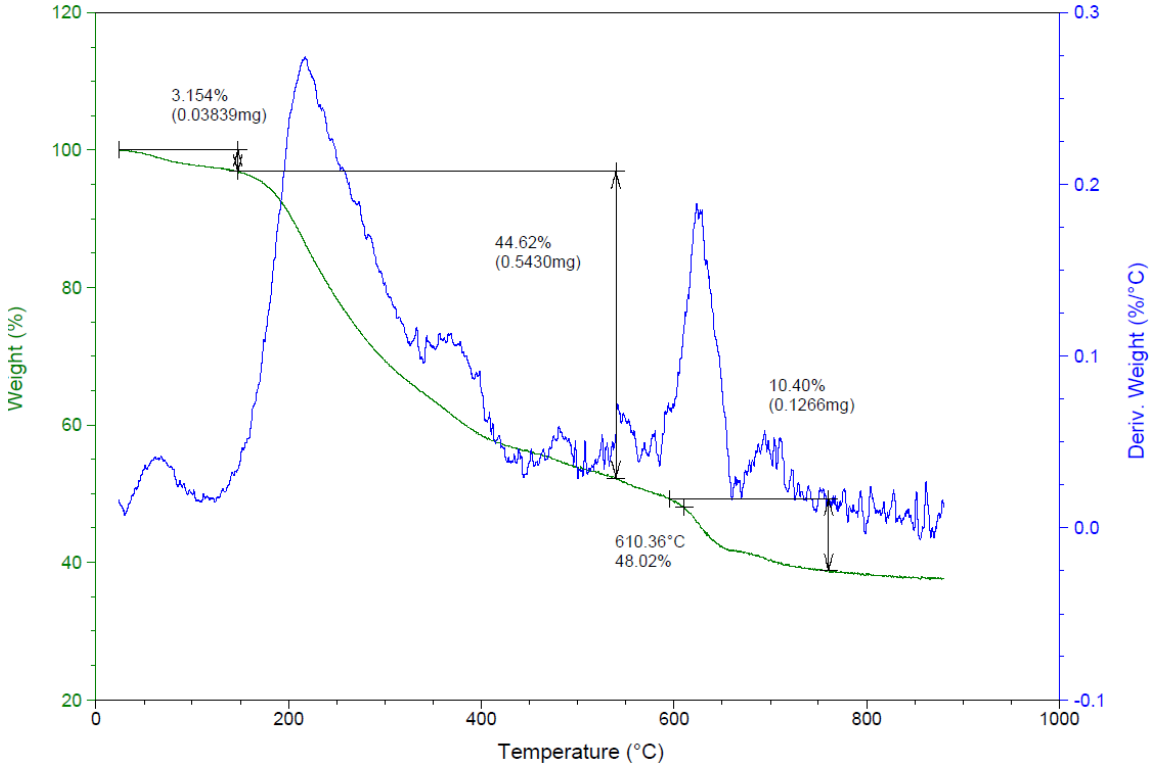

Figure 99: TGA curve and derivative weight profile for uncalcined Ni_2GaMo_3 under air in the range from room temperature to 900°C.

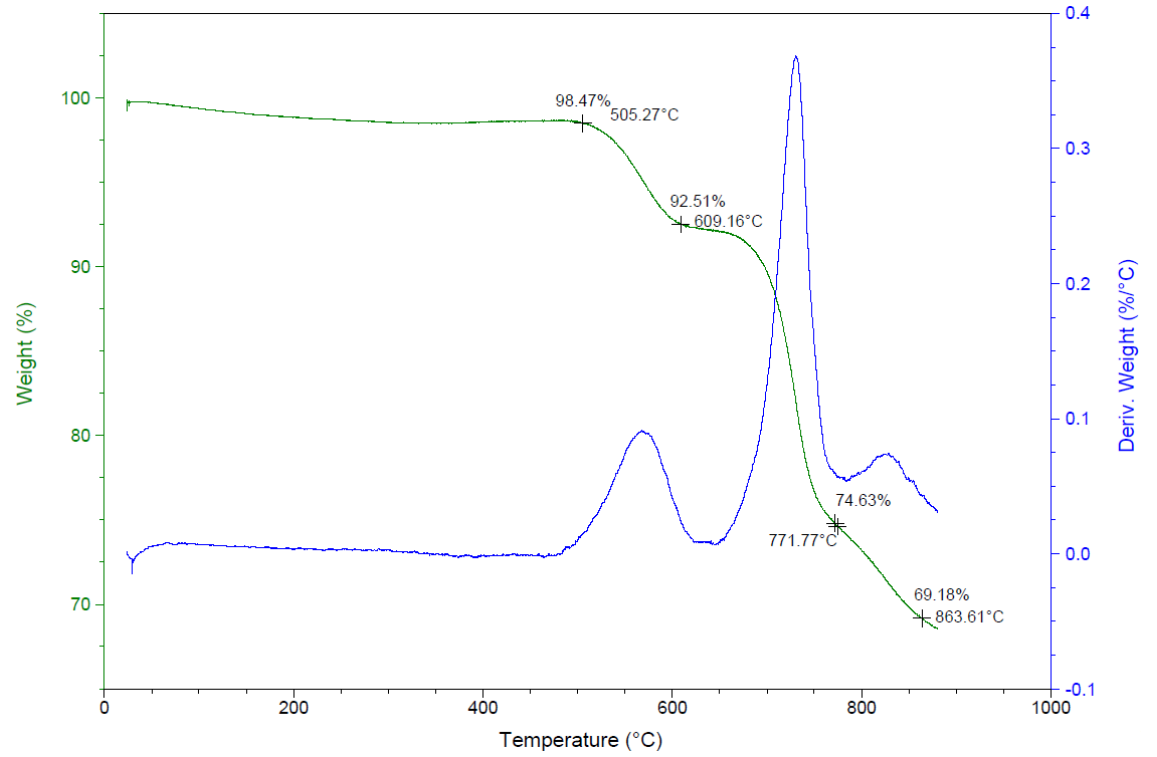

Figure 100: TGA curve and derivative weight profile for $Ni_2GaMo_3O_x$ calcined at 500°C under air in the range from room temperature to 900°C.

From the XRD pattern of the oxide as seen in Figure 101, it can be observed that the material consists of α-$NiMoO_4$ and MoO_3. Gallium oxide phases are also observed in the XRD pattern. Other peaks are observed in the XRD pattern and may relate to a mixed metal gallium phase but

these could not be identified with any files on the database (marked as red peaks). The XRD pattern is similar to the pattern obtained for $Ni_2Mo_3O_x$ that was prepared by the same sol-gel route. The mixture of oxides is desired due to the difference in the elemental ratios between the oxide and the nitride.

The elemental analysis showed that there was a trace amount of carbon present in the material after calcination and no nitrogen (C: 0.10 wt. %, H: 0.00 wt. % and N: 0.00 wt. %), suggesting that the higher calcination temperature was mostly sufficient to remove the nitrates and citric acid from the material.

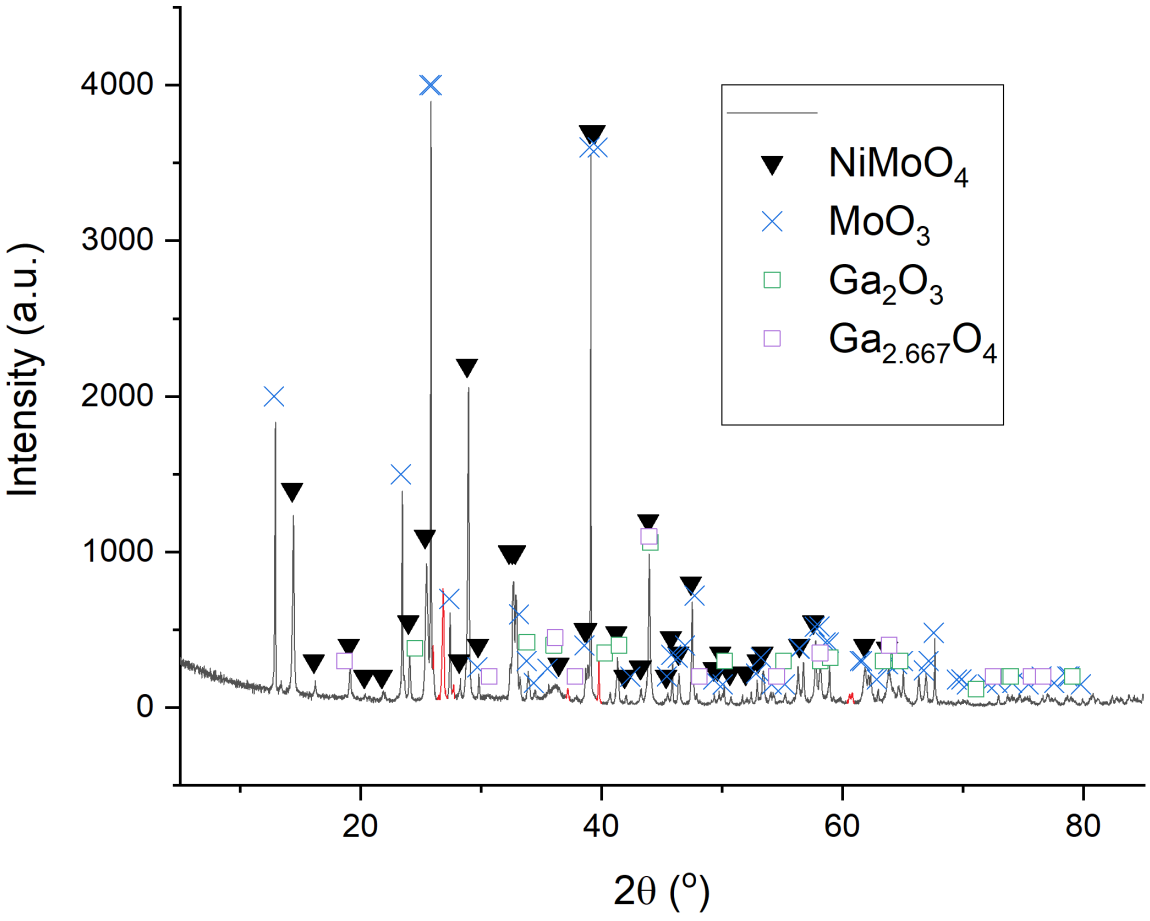

Figure 101: XRD pattern of nickel gallium molybdenum oxide calcined at 650°C ($Ni_2GaMo_3O_x$). Reflections marked: ▼ $NiMoO_4$ (JCPDS file number 00-033-0948), X MoO_3 (JCPDS file number 00-035-0609), □ α-Ga_2O_3 (JCPDS file number 01-074-1610) and □ $Ga_{2.667}O_4$ (JCPDS file number 01-074-7709).

The Raman spectrum of the oxide was analysed by comparing Figure 102 with the published spectra of $NiMoO_4$ and MoO_3. The Raman bands at positions of 960, 911 and 700, 381, 366 and 265 cm^{-1} were attributed to α-$NiMoO_4$ [89]. The bands at 960 and 911 cm^{-1} have been assigned in the literature as the symmetric and asymmetric stretching modes of the terminal Mo=O bond [90] and the band at 700 cm^{-1} was assigned to the Ni-O-

Mo symmetric stretch [67] [89]. The weak bands at 381 and 366 cm^{-1} are due to the bending mode of Mo−O [89] and the band at 265 cm^{-1} is attributed to the deformation mode of Mo−O−Mo [89]. Interestingly, there are no bands at approximately 994, 665 or 338 cm^{-1} that would be associated with MoO_3 [90]. Although, the band at 821 cm^{-1} could be attributed to the Mo-O-Mo asymmetric stretching mode of MoO_3 [90]. The presence of bands associated with $NiMoO_4$ agrees with the XRD result, which showed that the material contained this oxide.

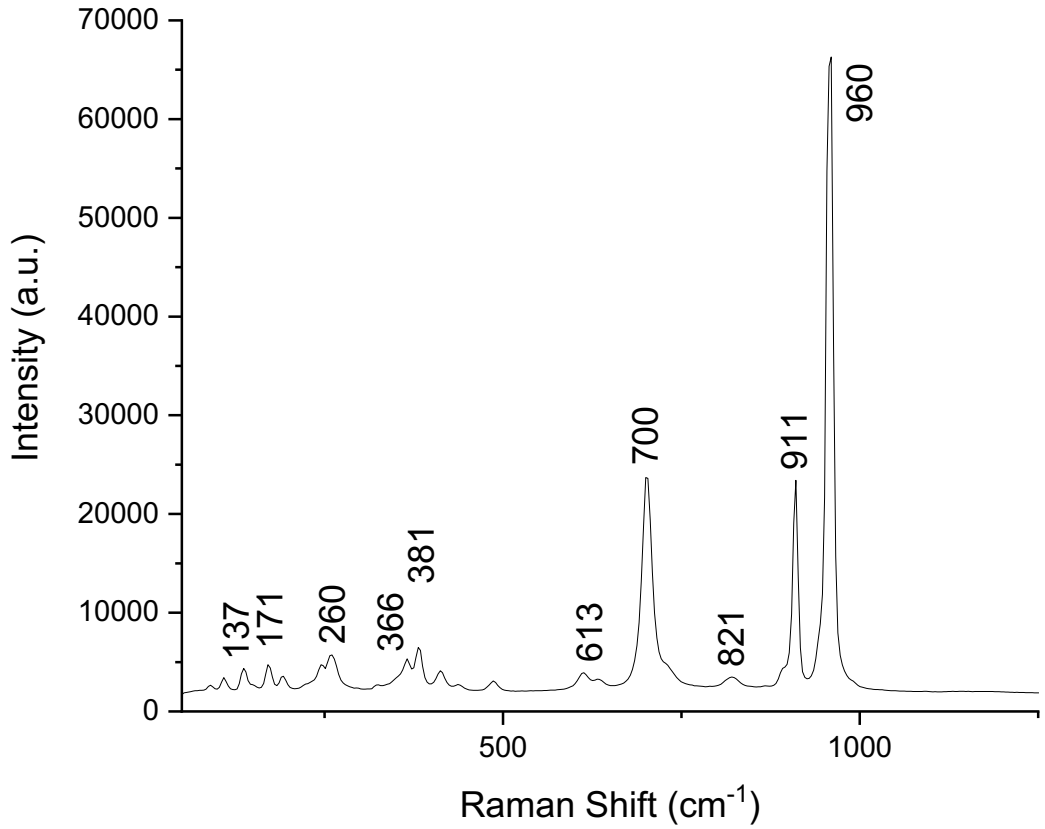

Figure 102: Raman spectrum of nickel gallium molybdenum oxide ($Ni_2GaMo_3O_x$).

Figure 103 gives the representative SEM images for the oxide. The sample consisted of porous particles with an uneven surface and also thin small needles. The stoichiometric percentage of nickel, gallium, molybdenum and oxygen in the theoretical $Ni_2GaMo_3O_{11}$ is 18.03 wt. %, 10.71 wt. %, 44.22 wt. % and 27.04 wt. %, respectively. From the EDX analysis in Table 24, it can be seen that the oxygen weight percentage was higher than predicted and the molybdenum percentage was lower. Therefore, the ratio of nickel, gallium and molybdenum was not 2:1:3 as expected. However, the XRD pattern shows that the material consisted of a separate molybdenum oxide phase and from the EDX data it can be seen that some areas contained more molybdenum than others.

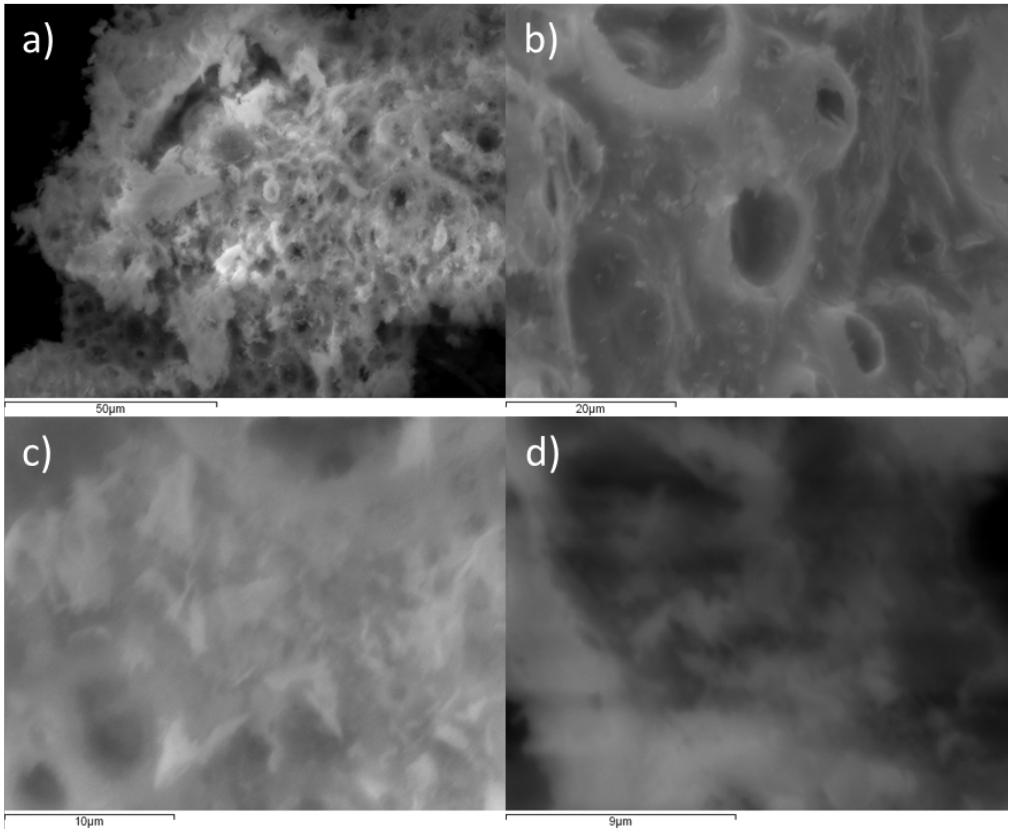

Figure 103: SEM images of nickel gallium molybdenum oxide ($Ni_2GaMo_3O_x$). a) 1000x magnification, b) 2000x magnification, c) 4000x magnification and d) 6000x magnification.

Area	Ni weight (%)	Ga weight (%)	Mo weight (%)	O weight (%)
1	13	10	34	42
2	2	2	59	37
3	13	9	32	45
4	20	16	33	32
5	22	18	31	28
6	18	14	30	37
7	19	14	32	35
8	16	12	29	43
9	20	15	31	35
10	19	15	29	37
11	14	11	31	45
12	11	9	34	46
13	11	7	36	46
14	13	11	32	44
15	20	15	31	34
16	21	15	30	34
Average	16	12	33	39

Table 24: EDX values for nickel gallium molybdenum oxide ($Ni_2GaMo_3O_x$).

3.2.4.2 Nickel Gallium Molybdenum Nitride (Ni_2GaMo_3N)

The η-carbide structured Ni_2GaMo_3N is a known phase that has previously been prepared by the reaction of MoO_3, hydrated gallium nitrate and nickel oxide under 10% H_2/N_2 with a heating regime up to 975°C [121]. In order to prepare the nitride at a lower temperature,

in this work the oxide was treated with ammonia gas at 785ºC via a temperature programmed regime. Pure phase η-carbide materials have previously been formed by the ammonolysis of their oxides [54] [35].

As can be seen in Figure 104, the desired quaternary nitride phase was formed. Ni_2GaMo_3N is not listed on the database; however, a CIF file from Springer materials [123] was plotted on VESTA to give the expected XRD reflections for the nitride. Impurities of GaNi and Mo_3N_2 were observed, suggesting that the material had not been completely nitrided. Prior and Battle observed a filled β-Mn structured impurity when they formed the nitride [121].

The elemental analysis shows that there was trace amounts of carbon and no hydrogen present in the material after ammonolysis (C: 0.14%, H: 0.00% and N: 3.73%). The percentage of nitrogen present in the material was higher than the expected stoichiometric value of 2.86 wt. %. This may be due to NH_x species on the surface of the nitride after ammonolysis, which is a common occurrence.

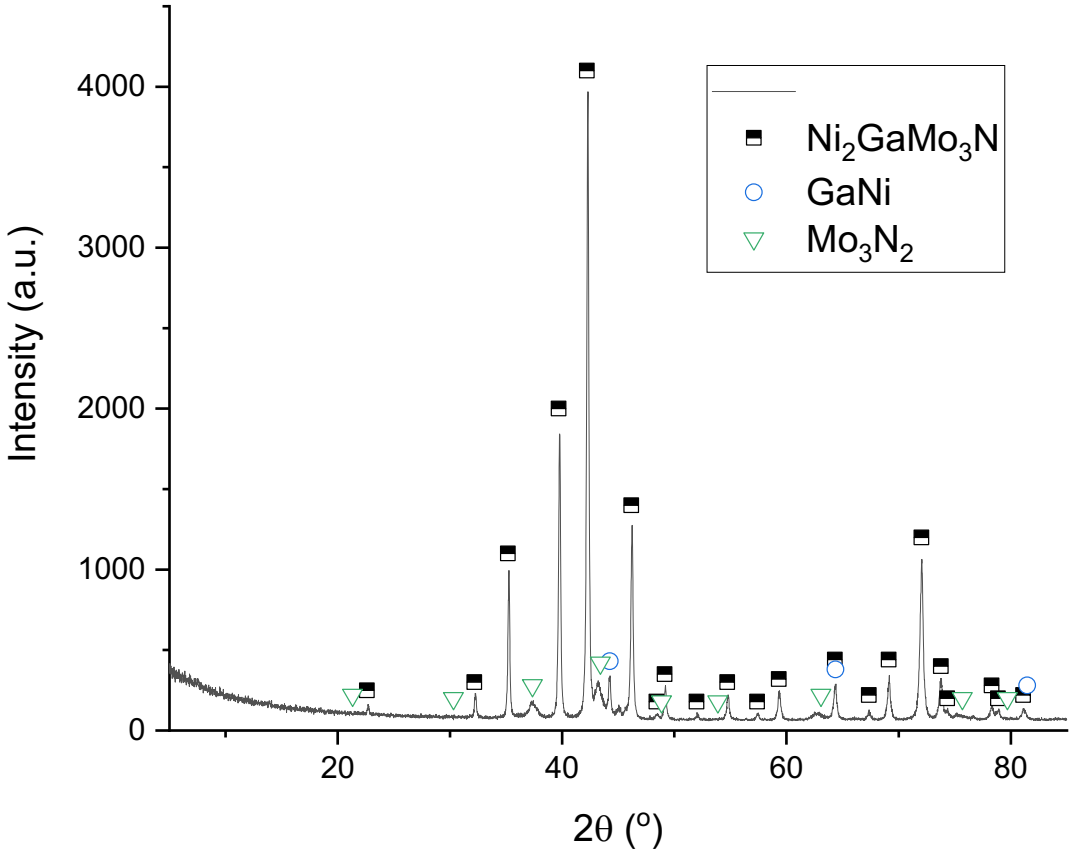

Figure 104: XRD pattern of nickel gallium molybdenum nitride (Ni_2GaMo_3N). Reflections marked: ■ Ni_2GaMo_3N (CIF file from Springer Materials [123]), ○ GaNi (JCPDS file number 01-071-8617) and ▽ Mo_3N_2 (JCPDS file number 03-065-4278).

Raman analysis was conducted for this material to investigate if there was any surface oxide species present. The Raman spectrum is presented in Figure 105 and shows that the material had formed a surface oxide layer. The positions of the Raman bands at 934, 886 and 812 cm^{-1} are observed in β-$NiMoO_4$ [96] [97] and $CoMoO_4$ [126]. These Raman bands are assigned to the Mo-O stretching vibrations or for the band at 820 cm^{-1} the asymmetric stretching mode of the Ni-O-Mo bond. To the author's knowledge, there is no published Raman spectrum of Ni_2GaMo_3N in the literature.

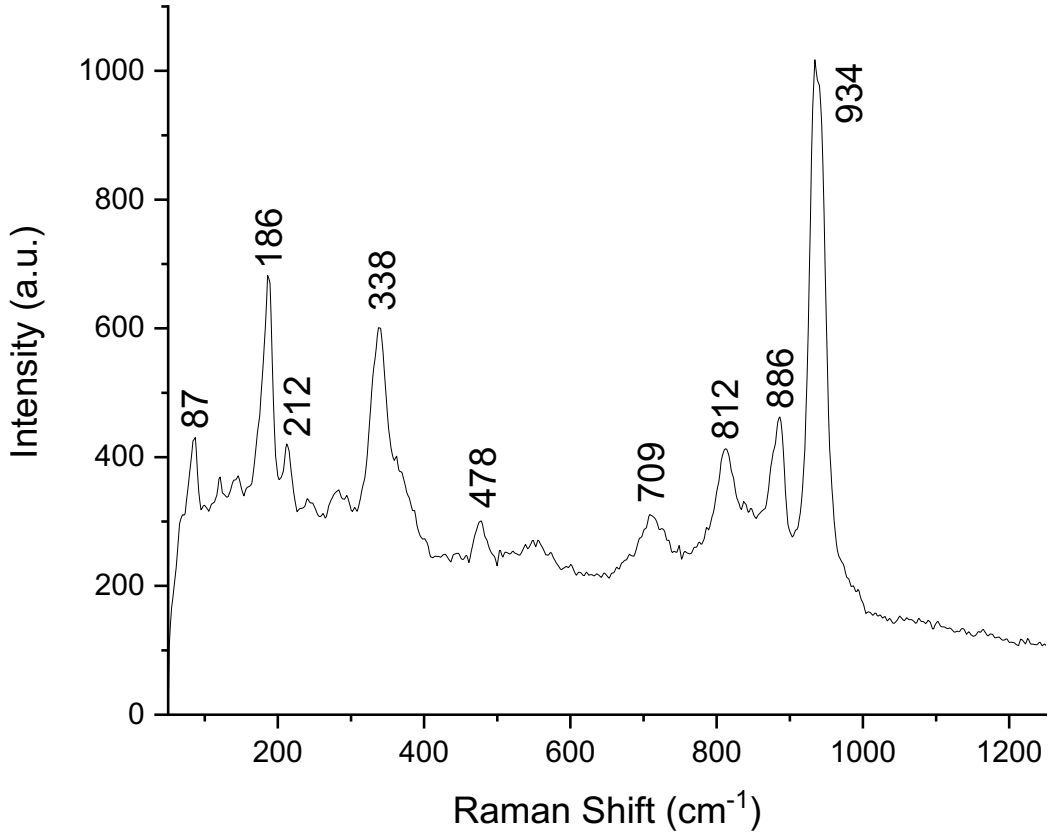

Figure 105: Raman spectrum of nickel gallium molybdenum nitride (Ni_2GaMo_3N).

As the morphology of a material can affect the ammonia synthesis activity, this was investigated by SEM analysis. The SEM images of the quaternary nitride are provided in Figure 106. The morphology of the material is similar to the pre-reaction material. However, there are more of the thin, small needles in the post-reaction material. The formation of needles has been observed for η-carbide structured Co_3Mo_3N that was prepared by ammonolysis [54]. The stoichiometric percentage of nickel, gallium, molybdenum and nitrogen in Ni_2GaMo_3N is 24.01 wt. %, 14.26 wt. %, 58.87 wt. % and 2.86 wt. %, respectively. The EDX data in Table 25 shows that the molybdenum percentage was slightly lower than expected and therefore, the ratio of the metals was not 2:1:3. Some areas contained more molybdenum and were observed as flat platelets as seen in Figure 106 (a) and may correspond to the Mo_3N_2 impurity. The nitrogen percentage was

higher than the expected stoichiometric amount and the 3.73 wt. % value obtained from CHN analysis. However, light elements are difficult to measure by EDX.

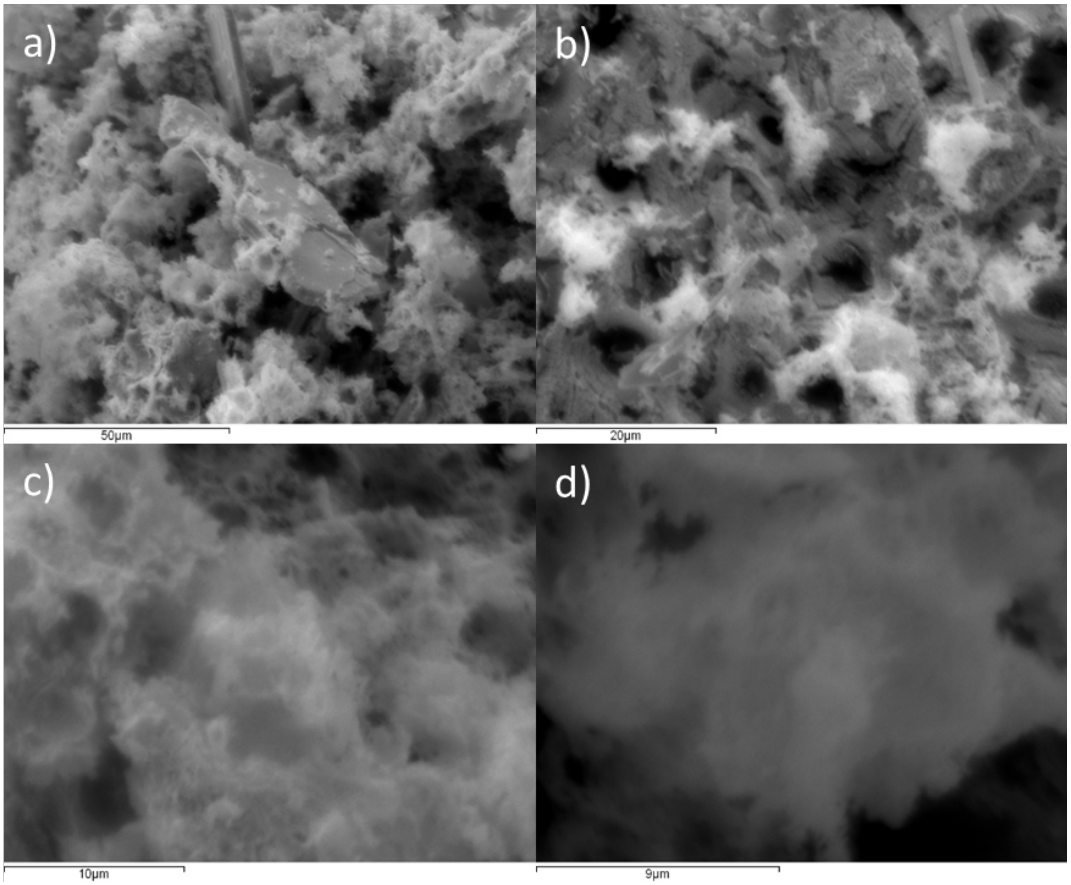

Figure 106: SEM images of nickel gallium molybdenum nitride (Ni_2GaMo_3N). a) 1000x magnification, b) 2000x magnification, c) 4000x magnification and d) 6000x magnification.

Area	Ni weight (%)	Ga weight (%)	Mo weight (%)	N weight (%)
1	26	20	50	4
2	18	14	56	11
3	18	14	59	9
4	23	17	53	6
5	34	28	37	0
6	25	18	52	4
7	29	21	44	6
8	24	20	50	6
9	21	17	57	6
10	27	23	45	5
11	27	21	44	8
12	29	21	45	5
13	22	16	55	8
14	21	16	53	10
15	22	15	57	6
16	20	15	53	11
17	22	18	50	10
18	25	19	49	7
19	23	17	52	8
20	25	19	49	7
Average	24	19	51	7

Table 25: EDX values for nickel gallium molybdenum nitride (Ni_2GaMo_3N).

3.2.4.2.1 Ammonia Synthesis for Ni_2GaMo_3N

In order to establish the relationship between structure and ammonia synthesis activity for ternary nitrides, Ni_2GaMo_3N was tested for its activity. The material was first pre-treated at 700°C for 2 hours under 3:1 H_2/N_2. Then, the material was tested under the same gas mixture at 400°C and 500°C. Figure 107 presents the plot of conductivity versus time for Ni_2GaMo_3N at the three temperatures tested. The rate of ammonia production at 700°C was 96 ± 12 μmol h^{-1} g^{-1} and at 500°C was 7 μmol h^{-1} g^{-1}. At 400°C, the activity was not steady state and therefore, a rate could not be calculated. The value was comparable to the rate for 'Ni_3Mo_3C' at 700°C (80 μmol h^{-1} g^{-1}) and lower than for 'Ni_6Mo_6C' (152 ± 89 μmol h^{-1} g^{-1}). However, the rate calculated for 500°C reaction temperature, was lower than for 'Ni_3Mo_3C' (41 μmol h^{-1} g^{-1}) and $Ni_2Mo_3C_xN_y$ (619 ± 14 μmol h^{-1} g^{-1}). These differences in activity suggest that the composition and structure have an effect, although morphology and surface area can also affect the rate. Although, Ni_3Mo_3C and Ni_2GaMo_3N both have a η-carbide structure and have a similar rate at 700°C, the carbide transforms to the filled β-Mn structured Ni_2Mo_3N during the reaction.

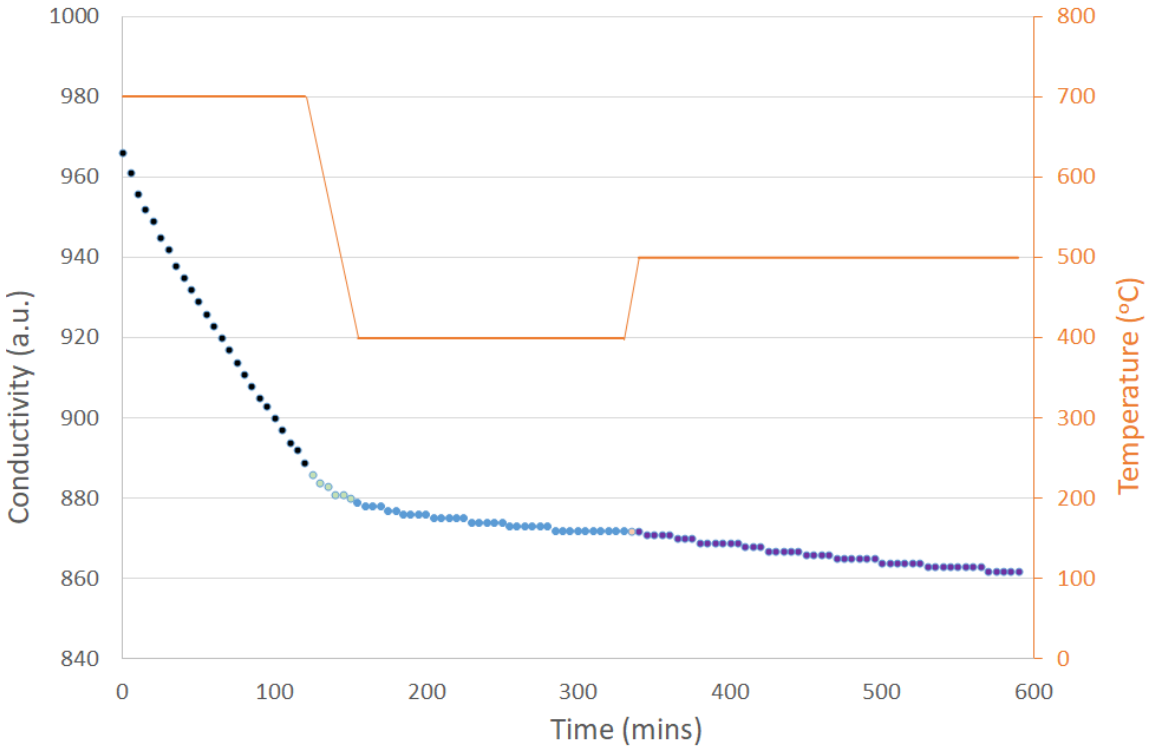

Figure 107: Conductivity profile for Ni_2GaMo_3N reacted with 3:1 H_2/N_2 at 700°C for 2 hours, 400°C for 3 hours and 500°C for 4 hours.

The XRD pattern in Figure 108 shows that the Ni_2GaMo_3N η-carbide structure was maintained after the reaction. The impurities of GaNi and Mo_3N_2 were also present in the material post-reaction.

The elemental analysis shows that the percentage of nitrogen present in the material after reaction with 3:1 H_2/N_2 had decreased (C: 0.12 wt. %, H: 0.00 wt. % and N: 2.77 wt. %) compared to pre-reaction (3.73 wt. %). The percentage of nitrogen present in the material agreed well with the expected stoichiometric value of 2.86 wt. % and may correspond to the loss of NH_x species form the surface. The Mo_3N_2 impurity had shifted to higher 2θ values as seen for the peak at 37.37° 2θ and suggests that it is losing nitrogen as the lattice parameter is getting smaller. Therefore, the decrease in nitrogen may also be due to the reduction of the Mo_3N_2.

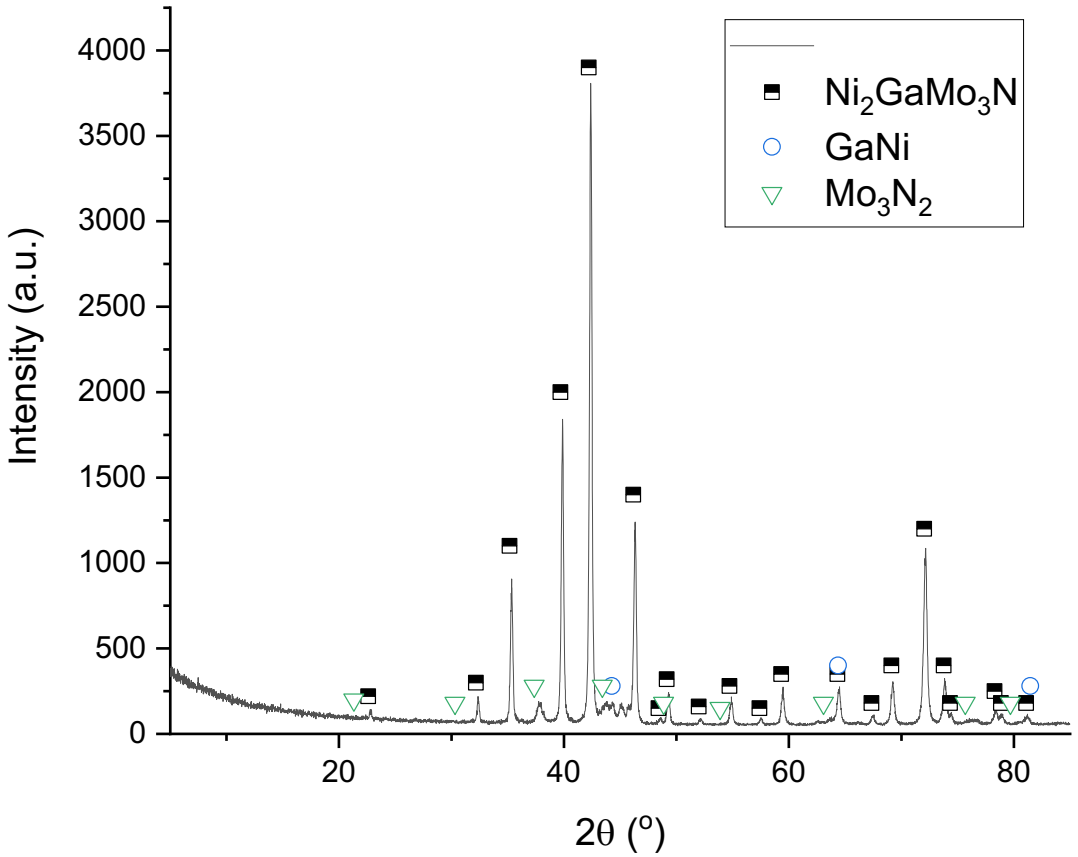

Figure 108: XRD pattern of Ni_2GaMo_3N post-reaction with 3:1 H_2/N_2. Reflections marked: ■ Ni_2GaMo_3N (CIF file from Springer Materials [123]), ○ GaNi (JCPDS file number 01-071-8617) and ▽ Mo_3N_2 (JCPDS file number 03-065-4278).

SEM analysis was performed on the material to observe any possible changes in morphology or structure during the reaction. Representative SEM images are provided in Figure 109. The material appears to have retained the morphology of the pre-reaction material and consists of porous surfaces, platelets and small needles. The platelets range in size and can be as large as 40 μm x 60 μm as observed in Figure 109 (b). The EDX data showed that these platelets consisted of a large percentage of molybdenum as seen in Table 26. The stoichiometric percentage of nickel, gallium, molybdenum and nitrogen in Ni_2GaMo_3N is 24.01 wt. %, 14.26 wt. %, 58.87 wt. % and 2.86 wt. %, respectively. As with the pre-reaction material, the molybdenum percentage was lower than expected and therefore, the ratio of metals was not as predicted. The EDX values of the pre- and post-reaction material were very similar suggesting that the phase does not change during the reaction.

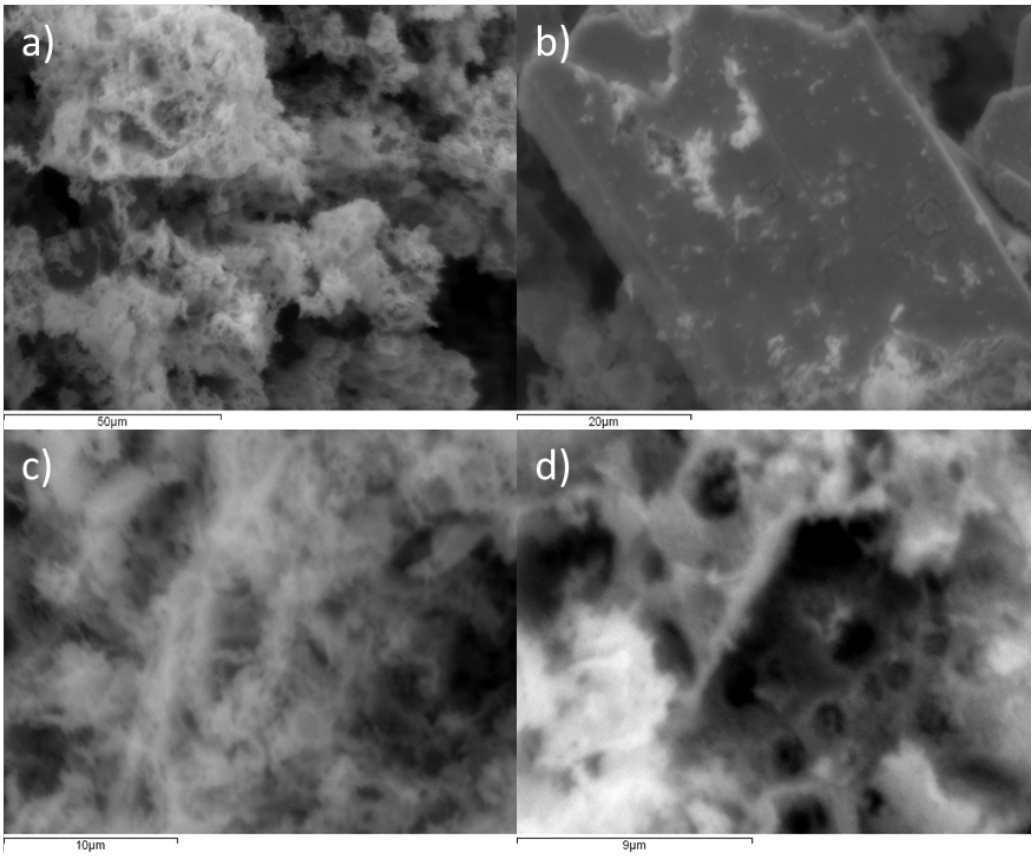

Figure 109: SEM images of Ni_2GaMo_3N post-reaction with 3:1 H_2/N_2. a) 1000x magnification, b) 2000x magnification, c) 4000x magnification and d) 6000x magnification.

Area	Ni weight (%)	Ga weight (%)	Mo weight (%)	N weight (%)
1	25	17	54	4
2	4	7	76	13
3	22	17	53	8
4	21	15	56	8
5	10	11	72	8
6	11	14	62	13
7	26	19	49	6
8	22	16	52	10
9	38	28	34	0
10	38	29	33	0
11	51	38	11	0
12	22	17	52	9
13	27	24	44	5
14	28	25	47	0
15	24	17	53	6
16	25	19	48	8
17	28	25	41	6
18	24	19	48	8
19	23	16	54	8
Average	25	20	49	6

Table 26: EDX values for Ni_2GaMo_3N post-reaction with 3:1 H_2/N_2.

3.2.4.2.2 Lattice Nitrogen Reactivity of Ni_2GaMo_3N at 700°C

In order to determine the reactivity of lattice nitrogen in Ni_2GaMo_3N, the material has been reacted under 3:1 H_2/Ar at 700°C. If the lattice nitrogen is reactive and the material operates via a Mars-van Krevelen mechanism, there would most likely be a reduction in the nitrogen percentage and occupancy of Ni_2GaMo_3N under these conditions. Figure 110 shows that the lattice nitrogen was only slightly reactive under Ar/H_2 at 700°C with only a small amount of ammonia being produced. There was a decrease in conductivity of 34 µS/cm over the 7 hours. This result is similar to Ni_2Mo_3N that has previously been tested under Ar/H_2 at 700°C [98] and was found that the lattice nitrogen was fairly unreactive. Ni_2Mo_3N has the filled β-Mn structure, suggesting that structure does not play a role in lattice nitrogen reactivity. Instead it appears that composition is more important. This result suggests that Ni_2GaMo_3N may not operate via a Mars-van Krevelen mechanism and could explain its low ammonia synthesis activity.

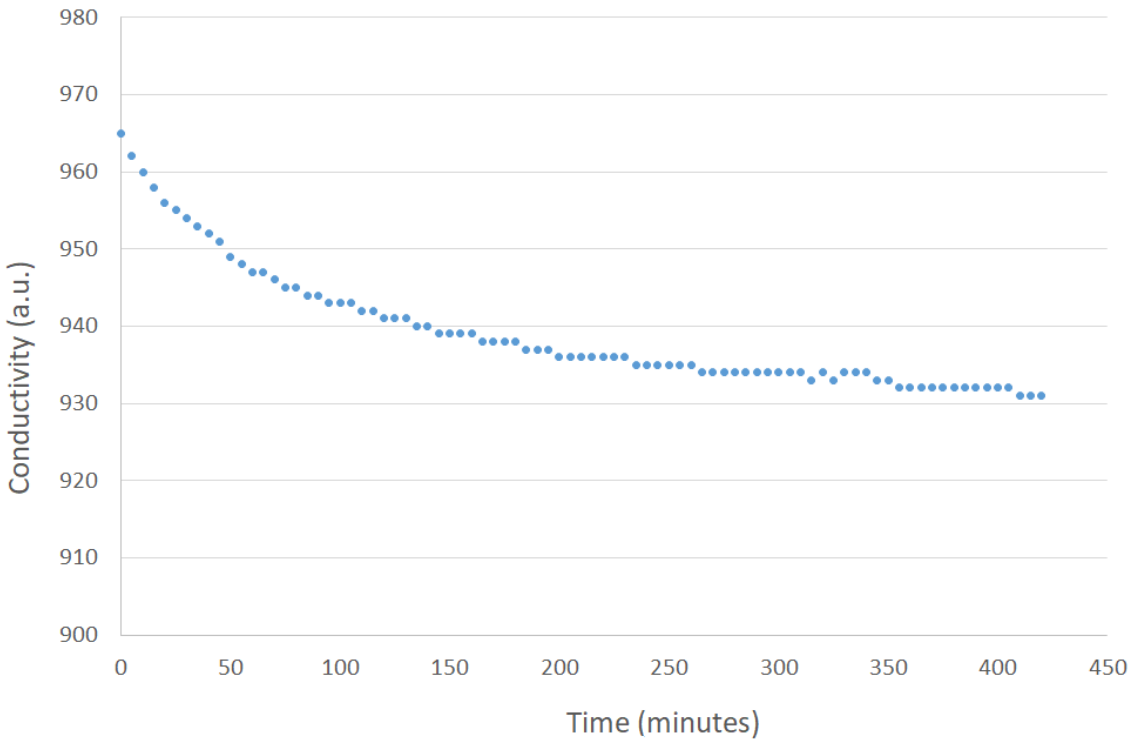

Figure 110: Conductivity profile for Ni_2GaMo_3N reacted with 3:1 H_2/Ar at 700°C for 7 hours.

The XRD pattern presented in Figure 111 demonstrates that there was no phase transition for the nitride during the reaction. The Mo_3N_2 impurity was reduced to β-Mo_2N during the reaction as evidenced from the XRD pattern. The XRD pattern confirms that the bulk lattice nitrogen in the material was unreactive as there was no shift of the XRD reflections to higher 2θ values as expected for a loss of nitrogen. Ni_2Mo_3N has also been shown to have no shift in the XRD reflections when tested under Ar/H_2 at 700°C [36] [92], whereas

Co_3Mo_3N has been shown to lose half of its lattice nitrogen to form Co_6Mo_6N when reacted under these conditions. Both Co_3Mo_3N and Ni_2GaMo_3N have a η-carbide structure but show different behaviour when reduced under Ar/H_2. This further suggests that the structure does not have an effect on the lattice nitrogen reactivity, but the composition may have a greater importance. However, in contrast to this inference, filled β-Mn structured $NiCoMo_3N$ has been previously prepared and tested for ammonia synthesis activity and lattice nitrogen reactivity and it was found to behave similar to Ni_2Mo_3N [92]. $NiCoMo_3N$ was prepared to explore the relationship between structure and lattice nitrogen activity and to move the electronic structure of Ni_2Mo_3N closer to Co_3Mo_3N. This could be used to probe how specific the material was to pure nickel. Therefore, as the quaternary nitride had a similar activity to Ni_2Mo_3N, it was proposed that electronic factors were not responsible for the material's activity.

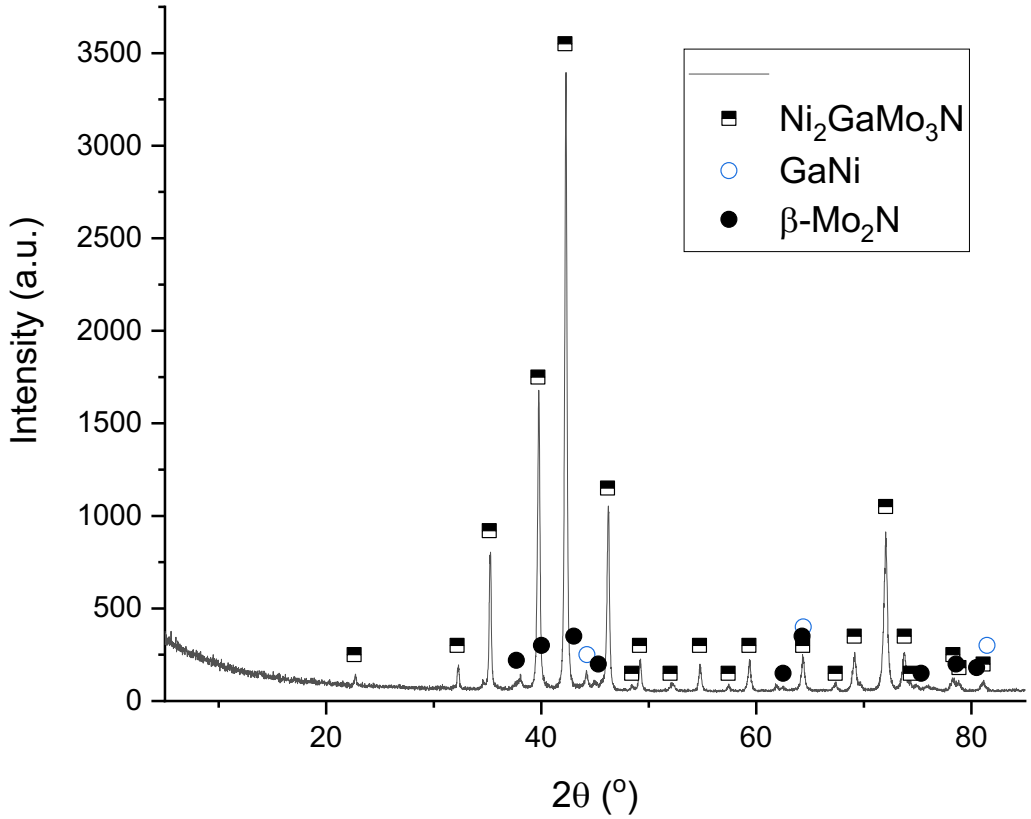

Figure 111: XRD pattern of Ni_2GaMo_3N post-reaction with 3:1 H_2/Ar at 700°C. Reflections marked: ⬒ Ni_2GaMo_3N (CIF file from Springer Materials [123]), ○ GaNi (JCPDS file number 01-071-8617) and ● β-Mo_2N (JCPDS file number 01-075-1150).

The elemental analysis shows that the percentage of nitrogen was similar after reduction with 3:1 H_2/Ar (C: 0.50 wt. %, H: 0.00 wt. % and N: 2.41 wt. %) to pre-reaction (2.40 wt. %). The percentage of nitrogen present in the material was lower than the expected stoichiometric value of 2.86 wt. %. This result confirms that the bulk lattice nitrogen in the material was unreactive.

In order to see if there was any change in morphology during the reaction, SEM analysis was performed. The representative SEM images of the post-reaction material are displayed in Figure 112. The sample consisted of porous particles with pores ranging in diameter from 1 μm to 20 μm and thin needles. The morphology had been retained compared to the pre-reaction material. The nickel, gallium, molybdenum and nitrogen appear to be fairly evenly distributed across the material as seen in the element map in Figure 113. This confirms that there had been no phase segregation under the reducing conditions.

The stoichiometric percentage of nickel, gallium, molybdenum and nitrogen for Ni_2GaMo_3N is 24.01 wt. %, 14.26 wt. %, 58.87 wt. % and 2.86 wt. %, respectively. The EDX analysis for the post-reaction sample is presented in Table 27 and shows that the nitrogen percentage had decreased compared to pre-reaction suggesting that some nitrogen may have been lost during the reaction. However, there are limitations to measuring light elements by EDX. The percentage of nickel and gallium had increased compared to pre-reaction and the molybdenum had decreased. Therefore, the ratio of Ni to Ga to Mo was not 2:1:3. This is in contrast to the XRD pattern, which showed that the Ni_2GaMo_3N phase had been retained.

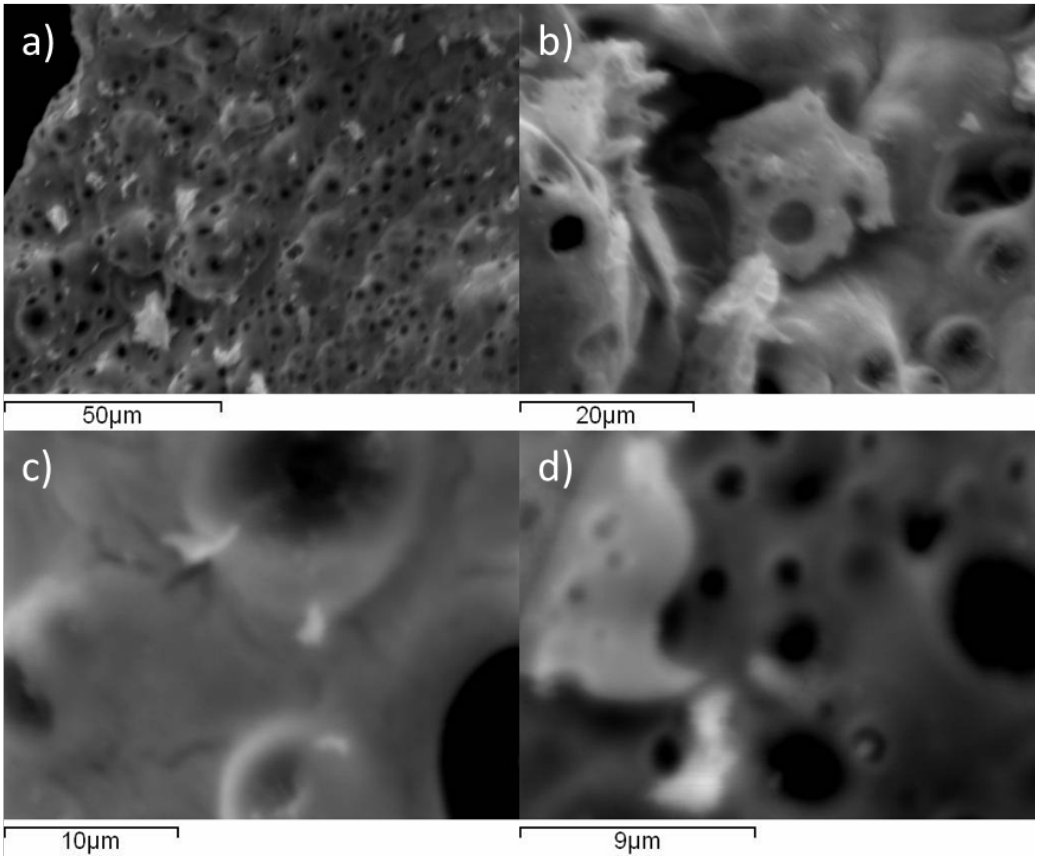

Figure 112: SEM images of Ni_2GaMo_3N post-reaction with 3:1 H_2/Ar at 700°C for 7 hours. a) 1000x magnification, b) 2000x magnification, c) 4000x magnification and d) 6000x magnification.

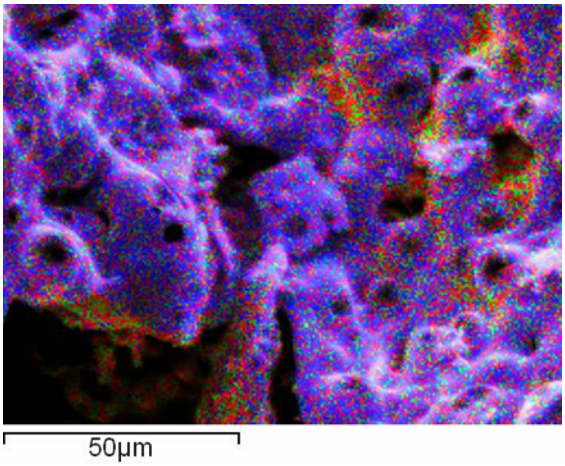

Figure 113: Element map for Ni_2GaMo_3N post-reaction with 3:1 H_2/Ar at 700°C for 7 hours. Elements: Ni (red), gallium (green), molybdenum (blue) and nitrogen (black).

Area	Ni weight (%)	Ga weight (%)	Mo weight (%)	N weight (%)
1	25	19	53	3
2	23	18	54	3
3	28	22	46	4
4	22	17	57	4
5	19	15	61	6
6	28	22	46	4
7	23	18	54	6
8	40	32	27	1
9	39	33	26	2
10	23	17	53	7
11	35	27	37	1
Average	28	22	47	4

Table 27: EDX values for Ni_2GaMo_3N post-reaction with 3:1 H_2/Ar at 700°C.

3.2.4.2.3 Lattice Nitrogen Reactivity of Ni_2GaMo_3N at 900°C

In order to investigate the possible reactivity of lattice nitrogen in Ni_2GaMo_3N, the material was reduced at a higher temperature. The material was tested at 900°C under 3:1 H_2/Ar for 7 hours. As observed from the conductivity data in Figure 114, the production of ammonia was minimal, with the conductivity decreasing by only 18 µS/cm over the 7 hours. However, it must be noted that ammonia production is unfavourable at this temperature and will decompose [99] and, therefore, the lattice nitrogen may be lost as N_2. No N_2 analysis was undertaken.

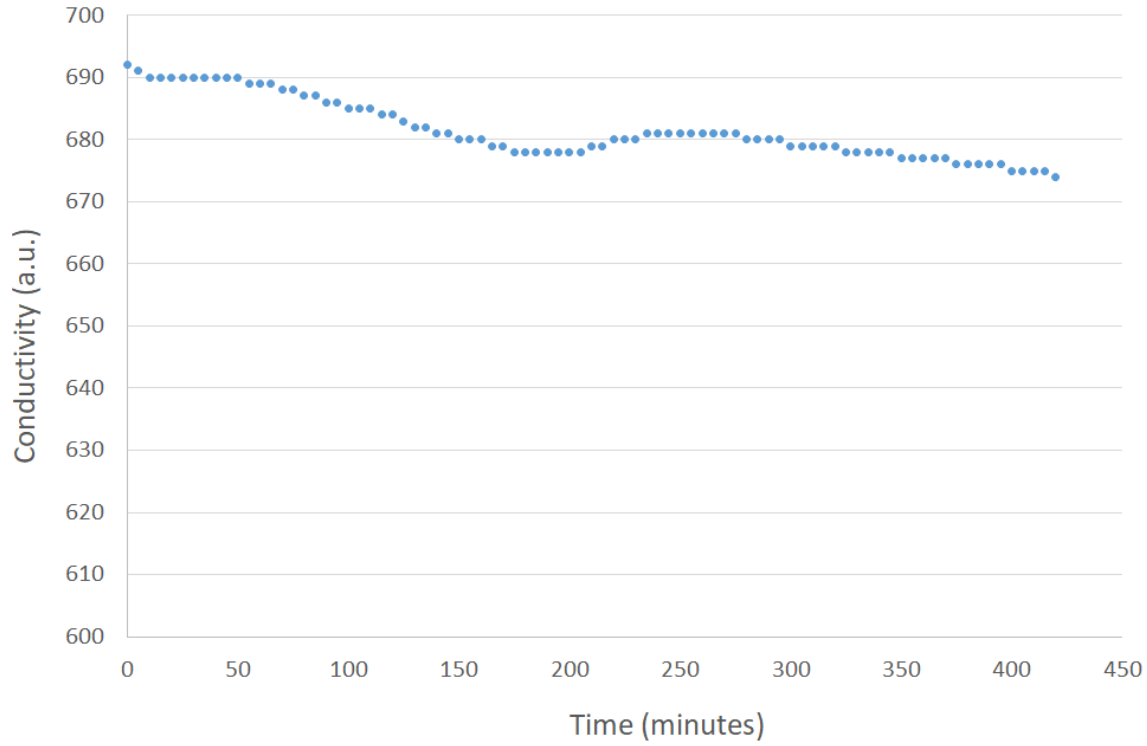

Figure 114: Conductivity profile for Ni_2GaMo_3N reacted with 3:1 H_2/Ar at 900°C for 7 hours.

The XRD pattern displayed in Figure 115 shows that the η-carbide structured Ni_2GaMo_3N was maintained after the reaction. There does not appear to have been any major change in phase compared to pre-reaction or shift in XRD reflections as seen in Figure 116. This suggests that the material is not reduced and does not loss a large percentage of nitrogen under these conditions. The Mo_3N_2 impurity was reduced during the reaction as seen from the XRD pattern. The XRD pattern confirms that the bulk lattice nitrogen in the material was unreactive. Ni_2Mo_3N also has no shift in its XRD reflections when tested under Ar/H_2 at 900°C as seen in section 3.2.1.2.1.

The elemental analysis shows that the percentage of nitrogen had decreased after reduction with 3:1 H_2/Ar at 900°C (C: 0.00 wt. %, H: 0.00 wt. % and N: 3.34 wt. %) compared to pre-reaction (4.17 wt. %). The reduction of the Mo_3N_2 phase or some loss of nitrogen from the quaternary nitride could account for the decrease in nitrogen. Assuming the loss of nitrogen was due only to the Ni_2GaMo_3N, the percentage of lattice nitrogen lost that was converted to ammonia was 14.62%.

This result suggests that the structure does not influence the lattice nitrogen reactivity, as similar behaviour was observed between the filled β-Mn structured Ni_2Mo_3N and the η-carbide structured Ni_2GaMo_3N.

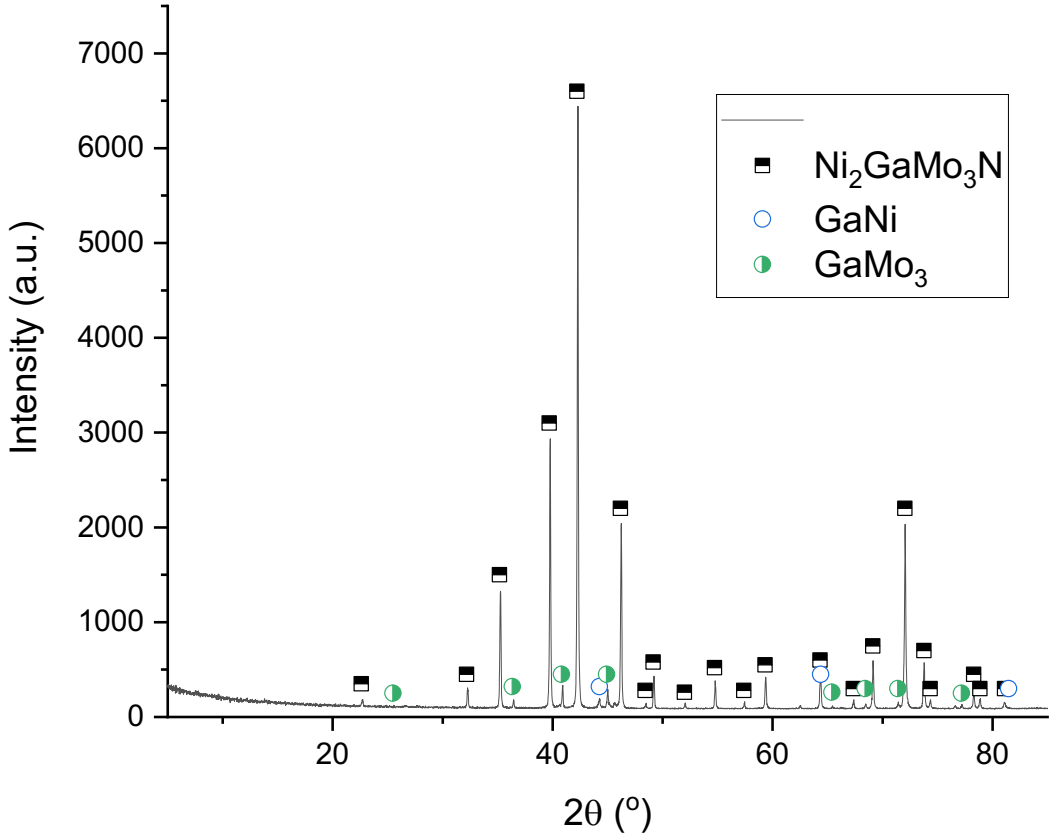

Figure 115: XRD pattern of Ni_2GaMo_3N post-reaction with 3:1 H_2/Ar at 900°C for 7 hours. Reflections marked: ■ Ni_2GaMo_3N (CIF file from Springer Materials [123]), ○ GaNi (JCPDS file number 01-071-8617) and ◐ $GaMo_3$ (JCPDS file number 03-065-3312).

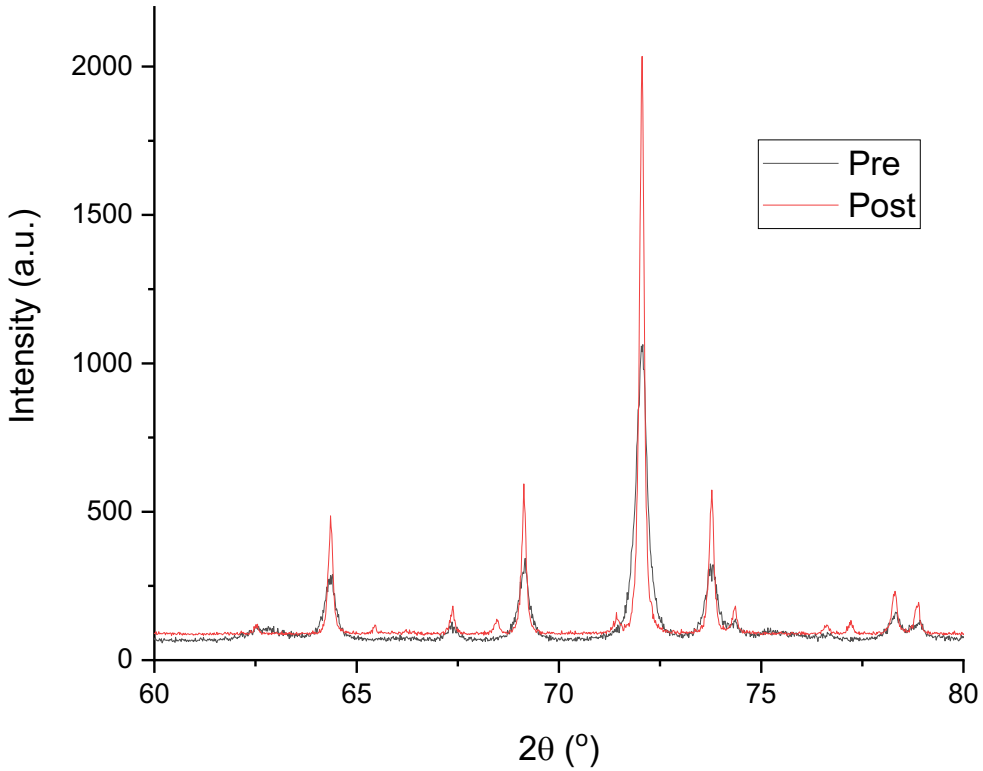

Figure 116: Comparison of XRD patterns between Ni_2GaMo_3N pre- (black) and post-reaction (red) with 3:1 H_2/Ar at 900°C for 7 hours.

SEM analysis was conducted to see if the reaction had an effect on the morphology of the material. Typical SEM images of Ni_2GaMo_3N post-reaction with 1:3 Ar/H_2 at 900°C are shown in Figure 117. The material consisted of a porous structure, platelets and small needles and the morphology was retained from the pre-reaction material. The morphology was slightly different from the Ni_2Mo_3N that was tested under the same conditions (Figure 26). The Ni_2Mo_3N did not contain platelets and there was not as many small needles. Therefore, the lattice nitrogen reactivity is not affected by the morphology of the material.

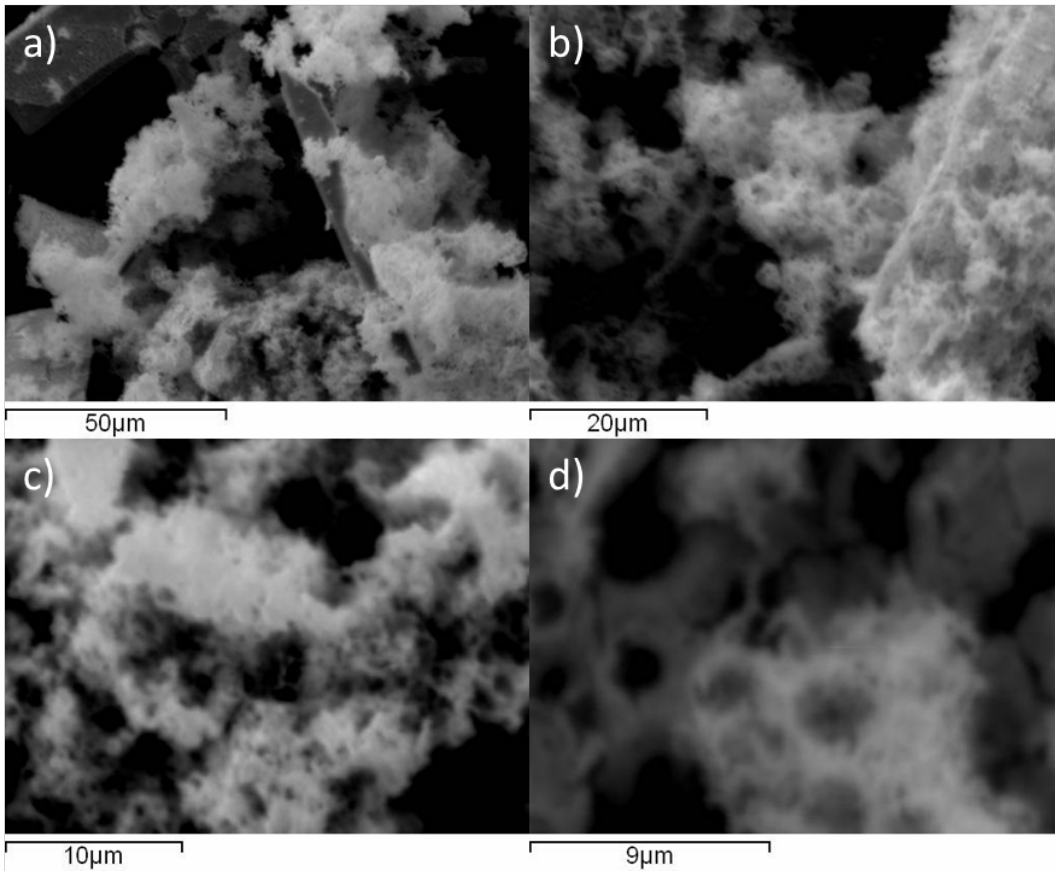

Figure 117: SEM images of Ni_2GaMo_3N post-reaction with 3:1 H_2/Ar at 900°C for 7 hours. a) 1000x magnification, b) 2000x magnification, c) 4000x magnification and d) 6000x magnification.

The element maps in Figure 118 illustrate that there was a fairly even distribution of nickel, gallium, molybdenum and nitrogen over the sample. Therefore, there had not been phase segregation during the reaction.

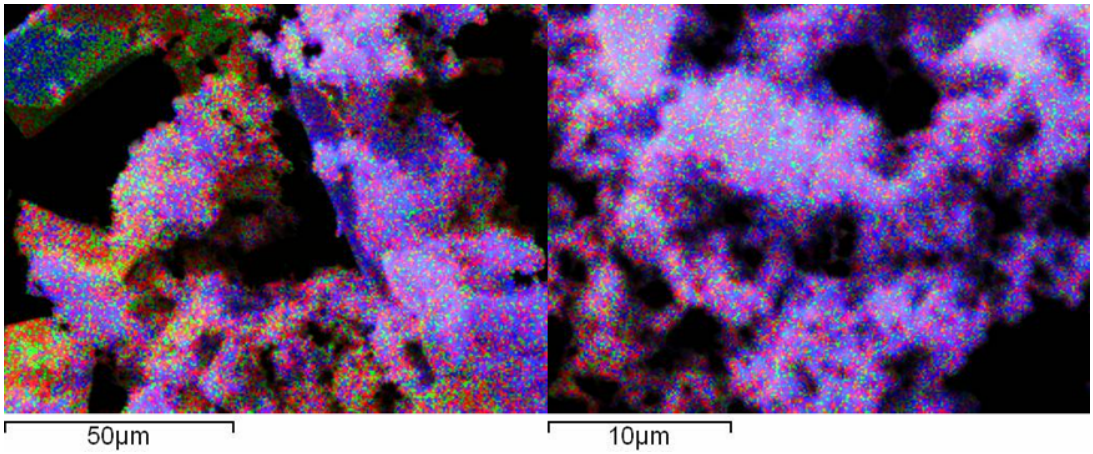

Figure 118: Element map for Ni_2GaMo_3N post-reaction with 3:1 H_2/Ar at 900°C for 7 hours. Elements: Ni (red), gallium (green), molybdenum (blue) and nitrogen (black).

The EDX data for the post-reaction sample is shown in Table 28. The stoichiometric percentage of nickel, gallium, molybdenum and nitrogen in Ni_2GaMo_3N is 24.01 wt. %, 14.26 wt. %, 58.87 wt. % and 2.86 wt. %, respectively. The nitrogen percentage had decreased compared to pre-reaction suggesting that some nitrogen was lost during the reaction. This agrees with the CHN analysis that showed the nitrogen percentage had decreased post-reaction. The percentage of nickel had decreased compared to pre-reaction and the amount of molybdenum had increased. Therefore, the ratio of the metals was closer to 2:1:3 compared to pre-reaction. This confirms that the Ni_2GaMo_3N phase had been retained as seen in the XRD pattern.

Area	Ni weight (%)	Ga weight (%)	Mo weight (%)	N weight (%)
1	7	33	60	0
2	27	20	53	0
3	24	17	56	3
4	21	15	57	6
5	28	20	49	4
6	24	18	53	5
7	26	18	52	5
8	24	18	52	6
9	22	15	55	7
10	24	17	54	5
11	22	16	55	7
12	30	22	46	3
13	11	23	64	2
14	25	18	51	6
Average	22	19	54	4

Table 28: EDX values for Ni_2GaMo_3N post-reaction with 3:1 H_2/Ar at 900°C.

3.3 Conclusions

The filled β-Mn structured Ni_2Mo_3N and $Ni_2Mo_3C_xN_y$ and η-carbide structured Ni_6Mo_6C, Ni_3Mo_3C and Ni_2GaMo_3N were prepared and tested for ammonia synthesis activity and lattice nitrogen reactivity. Unfortunately, Ni_2Mo_3C could not be synthesised by topotactic routes from Ni_2Mo_3N even though different carburisation sources were used. These materials were prepared and tested to give information on the influence structure and composition has on ammonia synthesis activity. All of these phases have the interstitial element (nitrogen and/or carbon) coordinated to six molybdenum species.

Ni_2Mo_3N and Ni_2GaMo_3N were reacted under 3:1 H_2/Ar at 900°C to determine their lattice nitrogen reactivity. The materials were found to not be reduced under these conditions, suggesting that the bulk lattice nitrogen was unreactive. Therefore, it appears that structure does not have an effect on the activity but perhaps composition has a greater importance.

Nickel molybdenum carbonitride ($Ni_2Mo_3C_xN_y$) was found to be active for ammonia synthesis at 400°C and was observed to undergo nitridation during the reaction as evidenced from elemental analysis. An induction period was observed for this material when it was tested at 500°C but was not observed when tested at 400°C. The effect of the passivation layer on the ammonia synthesis activity and its possible influence on the induction period was investigated by ToF-SIMS. It was seen that nitrogen and carbon were both present near the surface of the material at a depth of 10 nm.

Both Ni_6Mo_6C and Ni_3Mo_3C have been prepared and tested for ammonia synthesis activity to help establish structure-activity and composition-activity relationships. Ni_6Mo_6C was synthesised by using citric acid to carburise nickel molybdate under Ar/H_2 at 700°C. Ni_6Mo_6C phase was converted to Ni_3Mo_3C when reacted with 20% CH_4/H_2. The materials consisted of two main segregated phases, the carbide and Ni_2Mo_3N. 'Ni_6Mo_6C' and 'Ni_3Mo_3C' were not active for ammonia synthesis when tested at 400°C or 500°C, respectively. However, they were both active at 700°C under 3:1 H_2/N_2 with 'Ni_6Mo_6C' having the higher activity. The two materials were shown to undergo nitridation during the reaction as confirmed by the XRD patterns and elemental analysis. The carbides formed Ni_2Mo_3N rather than carry out a topotactic exchange mechanism as reported for Co_3Mo_3C, suggesting that the Ni_3Mo_3N phase is less stable. Interestingly, Mo_2C and $Mo_{0.09}Ni_{0.91}$ had good ammonia synthesis activity and also combined to form Ni_2Mo_3N during the reaction. It is not understood if the activity arises due to the nitridation of these materials and

therefore, the presence of lattice nitrogen is required or whether lattice nitrogen incorporates into these materials as they are active for ammonia synthesis.

Ni_2GaMo_3N was shown to have a very low activity for ammonia synthesis when tested at 400°C and 500°C and a rate of 96 ± 12 μmol h^{-1} g^{-1} at 700°C. This rate is lower than the reported rates for Ni_2Mo_3N in the literature (395 ± 6 μmol h^{-1} g^{-1} at 400°C [36]) and for $Ni_2Mo_3C_xN_y$ in this work (197 ± 23 μmol h^{-1} g^{-1} at 400°C). Therefore, it could be suggested that there is a possible relationship between structure and ammonia synthesis activity for nickel containing nitrides. However, it has been shown that nickel impurities can lower the rate of Ni_2Mo_3N (< 15 μmol h^{-1} g^{-1} at 400°C [36]). Therefore, the presence of GaNi in Ni_2GaMo_3N may affect its rate and a definite conclusion cannot be drawn for the structure-activity relationship.

A summary of the major phase transformations of the nickel molybdenum materials investigated within this chapter is presented in Figure 119.

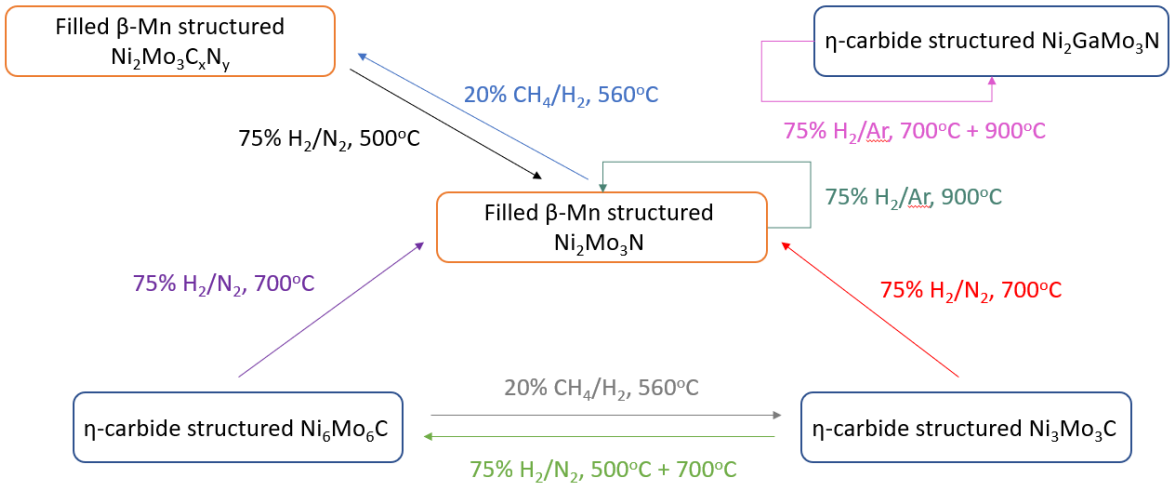

Figure 119: Phase transformations of the nickel molybdenum materials.

4. Cobalt Molybdenum Materials

4.1 Introduction

In order to continue to investigate the relationships between structure-ammonia synthesis activity and composition-activity, the filled β-Mn structured Co_2Mo_3N has been prepared. A comparison of the activity and lattice nitrogen reactivity of this nitride with the filled β-Mn structured Ni_2Mo_3N reported in Chapter 3 might give an insight into the role that metal composition has on the activity.

The η-carbide structured Co_3Mo_3N is a well known ammonia synthesis catalyst [35] [39] [54]. Co_3Mo_3N has been shown to have a higher activity than the Haber Bosch catalyst at ambient pressure [127] and also at more realistic Haber Bosch conditions [94]. The activity of Co_3Mo_3N can be enhanced by the addition of Cs^+ in low levels [128]. As this nitride has a high activity, most of the literature has focused upon it. Co_3Mo_3N has the η-6 carbide structure, which was explained in detail in Chapter 3 [59] [60].

In recent years, the filled β-Mn structured Co_2Mo_3N has been synthesised and investigated for its ammonia synthesis activity [129] [130]. In this structure, the Co atoms occupy the 8c sites and the Mo species are positioned on the 12d sites [73]. The N species are bonded to six Mo species as in the η-6 carbide structure. When this nitride is prepared, a mixture of Co_2Mo_3N and Co_3Mo_3N is formed, with the ratio of the two nitrides depending on the synthesis conditions. The activity of this material can be improved by the addition of potassium or chromium [129] [130]. These promoters alter the ratio of the Co_2Mo_3N/Co_3Mo_3N and increase the surface area [129] [131]. When potassium is added, the formation of the Co_2Mo_3N phase is favoured and the activity of this material can be increased by 2.4 times [129]. The activity of this material is also enhanced when the nitride is co-promoted with potassium and 1 wt. % Cr [130]. Adamski et al. state that the higher percentage of Co_2Mo_3N leads to a higher ammonia synthesis activity [132]. Therefore, it would be of interest to investigate the reason for the difference in activity between the two ternary nitrides. The difference in structure between the two nitrides may influence the activity and thus, this should be examined. The lattice nitrogen reactivity is one method that can be used to measure the activity of the materials.

The work in this chapter will aim to prepare the pure phase Co_2Mo_3N by using different preparation methods and different synthesis temperatures. The material was not doped in this chapter due to the complicating issues related to phase instability which are known to

occur for some related systems, such as Cs^+ on Co_3Mo_3N [39]. Furthermore, the initial aim was to understand the pure phase behaviour.

4.1.1 Lattice Nitrogen Reactivity

As discussed in more detail in Chapter 3, previous work has shown the lattice nitrogen of Co_3Mo_3N to be highly reactive, reversibly forming the Co_6Mo_6N phase [35] [50] [120] [77]. These results suggest that Co_3Mo_3N may operate via a Mars-van Krevelen mechanism for ammonia synthesis. This observation was further supported by work performed with the analogous Co_3Mo_3C phase [54].

In order to investigate the role structure has on the lattice nitrogen reactivity, a comparison of the filled β-Mn structured Co_2Mo_3N phase and the η-carbide structured Co_3Mo_3N phase would be of interest. Both the filled β-Mn structured Ni_2Mo_3N and η-carbide structured Ni_2GaMo_3N were stable and had minimal lattice nitrogen reactivity even at elevated temperature as discussed in Chapter 3. The study of the cobalt molybdenum nitrides would make a good comparison in order to see if this relationship is the same across the nitrides and to gain further insight into the structure-activity relationship in view of their similarity in composition but difference in structure. A mixture containing both Co_2Mo_3N and Co_3Mo_3N phases has been reduced under pure hydrogen at 700°C [133]. It was shown that Co_3Mo_3N was reduced to Co_6Mo_6N, as would be expected. However, Co_2Mo_3N was not reduced under these conditions and in-situ powder XRD showed that this phase was stable. Therefore, the lattice nitrogen in Co_2Mo_3N would appear to be less reactive than in Co_3Mo_3N. The work in this chapter will be performed in order to verify this previous observation and also to expand on the temperature conditions investigated to see whether a phase transition analogous to that for Co_3Mo_3N occurs at a higher temperature than 700 °C for Co_2Mo_3N. The cobalt molybdenum nitrides will be reduced under 3:1 H_2/Ar up to 900°C so that a comparison can be made with the nickel molybdenum nitrides reported in Chapter 3.

4.1.2 Synthesis of Co_2Mo_3N

Co_2Mo_3N was first synthesised by Prior and Battle [73]. This material was prepared by mixing MoO_3 and Co_3O_4 together and reacting under a flow of 10% H_2/N_2. A temperature programmed heating regime was used up to 1000°C and the material was ground together between each firing step. The XRD pattern of the resultant material showed that small amounts of molybdenum metal and Co_3Mo_3N were also present. The authors found that prolonged heating favoured the formation of Co_3Mo_3N and molybdenum metal.

Adamski et al. additionally observed that Co_2Mo_3N transforms to Co_3Mo_3N upon prolonged exposure to ammonia at 700°C through combination with an excess cobalt metal component [132]. They prepared the mixed phase Co_2Mo_3N/Co_3Mo_3N by first heating the oxide precursor to 700°C under pure nitrogen and then switching to either pure NH_3 [133] or 10% NH_3/N_2 [132]. This mixed phase Co_2Mo_3N/Co_3Mo_3N was also synthesised by heating the oxide under NH_3 to 700°C [129] [130] [131]. It was proposed that the time at which ammonia is introduced affects the composition of the nitride [132]. Through in-situ XRD studies, Adamski et al. showed that Co_3Mo_3N was the final product of the ammonolysis of $CoMoO_4$ precursor. The authors suggested the diffusion of Co atoms was the main factor in the final composition of the material and the restriction of this diffusion can be used to control the ratio of Co_2Mo_3N to Co_3Mo_3N. Moszynski et al. have observed that potassium encourages the formation of Co_2Mo_3N [129] and the addition of chromium prevents its development [131]. When potassium was added, the concentration of Co_2Mo_3N was observed to be 50 wt. %.

From comparing the XRD patterns of the mixed phase Co_2Mo_3N prepared by either N_2/H_2 or NH_3, it appears that the preparation of the nitride by N_2/H_2 resulted in the highest proportion of Co_2Mo_3N. Therefore, for this reason, a 3:1 H_2/N_2 mixture was used within this work.

4.2 Results and Discussion

4.2.1 Cobalt Molybdenum Nitride (Co_2Mo_3N)

4.2.1.1 Cobalt Molybdenum Oxide ($Co_2Mo_3O_x$)

Three preparation methods were applied to synthesise the cobalt molybdenum oxide. The modified Pechini method was the first method attempted as it had been used to successfully prepare the filled β-Mn structured Ni_2Mo_3N. The second method was similar to the one used to prepare Co_3Mo_3N [55] [53] and was based upon stoichiometric amounts of $(NH_4)_6Mo_7O_{24}.4H_2O$ and $Co(NO_3)_2 \cdot 6H_2O$ being added together in deionised water. The final method was similar to the second method but the material was not calcined prior to phase transformation.

The XRD pattern of the material prepared by the modified Pechini method is displayed in Figure 120. It can be seen that the oxide precursor was a mixture of $CoMoO_4$ and MoO_3 phases. This observation is consistent with the mixture of oxides that were synthesised when the sol-gel method was used to prepare Ni_2Mo_3N. Unique reflections of MoO_3 can be observed at 12.76°, 25.68°, 27.31°, 35.47° and 49.25° 2θ. This mixture of oxides was targeted as the

difference in metal ratios of the Co and Mo between the $CoMoO_4$ (1:1) and the nitride (2:3) could lead to impurities of cobalt metal when the nitride is synthesised similar to the observation for Ni_2Mo_3N, where nickel metal impurities are formed [36]. The other two preparation methods also comprised a mixture of phases but the intensities of the MoO_3 reflections were lower.

The elemental analysis showed that the material contained trace amounts of carbon and hydrogen when prepared by the modified Pechini method (C: 0.21 wt. %, H: 0.05 wt. %, N: 0.00 wt. %), which might be reflective of residues of the citric acid employed in the synthesis. However, for the method where the oxide was uncalcined, the material contained a larger percentage of nitrogen and hydrogen (C: 0.00 wt. %, H: 0.58 wt. %, N: 1.30 wt. %). The nitrogen and hydrogen likely originate from the starting precursors used in the synthesis.

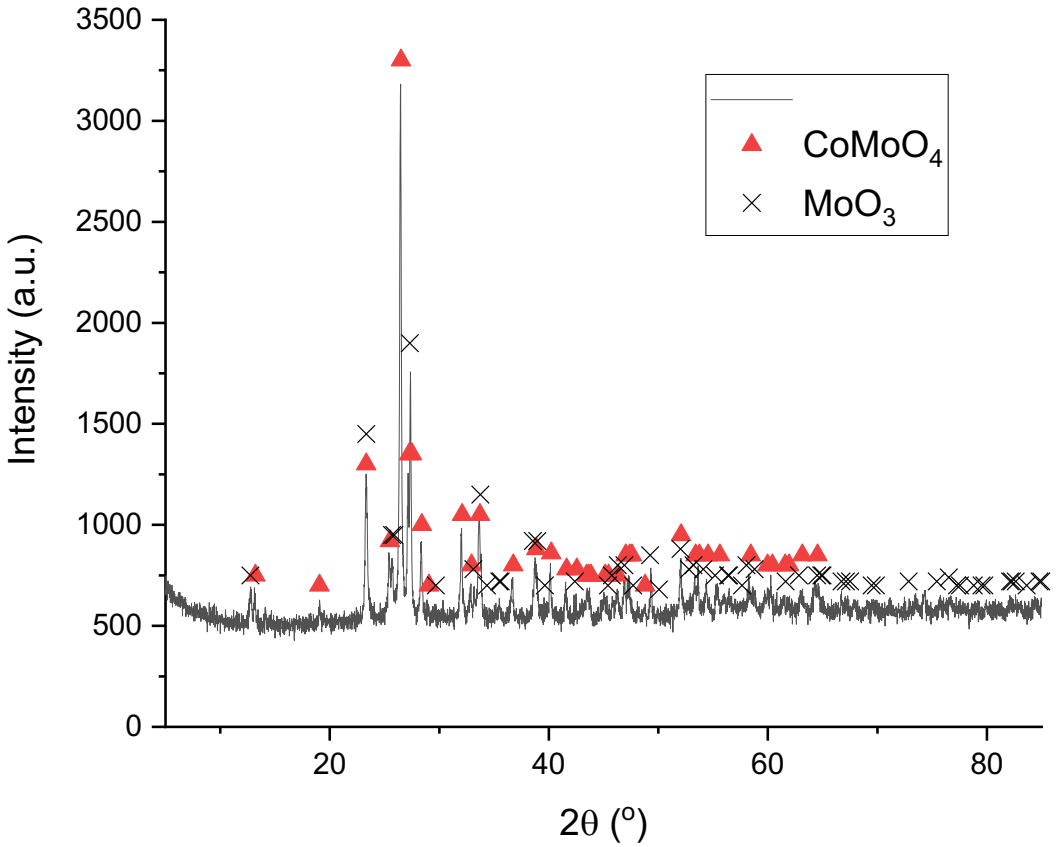

Figure 120: XRD pattern of cobalt molybdenum oxide ($Co_2Mo_3O_x$). Reflections marked: ▲ $CoMoO_4$ (JCPDS file number 00-021-0868) and X MoO_3 (JCPDS file number 01-074-7383).

Raman spectroscopy was used to determine the different oxide phases present in the material and to confirm that the two phases were present. A representative Raman spectrum of the mixed phase oxide is provided in Figure 121. The Raman spectrum of this

material was analysed by comparing it with the spectra of $CoMoO_4$ and MoO_3 in the literature.

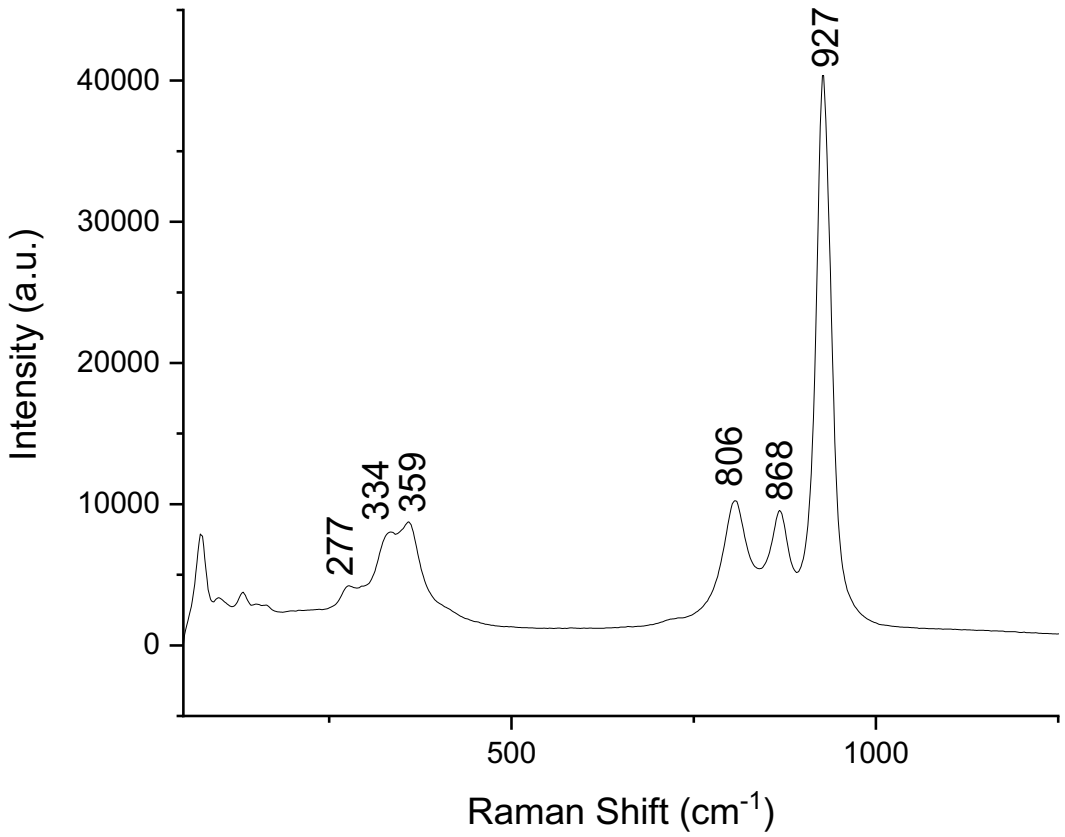

Figure 121: Raman spectrum of cobalt molybdenum oxide ($Co_2Mo_3O_x$).

The Raman bands at positions of 927, 868, 806 and 359 cm^{-1} were attributed to β-$CoMoO_4$ [126]. These Raman shifts are in very good agreement with $CoMoO_4$ spectra reported in the literature [126]. The bands at 927, 868 and 359 cm^{-1} have been assigned in the literature as the Mo-O-Co stretching vibrations in cobalt molybdate [126], with the strong band at 927 cm^{-1} being due to the A1 mode of Mo=O in MoO_4 [134]. The band at 806 cm^{-1} has also been reported as a band that occurs in the Raman spectrum for MoO_3 and is due to the Mo-O-Mo asymmetric stretching mode [67]. The Raman bands at 334 and 277 cm^{-1} have also been assigned to MoO_3 and are due to the Mo-O bending and Mo-O-Mo deformation mode [90]. However, the other expected bands for MoO_3 at approximately 995 and 665 cm^{-1} were not observed. This is unusual as the band at 995 cm^{-1} has a moderate intensity in the Raman spectrum for MoO_3. However, this can be dependent upon the edge plane and therefore, may be reflective of morphology. The SEM images for the cobalt molybdenum oxide ($Co_2Mo_3O_x$) are provided in Appendix IV. Morphologies related to MoO_3 cannot be identified and it is speculated that the MoO_3 morphology would be very anisotropic.

The presence of bands for both $CoMoO_4$ and MoO_3 agrees with the XRD results, which showed that both these oxides were present in the material. Alshibane [55] observed similar bands for the $CoMoO_4$ precursor.

EDX analysis was performed in order to determine if the ratio of cobalt to molybdenum was as desired for the formation of the Co_2Mo_3N phase from the oxide. This analysis may indicate the method that was best for preparing the oxide with the required $Co_2Mo_3O_x$ stoichiometry.

The EDX data in Table 29 details the weight percentages for each element for the material prepared by the modified Pechini method. The XRD pattern showed that the material consisted of both $CoMoO_4$ and MoO_3. Therefore, the stoichiometric percentage of cobalt, molybdenum and oxygen expected for this mixture of phases would be 20.26 wt. % Co, 49.48 wt. % Mo and 30.26 wt. % O, respectively. From the table, it can be seen that the values obtained from EDX agree quite well with the expected stoichiometric values. However, as stated before, the measure of low atomic number elements, such as oxygen, by EDX analysis is not reliable. This material had the correct ratio of cobalt to molybdenum to give the $Co_2Mo_3O_x$ stoichiometry.

Area	Co weight (%)	Mo weight (%)	O weight (%)
1	50	30	20
2	25	48	28
3	19	46	35
4	17	43	40
5	23	46	31
6	17	45	38
7	15	43	41
8	16	42	42
9	17	48	35
10	17	46	37
11	28	50	22
12	21	48	32
Average	22	44	33

Table 29: EDX values for cobalt molybdenum oxide ($Co_2Mo_3O_x$) prepared by modified Pechini method.

The EDX analysis in Table 30 provides the weight percentages for the material prepared by the second method. The stoichiometric percentage of cobalt, molybdenum and oxygen in the theoretical $Co_2Mo_3O_{11}$ is 20.26 wt. %, 49.48 wt. % and 30.26 wt. %, respectively. From the table, it can be seen that the oxygen weight percentage was higher than predicted. However, the oxygen analysis is not reliable in EDX. The weight ratio of cobalt to molybdenum in this material was not as expected as there was a much lower cobalt weight

percentage. This is in contrast to the XRD pattern and Raman spectroscopic result for this material, which showed that $CoMoO_4$ was the majority phase, which would suggest that the Co percentage would be higher. This result suggests that the modified Pechini method was superior at preparing the desired mixed phased oxide as the ratio of cobalt to molybdenum for that material was as required. This was also confirmed by the XRD pattern as the modified Pechini method had a better mixture of the $CoMoO_4$ and MoO_3 phases.

Area	Co weight (%)	Mo weight (%)	O weight (%)
1	5	41	54
2	6	41	53
3	6	42	52
4	4	41	56
5	8	42	50
6	14	33	53
7	7	47	47
8	19	40	41
Average	9	41	51

Table 30: EDX values for cobalt molybdenum oxide ($Co_2Mo_3O_x$) prepared from method 2.

4.2.1.2 Cobalt Molybdenum Nitride (Co_2Mo_3N)

The filled β-Mn structured Co_2Mo_3N was prepared via temperature programmed nitridation of the mixed oxides. A 1:3 N_2/H_2 gas mixture was used and the synthesis was performed at different temperatures in order to try to prepare the pure-phase nitride. The preparation of this material followed the method used to prepare relatively phase pure Ni_2Mo_3N as shown in Chapter 3. The mixed phase Co_2Mo_3N has previously been prepared by the reaction of MoO_3 and Co_3O_4 under 10% H_2/N_2 with a heating regime up to 1000°C [73]. As stated for Ni_2Mo_3N, an advantage of using N_2/H_2 gas mixture in the preparation is that it overcomes problems with using ammonia at a large scale [95].

Prior and Battle stated that prolonged heating favoured the formation of Co_3Mo_3N and molybdenum metal [73]. Therefore, it would be of interest to attempt to prepare the pure-phase Co_2Mo_3N by using different synthesis conditions, such as varying the length of time of the nitridation process.

Modified Pechini Method

The XRD patterns of the nitrides that were prepared by the modified Pechini method at either 600°C or 700°C reaction temperature are shown in Figure 122. The formation of Co_3Mo_3N is favoured at higher reaction temperatures under H_2/N_2 atmosphere and hence, a lower temperature was applied in order to try to prepare Co_2Mo_3N. Prior and Battle

observed that Co_3Mo_3N formation was favoured at higher temperature [73]. Furthermore, at 800°C and 900°C under 3:1 H_2/N_2 Co_3Mo_3N is favoured (Lucy Costley-Wood, 2019, personal communication). However, from the XRD pattern of the material prepared at 600°C, it can be seen that it contained a mixture of oxide phases and no evidence of any nitride phases and therefore, it appears that the reaction temperature was too low for the nitridation process to take place. Unique reflections for MoO_2 can be observed at 26.08°, 53.48°, 54.06° and 66.84° 2θ, for CoO at 42.72° 2θ and for $CoMoO_3$ at 56.29° 2θ. The elemental analysis in Table 31 shows that the material contained 1.37 wt. % of nitrogen. The expected percentage of nitrogen in Co_2Mo_3N based upon stoichiometry is 3.34 wt. % and for Co_3Mo_3N the stoichiometric amount of nitrogen is 2.93 wt. %. Therefore, it is suggested that a degree of nitridation of the material has occurred but the desired ternary phase was not synthesised at 600°C.

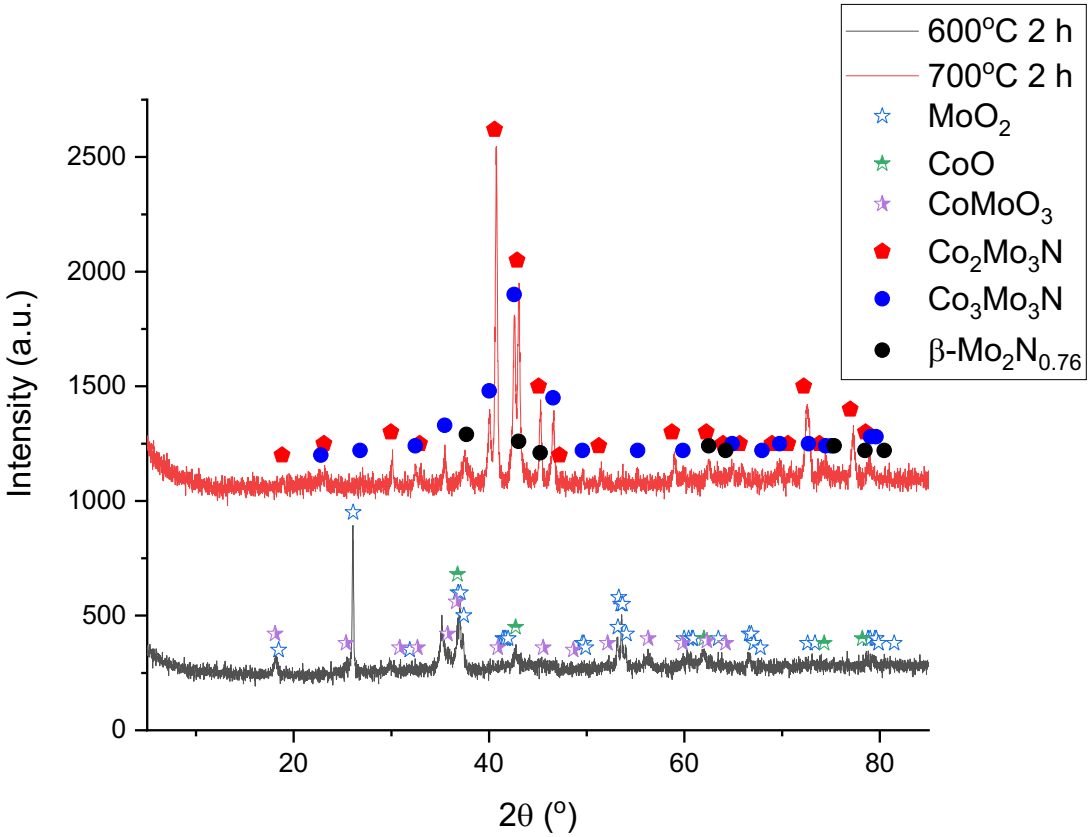

Figure 122: XRD pattern of Co_2Mo_3N prepared at 600°C for 2 hours and 700°C for 2 hours under 3:1 H_2/N_2. Reflections marked: ☆ MoO_2 (JCPDS file number 01-076-1807), ☆ CoO (JCPDS file number 01-070-2855), ☆ $CoMoO_3$ (JCPDS file number 00-021-0869), ⬟ Co_2Mo_3N (JCPDS file number 01-072-6570), ● Co_3Mo_3N (JCPDS file number 01-089-7953) and ● β-$Mo_2N_{0.76}$ (JCPDS file number 03-065-6236).

At 700°C, a mixture of the filled β-Mn structured Co_2Mo_3N and η-carbide structured Co_3Mo_3N were observed in the XRD pattern. However, the intensities of the Co_2Mo_3N reflections were greater than the Co_3Mo_3N reflections, suggesting that Co_2Mo_3N was the majority phase. A molybdenum nitride impurity was also observed in the XRD pattern. As both phases are prepared, an excess of molybdenum would be expected from the stoichiometry as a 2:3 ratio of Co to Mo was used to prepare the oxide. A unique reflection matching β-$Mo_2N_{0.76}$ can be seen at 37.68° 2θ. The elemental analysis of this material revealed that it contained 3.71 wt. % of nitrogen. This value was slightly higher than the expected stoichiometric value for Co_2Mo_3N. However, NH_x species formed on the surface of the material during the nitridation process may contribute to this value.

These results indicate that the preparation temperature needs to be higher than 600°C in order to form the nitride and that a mixture of phases is formed from the oxide prepared by the modified Pechini method.

Material	Carbon Content from Elemental Analysis (wt. %)	Hydrogen Content from Elemental Analysis (wt. %)	Nitrogen Content from Elemental Analysis (wt. %)
600°C 2 h	0.11	0.19	1.37
700°C 2 h	0.14	0.09	3.71

Table 31: Elemental Analysis for the cobalt molybdenum materials prepared at different temperatures with 3:1 H_2/N_2.

Method where the Oxide was Uncalcined

The XRD patterns of the nitrides that were prepared from the uncalcined oxide at either 650°C or 700°C reaction temperatures are presented in Figure 123. As the nitridation process did not appear to occur at 600°C, as shown before, the lowest temperature employed was above 600°C. For the material prepared at 650°C, it can be seen from the XRD pattern that it contained a mixture of oxide phases, which were the same phases as the material prepared at 600°C. Therefore, it appears that the temperature needs to be at 700°C in order for the nitridation process to take place. The elemental analysis shows that the material prepared at 650°C contained 2.01 wt. % nitrogen, suggesting that some nitridation resulting in XRD amorphous phases may possibly have occurred. Unique XRD reflections for MoO_2 can be observed at 26.08°, 53.48°, 54.06° and 66.84° 2θ, for CoO at 42.72° 2θ and for $CoMoO_3$ at 35.74° 2θ, which are indicative of reduction having commenced.

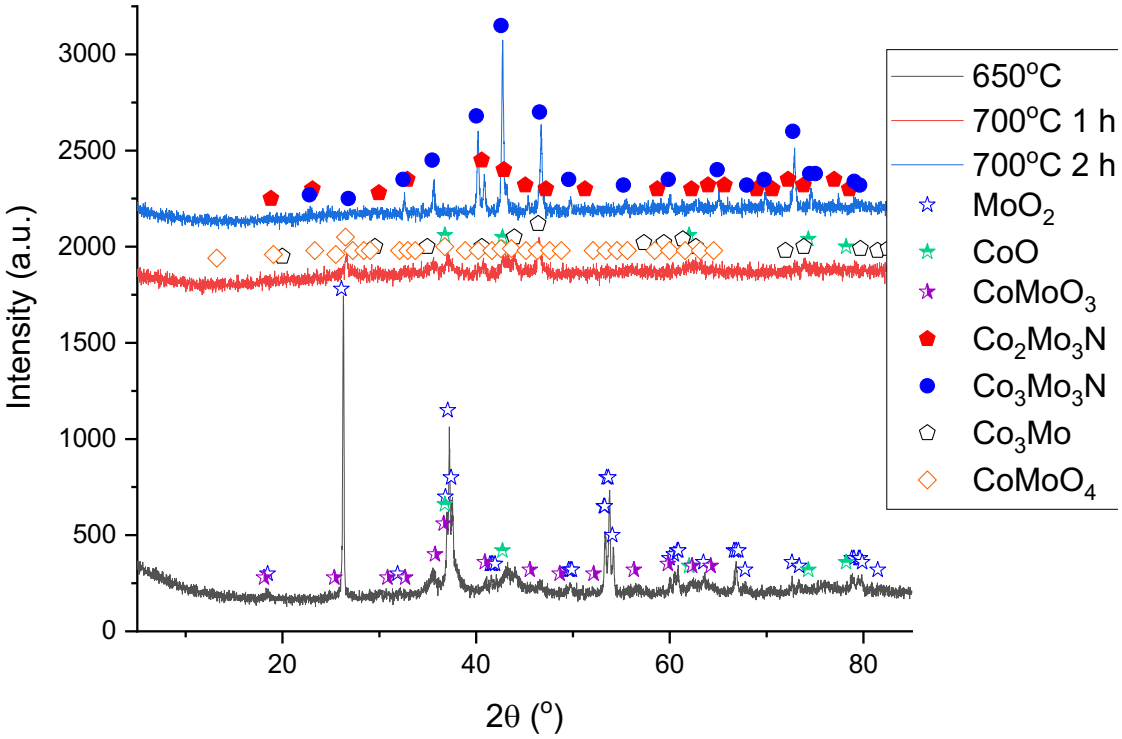

Figure 123: XRD pattern of Co_2Mo_3N prepared at 650°C for 3 hours, 700°C for 1 hour and 700°C for 2 hours under 3:1 H_2/N_2. Reflections marked: ☆ MoO_2 (JCPDS file number 01-076-1807), ☆ CoO (JCPDS file number 01-070-2855), ☆ $CoMoO_3$ (JCPDS file number 00-021-0869), ⬟ Co_2Mo_3N (JCPDS file number 01-072-6570), ● Co_3Mo_3N (JCPDS file number 01-089-7953), ⬠ Co_3Mo (JCPDS file number 03-065-3519) and ◊ $CoMoO_4$ (JCPDS file number 00-021-0868).

In an attempt to prepare the desired pure-phase nitride, nitridation at 700°C for either 1 hour or 2 hours was undertaken. As stated previously, it has been suggested that prolonged heating favours the formation of Co_3Mo_3N. However, when the material was prepared for 1 hour, it contained a mixture of oxides and Co_3Mo as seen from the XRD pattern. Unique XRD reflections for Co_3Mo can be observed at 46.41° 2θ, for $CoMoO_4$ at 26.51° 2θ and for CoO at 36.77° 2θ. Therefore, it appears that the nitride needs to be prepared at 700°C employing a longer time duration. The elemental analysis in Table 32, showed that, as expected from the XRD pattern, the percentage of nitrogen (2.30 wt. %) was lower than the expected stoichiometric value for Co_2Mo_3N. The XRD pattern of this material comprised a higher degree of amorphous component as evident from the intensity of its background. However, Co fluoresces when a Cu X-ray source is used, which results in adding to the background of the pattern. Therefore, the increased background may be due to increased Co fluorescence and not amorphous material.

When the material was synthesised at 700°C for 2 hours, a mixture of the ternary nitride phases were observed in the XRD pattern. Co_3Mo_3N was the majority phase as the

intensity of the reflections were greater than those for Co_2Mo_3N. This is in contrast to the material that was prepared from the modified Pechini method and therefore, that method would appear to be better in terms of preparation of the desired Co_2Mo_3N target. The material contained 4.00 wt. % nitrogen, which is higher than the expected stoichiometric value for either Co_2Mo_3N or Co_3Mo_3N. However, possible NH_x species on the surface of the material that result from the nitridation process would contribute to this percentage.

Material	Carbon Content from Elemental Analysis (wt. %)	Hydrogen Content from Elemental Analysis (wt. %)	Nitrogen Content from Elemental Analysis (wt. %)
650°C 3 h	0.00	0.10	2.01
700°C 1 h	0.00	0.00	2.30
700°C 2 h	0.00	0.00	4.00

Table 32: Elemental Analysis for the cobalt molybdenum materials prepared at different temperatures with 3:1 H_2/N_2.

Second Method

For the material prepared by the second method, where stoichiometric amounts of $(NH_4)_6Mo_7O_{24}.4H_2O$ and $Co(NO_3)_2 \cdot 6H_2O$ were added together in deionised water, Co_3Mo_3N appeared to be the majority phase and the intensity of the Co_2Mo_3N reflections were very small (the XRD pattern for this method is not provided).

Out of the three methods used, the oxide prepared by the modified Pechini route was the best method in order to prepare the desired Co_2Mo_3N phase in the highest ratio with respect to Co_2Mo_3N to Co_3Mo_3N. Therefore, the material that was synthesised by this route was investigated for its ammonia synthesis activity and lattice nitrogen reactivity.

Optimal Conditions for Preparing the Best Ratio of Co_2Mo_3N from the Oxide Prepared by the Modified Pechini Method

The filled β-Mn structured Co_2Mo_3N was prepared via temperature programmed nitridation of the mixed oxide at 700°C for three hours. These were found to be the optimal conditions to give the highest amount of Co_2Mo_3N. The XRD pattern of the material is displayed in Figure 124. The material also contained β-$Mo_2N_{0.76}$ and Co_3Mo_3N. The elemental analysis showed that the material contained 3.82 wt. % of nitrogen (C: 0.00 wt. %, H: 0.00 wt. %, N: 3.82 wt. %). This value agrees quite well with the expected stoichiometric amount of nitrogen for Co_2Mo_3N despite the fact that it comprises mixed phases.

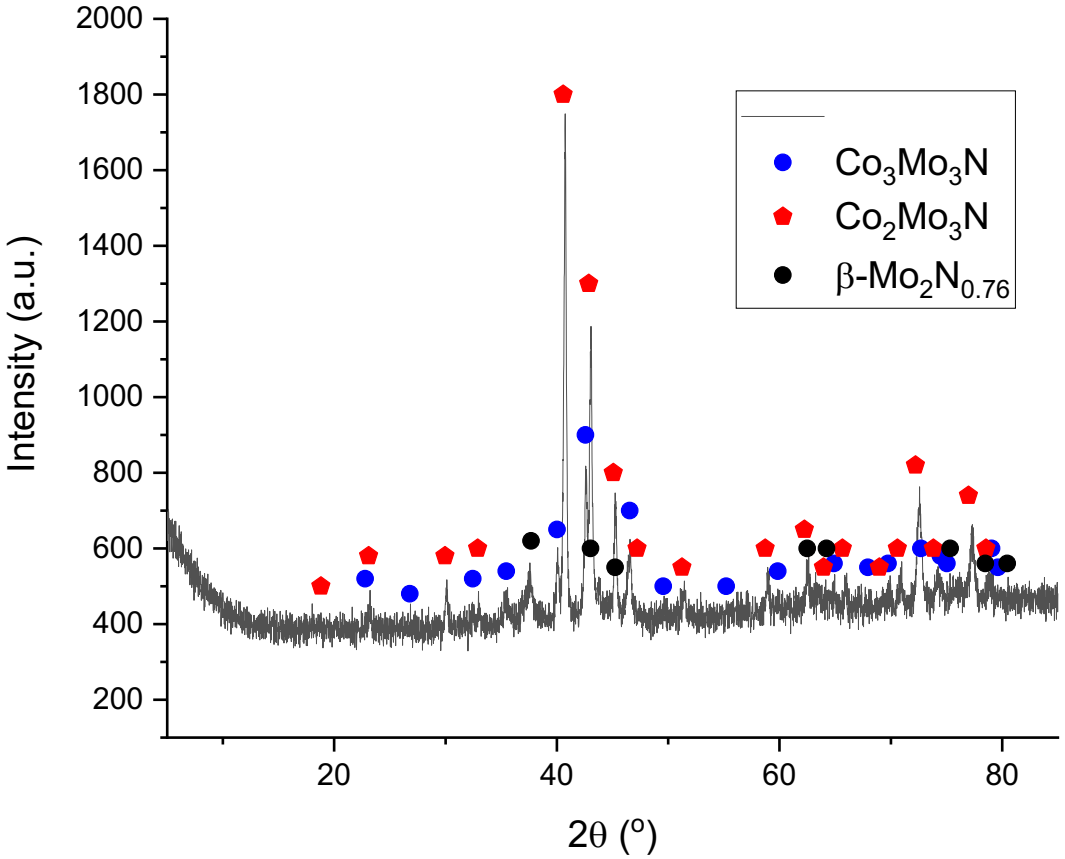

Figure 124: XRD pattern of cobalt molybdenum nitride (Co_2Mo_3N). Reflections marked: ⬟ Co_2Mo_3N (JCPDS file number 01-072-6570), ● Co_3Mo_3N (JCPDS file number 01-089-7953) and ● β-$Mo_2N_{0.76}$ (JCPDS file number 03-065-6236).

The Raman spectrum for the material is shown in Figure 125. The spectrum was similar to the one for the oxide, suggesting that the surface of the material possessed a passivation layer as expected based upon the air-sensitivity of nitrides. The Raman bands at 934, 877, 814 and 362 cm^{-1} were assigned to β-$CoMoO_4$ [126]. The bands at 934, 877 and 362 cm^{-1} are stated to be due to the Mo-O-Co stretching vibrations in cobalt molybdate [126]. The bands at 806 and 341 cm^{-1} have also been reported as bands that occur in the Raman spectrum for MoO_3 and are due to the Mo-O-Mo asymmetric stretching mode [67] and the Mo-O bending [90], respectively. The bands due to β-$CoMoO_4$ could be due to the surface oxide layer on Co_2Mo_3N and Co_3Mo_3N and the bands relating to MoO_3 could be due to a passivation layer on the molybdenum nitride impurity phase. Alshibane [55] and Alconchel et al. [105] observed similar bands for the Raman spectrum of Co_3Mo_3N.

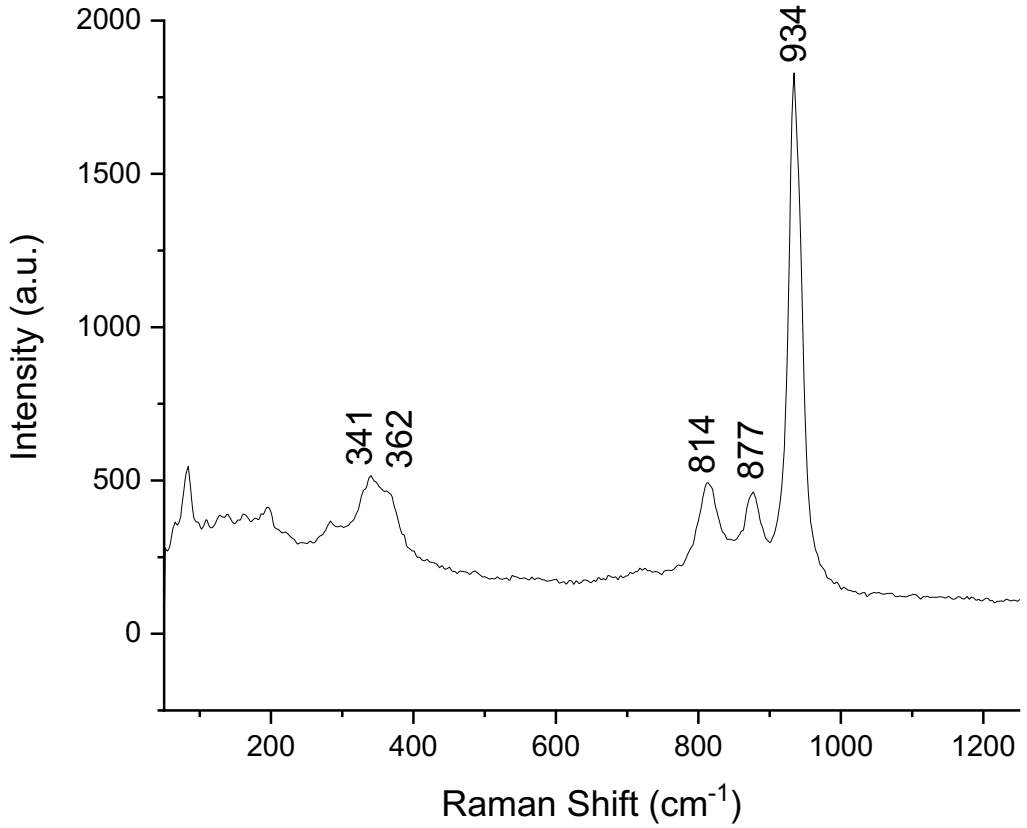

Figure 125: Raman spectrum of cobalt molybdenum nitride ('Co_2Mo_3N').

The representative SEM images of the material given in Figure 126 show that the morphology was retained with respect to the oxide precursor (SEM for oxide is provided in Appendix IV). The material had a porous and uneven surface, with the pores ranging in size from 1 to 10 μm.

The EDX analysis in Table 33 gives the weight percentages for the material. The stoichiometric percentage of cobalt, molybdenum and nitrogen in Co_2Mo_3N is 28.08 wt. %, 68.58 wt. % and 3.34 wt. %, respectively. It can be seen that the values obtained from EDX agree well with the expected stoichiometric values, even though the XRD pattern showed that the material consisted of both Co_3Mo_3N and β-$Mo_2N_{0.76}$ impurities. Therefore, the material had the desired weight ratio for Co_2Mo_3N. The values of the cobalt and molybdenum had increased compared to the oxide precursor, which is to be expected when considering that oxygen has been replaced with nitrogen. The weight ratio of cobalt and molybdenum in the oxide and nitride were as would be expected for these materials.

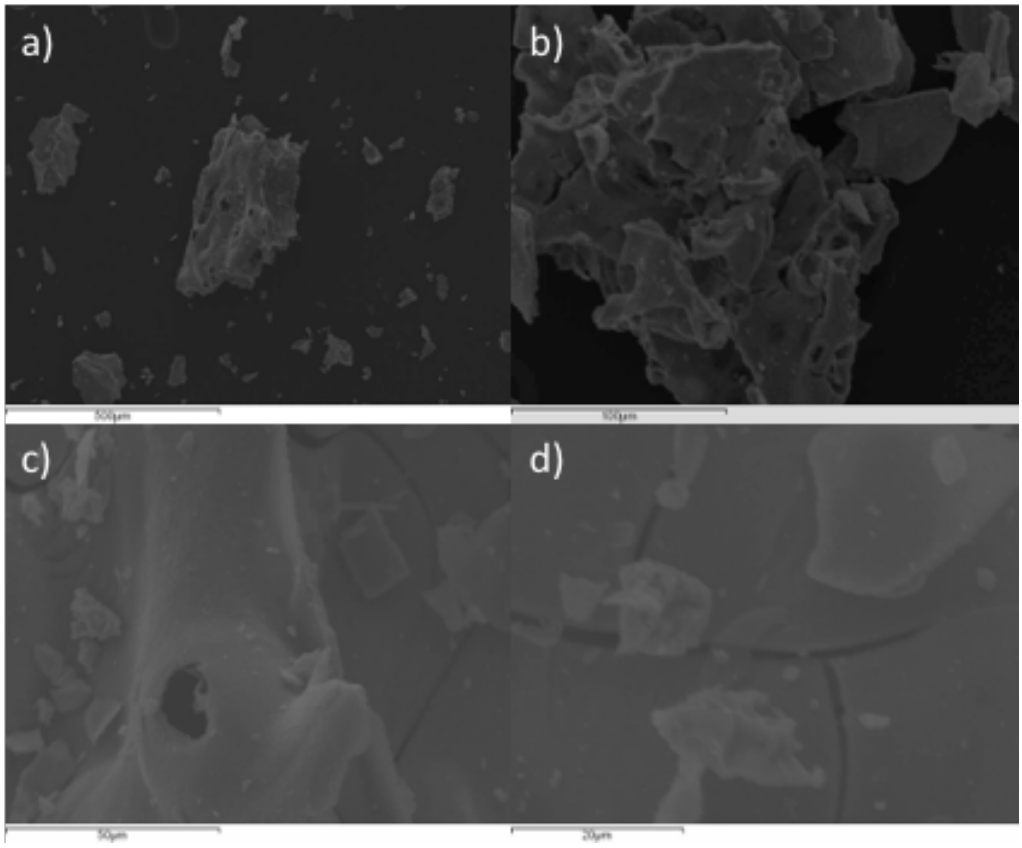

Figure 126: SEM images of cobalt molybdenum nitride ('Co_2Mo_3N'). a) 100x magnification, b) 500x magnification, c) 1000x magnification and d) 2000x magnification.

The elemental maps in Figure 127 indicate that the cobalt, molybdenum and nitrogen were fairly evenly disbursed across the material as would be expected.

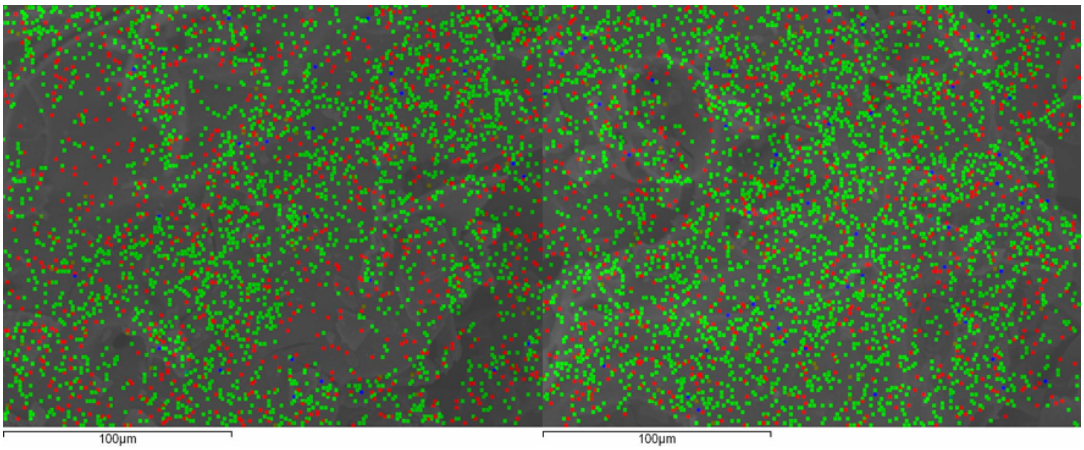

Figure 127: Element Maps for 'Co_2Mo_3N'. Elements: Co (red), Mo (green) and N (blue).

The number of EDX measurements for the samples are different and therefore, the samples with fewer measurements may not be as accurate due to the smaller sample size. There is also a significant variation in the nitrogen percentage between the areas examined. It has to be borne in mind that, in addition to being semi-quantitative, EDX analysis is not reliable in relation to nitrogen analysis.

Area	Co weight (%)	Mo weight (%)	N weight (%)
1	31	62	7
2	34	66	0
3	25	67	7
4	28	65	6
5	27	63	10
6	37	63	0
7	25	64	11
8	24	63	13
9	27	73	0
10	27	66	7
11	26	74	0
12	24	66	10
13	32	68	0
14	23	65	13
15	35	65	0
Average	28	66	6

Table 33: EDX values for cobalt molybdenum nitride ('Co_2Mo_3N').

4.2.2 Ammonia Synthesis at 400°C for Co_2Mo_3N

Mixed phase Co_2Mo_3N and Co_3Mo_3N has previously been tested for ammonia synthesis and was found to have a rate as reported by the authors as approximately 5.8 $g_{NH3}MPa^{0.5}$ g_{cat}^{-1} h^{-1} at 500°C and 10 MPa [130]. The quoted units for this rate are unusual and the origin is unclear from the reported literature. This rate was influenced by the addition of chromium and potassium, which altered the ratio of the ternary nitrides and the surface area [130] [131] [129].

The mixed phase Co_2Mo_3N prepared by the modified Pechini method in the current study was tested for ammonia synthesis at 400°C under 3:1 H_2/N_2 at atmospheric pressure for 8 hours. The material was first pre-treated at 700°C for 2 hours under the same gas mixture. The conductivity profile of the material is presented in Figure 128. The ammonia synthesis rate of 'Co_2Mo_3N' at 400°C was 208 μmol h^{-1} g^{-1} and at 700°C was 159 ± 8 μmol h^{-1} g^{-1}. The rate at 700°C was obtained during the pre-treatment, therefore, any phase changes during this period may consequently influence the rate. However, the rate was steady state during the pre-treatment. The lower rate of the material at 700°C may be expected as ammonia decomposes at this temperature. Co_3Mo_3N was previously reported to exhibit a rate of 166 ± 2 μmol h^{-1} g^{-1} under comparable reaction conditions at 400°C [35]. However, a direct comparison cannot be made as the relative surface areas between the materials is not known. An added consideration is that the materials have different morphologies. Unfortunately, there is not a surface area measurement value for the mixed phase nitride in this work as there were pro-longed technical issues with the equipment required to make

this measurement. Moszynski et al. [129] have previously stated that there is a direct relationship between the Co_2Mo_3N content and the ammonia synthesis activity. However, surface area was also a factor in this reported relationship.

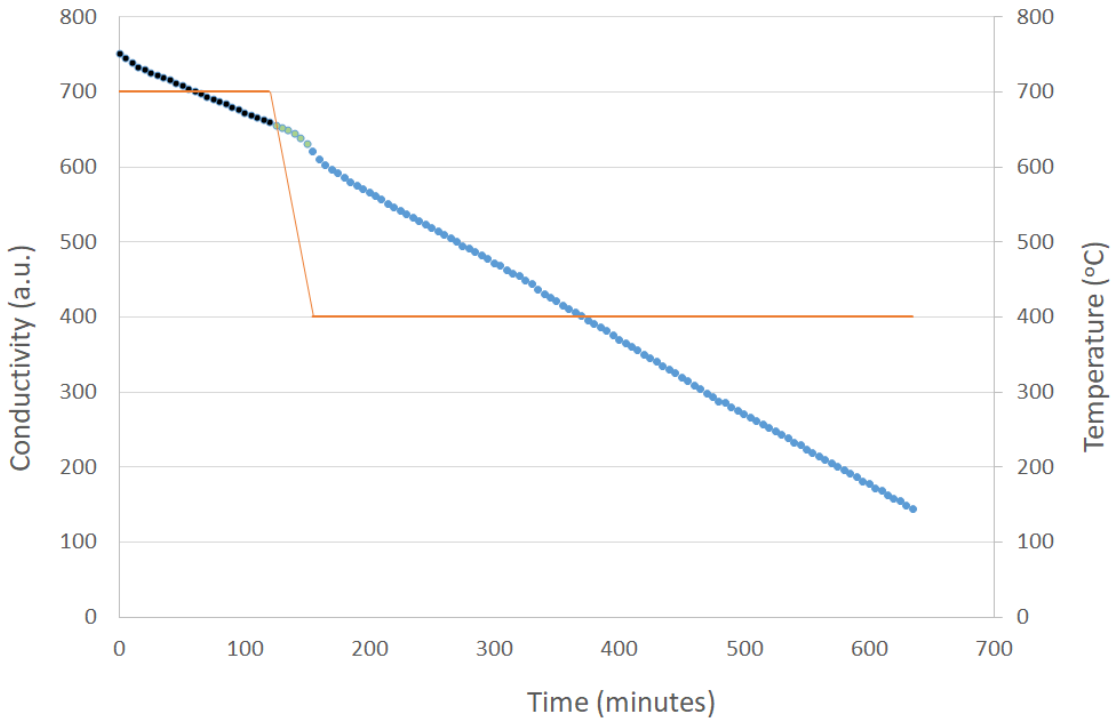

Figure 128: Conductivity profile for 'Co_2Mo_3N' reacted with 3:1 H_2/N_2 at 700°C for 2 hours and 400°C for 8 hours.

In the post-reaction XRD pattern (Figure 129) the ratio of Co_2Mo_3N to Co_3Mo_3N appeared to be the same as for the pre-reaction sample. This suggests that the material did not change phase during the reaction. The elemental analysis in Table 34 shows that the material had more nitrogen post-reaction and therefore, the pre-treatment may have further nitrided the material. The carbon present in the pre- and post-reaction material is most probably due to residues of citric acid used in the synthesis.

Material	Calculated Stoichiometric Nitrogen Content (wt. %)	Calculated Stoichiometric Carbon Content (wt. %)	Nitrogen Content from Elemental Analysis (wt. %)	Carbon Content from Elemental Analysis (wt. %)
'Co_2Mo_3N' Pre-reaction	3.34	-	2.67	0.20
'Co_2Mo_3N' Post-reaction	3.34	-	3.25	0.18

Table 34: Elemental Analysis for 'Co_2Mo_3N' comparing pre- and post-reaction with 3:1 H_2/N_2 at 700°C for 2 hours and 400°C for 8 hours as shown in the reaction profile in Figure 128.

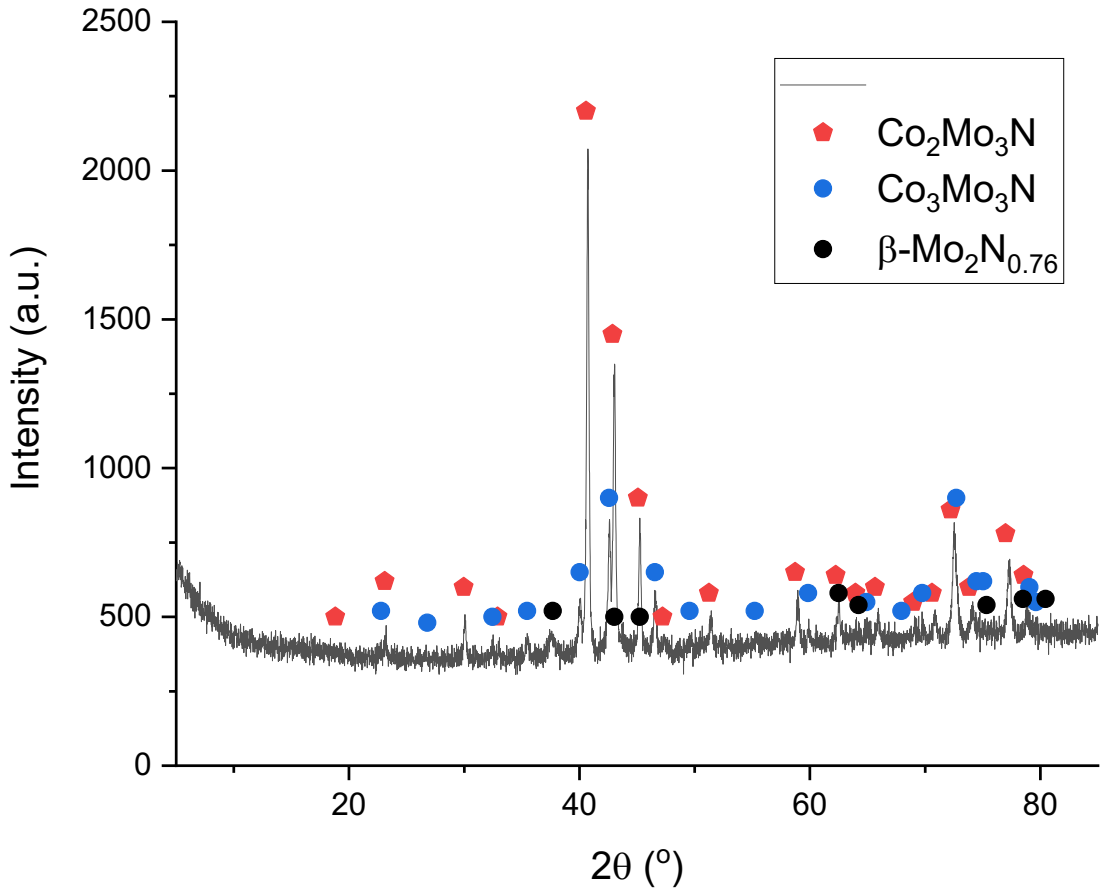

Figure 129: XRD pattern for 'Co_2Mo_3N' post-reaction with 3:1 H_2/N_2 at 400°C for 8 hours. Reflections marked: ⬟ Co_2Mo_3N (JCPDS file number 01-072-6570), ● Co_3Mo_3N (JCPDS file number 01-089-7953) and ● β-$Mo_2N_{0.76}$ (JCPDS file number 03-065-6236).

SEM analysis was conducted in order to investigate if there was any change in morphology and structure of 'Co_2Mo_3N' during the reaction. Figure 130 gives representative SEM images of the post-reaction material at different magnifications. The sample was porous and had an uneven surface. The pores ranged in diameter from approximately 1 µm to 10 µm. From the SEM images, it appears that the morphology had been retained compared to pre-reaction.

The cobalt, molybdenum and nitrogen were fairly evenly distributed across the material as evidenced by the element map in Figure 131. However, some areas appeared to have more cobalt, which suggests that there may have been some phase segregation of cobalt, although this was not evidenced in the XRD pattern. There did not appear to be any areas that had a larger percentage of cobalt in the EDX analysis (data not provided).

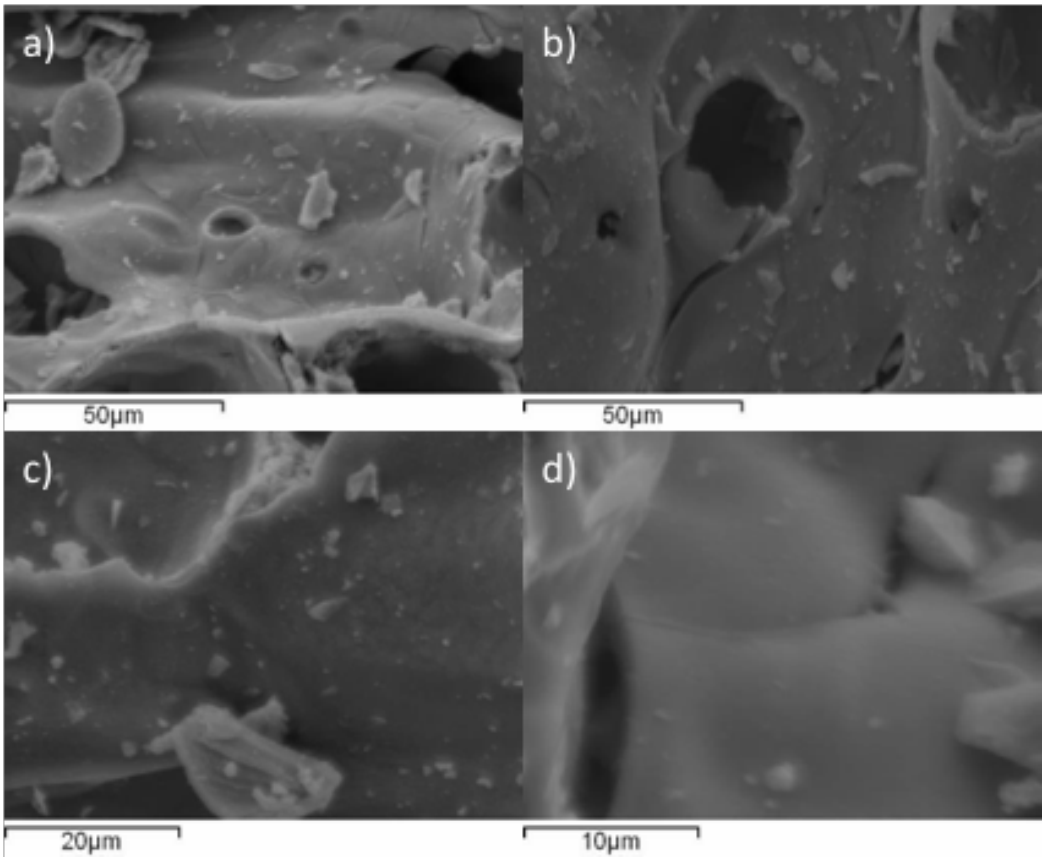

Figure 130: SEM images of 'Co_2Mo_3N' post reaction with 3:1 H_2/N_2 at 400°C for 8 hours. a) 1000x magnification, b) 1000x magnification, c) 2000x magnification and d) 4000x magnification.

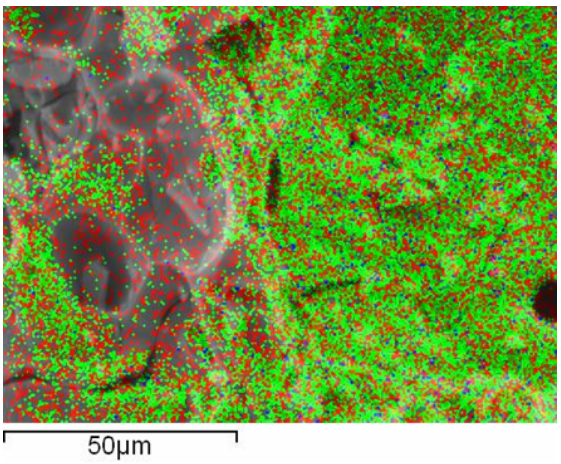

Figure 131: Element Map for 'Co_2Mo_3N' post-reaction with 3:1 H_2/N_2 at 400°C. Elements: Co (red), Mo (green) and N (blue).

4.2.3 Lattice Nitrogen Reactivity of Co_2Mo_3N

4.2.3.1 Lattice Nitrogen Reactivity of Co_2Mo_3N at 700°C

In order to determine the lattice nitrogen reactivity in Co_2Mo_3N, the material was reduced at 700°C under a flow of 3:1 H_2/Ar at ambient pressure for 7 hours. As observed from the conductivity profile data in Figure 132, for the first 60 minutes the conductivity decreased in a non-steady state manner. After the first 60 minutes, the rate became steady state with

ammonia production occurring at a rate of 13 μmol h^{-1} g^{-1} although at this temperature ammonia is thermodynamically unstable with respect to its decomposition. There was a total decrease in conductivity of 51 μS/cm over the 7 hours at 700°C. Co_3Mo_3N has been shown to have a linear decrease at 700°C when tested at this temperature for 1 hour [135]. However, the ammonia production rate was not reported.

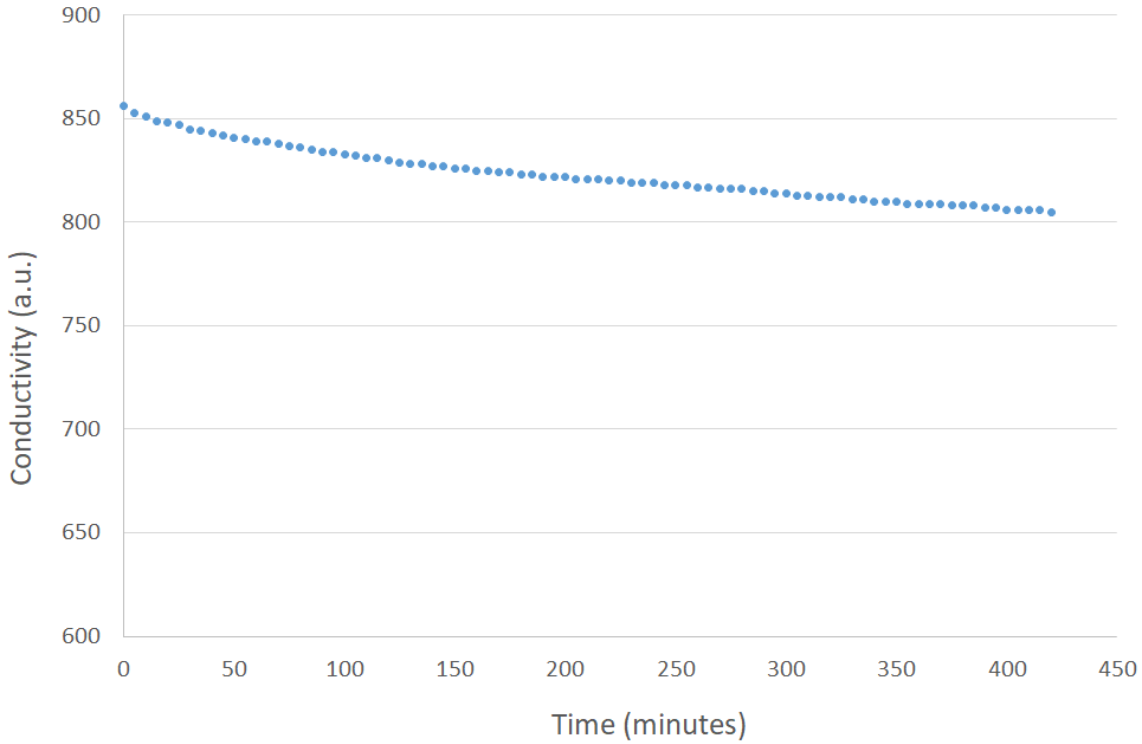

Figure 132: Conductivity profile for 'Co_2Mo_3N' reacted with 3:1 H_2/Ar at 700°C for 7 hours.

The XRD patterns of the pre- and post-reaction materials can be compared in Figure 133. The post-reaction XRD pattern shows a shift of the Co_3Mo_3N reflections to higher 2θ angles, which indicates that there was a decrease in the lattice nitrogen content of this phase as would be expected from its known phase transition to Co_6Mo_6N [55] [135] [35]. However, the analysis is complicated by the degree of overlap between reflections relating to the Co_6Mo_6N and Co_2Mo_3N phases. The reflections of Co_2Mo_3N did not appear to move to higher 2θ values post-reaction as clearly seen by the peak at approximately 45.08° 2θ. This suggests that this phase did not lose lattice nitrogen. This confirms the previous observations of Adamski et al. who have reported that the Co_2Mo_3N phase remains stable under pure hydrogen at 700°C [133], whereas Co_3Mo_3N does not. The molybdenum nitride impurity was reduced to molybdenum metal during the reaction, as would be expected on the basis of prior literature [135]. There are no unique reflections for molybdenum and hence, this phase cannot be completely established. However, the Raman spectrum for this material showed bands associated with MoO_3, suggesting that molybdenum metal, which oxidised upon standing in ambient air, was present in this material (spectrum not shown).

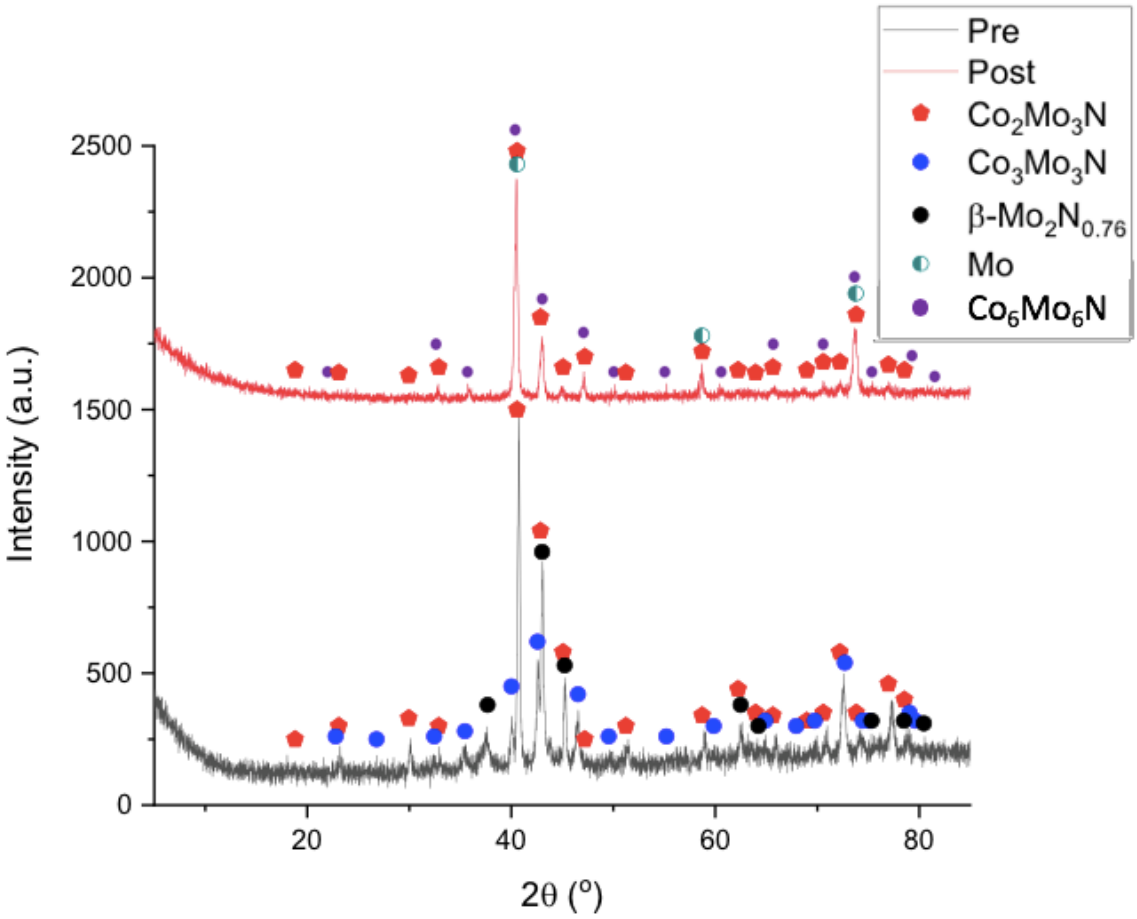

Figure 133: Comparison of XRD patterns for 'Co_2Mo_3N' pre- and post-reaction with 3:1 H_2/Ar at 700°C for 7 hours. Reflections marked: ⬟ Co_2Mo_3N (JCPDS file number 01-072-6570), ● Co_3Mo_3N (JCPDS file number 01-089-7953), ● β-$Mo_2N_{0.76}$ (JCPDS file number 03-065-6236), ◐ Mo (JCPDS file number 01-071-4645) and ● Co_6Mo_6N (data from [55]).

In addition, the elemental analysis showed that there was a loss of more than half the nitrogen content compared to pre-reaction as seen in Table 35. As the material contains Co_6Mo_6N, Co_2Mo_3N and Mo, the expected stoichiometric percentage of nitrogen in this material is 1.92 wt. %, assuming a 1:1:1 ratio. The experimental value was quite close to this expected value. The percentage of the overall nitrogen that was lost from the material that was converted to ammonia was ca. 25% (as determined from the change in conductivity of the H_2SO_4 solution through which the reactor effluent is passed) with the remainder of the nitrogen lost presumably being in the form of dinitrogen.

Material	Calculated Stoichiometric Nitrogen Content (wt. %)	Calculated Stoichiometric Carbon Content (wt. %)	Nitrogen Content from Elemental Analysis (wt. %)	Carbon Content from Elemental Analysis (wt. %)
‘Co_2Mo_3N’ Pre-reaction	3.34	-	4.41	0.12
‘Co_2Mo_3N’ Post-reaction	3.34	-	2.07	0.22

Table 35: Elemental Analysis for ‘Co_2Mo_3N’ comparing pre- and post-reaction with 3:1 H_2/Ar at 700°C for 7 hours.

The stability of the filled β-Mn structured Co_2Mo_3N is similar to the observations for the filled β-Mn structured Ni_2Mo_3N and η-carbide structured Ni_2GaMo_3N tested under the same conditions. This suggests that the lattice nitrogen reactivity of the ternary nitrides is a complex relationship between the metal composition and structure. The two nickel containing nitrides are stable, even though they have different structures, suggesting that the metal composition is more important than structure. However, this is not the case with the cobalt containing nitrides, suggesting that the structure also affects the stability. The local nitrogen environment between the two structures is similar with nitrogen coordinated to six molybdenum species in each case. Therefore, the influence of the other metal component on the Mo_6N species could possibly affect the lattice nitrogen reactivity. To the author’s knowledge, the bond distances in Co_2Mo_3N have not been reported in the literature and therefore, a comparison cannot be made with those for Co_3Mo_3N. In Co_3Mo_3N, the nitrogen relocates from the 16c site to the 8a site when the material transforms to Co_6Mo_6N. It could be suggested that for the filled β-Mn structure, nitrogen relocation within the crystallographic structure is less favourable and the Co_2Mo_3N phase is more stable. For the η-carbide structured Co_3Mo_3N, four Mo, six Co and two N species surround the molybdenum species, whereas in the filled β-Mn structure, the molybdenum species are bonded to six Co, six Mo and two N species [59]. Therefore, the Co atoms have a proportionately greater influence on the molybdenum species in the filled β-Mn structure and this in turn might affect the Mo-N interaction. This would suggest that the structure (i.e. η- carbide versus filled β-Mn) has some impact on the lattice nitrogen reactivity for materials of related composition (i.e. Co-Mo-N). The coordination diagrams of molybdenum in the η-carbide structured Co_3Mo_3N and the filled β-Mn structured Co_2Mo_3N are presented in Figure 134 and Figure 135, respectively.

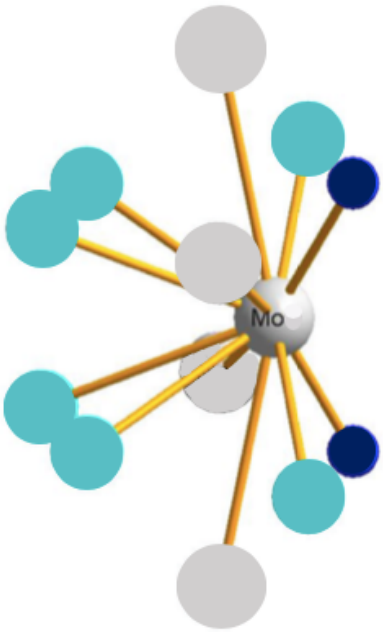

Figure 134: Coordination of molybdenum species in the η-carbide structure: molybdenum (grey), cobalt (green) and nitrogen (blue). Adapted from [135].

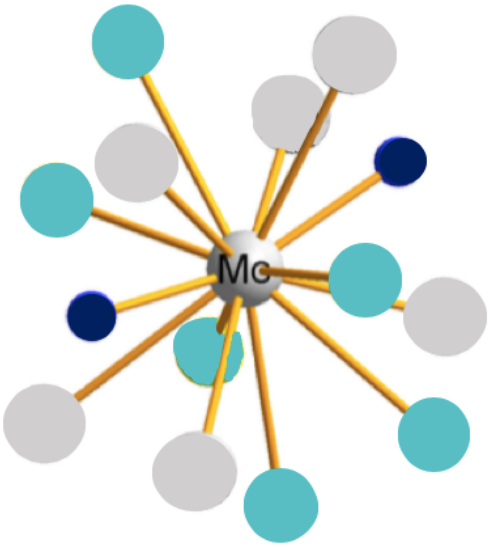

Figure 135: Coordination of molybdenum species in the filled β-Mn structure: molybdenum (grey), cobalt (green) and nitrogen (blue). Adapted from [135].

The SEM images in Figure 136 show that the morphology was similar to the pre-reaction material. The particles had an irregular shape with a smooth surface and pores. The morphology of the post-reaction nitrides (Ni_2Mo_3N, Ni_2GaMo_3N and mixed phase 'Co_2Mo_3N') tested under 3:1 H_2/Ar within this research are different.

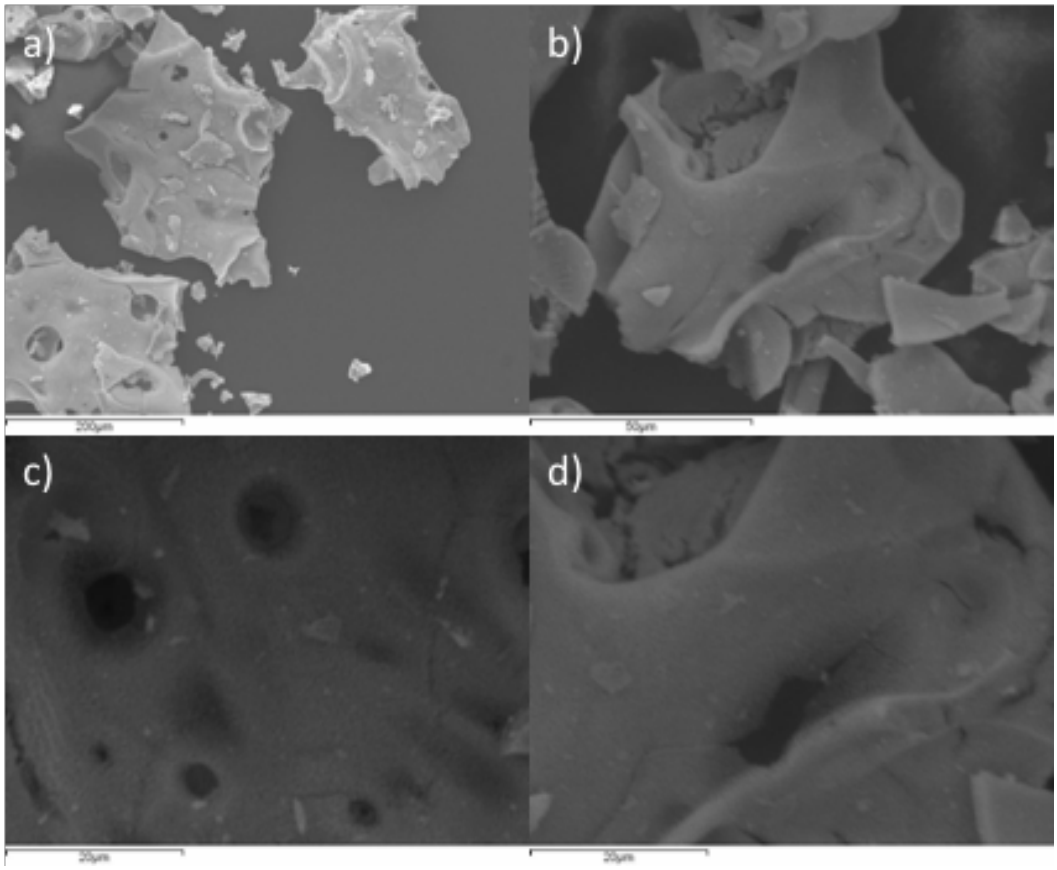

Figure 136: SEM images of 'Co_2Mo_3N' post-reaction with 3:1 H_2/Ar. a) 200x magnification, b) 1000x magnification, c) 2000x magnification and d) 2000x magnification.

The element map in Figure 137 shows that there was a fairly even distribution of cobalt and molybdenum over the sample, although as with the post N_2/H_2 reaction sample, there were areas that contained less molybdenum. This suggests that there may have been phase segregation during the reaction. However, this was not evidenced in the EDX analysis (data not provided).

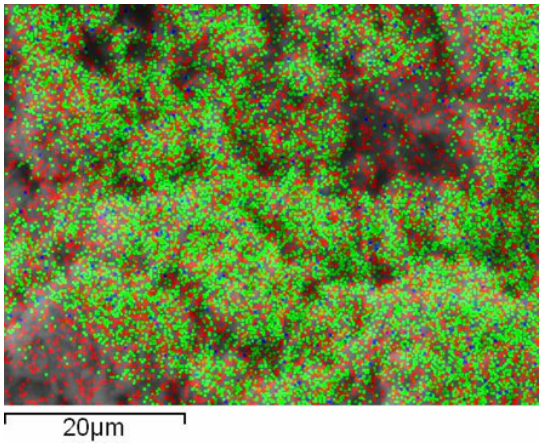

Figure 137: Element Map for 'Co_2Mo_3N' post-reaction with 3:1 H_2/Ar at 700°C. Elements: Co (red), Mo (green) and N (blue).

4.2.3.2 Lattice Nitrogen Reactivity of Co_2Mo_3N at 800°C and 900°C

The stability of Co_2Mo_3N and Co_6Mo_6N under reducing conditions and the possible lattice nitrogen reactivity of the material was investigated further by testing the material under 3:1 H_2/Ar at 800°C and 900°C. The material was tested at 900°C, in order to make a comparison with the other ternary nitrides examined elsewhere within this thesis. The conductivity data in Figure 138 for the 800°C reaction and in Figure 139 for the 900°C reaction show that the rate was non-steady state and the production of ammonia was minimal at both temperatures. There was a decrease in conductivity of 44 µS/cm at 800°C and of only 31 µS/cm at 900°C, over the 7 hours. This result is in accordance with the limited stability of ammonia under these conditions under which much of the lattice nitrogen would therefore be lost as N_2.

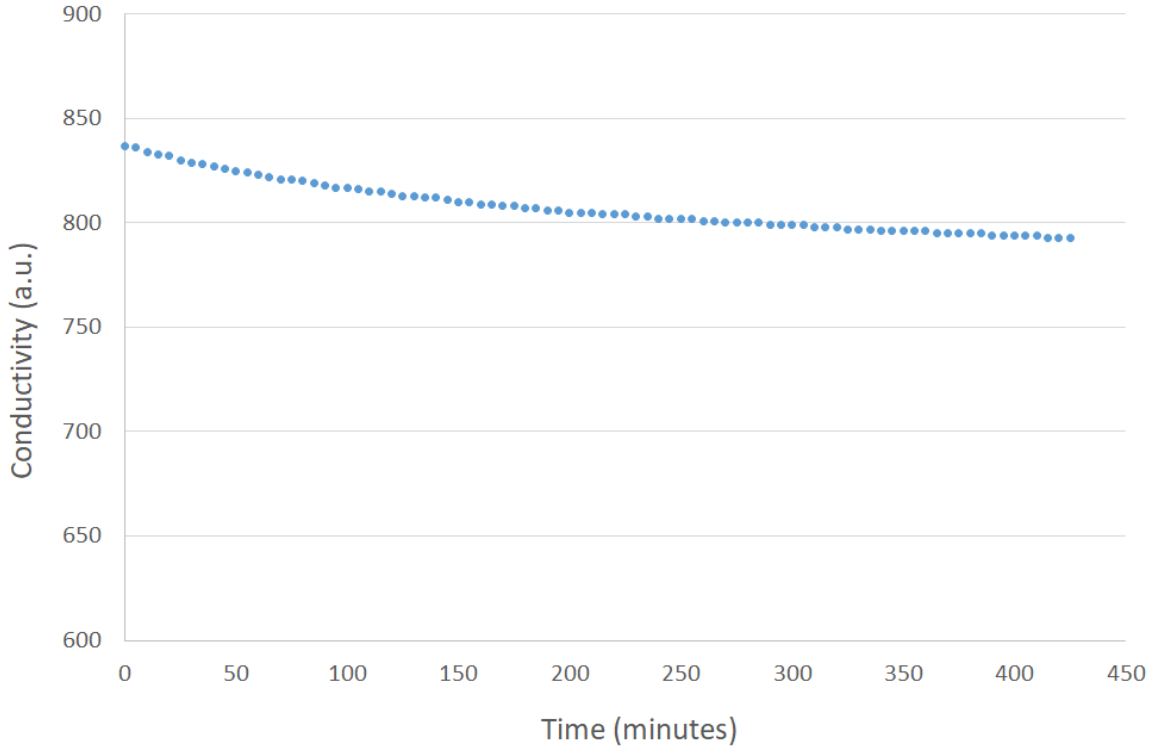

Figure 138: Conductivity profile for 'Co_2Mo_3N' reacted with 3:1 H_2/Ar at 800°C for 7 hours.

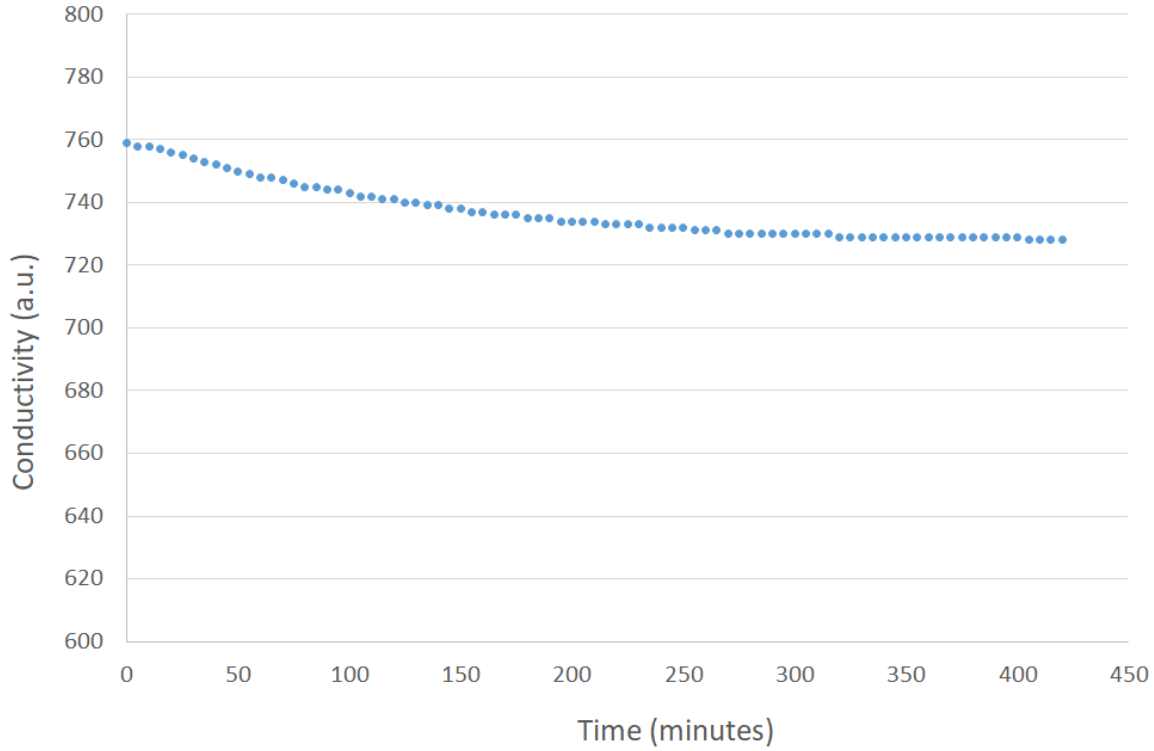

Figure 139: Conductivity profile for 'Co_2Mo_3N' reacted with 3:1 H_2/Ar at 900°C for 7 hours.

4.2.3.2.1 XRD Pattern and Elemental Analysis of Co_2Mo_3N Post 800°C Reaction

The pre- and post-reaction XRD patterns are provided in Figure 140. As was observed before, the Co_3Mo_3N phase shifted to higher 2θ values. This was most clearly seen when comparing the peak at approximately 35.46° 2θ, pre- and post-reaction. Moreover, the XRD reflections for Co_6Mo_6N appear to have shifted to even higher 2θ values than expected, suggesting that this phase has lost even more nitrogen. The Co_2Mo_3N appears to remain stable at this temperature, with no shift in the peak positions observed for this phase. The peak for Co_2Mo_3N at approximately 45.08° 2θ does not change position compared to pre-reaction. This suggests that the lattice nitrogen in this phase was unreactive. As was seen at 700°C, the molybdenum nitride impurity was reduced to molybdenum metal during the reaction. However, as there are not unique reflections for Mo, this phase cannot be completely confirmed as is the case at 700°C. However, the reduction of molybdenum nitride to Mo has been reported to occur under 3:1 Ar/H_2 at 700°C [135] and therefore, would be assumed to occur in this case as well.

The elemental analysis displayed in Table 36 shows that the nitrogen percentage decreased significantly compared to pre-reaction. If the material contained Co_6Mo_6N, Co_2Mo_3N and Mo, the expected stoichiometric percentage of nitrogen in this material is 1.92 wt. %, assuming a 1:1:1 ratio. The material had a lower percentage of nitrogen than this value, however, as the XRD pattern showed that the reflections of Co_6Mo_6N had shifted to higher 2θ values, this lower value is to be expected. The XRD pattern showed that the reflections

of Co_2Mo_3N had not shifted positions and therefore, the lower nitrogen value is not due to a loss of some nitrogen from this phase. Therefore, the loss of nitrogen is expected to be only from the Co_3Mo_3N phase. The percentage of nitrogen that was lost from the material that was converted to ammonia was ca. 24%. This value was similar to the calculated amount for the material reacted at 700°C. However, NH_3 becomes less stable as the temperature is increased.

Material	Calculated Stoichiometric Nitrogen Content (wt. %)	Calculated Stoichiometric Carbon Content (wt. %)	Nitrogen Content from Elemental Analysis (wt. %)	Carbon Content from Elemental Analysis (wt. %)
'Co2Mo3N' Pre-reaction	3.34	-	2.67	0.20
'Co2Mo3N' Post-reaction	3.34	-	0.72	0.34

Table 36: Elemental Analysis for 'Co_2Mo_3N' comparing pre- and post-reaction with 3:1 H_2/Ar at 800°C for 7 hours as shown in Figure 138.

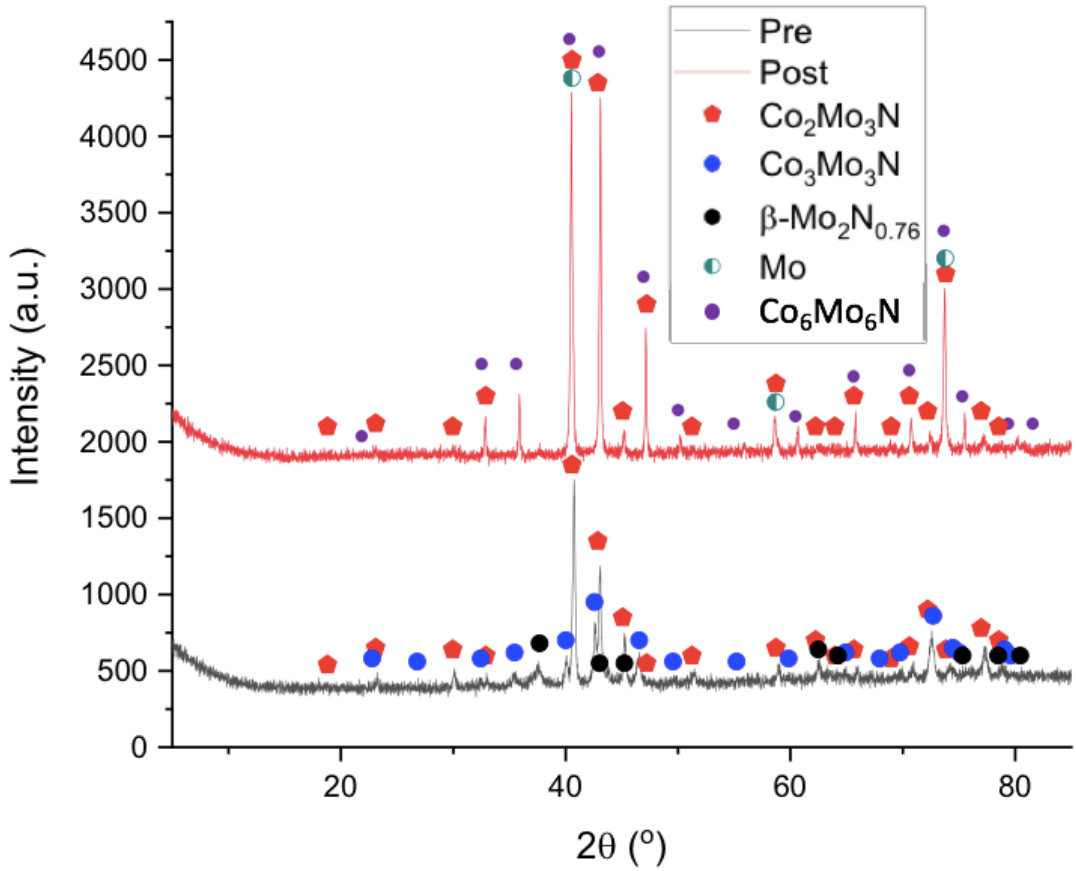

Figure 140: Comparison of XRD patterns for 'Co_2Mo_3N' pre- and post-reaction with 3:1 H_2/Ar at 800°C for 7 hours. Reflections marked: ⬟ Co_2Mo_3N (JCPDS file number 01-072-6570), ● Co_3Mo_3N (JCPDS file number 01-089-7953), ● β-$Mo_2N_{0.76}$ (JCPDS file number 03-065-6236), ◐ Mo (JCPDS file number 01-071-4645) and ● Co_6Mo_6N (data from [55]).

4.2.3.2.2 XRD Pattern and Elemental Analysis of Co_2Mo_3N Post 900°C Reaction

The XRD pattern in Figure 141 shows that there was a significant change in the post-reaction material compared to pre-reaction. The material was observed to have completely decomposed to $Co_{0.08}Mo_{0.92}$, α-Co and either a cobalt nitride phase or a cobalt molybdenum alloy.

It could be suggested that there was a lattice shift of Co_2Mo_3N to higher 2θ values as evidenced by two reflections at 40.57° and 42.87° 2θ pre-reaction and 40.65° and 43.52° 2θ post-reaction. However, the other two expected reflections for $Co_{0.08}Mo_{0.92}$ are evident in the XRD pattern. In addition, the other reflections due to Co_2Mo_3N are not apparent in the XRD pattern. Therefore, it is proposed that the material had decomposed under these conditions.

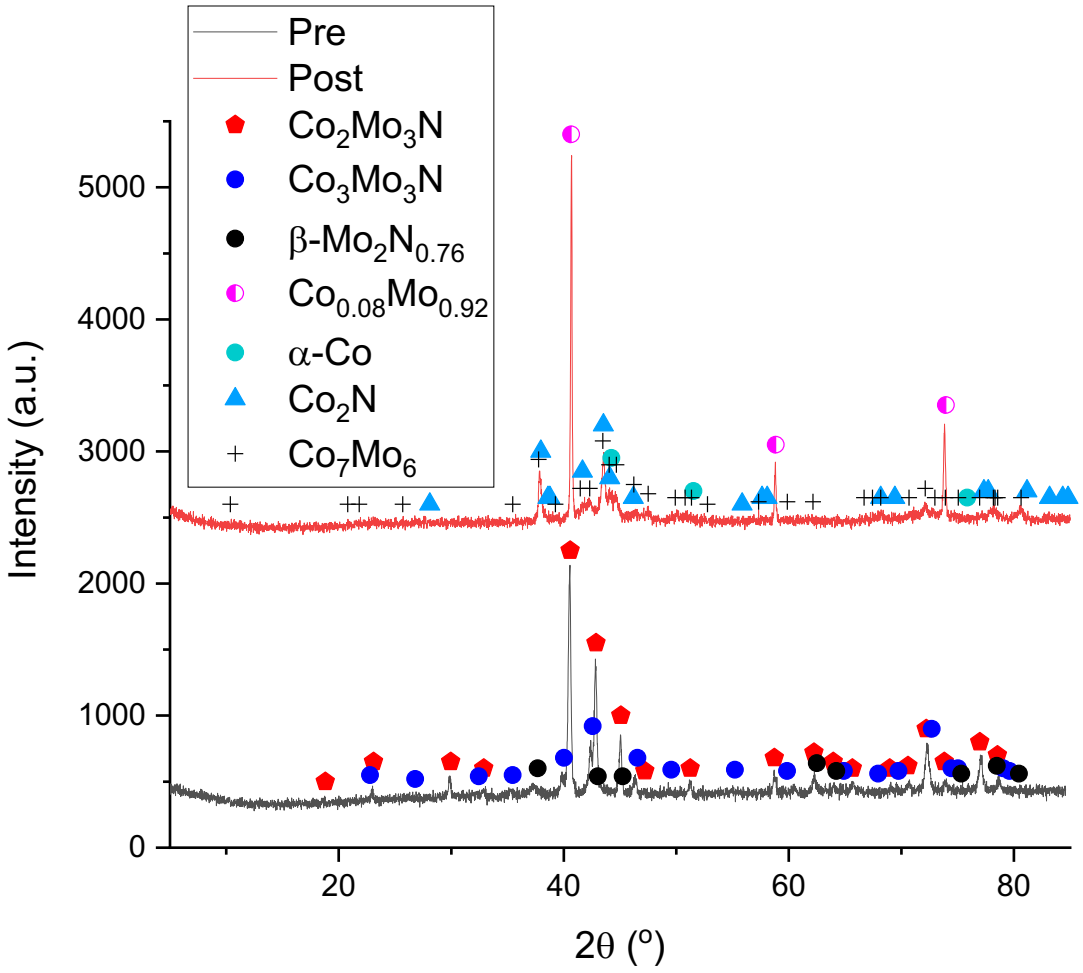

Figure 141: Comparison of XRD patterns for 'Co_2Mo_3N' pre- and post-reaction with 3:1 H_2/Ar at 900°C for 7 hours. Reflections marked: ⬟ Co_2Mo_3N (JCPDS file number 01-072-6570), ● Co_3Mo_3N (JCPDS file number 01-089-7953), ● β-$Mo_2N_{0.76}$ (JCPDS file number 03-065-6236), ◐ $Co_{0.08}Mo_{0.92}$ (JCPDS file number 01-071-7326), ● α-Co (JCPDS file number 01-089-4307), ▲ Co_2N (JCPDS file number 01-074-8393), + Co_7Mo_6 (JCPDS file number 00-029-0489).

This result suggests that the lattice nitrogen in the filled β-Mn structured Co_2Mo_3N was reactive at the elevated temperature and that the material was not as stable at 900°C compared to the filled β-Mn structured Ni_2Mo_3N and η-carbide structured Ni_2GaMo_3N. A possible explanation for this difference in stability and lattice nitrogen reactivity could be due to the bonding character of the M-Mo bond (M = Ni, Co) and its influence on the strength of the Mo-N interaction. The difference in electronegativity between Co (1.88) and Mo (2.16) is slightly greater than that for Ni (1.91) and therefore, the interaction is more ionic. The Mo-N bond distances in Co_3Mo_3N are calculated to be 2.113 Å [59] compared to 2.086 Å and 2.097 Å for Ni_2Mo_3N and Ni_2GaMo_3N, respectively [59] [121]. Unfortunately, the Mo-N distances in Co_2Mo_3N have not been reported in the literature to the writer's knowledge.

The elemental analysis shows that the amount of nitrogen had decreased significantly after reduction at 900°C as presented in Table 37 and as expected. The majority of the lattice nitrogen would have been lost as N_2 as the conductivity did not decrease as would be expected for the decrease in nitrogen observed. The percentage of lattice nitrogen removed from the material that was converted to ammonia was ca. 13%. Carbon was not detected in this sample pre- and post-reaction, contrasting with the other reported samples. However, the weight percentage of carbon in the other samples was very low and therefore, was unlikely to have affected the reduction process.

Material	Calculated Stoichiometric Nitrogen Content (%)	Calculated Stoichiometric Carbon Content (%)	Nitrogen Content from Elemental Analysis (%)	Carbon Content from Elemental Analysis (%)
'Co_2Mo_3N' Pre-reaction	3.34	-	3.82	0.00
'Co_2Mo_3N' Post-reaction	3.34	-	0.48	0.00

Table 37: Elemental Analysis for 'Co_2Mo_3N' comparing pre- and post-reaction with 3:1 H_2/Ar at 900°C for 7 hours.

4.2.3.2.3 SEM Analysis of Co_2Mo_3N Post 800°C Reaction

The SEM images of the post 800°C material are displayed in Figure 142. The morphology of this material resembled the one for the pre-reaction material and it consisted of a porous material with a rough surface. The pores ranged in size from 1 μm to 70 μm, which is larger than the pre-reaction material, although this observation is statistically limited in view of the comparatively small number of observations.

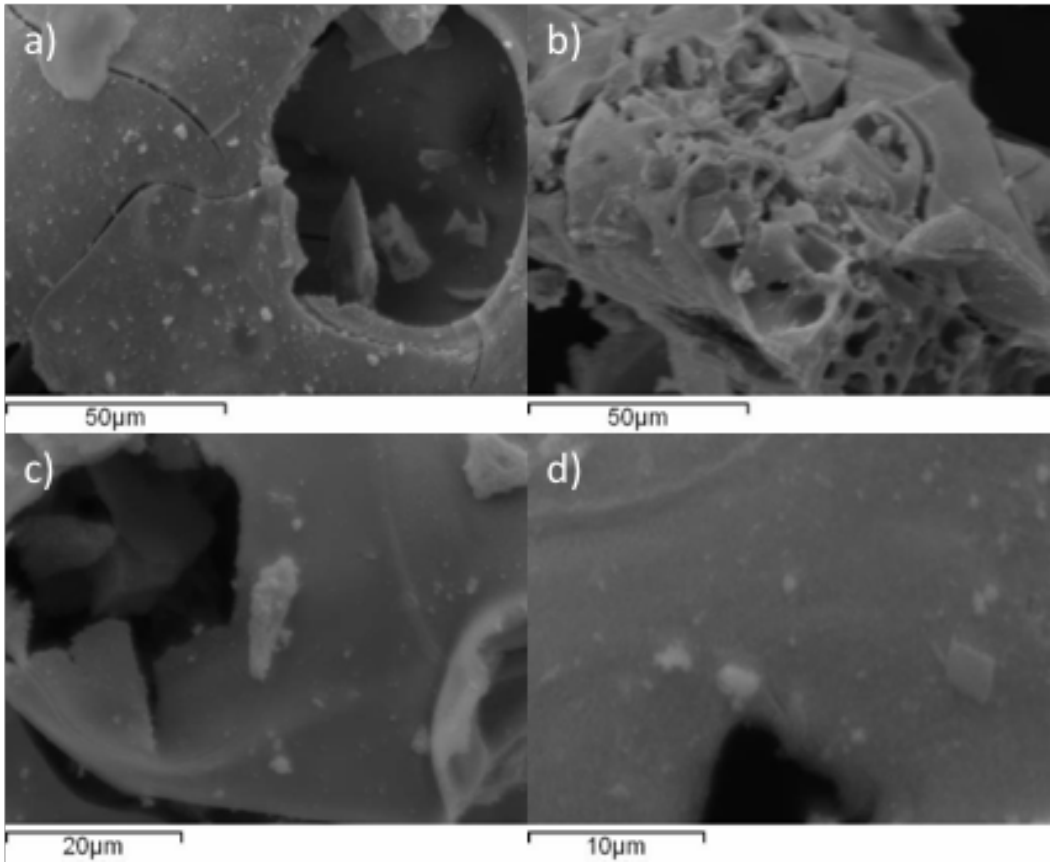

Figure 142: SEM images of 'Co_2Mo_3N' post-reaction with 3:1 H_2/Ar at 800°C. a) 1000x magnification, b) 1000x magnification, c) 2000x magnification and d) 4000x magnification.

The elemental map of the material illustrates that the cobalt and molybdenum were evenly distributed across the sample, as shown in Figure 143. In this sample, there was not an area with higher cobalt concentration as seen for the post 700°C material. This suggests that the material did not undergo segregation at this temperature. The reason for this difference is not clear.

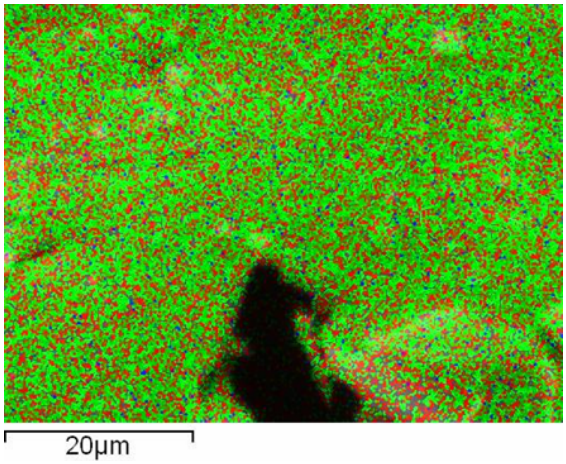

Figure 143: Element Map for 'Co_2Mo_3N' post-reaction with 3:1 H_2/Ar at 800°C. Elements: Co (red), Mo (green) and N (blue).

4.2.3.2.4 SEM Analysis of Co_2Mo_3N Post 900°C Reaction

SEM analysis was conducted on this sample to investigate if the decomposition of the material had an effect on the morphology. Previous materials that have decomposed under 3:1 H_2/Ar have been shown to have a porous nature after reduction [136], which might prove useful in terms of other applications. Therefore, it would be of interest to examine the morphology post-reaction. The morphology of the material was similar to the pre-reaction sample as observed from the SEM images displayed in Figure 144. The material contained pores and cracks that ranged in size from 1 μm to 100 μm, although as stated earlier, this observation is statistically limited. Therefore, although the material decomposed, there was not a large change in the morphology. However, the material did appear to be more porous post-reaction.

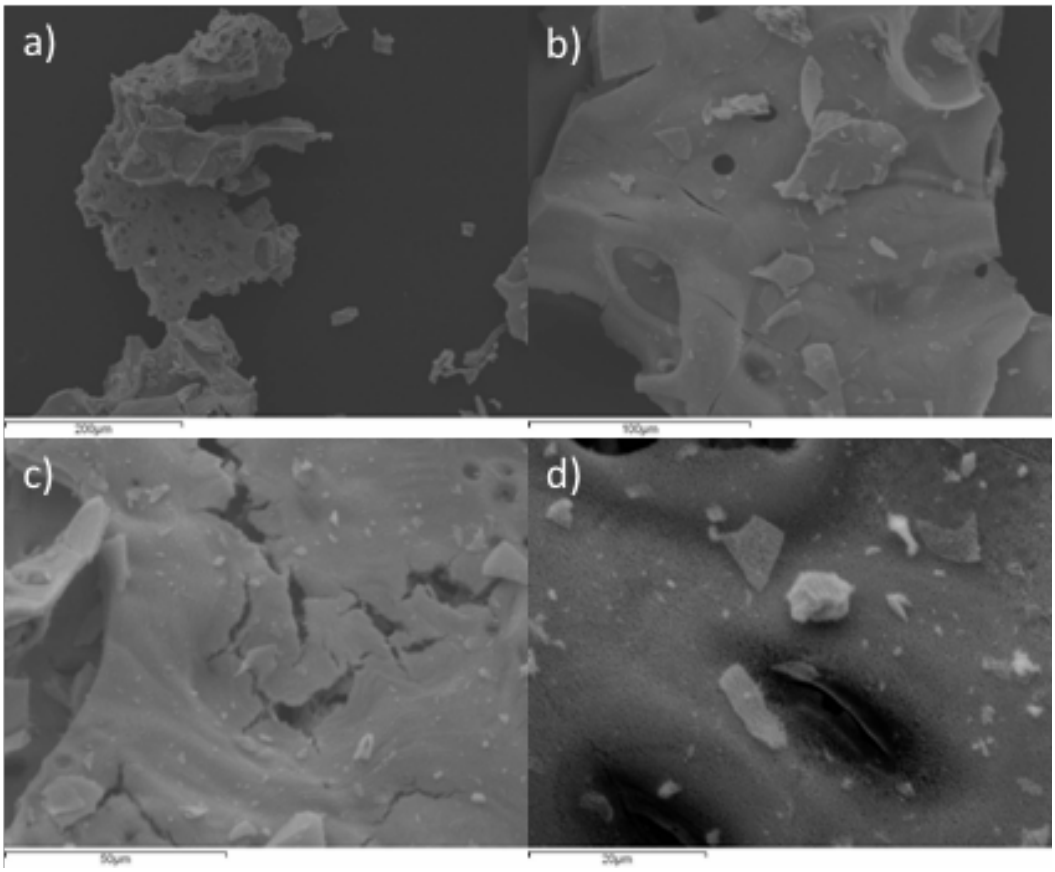

Figure 144: SEM images of 'Co_2Mo_3N' post-reaction with 3:1 H_2/Ar at 900°C. a) 200x magnification, b) 500x magnification, c) 1000x magnification and d) 2000x magnification.

The elemental maps in Figure 145 show that the cobalt and molybdenum were fairly evenly distributed across the sample, although, some areas of the elemental map did not show the presence of molybdenum. This somewhat agrees with the XRD pattern, as although the material had decomposed, cobalt molybdenum alloy phases had been formed and some segregation was observed.

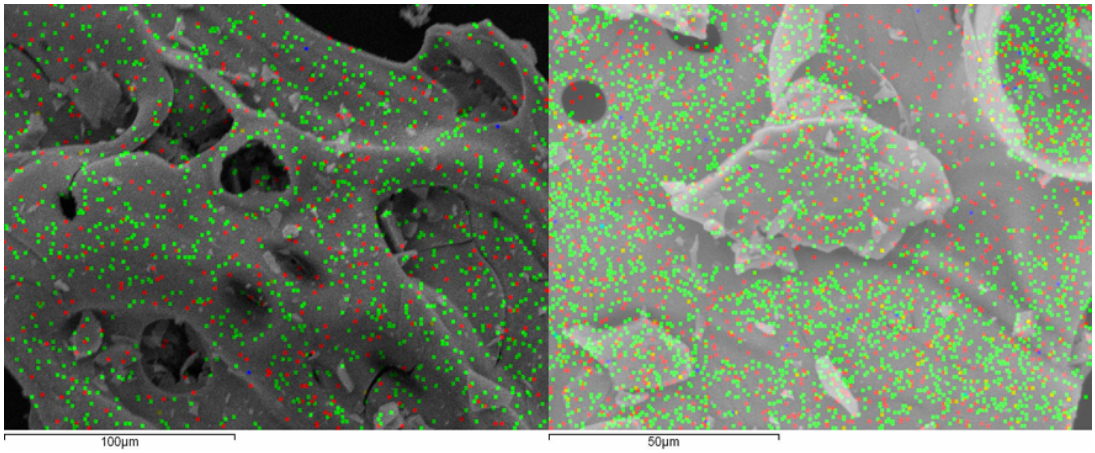

Figure 145: Element Maps for 'Co_2Mo_3N' post-reaction with 3:1 H_2/Ar at 900°C. Elements: Co (red), Mo (green) and N (blue).

4.3 Conclusions

In this chapter, the filled β-Mn structured Co_2Mo_3N and the η-carbide structured Co_3Mo_3N were examined for their ammonia synthesis activity and lattice nitrogen reactivity. This was performed in order to analyse the effect the metal composition and crystal structure had on the activity. A comparison could also be made with the filled β-Mn structured Ni_2Mo_3N and η-carbide structured Ni_2GaMo_3N discussed in Chapter 3.

Pure phase Co_2Mo_3N could not be synthesised and instead the material was a mixture of the filled β-Mn structured Co_2Mo_3N and the η-carbide structured Co_3Mo_3N, which is consistent with previous literature reports. Three preparation methods were used to synthesise a cobalt molybdenum oxide precursor. This was performed in an attempt to prepare the single phase Co_2Mo_3N from the oxide. It was found that the modified Pechini method, that was used to prepare β-Mn structured Ni_2Mo_3N, was the best route to preparing the highest ratio of Co_2Mo_3N to Co_3Mo_3N as indicated by the relative intensities in the powder XRD patterns. The optimal nitridation conditions were observed to be at 700°C for 3 hours.

The mixed phase 'Co_2Mo_3N' was shown to be active for ammonia synthesis. It exhibited a comparatively high activity of 208 µmol h^{-1} g^{-1} at 400°C and 159 ± 8 µmol h^{-1} g^{-1} at 700°C. Pure phase Co_3Mo_3N has previously been reported to have a rate of 166 ± 2 µmol h^{-1} g^{-1} at 400°C [35].

'Co_2Mo_3N' was reacted under 3:1 H_2/Ar at different temperatures to establish the lattice nitrogen reactivity and stability of the material. Co_2Mo_3N was shown to retain its structure up to 800°C. Co_3Mo_3N lost the majority of the lattice nitrogen at 700°C and 800°C yielding Co_6Mo_6N as expected. Therefore, the bulk lattice nitrogen in this phase was more reactive

than in Co_2Mo_3N. However, when reacted at 900°C, the mixed-phase material decomposed to the metal constituent components and most of the lattice nitrogen was lost. Therefore, it can be concluded that the Co_2Mo_3N, Co_6Mo_6N and Co_3Mo_3N phases were not stable under these conditions. In Chapter 3, it was shown that the filled β-Mn structured Ni_2Mo_3N and the η-carbide structured Ni_2GaMo_3N were not reduced at this temperature. Consequently, these results suggest that the lattice nitrogen reactivity of these ternary nitrides is a complex relationship between the metal composition and structure type.

5. Iron Molybdenum Materials

5.1 Introduction

As the lattice nitrogen reactivity of η-carbide Co_3Mo_3N and Ni_2GaMo_3N has been shown to be different, it would be of interest to investigate the activity and lattice nitrogen reactivity of another η-carbide structured nitride. If a nitride with a different metal composition was studied, it may be possible to gain yet further insight into the metal composition-activity relationship.

The η-carbide structured Fe_3Mo_3N is a known ammonia synthesis catalyst [35] [39] that has a lower activity than Co_3Mo_3N and therefore, has been less well studied [35] [135]. Fe_3Mo_3N is isostructural with Co_3Mo_3N as both have the η-6 carbide structure [59] [60]. The lattice nitrogen in Co_3Mo_3N has been shown to be highly reactive under Ar/H_2 atmosphere. Although Fe_3Mo_3N is isostructural with Co_3Mo_3N, the lattice nitrogen of this material has been revealed to be less reactive [35] [135]. Up to a temperature of 800°C, Fe_3Mo_3N has been observed to be stable under 3:1 H_2/Ar and the loss of lattice nitrogen was minimal. Powder neutron diffraction data showed that the nitride did not lose bulk nitrogen [135] and therefore, under 3:1 H_2/Ar, ammonia is not produced from the ternary nitride bulk lattice nitrogen. There is the possibility that the bulk nitrogen is not mobile within this system and that a surface Mars-van Krevelen type mechanism could still occur. In order to further investigate this possibility, η-carbide structured Fe_3Mo_3N and Fe_3Mo_3C have been synthesised and their comparative performance for ammonia synthesis is examined in this chapter.

5.1.1 Ammonia Synthesis Activity of Co_3Mo_3C and Fe_3Mo_3C

The replacement of lattice nitrogen with carbon is another method that can be used to investigate the activity of these materials. As stated in Chapter 3, there are two possible explanations for the high activity of Co_3Mo_3N.

As mentioned in the introduction of Chapter 3, Co_3Mo_3C has been studied for ammonia synthesis activity in order to see if the lattice nitrogen is required in this material [54]. It was found that the activity of this material occurred at higher temperatures than for Co_3Mo_3N and was associated with the substitution of lattice carbon with nitrogen.

As Fe_3Mo_3N was found to be less reducible than Co_3Mo_3N [35], it would be of interest to investigate the role the lattice nitrogen has in the iron molybdenum material. The synthesis

and testing of Fe_3Mo_3C would give an insight into the part the lattice nitrogen plays and comparisons could be made between Fe_3Mo_3C and Co_3Mo_3C.

5.1.2 Synthesis of Fe_3Mo_3N

One of the most widely applied ways of preparing Fe_3Mo_3N was devised by Bem et al. [49]. In this method, a 0.25 M aqueous solution of $FeCl_2$ and a 0.55 M aqueous solution of $Na_2MoO_4.2H_2O$ were mixed together and the resulting product was $FeMoO_4$. The nitride was then prepared by ammonolysis of the oxide precursor. Bem et al. also stated that the nitride can be formed by using a 5% H_2/N_2 nitridation mixture [49]. The XRD pattern of Fe_3Mo_3N revealed that the material was phase pure and therefore, this two-step method was shown to be successful. Other research that followed this method has also resulted in the formation of single phase Fe_3Mo_3N [135] [59] [74].

A modification of this method was investigated by McKay et al. [35], who used $Fe(NO_3)_3.9H_2O$ as the starting material. Unsurprisingly, the oxide precursor formed from this material was different from when $FeCl_2$ was used. The XRD pattern showed that the $Fe_2(MoO_4)_3$ phase was prepared instead of $FeMoO_4$. After ammonolysis of the oxide precursor, the XRD pattern showed that the desired nitride was formed along with substantial amounts of γ-Mo_2N impurity [35] [137], which is a consequence of the 2/3 Fe/Mo stoichiometric ratio in the precursor phase [135].

Another method of preparing Fe_3Mo_3N involves plasma nitridation of the oxide precursor with N_2/H_2 [74]. However, an FeMo alloy impurity was also formed alongside the desired ternary nitride. It was stated that the alloy was formed as the temperature was too high and hard to control due to thermal runaway. Fe_3Mo_3N has also been prepared by ball-milling of Mo_2N with iron [138] and heating hydrolysed alkanolamine complexed precursors in ammonia at 950°C [139]. A one step synthesis of Fe_3Mo_3N has been proposed by heating Fe_2O_3, molybdenum and sodium azide in an autoclave at 750°C for 10 hours [140]. Fe_3Mo_3N was also synthesised by heating iron powder and molybdenum powder under 10% H_2/N_2 at 975°C for 36 hours [60]. However, a small amount of molybdenum metal was observed in the XRD pattern when this method was used.

5.1.3 Synthesis of Fe_3Mo_3C

As with the formation of Ni_2Mo_3C, issues arose when the TPR method was used to synthesise Fe_3Mo_3C from the oxide precursor under CH_4/H_2 [141] [105]. Oyama et al. noted that the resulting product was a mixture of phases with the major phase having a hexagonal structure, which was not definitively identified [141]. Alconchel also observed a

mixture of phases, with the products being β-Mo_2N and $Mo_{12}Fe_{22}C_{10}$ [105]. Therefore, Alconchel et al. decided to prepare Fe_3Mo_3C by carburisation of Fe_3Mo_3N with CH_4/H_2 via topotactic lattice exchange of N by C [105]. The XRD pattern of this material showed that the single-phase ternary carbide was formed up to a temperature of 980 K.

Other methods have been used in order to prepare Fe_3Mo_3C, for example the ball milling of Fe, Mo and carbon in vacuum for 194 hours [142]. However, iron metal was also formed alongside the ternary carbide. Tsuchida attempted to prepare single phase Fe_3Mo_3C by ball milling Fe, Mo and carbon for 30 minutes at 700°C to 900°C, after having ground the sample together for 3 hours [143]. The author stated that the preparation of the carbide depended on the homogeneity of the mixture. Nevertheless, a mixture of Fe_3Mo_3C and $FeMoO_3$ was observed in the XRD pattern of the resultant material.

Other sources of carbon have also been used to synthesise Fe_3Mo_3C. The single-phase carbide has been prepared using decolourising carbon at 950°C under argon gas [48]. Fe_3Mo_3C was also prepared by a sol-gel method using chitosan solution, $FeCl_2$ and $(NH_4)_2MoO_4$ to form $FeMoO_4$, which was subsequently heat treated under Ar/H_2 [144]. However, Mo_2C was formed as an impurity when this method was used.

5.2 Results and Discussion

5.2.1 Iron Molybdenum Nitride (Fe_3Mo_3N)

5.2.1.1 Iron Molybdenum Oxide ($FeMoO_4$)

The $FeMoO_4$ precursor was targeted in order to synthesise pure phase Fe_3Mo_3N by the nitridation of the oxide with 3:1 H_2/N_2 mixture. The XRD pattern of the oxide precursor prepared in this work is displayed in Figure 146. It can be seen that the resultant material comprised a mixture of $FeMoO_4$, $Fe_2(MoO_4)_3$ and Fe_2O_3. Therefore, although iron (II) chloride tetrahydrate was used as a starting material, a mixture of phases comprising iron in different oxidation states (+2 and +3) was still observed. The elemental analysis showed that, as expected, the material did not contain any carbon, hydrogen or nitrogen.

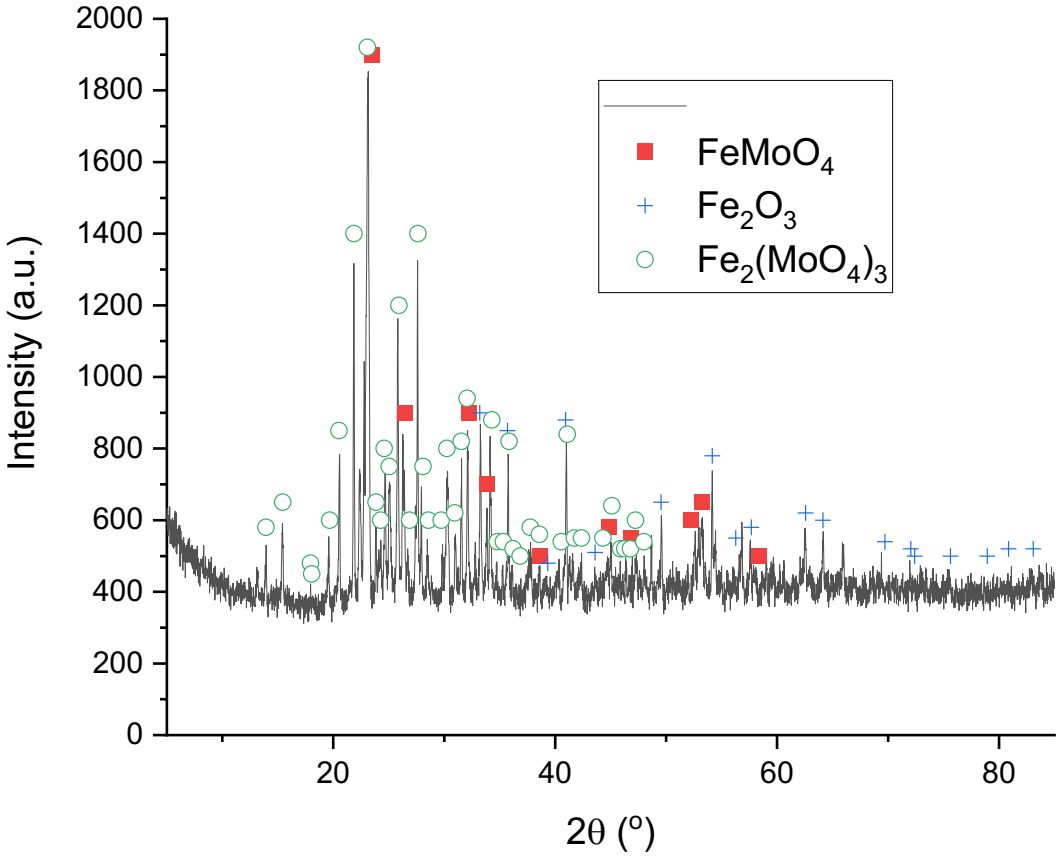

Figure 146: XRD pattern of iron molybdenum oxide ($FeMoO_4$). Reflections marked: ■ $FeMoO_4$ (JCPDS file number 00-028-0488), + Fe_2O_3 (JCPDS file number 01-076-4579) and ○ $Fe_2(MoO_4)_3$ (JCPDS file number 01-074-6404).

The Raman spectrum for the iron molybdenum oxide is presented in Figure 147. The Raman bands at positions of approximately 342, 775, 808, 921 and 967 cm^{-1} were attributed to $Fe_2(MoO_4)_3$. These Raman shifts are in very good agreement with $Fe_2(MoO_4)_3$ spectra reported in the literature [105] [145]. The band at 808 cm^{-1} is also observed in MoO_3 as a strong band. The bands at 921 and 967 cm^{-1} are assigned to the symmetric stretching modes of MoO_4 units, the bands at 775 and 808 cm^{-1} are the anti-symmetric stretching modes, the band at 342 cm^{-1} is assigned to a bending mode and the bands below 280 cm^{-1} are due to lattice modes [146]. The strong bands at 967 and 775 cm^{-1} have been assigned in the literature as Mo in a tetrahedral coordination in $Fe_2(MoO_4)_3$ [145]. It has also been suggested that the band at 808 cm^{-1} could be due to octahedrally coordinated Mo species, since MoO_3, which has octahedral Mo coordination, has a band at a similar wavenumber [145]. The bands at 593 and 212 cm^{-1} are observed in the Raman spectrum for Fe_2O_3 and the bands at 921, 342 and 276 cm^{-1} are seen in the Raman spectrum of β-$FeMoO_4$ [147], which corresponds to the XRD assignment presented above. However, the other bands expected for $FeMoO_4$ and Fe_2O_3 were not observed in the Raman spectrum in Figure 147. It is currently unclear why this is the case.

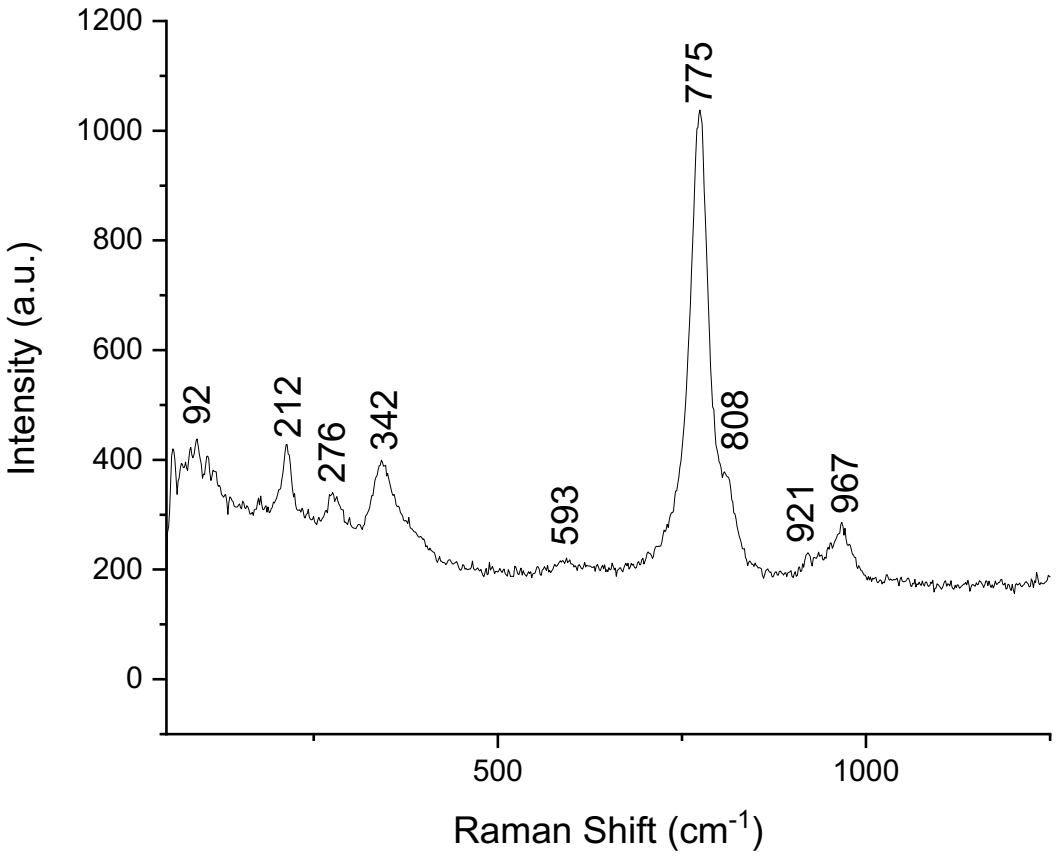

Figure 147: Raman spectrum of iron molybdenum oxide ($FeMoO_4$).

SEM analysis was performed in order to see if the different phases could be distinguished on the basis of, for example, differing morphology. The representative SEM images for the oxide precursor are shown in Figure 148. The material had an irregular morphology and appeared to consist of rounded particles. The material had a surface area of 1 m^2/g, a pore volume of 0.02 cc/g and an average pore radius of 20.31 Å. To the author's knowledge, other groups that used a similar preparation method did not publish SEM images of the iron molybdenum oxide [59] [148]. $Fe_2(MoO_4)_3$, for example, has been shown to have different morphologies depending on the preparation method [149] [150]. The different oxides did not appear to have distinguishable morphologies.

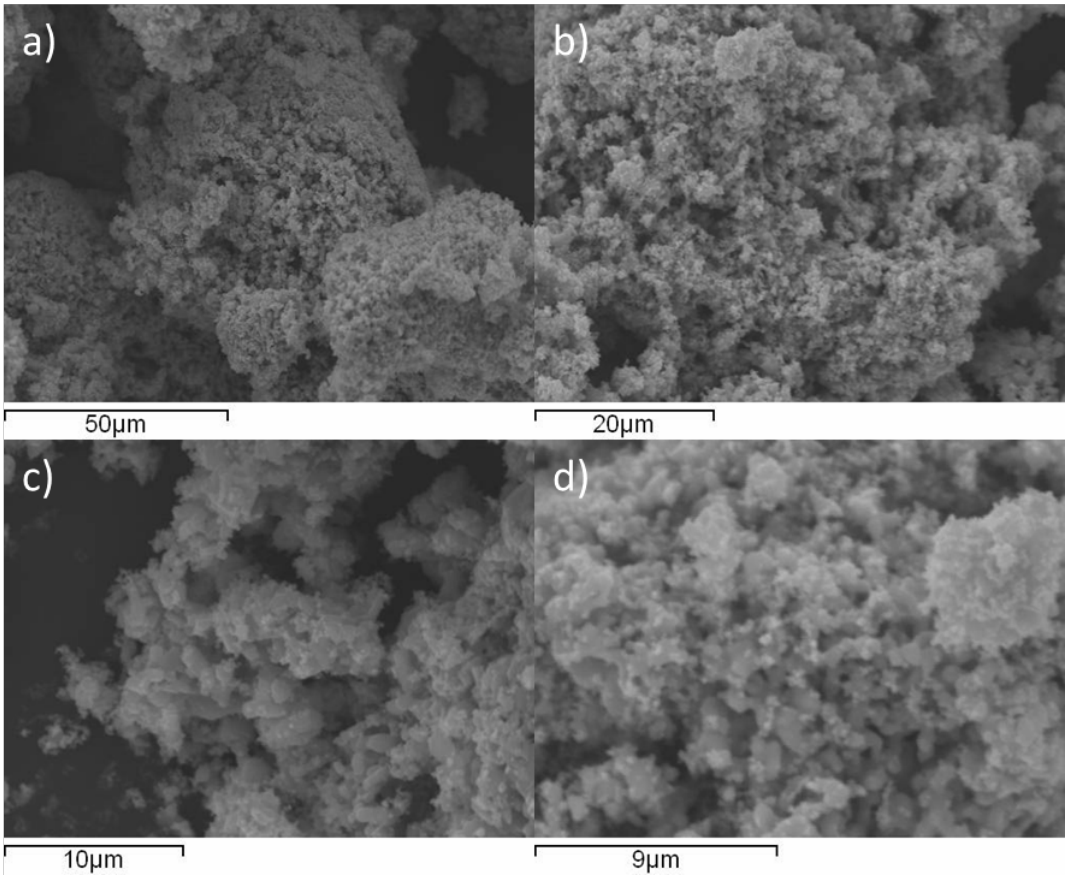

Figure 148: SEM images of iron molybdenum oxide ($FeMoO_4$). a) 1000x magnification, b) 2000x magnification, c) 4000x magnification and d) 6000x magnification.

The EDX weight percentages for each element in the oxide precursor are provided in Table 38. For $FeMoO_4$, the percentage of iron, molybdenum and oxygen in the sample should be 25.88 wt. %, 44.46 wt. % and 29.66 wt. % respectively. However, the XRD pattern showed that the material was a mixture of phases containing $Fe_2(MoO_4)_3$, $FeMoO_4$ and Fe_2O_3. From the EDX analysis, the calculated stoichiometry of this material is $Fe_5Mo_4O_{24}$. This suggests that the three oxides are present in equal proportions, although, the percentage of oxygen would be lower than the obtained value. Therefore, the three phases were present in the material, agreeing with the XRD pattern.

Area	Fe weight (%)	Mo weight (%)	O weight (%)
1	29	34	36
2	23	37	40
3	28	39	33
4	25	36	40
5	29	35	36
Average	27	36	37

Table 38: EDX values for iron molybdenum oxide ($FeMoO_4$).

5.2.1.2 Iron Molybdenum Nitride (Fe_3Mo_3N)

Although the XRD pattern of the oxide precursor showed it contained a mixture of $Fe_2(MoO_4)_3$, $FeMoO_4$, and Fe_2O_3, reasonably phase-pure Fe_3Mo_3N was formed after ammonolysis. However, small traces of MoN impurity were apparent in the XRD pattern as shown in Figure 149.

The elemental analysis showed that the material contained 4.27 wt. % nitrogen (C: 0.00 wt. %, H: 0.00 wt. %, N: 4.27 wt. %). The stoichiometric weight percentage of nitrogen in Fe_3Mo_3N is 2.98 wt. %. Therefore, the nitride contained a considerably higher percentage of nitrogen than the calculated stoichiometric content. However, the excess nitrogen will be due to the molybdenum nitride impurity and any NH_x species on the surface of the material. From the XRD pattern, the MoN phase content appeared to be very low and therefore, the contribution from this phase would be small. Hence, the excess nitrogen is more likely due to the NH_x species on the surface of the material.

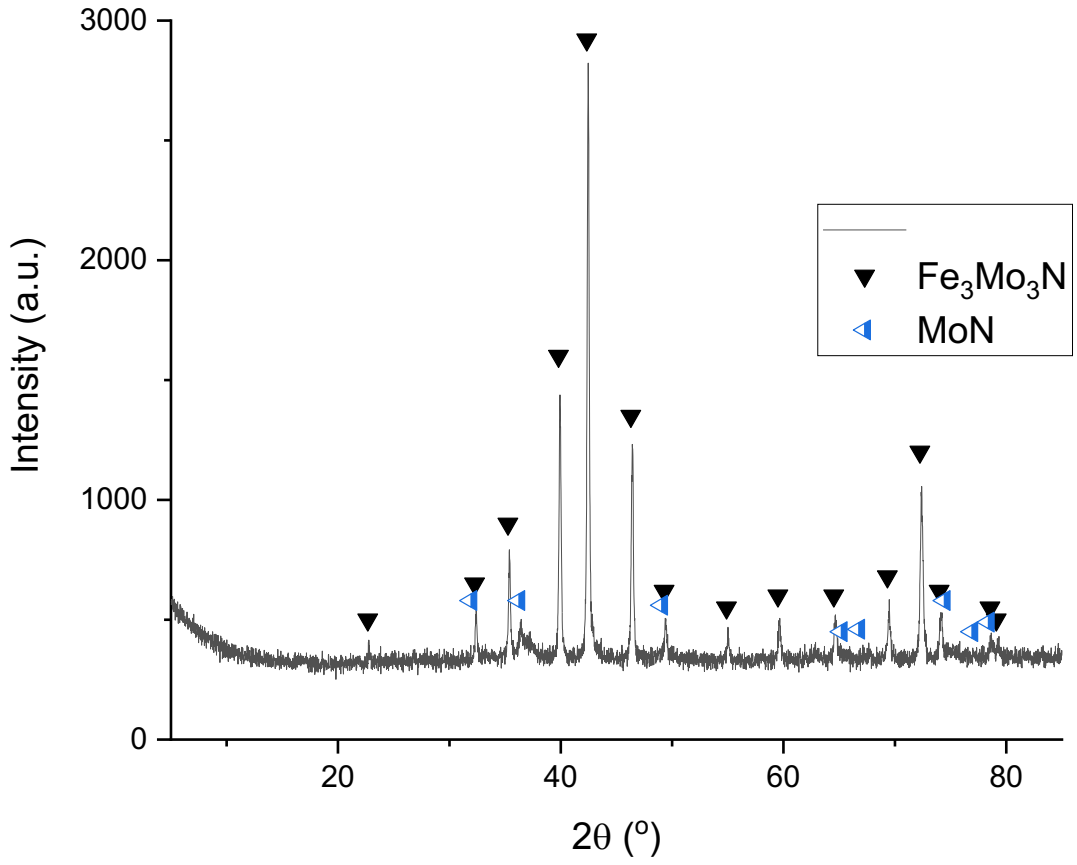

Figure 149: XRD pattern of iron molybdenum nitride (Fe_3Mo_3N). Reflections marked: ▼ Fe_3Mo_3N (JCPDS file number 00-048-1408) and ◁ MoN (JCPDS file number 01-073-9468).

Raman spectroscopy was used to characterise possible surface oxide species on the nitride. The presence of an oxide surface layer may affect the ammonia synthesis activity and

therefore, it is important to observe if one occurs on the surface of the material. The Raman spectra of Fe_3Mo_3N is presented in Figure 150. The Raman bands at positions of 967, 927, 806, 775 and 344 cm^{-1} were attributed to $Fe_2(MoO_4)_3$ [145] [146]. These Raman bands match the spectrum observed for the oxide precursor in Figure 147. These bands have been assigned in the literature to the MoO_4 vibrations [146]. However, it has been shown that $FeMoO_4$ has a similar Raman spectrum when a high-power laser is used [151]. It has been suggested by Boucherit et al. that the Fe^{2+} oxidises to Fe^{3+} and possibly transforms to $Fe_2(MoO_4)_3$. However, iron would need to be lost from the material in order for this process to occur. The presence of $Fe_2(MoO_4)_3$ in the Raman spectrum of Fe_3Mo_3N has been reported previously in the literature [105]. It has been shown that $Fe_2(MoO_4)_3$ and Fe_2O_3 are the products of the oxidation of the nitride [59].

The results from the Raman spectrum demonstrate that, as expected in view of the passivation treatment conducted prior to discharge from the ammonolysis reactor, there was a non-XRD apparent oxide layer covering the surface of the nitride.

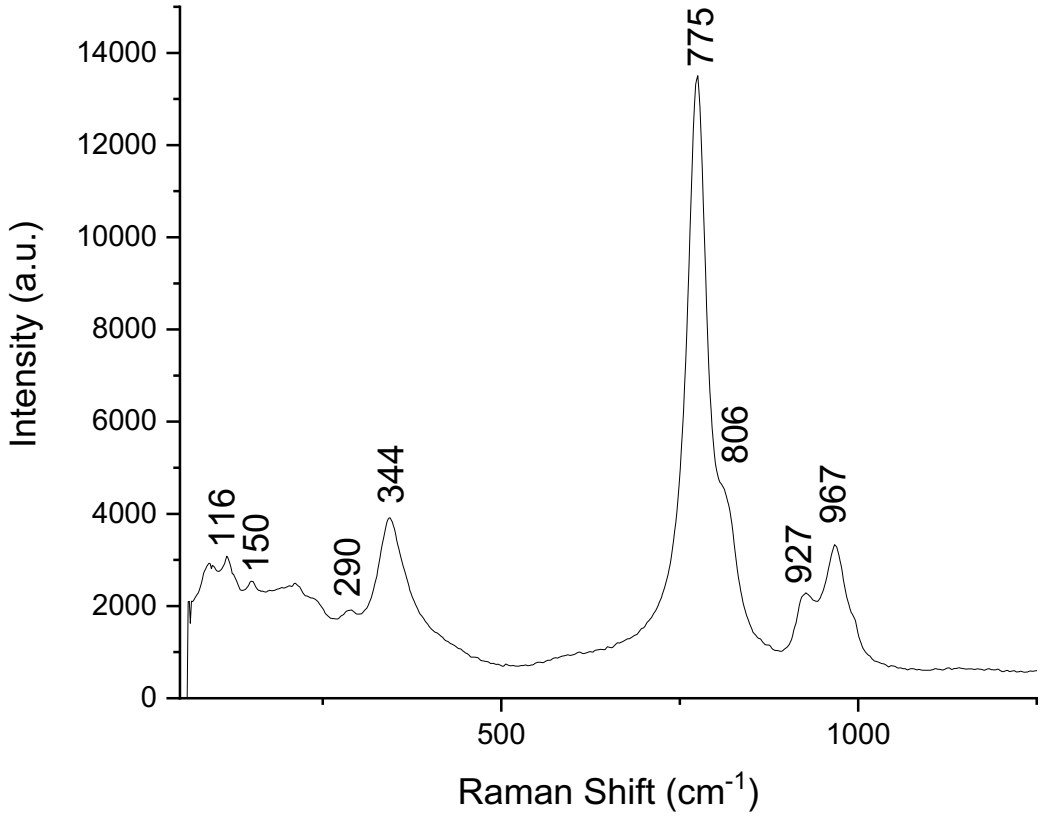

Figure 150: Raman spectrum of iron molybdenum nitride (Fe_3Mo_3N).

In order to compare the activity of the nitride and carbide, the morphology of the two materials has to be similar to remove any concerns that effects arising from structure sensitivity might be incorrectly ascribed to composition. Therefore, SEM analysis of the nitride was performed in order for a comparison with the topotactically synthesised carbide

to be discussed later to be made. Figure 151 shows representative SEM images for Fe_3Mo_3N. The SEM images show a similar morphology to that of the oxide precursor. It can be seen that the morphology of the sample appeared to consist of rounded particles. The material had a surface area of 13 m^2/g, a pore volume of 0.07 cc/g and an average pore radius of 30.78 Å. In the literature, the surface area of the nitride ranges from 4 to 18 m^2/g [148] [94] [152] and therefore, this result is in agreement with the published work. Since the sample had an oxide surface layer, the BET surface area may not be representative of the area exhibited by the sample during testing.

Previous studies by groups that used a similar preparation method had a different morphology. Their images showed smooth, rounded particles with an irregular morphology [59] [148] [137]. The η-carbide structured Co_3Mo_3N was shown to consist of needles when prepared by ammonolysis [54]. However, ammonolysis of an oxide precursor generally results in a pseudomorphic transformation. As there were three phases present in the oxide precursor, this transformation is complicated. However, there did not appear to be different morphologies in the oxide precursor.

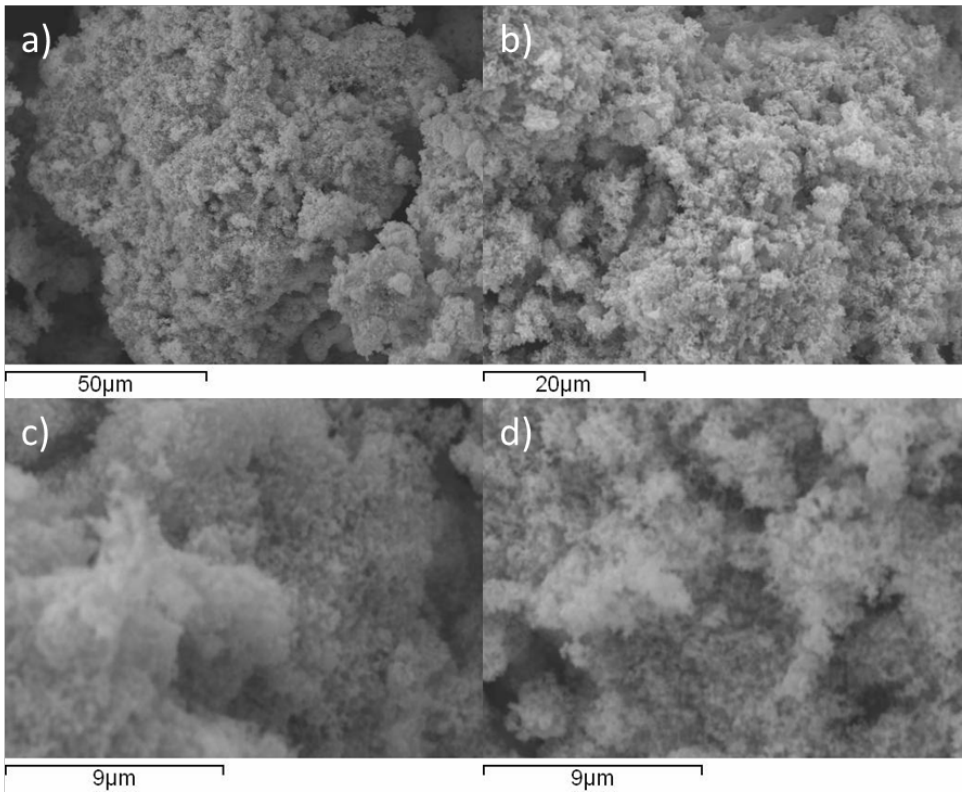

Figure 151: SEM images of iron molybdenum nitride (Fe_3Mo_3N). a) 1000x magnification, b) 2000x magnification, c) 6000x magnification and d) 6000x magnification.

An iron only containing component was observed in the XRD pattern for the oxide precursor and a molybdenum nitride impurity was seen in the XRD pattern of the nitride. Therefore, an elemental map was performed for this material in order to see if there were

areas of phase separation. The elemental map in Figure 152 shows that the iron, molybdenum and nitrogen were evenly dispersed across the sample.

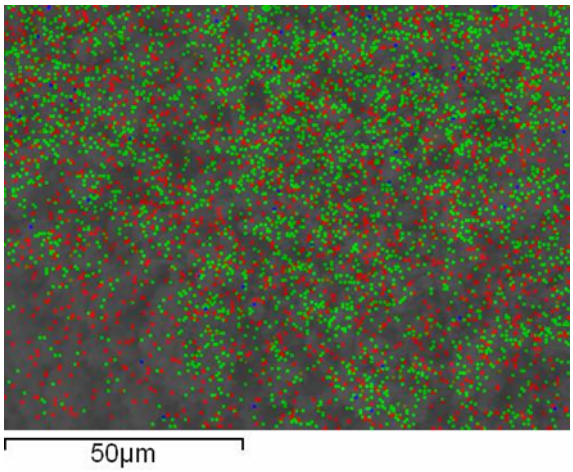

Figure 152: Element Map for Fe_3Mo_3N. Elements: Fe (red), Mo (green) and N (blue).

The EDX analysis for Fe_3Mo_3N is given in Table 39. The stoichiometric percentage of iron, molybdenum and nitrogen in the sample is 35.69 wt. %, 61.32 wt. % and 2.98 wt. %, respectively. The nitrogen weight percentage was greater than expected and was highly variable. However, the limitations of EDX for light element analysis should be taken into consideration. As with the oxide precursor, the percentage of molybdenum and iron were approximately the same as the expected stoichiometric values.

Area	Fe weight (%)	Mo weight (%)	N weight (%)
1	38	51	11
2	34	59	7
3	35	56	7
4	30	59	11
5	33	56	12
6	33	57	10
7	32	59	9
8	36	58	6
9	31	57	12
10	31	56	13
11	32	59	9
12	38	55	7
13	44	56	0
14	28	72	0
15	33	67	0
16	34	66	0
17	37	55	8
18	30	60	10
19	31	59	10
20	35	60	6
Average	34	58	8

Table 39: EDX values for iron molybdenum nitride (Fe_3Mo_3N).

5.2.1.3 Ammonia Synthesis at 400°C for Fe_3Mo_3N

Fe_3Mo_3N has previously been examined for its ammonia synthesis activity [35] [39] [94] and lattice nitrogen reactivity [35]. The highest ammonia synthesis rates for Fe_3Mo_3N at 400°C and ambient pressure which have been reported are 143 μmol h^{-1} g^{-1} [39] and 95 μmol h^{-1} g^{-1} [35]. However, these materials contained impurities, including γ-Mo_2N. The γ-Mo_2N phase is a known ammonia synthesis catalyst and therefore, it would be expected to contribute to the ammonia synthesis activity. The pure phase Fe_3Mo_3N has previously been reported to have a rate of 91 μmol h^{-1} g^{-1} at 400°C [135]. Therefore, it appears that the nitride has a similar activity to the material containing the impurity.

Fe_3Mo_3N was tested at 400°C under 1:3 ratio N_2/H_2 at atmospheric pressure for 7.75 hours in order to confirm the activity of the material and to make a comparison with the related carbide (as presented later in the chapter). The material was first pre-treated at 700°C for 2 hours under 1:3 ratio N_2/H_2 to remove the passivation layer, before the temperature was reduced to the reaction temperature. The conductivity profile of the material is shown in Figure 153. The ammonia synthesis rate of Fe_3Mo_3N at 400°C was 74 ± 1 μmol h^{-1} g^{-1} and at 700°C was 137 ± 7 μmol h^{-1} g^{-1}. This rate was lower than the ones reported previously and this may be due to the difference in morphology.

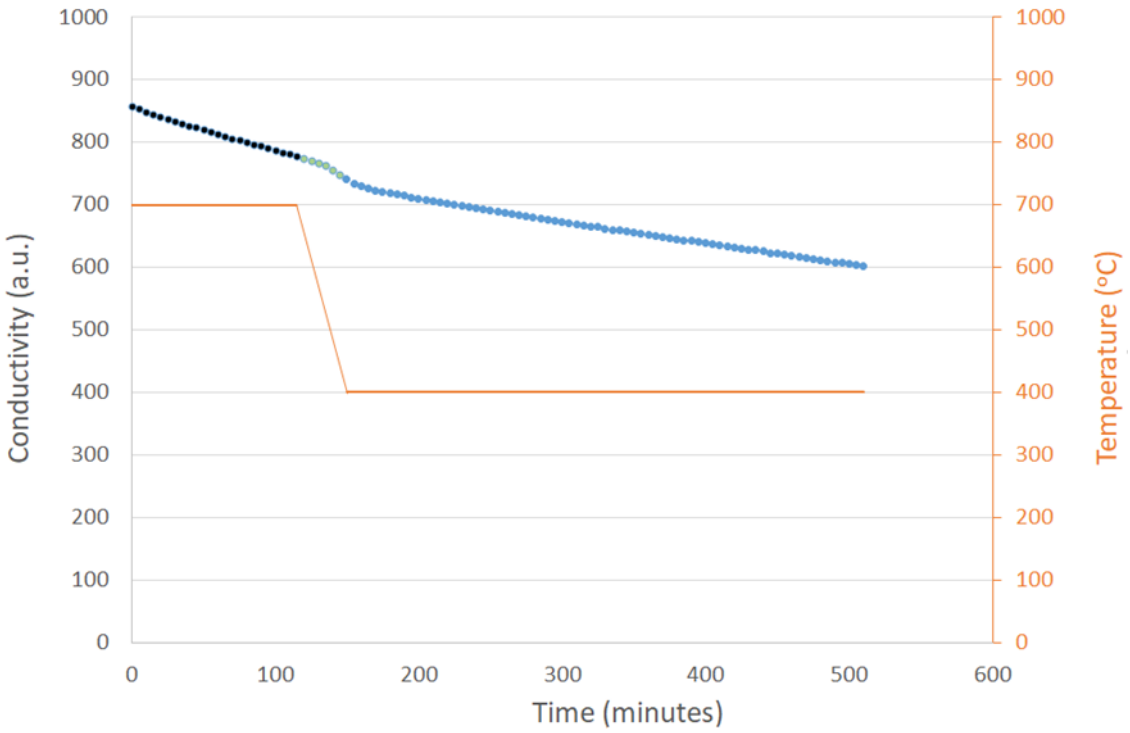

Figure 153: Conductivity profile for Fe_3Mo_3N reacted with 3:1 H_2/N_2 at 700°C for 2 hours and 400°C for 7.75 hours.

The XRD pattern in Figure 154 shows that there did not appear to be any major change in the Fe_3Mo_3N phase upon reaction. However, the MoN impurity present in the material was reduced to Mo_2N during the reaction. The elemental analysis in Table 40 shows that the percentage of nitrogen present in the material had decreased compared to pre-reaction. The percentage of nitrogen present in the material was comparable to the expected stoichiometric value of 2.98 wt. % for Fe_3Mo_3N. The decrease in nitrogen could be due to the reduction of the molybdenum nitride or the loss of some surface nitrogen from the ternary nitride. The total amount of N lost compared to the total amount of ammonia produced was ca. 55 %. Therefore, there is definitely a catalytic component to the results for Fe_3Mo_3N.

Material	Calculated Stoichiometric Nitrogen Content (wt. %)	Calculated Stoichiometric Carbon Content (wt. %)	Nitrogen Content from Elemental Analysis (wt. %)	Carbon Content from Elemental Analysis (wt. %)
Fe_3Mo_3N Post-reaction	2.98	-	2.86	0.00

Table 40: Elemental Analysis for Fe_3Mo_3N post-reaction with 3:1 H_2/N_2 at 700°C for 2 hours and 400°C for 7.75 hours.

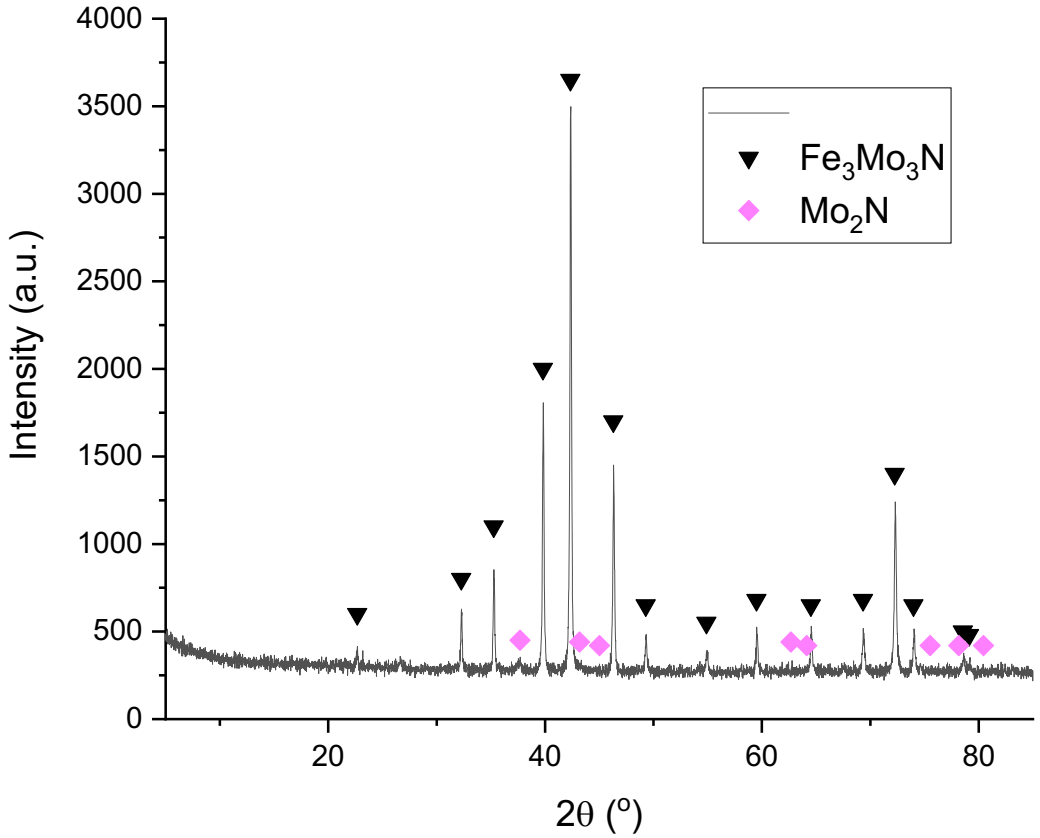

Figure 154: XRD pattern for Fe_3Mo_3N post-reaction with 3:1 H_2/N_2 at 400°C for 7.75 hours. Reflections marked: ▼ Fe_3Mo_3N (JCPDS file number 00-048-1408) and ♦ Mo_2N (JCPDS file number 00-025-1368).

SEM analysis was performed in order to examine if any changes occurred to the morphology or structure of Fe_3Mo_3N during the ammonia synthesis reaction. The representative SEM images of the post-reaction material are displayed in Figure 155. The material had an irregular structure and the morphology was similar to the pre-reaction material. The element map in Figure 156 shows that the even iron and molybdenum distribution had been retained from the pre-reaction sample.

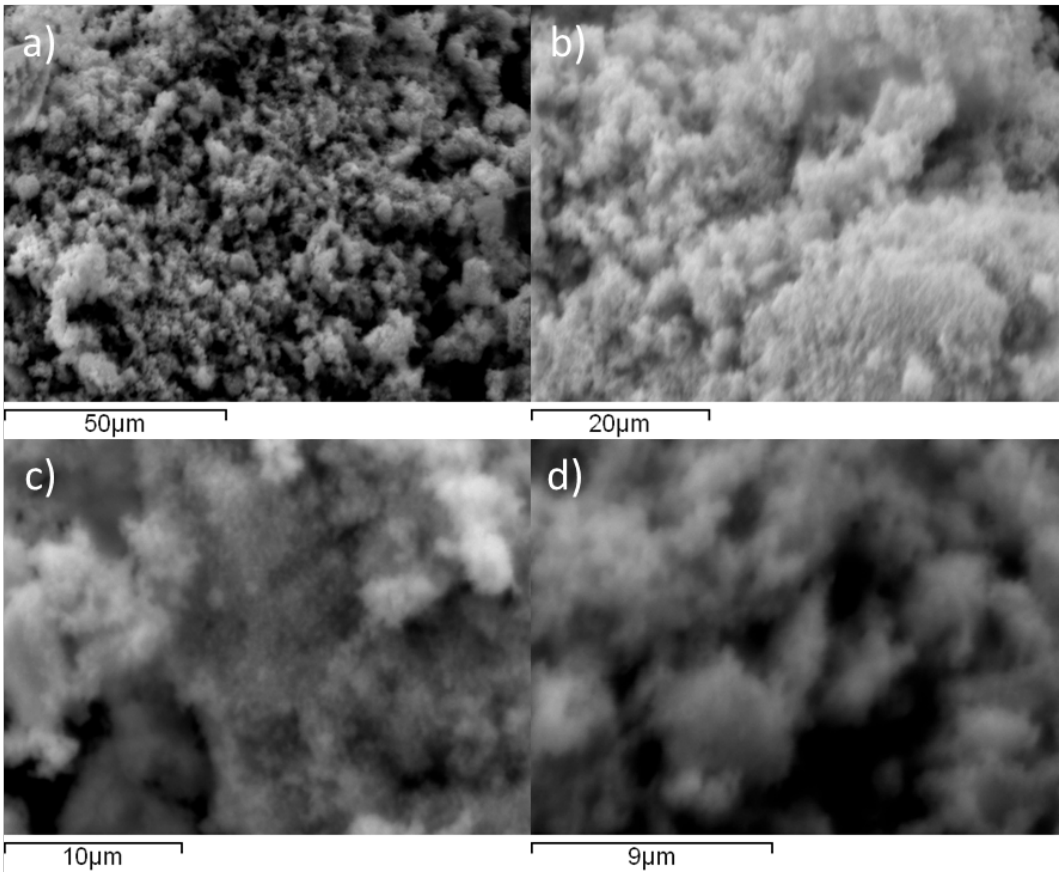

Figure 155: SEM images of Fe_3Mo_3N post reaction with 3:1 H_2/N_2 at 400°C for 7.75 hours. a) 1000x magnification, b) 2000x magnification, c) 4000x magnification and d) 6000x magnification.

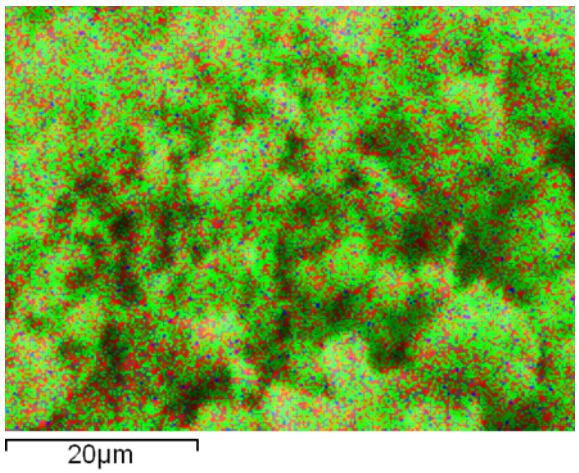

Figure 156: Element Map for Fe_3Mo_3N post-reaction with 3:1 H_2/N_2 at 400°C. Elements: Fe (red), Mo (green) and N (blue).

5.2.1.4 Ammonia Synthesis at 500°C for Fe_3Mo_3N

Fe_3Mo_3N was tested for ammonia synthesis activity at 500°C and atmospheric pressure under 3:1 H_2/N_2 in order to compare the activity of the nitride with the ternary carbide (as presented later). As before, the material was pre-treated at 700°C for 2 hours under 1:3 ratio N_2/H_2, before the temperature was reduced to 500°C. The reaction profile showed a linear decrease in conductivity over time and there was no induction period as seen in Figure 157. The ammonia synthesis rate of Fe_3Mo_3N was determined to be 403 μmol h^{-1} g^{-1} at 500°C. The material had a rate of 74 ± 1 μmol h^{-1} g^{-1} at 400°C. Therefore, the material was much more active at the higher temperature as might be expected. In comparison, Co_3Mo_3N has a rate of 489 ± 17 μmol h^{-1} g^{-1} [54] at 500°C and ambient pressure. This suggests that these two nitrides have similar specific activities as they have similar surface areas (Co_3Mo_3N: 18 m^2/g [55] and Fe_3Mo_3N: 13 m^2/g).

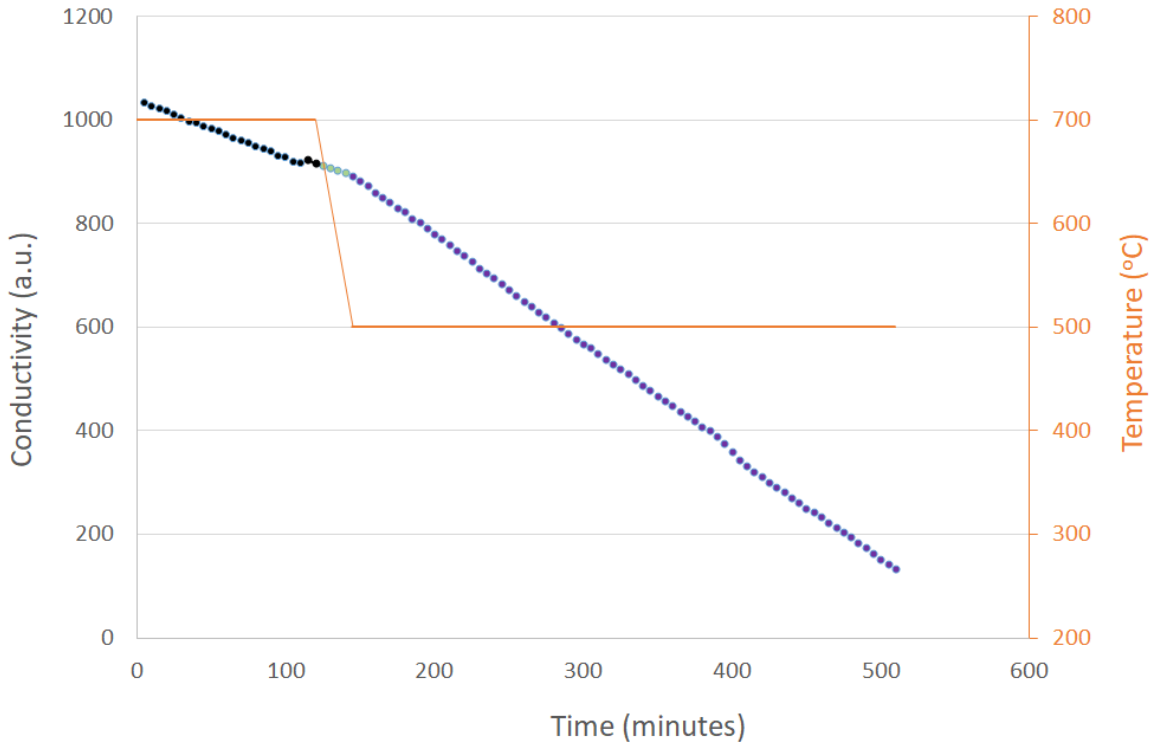

Figure 157: Conductivity profile for Fe_3Mo_3N reacted with 3:1 H_2/N_2 at 700°C for 2 hours and 500°C for 6 hours.

The XRD pattern in Figure 158 illustrates that the Fe_3Mo_3N did not change phase. However, as with the post 400°C reaction material, the MoN impurity present in the pre-reaction material was reduced during the reaction. The elemental analysis shows that there was a significant decrease in the percentage of nitrogen compared to the pre-reaction sample. This decrease in nitrogen could be due to the reduction of the molybdenum nitride or, more likely, the loss of NH_x species from the surface of the material. The post-reaction material had a similar percentage of nitrogen (2.91 wt. %) to the expected stoichiometric

value of 2.98 wt. % for Fe_3Mo_3N. The total amount of N lost versus the total amount of NH_3 produced was ca. 42 % and therefore, there was a catalytic component to the result. Additionally, the treatment stage at 700°C would be expected to lead to the loss of NH_x surface groups to form N_2.

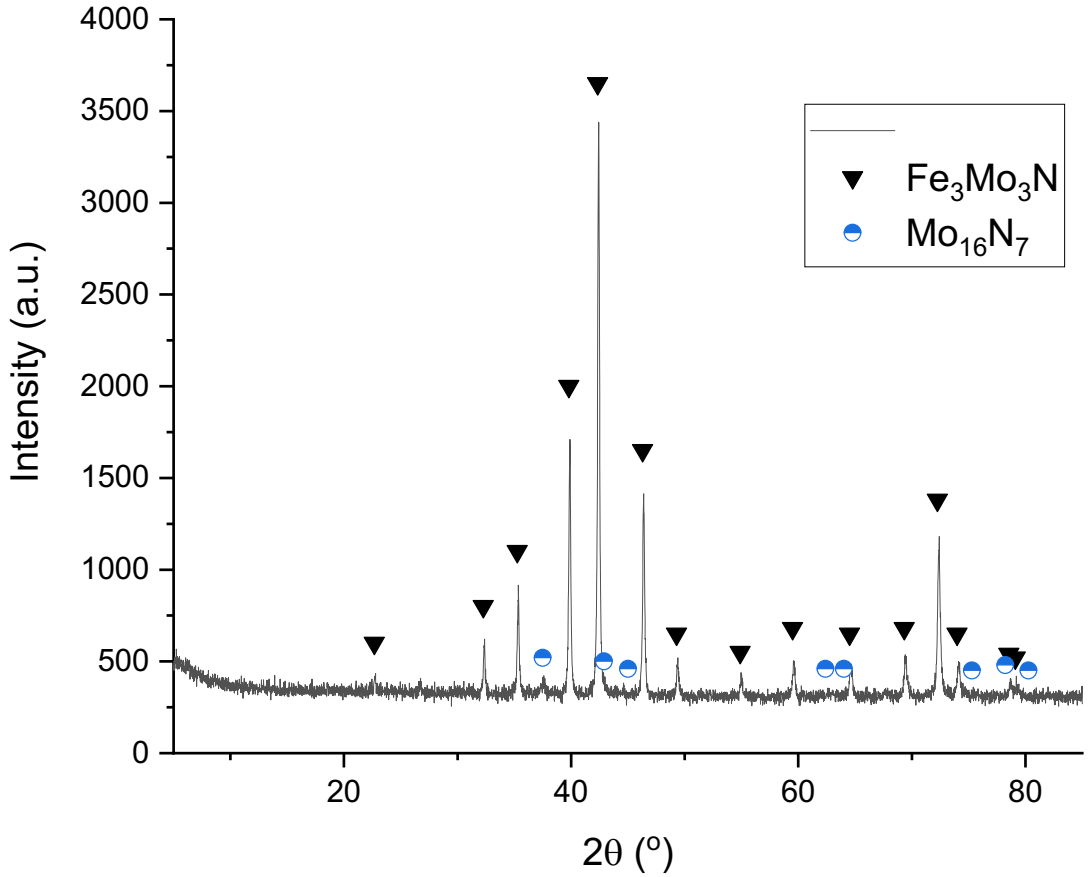

Figure 158: XRD pattern for Fe_3Mo_3N post-reaction with 3:1 H_2/N_2 at 500°C for 6 hours. Reflections marked: ▼ Fe_3Mo_3N (JCPDS file number 00-048-1408) and ◓ $Mo_{16}N_7$ (JCPDS file number 00-023-1256).

The SEM images of the material post 500°C reaction are exhibited in Figure 159. The morphology of the material was similar to the pre-reaction material. The material consisted of rounded particles.

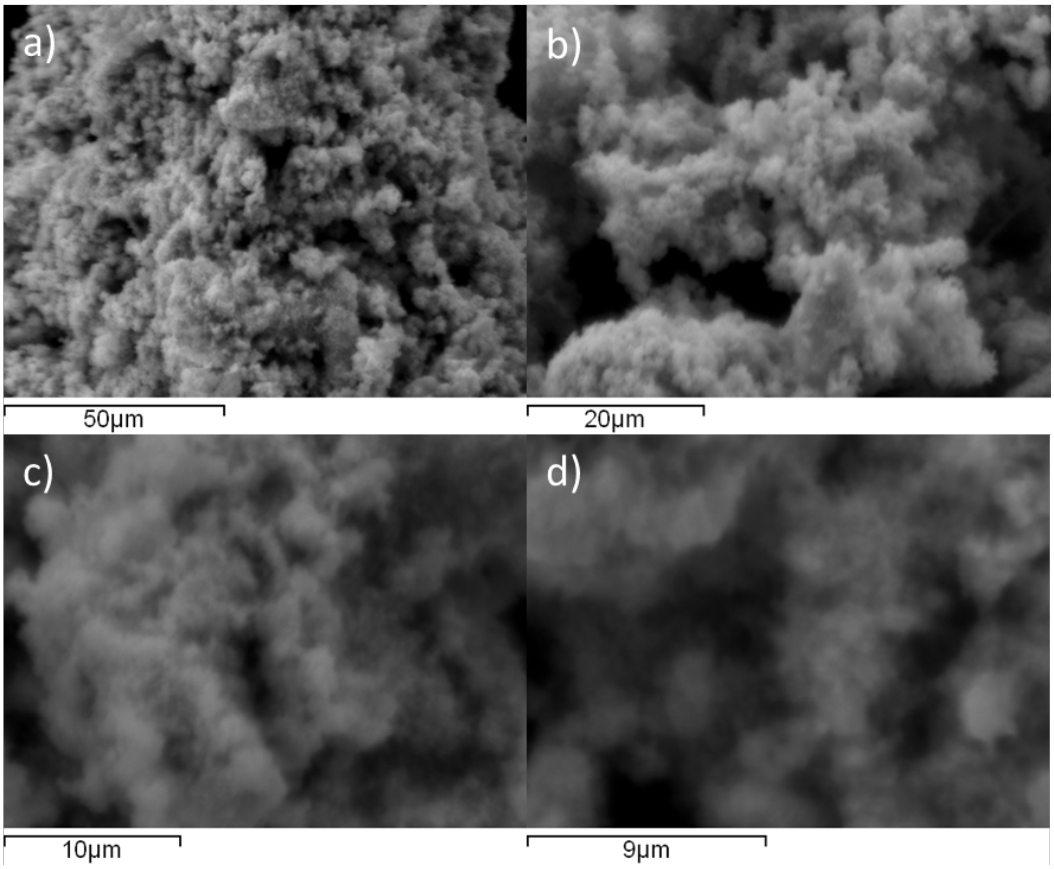

Figure 159: SEM images of Fe_3Mo_3N post reaction with 3:1 H_2/N_2 at 500°C. a) 1000x magnification, b) 2000x magnification, c) 4000x magnification and d) 6000x magnification.

The elemental map in Figure 160 shows that the iron and molybdenum were fairly evenly distributed across the sample.

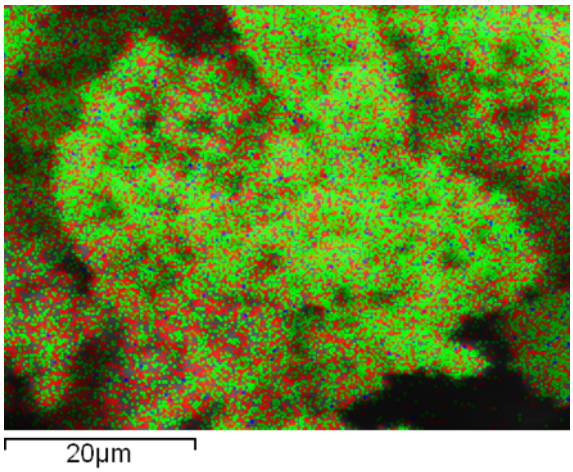

Figure 160: Element Map for Fe_3Mo_3N post-reaction with 3:1 H_2/N_2 at 500°C. Elements: Fe (red), Mo (green) and N (blue).

5.2.1.5 Lattice Nitrogen Reactivity of Fe_3Mo_3N at 900°C

In order to determine the reactivity of lattice nitrogen in Fe_3Mo_3N, the material has been reacted under 3:1 H_2/Ar at 900°C. The material has previously been investigated from 400°C to 800°C for its lattice nitrogen reactivity and it was found to be less reducible than

Co_3Mo_3N [35], even though they have the same structure. It was found that the molybdenum nitride component in the mixture of $FeMo_3N$ and γ-MoN decomposed to Mo metal whereas there was no shift in peak positions of the Fe_3Mo_3N in the resultant XRD pattern [135]. If the bulk lattice nitrogen was active for ammonia synthesis via a Mars-van Krevelen mechanism, it would be expected that a reduction in the bulk nitrogen content of Fe_3Mo_3N might occur when reduced under Ar/H_2.

Figure 161 shows that only a small amount of ammonia was produced and therefore, the lattice nitrogen was relatively unreactive in terms of ammonia production under Ar/H_2 at 900°C. There was a decrease in conductivity of 48 µS/cm over the 7 hours. However, as discussed in the previous chapter, ammonia synthesis is unfavourable at this temperature and ammonia will decompose [99] and, therefore, some lattice nitrogen may be lost as N_2.

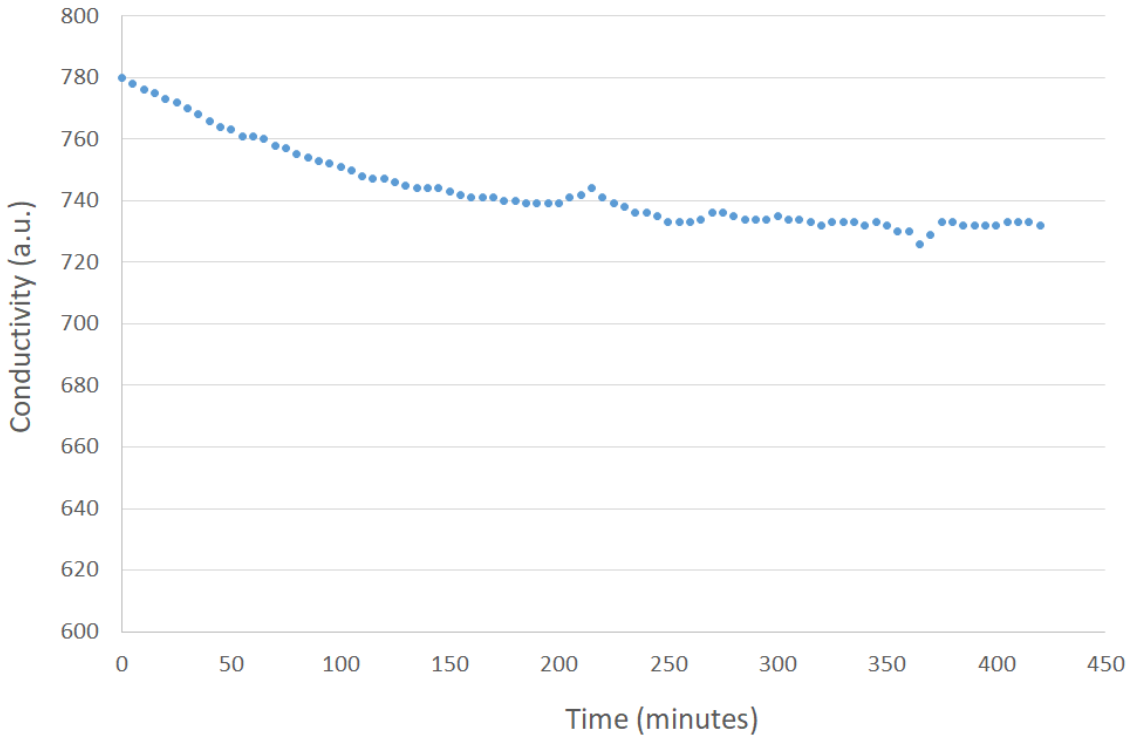

Figure 161: Conductivity profile for Fe_3Mo_3N reacted with 3:1 H_2/Ar at 900°C for 7 hours.

The XRD pattern in Figure 162 shows that the material decomposed to Mo metal and α-Fe and that there was an iron nitride phase. Minuscule peaks due to Fe_3Mo_3N can also be observed at 42° and 72° 2θ. This suggests that the lattice nitrogen was mainly lost as dinitrogen and that this loss is associated with the phase decomposition. In a number of respects, the XRD pattern of this material is reminiscent of the one for Co_2Mo_3N/Co_3Mo_3N post 900°C reaction, which was presented in Figure 141 in the previous chapter. Both Fe_3Mo_3N and Co_2Mo_3N/Co_3Mo_3N were not as stable at 900°C as Ni_2Mo_3N and Ni_2GaMo_3N. As stated for 'Co_2Mo_3N', one possible reason for this difference in stability

could be due to the bonding character in the materials. It has been shown that the bonding between the M-Mo (M = Ni, Fe, Co) is covalent in character [59]. In the case of Fe_3Mo_3N, the difference in electronegativity between Fe (1.83 on the Pauling scale) and Mo (2.16 on the Pauling scale) is larger than that of Ni (1.91 on the Pauling scale). This suggests that the Fe-Mo bond is more ionic than the Ni-Mo bond in Ni_2Mo_3N. Furthermore, the Mo-N bond distances in Fe_3Mo_3N, Ni_2Mo_3N and Ni_2GaMo_3N were calculated to be 2.111 Å, 2.086 Å and 2.097 Å, respectively [135] [59] [121]. Therefore, the difference in lattice nitrogen reactivity could be due to the secondary effect the iron, cobalt or nickel may have on the Mo-N sub-lattice.

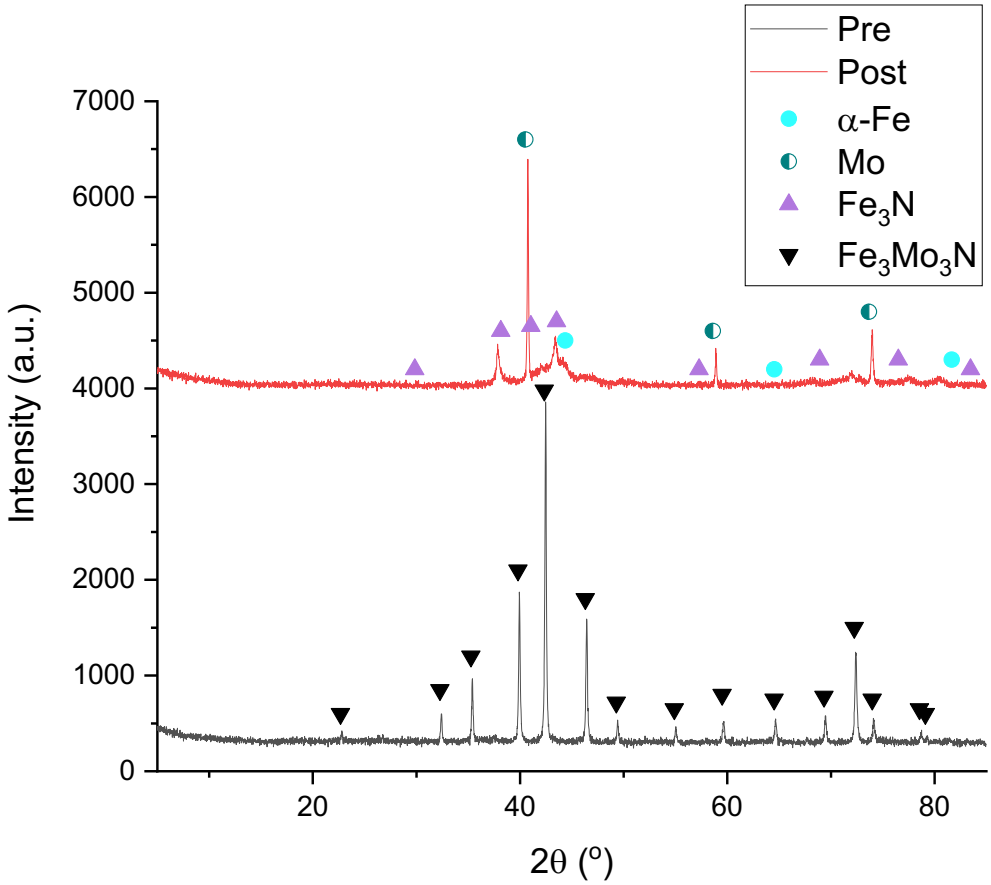

Figure 162: Comparison of XRD patterns for Fe_3Mo_3N pre- and post-reaction with 3:1 H_2/Ar at 900°C for 7 hours. Reflections marked: ▼ Fe_3Mo_3N (JCPDS file number 00-048-1408), ● α-Fe (JCPDS file number 01-085-1410), ◐ Mo (JCPDS file number 01-089-5023) and ▲ ε-Fe_3N (JCPDS file number 01-073-2101).

The elemental analysis shows that the percentage of nitrogen had significantly decreased after reduction with 3:1 H_2/Ar at 900°C compared to pre-reaction as shown in Table 41 as would be expected for the decomposition of the material. The percentage of lattice nitrogen that was lost from Fe_3Mo_3N that was converted to ammonia was ca. 5.6%.

Material	Calculated Stoichiometric Nitrogen Content (%)	Calculated Stoichiometric Carbon Content (%)	Nitrogen Content from Elemental Analysis (%)	Carbon Content from Elemental Analysis (%)
Fe_3Mo_3N Post-reaction	2.98	-	0.49	0.00

Table 41: Elemental Analysis for Fe_3Mo_3N post-reaction with 3:1 H_2/Ar at 900°C for 7 hours.

The Raman spectrum of the post reduction material, displayed in Figure 163, appears to be somewhat different compared to the pre-reaction spectrum as would be expected due to the material decomposing. The bands at 816 and 273 cm^{-1} could be due to MoO_3 [90]. This could result from a surface oxide layer on the molybdenum metal. The Raman bands at positions of 970, 924, 780 and 369 cm^{-1} could be attributed to $Fe_2(MoO_4)_3$ [146]. Although the XRD pattern only showed trace amounts of Fe_3Mo_3N were present in the material.

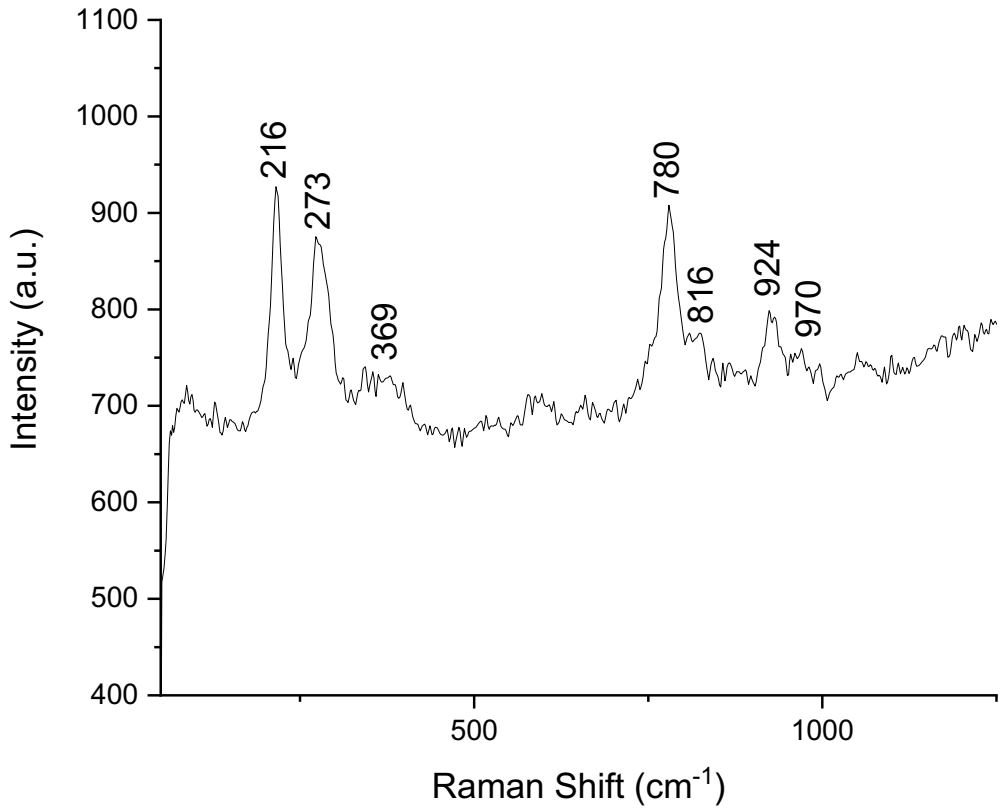

Figure 163: Raman spectrum of Fe_3Mo_3N post-reaction with 3:1 H_2/Ar at 900°C.

SEM analysis was conducted to see if the reduction of the material had an effect on the morphology. Typical SEM images of Fe_3Mo_3N post-reaction with 3:1 H_2/Ar are presented in Figure 164. The morphology was retained from the pre-reaction material and consisted of an irregular morphology and rounded particles. The morphology of the Fe_3Mo_3N, 'Co_2Mo_3N', Ni_2Mo_3N and Ni_2GaMo_3N post-reaction with 3:1 H_2/Ar were different

between each other, suggesting that the lattice nitrogen reactivity was not affected by the morphology of the material.

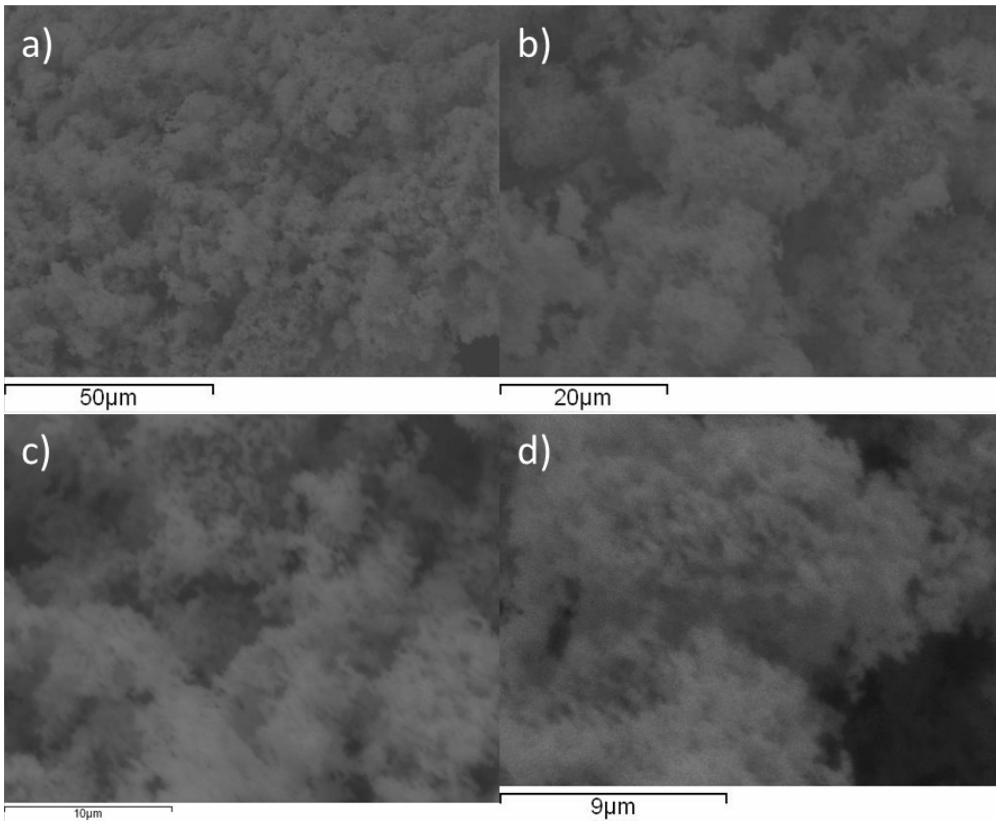

Figure 164: SEM images of Fe_3Mo_3N post-reaction with 3:1 H_2/Ar at 900°C. a) 1000x magnification, b) 2000x magnification, c) 4000x magnification and d) 6000x magnification.

The element maps in Figure 165 show that there was a fairly even distribution of nickel and molybdenum over the sample, even though the material decomposed.

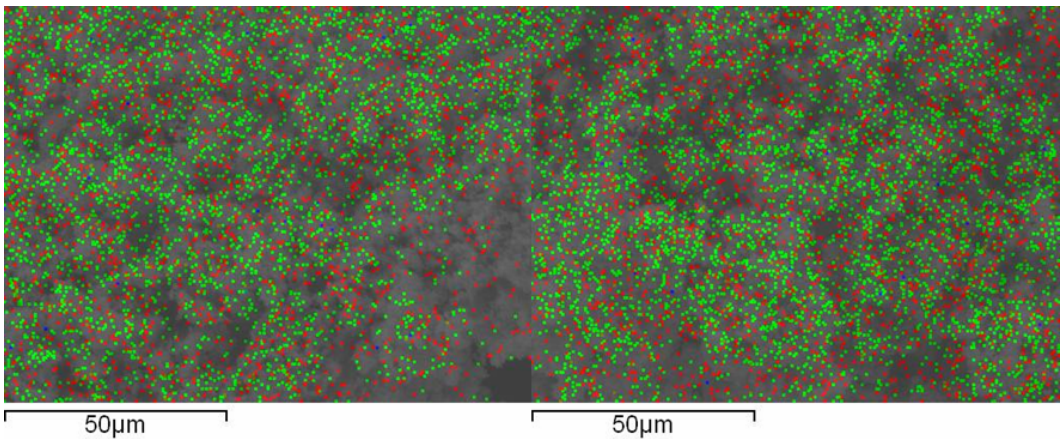

Figure 165: Element Maps for Fe_3Mo_3N post-reaction with 3:1 H_2/Ar at 900°C. Elements: Fe (red), Mo (green) and N (blue).

The EDX data for the post-reaction sample is provided in Table 42. Nitrogen was not detected in the areas measured by EDX. However, the elemental maps in Figure 165 detected some nitrogen, suggesting that it was present in the material in small amounts.

This agrees with the CHN analysis that showed a small amount of nitrogen remained in the material post-reaction. The ratio of iron to molybdenum is approximately as would be expected for this material.

Area	Fe weight (%)	Mo weight (%)	N weight (%)
1	41	59	0
2	36	64	0
3	36	64	0
4	44	56	0
5	39	61	0
6	40	60	0
7	36	64	0
8	51	49	0
9	38	62	0
10	36	64	0
11	39	61	0
Average	40	60	0

Table 42: EDX values for Fe_3Mo_3N post-reaction with 3:1 H_2/Ar at 900°C.

The decomposition of Fe_3Mo_3N was investigated by thermogravimetric analysis of the pre-reaction material under 3:1 H_2/Ar. The TGA curve and first derivative weight change of the material heated from room temperature to 1000°C at a ramp rate of 10°C/min under 3:1 H_2/Ar is provided in Figure 166. The first feature of the TGA curve is a weight loss of approximately 1.29 wt. % at 408°C and the second is a weight loss of 2.68 wt. % at 496°C. These could be due to the removal of the passivation layer or the loss of adsorbed water and needs to be investigated further.

At 668°C, a small feature is observed and results from a weight loss of 0.96 wt. %. This could be due to the decomposition of the molybdenum nitride to Mo metal as it has been previously shown to be reduced at this temperature under 1:3 Ar/H_2 [135]. The feature at 816°C is due to a weight loss of 3.25 wt. % and could be due to the decomposition of the material. It has previously been shown by *in-situ* powder neutron diffraction that the Fe_3Mo_3N does not decompose at 800°C under 1:3 Ar/H_2 and the nitrogen content remained unchanged [135]. Hence, the decomposition must occur between 800°C and 900°C. The expected weight loss due to the removal of nitrogen from the material and the decomposition of Fe_3Mo_3N to Fe and Mo metal is 2.98 wt. %. Therefore, this value agrees quite well with the weight loss of 3.25 wt. % that was observed.

The final feature at 929°C results in a weight loss of 6.94 wt. % and could be due to removal of some Mo metal from the material as it is volatile at high temperatures. However, this would need to be investigated further.

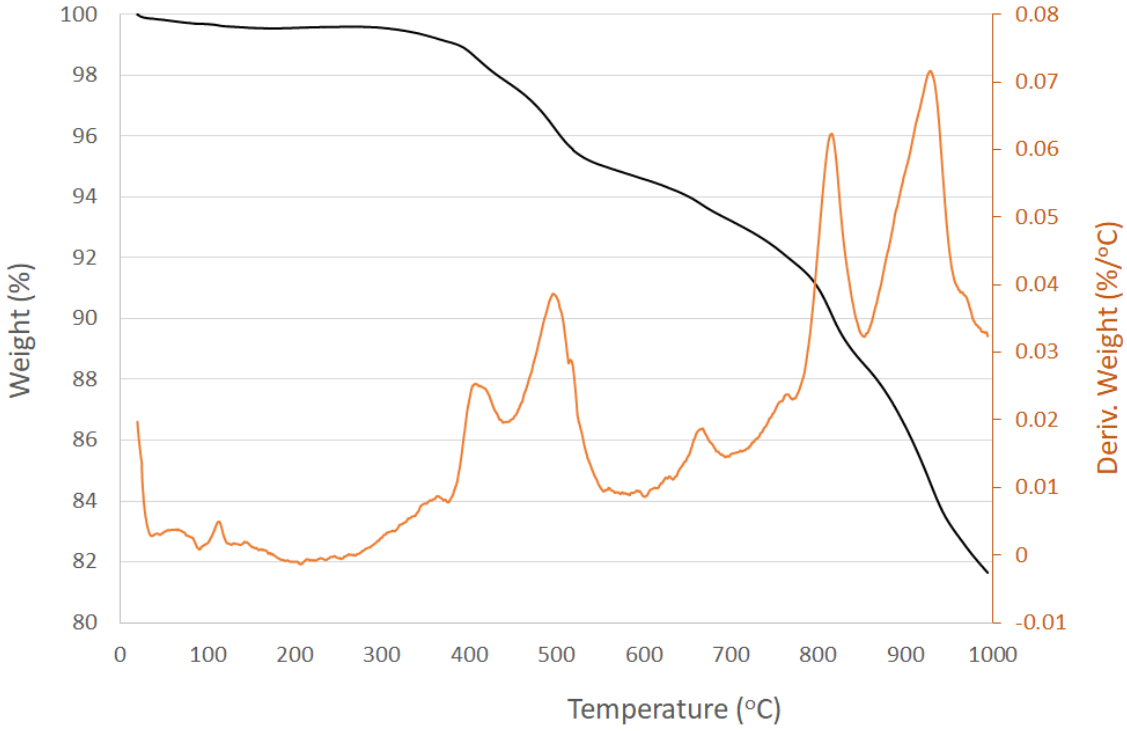

Figure 166: TGA and derivative weight profile of Fe_3Mo_3N under 75% H_2/Ar in the range from room temperature to 1000°C.

5.2.2 Iron Molybdenum Carbide (Fe_3Mo_3C)

Fe_3Mo_3C was prepared by carburisation of Fe_3Mo_3N with 20% CH_4/H_2 at 560°C. At this carburisation temperature, the η-carbide structure of the iron molybdenum material was maintained as seen in Figure 167.

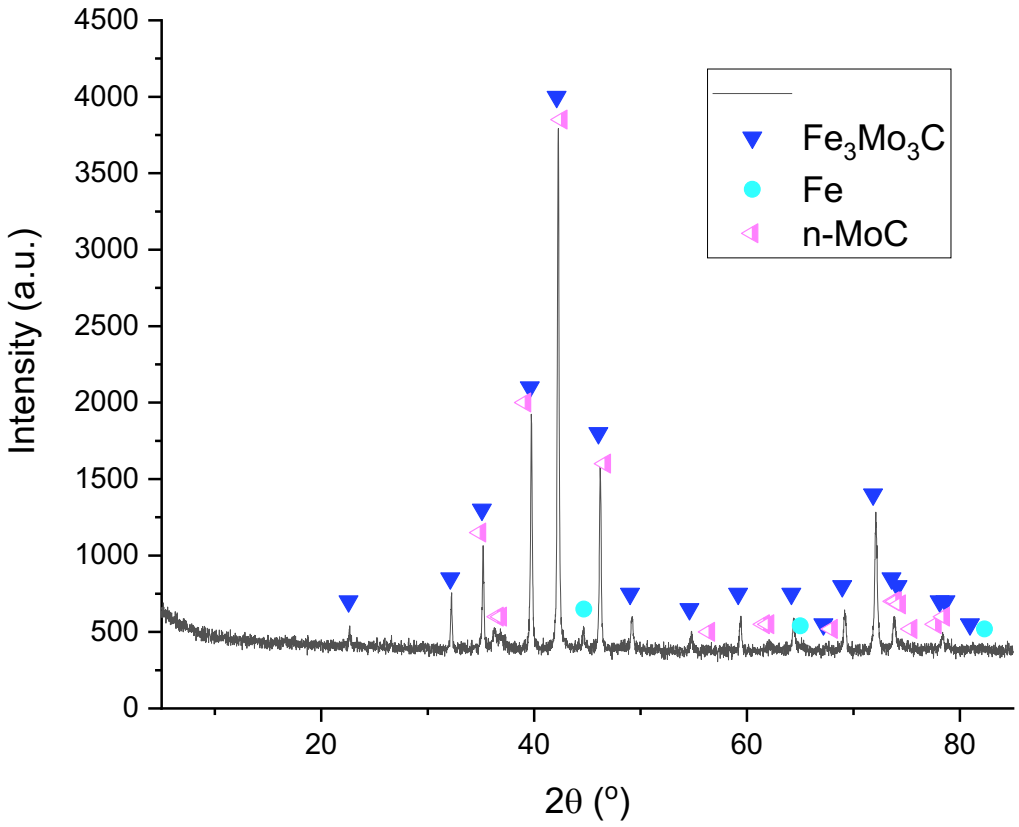

Figure 167: XRD pattern of iron molybdenum carbide (Fe_3Mo_3C). Reflections marked: ▼ Fe_3Mo_3C (JCPDS file number 00-047-1191), ● α-Fe (JCPDS file number 01-089-7194) and ◂ η-MoC (JCPDS file number 01-089-4305).

There appears to have been a shift in position of the peaks associated with the Fe_3Mo_3N to lower 2θ values as shown in Figures 168 and 169. This suggests that there was replacement of the lattice nitrogen with carbon and the formation of either Fe_3Mo_3C or a carbonitride phase. The atomic radii of carbon and nitrogen are 70 pm and 65 pm, respectively [125] and therefore, there is an increase in the unit cell size when carbon is incorporated. This carburisation process is topotactic and pseudomorphic in nature and therefore, the potentially complicating issue of changed morphology should not be a concern in this case. The MoN impurity had also undergone carburisation to form η-MoC. However, an iron phase was detected in the carburised material that was not present in the nitride sample. This suggests that there may have been a minor degree of phase instability, although the intensity of the reflections associated with the iron phase were very low. Reflections for Mo metal were not observed at 40.52° or 58.61° 2θ.

The elemental analysis showed that carbon was present in the material after carburisation and there was no nitrogen detected (C: 3.48%, H: 0.00% and N: 0.00%). Therefore, this would suggest that the material had been converted to the carbide. The expected stoichiometric value for carbon in Fe_3Mo_3C is 2.57%. The carbon content of the material

was greater than the calculated stoichiometric ratio. This could be a concern if the carbon encapsulates the ternary phase covering active sites.

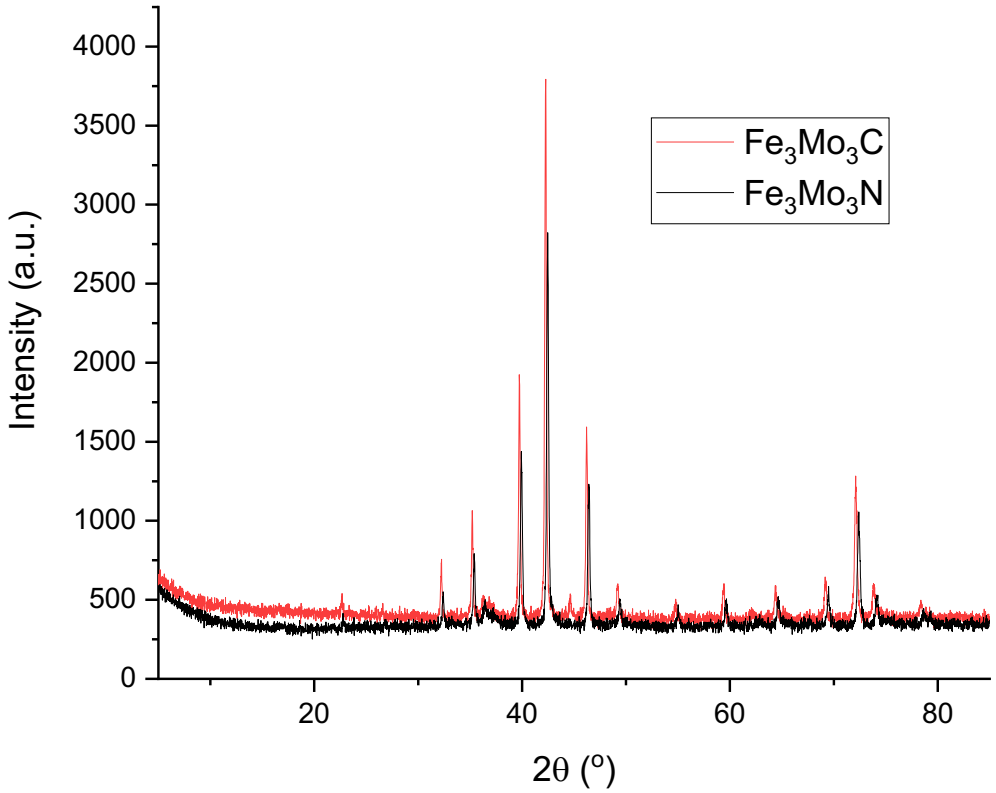

Figure 168: Comparison of XRD patterns for Fe_3Mo_3N and Fe_3Mo_3C showing shift in peaks associated with Fe_3Mo_3N.

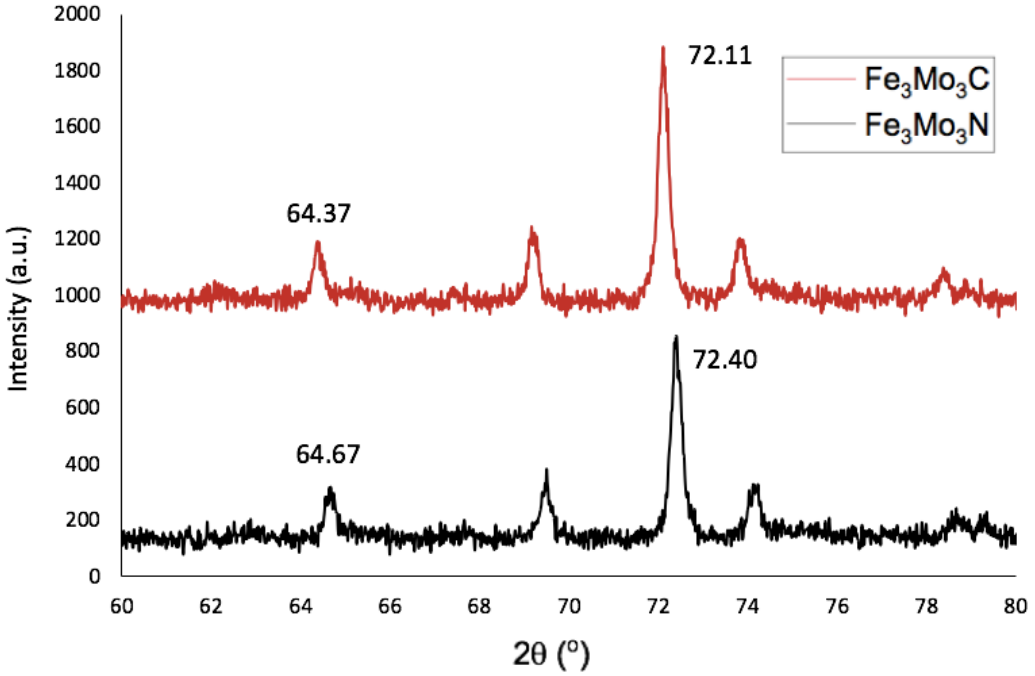

Figure 169: Comparison of XRD patterns between Fe_3Mo_3N (black) and Fe_3Mo_3C (red).

Raman spectroscopy was undertaken to investigate the nature of the excess carbon which was generated from carburisation. Bands associated with graphitic like carbon, which would be expected to occur at approximately 1320 and 1575 cm^{-1} were not observed in the spectrum, as shown in Figure 170. The bands at 973, 778 and 350 cm^{-1} were observed in the nitride and are assigned to $Fe_2(MoO_4)_3$ [146]. Therefore, an oxide layer was covering the surface of the carbide. Alconchel et al. did not detect any bands in the Raman spectrum of Fe_3Mo_3C [105]. However, these authors applied a lower laser power in their measurement. It has previously been shown that as the carbon content of a material increases, the fluorescence of the background increases [153]. Therefore, the fluorescence observed for this material may be due to the presence of carbon.

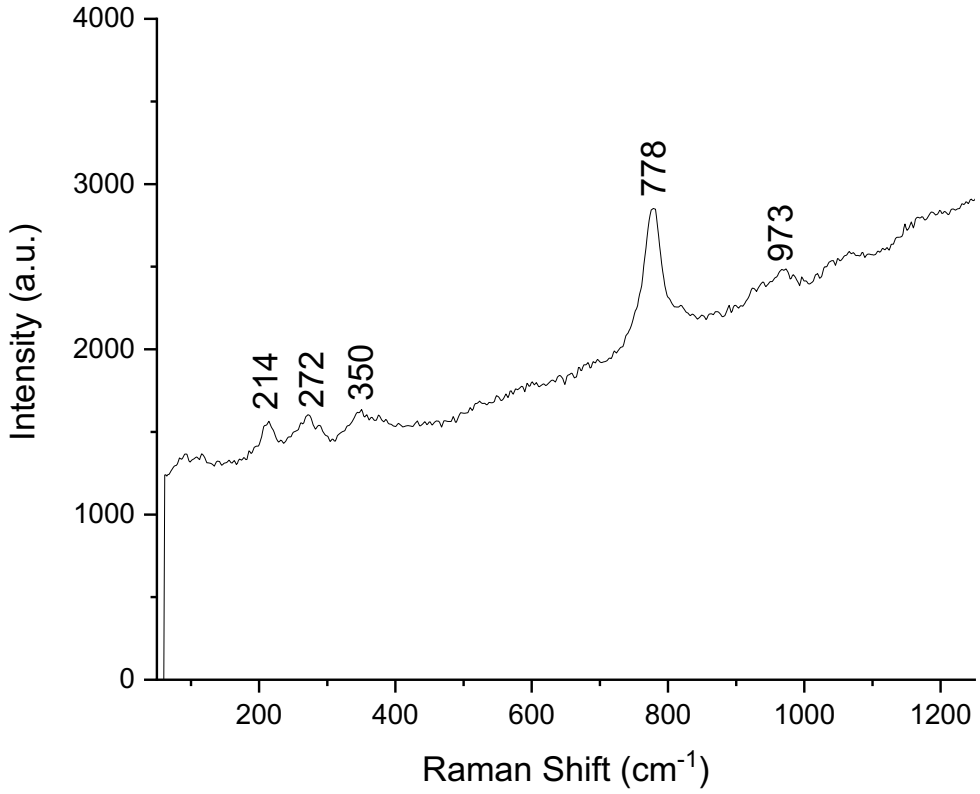

Figure 170: Raman spectrum of iron molybdenum carbide (Fe_3Mo_3C).

In order to compare the activity of the carbide with the nitride, it is important that the carburisation process was topotactic as reported. SEM images of the carbide have been taken in order to compare the morphology of the material with the nitride. Representative SEM images of Fe_3Mo_3C are displayed in Figure 171. These SEM images show the material had a very similar morphology to both the oxide precursor and the nitride as the material had an irregular morphology and contained rounded particles. The carburisation process is known to be topotactic and pseudomorphic for the iron molybdenum material [105]. It is important that the morphology of the nitride and carbide are the same, so that any differences in activity between the two materials cannot be related simply to a change

in morphology. There was no evidence that any additional structures, such as carbon nanotubes, had been formed, which is consistent with the Raman spectroscopic analysis presented above.

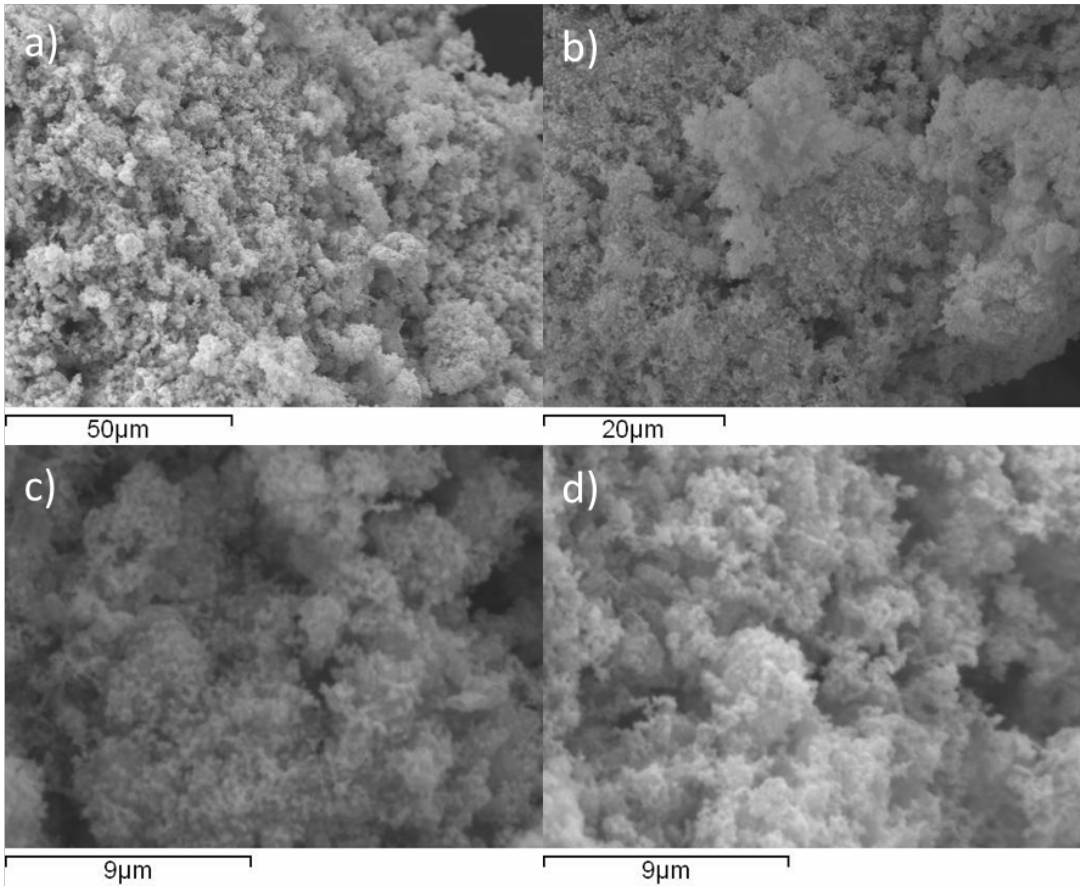

Figure 171: SEM images of iron molybdenum carbide (Fe_3Mo_3C). a) 1000x magnification, b) 2000x magnification, c) 6000x magnification and d) 6000x magnification.

The EDX analysis for Fe_3Mo_3C is provided in Table 43. The stoichiometric percentage of iron, molybdenum and carbon in the sample is 35.85 wt. %, 61.58 wt. % and 2.57 wt. %, respectively. The carbon weight percentage was greater than the expected stoichiometric percentage of carbon in Fe_3Mo_3C. However, EDX can be limited in analysing light elements and also it should be noted that in addition carbon stubs are used to mount the samples. Both the iron and molybdenum percentages were lower than the expected stoichiometric values due to the higher percentage of carbon.

Area	Fe weight (%)	Mo weight (%)	C weight (%)
1	29	51	19
2	27	54	18
3	29	49	22
4	28	50	22
5	31	48	21
Average	29	51	20

Table 43: EDX values for iron molybdenum carbide (Fe_3Mo_3C).

5.2.2.1 Ammonia Synthesis for Fe_3Mo_3C

Fe_3Mo_3C was tested for ammonia synthesis activity at 400°C and 500°C at atmospheric pressure under 3:1 H_2/N_2. This was performed to establish the influence the phase composition had upon ammonia synthesis activity. The material was not pre-treated before the reaction at 700°C as this would result in nitridation of the carbide and therefore, the activity would not be as a result of the carbide. Once the reaction had reached 400°C the conductivity values were recorded. The activity of the material at 400°C was very low and consequently, after 4 hours at 400°C, the temperature was increased to 500°C as shown in Figure 172.

The η-carbide structured Fe_3Mo_3C was not active for ammonia synthesis at 400 °C, unlike its corresponding nitride. The material became active at 500 °C and exhibited a steady state rate of 373 ± 55 μmol h^{-1} g^{-1}. There was an induction period of approximately 45 minutes before the material developed steady state ammonia synthesis activity when the reaction temperature was at 500°C. The Fe_3Mo_3N precursor was observed to have a rate of 403 μmol h^{-1} g^{-1} at 500°C. Therefore, these two materials have similar activities at this temperature. This behaviour is comparable to that reported for the isostructural Co_3Mo_3C [54]. Co_3Mo_3C required a temperature of 500°C and it also had an induction period that lasted for 40 minutes before it became active [54]. It was observed to undergo nitridation to form a carbonitride phase during the reaction. The carbonitride phase had a similar activity to its nitride at 500°C reaction temperature, with a rate of 461 ± 17 μmol h^{-1} g^{-1} [54].

The filled β-Mn structured $Ni_2Mo_3C_xN_y$ showed very different behaviour at 400°C reaction temperature. However, it is difficult to make comparisons between Fe_3Mo_3C and $Ni_2Mo_3C_xN_y$ as one of the materials contained lattice nitrogen prior to the determination of its activity for ammonia synthesis.

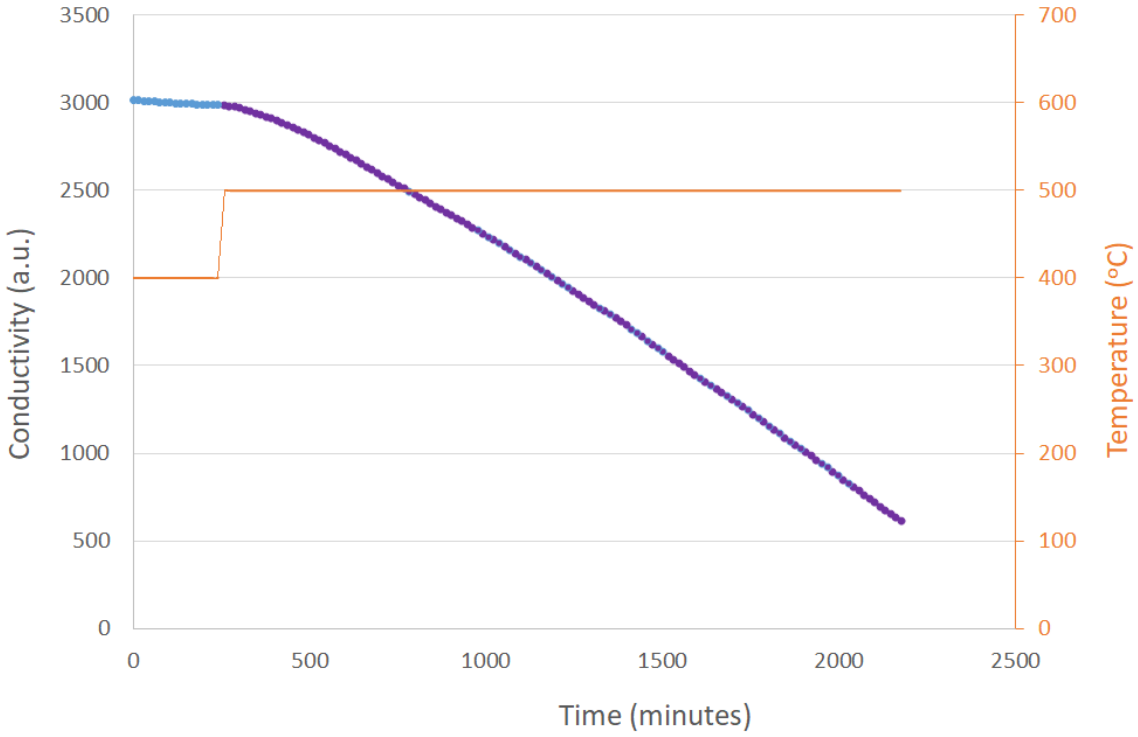

Figure 172: Conductivity profile for Fe_3Mo_3C reacted with 3:1 H_2/N_2 at 400°C for 4 hours and 500°C for 32 hours.

The XRD pattern in Figure 173 shows that the η-carbide structure was retained after the reaction and that the reflections had shifted to higher 2θ values. This can be more clearly seen in Figure 174. This suggests that some of the lattice carbon was replaced with nitrogen during the reaction, as this corresponds to a reduction in lattice parameter since nitrogen has a smaller atomic radius than carbon as discussed previously.

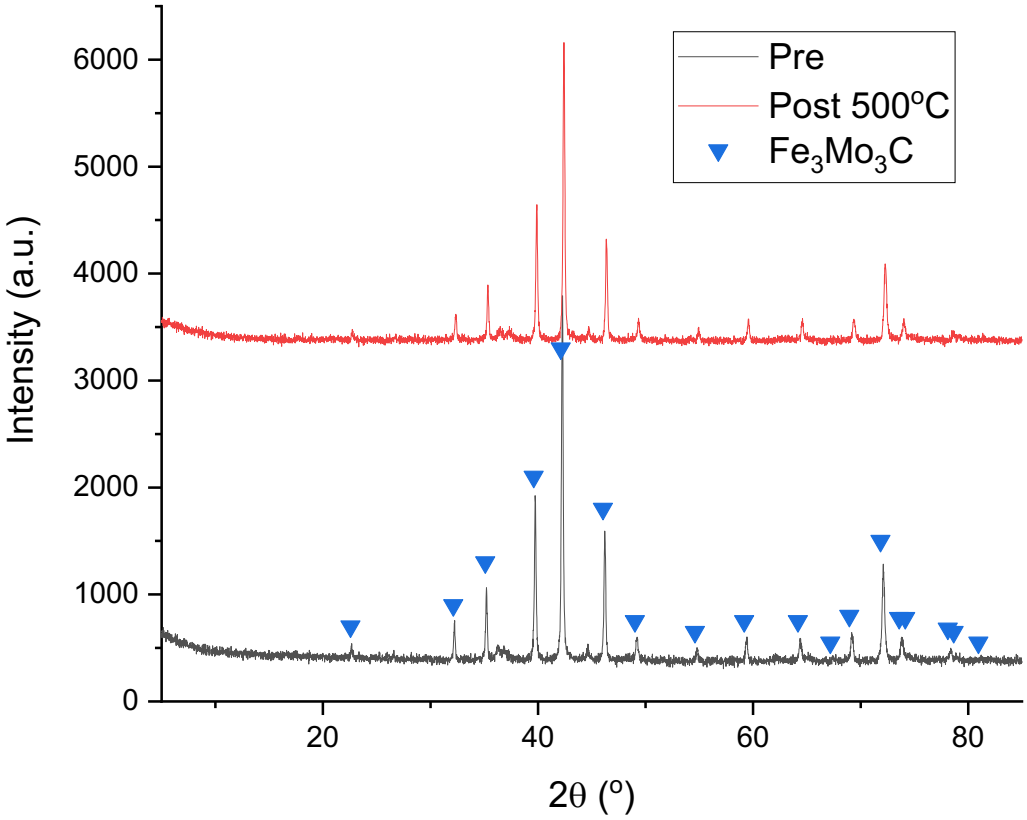

Figure 173: Comparison of XRD patterns for Fe_3Mo_3C pre- and post-reaction with 3:1 H_2/N_2 at 400°C for 4 hours and 500°C for 32 hours. Reflections marked: ▼ Fe_3Mo_3C (JCPDS file number 00-047-1191).

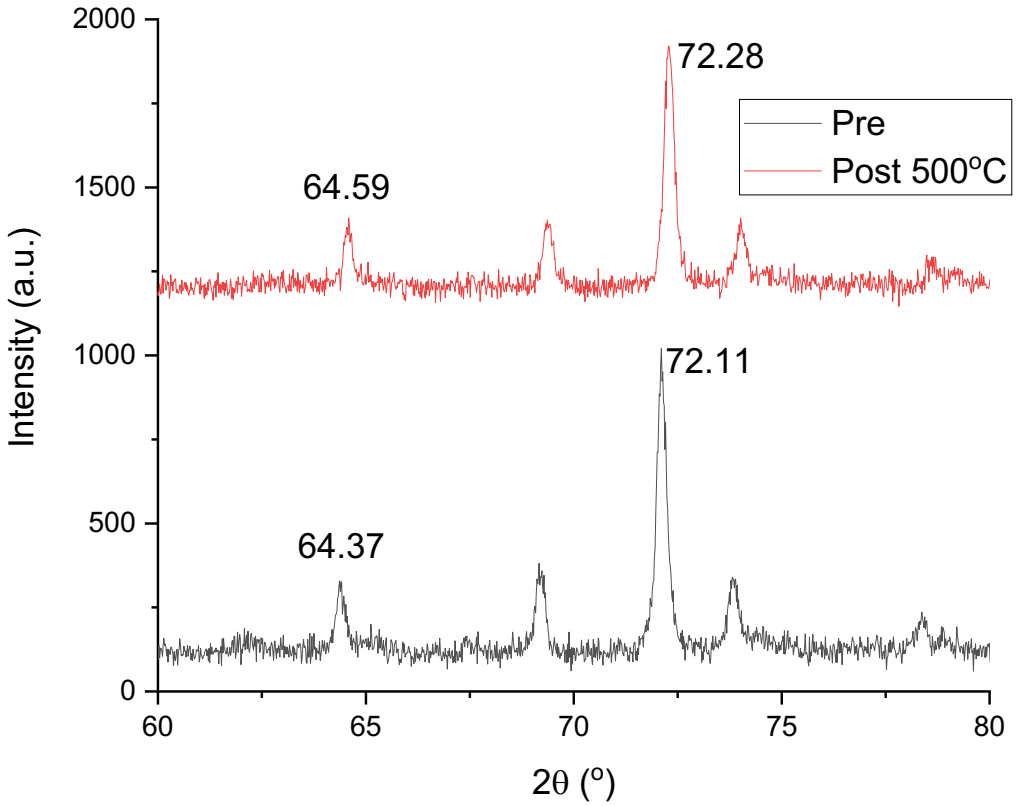

Figure 174: Comparison of XRD patterns between Fe_3Mo_3C pre- (black) and post-reaction (red) with 3:1 H_2/N_2 at 400°C for 4 hours and 500°C for 32 hours.

The elemental analysis presented in Table 44 for the material run in Figure 172 shows that there was substitution of lattice carbon by nitrogen during the reaction and therefore, a carbonitride phase had been formed. The stoichiometry calculated for the bulk sample post-reaction was $Fe_3Mo_3C_{0.41}N_{0.65}$. Therefore, it could be suggested that the induction period was due to the material not containing lattice nitrogen and once the material had enough lattice nitrogen, it became active. However, it is not clear whether the material was active because there was lattice nitrogen present or if lattice nitrogen resulted from the material being active for ammonia synthesis. The removal of the passivation layer and surface segregation/restructuring are also possible reasons for the induction period, which need to be taken into consideration.

Material	Calculated Stoichiometric Nitrogen Content (wt. %)	Calculated Stoichiometric Carbon Content (wt. %)	Nitrogen Content from Elemental Analysis (wt. %)	Carbon Content from Elemental Analysis (wt. %)
Fe_3Mo_3C Pre-reaction	-	2.57	0.00	3.48
Fe_3Mo_3C Post-reaction	-	2.57	1.94	1.05

Table 44: Elemental Analysis for Fe_3Mo_3C comparing pre- and post-reaction with 3:1 H_2/N_2 at 400°C for 4 hours and 500°C for 32 hours.

The representative SEM images of Fe_3Mo_3C post-reaction are given in Figure 175. The SEM images show a similar morphology to the oxide precursor, the nitride and the carbide pre-reaction. Therefore, the nitridation process did not result in a change in morphology. The material had a surface area of 3 m^2/g post-reaction, a pore volume of 0.03 cc/g and an average pore radius of 1002 Å.

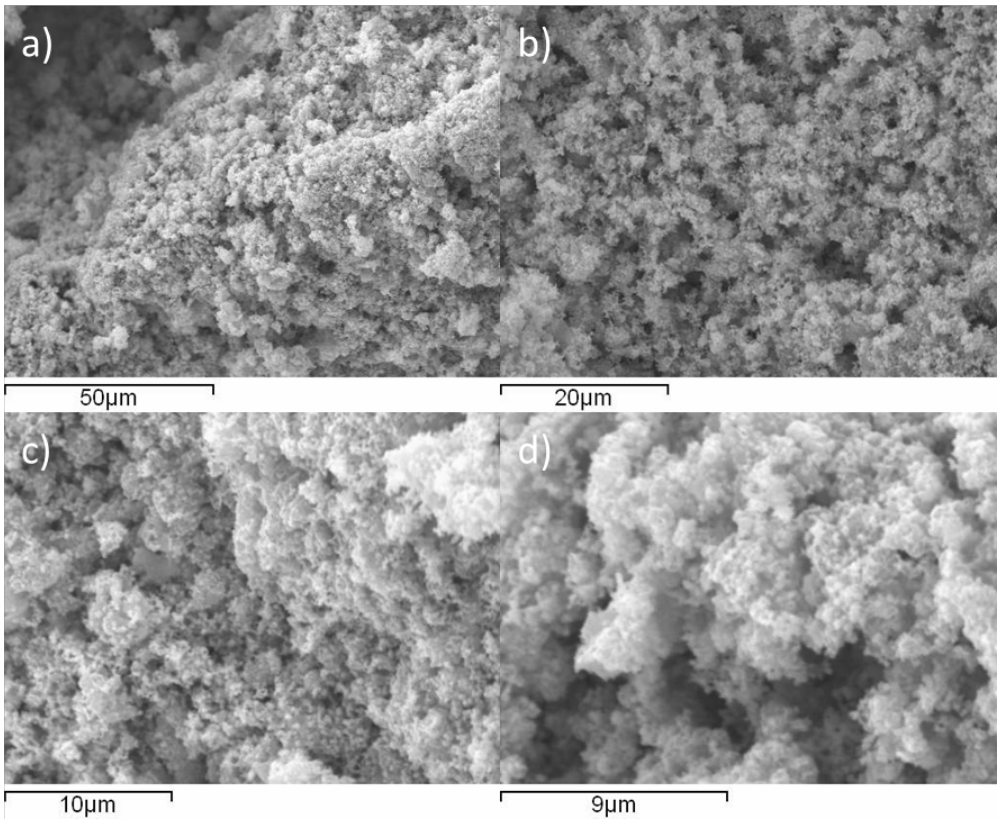

Figure 175: SEM images of Fe_3Mo_3C post-reaction with 3:1 H_2/N_2 at 400°C for 4 hours and 500°C for 32 hours. a) 1000x magnification, b) 2000x magnification, c) 4000x magnification and d) 6000x magnification.

The iron, molybdenum, carbon and nitrogen were evenly distributed across the sample as seen in the element map in Figure 176.

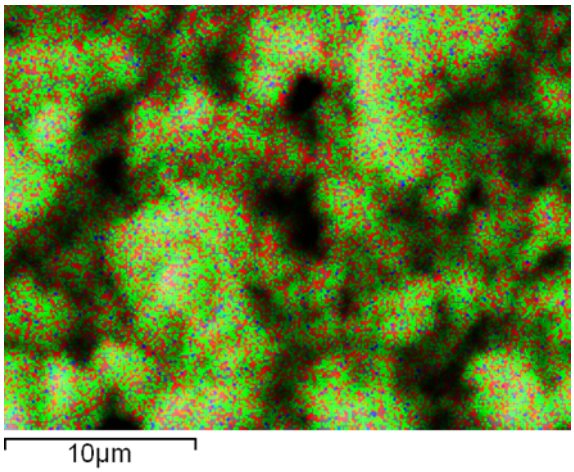

Figure 176: Element Maps for Fe_3Mo_3C post-reaction with 3:1 H_2/N_2 at 500°C. Elements: Fe (red), Mo (green), C (blue) and N (black).

Table 45 displays the weight percentage for each element given by the EDX analysis. From CHN analysis, the stoichiometry calculated for the bulk sample post 36 hour reaction at 500°C is $Fe_3Mo_3C_{0.41}N_{0.65}$. The stoichiometric percentage of iron, molybdenum, carbon and nitrogen in the sample should be 35.69 wt. %, 61.32 wt. %, 1.05 wt. % and 1.94 wt. %

respectively. As with the pre-reaction sample, the carbon percentage was higher than expected and the molybdenum percentage was lower. Nitrogen was detected in the post-reaction sample and this agrees with the elemental analysis that showed some lattice carbon had been replaced with nitrogen.

Area	Fe weight (%)	Mo weight (%)	C weight (%)	N weight (%)
1	30	53	12	4
2	33	53	11	3
3	31	49	20	0
4	32	51	11	6
5	34	55	8	3
6	34	55	6	5
7	35	54	7	4
Average	33	53	11	4

Table 45: EDX values for Fe_3Mo_3C post-reaction with 3:1 H_2/N_2 at 500°C.

The extent to which development of activity required the removal of the surface oxide layer and/or restructuring of the near surface region was investigated by ToF-SIMS. Analysis was performed on the pre- and post- 32 hour reaction materials. The ToF-SIMS data is provided in Appendix V. In Fe_3Mo_3C, the carbon is bonded to six molybdenum species and therefore, the mass fragments for this material would contain MoC species. As discussed before, the depth profiling of ^{92}MoC and ^{92}MoN mass fragments was used to determine if carbon and nitrogen were present near the surface of this material. For the pre-reaction carbide, nitrogen was detected, suggesting that the material may not have been completely carburised. However, the ToF-SIMS measurement has a sensitivity of the ppm/ppb range, which is far below that of the elemental analysis explaining the apparent discrepancy between the two techniques. Carbon was present in the material at a depth of 10 nm in both the pre- and post-reaction materials, suggesting that although there was an oxide layer, carbon was present near the surface.

For the post- 32 hour reaction material, the intensity of the ^{92}MoN fragment was approximately twice that of the pre-reaction material, which suggests that there was more nitrogen present near the surface of the material post-reaction. Furthermore, the intensity of the ^{92}MoC peak had decreased compared to pre-reaction. Although the intensities of the mass fragments were different compared to the pre-reaction material, there was no other change in the mass spectra, suggesting that the material had not undergone restructuring during the reaction.

As expected, oxygen was present in the pre- and post-reaction materials. The intensity of the oxygen mass fragments appeared to decrease as the depth increased, which is consistent with this being a surface oxide layer.

From the ToF-SIMS analysis, it can be stated that although there was a passivation layer, carbon and nitrogen were detected close to the surface of the material.

5.2.2.1.1 Ammonia Synthesis for Fe_3Mo_3C at 400°C

To examine the difference in activity between Fe_3Mo_3C and Fe_3Mo_3N at 400°C, the carbide has been investigated further post 400°C reaction. From the XRD pattern presented in Figure 177, it can be seen that the reflections have remained in the same position between pre- and post-reaction. This suggests that the lattice carbon had not been replaced with nitrogen during the reaction, although this conflicts with post-reaction CHN analysis which does indicate the introduction of 0.63 wt. % N content after reaction. This origin of this apparent contradiction is not clear and requires further investigation.

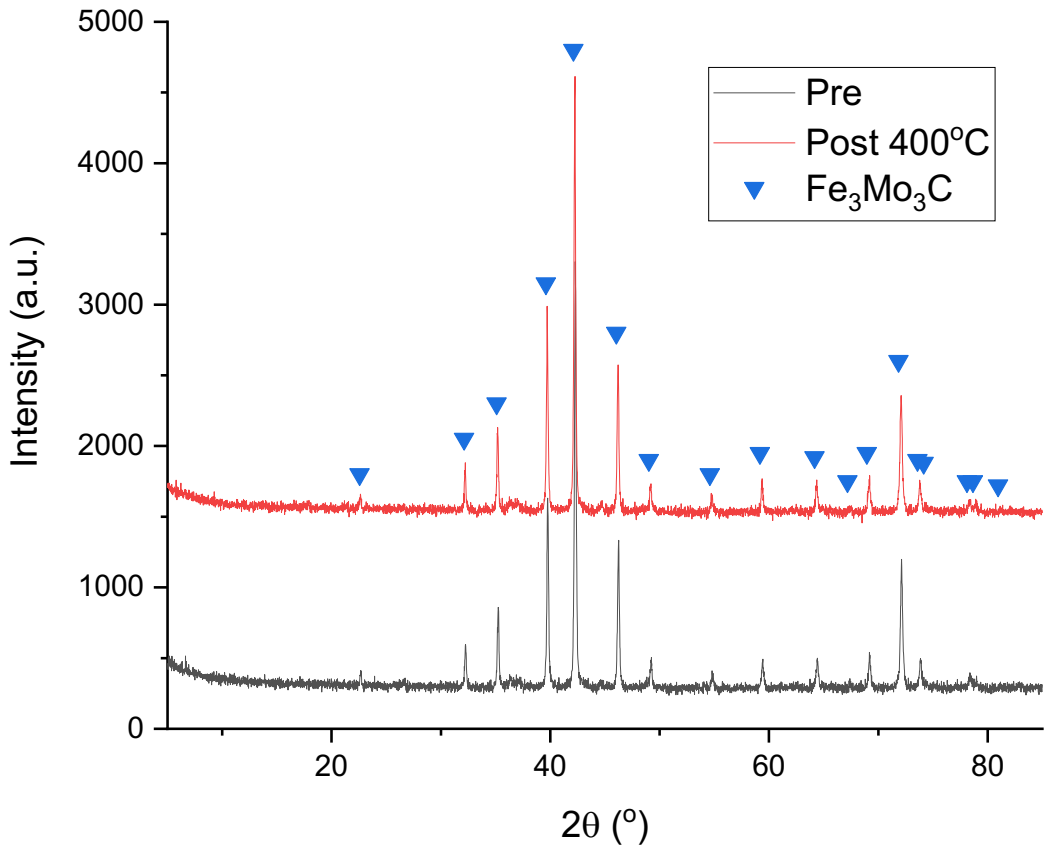

Figure 177: Comparison of XRD patterns for Fe_3Mo_3C pre- and post-reaction with 3:1 H_2/N_2 at 400°C for 7.5 hours. Reflections marked: ▼ Fe_3Mo_3C (JCPDS file number 00-047-1191).

The reduction of the carbide was investigated by thermogravimetric analysis of the pre-reaction material under 3:1 H_2/Ar. The TGA of the reduction of the carbide was performed

in order to investigate the difference in activity of the nitride and carbide and the reduction of the passivated layer. The TGA curve and first derivative weight change of Fe_3Mo_3C heated from room temperature to 1000°C at a ramp rate of 10°C/min under 3:1 H_2/Ar is displayed in Figure 178. Several weight loss steps are observed for Fe_3Mo_3C. The TGA curve appears to be similar to the TGA curve for Fe_3Mo_3N up to 750°C under the same conditions (Figure 166).

The first feature of the TGA curve is a weight loss of 0.63 wt. % at approximately 100°C and this possibly relates to the loss of water from the material. The second is a weight loss of 1.16 wt. % at 275°C. The mass spectra ion curve of m/z 44 shows a peak at this temperature as seen in Figure 179, suggesting the loss of either CO_2 or C_3H_8. The weight loss could be due to the reaction of lattice carbon to form propane or it could correspond to the removal of the passivation layer. The initial expectation would be that the removal of the passivation layer would generate water. However, the production of a mass spectral features with m/z 18 or 17 were not observed. CO_2 or C_3H_8 have different fragmentation pathways. Unfortunately, m/z 29, that would be observed as a mass fragment of propane, was not followed. However, the other m/z signals that were followed did not show any features. Therefore, the unique fragmentation pathways for both species were not observed and the species associated with the weight loss feature cannot be determined with any degree of certainty.

The third and fourth features of the TGA curve are weight losses of approximately 1.37 wt. % at 413°C and a weight loss of 1.99 wt. % at 493°C. These could be due to the reduction of an oxide surface layer producing water. M/z values of 2, 14, 15, 16, 17, 18, 28, 30, 32, 44 and 46 m/z were scanned but they did not show any features at these temperatures. When the reaction is run at 400°C, these features may not be removed from the material and this could explain the inactivity of the material at this temperature. However, the ToF-SIMS analysis for the pre-reaction material showed that carbon and nitrogen were observed near the surface of the material. Therefore, these features need to be investigated further.

A feature is observed at 662°C, which corresponds to a weight loss of 1.37 wt. %. The TGA profile of Co_3Mo_3C under H_2/Ar showed that the lattice carbon reacted to form methane resulting in a weight loss at 616°C [55]. Therefore, the weight loss at 662°C for Fe_3Mo_3C may be due to the loss of some lattice carbon from the ternary carbide. There was a mass feature for 44 m/z as shown in Figure 179 at a higher temperature at approximately 730°C.

The final feature that is observed above 900°C results in a weight loss of 1.97 wt. %. It is not clear what the weight loss corresponds to, as mass spectra of 2, 14, 15, 16, 17, 18, 28, 30, 32, 44 and 46 m/z did not show any features at this temperature. However, the weight loss above 900°C may be associated with decomposition of the material.

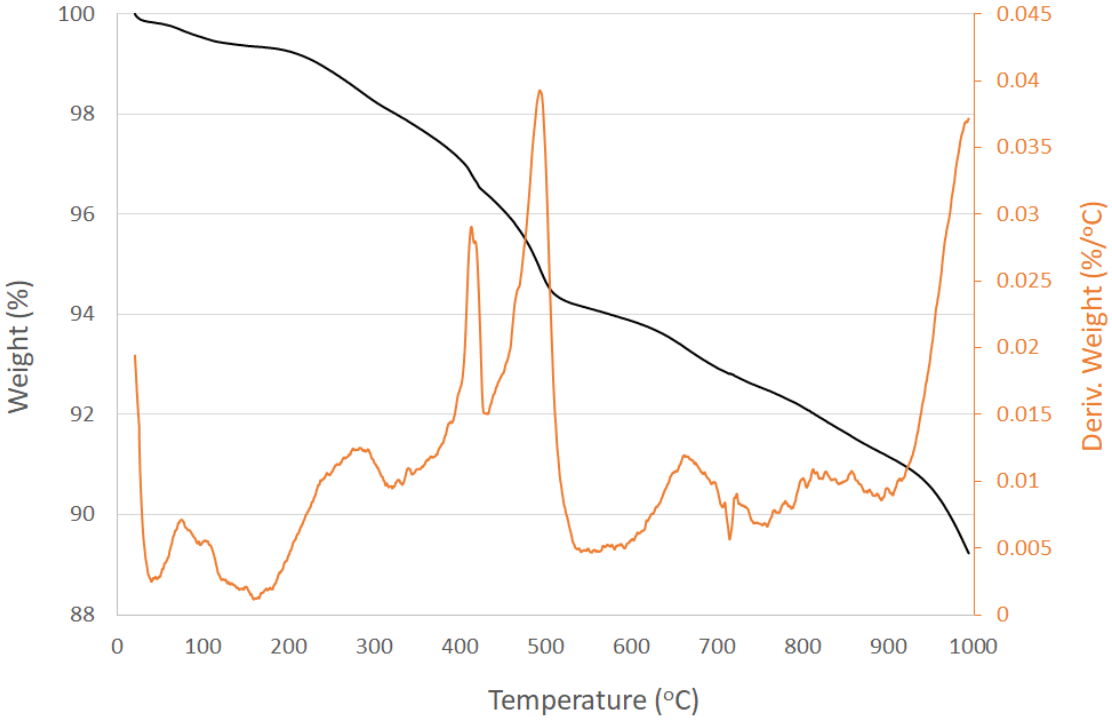

Figure 178: TGA and derivative weight profile of Fe_3Mo_3C under 75% H_2/Ar in the range from room temperature to 1000°C.

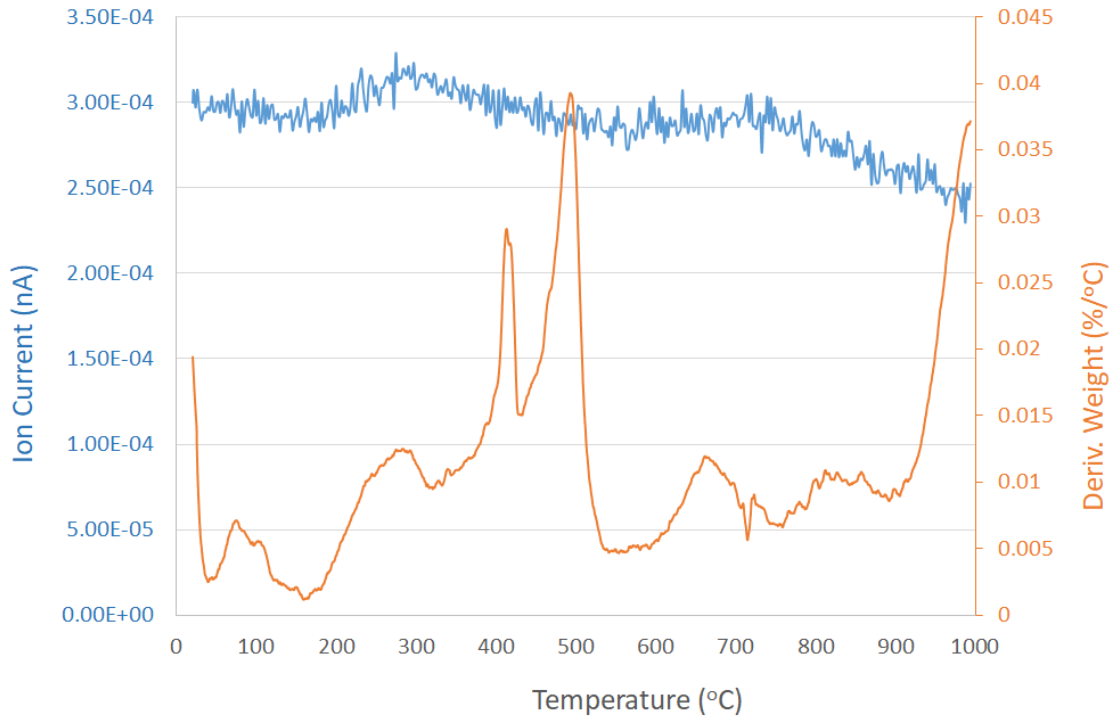

Figure 179: The mass spectrum ion curve for 44 m/z and the derivative weight profile.

5.3 Conclusions

In this chapter, the η-carbide structured Fe_3Mo_3N and Fe_3Mo_3C were examined for their ammonia synthesis activity. The lattice nitrogen reactivity of Fe_3Mo_3N was also investigated. The intention of this work was to gain a further insight into the effect the composition had on the activity. Although the bulk lattice nitrogen of Fe_3Mo_3N has previously been reported to be unreactive, the bulk mobility of the nitrogen may be limited and a Mars-van Krevelen type mechanism may still occur for the surface lattice nitrogen.

Fe_3Mo_3N was active for ammonia synthesis at 400°C and 500°C under 3:1 H_2/N_2. The nitride had a rate of 74 ± 1 μmol h^{-1} g^{-1} at 400°C and 403 μmol h^{-1} g^{-1} at 500°C. To determine the lattice nitrogen reactivity and stability of Fe_3Mo_3N, the nitride was reacted under 3:1 H_2/Ar at 900°C. The material decomposed and therefore, Fe_3Mo_3N was not stable under these conditions. In Chapter 4, the filled β-Mn structured Co_2Mo_3N and the η-carbide structured Co_3Mo_3N were shown to have a similar instability at 900°C.

The η-carbide structured Fe_3Mo_3C was also analysed for ammonia synthesis activity, to investigate the role the lattice nitrogen plays in Fe_3Mo_3N. The carbide was not active for ammonia synthesis at 400°C. A reaction temperature of 500°C was required and after an induction period, the material developed activity. The post-reaction XRD pattern and elemental analysis confirmed that the material underwent nitridation at 500°C and the material formed a carbonitride phase via a topotactic mechanism. These results were similar to those reported for the isostructural Co_3Mo_3N [55]. The difference in activity of Fe_3Mo_3N and Fe_3Mo_3C at 400°C suggests that the lattice nitrogen may be required in order for the material to be active. However, this needs to be investigated further as it is currently unknown whether the activity of Fe_3Mo_3C at 500°C occurs due to the nitridation of the carbide. There were a number of inconsistencies for the carbide tested at 400°C and therefore, this work should be repeated and this temperature would have to be investigated further. ToF-SIMS analysis was performed on the pre- and post-reaction Fe_3Mo_3C to investigate the effect the passivation layer had on the ammonia synthesis activity. Both carbon and nitrogen were detected in the near surface region of the material and therefore, it could be proposed that the passivation layer may have only a limited impact on the activity.

6. Osmium Based Compounds and Supported Mixed Metal Clusters

6.1 Introduction

6.1.1 Osmium

Osmium was discovered in 1803 by Smithson Tennant, who noticed that when platinum was added to dilute aqua regia, some powder remained. By using different acid and alkali treatments, Tennant separated the powder into two new elements, which he named osmium and iridium [154]. Osmium is a silver blue metal that is a member of the platinum group. The platinum group metals consist of six transition metals, which have high melting points and are corrosion resistant [11]. Osmium is the densest element with a value of 22.587 ± 0.009 g/cm^3 as calculated from X-ray diffraction [155]. It has a hexagonal close packed structure. In powdered form, osmium can be oxidised at room temperature to give osmium tetroxide. Due to the toxicity of the tetroxide, alloys of osmium are more commonly used than the pure metal. The metal can be used in pen nibs and needles of gramophones and also has applications as a catalyst [156] [157].

Osmium is found mainly with the other platinum group metals in mineral deposits, for example osmiridium, which consists of an alloy with iridium [11]. Osmium is obtained mostly from nickel refining and copper ores. It is estimated that only 10% of osmium is recovered from copper ore [158].

6.1.2 Osmium for Ammonia Synthesis

Osmium has had great historical interest as an ammonia synthesis catalyst, although there has been very little work in this area in recent years. In 1909, Haber discovered that osmium had a high activity towards ammonia synthesis with an 8% yield under reaction conditions of 175 atmospheres pressure and 600^{o}C [159]. Further work carried out by Mittasch [15] found that promoting the osmium with alkali metal oxides increased the yield from 2% ammonia to 4% at 550°C and 100 atmospheres pressure. However, osmium was a rare resource with approximately only 100 kg of it available in the world at that time [160]. Therefore, it was vital to find another catalyst that was cheaper as well as having a high ammonia synthesis rate. This led to the development of the promoted Fe catalyst that is used today in essentially unchanged form in the Haber-Bosch Process.

In 1982, Rambeau et al. [161] [162] reported their studies on the hydrogenation of nitrogen on an osmium powder at atmospheric pressure and over the temperature range 100 to 500^{o}C. They concluded that catalytic ammonia synthesis over osmium is limited by

adsorption of nitrogen and is inhibited by both hydrogen and ammonia. A decrease in the nitrogen pressure resulted in a decrease in the ammonia produced. The reaction order with respect to nitrogen was shown to be one. As hydrogen pressure decreased, both the ammonia pressure and inhibition due to ammonia, increased. A negative first order was observed for the hydrogen, which suggests hydrogen inhibition that is strong. As hydrogen inhibition affected the activity of osmium, Rambeau et al. proposed a cyclic operation for ammonia synthesis to overcome this problem [162]. Firstly, they saturated the surface of the osmium with pure nitrogen. Then, the adsorbed nitrogen was hydrogenated under pure hydrogen. By using this method, it was proposed that rates of industrial relevance could be achieved at atmospheric pressure. When 3:1 H_2/N_2 was used, a rate of approximately 0.5 x 10^{-6} mole NH_3/min was reported at 400°C and when the cyclic procedure was used the rate was approximately 0.9 x 10^{-4} mole NH_3/min [162].

Ozaki et al. [163] investigated the ammonia synthesis activity of different transition metals including osmium. The catalyst was prepared by supporting osmium tetroxide on coconut carbon and promoting it with potassium. A stoichiometric ammonia synthesis reactant mixture and a pressure of 0.79 atmospheres were utilised. The rate of ammonia synthesis was determined over a temperature range of 100 – 400°C. Of the transition metals tested, both ruthenium and osmium ranked highest for their activity. At 253°C, osmium had a reported rate of approximately 4 mL STP NH_3/hr and ruthenium had a rate of approximately 10 mL STP NH_3/hr [163]. It is interesting to note that the materials were inactive in the absence of potassium promotion. It was concluded that this effect was due to the potassium transferring electron density to the transition metal causing the adsorbed nitrogen to be converted to an anionic intermediate. When potassium was replaced with sodium, the activity decreased, which was explained as resulting from sodium's higher ionisation potential.

A recent DFT study by Ishikawa et al. examined the catalytic performance of osmium for ammonia synthesis [164]. It was proposed that the most active sites are step sites with an increase in turnover frequency of 10^4 for these sites compared to the sites on the (0001) surface terrace plane. The maximum concentration of the active step sites was expected to occur at an osmium particle diameter of 3-4 nm. However, it was proposed that NH_2 species can block these active sites, which prevents N_2 dissociation and results in a lower TOF (turnover frequency) than predicted. Ru has a similar value to Os for the activation barrier for N_2 dissociation at the step sites. Conversely, Ru has a higher catalytic activity than Os due to it having a higher number of vacant sites [164].

6.1.3 Comparison of Osmium with Iron and Ruthenium for Ammonia Synthesis

Osmium is located in the same group as iron and ruthenium in the periodic table. These two elements are used as commercial ammonia synthesis catalysts and therefore, it would be of interest to compare the activity and behaviour of osmium with them. The activity of ruthenium has been found to be higher than iron and hence, with osmium below ruthenium in the group, it would be of interest to further compare these three elements.

Ruthenium is considered to have the close to optimal binding energy for nitrogen [24], explaining the high activity of this metal. The metal is structure sensitive for ammonia synthesis, with B_5 sites being the active site for the reaction [165]. B_5 step sites are associated with three Ru atoms in one layer and two Ru atoms in the layer above, with some of the Ru having low-coordination, for example edge atoms. The B_5 sites have a particle size dependence, where particles of 1.8–2.5 nm have the optimum number of B_5 sites [165]. Therefore, Ru is the most active when it is supported as shown by the KAAP Process using Ru based catalyst supported on carbon. The choice of support is known to play an important role in the number of B_5 sites due to the support controlling the Ru morphology [165].

Ammonia synthesis on iron is also a structure sensitive reaction [166], with the Fe (111) plane having a much higher activity than the Fe (100) and the Fe (110) planes [167] [168] [169]. It was suggested that C_7 sites were the most active in iron catalysts [169]. C_7 sites consist of surface iron atoms with seven neighbours. Iron has been observed to have a higher activity when it is in bulk form [166]. Iron was shown to have a higher TOF when the iron particle size was large, showing a dependence on metal particle size.

Since, as stated above, osmium is in the same group as iron and ruthenium, it would be of interest to examine the nature of any potential structure sensitivity for osmium, which to the author's knowledge has not been investigated, to suggest potential strategies for further enhancing its catalytic performance. In order to undertake this, preliminary comparisons have been made between the performance of bulk metallic osmium and that for supported osmium prepared from a well-defined cluster compound precursor.

6.1.4 Osmium Carbonyl Clusters

Cotton first referred to a metal cluster as a material that contains metal-metal bonds [170]. A more specific definition is a collection of two or more metal atoms, which are bonded directly. Metal clusters are considered to be intermediate between mononuclear and polynuclear complexes. This means that they have similar properties to both; for example,

similar to mononuclear complexes, the clusters can be isolated and characterised by spectroscopy but they can also have delocalised metal to metal bonds. A common type of metal cluster is a metal carbonyl cluster. These are compounds that have two or more metals connected by metal bonds where the ligands are either entirely or predominately carbon monoxide. The nuclearity of the metal carbonyl clusters can vary greatly, with $Os_3(CO)_{12}$ being the compound of interest within this chapter. The structure of $Os_3(CO)_{12}$ is presented in Figure 180.

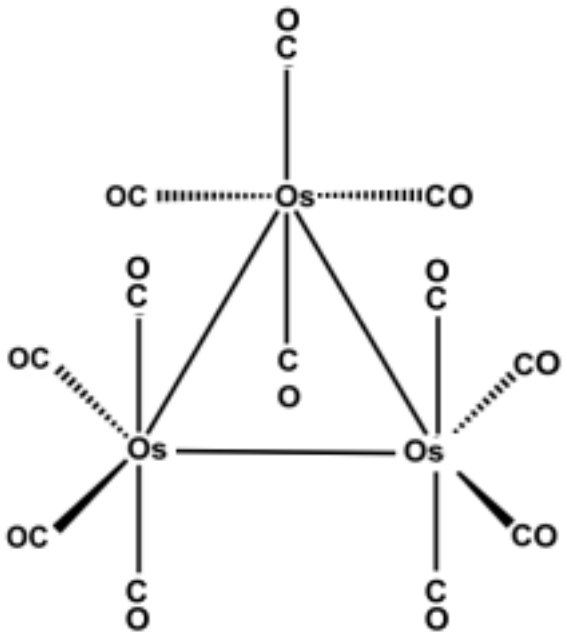

Figure 180: Structure of $Os_3(CO)_{12}$ at low temperature [171].

During the 1970s and 80s, there was growing interest in the application of metal carbonyl clusters as catalysts [36]. Metal carbonyl clusters have been utilised as heterogeneous catalysts by being used as precursors which can be impregnated onto supports such as silica and alumina. This provides some advantages over conventional heterogeneous catalysts. For example, if the cluster is retained on the support, there is extra control over its composition and nuclearity, which can have an effect on its activity and selectivity. Another advantage supported carbonyl clusters may have over conventional catalysts, is that their activity may sometimes be retained after being exposed to air, as is seen for supported osmium and ruthenium carbonyl clusters in the reaction of ethane hydrogenolysis [172]. When osmium on silica is exposed to air, an induction stage of a number of minutes is required before activity is restored. There is no such induction stage necessary for the cluster materials. Although the oxygen dissociates on adsorption, a reason for the catalysts not being affected by exposure to air could be due to the adsorption of oxygen being weak such that it is still reversible at 152°C.

As they are small molecules, the catalytic behaviour of clusters can be seriously affected by how they interact with the support. This strong interaction between the cluster and the support is of great interest and has been studied for $Os_3(CO)_{12}$ and $Os_6(CO)_{18}$ on silica, alumina and titania [51]. Previously, the osmium cluster compounds were thought to be reduced to monometallic species during the preparation of the precursor onto the oxide support [173]. The interaction of the support with the cluster was believed to occur through the hydroxyl groups. However, if the support is severely dehydroxylated before the precursor is impregnated, it has been shown from IR and UV-visible spectroscopy, that clusters remain intact on the support [51].

Yunusov et al have studied some carbonyl clusters for their ammonia synthesis activities [174]. They prepared $K_2[Ru_4(CO)_{13}]$, $K_2[Fe_2(CO)_8]$ and $K_2[Os_3(CO)_{11}]$ on two different carbon supports. The first carbon support was a commercial SKT and the second was an active carbon called sibunit. Sibunit was prepared from carbon black and differs from the other carbon support as it has a mainly mesoporous structure [175]. In addition, it has a very low amount of impurities with a carbon content of 99.4 wt. % compared to the 85.9 wt. % for SKT. The type of metal and carbon support had a great influence on the rate of ammonia produced. The ruthenium compound on sibunit was found to be the most active, with ammonia being produced from as low a temperature as 250^{o}C. Next active was the osmium on sibunit and the iron on sibunit was discovered to have the lowest activity. $K_2[Ru_4(CO)_{13}]$], $K_2[Os_3(CO)_{11}]$ and $K_2[Fe_2(CO)_8]$ on sibunit had a reported ammonia synthesis rate of 14.9 mL NH_3 h^{-1} g^{-1} cat., 11.3 mL NH_3 h^{-1} g^{-1} cat. and 0.7 mL NH_3 h^{-1} g^{-1} cat., respectively at 400^{o}C and atmospheric pressure [174]. When the SKT carbon was used, ammonia was only produced at 400^{o}C and the catalyst deactivated with the activity rapidly decreasing within the first hour of testing.

6.1.5 Mixed Metal Carbonyl Clusters

A variety of mixed metal carbonyl clusters can be formed from the Group 8 elements. Generally, these materials are prepared as part of a mixture of products, which need to be separated by chromatography techniques [176] [177]. Therefore, the percentage yield of the desired product can vary from low to reasonable yields depending on the synthesis method used [178] [179]. In a typical synthesis, the monometallic metal carbonyls are dissolved in a solvent and left for a period of time. After this, column chromatography or thin layer chromatography are used to isolate the mixed metal carbonyl cluster. For example, $Os_2Ru(CO)_{12}$ and $OsRu_2(CO)_{12}$ can be synthesised from thermal decomposition of $Ru_3(CO)_{12}$ and $Os_3(CO)_{12}$ in xylene [180].

The mixed metal carbonyl clusters are usually isostructural with one of the starting monometallic metal carbonyl precursors as observed by XRD and IR measurements [176] [178] [181]. For example, $FeOs_2(CO)_{12}$ has been suggested to be isostructural with $Os_3(CO)_{12}$, with one of the osmium being replaced with iron [176].

Kulkarni and Gates [52] have proposed that supported bimetallic clusters can be formed by heating metal carbonyls, resulting in decarbonylation and metal-metal bond formation. This was shown by supporting $Os_3(CO)_{12}$ and $Ru_3(CO)_{12}$ on MgO and heating the material under H_2. Through IR and EXAFS spectroscopy, it was observed that Ru-Os bond formation occurred at 125°C after partial decarbonylation of the two precursors. This is a promising method for forming supported mixed metal carbonyl clusters and overcomes the issue of separating the desired product by chromatography.

6.2 Results and Discussion

6.2.1 Bulk Osmium Metal

The XRD pattern in Figure 181 shows that only osmium metal was present, as expected. This demonstrates that the metal had not formed bulk osmium tetroxide while being in contact with air. However, a surface oxide layer may have formed, which would not be detectable by XRD analysis.

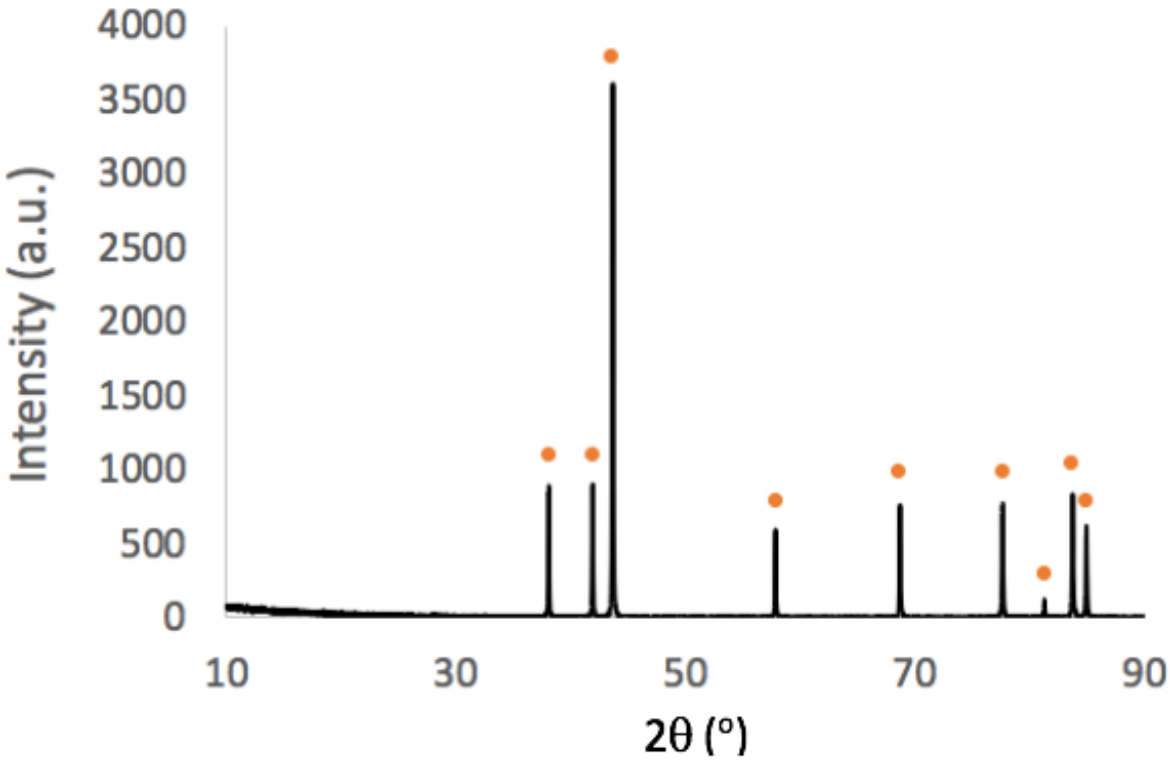

Figure 181: XRD pattern of osmium metal. Reflections marked: • Os (JCPDS file number 00-006-0662).

The BET surface area of the osmium was measured to be 2 m^2/g. According to Pinto and Paniego [182], osmium tetroxide can be formed when osmium is in the presence of oxygen or air. When the sample is in contact with air for a short time, a monolayer of oxygen is adsorbed onto the surface. If this is the case, then the BET surface area value for the osmium powder might not be a truly representative measurement in relation to that exhibited under reaction conditions.

The SEM images for osmium metal at different magnifications are presented in Figure 182. The material had an irregular structure with an agglomeration of small rounded crystallites. Some areas had a smoother surface as can be seen in Figure 182 (b). Only osmium was detected by EDX analysis for this material and no other element was observed.

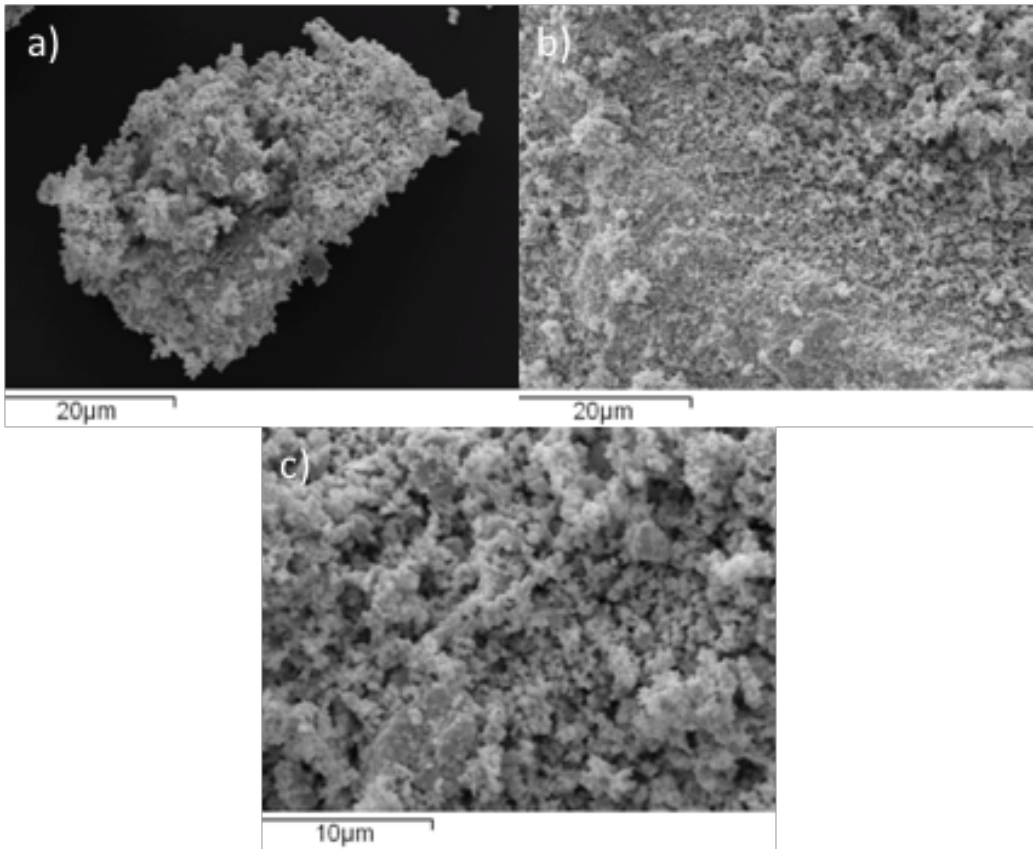

Figure 182: SEM images of the bulk osmium sample. a) 2000x magnification, b) 4000x magnification and c) 4000x magnification.

The bulk osmium sample was pre-treated with different gas mixtures to examine the potential inhibition of nitrogen and hydrogen on the surface. As stated in the introduction of this chapter, hydrogen was shown to inhibit the reaction and nitrogen coverage can also affect the rate [162]. These factors may therefore affect the ammonia synthesis rate of the osmium sample tested.

The metal was first pre-treated at 500°C for 2 hours with one of the following gas mixtures: 1:3 N_2/H_2, 1:3 Ar/H_2 or pure N_2. This pre-treatment temperature was employed to replicate the conditions used by Rambeau et al. [161] [162]. The temperature was then decreased to 400°C and the ammonia synthesis reaction was performed under 1:3 N_2/H_2. The ammonia production reaction profile for the osmium metal at 400°C after the three pre-treatments is presented in Figure 183. When 1:3 Ar/H_2 and pure N_2 were used as the pre-treatment gas, a lag period of approximately 20 minutes was observed before the material became active. However, when using a N_2/H_2 pre-treatment, this was not observed and the decrease in conductivity versus time resulted in a linear profile over the 12.5 hours of testing. Line flushing tests were undertaken to ensure that the lag period was not due to any experimental artefacts. For the 1:3 Ar/H_2 and N_2 pre-treated samples, beyond the induction period, the activity was observed to be steady state.

One possible explanation is that N_2, in the case of the N_2 pre-treatment, and H_2, in the case of the Ar/H_2 pre-treatment, cover the surface of the osmium during the pre-treatment. Hydrogen has been shown to inhibit the ammonia synthesis reaction for osmium and therefore, the coverage could block the active sites. The coverage of nitrogen may also block the active sites and thus delay the start of the reaction. The hydrogen may also reduce the osmium to an active phase and hence, would be required in the pre-treatment step. It might also be the case that the surface facets to an active form in the presence of the reactant mixture under these reaction conditions. The origin of this lag period, to eliminate any other potential artefacts, should be investigated further.

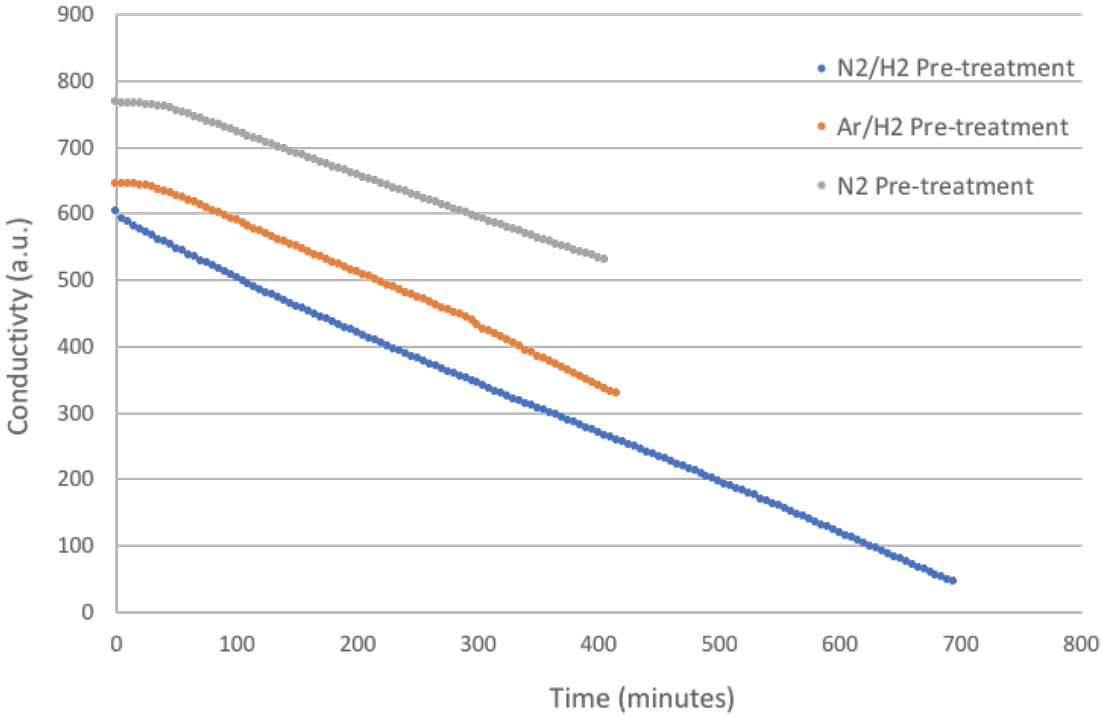

Figure 183: Conductivity profiles for osmium reacted with 3:1 H_2/N_2 at 400°C after different pre-treatments. Labels: 1:3 N_2/H_2 pre-treatment (blue), 1:3 Ar/H_2 pre-treatment (orange) and N_2 pre-treatment (grey).

The steady state ammonia synthesis rates relating to the tests employing the bulk osmium sample at 400°C are displayed in Table 46. In comparison, the rate of osmium metal at 500°C under 1:3 N_2/H_2 during the pre-treatment was 262 ± 21 μmol h^{-1} g^{-1}.

It can be seen that the pre-treatment gas possibly had a small effect on the ammonia synthesis activity of osmium. The metal had the highest activity at 400°C when the 1:3 N_2/H_2 pre-treatment was used. However, the three values for the different pre-treatment samples are within experimental error. In comparison, the promoted iron Haber Bosch catalyst has been reported to exhibit a rate of 330 μmol h^{-1} g^{-1} under comparable conditions [127]. A previous study on the comparative ammonia synthesis activity of Os and Fe, suggested that the activity of osmium was 100 times lower than iron powder at 1 atmosphere pressure and 400°C, when a stoichiometric ratio of N_2:H_2 was used [161]. The inhibition by hydrogen on osmium was proposed as the explanation for the lower activity compared to iron, which does not suffer from inhibition by hydrogen [161]. The rate of N_2 chemisorption on a bare osmium surface was reported to be 100 times higher than that for Fe and 100 times lower than that for Ru [161]. However, it is important to note that other studies show that osmium metal has a higher activity than iron [24] [15] [183].

Pre-treatment	NH_3 Synthesis Rate (μmol h^{-1} g^{-1})
1:3 N_2/H_2	79 ± 1
1:3 Ar/H_2	64 ± 16
N_2	69 ± 3

Table 46: Ammonia synthesis rates of osmium under 3:1 H_2/N_2 at 400°C after different pre-treatments.

The post-reaction XRD patterns for osmium that had undergone different pre-treatments are displayed in Figure 184. The XRD patterns were found to display only the pattern for osmium metal. CHN analyses undertaken for the pre-reaction and all the post-reaction samples did not evidence the formation of any bulk nitrogen or hydrogen content.

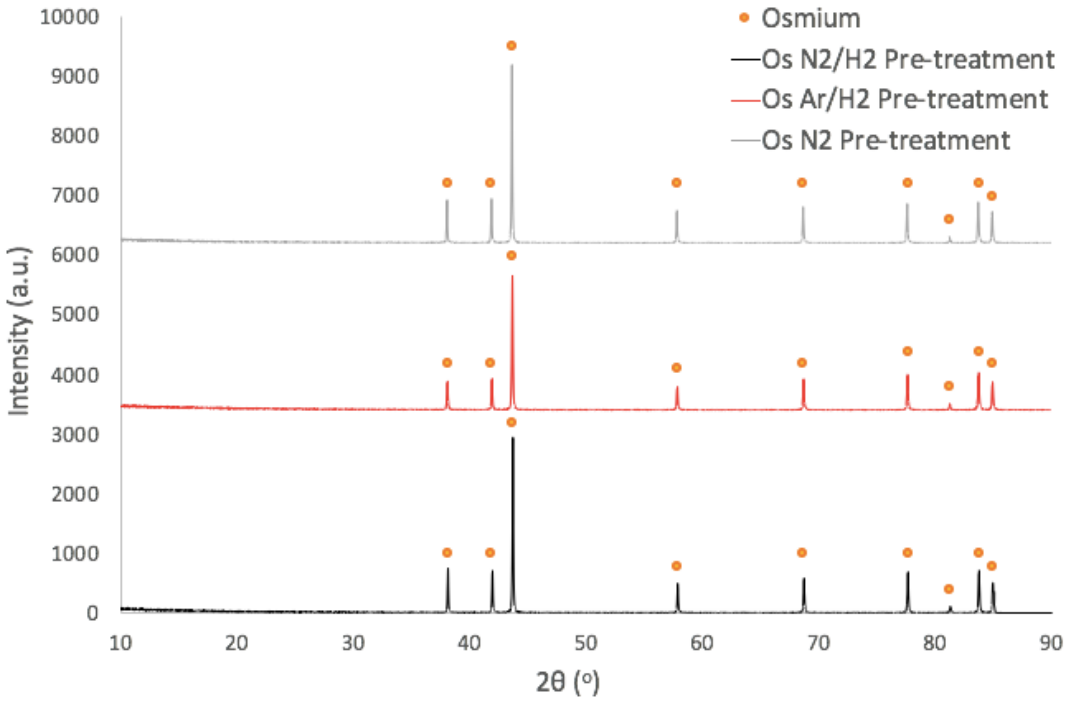

Figure 184: XRD patterns of osmium metal post-reaction with different pre-treatments. Reflections marked: • Os (JCPDS file number 00-006-0662).

Compared to pre-reaction, there did not appear to be a change in morphology of the osmium post-reaction for all three pre-treatments. Representative SEM images of osmium that had undergone the three pre-treatments are shown in Figure 185. The samples consisted of an irregular morphology, with small rounded crystallites. Therefore, the lag period did not appear to be due to a change in morphology between the pre-reaction and Ar/H_2 and N_2 pre-treated samples. Whilst the post-reaction material that was pre-treated with 3:1 H_2/N_2 had a surface area of 3 m^2/g, the small difference with respect to the pre-reaction material is not significant particularly in view of the uncertainties associated with the determination of such low BET surface areas.

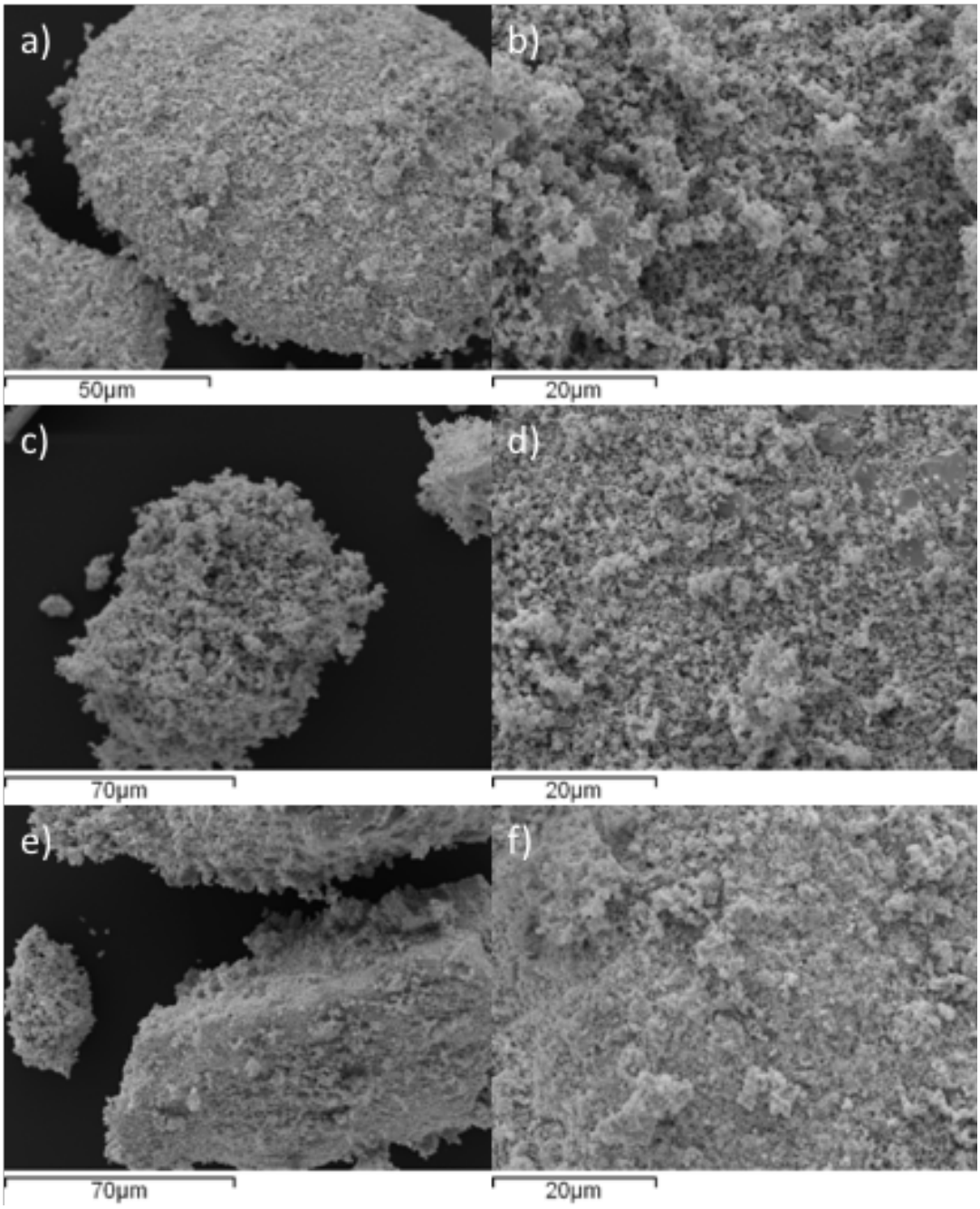

Figure 185: SEM images of osmium post-reaction with 3:1 H_2/N_2 at 400°C after different pre-treatments. a and b) 1:3 N_2/H_2 pre-treatment, c and d) 1:3 Ar/H_2 pre-treatment and e and f) N_2 pre-treatment.

Due to the possible inhibition of nitrogen and hydrogen on the surface of the osmium metal, a cyclic procedure was performed based upon the method reported by Rambeau et al. [162]. The osmium was first pre-treated at 500°C with 3:1 H_2/N_2 for 2 hours and then the temperature was decreased to 400°C. The line was switched to pure N_2 only and the nitrogen was flowed over the sample for 5 minutes. The line was then switched to a flow of pure H_2 and this was passed over the osmium for 5 minutes. This five minute cycling procedure was repeatedly performed for 1 h 30 min. After this, the cycling was switched to every two minutes for a further hour to explore the possible role of pulsing duration and

then to every eight minutes for another hour. Each time N_2 gas was the first gas to flow in the cycling step. Finally, the temperature was increased to 500°C and the cyclic procedure was performed every five minutes for 1 h 30 min.

The decrease in conductivity over time for the different stages outlined above is presented in Figure 186.

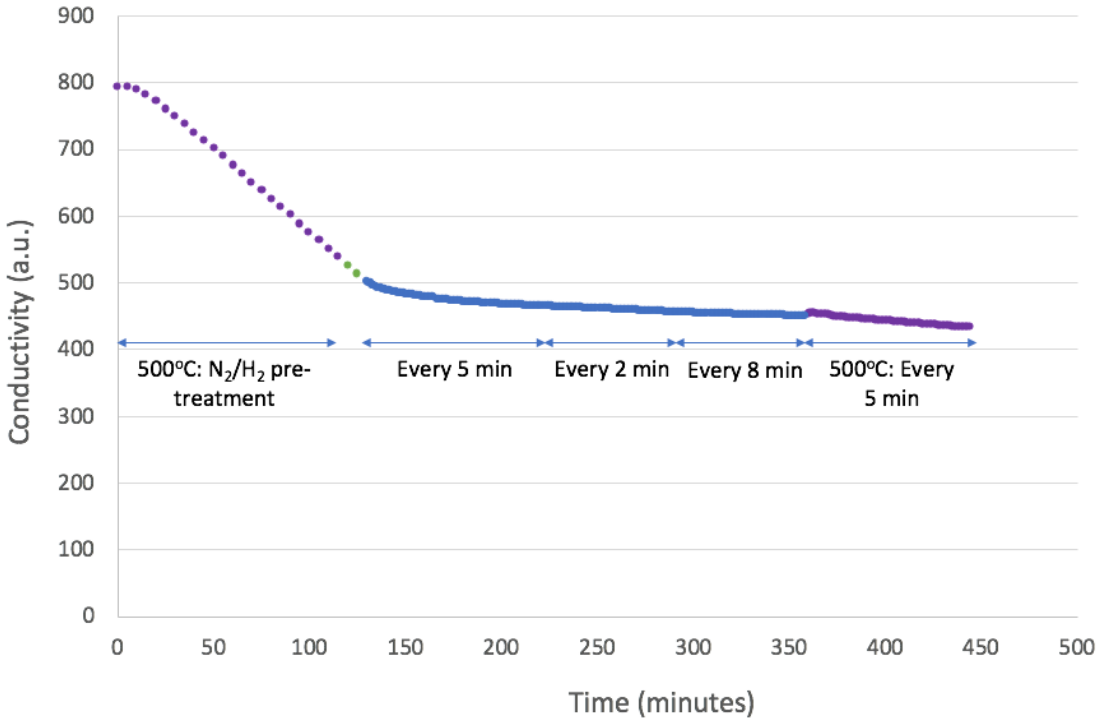

Figure 186: Conductivity profile for osmium cyclic procedure with 3:1 H_2/N_2 pre-treatment at 500°C.

The amount of ammonia produced in one hour for the different stages of the osmium cyclic procedure, detailed in Figure 186, is provided in Table 47. For the 5 min cycling at 400°C and 500°C, the values were calculated from when the conductivity had reached a steady decrease. When a continuous feed of 3:1 H_2/N_2 was used, the osmium that had been pre-treated with 3:1 H_2/N_2 produced 34.6 µmoles of ammonia in one hour at 400°C. These results suggest that the cyclic procedure was having a negative impact on the amount of ammonia produced at both 400°C and 500°C compared to when a continuous feed was used. It appears that the 5 minute cycling stage was the most effective at producing ammonia of the three stages investigated.

Conditions	Ammonia Produced in One Hour (µmoles)	Number of Cycles of H_2 Treatment
500°C 1:3 N_2/H_2 Pre-Treatment	108.0	-
400°C: Every 5 min	10.8	6
400°C: Every 2 min	5.8	15
400°C: Every 8 min	4.3	4
500°C: Every 5 min	11.5	6

Table 47: Amount of ammonia produced in one hour for each stage of the osmium cyclic procedure.

Rambeau et al. noted that at 400°C, the best conditions were when osmium was exposed to 10 s of nitrogen and 5 s of hydrogen [162]. Therefore, this would suggest that the cycling time needed to be shorter. However, this was not possible in this experimental setup. On the other hand, however, Rambeau et al. achieved satisfactory rates when the material was exposed to 5 minutes of nitrogen and 1 minute of hydrogen [162]. It would therefore be expected that the osmium should have a steady state rate in this work at these longer cycling times.

The ammonia synthesis rates of the osmium during the different cycling stages are provided in Table 48. During the pre-treatment stage at 500°C shown in Figure 186, beyond the lag period, the rate of ammonia production for the osmium was as expected according to the previous rate obtained. However, when the cycling procedure was performed at this temperature, the rate was significantly lower at 28 µmol h^{-1} g^{-1}. This suggests that the cycling procedure was having a negative effect on the ammonia synthesis process for osmium. This was also observed at 400°C when a 2 minute cycling period was used, with the rate of 15 µmol h^{-1} g^{-1} being much lower than the rates reported in Table 46 at the same temperature employing continuous feeding of reaction mixture. Therefore, these observations were not consistent with those reported by Rambeau et al. [162] who suggested that the rate could be increased by a factor of 5 at 400°C when the cyclic procedure was used.

Conditions	NH_3 Synthesis Rate (µmol h^{-1} g^{-1})
500°C 1:3 N_2/H_2 Pre-Treatment	261
400°C: Every 2 min	15
500°C: Every 5 min	28

Table 48: Ammonia synthesis rates of osmium under different conditions.

The XRD pattern for the post-reaction osmium that underwent a cyclic procedure is shown in Figure 187. Only osmium metal was observed in the pattern, as expected on the basis of the observations reported previously.

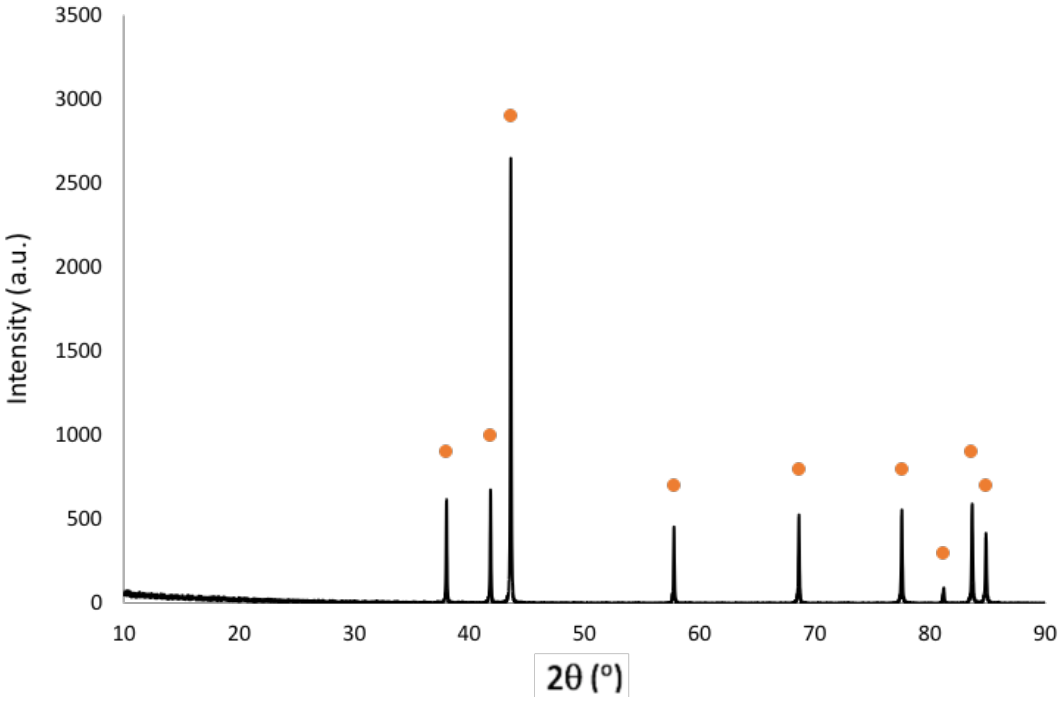

Figure 187: XRD patterns of osmium post cyclic procedure reaction. Reflections marked: • Os (JCPDS file number 00-006-0662).

Representative SEM images for the osmium post cyclic procedure showed that the material had a similar morphology to the pre-reaction material. Therefore, the cyclic procedure did not affect the morphology of the osmium.

6.2.2 Supported Osmium Compounds

6.2.2.1 $Os_3(CO)_{12}$ on Silica

To investigate potential structure sensitivity in the case of osmium catalysed ammonia synthesis, $Os_3(CO)_{12}$ was supported on amorphous silica. The material was prepared to give a 5 wt. % loading of osmium. In the literature, a 5 wt. % loading is used to prepare these materials and therefore, the same loading was used in this work. As the silica was not treated in order to remove hydroxyl groups, the silica support is referred to as hydroxylated. The XRD pattern of the 5% $Os_3(CO)_{12}$/silica hydroxylated is displayed in Figure 188. Reflections due to $Os_3(CO)_{12}$ can be observed in the pattern as well as a broad peak between 15-35° 2θ that is due to amorphous silica. The crystalline reflections related to the $Os_3(CO)_{12}$ suggest that there was not monolayer dispersion initially.

The elemental analysis of the silica showed that there was trace amounts of carbon and significant amounts of hydrogen, as to be expected due to the hydroxyl groups on the surface (C: 0.04 wt. %, H: 0.87 wt. %, N: 0.00 wt. %). For the 5% $Os_3(CO)_{12}$/silica, the elemental analysis indicated that there was carbon and hydrogen present in the material (C: 0.98 wt. %, H: 0.77 wt. %, N: 0.00 wt. %). As there was a 5 wt. % loading of osmium metal, the expected percentage of carbon in this supported material is 1.26 wt. %. Therefore, the percentage of carbon was lower than expected.

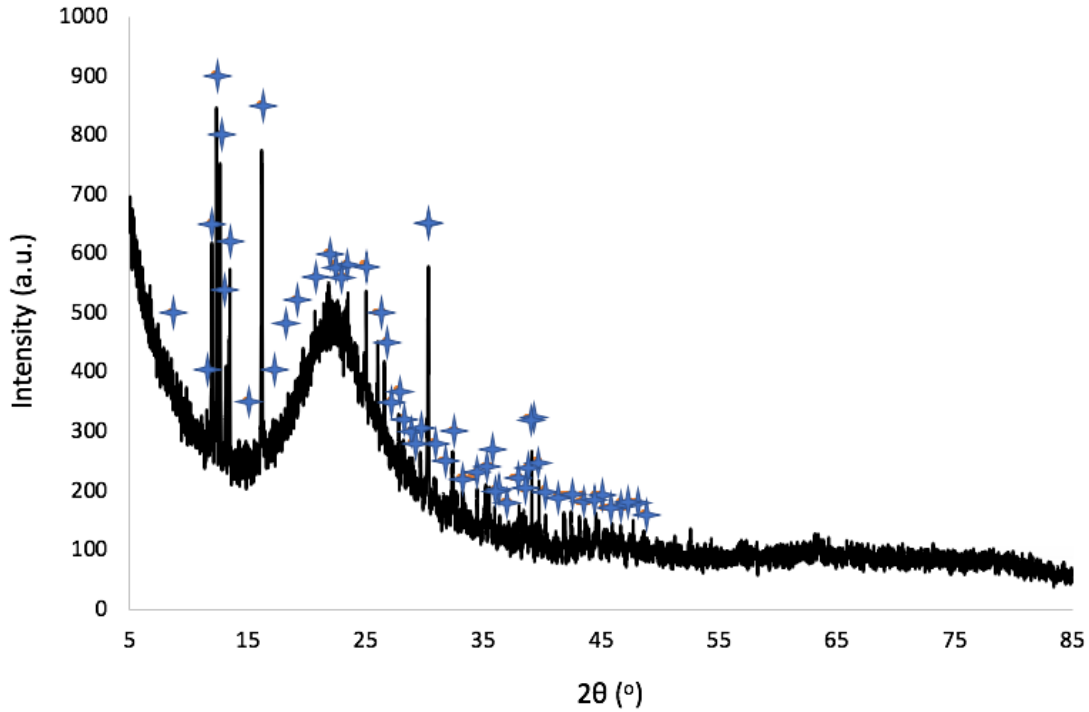

Figure 188: XRD pattern of 5% $Os_3(CO)_{12}$/silica hydroxylated. Reflections marked: ✦ $Os_3(CO)_{12}$ (JCPDS file number 01-070-0415).

FTIR spectroscopy was performed in the carbonyl region for the supported $Os_3(CO)_{12}$ material. The FTIR spectrum is provided in Figure 189. For the 5% $Os_3(CO)_{12}$/silica, IR frequencies were noted at 2068 cm^{-1} (s), 2035 cm^{-1} (m), 2014 cm^{-1} (w) and 2000 cm^{-1} (w). From the literature, $Os_3(CO)_{12}$ stretching frequencies have been reported to occur at 2068 cm^{-1} (s), 2035 cm^{-1} (s), 2014 cm^{-1} (m) and 2002 cm^{-1} (m) [181] [184]. Therefore, these results agree well with the literature values.

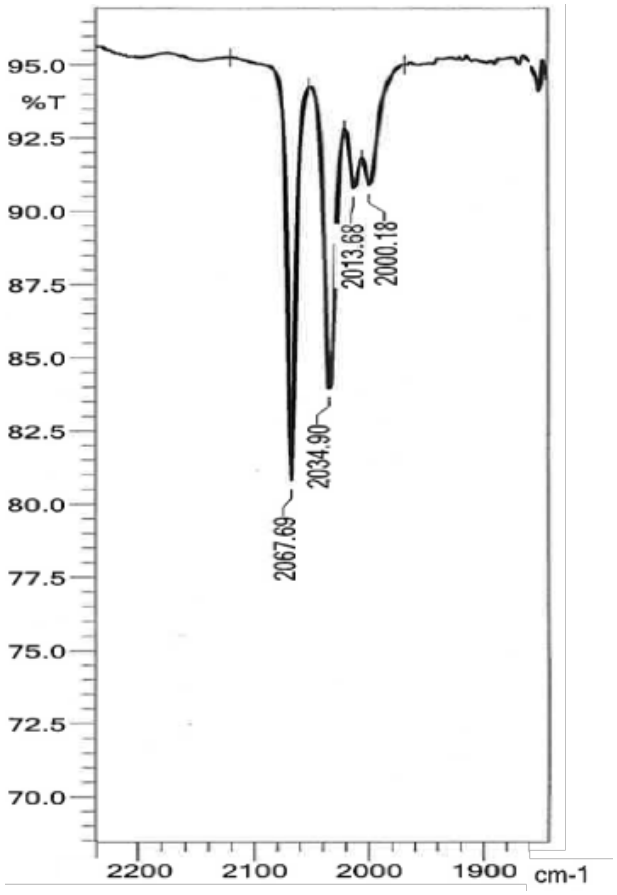

Figure 189: FTIR spectrum of 5% $Os_3(CO)_{12}$/silica hydroxylated.

The silica supported $Os_3(CO)_{12}$ was investigated for ammonia synthesis activity at 400°C and 500°C, in order to compare the rate of the material with the osmium metal. The reaction profile for this material is displayed in Figure 190. The material was reduced for 2 hours under N_2/H_2 at 500°C. This was performed in order to replicate the conditions used for the osmium metal. After 2 hours, the furnace was cooled to 400°C and kept at this temperature for 2 h 15 minutes. The temperature was then increased to 500°C, due to the low activity of the material at 400°C. The furnace was kept at 500°C for 4 hours. Finally, the furnace was cooled down again to 400°C and was kept at this temperature for 2 h and 25 minutes. The temperature was decreased to 400°C for a second time in order to investigate if there had been a change in the material when it was run at 500°C for a longer time. When the 5% $Os_3(CO)_{12}$/silica hydroxylated was run at 500°C for 36 hours, there was no indication of the material deactivating as seen in Figure 191.

The ammonia synthesis rate of the material at 400°C was 39 ± 6 μmol h^{-1} g^{-1}. The rate was calculated for the catalyst weight and was not normalised to osmium content. In comparison, the rate of the N_2/H_2 pre-treated osmium metal at 400°C was 79 ± 1 μmol h^{-1} g^{-1}. Therefore, the osmium metal was more active than the supported material at the lower temperature. However, when the activity is normalised to the mass of osmium, the supported material is much more active (770 ± 114 μmol h^{-1} g_{Os}^{-1}). The 5%

$Os_3(CO)_{12}$/silica hydroxylated had a rate of 265 ± 48 µmol h^{-1} g^{-1} at 500°C. Comparing this with the ammonia synthesis rate of the osmium metal at 500°C (262 ± 21 µmol h^{-1} g^{-1}), the rate was very similar, suggesting that osmium has the same activity whether in the bulk or supported form. However, a rate of 5306 ± 954 µmol h^{-1} g_{Os}^{-1} is obtained for the supported material when the rate is normalised to metal content. Therefore, the Os content is more efficient in the supported material and is much more active per unit mass of osmium. This possibly suggests that osmium is structure sensitive for ammonia synthesis. Osmium appears to possess structure sensitivity more similar to ruthenium, with osmium being more active when it is more highly dispersed.

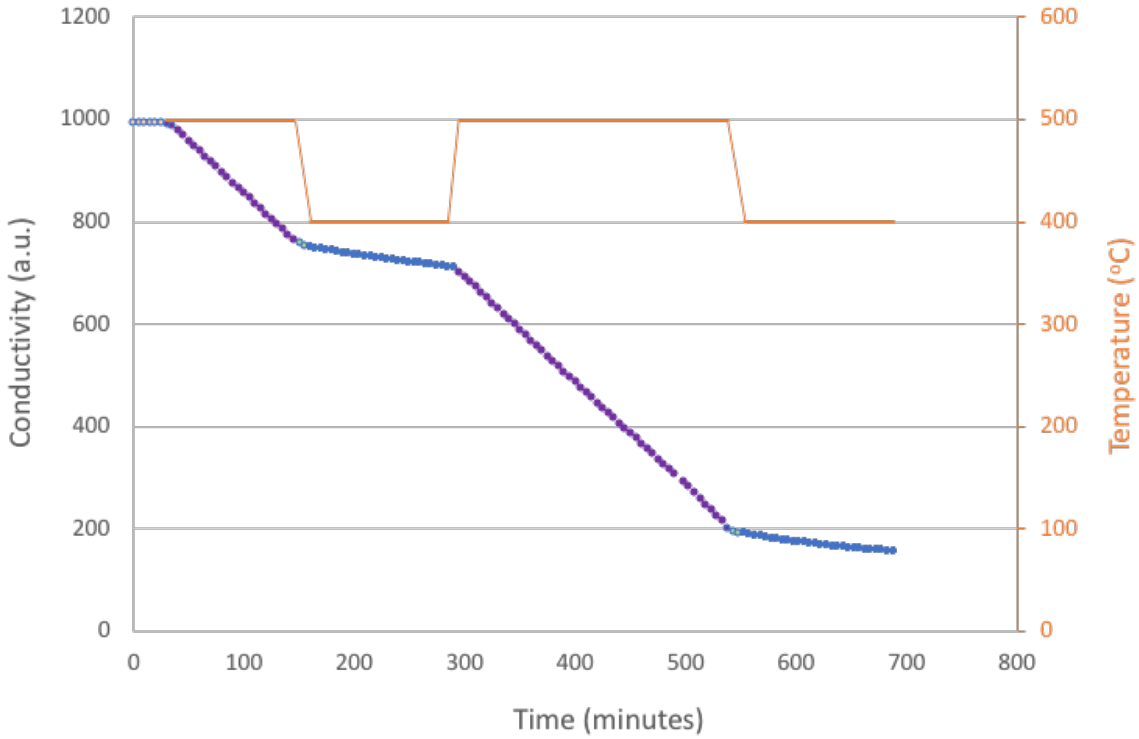

Figure 190: Conductivity profile for 5% $Os_3(CO)_{12}$/silica hydroxylated reacted with 3:1 H_2/N_2 at 400°C and 500°C.

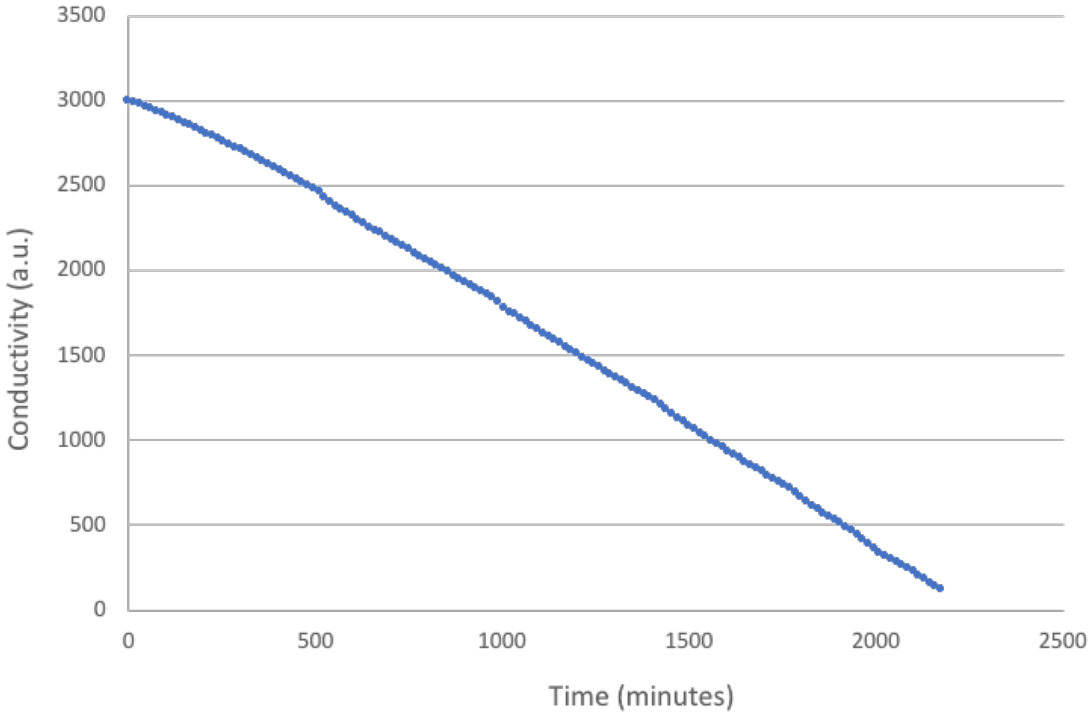

Figure 191: Conductivity profile for 5% $Os_3(CO)_{12}$/silica hydroxylated reacted with 3:1 H_2/N_2 at 500°C for 36 hours.

It has previously been suggested that $Os_3(CO)_{12}$ decomposes through a hydride intermediate when under hydrogen and supported on carbon [185]. At 400°C, it was shown that the $Os_3(CO)_{12}$ had decomposed to give well dispersed Os on the carbon support. A similar hydride intermediate has also been proposed for $Os_3(CO)_{12}$ supported on hydroxylated silica and alumina [186]. The retention of the Os-Os nuclearity has been questioned when the supported osmium carbonyl cluster decomposes [186] [187]. However, Collier et al. have claimed that Os-Os bonding is retained on dehydroxylated silica and alumina [51]. They observed that above 250°C, there were no spectral features of $Os_3(CO)_{12}$, suggesting that the carbonyl had decomposed.

The XRD pattern of the material post-reaction is displayed in Figure 192 and shows that, unlike the pre-reaction case, there were no reflections corresponding to $Os_3(CO)_{12}$. The broad peak between 15-35° 2θ due to amorphous silica was observed. An amorphous peak between 40 – 45° 2θ is observed that was not present in the pre-reaction material. This peak could be due to osmium as the metal has three high intensity reflections at this position. However, silica can also have similar features and therefore, some caution has to be taken. The XRD pattern indicates that $Os_3(CO)_{12}$ had decomposed during the reaction.

The elemental analysis of the post-reaction material showed that the amount of carbon and hydrogen had significantly decreased compared to pre-reaction (C: 0.04 wt.%, H: 0.26 wt. %, N: 0.07 wt.%). The loss of carbon is to be expected, if the $Os_3(CO)_{12}$ had decomposed.

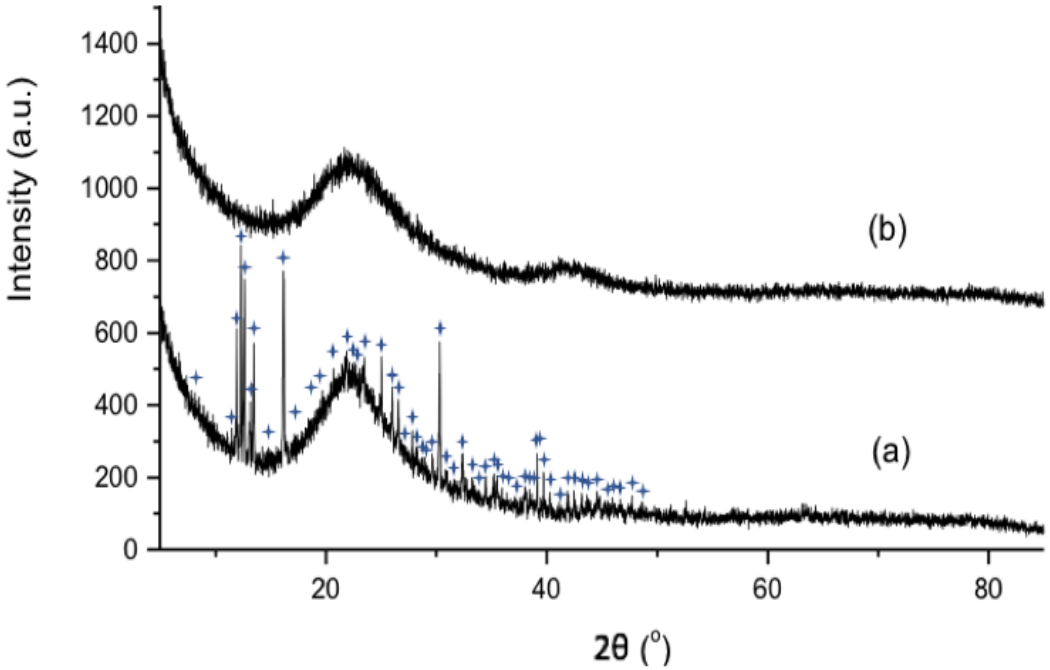

Figure 192: XRD patterns of 5% $Os_3(CO)_{12}$/silica hydroxylated: (a) pre-reaction and (b) post-reaction with 3:1 H_2/N_2. Reflections marked: ✦ $Os_3(CO)_{12}$ (JCPDS file number 01-070-0415).

An FTIR spectrum was taken for the post-reaction material, in order to see the effect the reaction had on the $Os_3(CO)_{12}$ structure and it is displayed in Figure 193. After the reaction, frequencies were recorded at 2043 cm^{-1} (vw), 2018 cm^{-1} (vw) and 1992 cm^{-1} (vw) in the carbonyl region. These bands are different from the literature values and those of the pre-reaction material. However, the bands are very weak and may be due to background noise. The intensity of the bands decreased after the ammonia synthesis reaction, suggesting that the $Os_3(CO)_{12}$ had largely decomposed. Such decomposition has been recorded in previous literature [188] and agrees with the information obtained from the XRD pattern and elemental analysis.

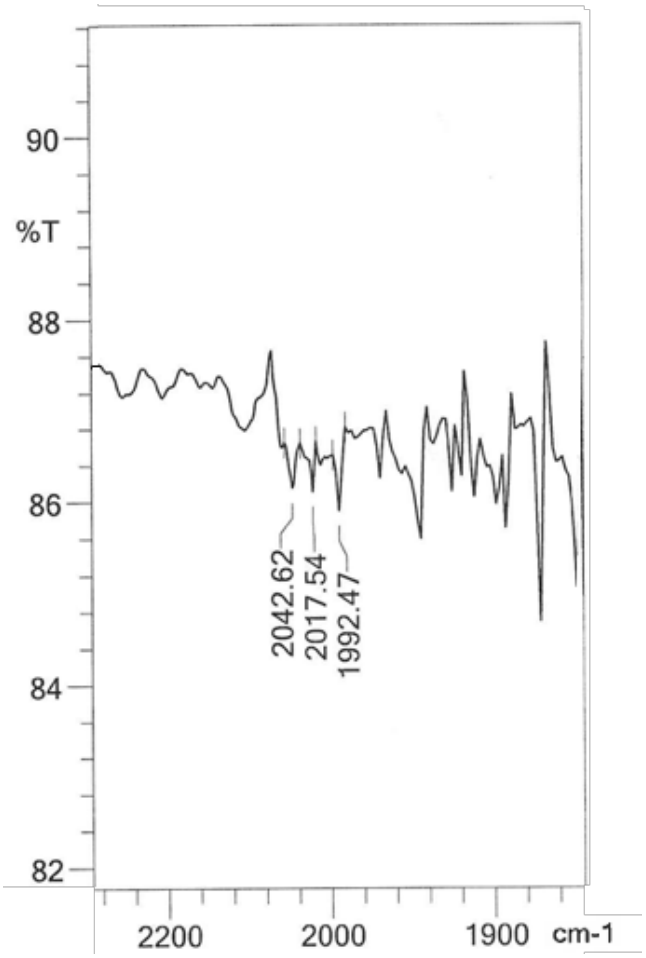

Figure 193: FTIR spectrum of 5% $Os_3(CO)_{12}$/silica hydroxylated post-reaction with 3:1 H_2/N_2 at 500°C for 36 hours.

EDX analysis of the $Os_3(CO)_{12}$/silica showed that it consisted of 1.27 wt. % Os, 14.27 wt.% C, 52.36 wt. % O and 32.09 wt. % Si. The post-reaction material consisted of 1.76 wt. % Os, 14.33 wt.% C, 46.44 wt. % O and 37.47 wt. % Si. The pre-reaction osmium percentage was lower than the 5 wt. % of osmium used to prepare the material. However, the osmium was not uniformly dispersed across the surface, as the EDX data showed a variation in the areas examined. The osmium was more evenly dispersed in the post-reaction material and the percentage had apparently increased compared to pre-reaction. However, as there was a variation in osmium content pre-reaction, this increase may be due to the higher dispersion. To calculate the coverage of the silica support with Os triangles, the bond lengths and angles of Os-Os in $Os_3(CO)_{12}$ [171] were used to calculate the cross-sectional area of the Os triangle. The cross-sectional area of the Os_3 complex was calculated to be 3.594×10^{-20} m^2 and the silica had a BET surface area of 427 m^2/g. Then, assuming the Os_3 structure lies flat on the silica support and that a monolayer was formed, the coverage of the silica support was calculated to be 0.44%.

To improve the activity of the silica supported $Os_3(CO)_{12}$, the material was modified in four different ways:

(1) The first method was the preparation of 5% $Os_3(CO)_{12}$/silica hydroxylated under a nitrogen atmosphere. This was to confirm that the metal carbonyl was not air sensitive as stated in the introduction. The sample was transferred into the reactor under nitrogen atmosphere and therefore, did not come into contact with air before the reaction.

(2) The second method resulted in the silica support being treated with nitrogen prior to being supported in order to remove surface hydroxyl groups. As Collier et al. suggested that there was retention of the cluster structure on dehydroxylated supports, a comparison of hydroxylated and dehydroxylated silica would be of interest.

(3) In the third method, the metal loading of osmium on the hydroxylated silica was increased to 7 wt. %.

(4) Finally, the 5% $Os_3(CO)_{12}$/silica hydroxylated was doped with 1% KOH as the ammonia synthesis activity of Ru/Al_2O_3 has been shown to increase when it is doped with alkali metals [26].

The ammonia synthesis activity of these materials at 400°C and 500°C are shown in Table 49. The activity of the "standard" 5% $Os_3(CO)_{12}$/silica hydroxylated material has been provided as a comparison. Only the materials that had a steady state rate at 400°C are listed in Table 49. For the sample prepared under N_2, there appeared to be minimal difference in activity compared to the 5% $Os_3(CO)_{12}$/silica hydroxylated material suggesting that the supported $Os_3(CO)_{12}$ material is not very air sensitive.

When comparing the hydroxylated and dehydroxylated silica supports, the hydroxylated silica supported material was more active at 400°C, with 5% $Os_3(CO)_{12}$/dehydroxylated silica not exhibiting a steady state rate at this temperature. However, at 500°C, there appeared to be an enhancement of the rate on the dehydroxylated system. Therefore, it could be suggested that the hydroxyl groups on the silica have an effect on the rate.

At 400°C, the 7% $Os_3(CO)_{12}$/silica hydroxylated had a lower activity than the 5% loaded material. When the catalyst weight was used to calculate the rate, the 7% loaded material was observed to be more active at 500°C. However, when the rate is normalised to the mass of osmium, the activity of the 5% $Os_3(CO)_{12}$/silica hydroxylated and 7% $Os_3(CO)_{12}$/silica hydroxylated were similar. If there was uniform dispersion of the

$Os_3(CO)_{12}$ on the silica surface, the rate should be 7/5 of the 5% $Os_3(CO)_{12}$/silica hydroxylated. Therefore, the rate is expected to be 7428 μmol h^{-1} g_{Os}^{-1} for the 7 wt. % loading material. The osmium mass normalised rate was lower than this expected value.

The Os supported material was not promoted by KOH at either 400°C or 500°C. At 400°C, the rate was non-steady state and at 500°C the rate was significantly reduced. These results suggest, surprisingly, that the KOH had a negative effect on the activity for this system.

Material	Temperature (°C)	NH_3 Synthesis Rate (μmol h^{-1} g^{-1})	NH_3 Synthesis Rate (μmol h^{-1} g_{Os}^{-1})
5% $Os_3(CO)_{12}$/silica hydroxylated	400	39 ± 6	770 ± 114
5% $Os_3(CO)_{12}$/silica hydroxylated	500	265 ± 48	5306 ± 954
5% $Os_3(CO)_{12}$/silica hydroxylated prepared under N_2 (1)	400	34	680
5% $Os_3(CO)_{12}$/silica hydroxylated prepared under N_2 (1)	500	284	5676
5% $Os_3(CO)_{12}$/silica dehydroxylated (2)	500	355 ± 19	7096 ± 385
7% $Os_3(CO)_{12}$/silica hydroxylated (3)	400	22	313
7% $Os_3(CO)_{12}$/silica hydroxylated (3)	500	349 ± 9	4972 ± 126
5% $Os_3(CO)_{12}$/silica hydroxylated + 1% KOH (4)	500	174 ± 11	3470 ± 202

Table 49: Ammonia synthesis rates of different $Os_3(CO)_{12}$/silica materials reacted with 3:1 H_2/N_2. (1), (2), (3) and (4) refers to the four different modifications detailed above.

6.2.2.1.1 5% $Os_3(CO)_{12}$/silica hydroxylated Prepared Under N_2

The XRD patterns of the material pre- and post-reaction are shown in Figure 194. The pattern was very similar to the material not prepared under nitrogen, with the reflections due to $Os_3(CO)_{12}$ not being present in the XRD pattern post-reaction. This indicates that $Os_3(CO)_{12}$ decomposed during the reaction. As before, the crystalline reflections of $Os_3(CO)_{12}$ suggests that there was not a monolayer dispersion.

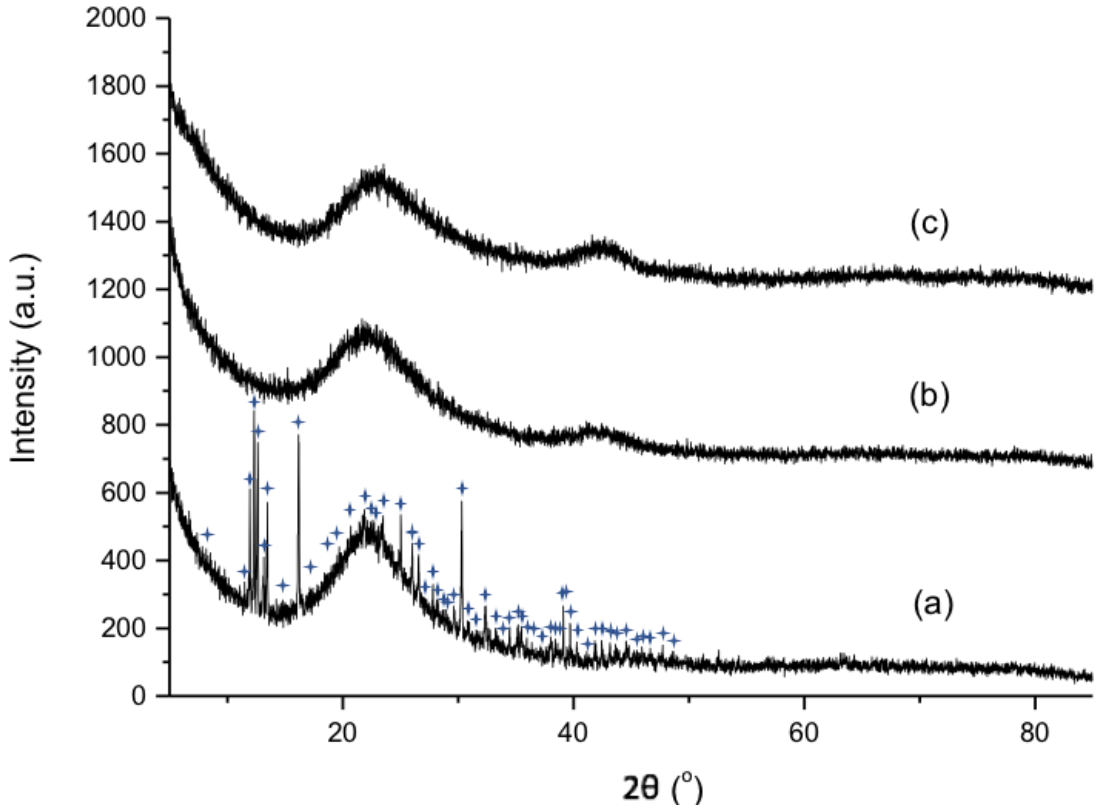

Figure 194: XRD patterns of 5% $Os_3(CO)_{12}$/silica hydroxylated: (a) pre-reaction, (b) post-reaction and (c) post-reaction prepared under N_2. Reflections marked: ✦ $Os_3(CO)_{12}$ (JCPDS file number 01-070-0415).

6.2.2.1.2 5% $Os_3(CO)_{12}$/silica dehydroxylated

The XRD patterns of the dehydroxylated material pre- and post-reaction appear to be very similar to the XRD patterns for the hydroxylated material as observed in Figure 195.

The silica post nitrogen treatment was shown to still contain some hydrogen (C: 0.03 wt. %, H: 0.20 wt. %, N: 0.00 wt. %). However, the amount was significantly lower than the sample that was not treated to remove hydroxyl groups, as would be expected. A degree of rehydroxylation may have occurred when the silica was in contact with air. The elemental analysis for the material pre- and post-reaction is provided in Table 50. The amount of carbon had significantly decreased post-reaction, which agrees with the XRD pattern that showed the $Os_3(CO)_{12}$ had decomposed.

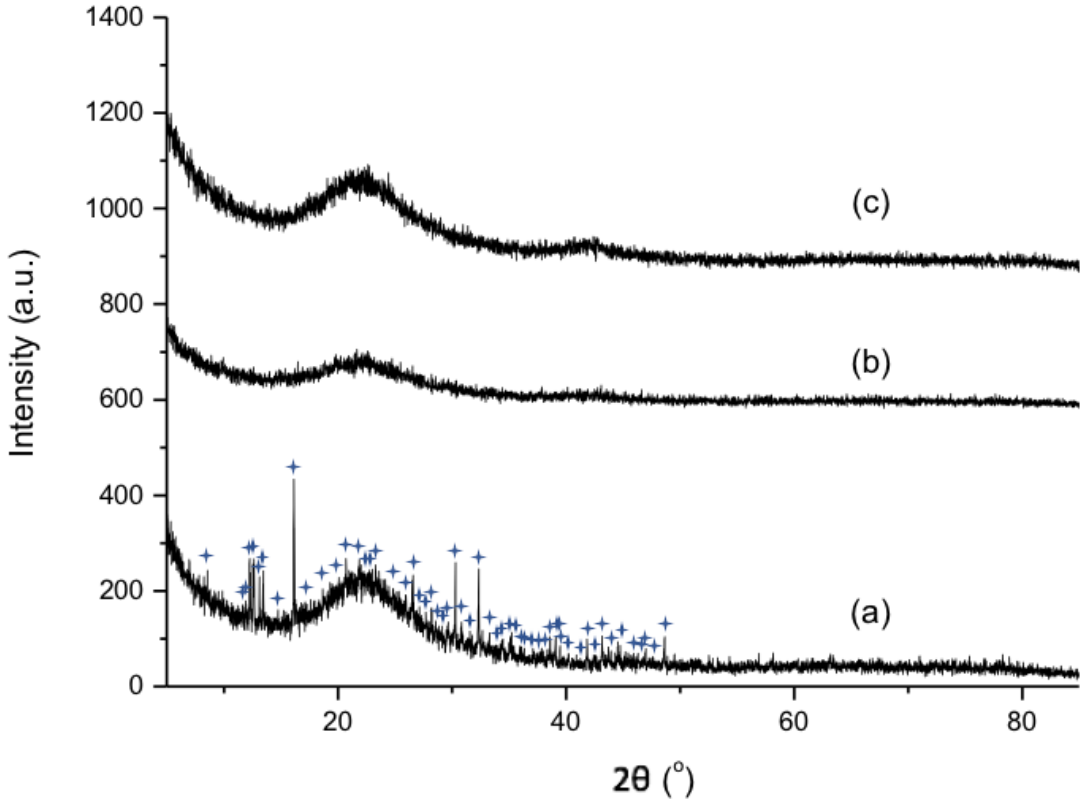

Figure 195: XRD patterns of 5% $Os_3(CO)_{12}$/silica dehydroxylated: (a) pre-reaction, (b) post-reaction at 400°C and (c) post-reaction at 500°C. Reflections marked: ✦ $Os_3(CO)_{12}$ (JCPDS file number 01-070-0415).

Material	Carbon Content from Elemental Analysis (wt. %)	Hydrogen Content from Elemental Analysis (wt. %)	Nitrogen Content from Elemental Analysis (wt. %)
Pre-reaction	2.42	0.52	0.03
Post-reaction	0.06	0.24	0.11

Table 50: Elemental Analysis for pre- and post-reaction 5% $Os_3(CO)_{12}$/silica dehydroxylated.

6.2.2.1.3 7% $Os_3(CO)_{12}$/silica hydroxylated

The XRD patterns of the material pre- and post-reaction are displayed in Figure 196. The $Os_3(CO)_{12}$ is not observed in the post-reaction pattern and therefore, it appears to have decomposed during the reaction. The pre- and post-reaction XRD patterns are similar to those for the 5% loaded material.

The elemental analysis of the 7% $Os_3(CO)_{12}$/silica hydroxylated is given in Table 51. For a 7 wt. % loading of osmium metal, the expected percentage of carbon in the supported material would be 1.76 wt. %. The carbon percentage of the pre-reaction material agrees quite well with this expected value. As observed with the other materials, the carbon content decreased after the reaction and therefore, this confirms that the $Os_3(CO)_{12}$ decomposed.

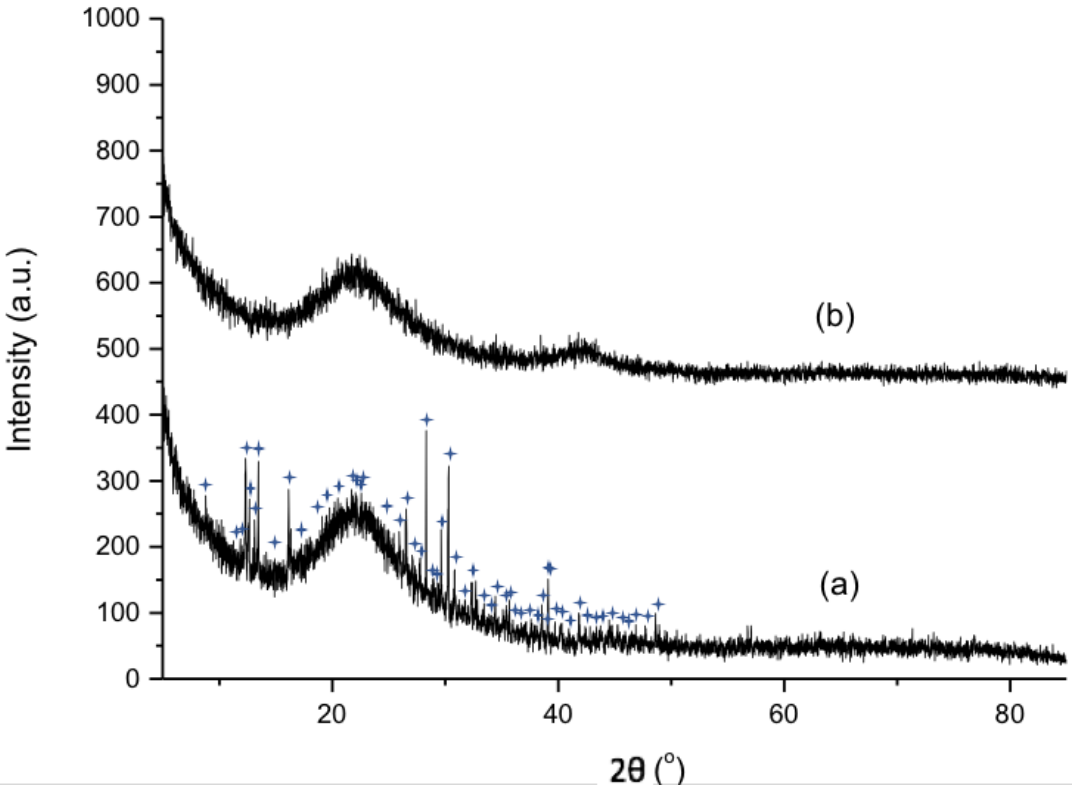

Figure 196: XRD patterns of 7% $Os_3(CO)_{12}$/silica hydroxylated: (a) pre-reaction and (b) post-reaction at 500°C. Reflections marked: ✦ $Os_3(CO)_{12}$ (JCPDS file number 01-070-0415).

Material	Carbon Content from Elemental Analysis (wt. %)	Hydrogen Content from Elemental Analysis (wt. %)	Nitrogen Content from Elemental Analysis (wt. %)
Pre-reaction	1.58	0.69	0.00
Post-reaction	0.03	0.33	0.04

Table 51: Elemental Analysis for pre- and post-reaction 7% $Os_3(CO)_{12}$/silica hydroxylated.

6.2.2.1.4 5% $Os_3(CO)_{12}$/silica hydroxylated + 1% KOH

The XRD patterns of the doped material were different to the undoped sample pre- and post-reaction as observed in Figure 197. For the pre-reaction sample, reflections due to $Os_3(CO)_{12}$ were not observed, with the only observed reflection being due to silica. In the post-reaction sample, the XRD pattern showed that osmium metal was present in the material. These differences in the XRD pattern of the doped material may provide an explanation for the lower activity compared to the undoped sample. The reflection widths of the osmium are large, suggesting that the osmium is highly dispersed consisting of small and/or disordered crystallites. As the osmium is more highly dispersed compared to the bulk osmium, this would suggest that there was a greater proportion of surface atoms.

Although $Os_3(CO)_{12}$ was not observed in the pre-reaction XRD pattern, the elemental analysis showed that there was carbon present in the material, suggesting that $Os_3(CO)_{12}$ was present pre-reaction. The carbon percentage was lower than expected, suggesting that the $Os_3(CO)_{12}$ percentage was also lower. This may be another reason for the lower activity of this material. The elemental analysis for the material pre- and post-reaction is provided in Table 52.

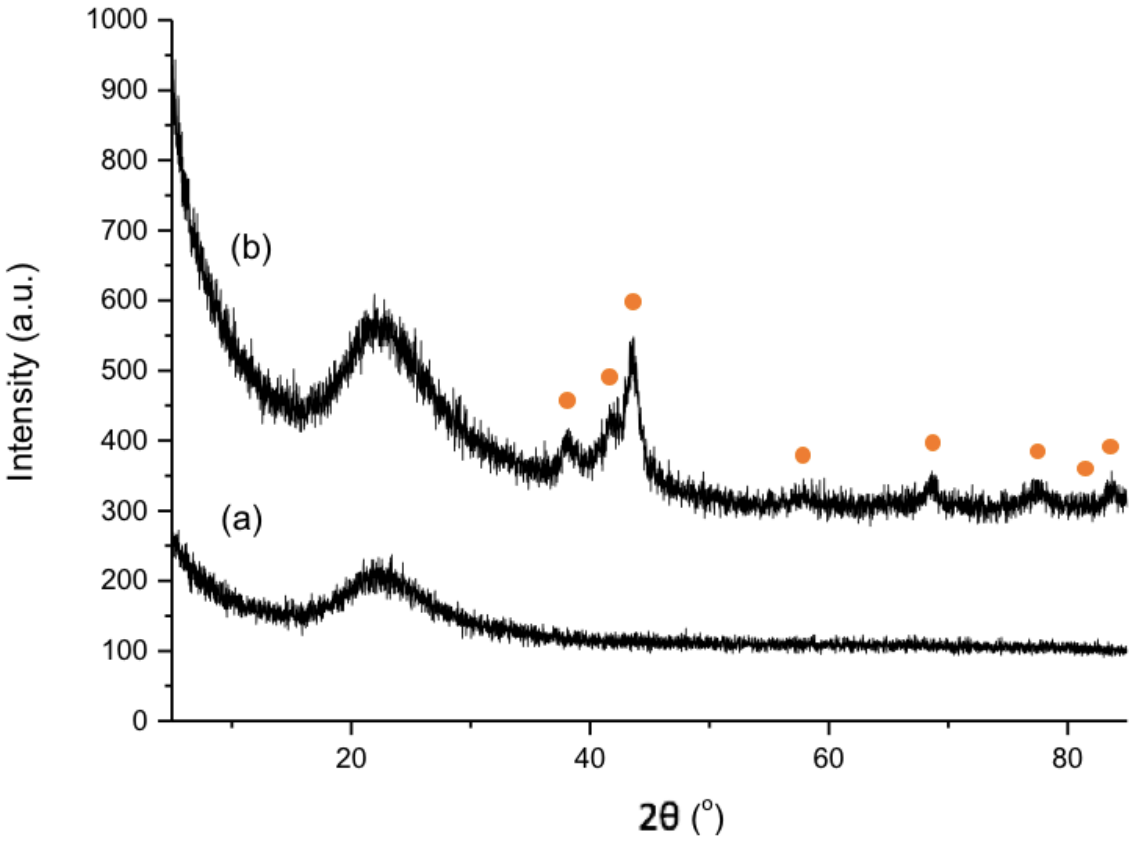

Figure 197: XRD patterns of 5% $Os_3(CO)_{12}$/silica hydroxylated + 1% KOH: (a) pre-reaction and (b) post-reaction at 500°C. Reflections marked: • Os (JCPDS file number 00-006-0662).

Material	Carbon Content from Elemental Analysis (wt. %)	Hydrogen Content from Elemental Analysis (wt. %)	Nitrogen Content from Elemental Analysis (wt. %)
Pre-reaction	0.75	0.78	0.01
Post-reaction	0.04	0.32	0.00

Table 52: Elemental Analysis for pre- and post-reaction 5% $Os_3(CO)_{12}$/silica hydroxylated + 1% KOH.

The elemental maps of osmium for the four samples is presented in Figure 198. The osmium appears to be evenly distributed across all four materials.

The EDX analysis of the four materials post-reaction is provided in Table 53. The osmium percentage for all four samples was higher than for the 5% $Os_3(CO)_{12}$/silica hydroxylated material discussed earlier, which contained 1.76 wt. % Os. There are a few interesting things to note. Firstly, although the doped material had a lower activity, this does not seem to be due to a lower percentage of osmium in the material. Next, as the 5% $Os_3(CO)_{12}$ on dehydroxylated silica apparently contained a higher percentage of osmium, this may explain the higher activity compared to the 5% $Os_3(CO)_{12}$/silica hydroxylated material. The osmium was not uniformly dispersed across the surface for all four samples, with variation in the osmium content observed in the EDX analysis. However, these results are statistically limited and this needs to be borne in mind. The lower loading may possibly suggest that the $Os_3(CO)_{12}$ was not completely loaded onto the support. However, as the Os was not evenly dispersed across the support, there were limitations to measuring the Os content by EDX analysis. Also, the monolayer coverage of Os_3 on silica was calculated to be only 0.44%.

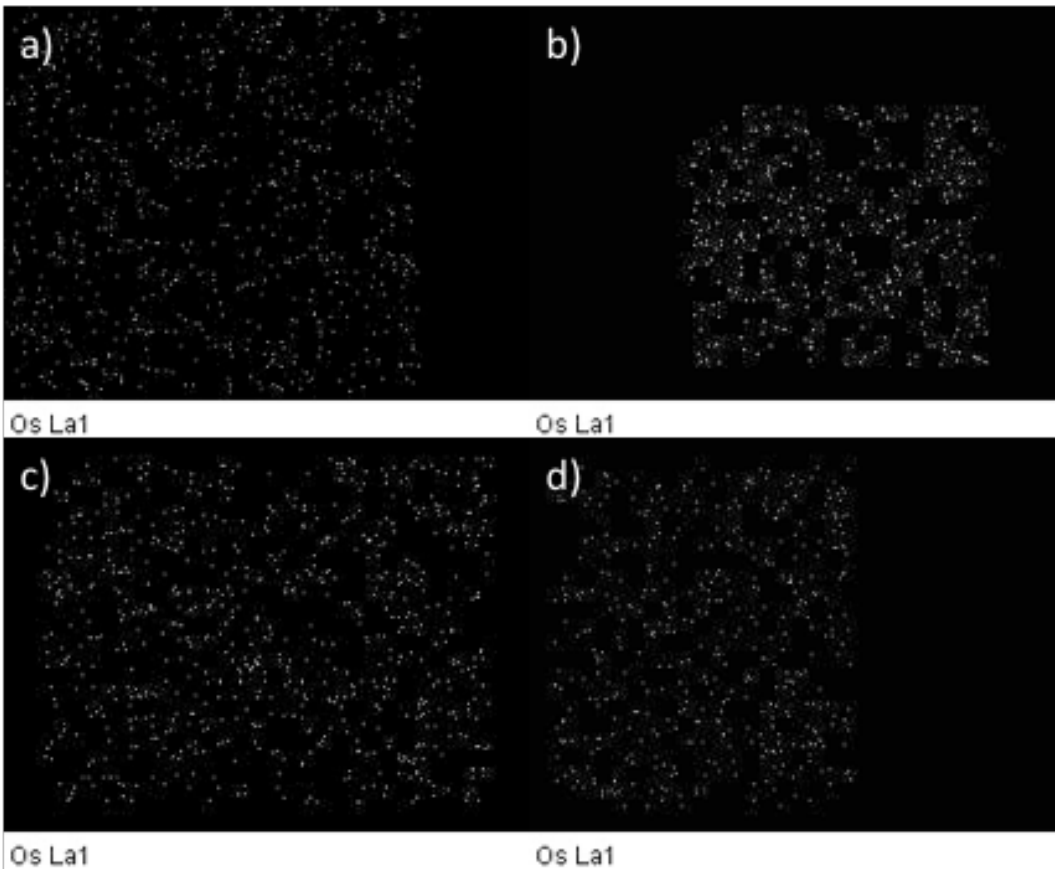

Figure 198: Elemental maps of osmium for $Os_3(CO)_{12}$/silica post-reaction with 3:1 H_2/N_2. a) 5% $Os_3(CO)_{12}$/silica hydroxylated prepared under N_2, b) 5% $Os_3(CO)_{12}$/silica dehydroxylated, c) 7% $Os_3(CO)_{12}$/silica hydroxylated and d) 5% $Os_3(CO)_{12}$/silica hydroxylated + 1% KOH.

Material	Os weight (%)	C weight (%)	O weight (%)	Si weight (%)
5% $Os_3(CO)_{12}$/silica Hydroxylated prepared under N_2. Average from 4 measurements	2	20	51	26
5% $Os_3(CO)_{12}$/silica Dehydroxylated. Average from 10 measurements	4	22	31	43
7% $Os_3(CO)_{12}$/silica Hydroxylated. Average from 15 measurements	3	23	34	40
5% $Os_3(CO)_{12}$/silica Hydroxylated + 1% KOH. Average from 11 measurements	4	18	31	47

Table 53: EDX values for $Os_3(CO)_{12}$/silica post-reaction with 3:1 H_2/N_2.

6.2.2.2 $Os_3(CO)_{12}$ on Gamma Alumina

$Os_3(CO)_{12}$ was supported on γ-alumina in order to investigate the effect the support may have on the ammonia synthesis activity. $Os_3(CO)_{12}$ was prepared on gamma alumina to give a percentage loading of 5% by weight of osmium. The material was first pre-treated at 500°C for 2 hours with N_2/H_2. Then, the temperature was decreased to 400°C. The temperature was subsequently changed as shown in Figure 199.

The material yielded an ammonia synthesis rate of 191 ± 43 μmol h^{-1} g^{-1} at 500°C when calculated from the catalyst weight. The rate was 3825 ± 860 μmol h^{-1} g_{Os}^{-1} when normalised to the mass of Os based on targeted loading. Although the material produced some ammonia at 400°C, it did not exhibit steady state activity. The performance of the material at 400°C did not change after being run at 500°C as can be seen in Figure 199. The material was run at 500°C for 36 hours as shown in Figure 200 and was found to exhibit a steady-state ammonia synthesis rate throughout the reaction, with no indication of deactivation. The $Os_3(CO)_{12}$ supported on silica possessed a higher ammonia synthesis rate than the gamma alumina equivalent. Although alumina is amphoteric [189] and therefore

the acidic sites of the support might retain some of the ammonia that is produced, this did not seem to be a significant issue.

Aika et al. prepared 2% $Ru_3(CO)_{12}$/alumina and 5% $Ru_3(CO)_{12}$/alumina and obtained a rate of 62 µmol h^{-1} g^{-1} and 202 µmol h^{-1} g^{-1}, respectively at 400°C and atmospheric pressure [25]. The mass was normalised to the total material weight. This suggests that the Ru metal is more active than the osmium at lower temperatures, even with a lower metal loading. This is to be expected as Ru has been shown to be more active than Os for ammonia synthesis [162] [163].

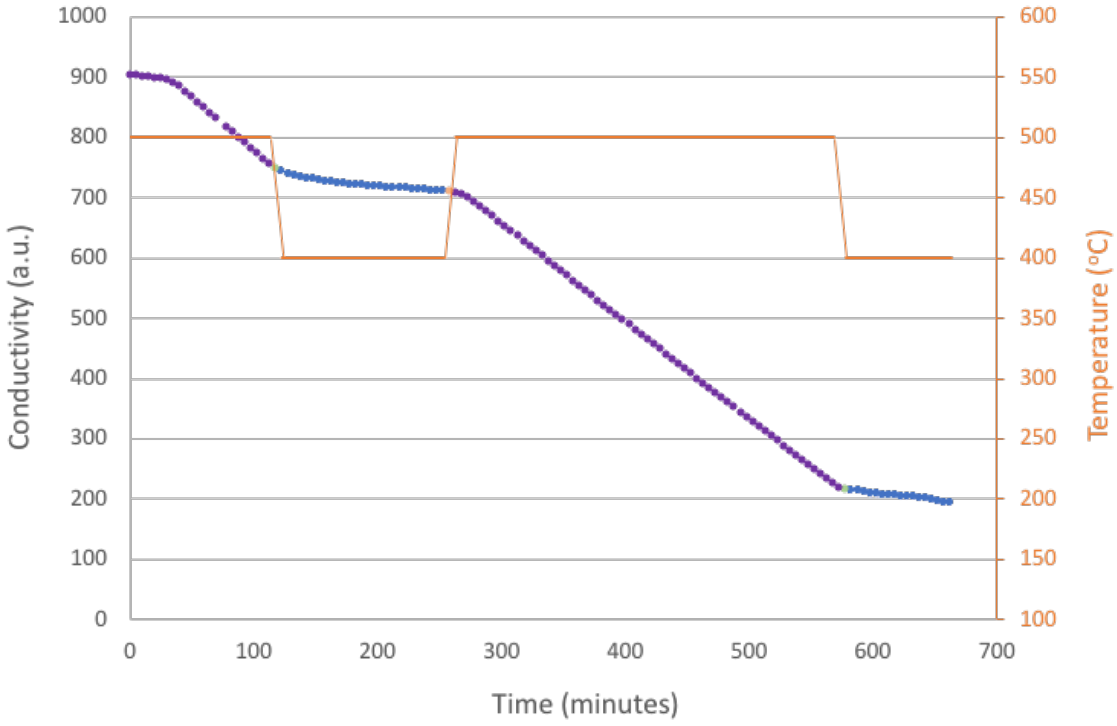

Figure 199: Conductivity profile for 5% $Os_3(CO)_{12}$/γ-alumina reacted with 3:1 H_2/N_2 at 400°C and 500°C.

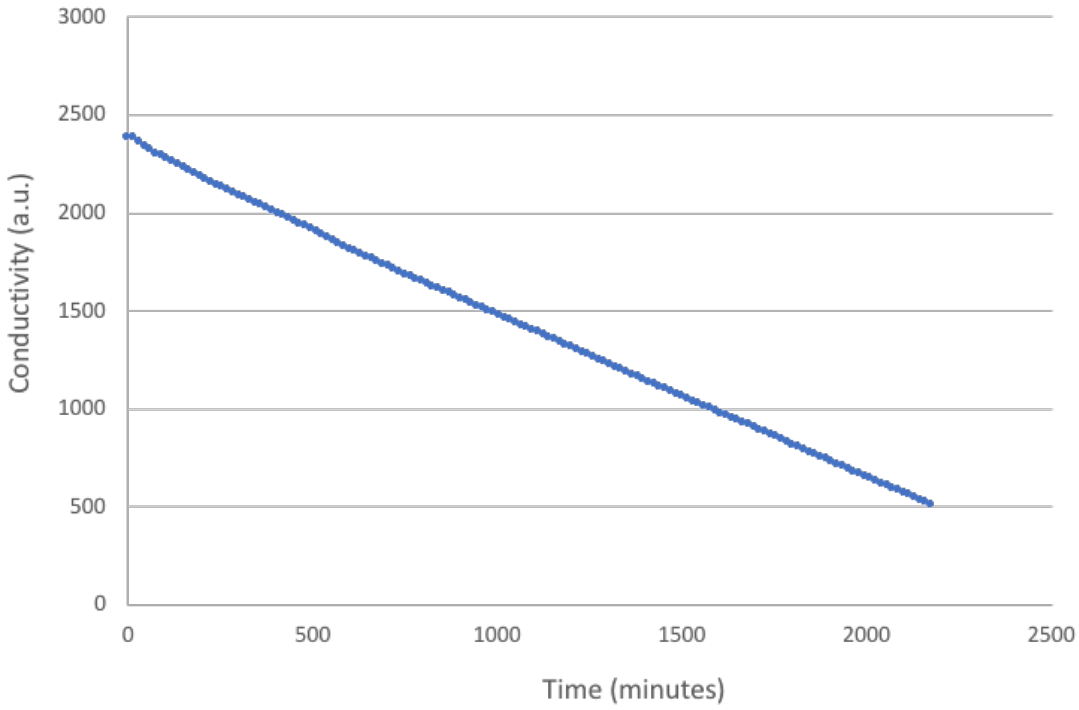

Figure 200: Conductivity profile for 5% $Os_3(CO)_{12}$/γ-alumina reacted with 3:1 H_2/N_2 at 500°C for 36 hours.

The FTIR spectrum of the 5% $Os_3(CO)_{12}$/γ-alumina pre-reaction is provided in Figure 201. An FTIR spectrum was taken of the post-reaction material in order to see the effect the reaction had on the $Os_3(CO)_{12}$ structure. For the pre-reaction 5% $Os_3(CO)_{12}$/γ-alumina, IR frequencies were recorded in the carbonyl region at 2068 cm^{-1} (m), 2033 cm^{-1} (w) 2014 cm^{-1} (vw) and 2003 cm^{-1} (vw). These values are similar to those for the silica supported $Os_3(CO)_{12}$ and those reported in the literature [181] [184].

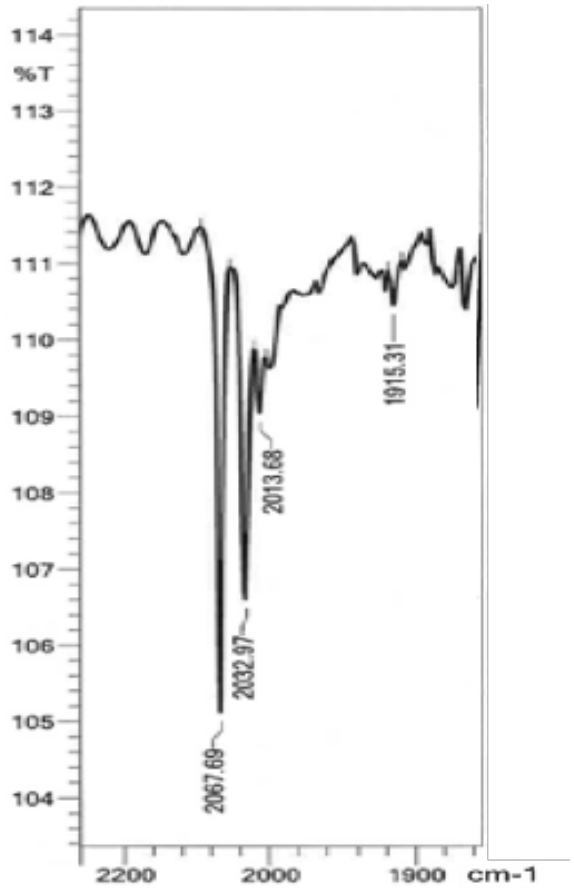

Figure 201: FTIR spectrum of 5% $Os_3(CO)_{12}$/γ-alumina.

$Os_3(CO)_{12}$ and γ-alumina can be seen in the XRD pattern of the supported gamma alumina material pre-reaction as shown in Figure 202. However, there is no evidence of $Os_3(CO)_{12}$ present in the material post-reaction, with reflections due to γ-alumina being the only peaks observed. Therefore, this suggests that $Os_3(CO)_{12}$ decomposed during the ammonia synthesis testing procedure. There does not appear to be a monolayer dispersion of $Os_3(CO)_{12}$ in the pre-reaction material as the reflections for $Os_3(CO)_{12}$ are crystalline.

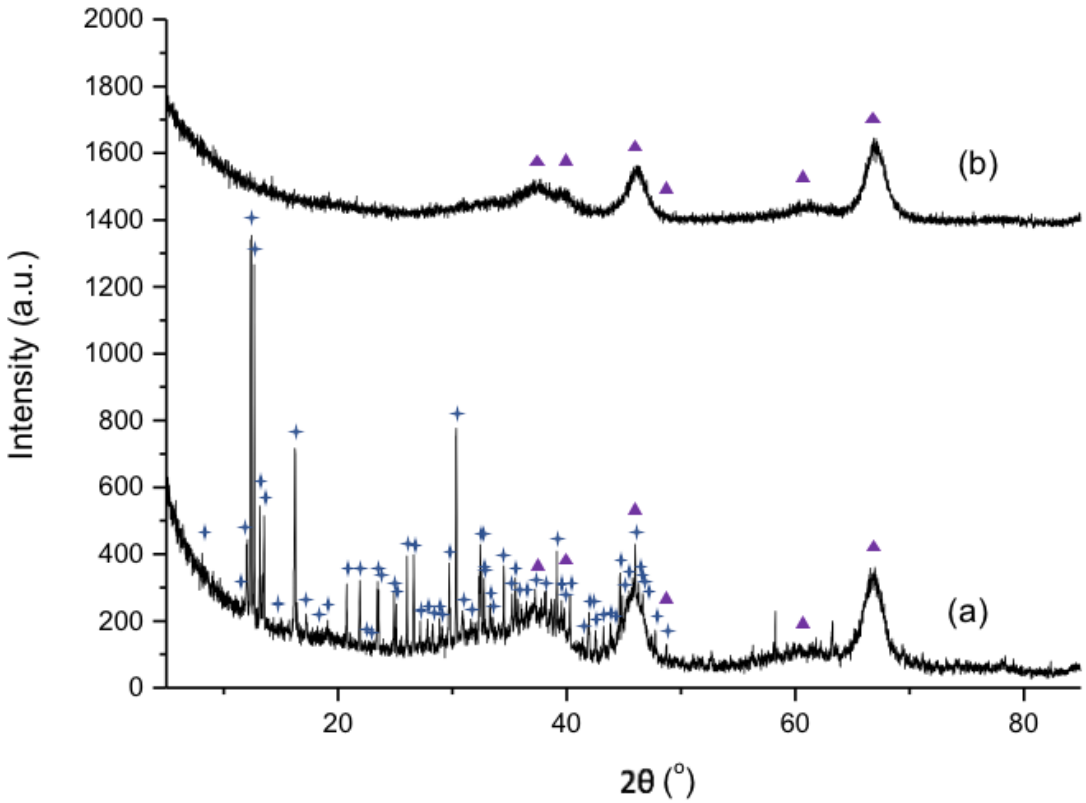

Figure 202: XRD patterns of 5% $Os_3(CO)_{12}/\gamma$-alumina: (a) pre-reaction and (b) post-reaction with 3:1 H_2/N_2 at 500°C for 36 hours. Reflections marked: ✦ $Os_3(CO)_{12}$ (JCPDS file number 01-070-0415) and ▲ γ-Al_2O_3 (JCPDS file number 00-001-1303).

The FTIR spectrum of the post-reaction material is displayed in Figure 203. There were no distinct bands in the post-reaction spectrum. As before, this indicates that the $Os_3(CO)_{12}$ has decomposed on the support. A similar observation has been previously reported by Knözinger and Zhao [190], who observed that $Os_3(CO)_{12}$ on alumina, experienced thermal degradation by loss of CO at temperatures as low as 200°C. The decomposition of the material agrees with the analysis from the XRD pattern.

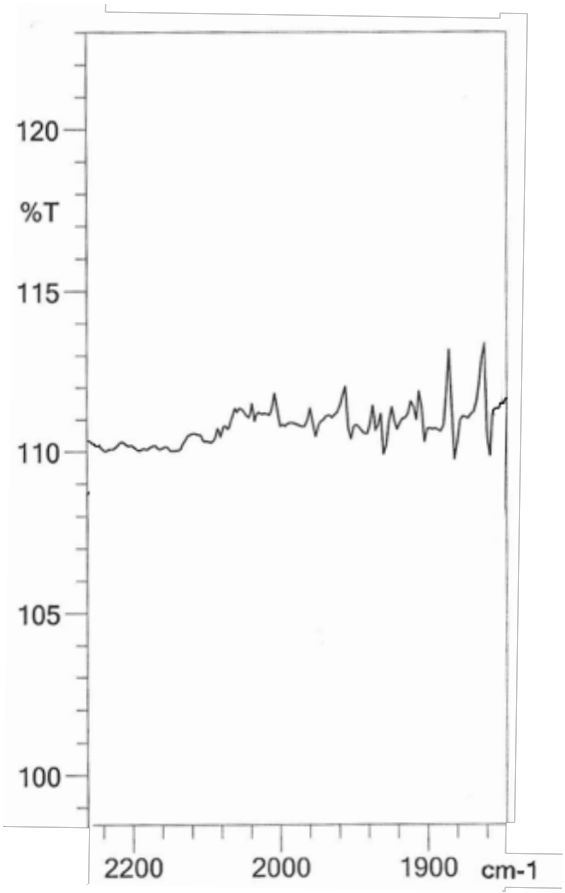

Figure 203: FTIR spectrum of 5% $Os_3(CO)_{12}$/γ-alumina post-reaction with 3:1 H_2/N_2 at 500°C for 36 hours.

The EDX analysis showed that the pre-reaction material consisted of 3.7 wt. % Os, 13 wt.% C, 54 wt. % O and 29 wt. % Al. For the post-reaction material, the EDX analysis indicated that the sample consisted of 2.1 wt. % Os, 12 wt.% C, 53 wt. % O and 32 wt. % Al. The osmium percentage of 3.7 wt. % was slightly lower than the targeted 5% osmium. However, there did not appear to be uniform dispersion of osmium on the catalyst surface. The coverage of γ-alumina with triangular Os complex was calculated to be 0.91% as the γ-alumina had a BET surface area of 208 m^2/g.

6.2.3 Supported Mixed Metal, Iron and Ruthenium Compounds

The other Group 8 metal carbonyls were investigated for ammonia synthesis activity, in order to make a comparison with the osmium compounds. The ammonia synthesis rates of the supported mixed metal, iron and ruthenium materials at 400°C and 500°C are presented in Table 54. Only those that had a steady state rate at these temperatures are provided. As can be observed, more materials were active at 500°C compared to 400°C.

Material	Temperature (°C)	NH_3 Synthesis Rate (μmol h^{-1} g^{-1})	NH_3 Synthesis Rate (μmol h^{-1} g_M^{-1})
5% Ru/Al_2O_3 + 1% KOH	400	461 ± 52	9207 ± 1038
5% Ru/Al_2O_3	400	42 ± 1	846 ± 21
2% $Ru_3(CO)_{12}$/γ-alumina	400	41 ± 5	2043 ± 265
2% $Ru_3(CO)_{12}$/silica hydroxylated	400	33 ± 6	1614 ± 274
1% $Fe_3(CO)_{12}$/γ-alumina	400	18 ± 2	1802 ± 228
5% Ru/Al_2O_3 + 1% KOH	500	544 ± 49	10875 ± 969
5% Ru/Al_2O_3	500	446 ± 63	8919 ± 1266
5% $Os_3(CO)_{12}$ + 2% $Ru_3(CO)_{12}$/silica hydroxylated	500	385 ± 34	5502 ± 491
2% $Ru_3(CO)_{12}$/γ-alumina	500	302 ± 19	15101 ± 934
2% $Ru_3(CO)_{12}$/silica hydroxylated	500	140 ± 51	6995 ± 2538
5% $Os_3(CO)_{12}$ + 1% $Fe_3(CO)_{12}$/silica hydroxylated	500	69 ± 1	1151 ± 14
1% $Fe_3(CO)_{12}$/γ-alumina	500	39 ± 10	3830 ± 944
2% $Ru_3(CO)_{12}$ + 1% $Fe_3(CO)_{12}$/silica hydroxylated	500	18 ± 3	587 ± 100
1% $Fe_3(CO)_{12}$/silica hydroxylated	500	4 ± 3	417 ± 317

Table 54: Ammonia synthesis rates of different mixed metal, iron and ruthenium supported materials reacted with 3:1 H_2/N_2 at 400°C and 500°C.

As supported Ru has previously been reported as having a high activity and is used in the KAAP process [29], Ru has been studied to give a reference. Commercial Ru/Al_2O_3 promoted with KOH gave the highest activity out of the materials studied at both 400°C and 500°C. In the literature, Ru is reported to have high activity as it is proposed to exhibit close to optimum nitrogen binding energy for ammonia synthesis [24]. At 400°C, there is a clearly evident enhancement due to the doping with KOH. This is in agreement with the literature, which states that doping of ruthenium with alkali metals increases activity via electron donation [26]. The promotional effect of KOH is less evident at 500°C, which could be due to loss of KOH at the elevated temperature. The choice of the support is also an important factor in enhancing the activity for Ru catalysts [191] [165]. It is suggested that the support controls the morphology of the Ru and therefore, the number of B_5 sites. In this study, the alumina supported Ru catalysts were more active than the

silica supported Ru catalyst at both 400°C and 500°C. This is in contrast to the $Os_3(CO)_{12}$, which exhibited better activity when supported on silica.

The supported iron based materials were shown to have the lowest activity of the samples investigated. As with the Ru based materials, the alumina supported Fe was more active at both 400°C and 500°C compared to when supported on silica. The higher activity of Os and Ru based materials compared to Fe is to be expected [24], although it must be noted that the loading of Fe was lower than for the other two metals. As stated in the introduction, iron has a higher activity when in the bulk form [192] [166] and therefore, the results of the supported Fe are as expected.

6.2.3.1 Supported Mixed Metal Compounds

Mixed metal supported materials were investigated in order to potentially optimise the ammonia synthesis activity and may provide the opportunity of tuning the activity of the dispersed clusters. The method performed by Kulkarni and Gates [52] was replicated in order to try and form supported mixed metal catalysts. As stated in the introduction, in this published work, mixed metal bonds were formed when the metal carbonyls underwent decarbonylation. Three mixed metal materials supported on hydroxylated silica have been prepared in this study: 5% $Os_3(CO)_{12}$ + 2% $Ru_3(CO)_{12}$, 5% $Os_3(CO)_{12}$ + 1% $Fe_3(CO)_{12}$ and 2% $Ru_3(CO)_{12}$ + 1% $Fe_3(CO)_{12}$.

None of the three materials were observed to exhibit a steady state ammonia synthesis rate at 400°C. As both 5% $Os_3(CO)_{12}$/silica hydroxylated and 2% $Ru_3(CO)_{12}$/silica hydroxylated were active at 400°C, it would possibly be expected that 5% $Os_3(CO)_{12}$ + 2% $Ru_3(CO)_{12}$/silica hydroxylated would also be active at this temperature. These results suggest that the metals were mixing due to the different effects on the rate.

At 500°C, the 5% $Os_3(CO)_{12}$ + 2% $Ru_3(CO)_{12}$/silica hydroxylated had the highest activity of the three mixed metal materials examined. This is possibly to be expected as the Os and Ru based materials displayed the highest activity. The activity of the mixed metal based material was higher than for both the 5% $Os_3(CO)_{12}$/silica hydroxylated (265 ± 48 μmol h^{-1} g^{-1}) and 2% $Ru_3(CO)_{12}$/silica hydroxylated (140 ± 51 μmol h^{-1} g^{-1}). The rate of the two separate monometallic materials added together is similar to the rate for the 5% $Os_3(CO)_{12}$ + 2% $Ru_3(CO)_{12}$/silica hydroxylated (385 ± 34 μmol h^{-1} g^{-1}). Therefore, it is difficult at this stage to confirm whether the higher rate is due to the possible Os-Ru bond formation. However, when the rate is normalised to the targeted metal content, the rate for 5% $Os_3(CO)_{12}$ + 2% $Ru_3(CO)_{12}$/silica hydroxylated is lower than for 2% $Ru_3(CO)_{12}$/silica

hydroxylated and is similar to the rate for 5% $Os_3(CO)_{12}$/silica hydroxylated. This suggests that the rate is not as a result of adding the two metals together and could suggest the formation of Os-Ru bonds.

Both the 5% $Os_3(CO)_{12}$ + 1% $Fe_3(CO)_{12}$/silica hydroxylated and 2% $Ru_3(CO)_{12}$ + 1% $Fe_3(CO)_{12}$/silica hydroxylated had lower activities than the monometallic Os based and Ru based silica supported materials at 500^{o}C. This could possibly suggest that there was mixing of the metals, which had an adverse effect on the catalytic performance. Ru-Fe bimetallic catalyst has previously been reported to have a lower ammonia synthesis rate than Ru and Fe [193].

The XRD patterns of the mixed metal supported samples pre- and post-reaction are provided in Figures 204, 205 and 206. The crystalline reflections for $Os_3(CO)_{12}$, $Ru_3(CO)_{12}$ and $Fe_3(CO)_{12}$ in the pre-reaction XRD patterns indicates that there was not a monolayer dispersion of the metal complexes. For all three samples, it can be observed that the reflections due to the starting metal carbonyls are not present in the post-reaction patterns. In the XRD post-reaction patterns of the 5% $Os_3(CO)_{12}$ + 2% $Ru_3(CO)_{12}$/silica hydroxylated and 5% $Os_3(CO)_{12}$ + 1% $Fe_3(CO)_{12}$/silica hydroxylated, the broad band between 40 – 45^o 2θ is observed. Furthermore, a reflection assigned to Ru metal can also be observed at 44^o 2θ in the XRD pattern for 5% $Os_3(CO)_{12}$ + 2% $Ru_3(CO)_{12}$/silica hydroxylated. Therefore, it is suggested that the metal carbonyls decomposed to their corresponding metal components. However, in the post-reaction XRD pattern of 2% $Ru_3(CO)_{12}$ + 1% $Fe_3(CO)_{12}$/silica hydroxylated, there were no reflections corresponding to Ru or Fe metal. This cannot be due to a lower metal loading, as Ru with the same loading was observed in the XRD pattern for 5% $Os_3(CO)_{12}$ + 2% $Ru_3(CO)_{12}$/silica hydroxylated. This may explain the reason for this material having the lowest activity of the three samples.

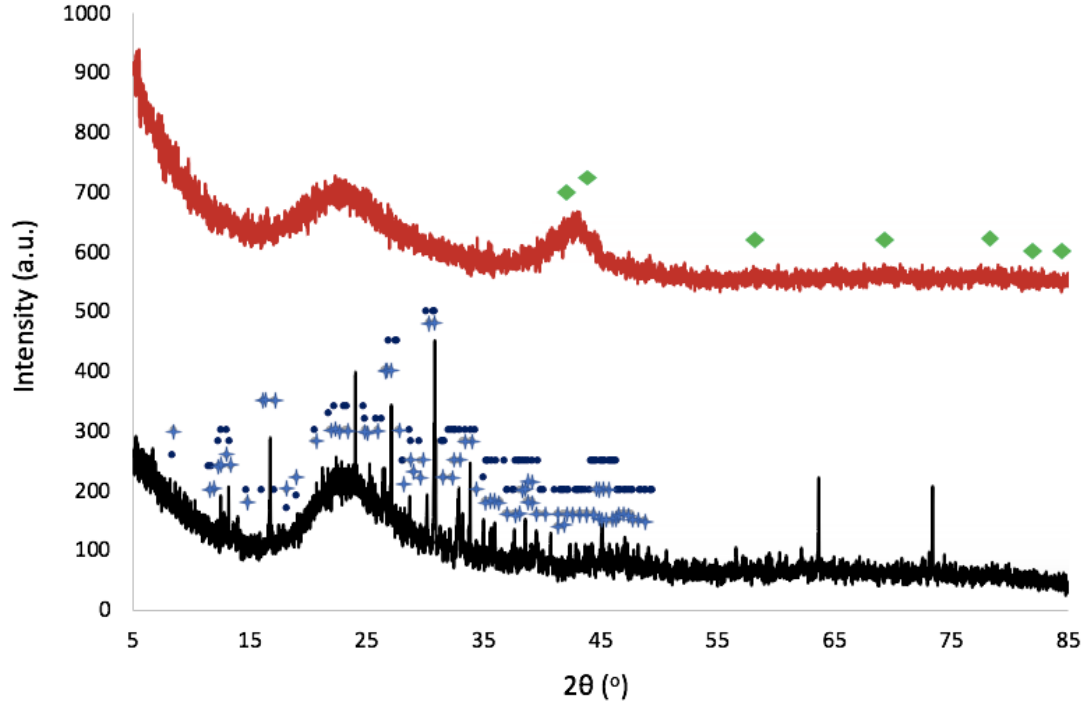

Figure 204: XRD patterns of 5% $Os_3(CO)_{12}$ + 2% $Ru_3(CO)_{12}$/silica hydroxylated pre- (black) and post-reaction (red) with 3:1 H_2/N_2. Reflections marked: ✦ $Os_3(CO)_{12}$ (JCPDS file number 01-070-0415), • $Ru_3(CO)_{12}$ (JCPDS file number 01-070-0553) and ◆ Ru (JCPDS file number 01-070-0274).

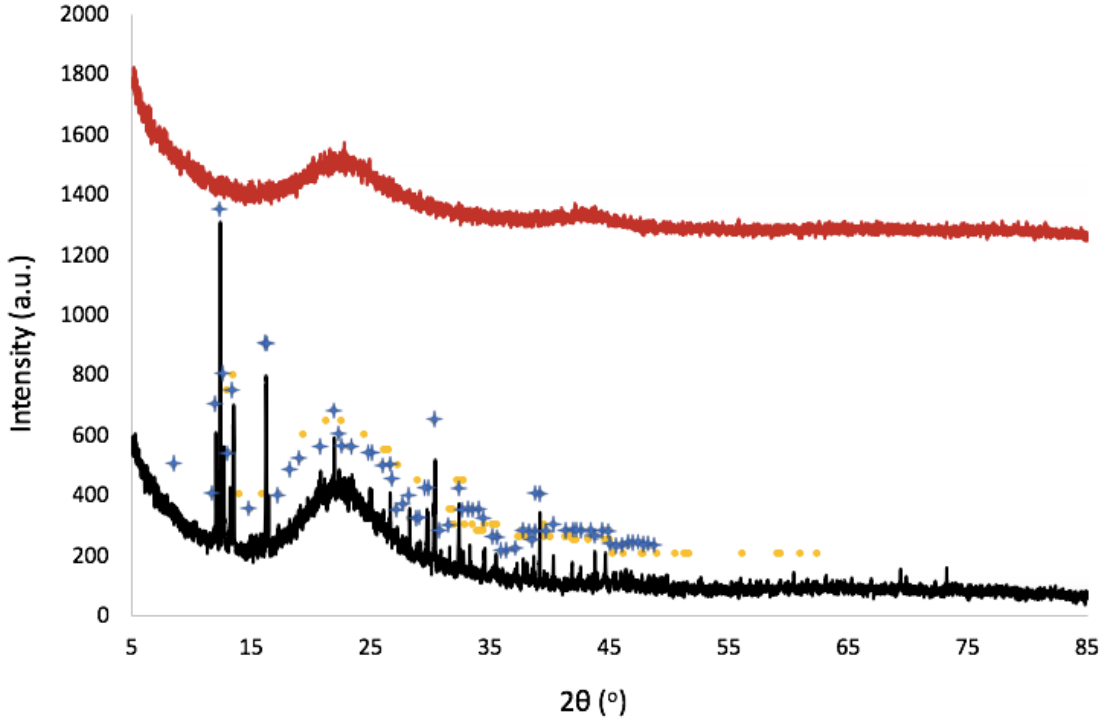

Figure 205: XRD patterns of 5% $Os_3(CO)_{12}$ + 1% $Fe_3(CO)_{12}$/silica hydroxylated pre- (black) and post-reaction (red) with 3:1 H_2/N_2. Reflections marked: ✦ $Os_3(CO)_{12}$ (JCPDS file number 01-070-0415) and • $Fe_3(CO)_{12}$ (JCPDS file number 01-082-2196).

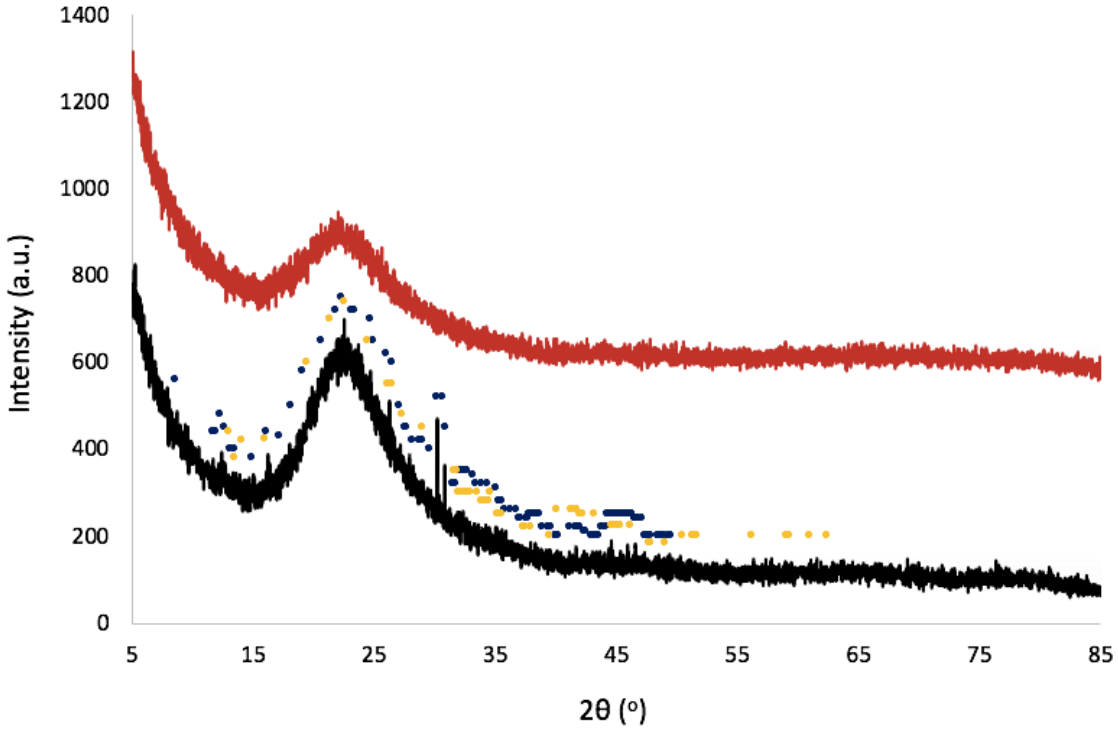

Figure 206: XRD patterns of 2% $Ru_3(CO)_{12}$ + 1% $Fe_3(CO)_{12}$/silica hydroxylated pre- (black) and post-reaction (red) with 3:1 H_2/N_2. Reflections marked: • $Ru_3(CO)_{12}$ (JCPDS file number 01-070-0553) and • $Fe_3(CO)_{12}$ (JCPDS file number 01-082-2196).

The FTIR spectra of the three supported mixed metal materials pre- and post-reaction are displayed in Figures 207, 208 and 209. For the 5% $Os_3(CO)_{12}$ + 2% $Ru_3(CO)_{12}$/silica hydroxylated pre-reaction spectrum, bands similar to those in the 5% $Os_3(CO)_{12}$/silica hydroxylated spectrum are observed. However, the IR bands for $Ru_3(CO)_{12}$ are at similar frequencies to those for $Os_3(CO)_{12}$ [184] [194]. Hence, overlapping of the bands due to $Os_3(CO)_{12}$ and $Ru_3(CO)_{12}$ may occur and will be difficult to distinguish.

The FTIR spectrum of 5% $Os_3(CO)_{12}$ + 1% $Fe_3(CO)_{12}$/silica hydroxylated pre-reaction is similar to the spectrum for 5% $Os_3(CO)_{12}$/silica hydroxylated. However, an additional band at 2046 (w) is also observed, which has been reported in the literature as a band for $Fe_3(CO)_{12}$ [195]. The expected bridging bands for $Fe_3(CO)_{12}$ between 1800 – 1900 cm^{-1} may be present in the spectrum in Figure 208. However, as there appears to be background noise in this region it was difficult to distinguish the bands.

The bands in the pre-reaction FTIR spectrum for 2% $Ru_3(CO)_{12}$ + 1% $Fe_3(CO)_{12}$/silica hydroxylated were very weak and therefore, difficult to differentiate from the background noise. This could possibly suggest that the content of the two metal carbonyls was low in the material and thus, may explain the low activity of this material.

For all three samples, no clear bands were observed in the spectra post-reaction. This is to be expected as the metal carbonyls will have decomposed during the reaction. Therefore, the metal carbonyls underwent decarbonylation as observed by Kulkarni and Gates [52].

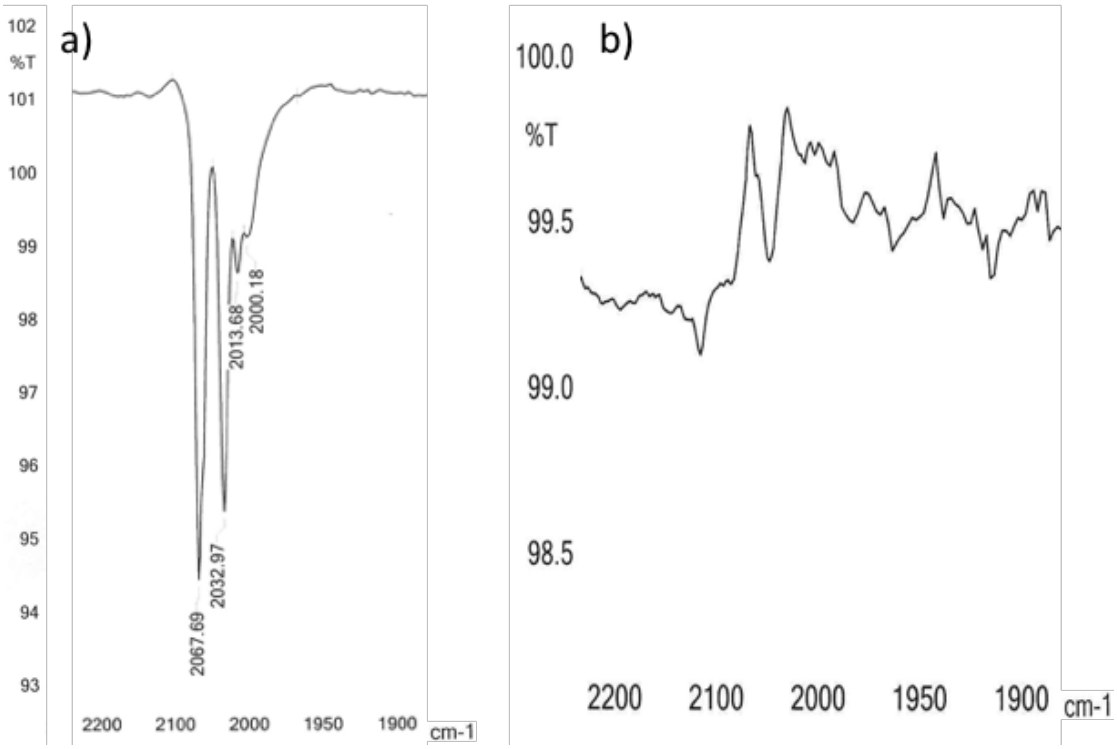

Figure 207: FTIR spectra of 5% $Os_3(CO)_{12}$ + 2% $Ru_3(CO)_{12}$/silica hydroxylated: a) pre-reaction and b) post-reaction.

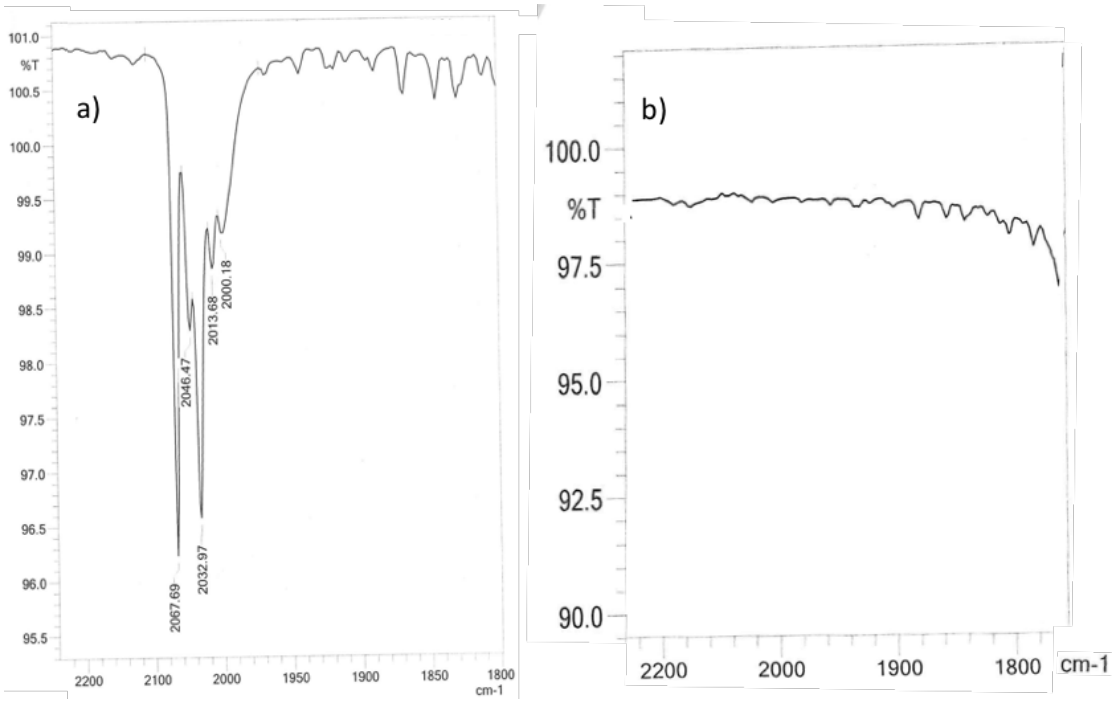

Figure 208: FTIR spectra of 5% $Os_3(CO)_{12}$ + 1% $Fe_3(CO)_{12}$/silica hydroxylated: a) pre-reaction and b) post-reaction.

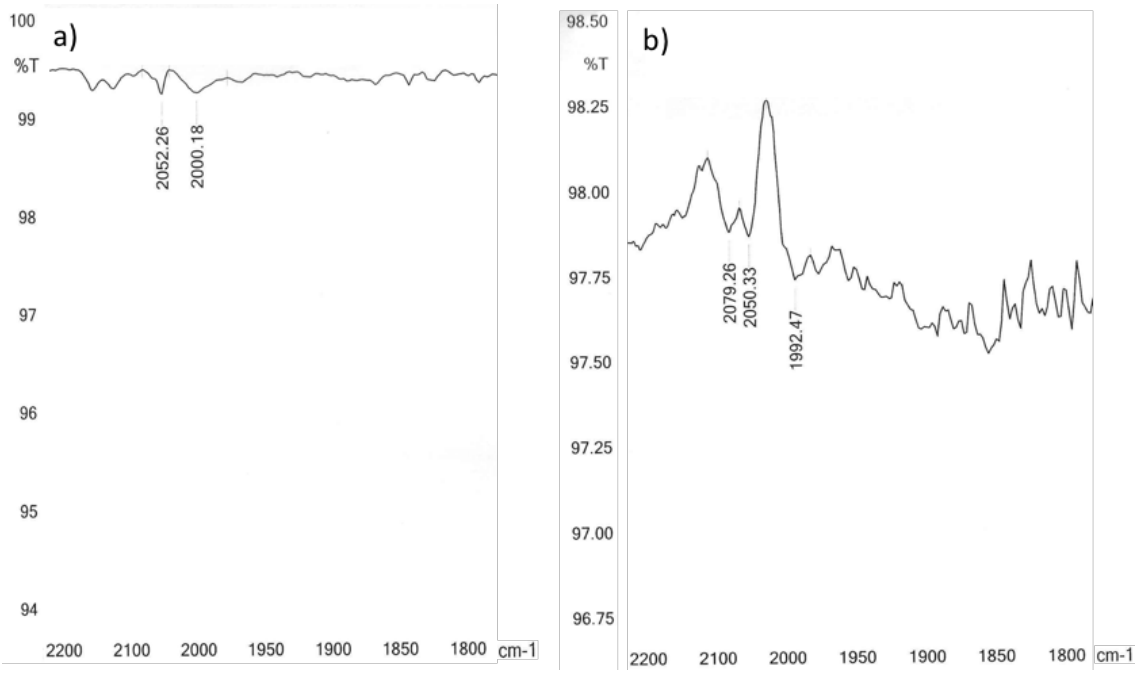

Figure 209: FTIR spectra of 2% $Ru_3(CO)_{12}$ + 1% $Fe_3(CO)_{12}$/silica hydroxylated: a) pre-reaction and b) post-reaction.

The pre and post-reaction EDX analysis is given in Table 55. The osmium percentage for 5% $Os_3(CO)_{12}$ + 2% $Ru_3(CO)_{12}$/silica hydroxylated was higher than for 5% $Os_3(CO)_{12}$ + 1% $Fe_3(CO)_{12}$/silica hydroxylated, which may explain the higher activity of this material. The osmium, ruthenium and iron percentages were observed to be higher post-reaction. The metal percentages were more varied across the areas examined in the pre-reaction materials and hence, this may suggest that there was better dispersion of the metals after the reaction.

Material	Os weight (%)	Ru weight (%)	Fe weight (%)	C weight (%)	O weight (%)	Si weight (%)
5% $Os_3(CO)_{12}$ + 2% $Ru_3(CO)_{12}$ /silica Pre-reaction. Average from 6 measurements.	1.5	0.5	-	14	55	29
5% $Os_3(CO)_{12}$ + 2% $Ru_3(CO)_{12}$ /silica Post-reaction. Average from 19 measurements.	2.3	0.7	-	12	52	32
5% $Os_3(CO)_{12}$ + 1% $Fe_3(CO)_{12}$ /silica Pre-reaction. Average from 10 measurements.	0.4	-	0.5	8	59	33
5% $Os_3(CO)_{12}$ + 1% $Fe_3(CO)_{12}$ /silica Post-reaction. Average from 11 measurements.	1	-	0.6	11	52	35

Table 55: EDX values for 5% $Os_3(CO)_{12}$ + 2% $Ru_3(CO)_{12}$/silica hydroxylated and 5% $Os_3(CO)_{12}$ + 1% $Fe_3(CO)_{12}$/silica hydroxylated pre- and post-reaction with 3:1 H_2/N_2.

6.3 Conclusions

In this chapter the activity of the bulk and supported osmium was compared. The osmium metal (262 ± 21 μmol h^{-1} g^{-1}) was found to have a similar activity as the supported $Os_3(CO)_{12}$ on silica (265 ± 48 μmol h^{-1} g^{-1}) at 500°C. However, when the rate is normalised to the metal content, the supported material is more efficient. Therefore, it appears that osmium was structure sensitive for ammonia synthesis. The area of the supported metal particles is not known and therefore, a conclusion based upon comparative turnover frequencies cannot be made.

When osmium metal was pre-treated with H_2/Ar or N_2, a lag period was observed before the material became active. This was not the case when H_2/N_2 was used as the pre-treatment mixture. The inhibition of hydrogen and nitrogen coverage of the surface may explain this lag period, as might surface restructuring under the reaction atmosphere. The osmium metal had steady state activity for all three pre-treatments after the lag periods. A cycling procedure was performed in order to try and overcome the possible inhibition of

hydrogen on the surface of the osmium. However, the cycling procedure resulted in the activity being reduced. Shorter cycling times appeared to be the most promising and therefore, this may be an avenue to be explored in future work.

$Os_3(CO)_{12}$ was supported on both silica and γ-alumina to give a 5 wt. % loading of osmium. 5% $Os_3(CO)_{12}$/silica hydroxylated and 5% $Os_3(CO)_{12}$/γ-alumina were observed to be stable when tested for 36 hours. The material was found to have the highest activity when supported on silica. To optimise the activity of the $Os_3(CO)_{12}$/silica hydroxylated, the material was modified by four different methods. It was found that the material had the highest activity when the silica was dehydroxylated. Promoting the material with KOH was shown to have a negative effect on the activity. The metal carbonyl was observed to largely decompose as a consequence of the reaction procedure. Further studies need to be performed in order to confirm if the Os nuclearity was preserved upon decomposition.

As the supported mixed metal materials had different activities compared to their monometallic equivalents, this may suggest that there was possible metal-metal bond formation between the different metals. However, this would need to be investigated further in order to gain an insight into the nature of the active phases. This study suggests that it may be possible to optimise these materials and this method may provide the opportunity of altering the activity of the metal particles. Furthermore, different sized metal carbonyl precursors could be used to control ensemble size.

A summary of the performance of the supported materials investigated within this chapter is provided in Figures 210 and 211.

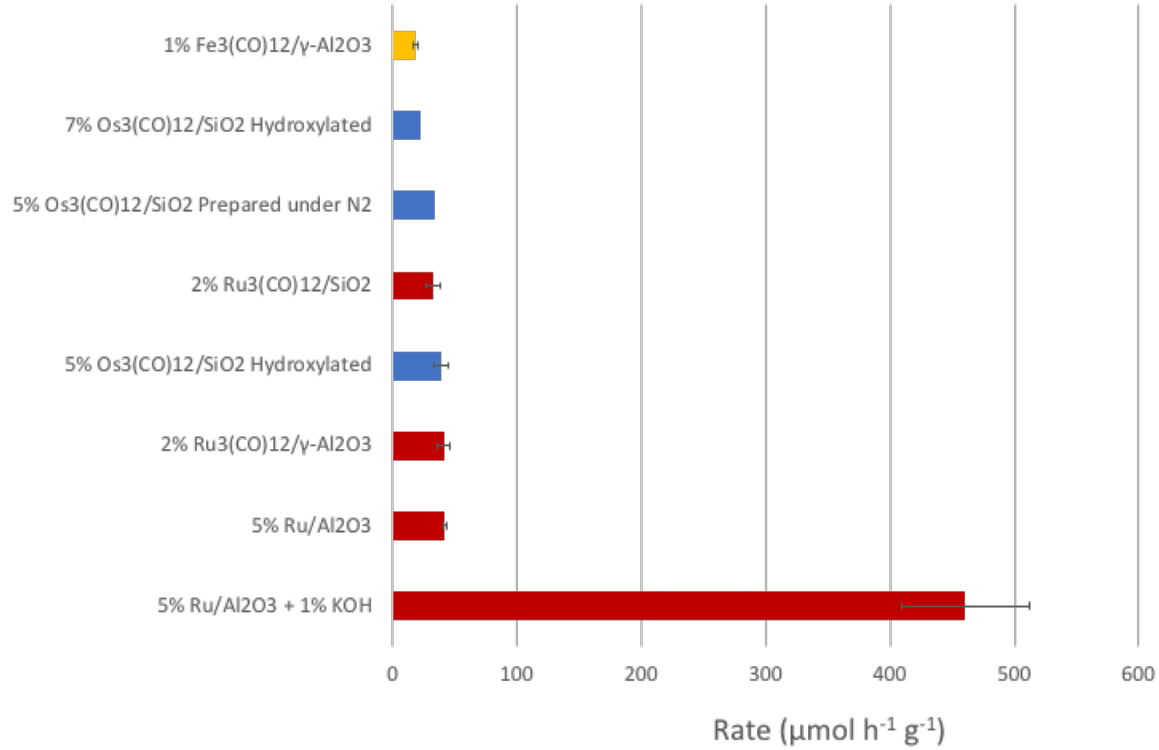

Figure 210: Ammonia synthesis activity of the supported materials reacted with 3:1 H_2/N_2 at 400°C.

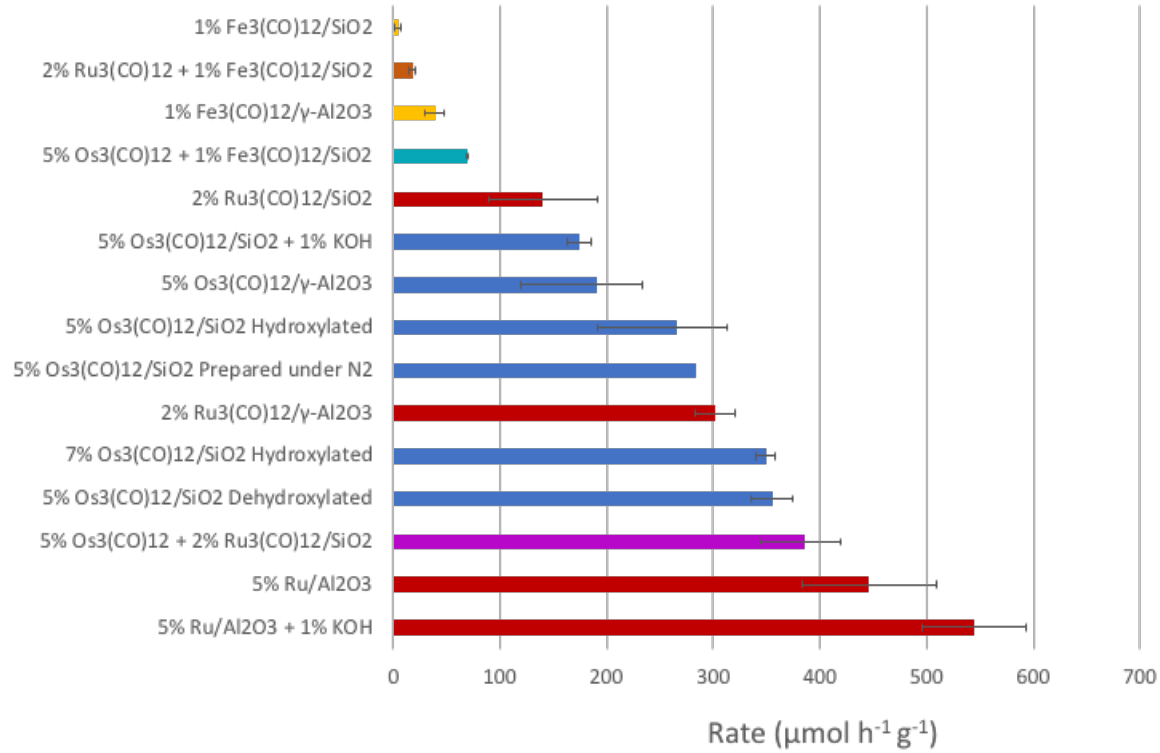

Figure 211: Ammonia synthesis activity of the supported materials reacted with 3:1 H_2/N_2 at 500°C.

7. Conclusions and Future Work

7.1 Conclusions

The main aim of this work was to investigate the role composition and structure type had on the ammonia synthesis activity of ternary and quaternary molybdenum containing materials and also the potential structure sensitivity of Group 8 metals. As a result, nitrides (Ni_2Mo_3N, Ni_2GaMo_3N, Co_2Mo_3N and Fe_3Mo_3N), a carbonitride ($Ni_2Mo_3C_xN_y$) and carbides (Ni_6Mo_6C, Ni_3Mo_3C and Fe_3Mo_3C) were synthesised that had different metal compositions and either a η-carbide structure or a filled β-manganese structure. Furthermore, the structure sensitivity of osmium was examined and compared with the other Group 8 metals.

The synthesis of some of the pure phase nitrides and carbides proved to be challenging. In the case of Co_2Mo_3N, the Co_3Mo_3N phase was also present and therefore, the optimal conditions had to be identified to give the highest ratio of Co_2Mo_3N to Co_3Mo_3N. For some other phases, minor impurities of monometallic nitrides/carbides or metal phases were observed. Hence, the careful choice of the synthesis conditions was required, with precursors, temperature and synthesis atmosphere all having an effect on the resulting product. The four nitrides investigated in this work were active for ammonia synthesis, with 'Co_2Mo_3N' having the highest activity of 208 μmol h^{-1} g^{-1} at 400°C.

The lattice nitrogen reactivity of the different nitrides was investigated up to 900°C, in order to examine the effect the crystal structure and metal composition had on the nitrogen mobility. The bulk lattice nitrogen in the filled β-manganese structured Ni_2Mo_3N and η-carbide structured Ni_2GaMo_3N were observed to be unreactive. However, the filled β-manganese structured Co_2Mo_3N and η-carbide structured Fe_3Mo_3N were shown to decompose when reacted under 3:1 H_2/Ar at 900°C. As the two filled β-manganese structured nitrides and the two filled η-carbide structured nitrides were shown to have different reactivities from one another, this could possibly suggest that the metal composition has a greater effect on the reactivity than the structure type. However, since the filled β-manganese structured Co_2Mo_3N and the η-carbide structured Co_3Mo_3N were observed to have different reactivities under 3:1 H_2/Ar up to 800°C, both structure and metal composition seem to play a role in the reactivity of the lattice nitrogen.

The effect of the interstitial element composition on the ammonia synthesis activity of the nickel molybdenum and iron molybdenum materials was also investigated. Preparation of Ni_2Mo_3C by nitridation of Ni_2Mo_3N proved to be unsuccessful, with instead a carbonitride

phase being formed. $Ni_2Mo_3C_xN_y$ was active for ammonia synthesis at 400°C and some replacement of lattice carbon was observed by elemental analysis. Ni_6Mo_6C, Ni_3Mo_3C and Fe_3Mo_3C were not active at this temperature. For Fe_3Mo_3C, unlike its corresponding nitride, a reaction temperature of 500°C was required before it developed activity. An induction period of 45 minutes was observed and through elemental analysis and analysis of the XRD patterns, it was discovered that substitution of some lattice carbon with nitrogen had taken place. This result may possibly suggest that the activity of Fe_3Mo_3N is due to the lattice nitrogen and therefore, the material may operate via a Mars-van Krevelen mechanism. The effect the passivation layer has on the reactivity of this system needs to be examined further but initial ToF-SIMS analysis suggests that this may have limited impact.

Ni_6Mo_6C and Ni_3Mo_3C required a much higher reaction temperature of 700°C before they were active. A small induction period was observed for both materials before there was development of activity. The two carbides were shown to undergo nitridation during the reaction. However, unlike Fe_3Mo_3C, the nitridation process did not occur through a topotactic exchange mechanism, with both carbides instead forming Ni_2Mo_3N. This possibly suggests that the Ni_3Mo_3N phase is unstable which is consistent with failed attempts to prepare it to date. This nitridation did not occur at the lower reaction temperatures examined and therefore, this may be the reason for the inactivity of these materials at these temperatures. Hence, it is possible that lattice nitrogen is required in order for these materials to be active.

The structure sensitivity of osmium was examined by comparing the ammonia synthesis activity of bulk osmium metal with triosmium dodecacarbonyl supported on silica and alumina. It was found that the bulk and supported osmium had similar activities at 500°C under 3:1 H_2/N_2. However, when the rate was normalised to take account of the differing mass of osmium present, the supported osmium materials were more active. This possibly suggests that the osmium is structure sensitive for ammonia synthesis, with the material being more active when the particle size is small. A comparison based upon turnover frequency is desirable. A cycling procedure was performed for osmium metal in order to try and improve ammonia production. Although production appeared to be reduced when this was implemented, shorter cycling times showed that there may be a benefit to this method.

Initial attempts were also performed in order to synthesise supported mixed metal clusters. Two of the osmium, ruthenium and iron metal carbonyl clusters were supported on silica and through FTIR analysis and analysis of the XRD patterns it was observed that the

materials underwent decarbonylation when reacted under 3:1 H_2/N_2. More detailed analysis using other techniques would need to be performed in order to determine if heterometallic bonds had formed. However, as the supported mixed metal materials had different activities to the supported monometallic equivalents, this possibly suggests that there may have been heterometallic bond formation. Therefore, this may be an interesting avenue to explore further.

7.2 Future Work

The formation of the η-carbide structured Ni_3Mo_3N, which is unprecedented to date, would give an interesting comparison to the isostructural Fe_3Mo_3N and Co_3Mo_3N. This would allow a further insight into the composition-activity relationship for ammonia synthesis and lattice nitrogen reactivity, which might be useful to feed into computational modelling for example. Furthermore, the comparison in performance between Ni_3Mo_3N and Ni_2Mo_3N would provide information on the structure-activity relationship. The study of anti-perovskites comprising the same elements but in different spatial and stoichiometric relationships could also provide information on the effect structure type has on activity.

The application of other complementary techniques such as X-ray photoelectron spectroscopy (XPS) and X-ray absorbance spectroscopy (XAS) could provide information on the effect structure and composition have on activity. XPS could also provide further information on the impact the passivation layer has on the activity of the carbides. XAS could be used to examine the possible heterometallic bond formation of the supported mixed metal clusters. This information could help towards the design of materials with high activity for ammonia synthesis.

Bibliography

[1] V. Smil, Enriching the Earth: Fritz Haber, Carl Bosch, and the Transformation of World Food Production, Cambridge: MIT Press, 2004.

[2] B. M. Hoffman, D. Lukoyanov, Z.-Y. Yang, D. R. Dean and L. C. Seefeldt, "Mechanism of Nitrogen Fixation by Nitrogenase: The Next Stage," *Chemical Reviews,* vol. 114, pp. 4041-4062, 2014.

[3] D. L. Drapcho, D. Sisterson and R. Kumar, "Nitrogen Fixation by Lightening Activity in a Thunderstorm," *Atmospheric Environment,* vol. 17, no. 4, pp. 729-734, 1983.

[4] S. Zhang, Y. Zhao, R. Shi, G. I. Waterhouse and T. Zhang, "Photocatalytic Ammonia Synthesis: Recent Progress and Future," *EnergyChem,* vol. 1, no. 2, p. 100013, 2019.

[5] R. R. Eady, "Structure-Function Relationships of Alternative Nitrogenases," *Chemical Reviews,* vol. 96, no. 7, pp. 3013-3030, 1996.

[6] O. Einsle, F. A. Tezcan, S. L. Andrade, B. Schmid, M. Yoshida, J. B. Howard and D. C. Rees, "Nitrogenase MoFe-Protein at 1.16 A Resolution: A Central Ligand in the FeMo-Cofactor," *Science,* vol. 297, no. 5587, pp. 1696-1700, 2002.

[7] H.-I. Lee, P. M. Benton, M. Laryukhin, R. Y. Igarashi, D. R. Dean, L. C. Seefeldt and B. M. Hoffman, "The Interstitial Atom of the Nitrogenase FeMo-Cofactor: ENDOR and ESEEM Show it is not an Exchangeable Nitrogen," *Journal of the American Chemical Society,* vol. 125, no. 19, pp. 5604-5605, 2003.

[8] T. Spatzal, M. Aksoyoglu, L. Zhang, S. L. Andrade, E. Schleicher, S. Weber, D. C. Rees and O. Einsle, "Evidence for Interstitial Carbon in Nitrogenase FeMo Cofactor," *Science,* vol. 334, no. 6058, p. 940, 2011.

[9] B. Hinnermann and J. K. Norskov, "Catalysis by Enzymes: The Biological Ammonia Synthesis," *Topics in Catalysis,* vol. 37, no. 1, pp. 55-70, 2006.

[10] N. Gruber and J. N. Galloway, "An Earth-System Perspective of the Global Nitrogen Cycle," *Nature,* vol. 451, pp. 293-296, 2008.

[11] F. R. Hartley, Chemistry of the Platinum Group Metals: Recent Developments, Elsevier Science, 2013.

[12] R. Michalsky and P. Pfromm, "An Ionicity Rationale to Design Solid Phase Metal Nitride Reactants for Solar Ammonia Production," *The Journal of Physical Chemistry,* vol. 116, pp. 23243 - 23251, 2012.

[13] F. Haber and R. L. Rossignol, "Production of Ammonia". United States Patent 1,202,995, 1916.

[14] M. Appl, "Ammonia," in *Ullmann's Encyclopedia of Industrial Chemistry*, Weinheim, Wiley-VCH Verlag GmbH & Co., 2006.

[15] A. Mittasch, "Early Studies of Multicomponent Catalysts," in *Advances in Catalysis, vol II*, vol. 2, New York, Academic Press, 1950, pp. 81-104.

[16] A. Mittasch and W. Frankenburger, “The Historical Development and Theory of Ammonia Synthesis,” *Journal of Chemical Education,* vol. 6, no. 12, pp. 2097-2103, 1929.

[17] T. Rayment, R. Schlogl, J. M. Thomas and G. Ertl, “Structure of the Ammonia Synthesis Catalyst,” *Nature,* vol. 315, pp. 311-313, 1985.

[18] G. Ertl, M. Weiss and S. B. Lee, “The Role of Potassium in the Catalytic Synthesis of Ammonia,” *Chemical Physics Letters,* vol. 60, no. 3, pp. 391-394, 1979.

[19] V. Palma, C. Ruocco, M. Martino, E. Meloni and A. Ricca, “Catalysts for Conversion of Synthesis Gas,” in *Bioenergy Systems for the Future*, Woodhead Publishing, 2017, pp. 217-277.

[20] V. Smil, “Detonator of the Population Explosion,” *Nature,* vol. 400, pp. 415 - 415, 1999.

[21] S. K. Ritter, “The Haber-Bosch Reaction: An Early Chemical Impact on Sustainability,” *Chemical & Engineering News,* vol. 86, no. 33, pp. 53 - 53, 2008.

[22] I. Rafiqul, C. Weber, B. Lehmann and A. Voss, “Energy Efficiency Improvements in Ammonia Production - Perspectives and Uncertainties,” *Energy,* vol. 30, no. 13, pp. 2487 - 2504, 2005.

[23] A. K. Rhodes, “New Ammonia Process, Catalyst Proven in Canadian Plant,” *Oil and Gas Journal,* vol. 94, no. 47, pp. 37-41, 1996.

[24] C. J. Jacobsen, S. Dahl, B. S. Clausen, S. Bahn, A. Logadottir and J. K. Norskov, “Catalyst Design by Interpolation in the Periodic Table: Bimetallic Ammonia Synthesis Catalysts,” *Journal of the American Chemical Society,* vol. 123, no. 34, pp. 8404-8405, 2001.

[25] K. -I. Aika, T. Takano and S. Murata, “Preparation and Characterization of Chlorine-Free Ruthenium Catalysts and the Promoter Effect in Ammonia Synthesis,” *Journal of Catalysis,* vol. 136, pp. 126-140, 1992.

[26] K. Aika, K. Shimazaki, Y. Hattori, A. Ohya, S. Ohshima, K. Shirota and A. Ozaki, “Support and Promoter Effect of Ruthenium Catalyst: I. Characterization of Alkali-Promoted Ruthenium/alumina Catalysts for Ammonia Synthesis,” *Journal of Catalysis,* vol. 92, no. 2, pp. 296-304, 1985.

[27] K.-i. Aika, H. Hori and A. Ozaki, “Activation of Nitrogen by Alkali Metal Promoted Transition Metal I. Ammonia Synthesis over Ruthenium Promoted by Alkali Metal,” *Journal of Catalysis,* vol. 27, no. 3, pp. 424-431, 1972.

[28] A. Ozaki, “Development of Alkali-Promoted Ruthenium as a Novel Catalyst for Ammonia Synthesis,” *Accounts of Chemical Research,* vol. 14, no. 1, pp. 16-21, 1981.

[29] D. E. Brown, T. Edmonds, R. W. Joyner, J. J. McCarroll and S. R. Tennison, “The Genesis and Development of the Commercial BP Doubly Promoted Catalyst for Ammonia Synthesis,” *Catalysis Letters,* vol. 144, pp. 545-552, 2014.

[30] R. B. Strait and I. Welch, “First Two 1,850 MTPD Grassroots Ammonia Plants,” *Ammonia Technical Manuel,* pp. 217-225, 2000.

[31] G. Rambeau and H. Amariglio, “Improvement of the Catalytic Performance of a Ruthenium Powder in Ammonia Synthesis by the Use of a Cyclic Procedure,” *Applied Catalysis,* vol. 1, no. 5, pp. 291-302, 1981.

[32] G. J. Leigh, The World's Greatest Fix: A History of Nitrogen and Agriculture, New York: Oxford University Press, 2004.

[33] F. Haber.Germany Patent 229,126, 1909.

[34] R. Kojima and K.-i. Aika, “Molybdenum Nitride and Carbide Catalysts for Ammonia Synthesis,” *Applied Catalysis A: General,* vol. 219, no. 1-2, pp. 141-147, 2001.

[35] D. McKay, J. S. Hargreaves, J. L. Rico, J. L. Rivera and X. L. Sun, “The Influence of Phase and Morphology of Molybdenum Nitrides on Ammonia Synthesis Activity and Reduction Characteristics,” *Journal of Solid State Chemistry,* vol. 181, no. 2, pp. 325-333, 2008.

[36] N. Bion, F. Can, J. Cook, J. S. Hargreaves, A. L. Hector, W. Levason, A. R. McFarlane, M. Richard and K. Sardar, “The Role of Preparation Route Upon the Ambient Pressure Ammonia Synthesis Activity of Ni2Mo3N,” *Applied Catalysis A: General,* vol. 504, pp. 44-50, 2015.

[37] R. Kojima and K. Aika, “Cobalt Molybdenum Bimetallic Nitride Catalysts for Ammonia Synthesis-Part 1. Preparation and Characterisation,” *Applied Catalysis A: General,* vol. 215, pp. 149-160, 2001.

[38] K. McAulay, J. S. Hargreaves, A. McFarlane, D. J. Price, N. A. Spencer, N. Bion, B. Can, M. Richard, H. F. Greer and W. Z. Zhou, “The Influence of Pre-treatment Gas Mixture Upon the Ammonia Synthesis Activity of Co-Re Catalysts,” *Catalysis Communications,* vol. 68, pp. 53-57, 2015.

[39] R. Kojima and K.-I. Aika, “Cobalt Molybdenum Bimetallic Nitride Catalysts for Ammonia Synthesis Part 1. Preparation and Charaterisation,” *Applied Catalysis A: General,* vol. 215, pp. 149-160, 2001.

[40] J. Norskov, J. Chen, R. Miranda, T. Fitzsimmons and R. Stack, “Sustainable Ammonia Synthesis – Exploring the Scientific Challenges Associated with Discovering Alternative, Sustainable Processes for Ammonia Production,” in *DOE Roundtable Report*, United States, 2016.

[41] Q. Wang, J. Guo and P. Chen, “Recent Progress Towards Mild-Condition Ammonia Synthesis,” *Journal of Energy Chemistry,* vol. 36, pp. 25-36, 2019.

[42] M. G. Heidlage, E. A. Kezar, K. C. Snow and P. H. Pfromm, “Thermochemical Synthesis of Ammonia and Syngas from Natural Gas at Atmospheric Pressure,” *Industrial and Engineering Chemistry Research,* vol. 56, no. 47, pp. 14014-14024, 2017.

[43] R. Michalsky, P. H. Pfromm and A. Steinfeld, “Rational Design of Metal Nitride Redox Materials for Solar-Driven Ammonia Synthesis,” *Interface Focus,* vol. 5, no. 3, p. 20150003, 2015.

[44] M. E. Galvez, M. Halmann and A. Steinfeld, “Ammonia Production via a Two-Step Al2O3/AlN Thermochemical Cycle 1. Thermodynamic, Environmental, and Economic

Analyses," *Industrial and Engineering Chemistry Research,* vol. 46, no. 7, pp. 2042-2046, 2007.

[45] M. E. Galvez, A. Frei, F. Meier and A. Steinfeld, "Production of AlN by Carbothermal and Methanothermal Reduction of Al2O3 in a N2 Flow Using Concentrated Thermal Radiation," *Industrial and Engineering Chemistry Research,* vol. 48, no. 1, pp. 528-533, 2009.

[46] R. Michalsky, A. M. Avram, B. A. Peterson, P. H. Pfromm and A. A. Peterson, "Chemical Looping of Metal Nitride Catalysts: Low Pressure Ammonia Synthesis for Energy Storage," *Chemical Science,* vol. 6, pp. 3965 - 3974, 2015.

[47] S. Laassiri, C. D. Zeinalipour-Yazdi, C. R. Catlow and J. S. Hargreaves, "The Potential of Manganese Nitride Based Materials as Nitrogen Transfer Reagents for Nitrogen Chemical Looping," *Applied Catalysis B: Environmental,* vol. 223, pp. 60-66, 2018.

[48] Y. N. Regmi and B. M. Leonard, "General Synthesis Method for Bimetallic Carbides of Group VIIIA First Row Transition Metals with Molybdenum and Tungsten," *Chemistry of Materials,* vol. 26, p. 2609−2616, 2014.

[49] D. S. Bem, C. P. Gibson and H. C. zur Loye, "Synthesis of Intermetallic Nitrides by Solid-state Precursor Reduction," *Chemistry of Materials,* vol. 5, no. 4, pp. 397-399, 1993.

[50] S. M. Hunter, D. McKay, R. I. Smith, J. S. Hargreaves and D. H. Gregory, "Topotactic Nitrogen Transfer: Structural Transformation in Cobalt Molybdenum Nitrides," *Chemistry of Materials,* vol. 22, pp. 2898-2907, 2010.

[51] G. Collier, D. J. Hunt, S. D. Jackson, R. B. Moyes, I. A. Pickering, P. B. Wells, A. F. Simpson and R. Whyman, "Chemisorption and Catalysis by Metal Clusters. I. Characterisation of Materials Obtained by Impregnation of Os3(CO)12 and Os6(CO)18 onto Silica, Alumina and Titania," *Journal of Catalysis,* vol. 80, pp. 154-171, 1983.

[52] A. Kulkarni and B. C. Gates, "Spectroscopic Elucidation of First Steps of Supported Bimetallic Cluster Formation," *Angewandte Chemie,* vol. 48, no. 51, pp. 9697-9700, 2009.

[53] D. McKay, "Catalysis over Molybdenum Containing Nitride Materials," PhD Thesis, University of Glasgow, 2008.

[54] I. AlShibane, A. Daisley, J. S. Hargreaves, A. L. Hector, S. Laassiri, J. L. Rico and R. I. Smith, "The role of Composition for Cobalt Molybdenum Carbide in Ammonia Synthesis," *ACS Sustainable Chemistry and Engineering,* vol. 5, no. 10, pp. 9214-9222, 2017.

[55] I. Alshibane, "Phase Transformations of Ternary Carbides, Nitrides and Carbonitrides," PhD Thesis, University of Glasgow, 2018.

[56] G. Jin, J. Zhu, X. Fan, G. Sun and J. Gao, "Effect of Ni Promoter on Dibenzothiophene Hydrodesulfurization Performance of Molybdenum Carbide Catalyst," *Chinese Journal of Catalysis,* vol. 27, no. 10, pp. 899-903, 2006.

[57] L. Zeng, S. Zhao and W. Li, "Ni3Mo3C as Anode Catalyst for High-Performance Microbial Fuel Cells," *Applied Biochemistry and Biotechnology,* vol. 175, pp. 2637-2646, 2015.

[58] S. Izhar, S. Otsuka and M. Nagai, “Application of Carbon Supported NiMo Carburised Catalyst to Fuel Cell Anode Electrocatalyst,” *Journal of New Materials for Electrochemical Systems,* vol. 11, pp. 15-20, 2008.

[59] S. Alconchel, F. Sapina, D. Beltran and A. Beltran, “Chemistry of Interstitial Molybdenum Ternary Nitrides MnMo3N (M = Fe, Co, n = 3; M = Ni, n = 2),” *Journal of Materials Chemistry,* vol. 8, no. 8, pp. 1901-1909, 1998.

[60] J. O. Conway and T. J. Prior, “Interstitial Nitrides Revisited - A Simple Synthesis of MxMo3N (M=Fe, Co, Ni),” *Journal of Alloys and Compounds,* vol. 774, pp. 69-74, 2019.

[61] S. Alconchel, F. Sapina, D. Beltran and A. Beltran, “A New Approach to the Synthesis of Molybdenum Bimetallic Nitrides and Oxynitrides,” *Journal of Materials Chemistry,* vol. 9, pp. 749-755, 1999.

[62] M. Nagai, A. M. Zahidul and K. Matsuda, “Nano-structured Nickel-Molybdenum Carbide Catalyst for Low-Temperature Water-Gas Shift Reaction,” *Applied Catalysis A: General,* vol. 313, pp. 137-145, 2006.

[63] W. Xu, P. J. Ramirez, D. Stacchiola, J. L. Brito and J. A. Rodriguez, “The Carburisation of Transition Metal Molybdates (MxMoO4, M=Cu, Ninor Co) and the Generation of Highly Active Metal/Carbide Catalysts for CO2 Hydrogenation,” *Catalysis Letters,* vol. 145, no. 7, pp. 1365-1373, 2015.

[64] J. M. Newsam, A. J. Jacobson, L. E. McCandlish and R. S. Polizzotti, “The Structures of the n-Carbides Ni6Mo6C, Co6Mo6C, and Co6Mo6C2,” *Journal of Solid State Chemistry,* vol. 75, pp. 296-304, 1988.

[65] T. Hirose, Y. Ozawa and M. Nagai, “Preparation of a Nickel Molybdenum Carbide Catalyst and Its Activity in the Dry Reforming of Methane,” *Chinese Journal of Catalysis,* vol. 32, no. 5, pp. 771-776, 2011.

[66] E. Puello-Polo and J. L. Brito, “Effect of the Type of Precursor and the Synthesis Method on Thiophene Hydrosulfurisation Activity of Activated Carbon Supported Fe-Mo, Co-Mo and Ni-Mo Carbides,” *Journal of Molecular Catalysis A: Chemical,* vol. 281, no. 1-2, pp. 85-92, 2008.

[67] S. Alconchel, B. Pierini, F. Sapina and E. Martinez, “Monitoring the Carburisation of Molybdenum Bimetallic Nitrides and Oxynitirdes with CH4/H2/Ar Mixtures: Identification of a New Carbonitride,” *Dalton Transactions,* vol. 0, no. 2, pp. 330-339, 2009.

[68] A. A. Smirnov, Z. Geng, S. A. Khromova, S. G. Zavarukhin, O. A. Bulavchenko, A. A. Saraev, V. V. Kaichev, D. Y. Ermakov and V. A. Yakovlev, “Nickel Molybdenum Carbides: Synthesis, Characterisation, and Catalytic Activity in Hydrodeoxygenation of Anisole and Ethyl Caprate,” *Journal of Catalysis,* vol. 354, pp. 61-77, 2017.

[69] L. Zhao, K. Fang, D. Jiang, D. Li and Y. Sun, “Sol-gel Derived Ni-Mo Bimetallic Carbide Catalysts and Their Preformance for CO Hydrogenation,” *Catalysis Today,* vol. 158, no. 3-4, pp. 490-495, 2010.

[70] S. T. Oyama, “Preparation and Catalytic Properties of Transition Metal Carbides and Nitrides,” *Catalysis Today,* vol. 15, no. 2, pp. 179-200, 1992.

[71] A. S. Kurlov and A. I. Gusev, Tungsten Carbides: Structure, Properties and Application in Hardmetals, 1 ed. ed., vol. 184, Springer International Publishing, 2013.

[72] V. Ponec and G. C. Bond, Catalysis by Metals and Alloys, 1 ed. ed., vol. 95, Elsevier Science, 1995.

[73] T. J. Prior and P. D. Battle, "Facile Synthesis of Interstitial Metal Nitrides with the Filled Beta-Manganese Structure," *Journal of Solid State Chemistry,* vol. 172, pp. 138-147, 2003.

[74] S. K. Jackson, R. C. Layland and H.-C. zur Loye, "The Simultaneous Powder X-ray and Neutron Diffraction Refinement of Two n-carbide Type Nitrides, Fe3Mo3N and Co3Mo3N, prepared by Ammonolysis and by Plasma Nitridation of Oxide Precursors," *Journal of Alloys and Compounds,* vol. 291, no. 1-2, pp. 94-101, 1999.

[75] P. Ettmayer and R. Suchentrunk, "Ueber die Thermische Stabilitaet der Eta-Carbide," *Monatshefte fuer Chemie,* vol. 101, no. 4, pp. 1098-1103, 1970.

[76] D. Errandonea, J. Ruiz-Fuertes, J. A. Sans, D. Santamaria-Perez, O. Gomis, A. Gomez and F. Sapina, "Compressibility and Structural Stability of Ultra-incompressible Bimetallic Interstitial Carbides and Nitrides," *Physical Review B,* vol. 85, p. 144103, 2012.

[77] S. M. Hunter, D. H. Gregory, J. S. Hargreaves, M. Richard, D. Duprez and N. Bion, "A Study of 15N/14N Isotopic Exchange over Cobalt Molybdenum Nitrides," *ACS Catalysis,* vol. 3, no. 8, pp. 1719-1725, 2013.

[78] Y. Tsuji, M. Kitano, K. Kishida, M. Sasase, T. Yokoyama, M. Hara and H. Hosono, "Ammonia Synthesis over Co-Mo Alloy Nanoparticle Catalyst Prepared via Sodium Naphthalenide-driven Reduction," *Chemical Communications,* vol. 52, pp. 14369-14372, 2016.

[79] Y. Tsuji, K. Ogasawara, M. Kitano, K. Kishida, H. Abe, Y. Niwa, T. Yokoyama, M. Hara and H. Hosono, "Control of Nitrogen Activation Ability by Co-Mo Bimetallic Nanoparticle Catalysts Prepared via Sodium Naphthalenide-reduction," *Journal of Catalysis,* vol. 364, pp. 31-39, 2018.

[80] S. Korlann, B. Diaz and M. E. Bussell, "Synthesis of Bulk and Alumina-Supported Bimetallic Carbide and Nitride Catalysts," *Chemistry of Materials,* vol. 14, no. 10, pp. 4049-4058, 2002.

[81] C. D. Zeinalipour-Yazdi, J. S. Hargreaves and C. R. Catlow, "Nitrogen Activation in a Mars–van Krevelen Mechanism for Ammonia Synthesis on Co3Mo3N," *The Journal of Physical Chemistry C,* vol. 119, no. 51, pp. 28368-28376, 2015.

[82] H. Ehrenberg, I. Svoboda, G. Wltschek, M. Wiesmann, F. Trouw, H. Weitzel and H. Fuess, "Crystal and Magnetic Structure of alpha-NiMoO4," *Journal of Magnetism and Magnetic Materials,* vol. 150, pp. 371-376, 1995.

[83] J. A. Rodriguez, S. Chaturvedi, J. C. Hanson, A. Albornoz and J. L. Brito, "Electronic Properties and Phase Transformations in CoMoO4 and NiMoO4: XANES and Time-Resolved Synchrotron XDD Studies," *The Journal of Physical Chemistry B,* vol. 102, no. 8, pp. 1347-1355, 1998.

[84] K. Eda, Y. Kato, Y. Ohshiro, T. Sugitani and M. S. Whittingham, “Synthesis, Crystal Structure, and Structural Conversion of Ni Molybdate Hydrate NiMoO4.nH2O,” *Journal of Solid State Chemistry,* vol. 183, no. 6, pp. 1334-1339, 2010.

[85] S. Al Sobhi, J. S. Hargreaves, A. L. Hector and S. Laassiri, “Citrate-gel Preparation and Ammonia Synthesis Activity of Compounds in the Quaternary (Ni,M)2Mo3N (M = Cu or Fe) Systems,” *Dalton Transactions,* vol. 48, pp. 16786-16792, 2019.

[86] D. Cai, D. Wang, B. Liu, Y. Wang, Y. Liu, L. Wang, H. Li, H. Huang, Q. Li and T. Wang, “Comparison of the Electrochemical Performance of NiMoO4 Nanorods and Hierarchical Nanospheres for Supercapacitor Applications,” *ACS Applied Materials and Interfaces,* vol. 5, no. 24, pp. 12905-12910, 2013.

[87] S. Baoyi, X. Aiju and W. Jiang, “The Impact of Preparation Methods on the Structure and Catalytic Performance of NiMoO4 for Oxidative Dehydrogenation of Propane,” *Integrated Ferroelectrics,* vol. 171, pp. 16-22, 2016.

[88] A. P. de Moura, L. H. de Oliveira, I. L. Rosa, C. S. Xavier, P. N. Lisboa-Filho, M. S. Li, F. A. La Porta, E. Longo and J. A. Varela, “Structural, Optical and Magnetic Properties of NiMoO4 Nanorods Prepared by Microwave Sintering,” *The Scientific World Journal,* vol. 2015, p. 315084, 2015.

[89] H. M. Abdel-Dayem, “Dynamic Phenomena during Reduction of α-NiMoO4 in Different Atmospheres: In-Situ Thermo-Raman Spectroscopy Study,” *Industrial and Engineering Chemistry Research,* vol. 46, no. 8, pp. 2466-2472, 2007.

[90] S. Chang, M. A. Leugers and S. R. Bare, “Surface Chemistry of Magnesium Oxide-Supported Molybdenum Oxide: An in Situ Raman Spectroscopic Study,” *The Journal of Physical Chemistry,* vol. 96, no. 25, pp. 10358-10365, 1992.

[91] P. R. Jothi, K. Shanthi, R. R. Salunkhe, M. Pramanik, V. Malgras, S. M. Alshehri and Y. Yamauchi, “Synthesis and Characterisation of alpha-NiMoO4 Nanorods for Supercapacitor Application,” *European Journal of Inorganic Chemistry,* vol. 2015, no. 22, pp. 3694-3699, 2015.

[92] S. Al Sobhi, N. Bion, J. S. Hargreaves, A. L. Hector, S. Laassiri, W. Levason, A. W. Lodge, A. R. McFarlane and C. Ritter, “The Reactivity of Lattice Nitrogen within the Ni2Mo3N and NiCoMo3N Phases,” *Materials Research Bulletin,* vol. 118, p. 110519, 2019.

[93] V. Umapathy, P. Neeraja, A. Manikandan and P. Ramu, “Synthesis of NiMoO4 Nanoparticles by Sol-gel Method and their Structural, Morphological, Optical, Magnetic and Photocatlytic Properties,” *Transactions of Nonferrous Metals Society of China,* vol. 27, no. 8, pp. 1785-1793, 2017.

[94] C. J. Jacobsen, “Novel Class of Ammonia Synthesis Catalysts,” *Chemical Communications,* no. 12, pp. 1057-1058, 2000.

[95] R. S. Wise and E. J. Markel, “Catalytic NH3 Decomposition by Topotactic Molybdenum Oxides and Nitrides: Effect on Temperature Programmed gamma-Mo2N Synthesis,” *Journal of Catalysis,* vol. 145, pp. 335-343, 1994.

[96] K. K. Naik, S. Ratha and C. S. Rout, “Phase and Shape Dependent Non-enzymatic Glucose Sensing Properties of Nickel Molybdate,” *ChemistrySelect,* vol. 1, pp. 5187-5195, 2016.

[97] H. Boukhlouf, R. Benrabaa, S. Barama and A. Barama, “Study of Unsupported and Al2O3 or SiO2-supported Nickel Molybdate for Oxireforming of Ethane,” in *Thin Films and Porous Materials, Materials Science Forum (Volume 609)*, Trans Tech Publications Ltd, 2009, pp. 145-148.

[98] J. S. Hargreaves and D. McKay, “A Comparison of the Reactivity of Lattice Nitrogen in Co3Mo3N and Ni2Mo3N Catalysts,” *Journal of Molecular Catalysis A: Chemical,* vol. 305, no. 1-2, pp. 125-129, 2009.

[99] G. Marnellos and M. Stoukides, “Ammonia Synthesis at Atmospheric Pressure,” *Science,* vol. 282, no. 5386, pp. 98-100, 1998.

[100] T. Xiao, A. P. York, K. S. Coleman, J. B. Claridge, J. Sloan, J. Charnock and M. L. Green, “Effect of Carburising Agent on the Structure of Molybdenum Carbides,” *Journal of Materials Chemistry,* vol. 11, pp. 3094-3098, 2001.

[101] T. Xiao, A. Hanif, A. P. York, J. Sloan and M. L. Green, “Study on Preparation of High Surface Area Tungsten Carbides and Phase Transition During the Carburisation,” *Physical Chemistry Chemical Physics,* vol. 4, pp. 3522-3529, 2002.

[102] J. B. Claridge, A. P. York, A. J. Brungs and M. L. Green, “Study of the Temperature-Programmed Reaction Synthesis of Early Transition Metal Carbide and Nitride Catalyst Materials from Oxide Precursors,” *Chemistry of Materials,* vol. 12, pp. 132-142, 2000.

[103] T. Xiao, A. P. York, V. Cliff Williams, H. Al-Megren, A. Hanif, X. Zhou and M. L. Green, “Preparation of Molybdenum Carbides Using Butane and Their Catalytic Performance,” *Chemistry of Materials,* vol. 12, no. 12, pp. 3896-3905, 2000.

[104] A. Maione and M. Devillers, “Solid Solutions of Ni and Co Molybdates in Silica-dispersed and Bulk Catalysts Prepared by Sol-gel and Citrate Methods,” *Journal of Solid State Chenistry,* vol. 177, no. 7, pp. 2339-2349, 2004.

[105] S. Alconchel, F. Sapina and E. Martinez, “From Nitrides to Carbides: Topotactic Synthesis of the n-carbides Fe3Mo3C and Co3Mo3C,” *Dalton Transactions,* no. 16, pp. 2463-2468, 2004.

[106] S. Chouzier, P. Afanasiev, M. Vrinat, T. Cseri and M. Roy-Auberger, “One-step Synthesis of Dispersed Bimetallic Carbides and Nitrides from Transition Metals Hexamethylenetetramine Complexes,” *Journal of Solid State Chemistry,* vol. 179, no. 11, pp. 3314-3323, 2006.

[107] T. Zhang, X. Guo and Z. Zhao, “Glucose-Assisted Preparation of a Nickel–Molybdenum Carbide Bimetallic Catalyst for Chemoselective Hydrogenation of Nitroaromatics and Hydrodeoxygenation of m-Cresol,” *ACS Applied Nano Materials,* vol. 1, no. 7, pp. 3579-3589, 2018.

[108] A. M. Stux, C. Laberty-Robert and K. E. Swider-Lyons, “Pechini Synthesis and Characterisation of Molybdenum Carbide and Nickel Molybdenum Carbide,” *Journal of Solid State Chemistry,* vol. 181, no. 10, pp. 2741-2747, 2008.

[109] Y. Chen, Y. Zhang, X. Zhang, T. Tang, H. Luo, S. Niu, Z. Dai, L. Wan and J. Hu, “Self-Templated Fabrication of MoNi4/MoO3-x Nanorod Arrays with Dual Active Components for Highly Efficient Hydrogen Evolution,” *Advanced Materials,* vol. 29, no. 39, p. 1703311, 2017.

[110] F. Dury, E. M. Gaigneaux and P. Ruiz, “The Active Role of Co2 at Low Temperature in Oxidation Processes: the Case of the Oxidative Dehydrogenation of Propane on NiMoO4 Catalysts,” *Applied Catalysis A: General,* vol. 242, no. 1, pp. 187 - 203, 2003.

[111] D. Ghosh, S. Giri and C. K. Das, “Synthesis, Characterisation and Electrochemical Performance of Graphene Decorated with 1D NiMoO4.nH2O Nanorods,” *Nanoscale,* vol. 5, pp. 10428 - 10437, 2013.

[112] H. Kagi, I. Tsuchida, M. Wakatsuki, K. Takahashi, N. Kamimura, K. Iuchi and H. Wada, “Proper Understanding of Down-shifted Raman Spectra of Natural Graphite: Direct Estimation of Laser-induced Rise in Sample Temperature,” *Geochimica et Cosmochimica Acta,* vol. 58, no. 16, pp. 3527 - 3530, 1994.

[113] A. C. Ferrari, “Raman Spectroscopy of Graphene and Graphite: Disorder, Electron-phonon Coupling, Doping and Nonadiabatic Effects,” *Solid State Communications,* vol. 143, pp. 47-57, 2007.

[114] M. Wall, “Raman Spectroscopy Optimizes Graphene Characterization,” *Advanced Materials and Processes,* vol. 170, no. 4, pp. 35-38, 2012.

[115] G. Mestl, P. Ruiz, B. Delmon and H. Knozinger, “Oxygen-Exchange Properties of MoO3: An in Situ Raman Spectroscopy Study,” *The Journal of Physical Chemistry,* vol. 98, pp. 11269 - 11275, 1994.

[116] Y. Kawashima and G. Katagiri, “Fundamentals, Overtones and Combinations in the Raman Spectrum of Graphite,” *Physical Review B,* vol. 52, no. 14, pp. 10053 -10059, 1995.

[117] L. M. Malard, M. A. Pimenta, G. Dresselhaus and M. S. Dresselhaus, “Raman Spectroscopy in Graphene,” *Physics Reports,* vol. 473, no. 5 - 6, pp. 51 - 87, 2009.

[118] T. Siciliano, A. Tepore, E. Filippo, G. Micocci and M. Tepore, “Characteristics of Molybdenum Trioxide Nanobelts Prepared by Thermal Evaporation Technique,” *Materials Chemistry and Physics,* vol. 114, no. 2-3, pp. 687-691, 2009.

[119] I. AlShibane, S. Laassiri, J. L. Rico and J. S. Hargreaves, “Methane Cracking over Cobalt Molybdenum Carbides,” *Catalysis Letters,* vol. 148, no. 6, pp. 1643-1650, 2018.

[120] D. H. Gregory, J. S. Hargreaves and S. M. Hunter, “On the Regeneration of Co3Mo3N from Co6Mo6N with N2,” *Catalysis Letters,* vol. 141, pp. 22-26, 2011.

[121] T. J. Prior and P. D. Battle, “Supermagnetism and Metal-site Ordering in Quaternary Nitrides with the n-carbide Structure,” *Journal of Materials Chemistry,* vol. 14, pp. 3001-3007, 2004.

[122] B. Huneau, J. J. Ding, P. Rogl, J. Bauer, X. Y. Ding and M. Bohn, “Experimental Investigation in the Quaternary Systems Ti-Ni-Al-N and Ti-Ni-Al-O,” *Journal of Solid State Chemistry,* vol. 155, pp. 71-77, 2000.

[123] P. Villars, “Ni2GaMo3N (Mo3Ni2GaN, T = 300 K) Crystal Structure, SpringerMaterials (online database),” Springer, [Online]. Available: https://materials.springer.com/isp/crystallographic/docs/sd_1201022. [Accessed 01 11 2019].

[124] L. A. Sviridov, P. D. Battle, F. Grandjean, G. J. Long and T. J. Prior, “Magnetic Ordering in Nitrides with the n-Carbide Structure, (Ni, Co, Fe)2(Ga, Ge)Mo3N,” *Inorganic Chemistry,* vol. 49, no. 3, pp. 1133-1143, 2010.

[125] J. C. Slater, “Atomic Radii in Crystals,” *The Journal of Chemical Physics,* vol. 41, pp. 3199-3204, 1964.

[126] J. E. Herrera and D. E. Resasco, “Role of Co-W Interaction in the Selective Growth of Single-Walled Carbon Nanotubes from CO Disproportionation,” *The Journal of Physical Chemistry B,* vol. 107, no. 16, pp. 3738-3746, 2003.

[127] R. Kojima and K.-i. Aika, “Cobalt Molybdenum Bimetallic Nitride Catalysts for Ammonia Synthesis: Part 2. Kinetic Study,” *Applied Catalysis A: General,* vol. 218, no. 1-2, pp. 121-128, 2001.

[128] R. Kojima and K.-I. Aika, “Cobalt Molybdenum Bimetallic Nitride Catalysts for Ammonia Synthesis,” *Chemistry Letters,* vol. 29, no. 5, pp. 514-515, 2000.

[129] D. Moszynski, R. Jedrzejewski, J. Ziebro and W. Arabczyk, “Surface and Catalytic Properties of Potassium-modified Cobalt Molybdenum Catalysts for Ammonia Synthesis,” *Applied Surface Science,* vol. 256, pp. 5581-5584, 2010.

[130] D. Moszynski, P. Adamski, M. Nadziejko, A. Komorowska and A. Sarnecki, “Cobalt Molybdenum Nitrides Co-promoted by Chromium and Potassium as Catalysts for Ammonia Synthesis,” *Chemical Papers,* vol. 72, pp. 425-430, 2018.

[131] D. Moszynski, “Controlled Phase Composition of Mixed Cobalt Molybdenum Nitrides,” *International Journal of Refractory Metals and Hard Materials,* vol. 41, pp. 449-452, 2013.

[132] P. Adamski, D. Moszynski, A. Komorowska, M. Nadziejko, A. Sarnecki and A. Albrecht, “Ammonolysis of Cobalt Molybdenum Oxides - In Situ XRD Study,” *Inorganic Chemistry,* vol. 57, pp. 9844-9850, 2018.

[133] P. Adamski, D. Moszynski, M. Nadziejko, A. Komorowska, A. Sarnecki and A. Albrecht, “Thermal Stability of Catalyst for Ammonia Synthesis Based on Cobalt Molybdenum Nitrides,” *Chemical Papers,* vol. 73, pp. 851-859, 2019.

[134] T.-C. Xiao, A. P. York, H. Al-Megren, C. V. Williams, H.-T. Wang and M. L. Green, “Preparation and Characterisation of Bimetallic Cobalt and Molybdenum Carbides,” *Journal of Catalysis,* vol. 202, no. 1, pp. 100-109, 2001.

[135] S. M. Hunter, “Molybdenum Nitrides: Structural and Reactivity Studies,” PhD thesis, University of Glasgow, 2012.

[136] A. -M. Alexander and J. S. Hargreaves, “The Reduction of Various Nitrides under Hydrogen: Ni3N, Cu3N, Zn3N2 and Ta3N5,” *Topics in Catalysis,* vol. 55, pp. 1046-1053, 2012.

[137] I. A. Amar, R. Lan, C. T. Petit and S. Tao, “Electrochemical Synthesis of Ammonia Using Fe3Mo3N Catalyst and Carbonate-Oxide Composite Electrolyte,” *International Journal of Electrochemical Science,* vol. 10, pp. 3757-3766, 2015.

[138] C. J. Jacobsen, J. J. Zhu, H. Lindelov and J. Jiang, “Synthesis of Ternary Nitrides by Mechanochemical Alloying,” *Journal of Materials Chemistry,* vol. 12, no. 10, pp. 3113-3116, 2002.

[139] K. S. Weil and P. N. Kumta, “Synthesis of Ternary Transition Metal Nitrides using Chemically Complexed Precursors,” *Materials Science and Engineering B,* vol. 38, pp. 109-117, 1996.

[140] L. Wang, W. Xian, K. Zhang, W. Liu, H. Qin, Q. Zhou and Y. Qian, “One-step Solid State Reaction for the Synthesis of Ternary Nitrides Co3Mo3N and Fe3Mo3N,” *Inorganic Chemistry Frontiers,* vol. 4, pp. 2055-2058, 2017.

[141] S. T. Oyama, C. C. Yu and S. Ramanathan, “Transition Metal Bimetallic Oxycarbides: Synthesis, Characterisation, and Activity Studies,” *Journal of Catalysis,* vol. 184, pp. 535-549, 1999.

[142] L. M. Di, A. Calka, Z. L. Li and J. S. Williams, “The Formation of Ternary Compound Fe3Mo3C by Ball Milling,” *Journal of Applied Physics,* vol. 78, pp. 4118-4122, 1995.

[143] T. Tsuchida, “Formation of Ternary Carbide Fe3Mo3C by Mechanical Activation and Subsequent Heat Treatment,” *Journal of Materials Science,* vol. 36, pp. 1735-1740, 2001.

[144] Z. Cui, Y. Li, G. Fu, X. Li and J. B. Goodenough, “Robust Fe3Mo3C Supported IrMn Clusters as Highly Efficient Bifunctional Air electrode for Metal-Air Battery,” *Advanced Materials,* vol. 29, p. 1702385, 2017.

[145] E. Soderhjelm, M. P. House, N. Cruise, J. Holmberg, M. Bowker, J. Bovin and A. Andersson, “On the Synergy Effect in MoO3–Fe2(MoO4)3 Catalysts for Methanol Oxidation to Formaldehyde,” *Topics in Catalysis,* vol. 50, pp. 145 - 155, 2008.

[146] J. V. Moura, G. S. Pinheiro, P. T. Freire, J. Mendes Filho, G. D. Saraiva, B. C. Viana and C. Luz-Lima, “High-pressure Raman Scattering on Fe2(MoO4)3 Microcrystals Obtained by a Hydrothermal Method,” *Vibrational Spectroscopy,* vol. 87, pp. 88-93, 2016.

[147] K. V. Raun, L. F. Lundegaard, J. Chevallier, P. Beato, C. C. Appel, K. Nielsen, M. Thorhauge, A. D. Jensen and M. Hoj, “Deactivation Behavior of an Iron-Molybdate Catalyst During Selective Oxidation of Methanol to Formaldehyde,” *Catalysis Science & Technology,* vol. 8, pp. 4626-4637, 2018.

[148] N. Perret, A. Alexander, S. M. Hunter, P. Chung, J. S. Hargreaves, R. F. Howe and M. A. Keane, “Synthesis, Characterisation and Hydrogenation Performance of Ternary Nitride Catalysts,” *Applied Catalysis A: General,* vol. 488, pp. 128-137, 2014.

[149] D. Zhang, L. Zhang, W. Zhang, M. Huo, J. Yin, G. Dang, Z. Ren, Q. Zhang, J. Xie and S. S. Mao, “Morphology-dependent Electrocatalytic Performance of Fe2(MoO4)3 for Electro-oxidation of Methanol in Alkaline Medium,” *Journal of Materiomics,* vol. 3, no. 2, pp. 135-143, 2017.

[150] J. Shirakawa, M. Nakayama, M. Wakihara and Y. Uchimoto, “Changes in Electronic Structure upon Lithium Insertion into Fe2(SO4)3 and Fe2(MoO4)3 Investigated by X-ray Absorption Spectroscopy,” *The Journal of Physical Chemistry B,* vol. 111, no. 6, pp. 1424-1430, 2007.

[151] N. Boucherit, A. Hugot-Le Goff and S. Joiret, “Raman Studies of Corrosion Films Grown on Fe and Fe-6Mo in Pitting Conditions,” *Corrosion Science,* vol. 32, no. 5/6, pp. 497-507, 1991.

[152] R. N. Panda and N. S. Gajbhiye, “Electronic and Magnetic Properties of Fe3Mo3N,” *Journal of Alloys and Compounds,* vol. 256, pp. 102-107, 1997.

[153] M. N. Ess, D. Ferry, E. D. Kireeva, R. Niessner, F. -X. Ouf and N. P. Ivleva, “In situ Raman Microspectroscopic Analysis of Soot Samples with Different Organic Carbon Content: Structural Changes During Heating,” *Carbon,* vol. 105, pp. 572-585, 2016.

[154] S. Tennant, “On Two Metals, Found in the Black Powder Reamining after the Solution of Platina,” *Philosophical Transactions of the Royal Society of London,* vol. 94, pp. 411-418, 1804.

[155] J. W. Arblaster, “Osmium, the Densest Metal Known,” *Platinum Metals Review,* vol. 39, no. 4, p. 164, 1995.

[156] M. Bertoli, A. Choualeb, A. J. Lough, B. Moore, D. Spasyuk and D. G. Gusev, “Osmium and Ruthenium Catalysts for Dehydrogenation of Alcohols,” *Organometallics,* vol. 30, no. 13, pp. 3479-3482, 2011.

[157] M. L. Buil, M. A. Esteruelas, J. Herrero, S. Izquierdo, I. M. Pastor and M. Yus, “Osmium Catalyst for the Borrowing Hydrogen Methodology: alpha-Alkylation of Arylacetonitriles and Methyl Ketones,” *ACS Catalysis,* vol. 3, no. 9, pp. 2072-2075, 2013.

[158] I. C. Smith, B. L. Carson and T. L. Ferguson, “Osmium: An Appraisla of Environmental Exposure,” *Environmental Health Perspectives,* vol. 8, pp. 201-213, 1974.

[159] J. M. Modak, “Haber Process for Ammonia Synthesis,” *Resonance,* vol. 7, no. 9, pp. 69-77, 2002.

[160] H. Liu, Ammonia Synthesis Catalysts: Innovation and Practice, World Scientific Publishing Company, 2013.

[161] G. Rambeau, A. Jorti and H. Amariglio, “Ammonia Synthesis on Osmium Powder and Hydrogenation of Preadsorbed Nitrogen from 100 to 500oC,” *Journal of Catalysis,* vol. 74, no. 1, pp. 110-120, 1982.

[162] G. Rambeau, A. Jorti and H. Amariglio, “Improvement of the Catalytic Performance of an Osmium Powder in Ammonia Synthesis by the Use of a Cyclic Procedure,” *Applied Catalysis,* vol. 3, no. 3, pp. 273-282, 1982.

[163] A. Ozaki, K. Aika and H. Hori, “A New Catalyst System for Ammonia Synthesis,” *Bulletin of the Chemical Society of Japan,* vol. 44, no. 11, pp. 3216-3216, 1971.

[164] A. Ishikawa, T. Doi and H. Nakai, “Catalytic Performance of Ru, Os and Rh nanoparticles for Ammonia Synthesis: A Density Functional Theory Analysis,” *Journal of Catalysis,* vol. 357, pp. 213-222, 2018.

[165] C. J. Jacobsen, S. Dahl, P. L. Hansen, E. Tornqvist, L. Jensen, H. Topsoe, D. V. Prip, P. B. Moenshaug and I. Chorkendorff, “Structure Sensitivity of Supported Ruthenium Catalysts

for Ammonia Synthesis," *Journal of Molecular Catalysis A: Chemical,* vol. 163, no. 1-2, pp. 19-26, 2000.

[166] J. A. Dumesic, H. Topsoe, S. Khammouma and M. Boudart, "Surface, Catalytic and Magnetic Properties of Small Iron Particles: II. Structure Sensitivity of Ammonia Synthesis," *Journal of Catalysis,* vol. 37, no. 3, pp. 503-512, 1975.

[167] F. Bozso, G. Ertl, M. Grunze and M. Weiss, "Interaction of Nitrogen with Iron Surfaces I. Fr (100) and Fe (111)," *Journal of Catalysis,* vol. 49, pp. 18-41, 1977.

[168] F. Bozso, G. Ertl and M. Weiss, "Interaction of Nitrogen with Iron Surfaces II. Fe (110)," *Journal of Catalysis,* vol. 50, pp. 519-529, 1977.

[169] D. R. Strongin, J. Carrazza, S. R. Bare and G. A. Somorjai, "The Importance of C7 Sites ans Surface Roughness in the Ammonia Synthesis Reaction over Iron," *Journal of Catalysis,* vol. 103, pp. 213-215, 1987.

[170] F. A. Cotton, "Metal—Metal Multiple Bonds and Metal Clusters," in *Reactivity of Metal-Metal Bonds*, AMERICAN CHEMICAL SOCIETY, 1981, pp. 1-16.

[171] E. R. Corey and L. F. Dahl, "The Molecular and Crystal Structure of Os3(CO)12," *Inorganic Chemistry,* vol. 1, no. 3, pp. 521-526, 1962.

[172] D. J. Hunt, S. D. Jackson, R. B. Moyes and P. B. Wells, "Air Stability of Catalysts Derived from Osmium and Ruthenium Cluster Carbonyls," *Journal of the Chemical Society, Chemical Communications ,* no. 1, pp. 85-86, 1982.

[173] G. Rambeau, A. Jorti and H. Amariglio, "Ammonia Synthesis on Osmium Powder and Hydrogenation of Preadsorbed Nitrogne from 100 to 500oC," *Journal of Catalysis,* vol. 74, no. 1, pp. 110-120, 1982.

[174] S. M. Yunusov, E. S. Kalyuzhnaya, H. Mahapatra, V. K. Puri, V. A. Likholobov and V. B. Shur, "Supported Ammonia Synthesis Catalysts Based on Potassium Derivatives of Anionic Ruthenium, Osmium and Iron Carbonyl Clusters.," *Journal of Molecular Catalysis A: Chemical ,* vol. 139, no. 2-3, pp. 219-225, 1999.

[175] Y. I. Yermakov, V. F. Surovikin, G. V. Plaksin, V. A. Semikolenov, V. A. Likholobov, L. V. Chuvilin and S. V. Bogdanov, "New Carbon Material as Support for Catalysts," *Reaction Kinetics and Catalysis Letters,* vol. 33, no. 2, pp. 435-440, 1987.

[176] J. R. Moss and W. A. Graham, "A New Route to Mixed-Metal Carbonyls Containing Osmium," *Journal of Organometallic Chemistry,* vol. 23, no. 2, pp. C23-C24, 1970.

[177] V. A. Maksakov, V. P. Kirin, A. V. Virovets, N. V. Podberezskaya and P. P. Semyannikov, "Sythesis of Trinuclear Mixed-metal Clusters Os2Fe(CO)10L2 (L=OH,I,CO). The Crystal 45 Structures of Os2Fe(CO)10(u-OH)2 and Os2Fe(CO)12.0.41Os3(CO)12," *Journal of Organometallic Chemistry,* vol. 543, pp. 57-62, 1997.

[178] W. A. Graham and J. R. Moss, "The Synthesis of Some Mixed Metal Cluster Complexes of Osmium with Cobalt and Iron," *Journal of Organometallic Chemistry,* vol. 270, no. 2, pp. 237-243, 1984.

[179] R. Giordano and E. Sappa, "Heterometallic Clusters in Homogeneous Catalysis. Hydrogenation of Diphenylacetylene and Isomerization of cis-stilbene in the Presence of

[Fe2Ru(CO)12], [FeRu2(CO)12], [H2FeRu3(CO)13], [H2Ru4(CO)13], and Related Compounds," *Journal of Organometallic Chemistry,* vol. 448, no. 1-2, pp. 157-166, 1993.

[180] B. F. Johnson, R. D. Johnson, J. Lewis, I. G. Williams and P. A. Kilty, "Relative Reactivity of Triruthenium and Triosmium Dodecacarbonyls," *Chemical Communications (London),* no. 15, pp. 861-862, 1968.

[181] D. B. Yawney and F. G. Stone, "Chemistry of the Metal Carbonyls. Part LV. Synthesis of Polynuclear Carbonyl (iron–ruthenium) Complexes," *Journal of the Chemical Society A: Inorganic, Physical, Theoretical,* vol. 0, pp. 502-506, 1969.

[182] J. M. Guil Pinto and A. Ruiz Paniego, "Specific Surface Area of Osmium Powder," *Studies in Surface Science and Catalysis,* vol. 10, pp. 361 - 366, 1982.

[183] K. Aika and A. Ozaki, in *Catalysis Science and Technology*, Berlin, Springer Verlag, 1981, p. 87.

[184] G. A. Battiston, G. Bor, U. K. Dietler, S. F. A. Kettle, R. Rossetti, G. Sbrignadello and P. L. Stanghellini, "Comparative Infrared and Raman Spectroscopic v{CO) Study of Ru3(CO)12, Os3(CO)12, Their Mixed Crystals, and the Mixed Triangulo Cluster Carbonyls Ru2Os(CO)12 and RuOs2(CO)12," *Inorganic Chemistry,* vol. 19, pp. 1961-1973, 1980.

[185] J. J. Venter and M. A. Vannice, "An Investigation of the Decomposition of Osmium Carbonyl Clusters on Carbon Using Diffuse Reflectance Fourier Transform IR Spectroscopy," *Journal of the American Chemical Society,* vol. 111, no. 7, pp. 2377-2387, 1989.

[186] A. K. Smith, B. Besson, J. M. Basset, R. Psaro, A. Fusi and R. Ugo, "Surface Supported Metal Cluster Carbonyls. The Surface Organometallic Chemistry of Polymetallic and Monometallic Osmium Carbonyl species formed by Depositing Various Osmium Clusters on Silica and Alumina," *Journal of Organometallic Chemistry,* vol. 192, pp. C31-C34, 1980.

[187] C. Dossi, A. Fusi, E. Grilli, R. Psaro, R. Ugo and R. Zanoni, "FTIR, XPS and TPD Studies on the Thermal Decomposition of Os3(CO)12/silica: A Multitechnique Approach to the Resolution of some Controversial Problems," *Catalysis Today,* vol. 2, pp. 585-594, 1988.

[188] B. C. Gates, H. Knozinger, G. Marie, R. Psaro and R. Ugo, in *Metal Clusters in Catalysis*, vol. 29, Amsterdam, Elseveir, 1986, pp. 415-543.

[189] S.-J. Park and M.-K. Seo, "Element and Processing," in *Interface Science and Technology*, vol. 18, Elsevier, 2011, pp. 431-499.

[190] H. Knozinger and Y. Zhao, "Infrared Characterisation of Mononuclear Osmium Carbonyl Species on Alumina," *Journal of Catalysis,* vol. 71, no. 2, pp. 337-347, 1981.

[191] O. Hinrichsen, F. Rosowski, A. Hornung, M. Muhler and G. Ertl, "The Kinetics of Ammonia Synthesis over Ru-Based Catalysts 1. The Dissociative Chemisorption and Associative Desorption of N2," *Journal of Catalysis,* vol. 165, pp. 33-44, 1997.

[192] R. Schlogl, "Ammonia Synthesis," in *Handbook of Heterogeneous Catalysis*, Wiley, 2008, pp. 2501-2575.

[193] K. Urabe and A. Ozaki, "Activation of Nitrogen on Ru-Fe Bimetallic Catalyst," *Journal of Catalysis,* vol. 52, pp. 542-543, 1978.

[194] X. Dong, F. Yang, J. Zhao and J. Wang, “Efficient Intramolecular Vibrational Excitonic Energy Transfer in Ru3(CO)12 Cluster Revealed by Two-Dimensional Infrared Spectroscopy,” *The Journal of Physical Chemistry B,* vol. 122, pp. 1296-1305, 2018.

[195] M. Poliakoff and J. J. Turner, “The Infrared Spectra of Trimetal Carbonyl Species in Frozen Gas Matrices at 20K,” *Journal of the Chemical Society D: Chemical Communications,* no. 16, pp. 1008-1009, 1970.

Appendices

Appendix I

The following calculation was used to determine the ammonia synthesis rate for each reaction that had a steady state reaction profile. The change in conductivity of 200 mL of 0.00108 mol/L sulfuric acid solution was used to measure the production of ammonia.

The first stage was to calculate the number of moles of H_2SO_4 within the flask.

$$\text{Moles } (H_2SO_4) = 0.00108 \text{ mol/L} \times 200 \text{ mL}$$

$$= 2.16 \times 10^{-4} \text{ moles}$$

This value is then multiplied by 2 to account for the equivalent H^+ in the ammonia needed to react with H_2SO_4.

$$= 4.32 \times 10^{-4} \text{ moles of ammonia required}$$

The mean conductivity change of the 0.00108 mol/L sulfuric acid solution for complete consumption by reaction with ammonia was observed to be 600 µS/cm.

The number of moles of ammonia required is divided by the mean conductivity to give the number of moles of H_2SO_4 used.

$$= 4.32 \times 10^{-4} \text{ moles}/600 = 7.20 \times 10^{-7} \text{ mol/µScm}^{-1}$$

The gradient of the conductivity vs. time graph is multiplied by 60, to convert the value from minutes to hours, and 7.20×10^{-7} mol/µScm^{-1} to give a value X. Then, this value is divided by the mass of the material to obtain the ammonia synthesis rate in units of µmol hr^{-1} g^{-1} catalyst.

Appendix II

EDX Tables for Nickel Molybdenum Materials Prepared at Different Carburisation Temperatures with 20% CH_4/H_2

Area	Ni weight (%)	Mo weight (%)	C weight (%)	N weight (%)
1	24	62	7	7
2	25	60	9	6
3	34	59	7	0
4	25	56	11	8
5	34	54	8	4
6	25	62	8	5
7	22	56	14	8
8	26	63	9	2
9	19	56	15	10
10	25	59	10	6
11	22	60	11	7
12	26	57	13	5
13	21	34	42	3
14	34	58	8	0
15	6	9	81	5
Average	24	54	17	5

Table 56: EDX values for nickel molybdenum material prepared at 560°C with 20% CH_4/H_2

Area	Ni weight (%)	Mo weight (%)	C weight (%)	N weight (%)
1	49	40	10	2
2	26	55	20	0
3	19	54	24	2
4	24	50	23	4
5	27	55	13	5
6	50	39	12	0
7	39	42	16	2
8	22	50	28	0
9	30	53	15	2
10	21	50	29	0
11	27	57	15	0
12	22	49	29	0
13	24	55	21	0
14	26	59	15	0
15	21	62	17	0
Average	28	51	19	1

Table 57: EDX values for nickel molybdenum material prepared at 600°C with 20% CH_4/H_2

Area	Ni weight (%)	Mo weight (%)	C weight (%)	N weight (%)
1	20	44	36	0
2	19	55	26	0
3	17	49	34	0
4	20	47	33	0
5	20	48	32	0
6	26	55	19	0
7	23	57	20	0
8	26	53	20	0
9	24	55	22	0
10	24	60	16	0
11	20	60	20	0
12	27	56	17	0
13	29	59	12	0
14	32	57	11	0
15	22	52	26	0
16	20	48	32	0
17	27	55	18	0
18	19	52	28	0
19	35	57	8	0
20	22	54	24	0
21	19	53	28	0
22	20	57	22	0
23	25	52	23	0
24	20	53	27	0
25	35	52	13	0
26	27	55	18	0
27	23	57	20	0
Average	24	54	22	0

Table 58: EDX values for nickel molybdenum material prepared at 650°C with 20% CH_4/H_2

Area	Ni weight (%)	Mo weight (%)	C weight (%)	N weight (%)
1	29	44	28	0
2	19	36	44	0
3	32	41	27	0
4	38	34	28	0
5	31	50	19	0
6	42	45	13	0
7	18	42	39	0
8	12	44	44	0
9	13	45	42	0
10	19	47	33	0
11	15	41	44	0
12	15	40	44	0
13	19	44	37	0
14	17	48	35	0
15	42	41	18	0
Average	24	43	33	0

Table 59: EDX values for nickel molybdenum material prepared at 700°C with 20% CH_4/H_2

Area	Ni weight (%)	Mo weight (%)	C weight (%)	N weight (%)
1	13	49	38	0
2	48	34	19	0
3	17	45	39	0
4	15	40	45	0
5	17	46	37	0
6	18	44	39	0
7	17	45	39	0
8	15	48	37	0
9	16	37	47	0
10	14	43	43	0
11	19	42	39	0
12	13	46	41	0
13	19	35	46	0
14	20	30	50	0
15	15	37	47	0
16	21	42	37	0
17	14	44	41	0
18	25	47	29	0
19	17	45	38	0
20	20	47	33	0
21	25	49	26	0
22	19	43	38	0
Average	19	43	38	0

Table 60: EDX values for nickel molybdenum material prepared at 725°C with 20% CH_4/H_2

Appendix III

ToF-SIMS Data for $Ni_2Mo_3C_xN_y$

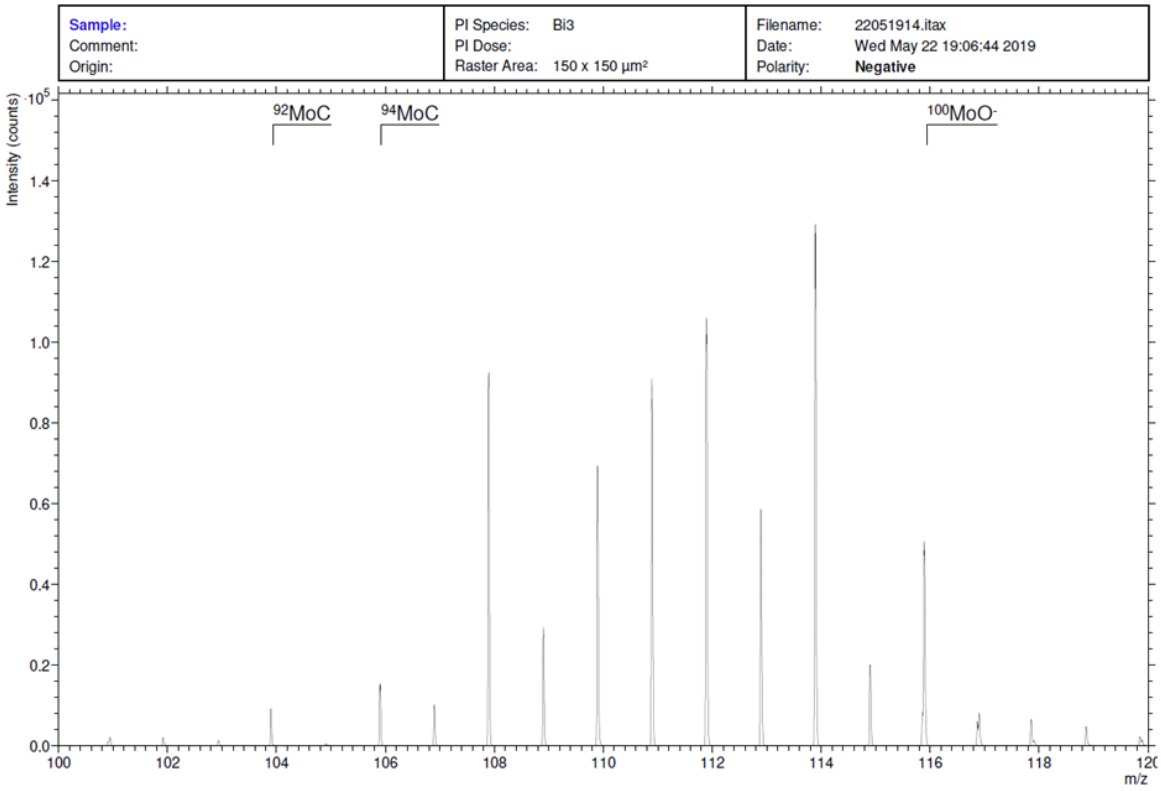

Figure 212: ToF-SIMS analysis from 100 – 120 m/z for $Ni_2Mo_3C_xN_y$

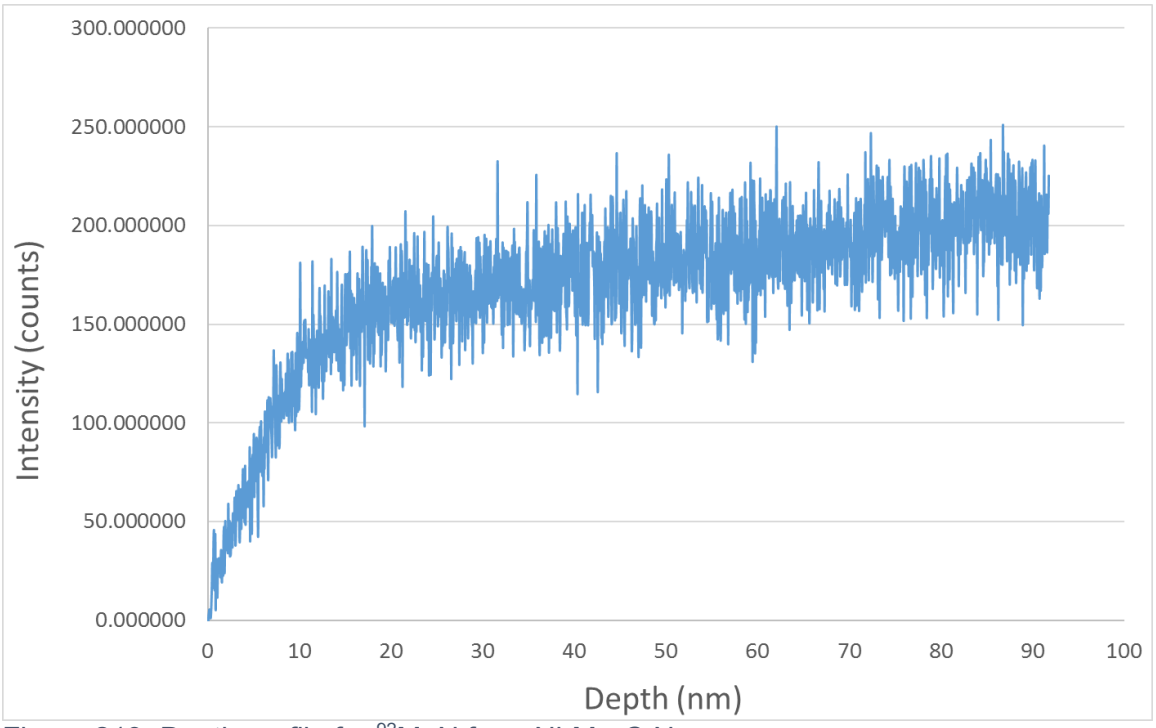

Figure 213: Depth profile for ^{92}MoN from $Ni_2Mo_3C_xN_y$

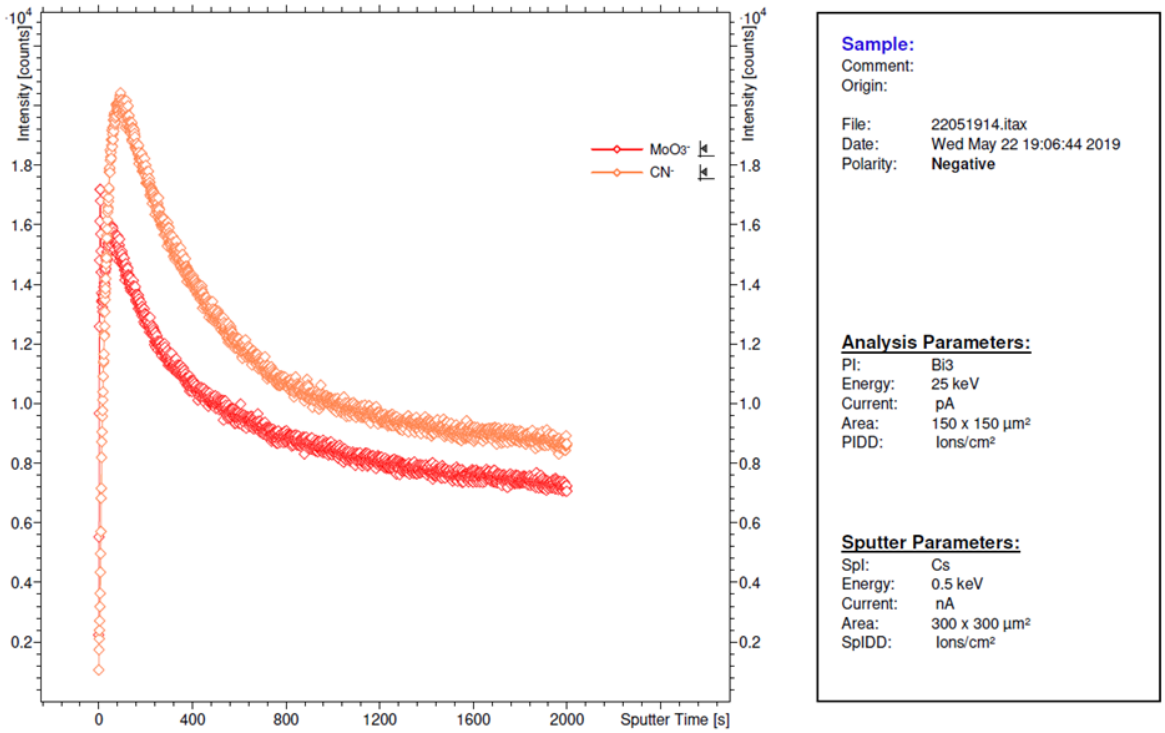

Figure 214: Depth profiles for MoO^{3-} (red) and CN^- (orange) from $Ni_2Mo_3C_xN_y$

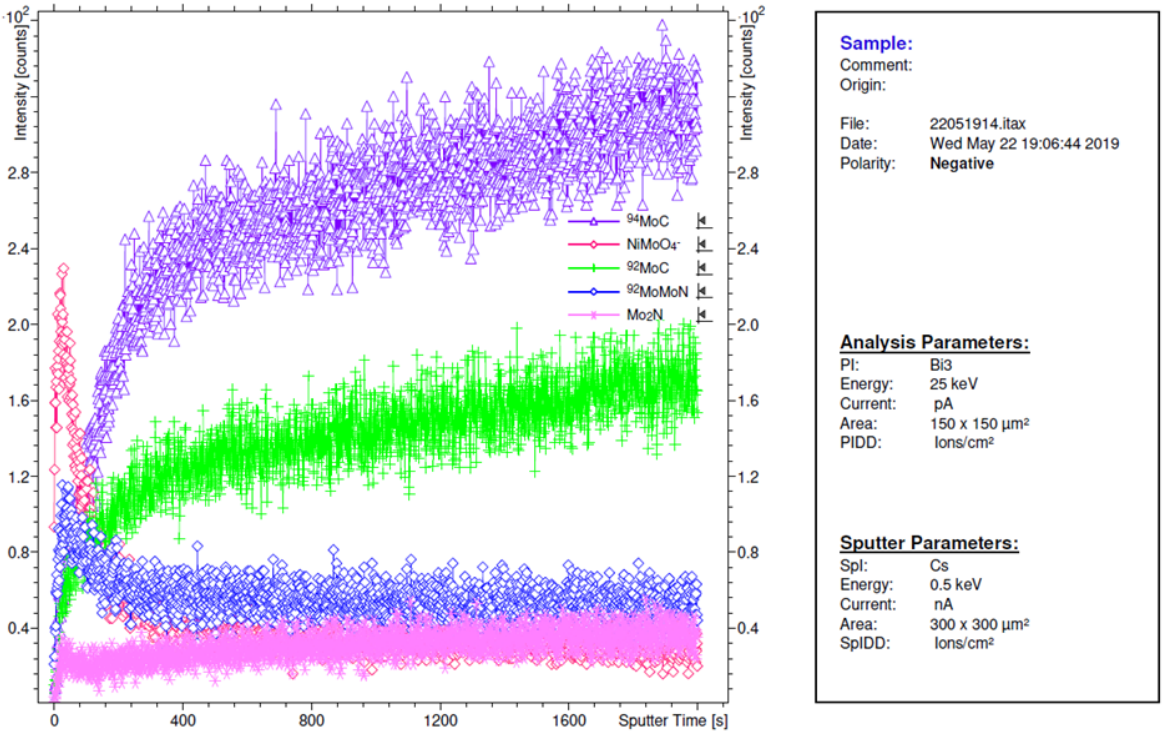

Figure 215: Depth profiles for $NiMoO_4^-$ (red), $^{92}MoC^-$ (green), ^{94}MoC (purple), Mo_2N (pink) and $^{92}MoMoN$ (blue) from $Ni_2Mo_3C_xN_y$

ToF-SIMS Data for $Ni_2Mo_3C_xN_y$ Post-Reaction with 3:1 H_2/N_2 at 400°C for 36 Hours

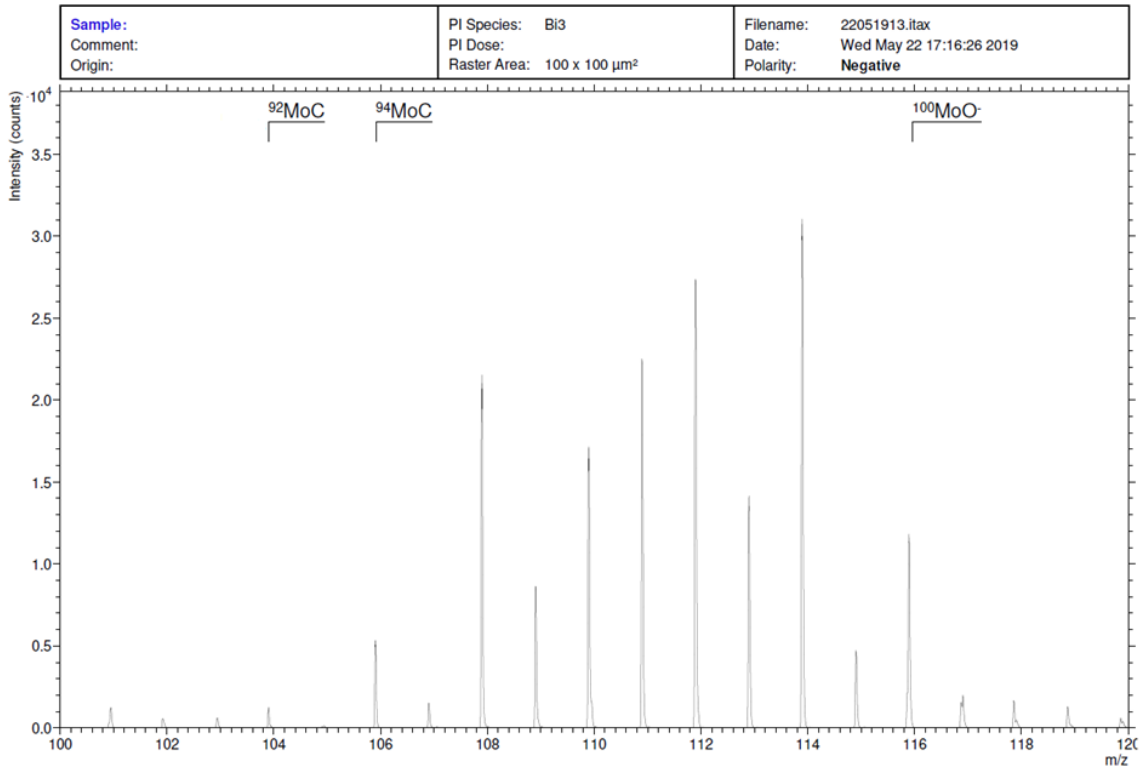

Figure 216: ToF-SIMS analysis from 100 – 120 m/z for $Ni_2Mo_3C_xN_y$ post reaction with 3:1 H_2/N_2 at 400°C for 36 hours.

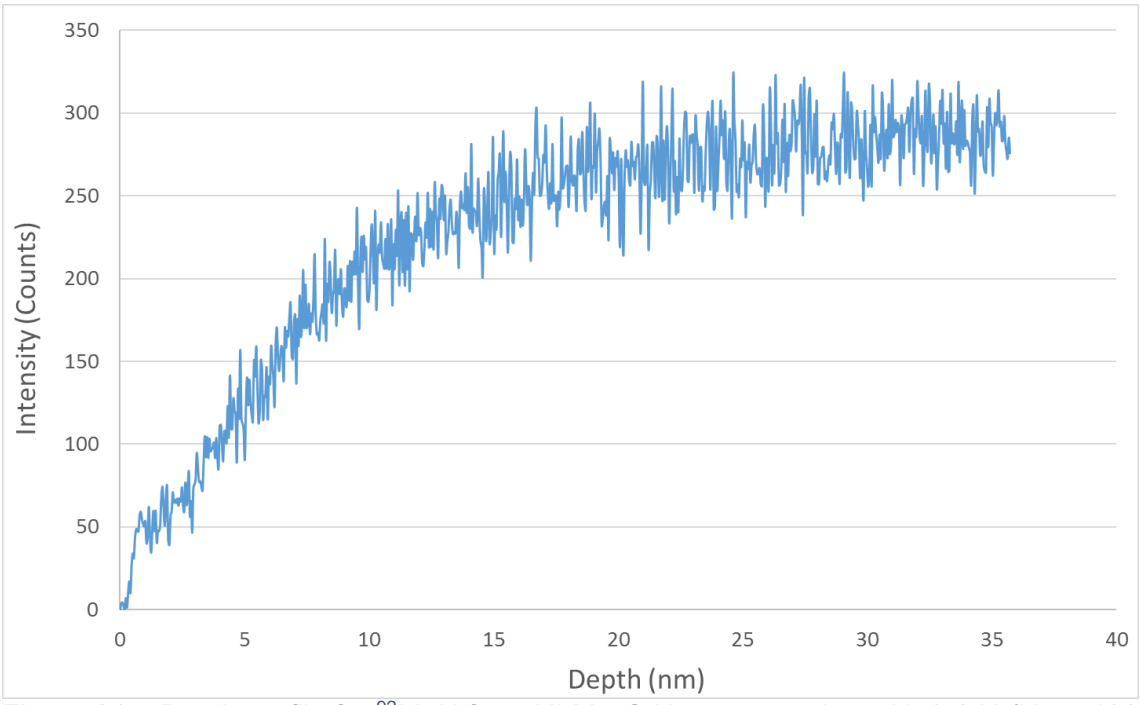

Figure 217: Depth profile for ^{92}MoN from $Ni_2Mo_3C_xN_y$ post reaction with 3:1 H_2/N_2 at 400°C for 36 hours.

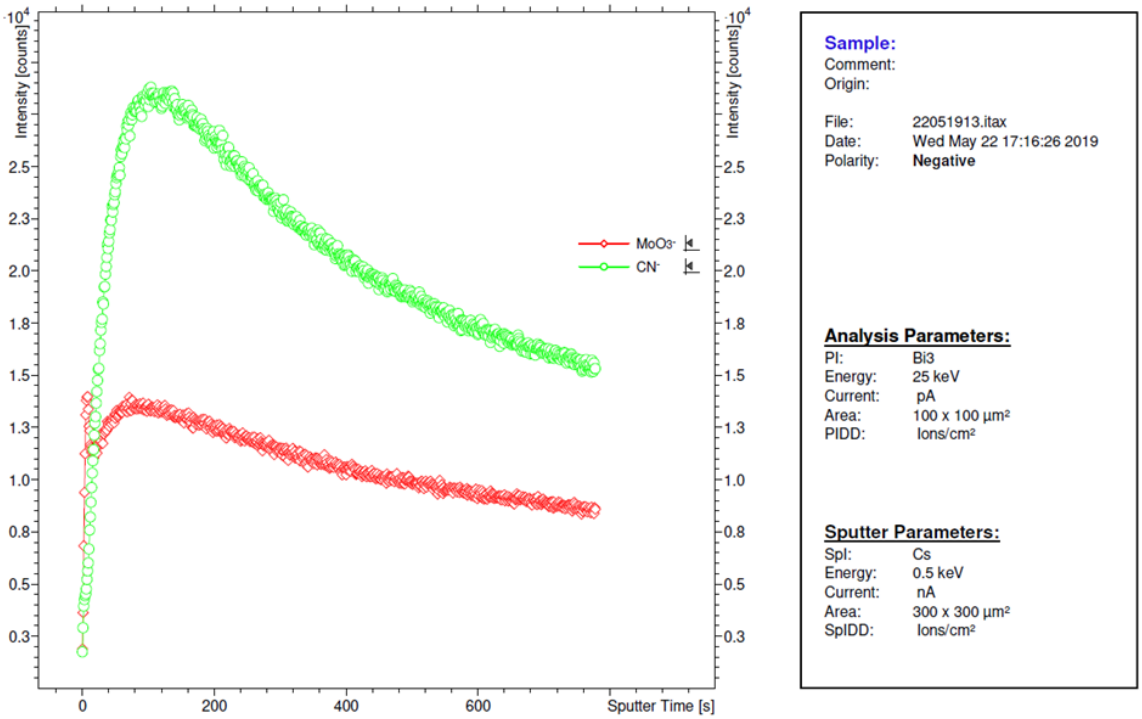

Figure 218: Depth profiles for MoO^{3-} (red) and CN^- (green) from $Ni_2Mo_3C_xN_y$ post reaction with 3:1 H_2/N_2 at 400°C for 36 hours.

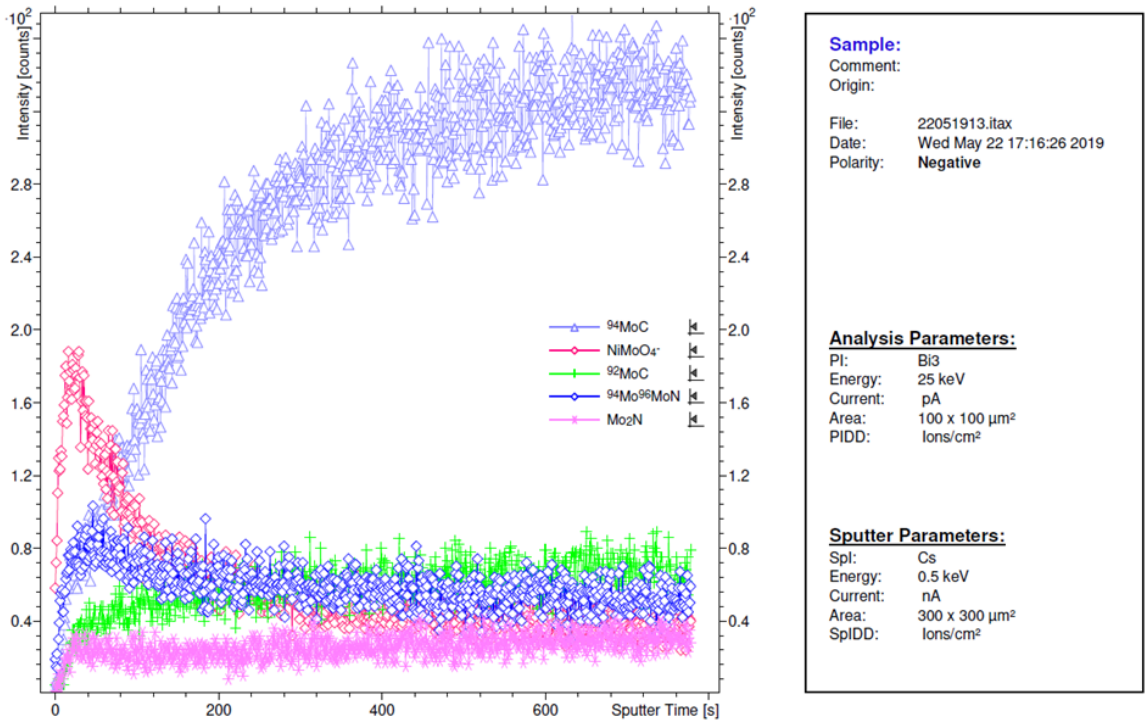

Figure 219: Depth profiles for $NiMoO_4^-$ (red), $^{92}MoC^-$ (green), ^{94}MoC (light blue), Mo_2N (pink) and $^{94}Mo^{96}MoN$ (blue) from $Ni_2Mo_3C_xN_y$ post reaction with 3:1 H_2/N_2 at 400°C for 36 hours.

ToF-SIMS Data for $Ni_2Mo_3C_xN_y$ Post-Reaction with 3:1 H_2/N_2 at 500°C for 7.5 Hours

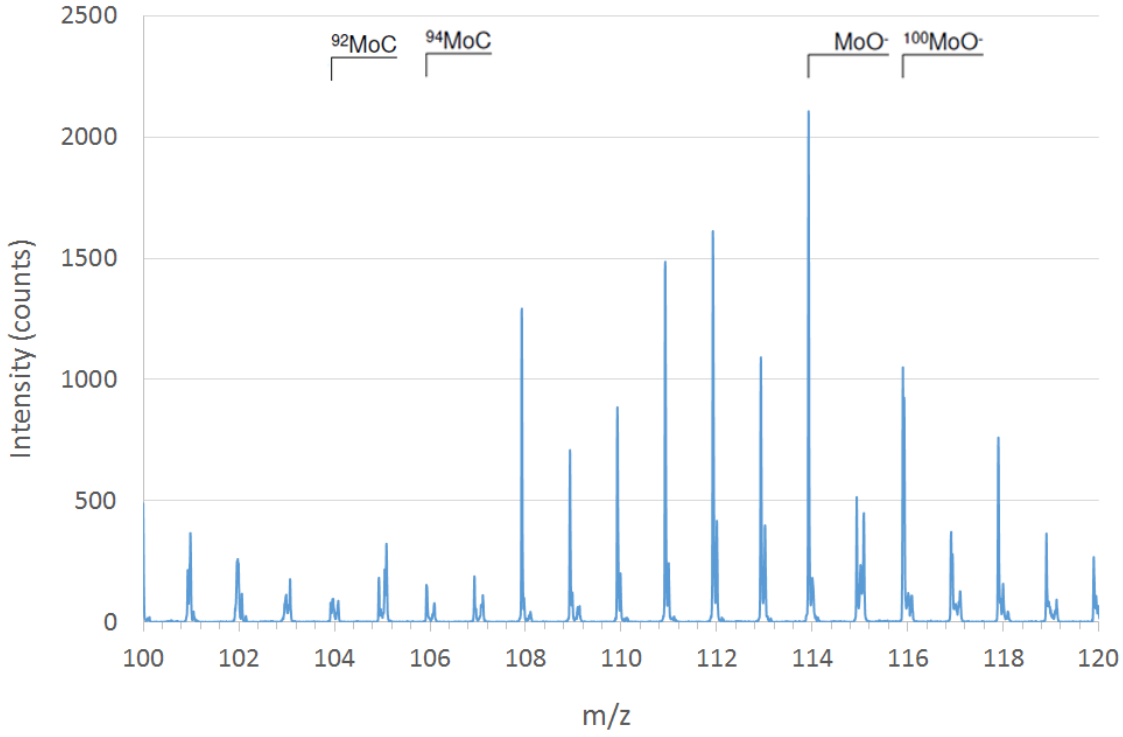

Figure 220: ToF-SIMS analysis from 100 – 120 m/z for $Ni_2Mo_3C_xN_y$ post-reaction with 3:1 H_2/N_2 at 500°C for 7.5 hours. Measurement was taken in static mode.

Appendix IV

SEM Images for Cobalt Molybdenum Oxide Prepared by Modified Pechini Method

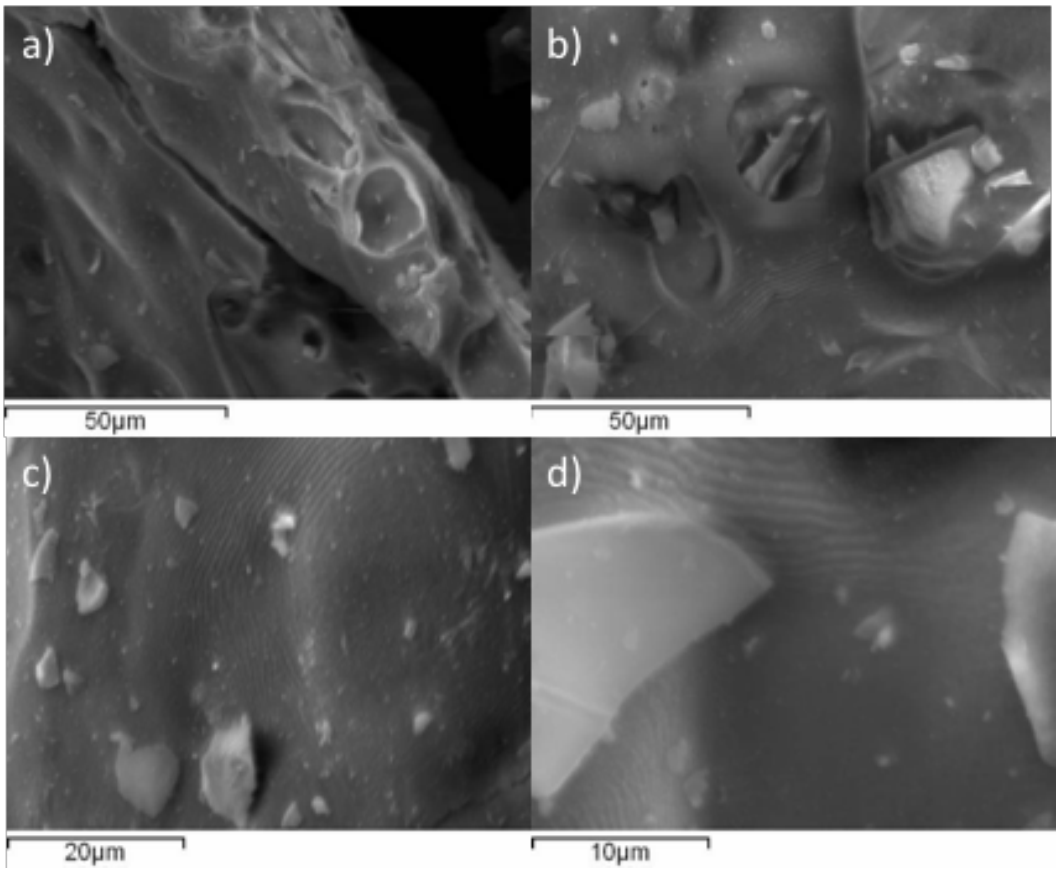

Figure 221: SEM images of cobalt molybdenum oxide prepared by modified Pechini method ($Co_2Mo_3O_x$). a) 1000x magnification, b) 1000x magnification, c) 2000x magnification and d) 4000x magnification.

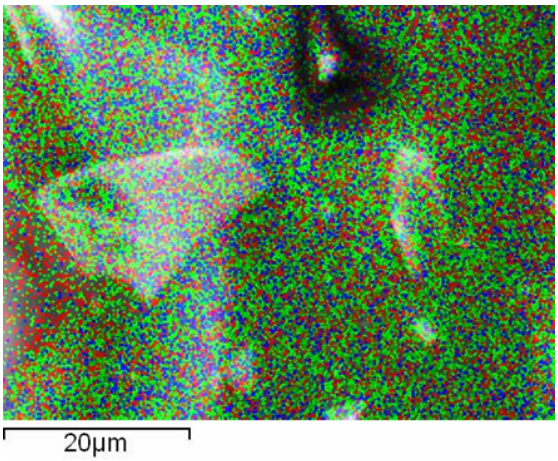

Figure 222: Element Map for cobalt molybdenum oxide ($Co_2Mo_3O_x$) prepared by modified Pechini method. Elements: Co (red), Mo (green) and O (blue).

SEM Images for Cobalt Molybdenum Oxide Prepared from Mixing of $(NH_4)_6Mo_7O_{24}.4H_2O$ and $Co(NO_3)_2 \cdot 6H_2O$ (Method 2)

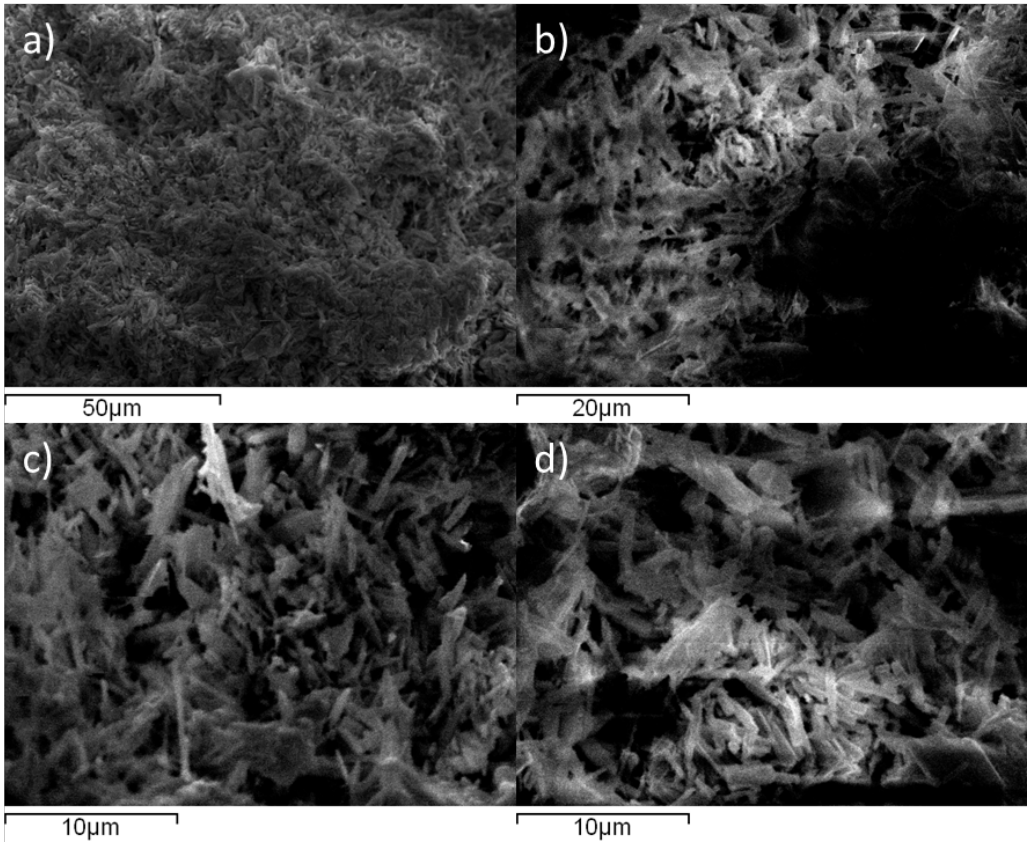

Figure 223: SEM images of cobalt molybdenum oxide ($Co_2Mo_3O_x$) prepared from method 2. a) 1000x magnification, b) 2000x magnification, c) 4000x magnification and d) 4000x magnification.

Appendix V

ToF-SIMS Data for Fe_3Mo_3C

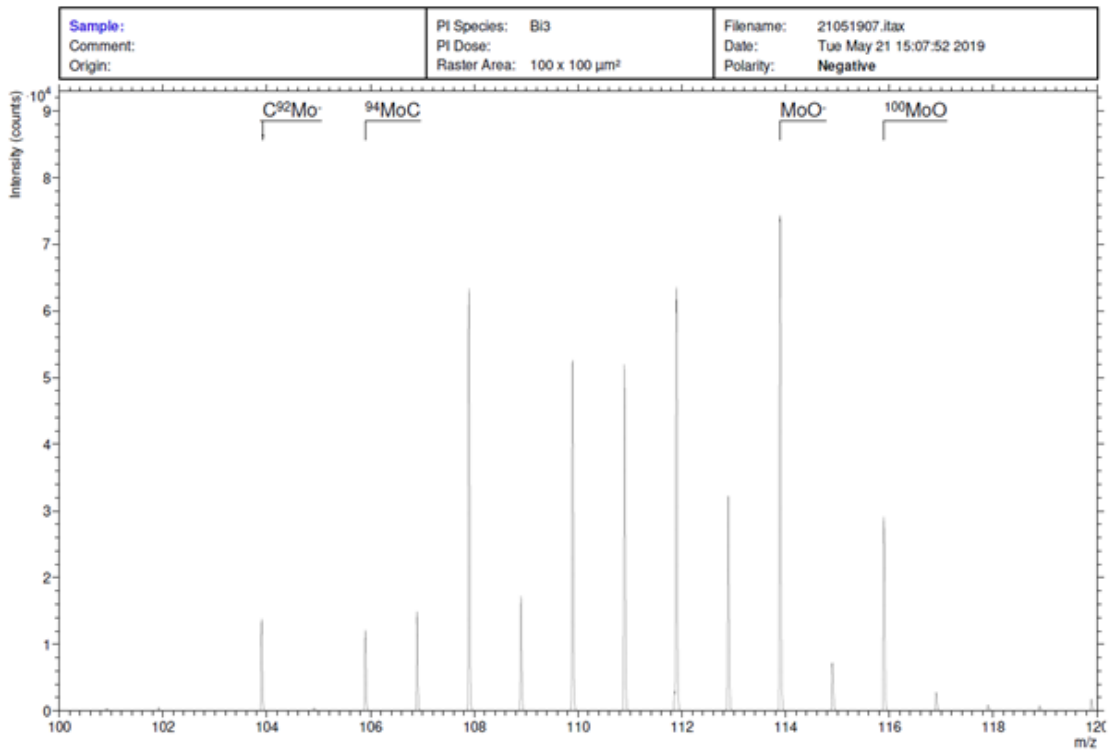

Figure 224: ToF-SIMS analysis from 100 – 120 m/z for Fe_3Mo_3C.

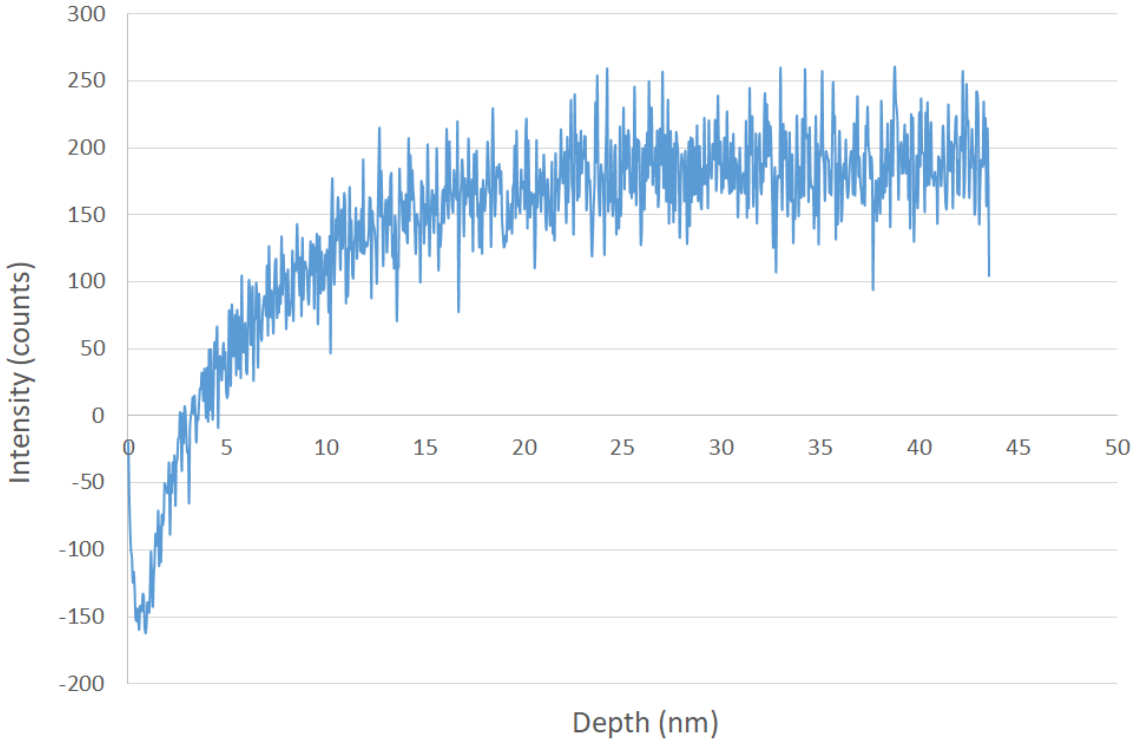

Figure 225: Depth profile for ^{92}MoN from Fe_3Mo_3C.

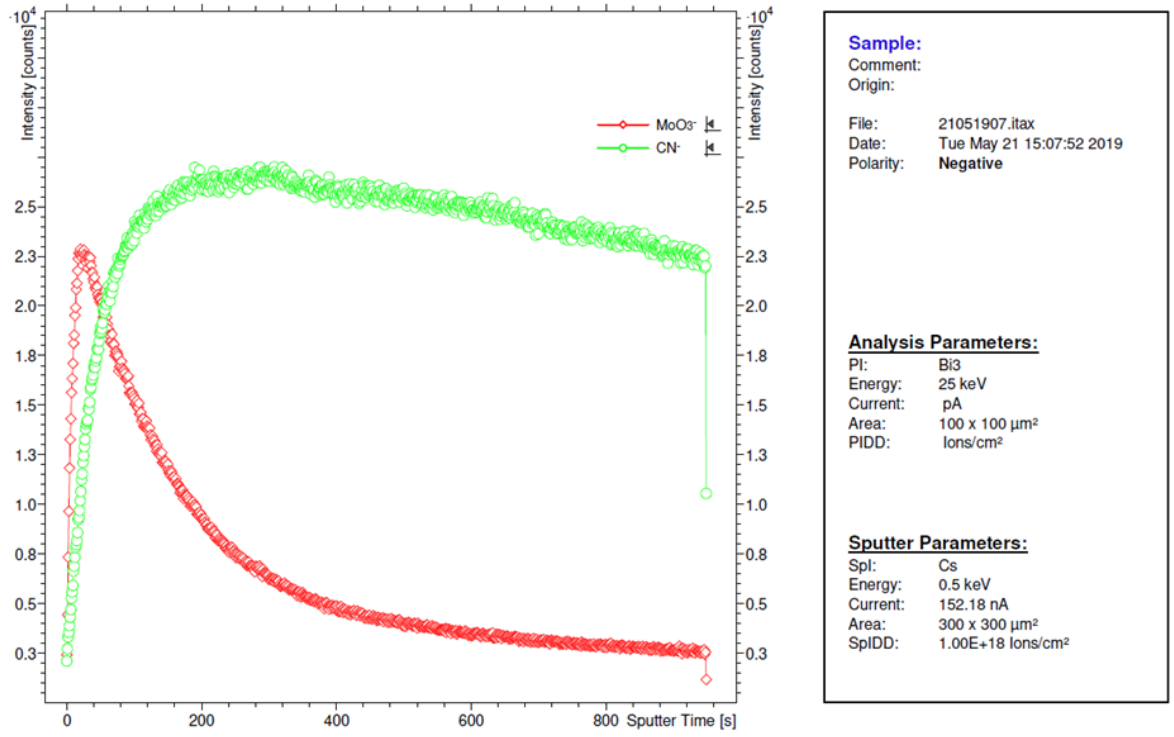

Figure 226: Depth profiles for MoO^{3-} (red) and CN^- (green) from Fe_3Mo_3C.

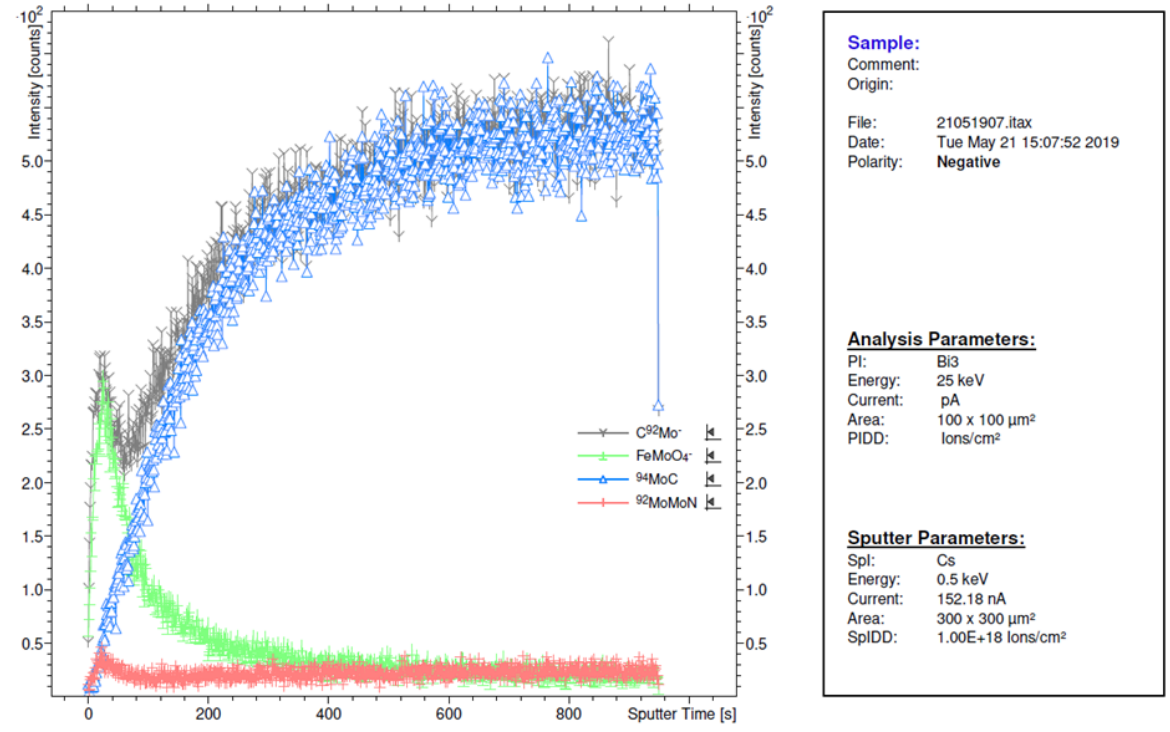

Figure 227: Depth profiles for $FeMoO4^-$ (green), $^{92}MoC^-$ (grey), ^{94}MoC (blue) and $^{92}MoMoN$ (pink) from Fe_3Mo_3C.

ToF-SIMS Data for Fe_3Mo_3C Post-Reaction with 3:1 H_2/N_2 at 400°C for 4 Hours and 500°C for 32 Hours

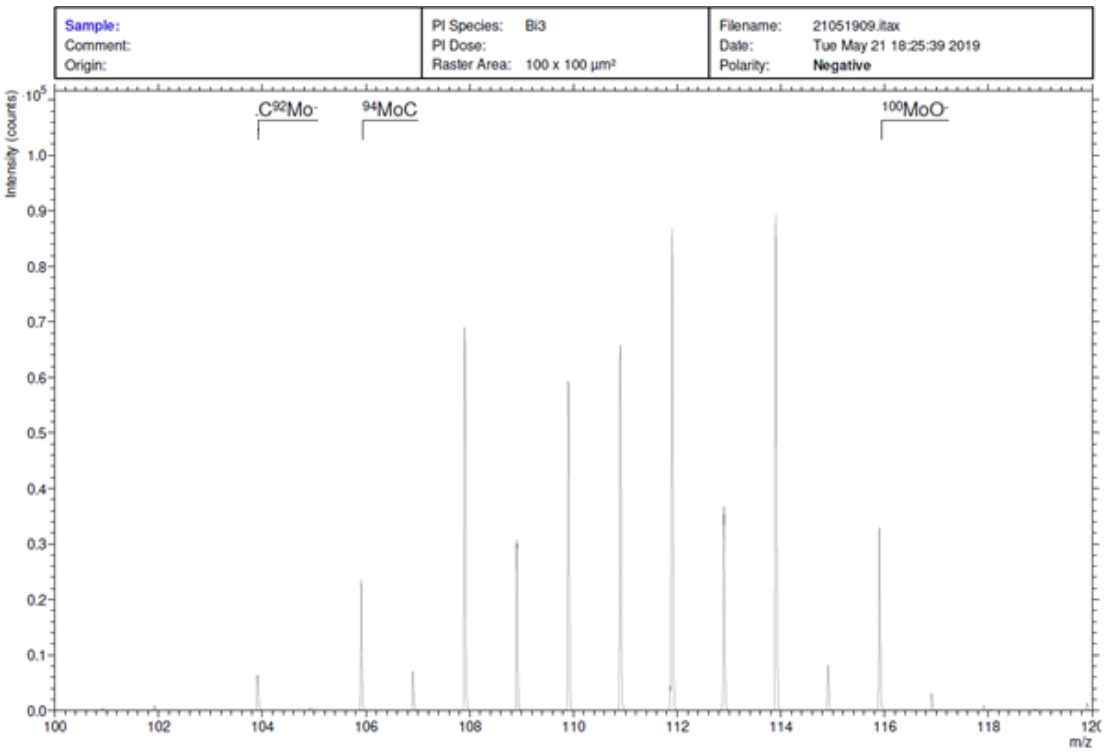

Figure 228: ToF-SIMS analysis from 100 – 120 m/z for Fe_3Mo_3C post-reaction with 3:1 H_2/N_2 at 400°C for 4 hours and 500°C for 32 hours.

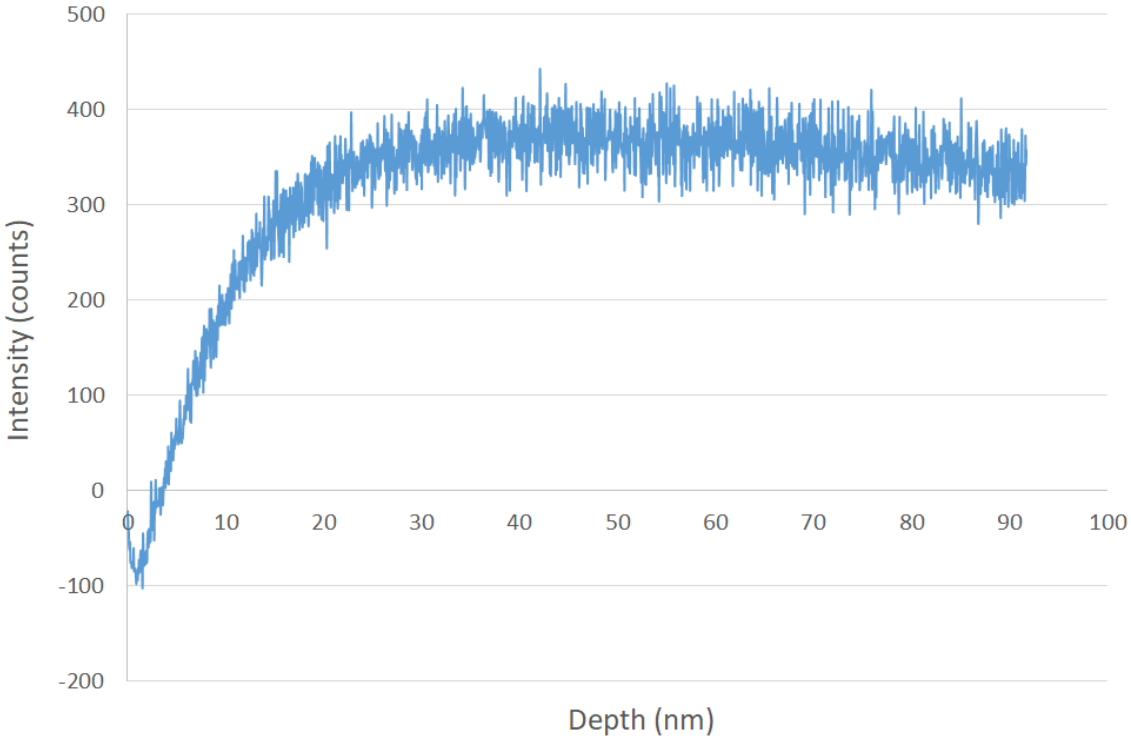

Figure 229: Depth profile for ^{92}MoN from Fe_3Mo_3C post-reaction with 3:1 H_2/N_2 at 400°C for 4 hours and 500°C for 32 hours.

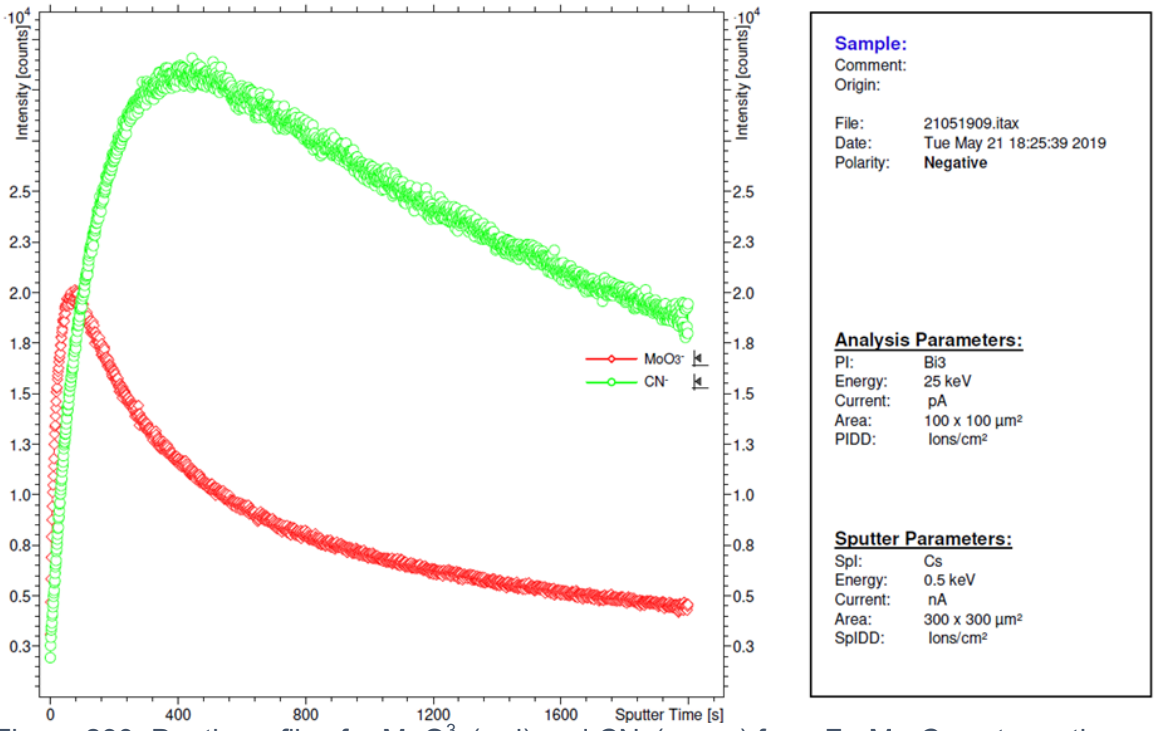

Figure 230: Depth profiles for MoO^{3-} (red) and CN^- (green) from Fe_3Mo_3C post-reaction with 3:1 H_2/N_2 at 400°C for 4 hours and 500°C for 32 hours.

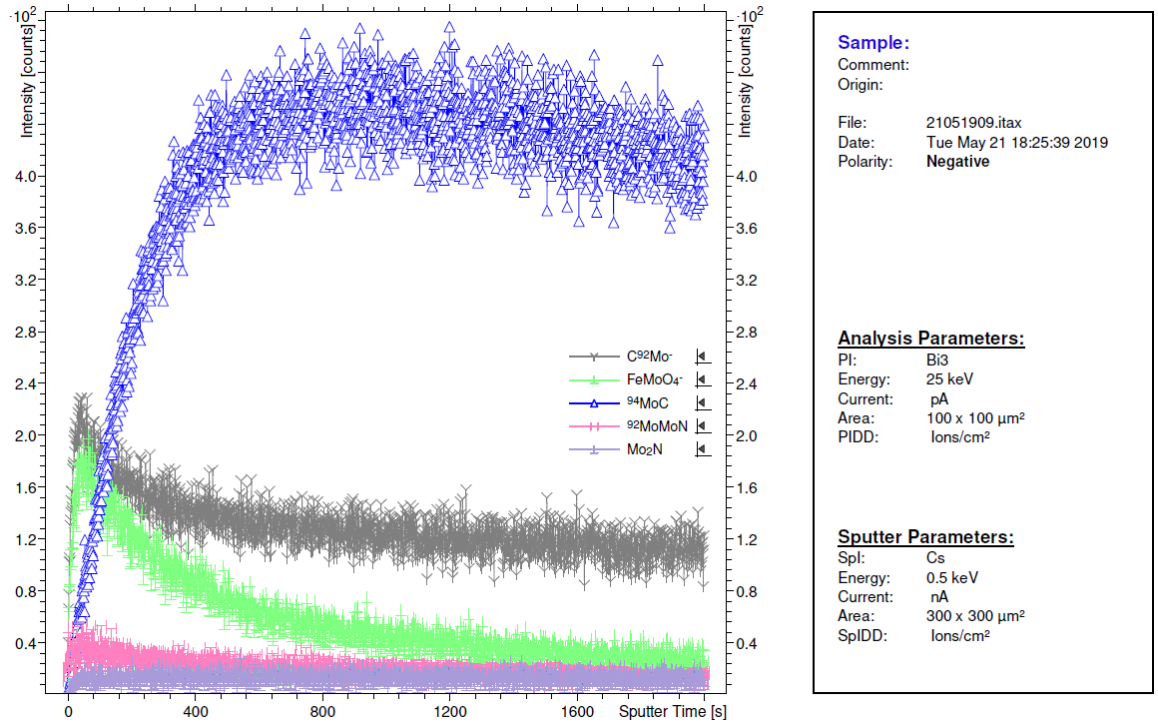

Figure 231: Depth profiles for $FeMoO4^-$ (green), $^{92}MoC^-$ (grey), ^{94}MoC (blue), $^{92}MoMoN$ (pink) and Mo_2N (purple) from Fe_3Mo_3C post-reaction with 3:1 H_2/N_2 at 400°C for 4 hours and 500°C for 32 hours.

ToF-SIMS Data for Fe_3Mo_3C Post-Reaction with 3:1 H_2/N_2 at 500°C for 8 Hours

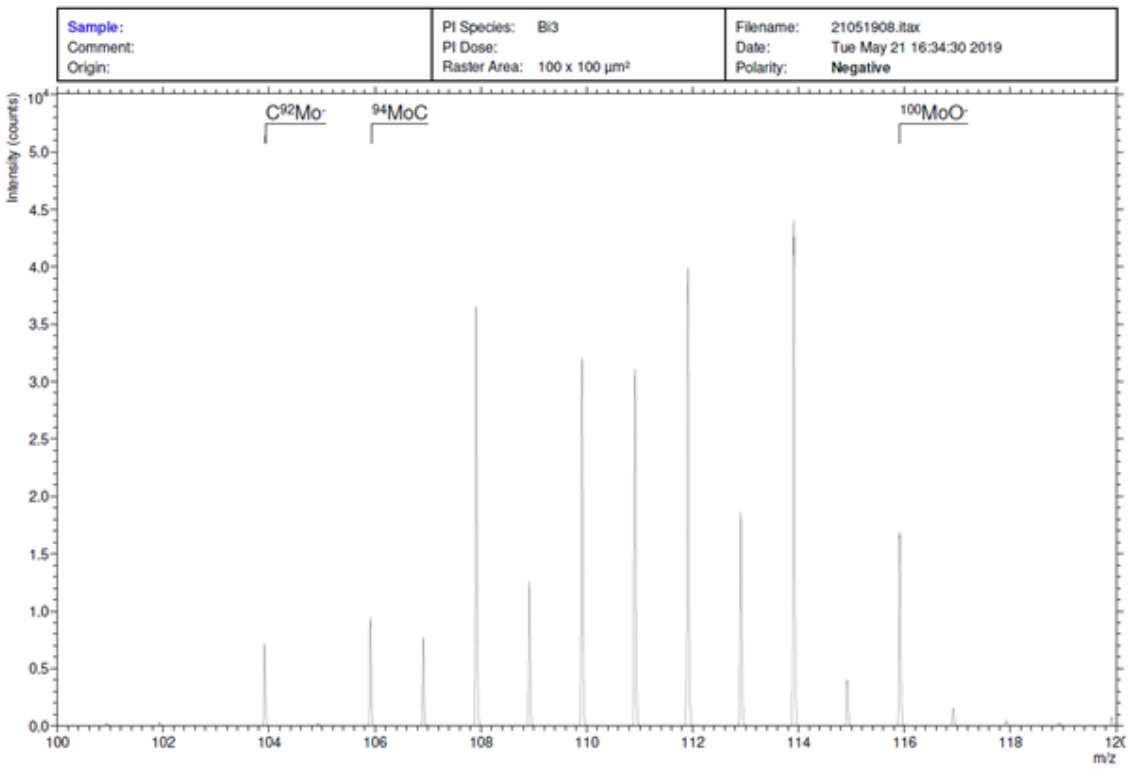

Figure 232: ToF-SIMS analysis from 100 – 120 m/z for Fe_3Mo_3C post-reaction with 3:1 H_2/N_2 at 500°C for 8 hours.

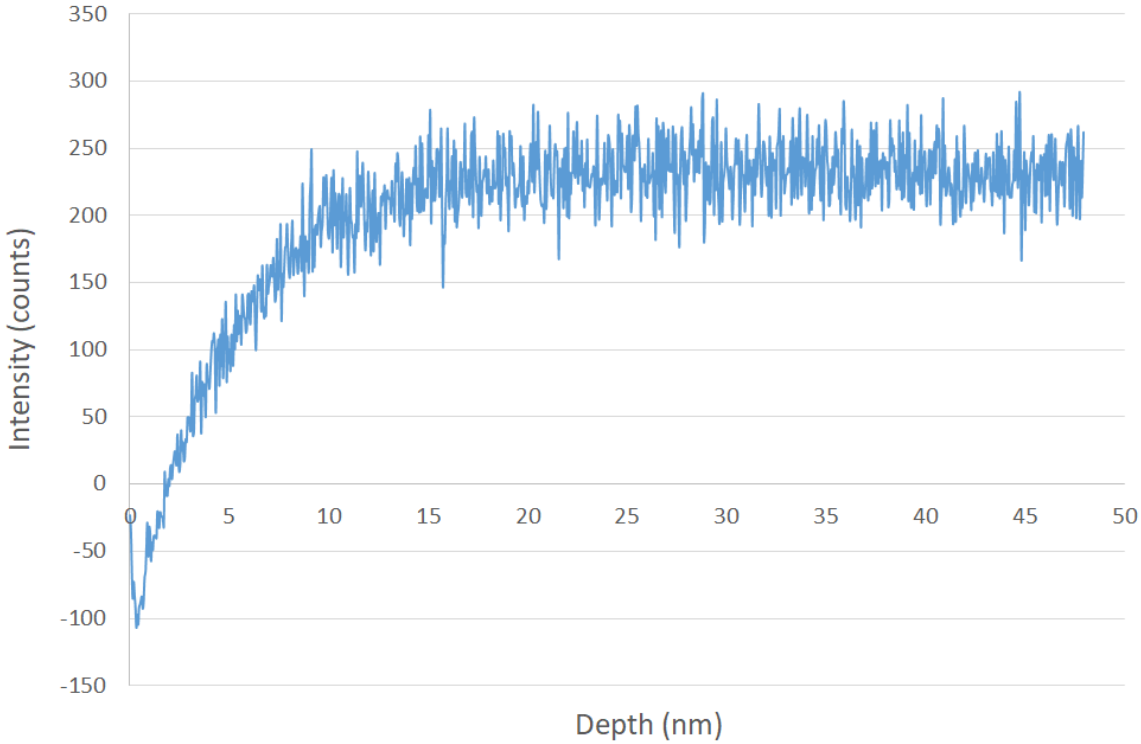

Figure 233: Depth profile for ^{92}MoN from Fe_3Mo_3C post-reaction with 3:1 H_2/N_2 at 500°C for 8 hours.

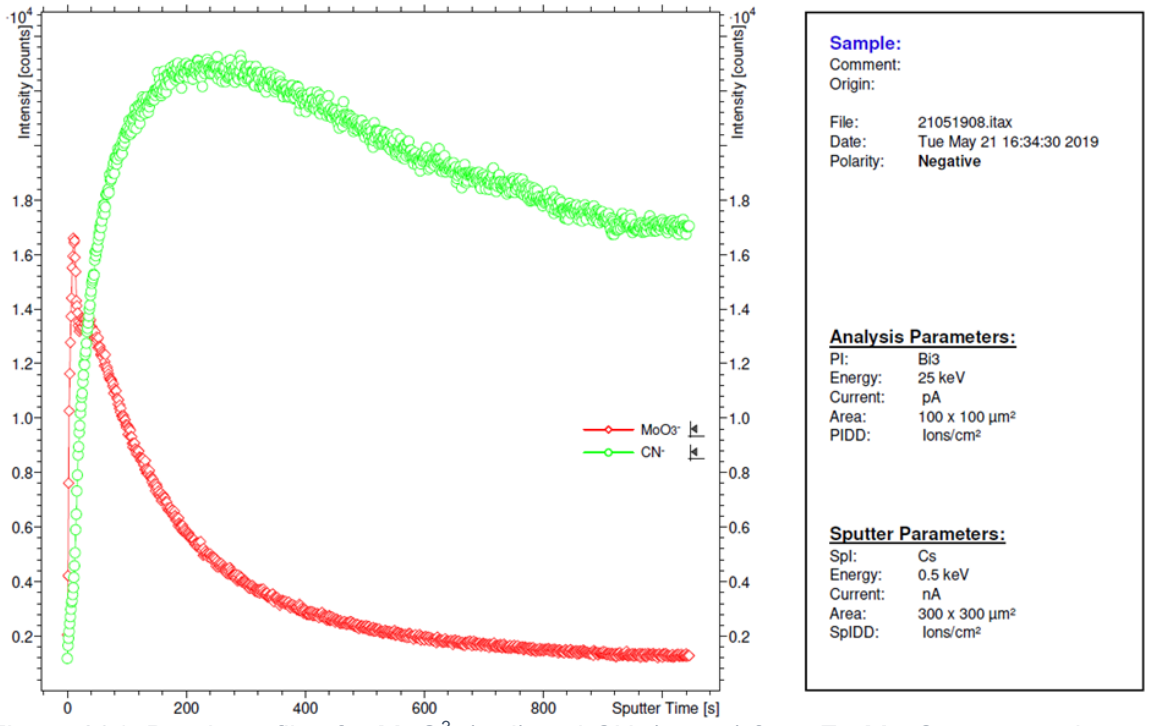

Figure 234: Depth profiles for MoO^{3-} (red) and CN^- (green) from Fe_3Mo_3C post-reaction with 3:1 H_2/N_2 at 500°C for 8 hours.

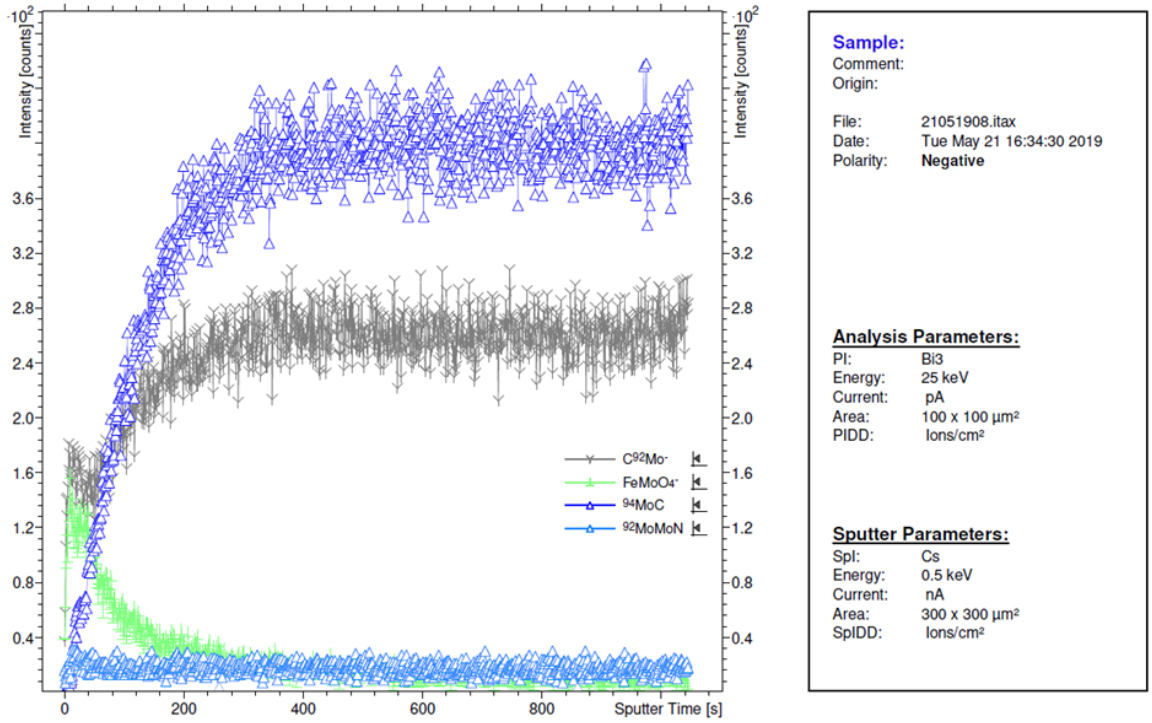

Figure 235: Depth profiles for $FeMoO4^-$ (green), $^{92}MoC^-$ (grey), ^{94}MoC (dark blue) and $^{92}MoMoN$ (light blue) from Fe_3Mo_3C post-reaction with 3:1 H_2/N_2 at 500°C for 8 hours.